Phenomenological Modeling of Deformation and Fracture in Metallic Materials with Evolving Microstructures

Habilitationsschrift
zur Erlangung der Lehrbefugnis
für das Fach

Festkörpermechanik

in der

Fakultät für Maschinenbau und Sicherheitstechnik

in der

Bergischen Universität Wuppertal

vorgelegt von:

Ph.D. METU Celal Soyarslan
aus Elazığ (Türkei)

Wuppertal, den 04.06.2018

The habilitation can be quoted as follows:

Acknowledgement

Contents

Kurzfassung

In dieser Arbeit werden phänomenologische Modellierungsansätze zur Beschreibung konstitutiver Gesetze von sich entwickelnden Mikrostrukturen metallischer Materialien untersucht. Die Arbeit gliedert sich in vier Teile. Der erste Teil befasst sich mit dem Levkovitch - Svendsen Querverfestigungsmodell als Repräsentant eines pfadabhängigen Verfestigungsansatzes. Dabei erfolgt eine Erweiterung des bestehenden Modells in Form eines ratenabhängigen Johnson-Cook Formalismusses. Mittels Finite Elemente Simulationen stochastischer Marciniak-Kuczyński Versuche und Nakazima Versuche wird eine Verbesserung der materiellen Stabilität der Berechnungen aufgezeigt. Diese Stabilität rührt von einer verringerten lokalen Krümmung der Fließfläche im Belastungspunkt mit Querverfestigung her. Eine Modifikation durch die Verfestigungsbeschreibung in radialen Richtungen mittels parallelen und orthogonalen Projektionen des sich entwickelnden plastischen, anisotropen Verfestigungstensors 4. Ordnung wird vorgeschlagen. Diese Modifikation behebt das Problem eines verschränkten Verfestigungsverhaltens des originalen Models.

In Teil zwei werden die Phänomene der Dehnungslokalisierung und des Bruchs induziert durch duktile Schädigung bei Raumtemperatur untersucht. Das poröse Gurson Plastizitätsmodell mit Schermodifikation wird verwendet um gemischte Modus I und Modus II Beanspruchung zu modellieren. Insbesondere wird der Fall der freien Biegung sowie des kleinen Stempel-Tests für verschiedene Probendicken untersucht. Dabei kommt eine nichtlokale Formulierung mit einem materialabhängigen Längenparameter, der mit der duktilen Schädigung assoziiert ist, zum Einsatz. Dies ermöglicht nicht nur die Berücksichtigung werkstoffcharakteristischer Größeneffekte, sondern beseitigt auch die pathologische Netzabhängigkeit der numerischen Berechnungen, die typisch für eine schädigungsindutzierte Entfestigung ist. Zwei empirische Erweiterungen des klassischen Schädigungsmodells nach Lemaitre in Form von quasi-unilateraler Schädigungsentwicklung und Lode Parameterabhängigkeit werden mit einer minimalen Anzahl von zusätzlichen Materialparameter vorgestellt. Die Modifikationen erweisen sich als nützlich, da sie eine Grenzdehnung unter einachsiger Kompression liefern und Flexibilität bei der Modellierung von Bruchvorgängen bei generalisierter Scherung ermöglichen.

Teil drei dieser Arbeit befasst sich mit dem Einfluss der Temperatur auf die Dehnungslokalisierung, Schädigung und auf Bruchvorgänge. Simulationen des temperaturgetriebenen Übergangsprozesses von duktilem Bruch zu Sprödbruch in kleinen Stempel-Test mit gekerbten (kleinskaliges plastisches Fließen) und ungekerbten (großskaliges plastisches Fließen) Proben nachgewiesen. Diese Simulationen verwenden ein generalisiertes thermoplastisches Konstitutivmodell, das nichtlokale RKR Sprödschädigung mit dem porösen Gurson-Plastizitätsmodell kombiniert. Schlüsselkomponente des Models ist die Temperaturabhängigkeit der Fließspannung. Darüber hinaus werden zwei thermo-mechanische Modellansätze vorgestellt. Diese verwenden im Rahmen der Thermodynamik das Konzept der internen Variablen für schädigungsgekoppelte finite Plastizität. Das erste Modell verwendet eine einzige Schädigungsvariable während das zweite Modell zwei Schädigungsvariablen benutzt, die mit spröder und duktiler Schädigung verknüpft sind. Diese Wahl erweist sich als brauchbar um den Übergang von duktiler zu spröder Schädigung in ther-

modynamisch konsistenter Weise zu modellieren. Schließlich konzentriert sich Teil vier dieser Arbeit auf Versuche zur mechanischen Materialcharakterisierung von Metallblechen. Zunächst wird der Einsatz von optischen Dehnungsfeldmessungen bei Zugversuchen von stumpf gekerbten Proben mit einem breiten Dehnungspfadspektrum bei inversen Parameteridentifikationen und plastischer Anisotropie rezensiert. Diese Versuche ermöglichen die Identifizierung von Parametern komplexer plastischer Anisotropiemodelle, wobei die Anzahl der erforderlichen Charakterisierungsversuche in einem angemessenen Rahmen bleiben.

Der letzte Teil von Abschnitt vier dieser Arbeit befasst sich mit verschiedenen Varianten von ebenen Torsionsversuchen. Zum Zweck der kinematischen Verfestigungscharakterisierung werden zyklische Doppelbrücken-Scherversuche mit geschlitzten Scheibenproben als erstes und als zweites, monotone ebene Torsionsversuche mit runden, radial genuteten Scheiben für Scherbruch betrachtet. Durch die Eliminierung von Knickung ist die erste Versuchsanordnung dem zyklischen einachsigen Zug-Druckversuch für dünne Bleche überlegen. Der zweite Versuch liefert nicht nur Scherbruch unter idealen Scherbedingungen, d.h. verschwindende Spannungsdreiachsigkeit mit $\eta = 0$ und einen Lode Parameter von $\bar{\theta} = 0$, sondern ermöglicht auch eine in situ Identifizierung der Bruchdehnung in der Bruchzone der Nut durch die Verwendung digitaler Bildkorrelationssysteme. Obwohl die Anwendbarkeit der konstitutiven Modelle nicht auf spezielle Materialien limitiert ist, befasst sich diese Arbeit vor allem mit Stahl und Aluminiumlegierungen wie z.B.: interstitiellfreier (IF) Stahl DC06, Dualphasenstähle DP600 und DP1000, P91 Stahl, die umwandlungsbewirkten Plastizitätsstähle (TRIP-Stahl) TRIP690 und TRIP700 sowie den Aluminiumlegierungen AA6016-T4 und Al2024. An entsprechender Stelle werden die algorithmische Umsetzung der lokalen Return-Mapping-Strategien der vorgestellten konstitutiven Modelle ausgeführt.

Abstract

In this thesis, phenomenological constitutive modeling approaches to evolving microstructure in metallic materials are explored in four parts. In Part I, Levkovitch–Svendsen cross hardening model as a path dependent hardening model is considered. An extension to rate dependence in a Johnson–Cook formalism is introduced. Through finite element simulations of stochastic Marciniak-Kuczyński tests and Nakazima tests, the stability increase due to decreased local curvature of the yield locus at the loading point by cross hardening is demonstrated. A modification by using the radial direction in parallel and orthogonal projections of the fourth-order evolving plastic anisotropy tensor is proposed. In doing so, the hardening entanglement problem in the original model is remedied. In Part II, ductile damage driven localization and fracture at room temperature is investigated. To this end, Gurson's porous plasticity model with shear modification is used in modeling blended Mode I Mode II fracture in both free bending and small punch tests for various specimen thicknesses. A nonlocal formulation incorporating material length parameter associated with ductile damage is devised. This not only allowed reflecting characteristic size effects but also remedied pathological mesh dependence problem associated with damage driven softening. Moreover, two empirical extensions to the classical Lemaitre's damage model is introduced with least number of additional material parameters. The first one of these extensions considers quasi-unilateral damage evolution and the second one Lode parameter dependence. The modifications prove useful by providing cut-off strain under uniaxial compression and flexibility to model fracture under generalized shear. In Part III, the role of temperature on damage, localization and fracture is examined. Predictive simulations of temperature driven ductile-brittle transition in small punch test with notched (small-scale yielding) and unnotched (large-scale yielding) specimens are demonstrated. These make use of a unified thermo-plastic constitutive model by combining the nonlocal RKR brittle damage model with the nonlocal Gurson's porous plasticity. It is shown that temperature dependence of the yield stress constitutes the key ingredient. Moreover, two thermomechanical model frameworks, which make use of the internal variable theory of thermodynamics for damage-coupled finite plasticity, are established. The first model uses a single damage variable, whereas the second model considers two damage variables associated with brittle and ductile damage, respectively. Such a choice is shown to prove useful in modeling ductile-brittle transition in a thermodynamically consistent setting. Finally in Part IV, mechanical material characterization tests for metallic sheets are focused on. First the use of optical strain field measurements over tensile tests of smoothly notched specimens, spanning a wide strain path spectrum, in inverse parameter identification of plastic anisotropy is investigated. This allows identification of parameters of complex plastic anisotropy models, while keeping the number of required characterization tests at a reasonable limit. In the rest of the thesis, variants of in-plane torsion test are explored. Cyclic twin bridge shear test with slitted disk specimens is considered for kinematic hardening characterization and monotonic in-plane torsion test. Radial grooves are considered for testing shear fracture. The former test is superior to cyclic uniaxial tension-compressive tests for thin sheets, for it eliminates the risk of buckling. On the other hand, the latter test delivers shear fracture under ideal shear conditions, i.e., vanishing stress triaxiality $\eta = 0$ and Lode parameter

$\bar{\theta} = 0$. Furthermore, it allows in situ identification of fracture strain through digital image correlation systems by trapping fracture zone within the groove. This work collects applications mainly to steels and aluminum alloys such as: interstitial free (IF) steel DC06, dual phase steels DP600 and DP1000, P91 steel, transformation induced plasticity steels TRIP690 and TRIP700; aluminum alloys AA6016-T4 and Al2024. However, the applicability of the constitutive models is not limited to these materials. Finally, algorithmic treatment of local return mapping for presented constitutive models is elaborated when necessary.

This thesis consists of an introduction and 12 papers presenting results on computational modeling of different phenomena in different materials. These results have been published in or submitted to international scientific peer-reviewed journals. The original papers are slightly modified in order to illustrate connections, extend explanations and avoid unnecessary repetitions, the original papers are slightly modified wherever it is beneficial. An overview of the research content of this thesis is given in the introduction, i.e. Chapter 1. This thesis consists of the following papers:

Chapter 2. Behrouzi, A.; Soyarslan, C.; Klusemann, B.; Bargmann, S.: [49]
Inherent and induced anisotropic Finite visco-plasticity with applications to the forming of DC06 sheets, International Journal of Mechanical Sciences, Vol. 89, Pages 101–111, 2014.

Chapter 3. Soyarslan, C.; Klusemann, B.; Bargmann, S.: [283]
The effect of yield surface curvature change by cross hardening on forming limit diagrams of sheets, International Journal of Mechanical Sciences, Vol. 117, Pages 53–66, 2016.

Chapter 4. Soyarslan, C.; Klusemann, B.; Bargmann, S.: [282]
A directional modification of the Levkovitch-Svendsen cross-hardening model based on the stress deviator, Mechanics of Materials, Vol. 86, Pages 21–30, 2015.

Chapter 5. Soyarslan, C.; Malekipour Gharbi, M.; Tekkaya, A.E.: [280]
A combined experimental-numerical investigation of ductile fracture in bending of a class of a ferritic-martensitic steel, International Journal of Solids and Structures, Vol. 49, Issue 13, Pages 1608–1626, 2012.

Chapter 6. Gülçimen Çakan, B.; Soyarslan, C.; Bargmann, S.; Hähner, P.: [68]
Ductile fracture under large-scale yielding conditions: Experimental and computational study of the small punch test, Materials, Vol. 10(10), 1185, 2017.

Chapter 7. Soyarslan, C.; Richter, H.; Bargmann, S.: [285]
Variants of Lemaitre's damage model and their use in formability prediction of metallic materials, Mechanics of Materials, Vol. 92, Pages 58–79, 2016. (with additional results from [284])

Chapter 8. Soyarslan, C.; Gülçimen, B.; Bargmann, S.; Hähner, P.: [281]
Modeling of fracture in small punch tests for small- and large-scale yielding conditions at various temperatures, International Journal of Mechanical Sciences, Vol. 106, Pages 266–285, 2016.

Chapter 9. Soyarslan, C.; Bargmann, S.: [279]
Thermomechanical formulation of ductile damage coupled to nonlinear isotropic hardening and multiplicative viscoplasticity, Journal of the Mechanics and Physics of Solids, Vol. 91, Pages 334–358, 2016.

Chapter 10. Soyarslan, C.; Türtük, I.; Deliktaş, B.; Bargmann, S.: [289]
A thermodynamically consistent constitutive theory for modeling micro-void and/or micro-crack driven failure in metals at finite strains, International Journal of Applied Mechanics, Vol. 8, No. 1, 1650009 (20 pages), 2016.

The papers were prepared in collaboration with several co-authors. The author of this thesis took part in planning of the papers [49, 282, 283, 280, 68, 285, 281, 279, 289, 109, 342, 343], took part in outlining and developing the theory [49, 282, 283, 280, 68, 285, 281, 279, 289, 109, 342, 343], did the algorithmic treatment and numerical implementation of the user defined material subroutines (`UMAT`, `VUMAT`, `USDFLD`, `VUSDFLD`, `UMATHT`) for ABAQUS, MATLAB or MATHEMATICA codes for return mapping [49, 282, 283, 280, 68, 285, 281, 279, 289, 109, 342, 343], for example.

1. Introduction

High specific structural strength, flexibility, high manufacturability, weldability, toughness, corrosion resistance, cost and reparability are some of their unique and valuable properties[1] that make some metals and metal alloys indispensable for many industrial industries such as marine/ship building industry (e.g., hull structure of ships, high-speed sea and river vessels, hydrofoil ships, aerostatic crafts), construction industry (e.g., high-rise buildings, bridges), automotive industry (e.g., pistons, cylinders, power screws, suspension assemblies, car doors, hoods), aircraft industry (e.g., landing gear parts, aircraft wheel, wings, fuselage), aerospace industry (e.g., rockets, launch vehicles, space vehicles), home appliances industry (e.g., sinks, freezers), food industry (e.g., cooking pots, canned goods). This immense demand on metals and alloys creates an exhaustive interest on their physical, chemical and mechanical properties which are not invariant.

Metallic materials possess crystalline structure which makes up their unique behavior. When subjected to sufficiently intense load levels various microstructural changes occur: new dislocations nucleate in addition to the existing ones, they gain mobility and interact with barriers, e.g., grain boundaries, inclusions, solid solutions, as well as each other, micro-voids and/or micro-cracks nucleate, grow and coalesce causing localization into deformation bands, as a precursor to fracture. The way these interactions occur closely depends on the mechanical and thermal loading history and identifies the macroscopic response of the material.

Various approaches are developed so far in order to undertake the mathematical modeling of various phenomena pertaining to the deformation and failure mechanisms of metallic materials. To name some, in an ascending time- and lengthscale order, one can mention quantum mechanics, molecular mechanics, discrete dislocation dynamics. As compared to the experimental sample sizes in usual engineering practice and/or mechanical process loading rates, the specified methods are often limited to specific length- and timescales and hence mostly not applicable. To overcome these drawbacks, the theory of continuum mechanics has served as a good basis for the modeling of solid materials over several length and timescales. Continuum dynamics equations are continuous representation of balance of linear momentum equations and they make no reference to the underlying material material behaviour observed. Constitutive models, which can be postulated at any scale, by relating deformations and forces, complete the definition of the boundary value problem. Phenomenological constitutive assumptions, traditionally established experimentally, in description of geometric state of a deformed body with structural transformations[2] are indispensable for phenomenological realism and help obtaining new insight into relevant physical mechanisms at relevant scales.

---

[1]Unfortunately, all of these properties are not always possessed by a single metal or its alloy.

[2]More specifically, phenomenological constitutive approaches aim at modeling meso- or macroscale material response through state and evolutionary equations of mathematical constructs which can relate to physically measurable quantities (strain, temperature,time) or those that are not directly measurable, often referred to as internal state variables representing smeared definitions of microstructural phenomena.

Once the emerging set of equations is not tractable, any constitutive model remains out of reach. Their inherent complexity does not allow for the analytical solution to many initial boundary value problems together with the constitutive models. For this purpose, numerical solution methods which rely on temporal and spatial discretization schemes where the unknown continuous fields are replaced with their discrete counterparts are used. With the advent of powerful computers, these computations are made possible to be conducted over large systems. One of the most widely used methods of this kind in the field of nonlinear solid and structural mechanics is the finite element method which is also made available for large scale computations through commercial softwares, such as ABAQUS. This gives the user chance to concentrate purely on the stress update routines making up the constitutive model updates whereas many complicated phenomena such as contact handling, global data management, assembly operations and solution of global system of equations are carried out by the code. With these properties finite element method constitutes an efficient way to predict the material and structural behavior and it is nowadays standard in industrial practice. Hence, only the implementation of the postulated frameworks makes the models accessible for the solution of industrial scale problems.

The parameters making up the mathematical models must be identified through characterization experiments. This is not an easy task, especially considering the complexity of the material model and technological limitations against investigation of a specific material response and/or limitations of the specimens, e.g., buckling of thin plates. Hence,

- postulation of micromechanically informed phenomenological constitutive models,

- their implementation into existing simulation software,

- development of experimental procedures for mechanical material characterization

constitute complementary integral directions that process design for functional yet lightweight components with exploitation of the material potential, accurate prediction of post-manufacturing material and geometrical properties in reasonable computational times, the service life or performance under extreme operating conditions require.

The current work collects the studies which the author contributed, to fulfill these challenging requirements. The thesis consists of mainly four parts each of which includes three papers. Part I, composed of [49, 283, 282], is after outlining a path dependent hardening model for metallic sheets. Part II, composed of [280, 68, 285], is after outlining room temperature localization and fracture making use of Gurson's porous plasticity model as well as Lemaitre's damage model including low triaxiality shear fracture enhancements. Here, nonlocal extensions of Gurson's porous plasticity model is also discussed. Part III, composed of [281, 279, 289], is after outlining the role of temperature in localization and fracture of metallic materials. Specifically ductile-brittle transition is studied in which each brittle and ductile damage processes shows their corresponding length-scales, hence, necessitates a nonlocal formulation. Finally, Part IV, composed of [109, 342, 343], summarizes experimental approaches used in identification of material parameters for anisotropy, path dependent hardening and finally low triaxiality ductile fracture in metallic sheets.

1.1.   **Path Dependent Hardening**

Anisotropic mechanical response of materials can be sourced from geometry or material. The former is purely due to the microstructural form, whereas the latter is due to lattice system in

metals or chain orientations or damage in polymers. The material-sourced anisotropy can be either inherent or induced, e.g., by damage or additional dislocation motion driven by loading path changes. The Bauschinger effect is a path dependent (kinematic) hardening which occurs by partial dissolution of dislocation pile-ups upon load reversals causing early reyielding [44]. Cross hardening, on the other hand, is sensitivity to orthogonal loading path changes by which the slip on the newly activated slip systems is hindered by prevailing dislocations resulting in a latent resistance to yielding and hardening rate increase [104, 257, 258, 231, 96].

Levkovitch and Svendsen proposed a phenomenological model through evolving fourth-order structural tensor associated with the form of plastic anisotropy [181]. In accordance with the dynamics of dislocation structures, the evolution is considered in two parts such as dynamic and latent. The former is the strength evolution associated with the currently active slip systems whereas the latter is the *cross hardening* linked to the latent slip systems. Mathematically, the split is carried out elegantly through parallel and orthogonal projections to a selected direction. In the original work of Levkovitch and Svendsen this direction is selected as the unit plastic flow direction $\boldsymbol{n}_p = \dot{\boldsymbol{\varepsilon}}_p / |\dot{\boldsymbol{\varepsilon}}_p|$.

This part starts with examination of the application of a consistency-type viscoplastic extension of the model in an industrial forming process materializing interstitial-free (IF) steel sheets in Chapter 2. The rate extension is motivated by the relatively high strain rate sensitivity of this steel class compared to others used in automotive industries [168]. The initial plastic anisotropy anisotropy of the sheet is described by the quadratic Hill-48 model [122]. Bauschinger effect is also considered. The finite strain extension of the model is realized through Green–Naghdi–McInnis-type hypo-elastic plastic formulation which uses additivity of the rate of deformation tensor into elastic and plastic parts in the rotationally neutralized configuration. Making use of the developed subroutine and a set of experiments involving monotonic shear, uniaxial tension, forward to reverse shear and plane strain tension followed by shear tests the model parameters are identified. As an application, the channel forming process is studied where a good agreement with the experimental findings is reported.

Formability describes the capability of a material to undergo plastic deformation to a given shape without defects [24]. Uniaxial tension tests under monotonic loading which is generally used in mechanical characterization studies fall short to reflect the complexity inherent to the real forming processes which involve a number of strain path changes and associated formability of the material [323]. This gains further importance for hardening models with path dependence. Thus, in Chapter 3, the additional formability gained by the choice of cross hardening plasticity with reduction in yield locus curvature is clarified quantitatively. In absence of dynamic hardening contribution, the selected formulation for the cross hardening plasticity does not result in any difference under strictly proportional loading paths. Hence a Marciniak-Kuczyński-based finite element modeling approach is followed with spatially correlated random defect distribution as localization triggering mechanism in numerical determination of the first quadrants of forming limit diagrams. This allows modeling gained expansion of the yield locus with latent hardening and consequent reduction of the sensitivity to small loading path changes which results in increased stability as compared to the non-cross hardening model. For the applications thin shell elements, reduced plane-stress vector formulations are elaborated. It is shown that although for plane strain loading path there occurs no difference in localization predictions of the models with and without cross hardening, for biaxial strain paths a delayed localization is observed in the cross hardening model as compared to the one without cross hardening effects.

In Chapter 4, an undesired feature of the original Levkovitch-Svendsen model is brought to the attention of the reader: For materials with initial plastic anisotropy, the material model predicts additional strengthening in loading direction due to latent hardening even if the dynamic hardening component is bypassed. First, the source of this *hardening entanglement* problem is identified as the broken coaxiality of the stress deviator and plastic strain rate tensor with initial anisotropy. A simple solution is then proposed through the use of the so–called radial direction $\boldsymbol{n}_s = [\boldsymbol{S} - \boldsymbol{X}]/|\boldsymbol{S} - \boldsymbol{X}|$ in parallel and orthogonal projections used in the evolution equation of the fourth-order structural tensor $\boldsymbol{\mathcal{H}}$ where $\boldsymbol{S} = \mathrm{dev}(\boldsymbol{\sigma})$. This modification, through resolving the hardening entanglement problem with isolation of each dynamic and latent hardening source, expedites the parameter identification stage. The findings are complemented with analytical and numerical derivations for various material model combinations.

1.2. Damage Driven Localization and Fracture

Cavitation as a source of the localization into deformation bands as a precursor to fracture shows strong dependence on the stress state during plastic flow. An exponential growth of voids is observed under triaxial tensile stress states whereas shear stress state promotes void sheeting, void nucleation, void distortion and void interaction with material rotation and associated degradation of stiffness and strength of the material. In mathematical modeling of this phenomenon, dependence on the Lode parameter or third invariant of the deviatoric Cauchy (true) stress tensor is proposed in [339] and [224], respectively. In this part ductile damage at room temperature is studied.

In Chapters 5 and 6, fracture initiation by progressive material deterioration due to cavitation, i.e. nucleation, growth, and coalescence of micro-voids, see e.g. [340, 228, 265, 305] during free bending of a class of ferritic-martensitic DP1000 steel and during small punch testing of P91 steel (unnotched) disks are investigated, respectively. Free bending is a frequently used manufacturing process whereas small punch testing is an *almost non-destructive test* used to investigate fracture properties such as yield stress, ultimate stress or fracture toughness which requires small specimen sizes as compared to standard mechanical tests. In both tests rather large-scale yielding prevails as compared to tests utilizing notched samples. Both experimental and numerical studies are accounted for. Simulations are realized using Gurson's dilatant plasticity model with a recent shear modification, strain-based void nucleation, and coalescence effects. An integral-type nonlocal formulation is also introduced in Chapter 6. This formulation requires a characteristic length hence allowing incorporating the size effect in the model. Various parametric studies are presented depicting the effect of certain material parameters (initial porosity, damage at coalescence and failure, shear modification term, etc.), plane strain constraint and mesh size on the localization and the fracture behavior. The parametric studies show that in absence of sufficient softening, a cleavage-type brittle fracture pattern orthogonal to the maximum stress direction is carried out. With sufficient softening, on the other hand, fracture pattern follows plastic localization bands which are oriented approximately 45° to the maximum stress direction, in agreement with the observations presented in, e.g., [339, 185].

Lemaitre's damage model constitutes one of the widely used continuum damage mechanics approaches [175]. In Chapter 7 two successive enhancements of Lemaitre's model and the implications of their use in formability prediction of today's modern steels are presented. These are quasi-unilateral damage evolution and shear stress dependence. The former, by scaling the elastic energy release rate due to compressive principal stress, allows controlling fracture under low

and negative stress triaxialities whereas the latter accounts for nonmonotonic dependence of the fracture strain on the stress triaxiality ratio especially modifying generalized shear points. This section introduces closed form expressions for the isochronous fracture surfaces of deformation decoupled versions of the proposed models variants for linear strain paths. The performance of each model is demonstrated with providing parameter identification studies for the given test data from the literature. Also, an application with prediction of crack formation in deep-drawing punch tests is presented.

1.3. Temperature Effects on Damage Driven Localization and Fracture

Thermal expansion, temperature induced elastic softening with temperature dependence of elastic material properties, temperature induced plastic softening with yield locus shrinkage are examples for the influence of temperature on mechanical fields. Geometric coupling on heat flux, heat generation by inelastic dissipation, structural elastic heating: the GOUGH-JOULE effect, on the other hand constitute examples for the influence of of the mechanical field on the thermal field. In this part, investigation of the influence of temperature on material damage and fracture is aimed at.

One typical example of this type is the ductile–brittle transition, typically seen in bcc and hcp metals. Mechanistically, nucleation, growth and coalescence of microvoids define ductile fracture whereas inter- or intra-granular cleavage with microcrack nucleation, growth and coalescence causes brittle fracture, [11]. In Chapter 8, the small punch test is revisited but this time for temperatures varying from $-196°$C to $25°$C and for notched and unnotched specimens of P91 steel representative for small- and large-scale yielding conditions, respectively, in order to investigate ductile-brittle transition phenomenon. A combined experimental-numerical is presented on temperature dependent fracture mode change. The conducted experiments reveal fracture by cleavage at $-196°$C whereas at $25°$C shear localization with voidage precursor to ductile fracture was observed where the observed deformation energy to fracture for the former is considerably lower than the latter. Moreover, for brittle fracture the crack propagation direction is normal to the maximum tensile principal stress whereas for ductile fracture, fracture pattern follows that of shear localization patterns parallel to the punch displacement. In numerical simulations, a thermo-inelastic constitutive approach is used with Gurson's porous metal plasticity accounting for the ductile damage. A temperature dependent flow stress is considered. For brittle fracture, Ritchie–Knott–Rice's maximum principal stress criterion is used. Each ductile and brittle damage models are formulated with nonlocal manner incorporating corresponding length scales which are computed based on the average inclusion distance and average grain size, respectively. This allowed capturing a good agreement with the experimentally obtained fracture modes, patterns and corresponding deformation energies up to fracture. One crucial output of this part is the role of stress gradients in identification of the length scales and critical fracture thresholds associated with brittle fracture.

Chapters 9 and 10 focus on development of isotropic damage coupled finite strain plasticity frameworks through a systematic use of the internal variable theory of thermodynamics and multiplicative kinematics. In Chapters 9, a single damage variable is used with a viscous plasticity model. Following [275], inelastic entropy rate is derived to be additively composed of plastic and damage parts through a temperature dependent damage dissipation potential. A staggered solution scheme is applied for the thermomechanical problem with a so-called isother-

mal split. Corresponding subroutine implementations allowed simulation of a set of 2D and 3D problems which demonstrate the mutual effects of damage localization and inelastic heating on each other. In Chapters 10, in the spirit of Chaboche and coworkers [71], Gurson's porous plasticity model is blended with Lemaitre's continuum damage mechanics to result in a two damage variable formulation. The first *brittle* damage variable d is responsible for cleavage-type of damage in absence of any volume change whereas the second *ductile* one f responsible for ductile damage due to plastic growth of microvoids as the void volume fraction in Gurson's model. It is shown that the evolution of d requires postulation of an appropriate damage dissipation potential in terms of its conjugate variable, the elastic energy release rate. On the other hand, since the evolution of f is formulated through the conservation of mass, any resultant dissipation with microvoid growth encapsulated in the plastic flow. It is shown through application problems that, the developed model framework is capable to model ductile-brittle fracture through use of a temperature dependent flow stress is considered.

1.4.   Experimental Approaches for Mechanical Characterization of Plasticity and Damage

According to [7], rational formulation of constitutive theories necessitate three types of experiments: exploratory tests, characterization tests and validation tests. Exploratory tests are after clarification of significant features of material response such as loading path dependence, rate dependence, sensitivity to Lode parameter and stress triaxiality, etc, where these ingredients shape the mathematical structure of the model. Hence such tests are indispensable for development of phenomenological constitutive theories. Characterization tests aim at an accurate identification of the constants used in the mathematical model usually under specific conditions, e.g., uniaxial state of stress. Only through properly identified set of material parameters, one can use the constitutive models in structural analysis or engineering design. Finally, validation tests enable corroboration of a constitutive model by comparing the predictions with the structural response under multiaxial states of stress and strain. At this stage, a disagreement means an imperative need for reconsideration or tailoring of certain parts of the mathematical structure.

In this last part of the thesis, mechanical material characterization tests for path dependent hardening, directional plastic response and fracture for metallic sheets are considered. As compared to bulk metals, metallic sheets are thinner and hence more sensitive to geometrical instability mechanisms such as buckling. Hence, most tests that are readily available for bulk materials, e.g. uniaxial compression test, cannot be applied to the sheets easily. Moreover, sheet metals exhibit a certain texture which leads to directional dependence in their planar plastic behavior. For plane stress space, various yield functions are defined to define the plastic anisotropy of metallic sheets. The 3 parameter quadratic Hill'48 model [122], the 7 parameter BBC2000 model [27], 8 parameter Yld2000-2D [34] and 17 parameter Vegter model [317] are just to mention some. Identification of the increased number of parameters requires various test set ups including uniaxial tensile test, shear test, biaxial tension test, plane strain tensile test, layer compressions test, etc. [163]. From an industrial point of view keeping the number of required tests is crucial.

In Chapter 11 a characterization methodology for identification of the plastic anisotropy of sheets is proposed. Unlike classical tensile tests which aim at development of strain uniformity at the gauge length, the proposed scheme uses tensile tests which intends nonuniform strain field development through use of smoothly notched specimens. Emergent nonuniform fields are

then measured with optically to form a database. Through repetitive finite element simulations, which aim at minimizing the gap between predictions and the experimental database, the material set controlling plastic anisotropy is identified through a Levenberg-Marquardt algorithm. In the tests, deformation states from uniaxial tension to plane strain tension prevail. This wide coverage of deformation space allows reduction of the number of material tests conventionally required for identification of constants for complex anisotropy models. In the applications, tests performed on sheets made of aluminum alloy AA6016-T4 is used. Yld2000-2D model, a non-quadratic plane stress yield function having 8 material parameters, which is implemented as a VUMAT subroutine for ABAQUS/EXPLICIT, is selected to define the initial anisotropy of the material. The results showing the agreement between the yield loci and $r-$values obtained with the proposed methodology and those obtained with conventional methodologies making use of higher number of tests confirm the effectiveness of the proposed methodology.

The main focus of the Chapters 12 and 13 is the so called in-plane torsion test. In the test, a circular sheet is clamped internally and externally. In plane torsion is provided rotating the external clamping device whereas keeping the internal clamping device fixed. In retrospect, this test was proposed for investigation of the work hardening and fracture of the metallic sheets by [200] a decade before the Miyauchi test. This test set up is used for stress and strain curve determination in [297]. Since the test proves practical and insensitive to geometrical instability mechanisms such as buckling or necking, up to date, many variants have been proposed through changing the specimen geometry. In particular, so-called twin bridge specimen with slitted circular disk geometry was introduced in [61]. The introduced cuts limit the deformation zone and the effect of anisotropy as compared to a continuous specimen. This also reduces the load demand from the experimental device. Still the shear region should be kept sufficiently wide to reduced edge effects. In Chapter 12 identification of kinematic hardening parameters using a twin bridge *cyclic* shear test specimen is considered. Tests are conducted for three different steel sheet materials: mild steel DC06, dual phase steel DP600 transformation induced plasticity steel TRIP700. Since an analytical form for the solution of the initial value problem is not available for the test, an inverse parameter identification methodology is used in determination of the hardening parameters. This way, the identification of the parameters of a combined Voce-type nonlinear isotropic and Armstrong-Frederick-type kinematic hardening model is realized, where the model is made available through implementation as a VUMAT subroutine for ABAQUS/EXPLICIT. The results illuminate salient kinematic hardening response of advanced high strength steels DP600 and TRIP700 for which Armstrong-Frederick model falls short.

Finally, Chapter 13 is concerned with monotonic in plane torsion test with radially grooved specimens in order to characterize shear fracture in sheet materials. Radial continuity in the specimen material [200] avoids edge cracks whereas the radial groove controls the fracture zone and keeps it away from the clamping area. The emergent fracture in the groove zone occurs under vanishing triaxiality $\eta = 0$ and Lode parameter $\theta = 0$ to be qualified as a shear fracture as desired. Moreover, since the fracture occurs in the visible region, the test makes a direct determination of the equivalent strain at fracture from digital image correlation (DIC) system possible. Hence, the test is ideal for identification of the recent shear extended damage and fracture models. Moreover it is possible to use the test as an exploratory test to illuminate the shear fracture sensitivity of the material. As an application, the fracture behavior of DP1000 steel is investigated.

1.5.   A Word on Notation

In this work, unless otherwise stated, the following notation will be used. Assuming $\boldsymbol{a}$, $\boldsymbol{b}$, and $\boldsymbol{c}$ as three second-order tensors, together with the EINSTEIN's summation convention on repeated indices, $\boldsymbol{c} = \boldsymbol{a} \cdot \boldsymbol{b}$ represents the product with $c_{ik} = a_{ij}b_{jk}$. $d = \boldsymbol{a} : \boldsymbol{b} = a_{ij}b_{ij}$ represents the inner product with where d is a scalar. $\boldsymbol{\mathcal{E}} = \boldsymbol{a} \otimes \boldsymbol{b}$, $\boldsymbol{\mathcal{F}} = \boldsymbol{a} \oplus \boldsymbol{b}$ and $\boldsymbol{\mathcal{G}} = \boldsymbol{a} \ominus \boldsymbol{b}$ represent the tensor products with $\mathcal{E}_{ijkl} = a_{ij}b_{kl}$, $\mathcal{F}_{ijkl} = a_{ik}b_{jl}$ and $\mathcal{G}_{ijkl} = a_{il}b_{jk}$, where $\boldsymbol{\mathcal{E}}$, $\boldsymbol{\mathcal{F}}$ and $\boldsymbol{\mathcal{G}}$ represent fourth-order tensors. $\mathrm{dev}\,(\bullet) = [\bullet] - 1/3\,\mathrm{tr}(\bullet)\,\mathbf{1}$ and $\mathrm{tr}\,(\bullet)$ stand for the deviatoric part of and trace of $[\bullet]$, respectively, with $\mathbf{1}$ denoting the second-order identity tensor. $\mathrm{sym}\,(\bullet)$ and $\mathrm{skw}\,(\bullet)$ denote symmetric and skew-symmetric parts of $[\bullet]$. $[\dot{\bullet}]$ gives the material time derivative of $[\bullet]$. $[\bullet]^{\top}$ and $[\bullet]^{-1}$ denote the transpose and the inverse of $[\bullet]$, respectively. The norm of $\boldsymbol{a}$ is denoted by $|\boldsymbol{a}| = \sqrt{\boldsymbol{a} : \boldsymbol{a}}$. Moreover, $[\hat{\bullet}]$ gives any $[\bullet]$ represented at the rotationally neutralized, i.e. corotational, configuration. $\mathrm{Div}(\bullet)$ and $\mathrm{div}(\bullet)$ respectively designate the divergence operators with respect to the coordinates in the reference and current configurations. Analogously, $\mathbf{Grad}(\bullet)$ and $\mathbf{grad}(\bullet)$ respectively designate the gradient operators with respect to the coordinates in the reference and current configurations. $\langle\bullet\rangle$ stands for the ramp function with $\langle\bullet\rangle = 1/2\,[\bullet + |\bullet|]$. $\log\,(\bullet)$ represents natural logarithm. Square brackets $[\ldots]$ are used to collect mathematical expressions, row-ordered vector components whereas round brackets $(\ldots)$ collect function arguments. Otherwise they respectively represent closed and open interval boundaries in a real space.

Part I.

Path Dependent Hardening

2. Inherent and Induced Anisotropic Finite Visco-Plasticity with Applications to the Forming of DC06 Sheets

In this chapter, a finite visco-plasticity model accounting for inherent and induced plastic anisotropy as well as Bauschinger effect for the interstitial free (IF) steels is presented with an application to a forming process simulation of DC06 sheets. The inherent plastic anisotropy uses a Hill-48 type structural tensor whereas the induced anisotropy is modeled via its evolution accounting for dynamic (active) and latent (inactive) parts. The latter appears to be an eminent requirement for predicting the qualitative effect of the evolving dislocation microstructures under orthogonal loading path changes, i.e., the cross hardening. A nonlinear isotropic and Armstrong–Frederick type kinematic hardening is also involved. Finally, the rate dependence of the plastic response is incorporated using Johnson–Cook type formulation. The model is implemented as VUMAT user defined material subroutine for ABAQUS and used in a set of sensitivity analyses to present mentioned model features. The model parameters are identified based on a set of experiments involving monotonic shear, uniaxial tension, forward to reverse shear and plane strain tension followed by shear tests. Finally, the channel forming process of a DC06 sheet is simulated. A good agreement with the experimental findings is observed, in both the tool response history curves and the extent of spring-back which is conclusive on the final product geometry.

2.1. Introduction

The macroscopic behavior of the polycrystalline metals is closely linked to the underlying microstructure and its evolution. Under sufficiently intense load levels, new dislocations nucleate in addition to the existing ones: they gain mobility and interact with barriers, e.g., grain boundaries, inclusions, solid solutions, as well as each other. The way how these interactions occur, depends on the loading history, i.e., the loading path being monotonic, reverse or, e.g., orthogonal. Under monotonic loading paths dislocations accumulate in front of barriers to form pile-ups. The consequent increase in the resistance to flow is referred to as strain hardening. Once the load is reversed at proceeding stages, the pile-ups are partially dissolved, with the dislocations departing from the barriers. This early re-yielding at load reversals is referred to as the Bauschinger effect [44]. On the other hand, if instead of a complete load reversal, an orthogonal loading is pursued, prevailing dislocations hinder the slip on the newly activated slip systems. Resultant latent resistance to yielding and hardening rate increase is named as cross hardening, see, e.g., Ghosh and Backofen [104] for one of the pioneering reports and Rauch and Schmitt [257] as well as Rauch and Thuillier [258] who reported dislocation microstructure alterations under tension followed by shear as subsequently orthogonal loading paths. Nesterova et al. [231] investigated the microstructure under two strain path changes (simple-shear/simple-shear and uniaxial-tension/simple-shear) in an interstitial free (IF) steel where the influence of

the grain orientation is discussed as well. Gardey et al. [96] studied the dislocation structures in dual-phase steel under different loading paths, including orthogonal loading and the effect of the different strain paths on the dislocation structure is discussed in detail.

Mathematical modeling approaches associated with such micro-macro interactions differ by the scale at which the mathematical constructs and their emerging relations are formulated. The microscale based mechanistic approaches use mathematical entities in direct association with corresponding microstructural phenomena. Within the current context, glide-system level resolutions with crystal plasticity (e.g., [147, 203, 125] and for a recent overview see Roters et al. [262]) as well as gradient extended crystal plasticity ([9, 31, 32, 89, 130, 236]) were presented. These approaches, while supplying higher accuracy with less approximations require relatively high computational cost as compared to their phenomenological counterparts which base their formulations at the meso- or macroscale using smeared microstructural properties. Since the current chapter aims at simulation of a metal forming process of DC06 steel sheets at the macroscale, a phenomenological modeling approach is adopted here.

The phenomenological approaches account for the micromechanical phenomena mentioned above through subjecting the yield surface to various transformations, such as proportional expansion, translation, rotation and distortion [162]. Standard models involving combined isotropic and kinematic hardening effects are limited to modeling only proportional expansion and translation which might not be sufficient in accurate modeling of multistage metal forming processes involving strong load path changes. Baltov and Sawczuk [23] represent one of the early works that takes into account the shape change of the yield surface during deformation known as distortional hardening. The frameworks of Baltov and Sawczuk [23], Levkovitch and Svendsen [181], Clausmeyer et al. [77], Pietryga et al. [245], Barthel et al. [40] and Barlat et al. [36] account for the texture evolution due to the interaction of dislocation structures using evolving structural tensors besides initial anisotropy and combined isotropic and kinematic hardening. The models of the Teodosiu group, e.g., [298, 124, 113, 182] with modifications proposed by Wang et al. [324] constitute other phenomenological approaches for modeling distortional hardening effects which, as opposed to the formerly listed models, involve strong coupling between the kinematic hardening and distortional hardening formulation. This makes basic model interpretation and parameter identification relatively tough. Uenishi and Teodosiu [310] presented an extension of the previous model of the Teodosiu group to include the rate effects to describe the behavior of IF steel in crash analysis correctly. Finally, the works of Feigenbaum and Dafalias [90, 91] and Plesek et al. [249] represent thermodynamically consistent distortional hardening models where the yield surface curvature at the vicinity of the loading and flattening at the opposing region can be modeled.

In the present chapter, following in the footsteps of the approaches proposed by Levkovitch and Svendsen [181] and Barthel et al. [40], a framework for rate-dependent plasticity accounting for inherent and induced plastic anisotropy as well as Bauschinger effect is presented aiming at modeling of the interstitial free (IF) steel behavior, specifically for DC06. For this purpose an anisotropic yield function of Hill-48 type is devised (cf. [122]). The fourth-order structural tensor is not taken as an invariant. However, it is assumed to evolve, where its evolution is formulated in two parts such as dynamic and latent parts in accordance with the dynamics of dislocation structures. In this way, the strength evolution associated not only with the currently active slip systems but also with the latent slip systems is taken into account, the latter of which is also known as cross hardening. The geometrical implications of the current formulation are determined by the quadratic structure of the yield locus which is preserved even during

its evolution. Within this limit, e.g., rotation of the axes and the change of the aspect ratio of the ellipse representing the yield locus at the plane stress space is captured. The uniform extension of the yield locus and its shift are taken into account using a combined nonlinear isotropic and Armstrong–Frederick type kinematic hardening. This way the early re-yielding at the load reversals, i.e., the Bauschinger effect, and successive transient hardening is incorporated in the model as an eminent requirement for DC06. The IF steel DC06 is reported as the most strain rate sensitive IF steel among those being applied in automotive industries [168]. A strain rate dependent model is formulated in the current chapter in terms of a Johnson–Cook type formulation. The experimental curves for DC06 at different strain rates reported by van Riel [314] as well as the experimental data from [77, 76, 131] are used to identify the corresponding material parameters. The Teodosiu and Hu model [298] and the Levkovich model [181] both are capable of predicting the cross hardening behavior, however the strain rate effect is not included in the Levkovich model. The Teodosiu and Hu model on the other hand is also considers strain rate effects however at a cost of totally 7 parameters devoted to the cross hardening(cf. [314]). In the current model, as compared to Teodosiu and Hu only 4 parameters are used for this purpose. Finally, possible change of the Young's modulus due to plastic strain or anisotropy is not accounted for in this work.

The finite strain formulation is based on a Green–Naghdi–McInnis-type hypo-elastic plastic formulation. Accordingly, additivity of the rate of deformation tensor into elastic and plastic parts is assumed. By expressing the yield function in terms of the rotated Cauchy (true) stresses the material frame indifference is naturally satisfied. The developed framework is implemented as a VUMAT user defined material subroutine for ABAQUS/EXPLICIT. First, sensitivity analyses are performed using single finite element tests. Hereby, plane strain tension followed by simple shear, cyclic simple shear with varying amplitudes and cyclic simple shear with varying loading rates are realized in a strain controlled fashion. These analyses show that the proposed model appropriately reflects the targeted features such as cross hardening at orthogonal loading path changes, early re-yielding and transient hardening with reversed cyclic loading paths and positive rate dependence of the plastic hardening. Finally, following the corresponding material characterization studies the model is used in the simulation of a channel forming process of DC06 steel sheet. Comparisons of the simulation results with the experimental observations show very good agreement in both the tool response, i.e., the punch force demand history curve, such as the extent of the spring-back which is conclusive on the final product geometry.The key features in the current approach can be listed as follows:

- Inclusion of rate dependence using a Johnson–Cook type formulation with parameter identification.

- Consistent implementation in ABAQUS/EXPLICIT as VUMAT.

- Sensitivity analysis of the material model with respect to different hardening effects.

- Application of the model to an actual metal forming experimental process.

2.2. Theory

2.2.1. Material Model - Small Strain Formulation

The stage is set by assuming the additivity of the total strain tensor $\boldsymbol{\varepsilon}$ into elastic $\boldsymbol{\varepsilon}^e$ and plastic $\boldsymbol{\varepsilon}^p$ parts viz.

$$\boldsymbol{\varepsilon} = \boldsymbol{\varepsilon}^e + \boldsymbol{\varepsilon}^p \,. \tag{2.2.1}$$

The stress tensor $\boldsymbol{S}$ is computed from the quadratic elastic strain energy $\Psi^e = [1/2]\,[\boldsymbol{\varepsilon}^e : \boldsymbol{\mathcal{C}}^e : \boldsymbol{\varepsilon}^e]$ with $\boldsymbol{\mathcal{C}}^e$ denoting the elastic constitutive tensor with

$$\boldsymbol{\mathcal{C}}^e := \left[\kappa - \frac{2\mu}{3}\right][\mathbf{1} \otimes \mathbf{1}] + \mu\,[\mathbf{1}\overline{\otimes}\mathbf{1} + \mathbf{1}\underline{\otimes}\mathbf{1}] \,, \tag{2.2.2}$$

where κ and μ are the elastic bulk and the shear moduli which are treated as constants. Hence, the time rate of change of $\boldsymbol{S}$ reads

$$\dot{\boldsymbol{S}} = \boldsymbol{\mathcal{C}}^e : \dot{\boldsymbol{\varepsilon}}^e = \kappa\,\mathrm{tr}(\dot{\boldsymbol{\varepsilon}}^e)\mathbf{1} + 2\mu\,\mathrm{dev}(\dot{\boldsymbol{\varepsilon}}^e) \,. \tag{2.2.3}$$

The material behavior of polycrystalline sheet metals during forming processes is predominantly determined by a changing dislocation microstructure and attendant evolving anisotropic yield behavior. In addition to the shift of the yield surface and its proportional expansion as in the case of conventional combined hardening, the current model also accounts for an evolving yield surface shape, i.e., cross hardening. Under these effects the plastic flow potential ϕ^p is represented by

$$\phi^p := \sqrt{[\sigma_{\mathrm{eq}}]^2 + [\boldsymbol{S} - \boldsymbol{X}] : \boldsymbol{\mathcal{H}} : [\boldsymbol{S} - \boldsymbol{X}]} - \sigma_y\,(e^p, \dot{e}^p) \leq 0 \,, \tag{2.2.4}$$

Here, σ_{eq} denotes an equivalent stress measure of any kind, e.g., Hill-48 [122], Hosford [126], Karafillis and Boyce [148], or Barlat [37]. Since in the current application a Hill-48 type initial anisotropy is aimed at, the condition $[\sigma_{\mathrm{eq}}]^2 = [\boldsymbol{S} - \boldsymbol{X}] : \boldsymbol{\mathcal{A}} : [\boldsymbol{S} - \boldsymbol{X}]$ is made use of. Thus, Equation (2.2.4) is rearranged to give

$$\phi^p := \sqrt{[\boldsymbol{S} - \boldsymbol{X}] : [\boldsymbol{\mathcal{A}} + \boldsymbol{\mathcal{H}}] : [\boldsymbol{S} - \boldsymbol{X}]} - \sigma_y\,(e^p, \dot{e}^p) \leq 0 \,, \tag{2.2.5}$$

In above the initial (Hill-48-type) and the evolving fourth-order flow anisotropy tensors are respectively denoted by $\boldsymbol{\mathcal{A}}$ and $\boldsymbol{\mathcal{H}}$. $\boldsymbol{X}$ is the back stress tensor. $\sigma_y\,(e^p, \dot{e}^p)$ denotes the flow stress accounting for the isotropic hardening of the material with strain and strain rate effects. Hence, letting e^p denote the equivalent plastic strain and $\dot{e}^p$ its rate, $\sigma_y\,(e^p, \dot{e}^p)$ follows a Johnson–Cook type, [142], multiplicative form in which thermal effects are omitted

$$\sigma_y\,(e^p, \dot{e}^p) := h_y\,(e^p)\,r_y\,(\dot{e}^p) \,. \tag{2.2.6}$$

Here, $h_y\,(e^p)$ and $r_y r_y\,(\dot{e}^p)$ denote the functions of strain hardening and strain rate hardening which are defined as

$$\left.\begin{aligned} h_y\,(e^p) &:= h\,e^p + b - [b - \sigma_{y0}]\exp\left(-m\,[e^p]^n\right), \\ r_y\,(\dot{e}^p) &:= 1 + c\log\left(\dot{e}^p/\dot{e}_0^p\right), \end{aligned}\right\} \tag{2.2.7}$$

where σ_{y0}, b, c, n and m are material parameters. The reference rate is denoted by $\dot{e}_0^p$. During fully developed plastic flow the consistency condition is satisfied, i.e., $\phi^p = 0$. Hence, the current visco-plastic formulation is referred to as a consistency type visco-plastic formulation, see, e.g.,

[326]. Thus, the proposed model is capable of reflecting strain rate effects in contrast to similar models, e.g., [181, 77]. An associative form is selected for the evolution of the plastic flow

$$\dot{\boldsymbol{\varepsilon}}^p / \dot{e}^p = \partial_{\boldsymbol{S}} \phi^p = \frac{[\boldsymbol{\mathcal{A}} + \boldsymbol{\mathcal{H}}] : [\boldsymbol{S} - \boldsymbol{X}]}{\sqrt{[\boldsymbol{S} - \boldsymbol{X}] : [\boldsymbol{\mathcal{A}} + \boldsymbol{\mathcal{H}}] : [\boldsymbol{S} - \boldsymbol{X}]}} . \tag{2.2.8}$$

For definition of the equivalent plastic strain rate, following [173] the rate of plastic work $\dot{w}^p$ is defined as

$$\dot{w}^p = \boldsymbol{S} : \dot{\boldsymbol{\varepsilon}}^p = \underbrace{[\boldsymbol{S} - \boldsymbol{X}] : \dot{\boldsymbol{\varepsilon}}^p}_{=: \dot{w}^p_{\text{stationary}}} + \underbrace{\boldsymbol{X} : \dot{\boldsymbol{\varepsilon}}^p}_{=: \dot{w}^p_{\text{translation}}} . \tag{2.2.9}$$

Using Hill-48 type σ_{eq}, $[\boldsymbol{S} - \boldsymbol{X}] : [\boldsymbol{\mathcal{A}} + \boldsymbol{\mathcal{H}}] : [\boldsymbol{S} - \boldsymbol{X}]$ is degree-one homogeneous with respect to $[\boldsymbol{S} - \boldsymbol{X}]$. Thus, substituting Equation (2.2.8) into Equation (2.2.9), with an abuse of notation $\sigma_y = \sigma_y (e^p, \dot{e}^p)$, one has

$$\dot{w}^p_{\text{stationary}} = [\boldsymbol{S} - \boldsymbol{X}] : \dot{\boldsymbol{\varepsilon}}^p = \dot{e}^p \frac{[\boldsymbol{S} - \boldsymbol{X}] : [\boldsymbol{\mathcal{A}} + \boldsymbol{\mathcal{H}}] : [\boldsymbol{S} - \boldsymbol{X}]}{\sqrt{[\boldsymbol{S} - \boldsymbol{X}] : [\boldsymbol{\mathcal{A}} + \boldsymbol{\mathcal{H}}] : [\boldsymbol{S} - \boldsymbol{X}]}} = \dot{e}^p \sigma_y . \tag{2.2.10}$$

Hence,

$$\dot{e}^p = \frac{[\boldsymbol{S} - \boldsymbol{X}] : \dot{\boldsymbol{\varepsilon}}^p}{\sigma_y} . \tag{2.2.11}$$

The kinematic hardening behavior is modeled via a variant of the Armstrong–Frederick form

$$\dot{\boldsymbol{X}} / \dot{e}^p = c_x [s_x \boldsymbol{N}^p - \boldsymbol{X}] , \tag{2.2.12}$$

where c_x and s_x are associated with the saturation rate and magnitude with the back stress tensor $\boldsymbol{X}$, respectively. $\boldsymbol{N}^p$ denotes the unit direction of the inelastic deformation with $\boldsymbol{N}^p = \dot{\boldsymbol{\varepsilon}}^p / |\dot{\boldsymbol{\varepsilon}}^p|$ where $\boldsymbol{N}^p : \boldsymbol{N}^p = 1$. The evolution of the flow anisotropy tensor determines the shape changes in the yield surface due to the microstructure evolution and is modeled introducing the following evolutionary relation (see, e.g., [181])

$$\dot{\boldsymbol{\mathcal{H}}} / \dot{e}^p = c_d \left[s_d \boldsymbol{N}^p \otimes \boldsymbol{N}^p - \boldsymbol{\mathcal{H}}^d \right] + c_l \left[s_l \left[\boldsymbol{N}^p \otimes \boldsymbol{N}^p - \boldsymbol{\mathcal{I}}^{\text{dev}} \right] - \boldsymbol{\mathcal{H}}^l \right] . \tag{2.2.13}$$

$\boldsymbol{\mathcal{I}}^{\text{dev}}$ is the deviatoric part of the fourth-order symmetric identity tensor, $\boldsymbol{\mathcal{I}}^{\text{sym}} = 1/2 [\boldsymbol{1} \overline{\otimes} \boldsymbol{1} + \boldsymbol{1} \underline{\otimes} \boldsymbol{1}]$, with $\boldsymbol{\mathcal{I}}^{\text{dev}} = \boldsymbol{\mathcal{I}}^{\text{sym}} - 1/3 [\boldsymbol{1} \otimes \boldsymbol{1}]$. $\boldsymbol{\mathcal{H}}^d = [\boldsymbol{N}^p : \boldsymbol{\mathcal{H}} : \boldsymbol{N}^p] [\boldsymbol{N}^p \otimes \boldsymbol{N}^p]$ and $\boldsymbol{\mathcal{H}}^l = \boldsymbol{\mathcal{H}} - \boldsymbol{\mathcal{H}}^d$ represent the projections of $\boldsymbol{\mathcal{H}}$ parallel and orthogonal to $\boldsymbol{N}^p$, respectively. This form is based on the idea of growth and saturation of the dynamic ($\boldsymbol{\mathcal{H}}^d$) and latent ($\boldsymbol{\mathcal{H}}^l$) parts of the flow anisotropy tensor $\boldsymbol{\mathcal{H}}$. Here, c_d and s_d represent the saturation rate and magnitude associated with $\boldsymbol{\mathcal{H}}^d$, respectively. Analogously, c_l and s_l are the saturation rate and magnitude associated with $\boldsymbol{\mathcal{H}}^l$.

2.2.2. Extension to Finite Strains

Let $\boldsymbol{X}$ and $\boldsymbol{x} := \boldsymbol{\varphi}(\boldsymbol{X}, t)$ denote the particle positions at the reference (undeformed) configuration Ω_0 and current (deformed) configuration Ω respectively. $\boldsymbol{F} := \partial_{\boldsymbol{X}} \boldsymbol{\varphi}(\boldsymbol{X}, t)$ defines the deformation gradient of the nonlinear map $\boldsymbol{\varphi} : \Omega_0 \times \mathbb{R} \to \mathbb{R}^3$. Any infinitesimal material vector $d\boldsymbol{X}$ at the reference configuration is transformed to its final setting $d\boldsymbol{x}$ at the current configuration via

$$d\boldsymbol{x} := \boldsymbol{F} \cdot d\boldsymbol{X} . \tag{2.2.14}$$

Let $\boldsymbol{l} := \dot{\boldsymbol{F}} \cdot \boldsymbol{F}^{-1} = \partial_{\boldsymbol{x}} \boldsymbol{v}$ denote the spatial velocity gradient, with $\boldsymbol{v} = \dot{\boldsymbol{x}}$. Various forms of rate additive splits can be recovered through a multiplicative decomposition of $\boldsymbol{F}$ into elastic $\boldsymbol{F}^e$ and

plastic $\boldsymbol{F}^p$ parts with $\boldsymbol{F} := \boldsymbol{F}^e \cdot \boldsymbol{F}^p$ making use of $\dot{\boldsymbol{F}} = \dot{\boldsymbol{F}}^e \cdot \boldsymbol{F}^p + \boldsymbol{F}^e \cdot \dot{\boldsymbol{F}}^p$ and $[\boldsymbol{F}]^{-1} = [\boldsymbol{F}^p]^{-1} \cdot [\boldsymbol{F}^e]^{-1}$. Accordingly one has $\boldsymbol{l} = \boldsymbol{l}^e + \boldsymbol{l}^p$ where $\boldsymbol{l}^p \to \boldsymbol{F}^e \cdot \boldsymbol{L}^p \cdot [\boldsymbol{F}^e]^{-1}$ with $\boldsymbol{l}^e := \dot{\boldsymbol{F}}^e \cdot [\boldsymbol{F}^e]^{-1}$ and $\boldsymbol{L}^p := \dot{\boldsymbol{F}}^p \cdot [\boldsymbol{F}^p]^{-1}$. For small elastic strains and rigid body rotations with $\boldsymbol{F}^e \simeq \boldsymbol{1}$ one governs $\boldsymbol{l}^p \to \boldsymbol{L}^p$. Using $\boldsymbol{F}^e := \boldsymbol{R}^e \cdot \boldsymbol{U}^e$ and assuming small elastic strains but finite rotations, i.e., $\boldsymbol{U}^e \simeq \boldsymbol{1}$, supplies $\boldsymbol{l}^p \to \boldsymbol{R}^e \cdot \boldsymbol{L}^p \cdot [\boldsymbol{R}^e]^{-1}$. Taking the symmetric part of both sides one reaches the following additive split from a multiplicative split

$$\boldsymbol{d} = \boldsymbol{d}^e + \boldsymbol{d}^p. \tag{2.2.15}$$

This forms the basis of hypoelastic-plastic formulations which rely on certain objective rates of the selected stress measures. ABAQUS/VUMAT convention uses the Green–Naghdi–McInnis rate of the Cauchy (true) stress $\boldsymbol{\sigma}$ which requires the rotationally neutralized rate of deformation tensor $\dot{\hat{\boldsymbol{\epsilon}}}$ which is defined as

$$\dot{\hat{\boldsymbol{\epsilon}}} = \boldsymbol{R}^\top \cdot [\boldsymbol{d}^e + \boldsymbol{d}^p] \cdot \boldsymbol{R} = \dot{\hat{\boldsymbol{\epsilon}}}^e + \dot{\hat{\boldsymbol{\epsilon}}}^p, \tag{2.2.16}$$

with $\dot{\hat{\boldsymbol{\epsilon}}}^e := \boldsymbol{R}^\top \cdot \boldsymbol{d}^e \cdot \boldsymbol{R}$, $\dot{\hat{\boldsymbol{\epsilon}}}^p := \boldsymbol{R}^\top \cdot \boldsymbol{d}^p \cdot \boldsymbol{R}$. Here, $\boldsymbol{R}$ denotes the rotation tensor, carried out by the polar decomposition of the deformation gradient, $\boldsymbol{F} := \boldsymbol{R} \cdot \boldsymbol{U}$, with $\boldsymbol{U}$ representing the symmetric right stretch tensor. Similarly, a pull back operation on the Cauchy (true) stress tensor $\boldsymbol{\sigma}$ with the rotation tensor gives its rotationally neutralized counterpart viz $\hat{\boldsymbol{\sigma}} := \boldsymbol{R}^\top \cdot \boldsymbol{\sigma} \cdot \boldsymbol{R}$ whose material time derivative $\dot{\hat{\boldsymbol{\sigma}}}$ can be objectively integrated. Hence, the finite strain extension of the presented framework is simply realized using the replacements $\dot{\boldsymbol{S}} \rightsquigarrow \dot{\hat{\boldsymbol{\sigma}}}$ and $\dot{\boldsymbol{\varepsilon}} \rightsquigarrow \dot{\hat{\boldsymbol{\epsilon}}}$ and representing the expressions at the rotationally neutralized configuration.

The developed material model is implemented as an ABAQUS/VUMAT subroutine and used in the simulations given in the subsequent sections. The details of the implementation using the Voigt notation can be found in the Appendix.

2.3. Parameter Identification for DC06

Cold-rolled steel sheet DC06 is an interstitial free steel type commonly applied for forming processes. Many difficult automotive parts such as oil pans, side panels and interior door parts are manufactured through forming DC06 sheets. As DC06 shows high strain path sensitivity, it is known as a material with a complex anisotropic hardening behavior. The evolution of dislocation microstructure during plastic deformation determines the hardening behavior of this material. A cellular structure is formed by dislocations after inducing plastic deformation and the dislocation density will increase at the cell boundaries when more plastic strain is induced. The microstructural evolution of a DC06 sample under uniaxial tensile deformation (captured by TEM) is shown in Figure 2.1. Cold-rolled steel sheet DC06 is an interstitial free steel type commonly applied for forming processes. Many difficult automotive parts such as oil pans, side panels and interior door parts are manufactured through forming DC06 sheets. As DC06 shows high strain path sensitivity, it is known as a material with a complex anisotropic hardening behavior. The evolution of dislocation microstructure during plastic deformation determines the hardening behavior of this material. A cellular structure is formed by dislocations after inducing plastic deformation and the dislocation density will increase at the cell boundaries when more plastic strain is induced. The microstructural evolution of a DC06 sample under uniaxial tensile deformation (captured by TEM) is shown in Figure 2.1.

Cross hardening is one of the observed hardening modes of this material that evolves during orthogonal loading path changes. This phenomenon is dominated by the evolutionary changes in
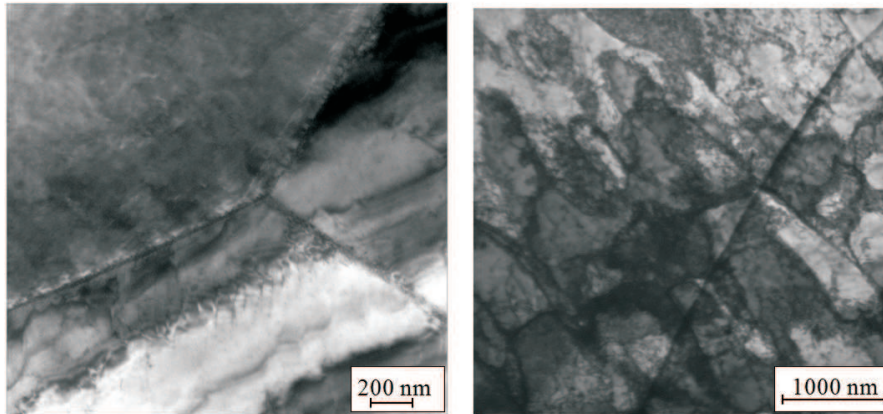
Figure 2.1.: TEM-images of DC06. Left: initial state. Grain boundaries at the triple point are clearly visible. Right: dislocations structure after 5% uniaxial tension. Cell walls inside a grain can be seen.

dislocation microstructures. In general, such phenomena are not captured in classical material models. As a consequence, materials like DC06, that show complex microstructure behavior, are challenging ones to predict the material behavior correctly. The DC06 sheets used in this study are prepared by cold rolling followed by annealing and finishing by skin pass process. The steel sheets in this work are of 1.0 mm thickness and provided and chemically analyzed by ThyssenKrupp Steel Europe AG (cf. [77, 76]) . The material specifications are obtained from the performed test on the DC06 sheet. The average Lankford's coefficients in 0°, 45° and 90° with respect to the rolling direction are determined as r_0=2.31, r_{45}=1.95 and r_{90}=2.77, respectively [77]. Their relation with the Hill-48 constants, F, G, H, L, M, and N are given below,

$$F = \frac{r_0}{r_{90}[1+r_0]} \,, \ G = \frac{1}{[1+r_0]} \,, \ H = \frac{r_0}{[1+r_0]} \,, \ L = \frac{1}{2}\frac{[r_0+r_{90}][1+2r_{45}]}{r_{90}[1+r_0]} \,. \tag{2.3.1}$$

with $M = N = L$.

Table 2.1.: Chemical composition of DC06. All values are given as multiples of 10^{-5} mass fraction. The data set is determined by ThyssenKrupp Steel Europe AG [77, 76].

alloying component	C	Si	Mn	P	S	Al	N	Ti
10^{-5} mass fraction	3	18	137	13	10	35	2.7	79

To identify the material parameters in the formulated material model, experimental data for monotonic shear, uniaxial tension, forward to reverse shear and plane strain tension followed by shear tests are used (cf. [314, 77, 76, 131]). The simple shear tests and the combined plane strain tension to shear tests were conducted on a biaxial tester (equipped with two axes which can be moved independently) at Applied Mechanics Group, Faculty of Engineering Technology, University of Twente, Netherlands (cf. [315, 314]).

The isotropic hardening parameters in the Johnson–Cook model (σ_{y0}, b, m and n) in Equation (3.2.4) are identified based on the monotonic shear and the plane strain tension results. The plane strain tension followed by shear test is used to identify the model parameters associated with cross hardening (s_d, c_d, s_l and c_l). The simulation results of the presented model are compared with the experimental data for monotonic shear and the plane strain tension followed by the shear tests in Fig. 2.2. The Frederick–Armstrong kinematic hardening parameters are adopted as the ones in Clausmeyer et al. [77].
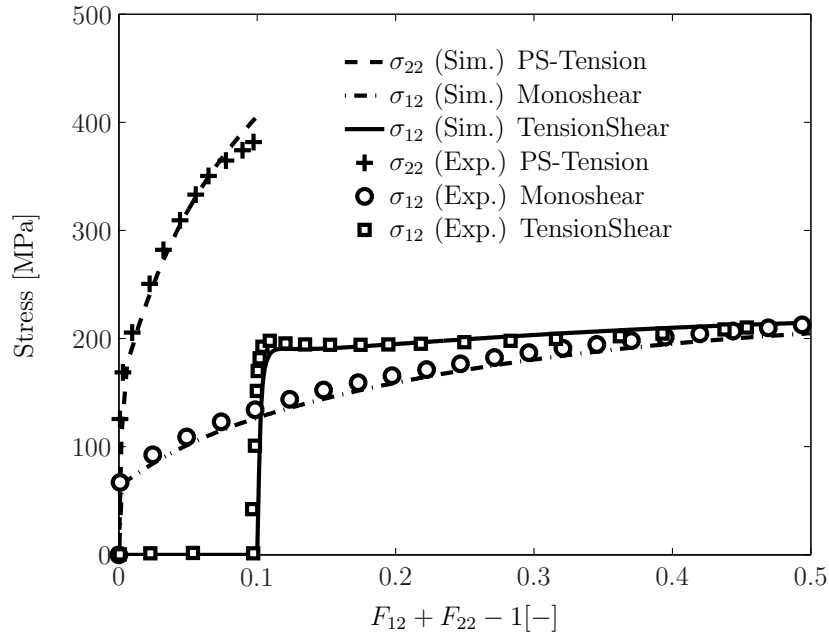
Figure 2.2.: Comparison of the model response to the monotonic shear test and the plane strain tension followed by shear test with the experiments data from [314, 77].
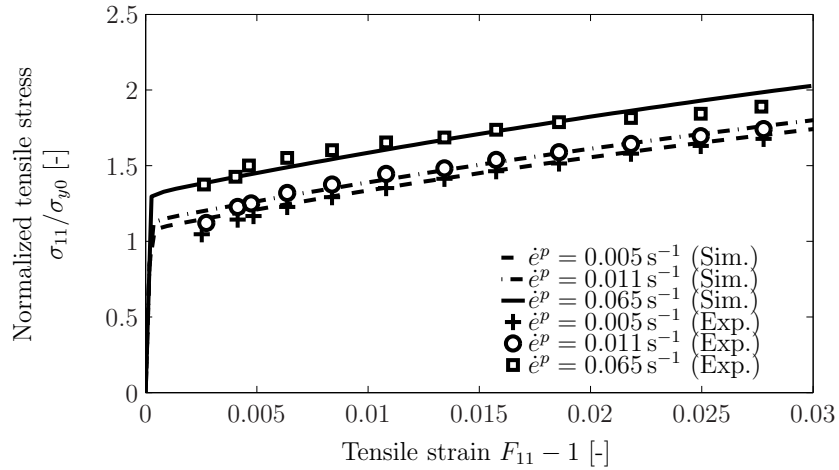
Figure 2.3.: Identification of strain rate sensitivity in Johnson–Cook model using the experimental results represented in [314].

The strain rate parameters in Johnson–Cook model ($\dot{e}_0^p$ and c) in Equation (3.2.4) are identified using the experimental stress-strain curves represented in van Riel [314] for the strain rates $\dot{e} = [0.005\,\text{s}^{-1}, 0.011\,\text{s}^{-1}, 0.065\,\text{s}^{-1}]$. The reference strain rate parameter $\dot{e}_0^p$ is identified to $0.005\,\text{s}^{-1}$ and the strain rate sensitivity parameter c as 0.0857. In Fig. 2.3 the strain rate sensitivity of the model is compared to the corresponding experimental curves in plane strain tensile loading [314]. The identified material parameters for DC06 are summarized in Table 2.2.

Table 2.2.: Identified material parameters for interstitial free DC06. Parameter values determined from uniaxial tension, monotonic shear, cyclic shear, and orthogonal tension-shear experimental test data, see [315, 77].

Parameter	Symbol	Value	Dimension
Elastic constants	κ	150.833	[GPa]
	μ	69.615	[GPa]
Johnson–Cook constants	σ_{y0}	108.0	[MPa]
	b	320.0	[MPa]
	m	7.60	[−]
	n	1.18	[−]
	$\dot{e}_0^p$	0.005	[s^{-1}]
	c	0.086	[−]
Hill-48 constants	F	0.252	[−]
	G	0.302	[−]
	H	0.698	[−]
	L	1.357	[−]
	M	1.357	[−]
	N	1.357	[−]
Kinematic hardening constants	s_x	56.0	[MPa]
	c_x	33.1	[−]
Cross hardening constants	s_d	0	[−]
	c_d	23.90	[−]
	s_l	0.83	[−]
	c_l	87.30	[−]

2.4. Applications

In order to assess the presented material model two sets of numerical simulation have been used. First, in a one element test the capability of the model in capturing different aspects of material hardening under strain path changes is investigated. The response of each single hardening mode in terms of a sensitivity analysis is represented at first.

Afterwards, by simulation of an experimentally performed drawing process, the applicability of the model to industrial problems is tested. The description and results of each case study are represented in the next subsections.

2.4.1. Single Element Tests and Sensitivity Analyses

The one element tests are performed with a cubic 8 node element C3D8 element with unity size. To concentrate on the effect of the induced anisotropy only, an initial yield surface of von-Mises type is assumed in this section. Three sets of numerical tests are performed to investigate the model's performance. First, the simulations are run for a combined plane strain tension and simple shear loading path. The displacement in $x-$direction is constrained and the uniaxial displacement in $y-$direction is applied in the plane strain load case. The simple shear loading is examined by inducing the shear deformation in the $xy-$plane. The effect of each single hardening mode (isotropic, kinematic and cross) as well as combinations of them are presented in Figures 2.4 and 2.5. For this purpose, single hardening models are turned off by setting the

corresponding material parameters accordingly.
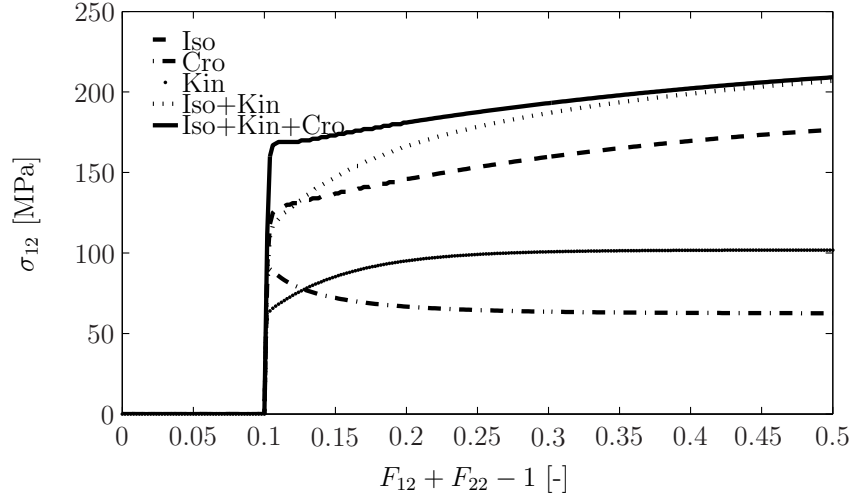
Figure 2.4.: Plane strain tension followed by simple shear test. Cauchy stress σ_{12} versus sum of deformation gradient components $F_{11} + F_{12} - 1$ for different hardening contributions active: Iso, Kin and Cro refer to isotropic, kinematic, and cross hardening, respectively.

The Cauchy shear stress component σ_{12} versus the sum of the deformation gradient components $F_{11} + F_{12} - 1$ are depicted in Figure 2.4. The share of each hardening mode is clearly observable. In addition, the Cauchy stress component σ_{22} during the considered loading path is shown in Figure 2.5.
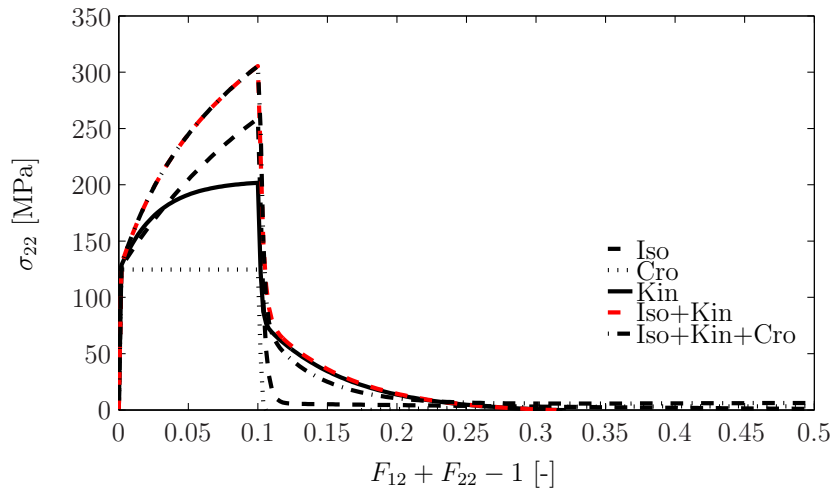
Figure 2.5.: Plane strain tension test. Cauchy stress σ_{22} versus strain $F_{12} + F_{22} - 1$ for different hardening contributions active. As expected, cross hardening does not play a role. Iso, Kin and Cro refer to isotropic, kinematic, and cross hardening, respectively.

The results show that the isotropic, kinematic and cross hardening contributions are accounted for in the proposed model formulation. In the first part of the loading path (plane strain tension), the full model (Iso+Kin+Cro) yields the same stress response as combined isotropic and kinematic hardening (Iso+Kin). As expected, the cross hardening mode does not contribute to the stress in the first part of the applied loading path. Conversely, a significant stress overshoot in the Cauchy stress component σ_{12} is observable in the full hardening model at the beginning

of simple shear loading (cf. Figure 2.4). This is not captured in the combined isotropic and kinematic hardening model due to the evolved cross hardening. The Bauschinger effect and its saturation at higher strain amplitudes are observable.

To illustrate the effect of kinematic hardening in more detail, the model is analyzed for three simple shear loading cycles of different strain amplitudes as shown in Figure 2.6. The Bauschinger effect, i.e., a reduction of the yield stress after reversal loading, is clearly observed.
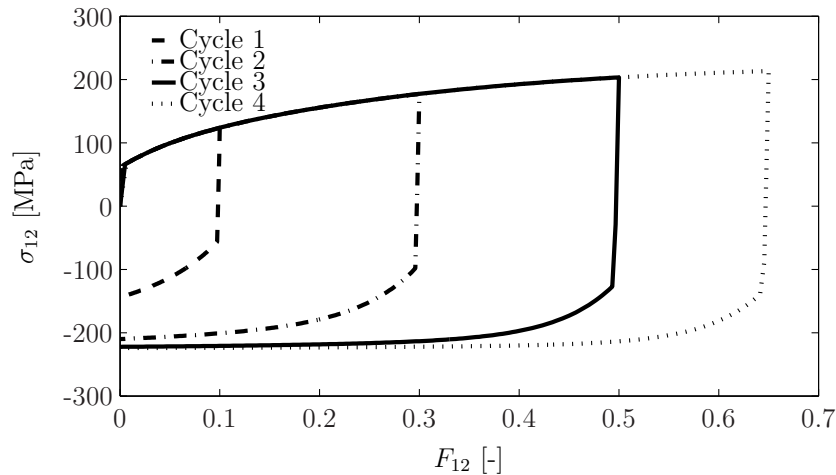
Figure 2.6.: Three simple shear loading cycles with different strain amplitudes. Cauchy stress component σ_{12} versus strain F_{12}. The Bauschinger effect and its saturation are observable.

In addition to the obtained results for DC06, further numerical investigations of the proposed model with different set of model parameters associated with flow anisotropy tensor have been performed. The results showed that a wide range of cross hardening sensitivity was covered by the model. The results of the sensitivity analysis with respect to the magnitude of the latent hardening part s_l under plane strain followed by simple shear loading are shown in Figure 2.7. The represented curves in this figure show the material response in the plane strain loading followed by the simple shear loading for the different values of s_l parameter. The results show the flexibility of the material model in reflecting the cross hardening behavior in other materials with different sensitivities to load path changes.

The capability of the material model to predict the evolving yield surface in the considered loading path is demonstrated in Figures 2.8.(a) and 2.8.(b). The evolution of yield surface at the end of each part of loading path as well as its initial state is depicted in Figure 2.8.(a) for the full hardening model. Comparing the yield surface at the end of plane strain tension with the initial yield surface clearly shows the shift in center of the curve due to the kinematic hardening. The cross hardening effect is reflected in this figure through orientation change of the yield surface. The change in the aspect ratio of the yield surface is observable as well. According to the definition of the cross hardening part in the formulation of the material model, it is expected to see the expansion of yield surface in the parallel and perpendicular directions respect to the loading direction due to the dynamic and latent parts of induced anisotropy, respectively. In the first loading phase (plane strain tension), the projection of loading direction on the major axis of the yield ellipse is greater than that on the minor axis. In this regard, if the contribution of the cross hardening mode is focused on, the expansion of the yield surface toward its minor axis is mainly the effect of the latent part. In the second loading path, the direction of loading is toward the minor axis of the initial yield surface and the effect of the latent part due to cross
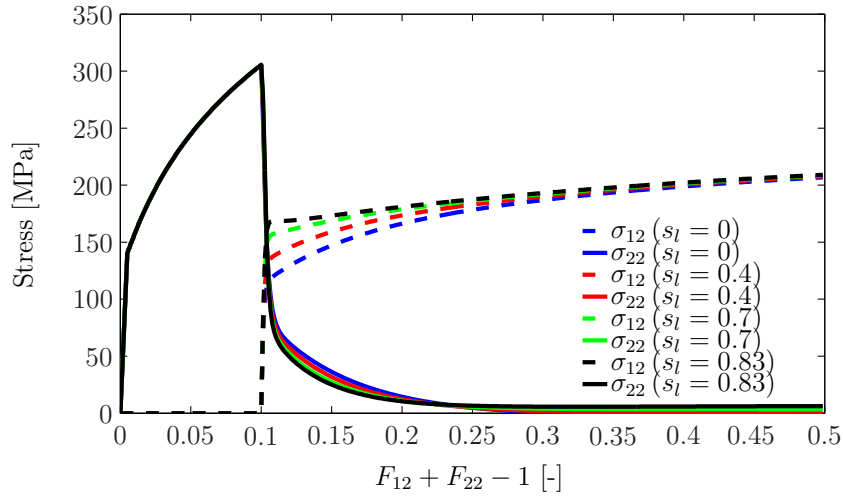
Figure 2.7.: Sensitivity analysis with respect to s_l for the plane strain tension followed by the simple shear loading (σ_{11}, σ_{22} and σ_{12} versus strain $F_{12} + F_{22} - 1$).

hardening is the growth of the yield surface in the direction of the major axis of initial yield surface. The growth of the yield surface in this direction at the end of second part of the loading path is clearly observable in Figure 2.8.(a), as anticipated. Finally, inspecting the normals to the yield loci at uniaxial stress points, the evolution of the in-plane anisotropy, i.e., the Lankford's coefficients, is observable.
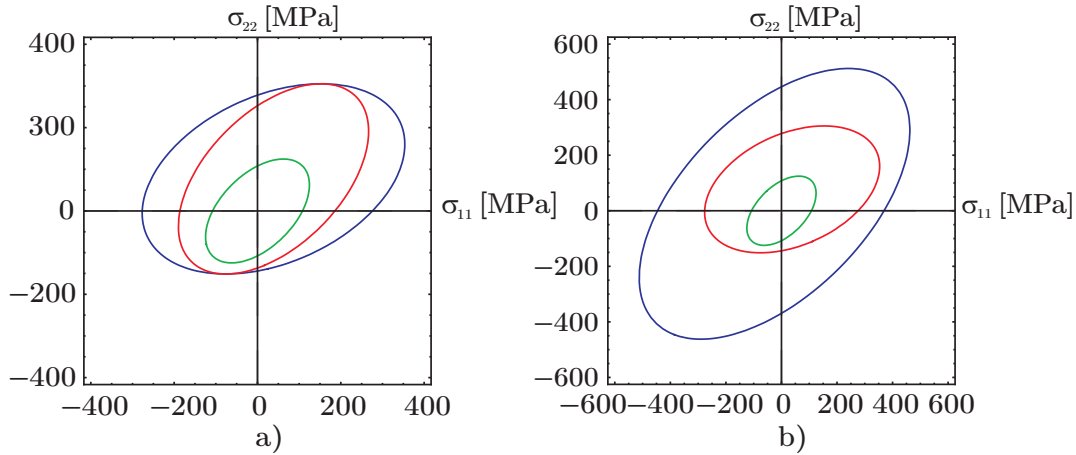
Figure 2.8.: (a) Yield loci at the initial condition, the end of plane strain tension loading and the end of simple shear loading. (b) Yield loci at the initial condition and at the end of plane strain tension for Iso+Kin and Iso+Kin+Cro model.

To investigate the effect of cross hardening to the yield surface evolution, the yield surface at the end of the first part of loading path (plane strain tension) is plotted in Figure 2.8.(b) for two combination of hardening modes: one for the complete model considering the effect of isotropic, kinematic and cross hardening and the other without the cross hardening contribution. Both combinations predict the same yield points on the loading path. That is in agreement with the depicted curves in Figure 2.5 for the first part of the loading path. Moreover, the effect of cross hardening in determining the orientation and the expansion of yield surface is obviously reflected in this figure. Further, it is seen for a following orthogonal loading path, the full

model predicts higher yield that is in accordance with the shear stress curve in Figure 2.4 at the beginning of the simple shear loading. Accordingly, the latent slip system orthogonal to the current loading direction is taken into account in the proposed model. In addition, to reflect the cross hardening effect in predicting the yield surface, the investigation of the yield surface evolution after orthogonal loading change shows that the orientation of the yield surface returns to its initial one after a slight loading. Further, shear loading results in the expansion of the yield surface in this orientation (cf. Figure 2.8.(a)). According to the above results, the introduced model captures all the target features well, but the feasibility investigation of the model for the real sheet forming process remains - this is done in the following.

2.4.2. An Industrial Process Simulation

An open section channel (cf. Figure 2.9) is selected for the experimental drawing process and the results are recorded to verify the simulation results. As the selected geometry comprises different complex curves, different plastic strain paths occur in different zones of the DC06 sheet during the forming process. Consequently, the various hardening modes such as isotropic, kinematic and cross hardening take part during the deformation. The forming processes were performed at the Institute of Forming Technology and Lightweight Construction, Technical University of Dortmund, Germany, on a double acting hydraulic press with maximum 1000 kN capacity. The die components comprising punch, matrix and blank-holder are made of tool steel C60 according to DIN EN 10027-2. The blank-holder force is provided hydraulically at the constant value of 200 kN during loading step. However, due to the hydraulic oscillation, this was not completely achieved (see Figure 2.10). Contacting surfaces are covered by a lubrication formulated on solvent refined mineral oil with a viscosity of $67\,\mathrm{mm}^2/\mathrm{s}$ at $40°\,\mathrm{C}$. To determine the Coulomb friction coefficient, the contact conditions in the channel forming process are simulated in several simple experimental tests (cf. [332]). For each contact test, rectangular metal strips ($300\,\mathrm{mm} \times 400\,\mathrm{mm}$) are prepared and lubricated corresponding to the contact conditions of the considered contact set. The prepared strips are pressed against each other with a definite force and the required pulling force for each test is measured. The friction coefficient has experimentally been identified as μ=0.15. During the forming process, the die displacement, the blank-holder force and the force acting on the die are recorded with a frequency of 50 Hz. For homogeneous load distribution, avoiding dynamic effect and geometry precision, the forming process is performed at the low rate of loading about $4\,\mathrm{mm/s}$. Moreover, the final geometry is measured by ATOS machine to compare to the obtained final geometry from process simulation. Three tests with the identical conditions are carried out to check the test repeatability. Comparing the force-time recorded results and the final geometry of workpiece obtained from each repetition shows no considerable differences.

In the following, the above experimental forming process is modeled and the numerical results are compared to the experimental data. The meshed parts of the channel forming process in the simulation are shown in Figure 2.11. The die parts are meshed by rigid shell elements R3D4 and the blank is meshed by 8-node elements C3D8R with reduced integration and 1 mm approximate element size. Five layers of elements are used with the total number of 75030 elements for the blank mesh. The simulation is performed using a VUMAT subroutine in ABAQUS/EXPLICIT. The initial anisotropy is considered using the Hill-48 constants listed in Table 2.2.

The load is applied according to the experimental time scale. In accordance to the measured value during the experiment, the blank-holder force is approximated as 200 kN and kept unchanged during the following forming process. The blank-holder force measured in the exper-
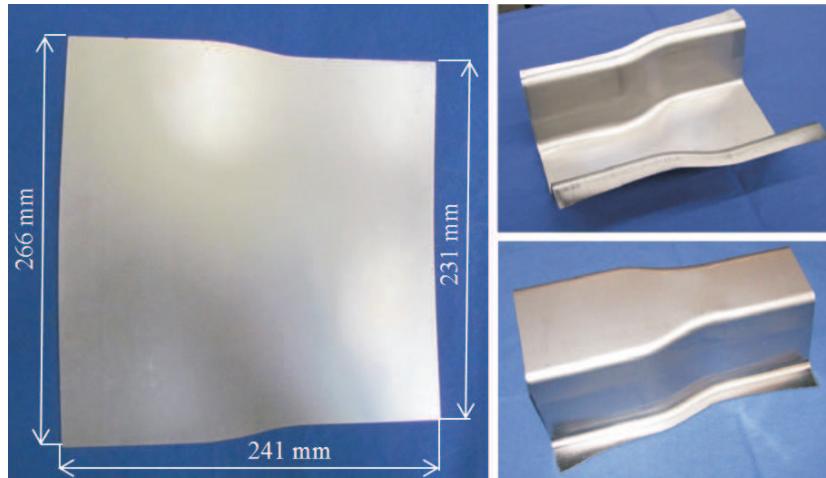
Figure 2.9.: Undeformed blank (left) and channel die geometry after forming (right).
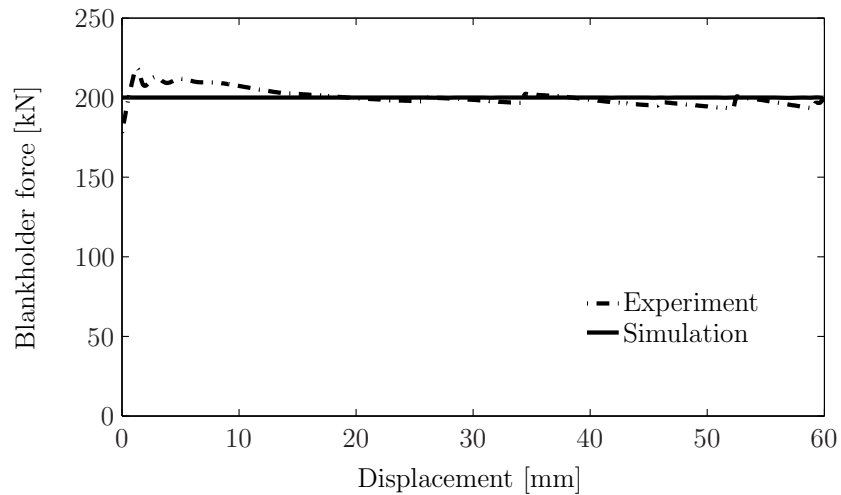
Figure 2.10.: Experimentally determined blank-holder force in channel forming process. The applied force in the simulation is approximated as a constant value of 200 kN.

iment as well as the one from the simulation are plotted in Figure 2.10. Tangential contact behavior is defined by Coulomb friction law with the friction coefficient of $\mu = 0.15$.

The simulation results of the channel forming process are shown in Figures 2.12-2.16. First, the die force from the finite element simulation is compared to the recorded die force during the experiment (cf. Figure 2.12). These two curves represent the die force versus punch displacement and an acceptable downstream following the experimental curve is observed. A local increase in the experimental die force is seen at the end of loading in Figure 2.12. The tapered shape of the die may be a reason for such an increase due to the blank clamping at the end of the punch course at the upper region. This local increase of the die force is captured in the simulation, but it is less pronounced.

The geometry of the workpiece before and after spring-back, obtained from simulation is compared to the measured experimental one in Figures 2.13 and 2.14. An acceptable agreement between the simulation and experiment is achieved in the curved areas and the flange angles. The comparisons are presented for the both ends of the channel.

Figure 2.11.: Simulation set up of channel forming process.
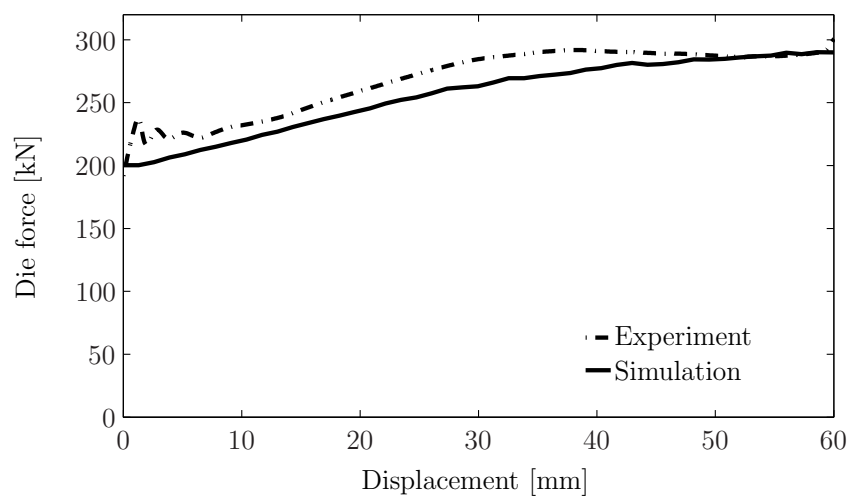
Figure 2.12.: Die force (kN) in the channel forming process determined in experiment and simulation.

Figure 2.13.: Comparison of the obtained final shapes before and after spring-back from simulation with the final shapes after spring-back from experiment at wider opening end. The numerical result agrees well with the experimental data.

The final flange shapes, obtained from simulation and experiment, are compared in Figure 2.15.
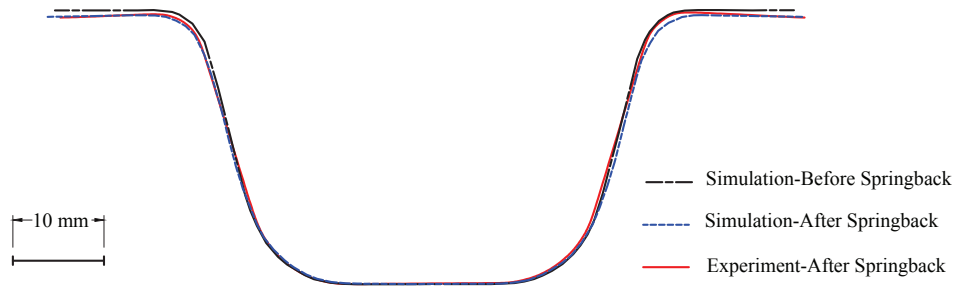
Figure 2.14.: Comparison of the obtained final shapes before and after spring-back from simulation with the final shapes after spring-back from experiment at narrower opening end. The numerical result is in good accordance to the experimental data.

Here, a small difference is seen between the two geometries. In spite of the homogeneous flange widths in the simulated one, the experimental flange shape has varying flange width especially at both ends. The non-uniform distribution of the blank-holder force in experimental process could be one reason of such difference in the flange widths. In conventional industrial problems, the main target in blank shape design is having the equal flange width all over the final part. This target decreases the required blank-holder force for controlling the wrinkling effect as well as the wasted material in final cutting.
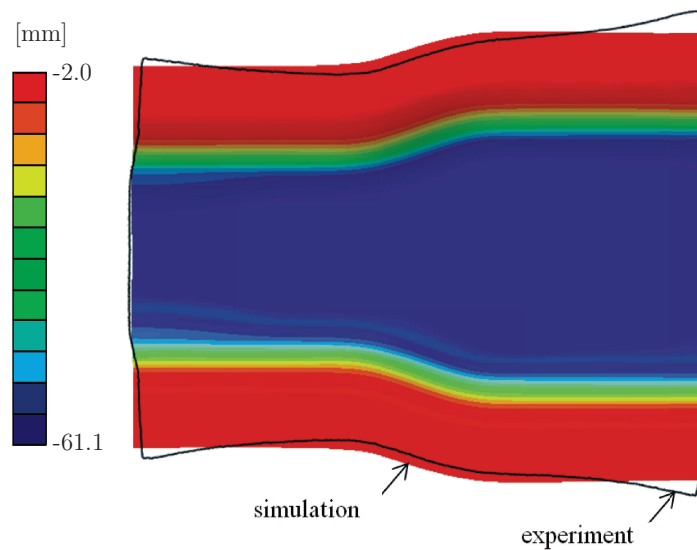
Figure 2.15.: Comparison of the flange shape after spring-back in the final workpiece obtained from experiment and simulation. The displacement [mm] in $z-$direction is plotted.

The strain rate distribution in the workpiece at the 60% of the total forming process is shown in Figure 2.16. It is observable that the strain rates in some areas (especially at the die edges) are considerably high - leading to a strain rate hardening effect in the material. As the sheet suddenly bends at the die edges during draw-in process, it is expected that high strain rates occur in such areas. In this regard, the strain rate values strongly depend on the die radii as well as the loading speed. The strain rate distribution shows that the strain rate effect is a phenomenon in the selected forming process which should not be neglected.
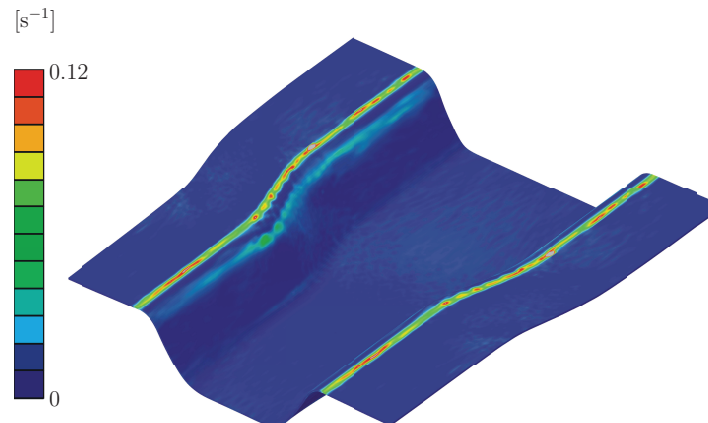
Figure 2.16.: Strain rate distribution after 60% of loading. The strain rates at the die edges are considerably high leading to a strain rate hardening effect in the material. Thus, the strain rate effect should be accounted for in the simulations.

2.5. Conclusion:

A micromechanically motivated visco-plastic material model is applied to interstitial free DC06 steel. The microstructure evolution of the material during plastic deformation is mapped via the flow potential function by an evolutionary approach. This evolutionary approach implements the change of dislocation structures parallel and orthogonal to the direction of inelastic deformation as the dynamic and the latent part of hardening via an the induced anisotropy tensor of fourth-order. This model is implemented into a VUMAT subroutine and its capabilities for taking into account the isotropic, kinematic hardening and cross hardening modes are investigated.

Considering the presented results in the one element simulation tests, the isotropic and kinematic hardening modes are successfully captured by the proposed material model. In addition, cross hardening in orthogonal loading paths is correctly predicted by the model as well. The evolution of the yield surface under the applied orthogonal loading path is depicted and the reflection of each hardening mode is well observed. In addition, the results are consistent with the microstructural hypothesis of plastic deformation in the active and the non-active slip systems, so that the cross hardening effect is clearly observed in the obtained results. The strain rate effect is successfully considered in the model via the Johnson–Cook formulation and fitted to the experimental stress-strain curves of the considered material DC06. The strain rate effect in the channel forming case study is reflected as well.

Furthermore, its applicability to an experimental channel forming process is shown. The sheet undergoes a wide range of strain paths at different locations, during the selected channel forming process with non-homogeneous section. The simulation of the selected industrial (case study) process has been carried out successfully and the obtained results are in very good agreement with the measured experimental results. Satisfactory coincidence of the spring-back shape between the simulation and experiment shows that the material behavior is succeeded in modeling effective hardening mechanisms in different strain paths during the forming process.

According to the presented results the strain rate effect is an active phenomenon in the se-

lected process and material, although the selected process is not perfect to investigate the strain rate effect in detail. The cross hardening evolution also shows the importance of the induced anisotropy during the process and the mechanical characteristics of the final product. Making use of this material model via the commercial finite element software ABAQUS is a practical way for precise simulating the industrial sheet forming processes. In this way, different modes of hardening consisting isotropic, kinematic and cross hardening as well as the strain rate effect are considered in the simulation of forming processes. A final word is that, the induced anisotropy is not only affecting the material behavior in non-proportional loading paths but also the product characteristics in the post production investigations (e.g., crashworthiness [290]). Therefore, even for the areas that do not experience a non-proportional loading during production, the induced anisotropy might gain importance during service-life.

2.A. Details of Vumat Implementation

2.A.1. Voigt Notation

Implementation of the material models preserving tensorial forms often result in inefficient codes. For a three-dimensional application this can be remedied by the use of Voigt notation, i.e., using 6×1 vectors and 6×6 matrices for the representation of symmetric second-order tensors and fourth-order tensors with at least minor-symmetries. This allows application of standard matrix algebra.

The 6×1 vector representations for the strain tensor is $\boldsymbol{\varepsilon} = [\varepsilon_{11}, \varepsilon_{22}, \varepsilon_{33}, 2\varepsilon_{12}, 2\varepsilon_{23}, 2\varepsilon_{13}]^\top$. where the strain tensor norm $|\boldsymbol{\varepsilon}| = \sqrt{\varepsilon_{ij}\varepsilon_{ij}}$ is computed using $|\boldsymbol{\varepsilon}| = \sqrt{\boldsymbol{\varepsilon}^\top \boldsymbol{\mathcal{Q}} \boldsymbol{\varepsilon}}$, with

$$\boldsymbol{\mathcal{Q}} = \frac{1}{2} \left[\begin{array}{ccc|ccc} 2 & 0 & 0 & 0 & 0 & 0 \\ 0 & 2 & 0 & 0 & 0 & 0 \\ 0 & 0 & 2 & 0 & 0 & 0 \\ \hline 0 & 0 & 0 & 1 & 0 & 0 \\ 0 & 0 & 0 & 0 & 1 & 0 \\ 0 & 0 & 0 & 0 & 0 & 1 \end{array} \right] . \tag{2.A.1}$$

All the strain and strain-like tensors follow the stencil $\left[\begin{array}{c|c} 1 & 2 \end{array} \right]^\top$, where the shear components are multiplied by two

$$\left. \begin{array}{ll} \boldsymbol{\varepsilon}^e & = [\varepsilon_{11}^e, \varepsilon_{22}^e, \varepsilon_{33}^e, 2\varepsilon_{12}^e, 2\varepsilon_{23}^e, 2\varepsilon_{13}^e]^\top , \\ \boldsymbol{\varepsilon}^p & = [\varepsilon_{11}^p, \varepsilon_{22}^p, \varepsilon_{33}^p, 2\varepsilon_{12}^p, 2\varepsilon_{23}^p, 2\varepsilon_{13}^p]^\top , \\ \boldsymbol{N}^p & = [N_{11}^p, N_{22}^p, N_{33}^p, 2N_{12}^p, 2N_{23}^p, 2N_{13}^p]^\top . \end{array} \right\} \tag{2.A.2}$$

The 6×1 vector representations for the stress and stress-like tensors follow the stencil $\left[\begin{array}{c|c} 1 & 1 \end{array} \right]^\top$, where the shear components are multiplied by unity

$$\left. \begin{array}{l} \boldsymbol{S} = [S_{11}, S_{22}, S_{33}, S_{12}, S_{23}, S_{13}]^\top , \\ \boldsymbol{X} = [X_{11}, X_{22}, X_{33}, X_{12}, X_{23}, X_{13}]^\top , \end{array} \right\} \tag{2.A.3}$$

where the tensor norm, e.g., $|\boldsymbol{S}| = \sqrt{S_{ij}S_{ij}}$, is computed using $|\boldsymbol{S}| = \sqrt{\boldsymbol{S}^\top \boldsymbol{\mathcal{Q}}^{-1} \boldsymbol{S}}$. A similar distinction also applies for the 6×6 matrix representations of the fourth-order tensors acting

on the stress-like or strain-like tensors. Hence while representing $\boldsymbol{\varepsilon}^e : \boldsymbol{\mathcal{C}}^e : \boldsymbol{\varepsilon}^e$ as $[\varepsilon^e]^\top \boldsymbol{\mathcal{C}}^e \varepsilon^e$, the matrix form of $\boldsymbol{\mathcal{C}}^e$ reads

$$
\boldsymbol{\mathcal{C}}^e = \left[\begin{array}{ccc|ccc}
\mathcal{C}^e_{1111} & \mathcal{C}^e_{1122} & \mathcal{C}^e_{1133} & \mathcal{C}^e_{1112} & \mathcal{C}^e_{1123} & \mathcal{C}^e_{1113} \\
\mathcal{C}^e_{2211} & \mathcal{C}^e_{2222} & \mathcal{C}^e_{2233} & \mathcal{C}^e_{2212} & \mathcal{C}^e_{2223} & \mathcal{C}^e_{2213} \\
\mathcal{C}^e_{3311} & \mathcal{C}^e_{3322} & \mathcal{C}^e_{3333} & \mathcal{C}^e_{3312} & \mathcal{C}^e_{3323} & \mathcal{C}^e_{3313} \\
\hline
\mathcal{C}^e_{1211} & \mathcal{C}^e_{1222} & \mathcal{C}^e_{1233} & \mathcal{C}^e_{1212} & \mathcal{C}^e_{1223} & \mathcal{C}^e_{1213} \\
\mathcal{C}^e_{2311} & \mathcal{C}^e_{2322} & \mathcal{C}^e_{2333} & \mathcal{C}^e_{2312} & \mathcal{C}^e_{2323} & \mathcal{C}^e_{2313} \\
\mathcal{C}^e_{1311} & \mathcal{C}^e_{1322} & \mathcal{C}^e_{1333} & \mathcal{C}^e_{1312} & \mathcal{C}^e_{1323} & \mathcal{C}^e_{1313}
\end{array} \right] .
\tag{2.A.4}
$$

Hence, the stencil $\left[\begin{array}{c|c} 1 & 1 \\ \hline 1 & 1 \end{array} \right]$ is used over the continuum components. Note that with Equations (2.A.3) and (3.3.4), the stress definition in Equation (2.2.3) naturally replaces with its corresponding Voigt form

$$
\boldsymbol{S} = \boldsymbol{\mathcal{C}}^e \, \boldsymbol{\varepsilon}^e ,
\tag{2.A.5}
$$

and hence $[\varepsilon^e]^\top \boldsymbol{\mathcal{C}}^e \varepsilon^e = [\varepsilon^e]^\top \boldsymbol{S} = [\boldsymbol{S}^e]^\top \varepsilon^e$. The matrix representation of $[\boldsymbol{S} - \boldsymbol{X}] : [\boldsymbol{\mathcal{A}} + \boldsymbol{\mathcal{H}}] : [\boldsymbol{S} - \boldsymbol{X}]$ reads $[\boldsymbol{S} - \boldsymbol{X}]^\top [\boldsymbol{\mathcal{A}} + \boldsymbol{\mathcal{H}}] [\boldsymbol{S} - \boldsymbol{X}]$. The matrix form of $\boldsymbol{\mathcal{A}}$ and $\boldsymbol{\mathcal{H}}$, which preserve both major- and minor-symmetries with $\mathcal{A}_{ijkl} = \mathcal{A}_{jikl} = \mathcal{A}_{ijlk} = \mathcal{A}_{klij}$ and $\mathcal{H}_{ijkl} = \mathcal{H}_{jikl} = \mathcal{H}_{ijlk} = \mathcal{H}_{klij}$, read

$$
\boldsymbol{\mathcal{A}} = \left[\begin{array}{ccc|ccc}
\mathcal{A}_{1111} & \mathcal{A}_{1122} & \mathcal{A}_{1133} & 2\mathcal{A}_{1112} & 2\mathcal{A}_{1123} & 2\mathcal{A}_{1113} \\
\mathcal{A}_{2211} & \mathcal{A}_{2222} & \mathcal{A}_{2233} & 2\mathcal{A}_{2212} & 2\mathcal{A}_{2223} & 2\mathcal{A}_{2213} \\
\mathcal{A}_{3311} & \mathcal{A}_{3322} & \mathcal{A}_{3333} & 2\mathcal{A}_{3312} & 2\mathcal{A}_{3323} & 2\mathcal{A}_{3313} \\
\hline
2\mathcal{A}_{1211} & 2\mathcal{A}_{1222} & 2\mathcal{A}_{1233} & 4\mathcal{A}_{1212} & 4\mathcal{A}_{1223} & 4\mathcal{A}_{1213} \\
2\mathcal{A}_{2311} & 2\mathcal{A}_{2322} & 2\mathcal{A}_{2333} & 4\mathcal{A}_{2312} & 4\mathcal{A}_{2323} & 4\mathcal{A}_{2313} \\
2\mathcal{A}_{1311} & 2\mathcal{A}_{1322} & 2\mathcal{A}_{1333} & 4\mathcal{A}_{1312} & 4\mathcal{A}_{1323} & 4\mathcal{A}_{1313}
\end{array} \right]
\tag{2.A.6}
$$

and

$$
\boldsymbol{\mathcal{H}} = \left[\begin{array}{ccc|ccc}
\mathcal{H}_{1111} & \mathcal{H}_{1122} & \mathcal{H}_{1133} & 2\mathcal{H}_{1112} & 2\mathcal{H}_{1123} & 2\mathcal{H}_{1113} \\
\mathcal{H}_{2211} & \mathcal{H}_{2222} & \mathcal{H}_{2233} & 2\mathcal{H}_{2212} & 2\mathcal{H}_{2223} & 2\mathcal{H}_{2213} \\
\mathcal{H}_{3311} & \mathcal{H}_{3322} & \mathcal{H}_{3333} & 2\mathcal{H}_{3312} & 2\mathcal{H}_{3323} & 2\mathcal{H}_{3313} \\
\hline
2\mathcal{H}_{1211} & 2\mathcal{H}_{1222} & 2\mathcal{H}_{1233} & 4\mathcal{H}_{1212} & 4\mathcal{H}_{1223} & 4\mathcal{H}_{1213} \\
2\mathcal{H}_{2311} & 2\mathcal{H}_{2322} & 2\mathcal{H}_{2333} & 4\mathcal{H}_{2312} & 4\mathcal{H}_{2323} & 4\mathcal{H}_{2313} \\
2\mathcal{H}_{1311} & 2\mathcal{H}_{1322} & 2\mathcal{H}_{1333} & 4\mathcal{H}_{1312} & 4\mathcal{H}_{1323} & 4\mathcal{H}_{1313}
\end{array} \right]
\tag{2.A.7}
$$

Hence, the stencil $\left[\begin{array}{c|c} 1 & 2 \\ \hline 2 & 4 \end{array} \right]$ applies over the continuum components. This notation leads to the following matrix form of the Hill-48-type structural tensor

$$
\boldsymbol{\mathcal{A}} = \left[\begin{array}{cccccc}
G + H & -H & -G & 0 & 0 & 0 \\
-H & F + H & -F & 0 & 0 & 0 \\
-G & -F & F + G & 0 & 0 & 0 \\
0 & 0 & 0 & 2N & 0 & 0 \\
0 & 0 & 0 & 0 & 2L & 0 \\
0 & 0 & 0 & 0 & 0 & 2M
\end{array} \right] .
\tag{2.A.8}
$$

Note that with Equations (3.3.7) and (3.3.6), the flow rule in Equation (2.2.8) naturally replaces with its corresponding Voigt form

$$
\dot{\varepsilon}^p / \dot{e}^p = \frac{[\boldsymbol{\mathcal{A}} + \boldsymbol{\mathcal{H}}] \, [\boldsymbol{S} - \boldsymbol{X}]}{\sqrt{[\boldsymbol{S} - \boldsymbol{X}]^\top \, [\boldsymbol{\mathcal{A}} + \boldsymbol{\mathcal{H}}] \, [\boldsymbol{S} - \boldsymbol{X}]}} .
\tag{2.A.9}
$$

The Voigt representation of the tensorial expressions which uses different types in each side of the equation, like in Equation (2.2.12), needs additional transformation operators. For example the Voigt form of Equation (2.2.12) reads $\dot{\boldsymbol{X}}/\dot{e}^p = c_x \left[s_x \boldsymbol{\mathcal{Q}} \, \boldsymbol{N}^p - \boldsymbol{X} \right]$, where $\boldsymbol{N}^p = \dot{\boldsymbol{\varepsilon}}^p/|\dot{\boldsymbol{\varepsilon}}^p|$.

Finally, the Voigt representation of Equation (3.3.10) is given as

$$\dot{\boldsymbol{\mathcal{H}}}/\dot{e}^p = c_d \left[s_d \boldsymbol{N}^p \left[\boldsymbol{N}^p \right]^\top - \boldsymbol{\mathcal{H}}^d \right] + c_l \left[s_l \left[\boldsymbol{N}^p \left[\boldsymbol{N}^p \right]^\top - \boldsymbol{\mathcal{I}}^{\mathrm{dev}} \right] - \boldsymbol{\mathcal{H}}^l \right] , \qquad (2.\mathrm{A}.10)$$

where

$$\boldsymbol{N}^p \left[\boldsymbol{N}^p \right]^\top = \left[\begin{array}{ccc|ccc} N^p_{11}N^p_{11} & N^p_{11}N^p_{22} & N^p_{11}N^p_{33} & 2N^p_{11}N^p_{12} & 2N^p_{11}N^p_{23} & 2N^p_{11}N^p_{13} \\ N^p_{22}N^p_{11} & N^p_{22}N^p_{22} & N^p_{22}N^p_{33} & 2N^p_{22}N^p_{12} & 2N^p_{22}N^p_{23} & 2N^p_{22}N^p_{13} \\ N^p_{33}N^p_{11} & N^p_{33}N^p_{22} & N^p_{33}N^p_{33} & 2N^p_{33}N^p_{12} & 2N^p_{33}N^p_{23} & 2N^p_{33}N^p_{13} \\ \hline 2N^p_{12}N^p_{11} & 2N^p_{12}N^p_{22} & 2N^p_{12}N^p_{33} & 4N^p_{12}N^p_{12} & 4N^p_{12}N^p_{23} & 4N^p_{12}N^p_{13} \\ 2N^p_{23}N^p_{11} & 2N^p_{23}N^p_{22} & 2N^p_{23}N^p_{33} & 4N^p_{23}N^p_{12} & 4N^p_{23}N^p_{23} & 4N^p_{23}N^p_{13} \\ 2N^p_{13}N^p_{11} & 2N^p_{13}N^p_{22} & 2N^p_{13}N^p_{33} & 4N^p_{13}N^p_{12} & 4N^p_{13}N^p_{23} & 4N^p_{13}N^p_{13} \end{array} \right] , \qquad (2.\mathrm{A}.11)$$

and

$$\boldsymbol{\mathcal{I}}^{\mathrm{dev}} = \frac{1}{3} \left[\begin{array}{ccc|ccc} 2 & -1 & -1 & 0 & 0 & 0 \\ -1 & 2 & -1 & 0 & 0 & 0 \\ -1 & -1 & 2 & 0 & 0 & 0 \\ \hline 0 & 0 & 0 & 6 & 0 & 0 \\ 0 & 0 & 0 & 0 & 6 & 0 \\ 0 & 0 & 0 & 0 & 0 & 6 \end{array} \right] . \qquad (2.\mathrm{A}.12)$$

Finally, the Voigt form of $\boldsymbol{\mathcal{H}}^d$ reads $\boldsymbol{\mathcal{H}}^d = \left[\left[\boldsymbol{\mathcal{Q}} \, \boldsymbol{N}^p \right]^\top \boldsymbol{\mathcal{H}} \left[\boldsymbol{\mathcal{Q}} \, \boldsymbol{N}^p \right] \right] \left[\boldsymbol{N}^p \left[\boldsymbol{N}^p \right]^\top \right]$.

2.A.2.   Algorithm

The staggered algorithmic treatment of the material model implementation is summarized in Algorithm 1. This approach shows required accuracy with sufficiently small stable time steps adapted in the dynamic-explicit finite element code.

Algorithm 1 Algorithmic treatment of the framework.

---

1. Initialize the matrix form of the structural tensor for the induced anisotropy with the 6×6 zero matrix $\mathcal{O}$:

$$\mathcal{O} \longrightarrow \mathcal{H}\,.$$

2. For the given strain increment $\Delta \boldsymbol{\varepsilon}$ compute the elastic trial state:

$$\Delta \boldsymbol{\varepsilon} \longrightarrow \Delta \boldsymbol{\varepsilon}^e\,,$$
$$\boldsymbol{S} + \boldsymbol{\mathcal{C}}^e\, \Delta \boldsymbol{\varepsilon}^e \longrightarrow \boldsymbol{S}\,,$$
$$\sqrt{[\boldsymbol{S} - \boldsymbol{X}]^\top\, [\boldsymbol{\mathcal{A}} - \boldsymbol{\mathcal{H}}]\, [\boldsymbol{S} - \boldsymbol{X}]} - \sigma_y\, (e^p, \dot{e}^p) \longrightarrow \phi^p.$$

3. **IF** $\phi^p < 0$ **THEN GOTO 4.**
   ELSE GOTO 5.

4. **Elastic Step:** Trial step does not need correction. **GOTO 2.**

5. **Elasto-Plastic Step:** Trial step needs correction. Apply the cutting-plane return mapping algorithm to update the elastic and inelastic solution dependent state variables including the equivalent plastic strain increment Δe^p and the plastic strain increment $\Delta \boldsymbol{\varepsilon}^p$ for $\dot{\boldsymbol{\mathcal{H}}} = \boldsymbol{\mathcal{O}}$.

6. Compute the normal $\boldsymbol{N}^p$ in the plastic flow direction:

$$\Delta \boldsymbol{\varepsilon}^p / |\Delta \boldsymbol{\varepsilon}^p| \longrightarrow \boldsymbol{N}^p.$$

7. Integrate $\boldsymbol{\mathcal{H}}$ with the incremental form of Equation (2.A.10):

$$[\boldsymbol{\mathcal{Q}}\, \boldsymbol{N}^p]^\top\, \boldsymbol{\mathcal{H}}\, [\boldsymbol{\mathcal{Q}}\, \boldsymbol{N}^p] \longrightarrow \boldsymbol{\mathcal{H}}^d$$
$$\boldsymbol{\mathcal{H}} - \boldsymbol{\mathcal{H}}^d \longrightarrow \boldsymbol{\mathcal{H}}^l$$
$$c_d \left[s_d \boldsymbol{N}^p\, [\boldsymbol{N}^p]^\top - \boldsymbol{\mathcal{H}}^d \right] \Delta e^p \longrightarrow \Delta \boldsymbol{\mathcal{H}}^d,$$
$$c_l \left[s_l \left[\boldsymbol{N}^p\, [\boldsymbol{N}^p]^\top - \boldsymbol{\mathcal{I}}^{\mathrm{dev}} \right] - \boldsymbol{\mathcal{H}}^l \right] \Delta e^p \longrightarrow \Delta \boldsymbol{\mathcal{H}}^l,$$
$$\Delta \boldsymbol{\mathcal{H}}^d + \Delta \boldsymbol{\mathcal{H}}^l \longrightarrow \Delta \boldsymbol{\mathcal{H}},$$
$$\boldsymbol{\mathcal{H}} + \Delta \boldsymbol{\mathcal{H}} \longrightarrow \boldsymbol{\mathcal{H}}.$$

8. **GOTO 2.**

---

3. The effect of yield surface curvature change by cross hardening on forming limit diagrams of sheets

In this chapter, clarification of the role of reduction in yield locus curvature on forming limit diagrams is aimed at. To this end, a cross-hardening model showing a reduction of yield surface curvature is used which accounts for dynamic and latent hardening effects associated with dislocation motion during loading. The model's three-dimensional tensorial as well as reduced plane-stress vector formulations are given. The first quadrants of forming limit diagrams are numerically produced using finite element models of the Marciniak-Kuczyński test with spatially correlated random defect distribution as localization triggering mechanism. The effect of cross hardening is investigated in detail. It is demonstrated that for plane strain loading path there occurs no difference in localization predictions of the models with and without cross hardening whereas for biaxial strain paths a delayed localization is observed in the cross hardening model as compared to the one without cross hardening effects. This is in accordance with the relative bluntness of the yield surface at the points of load path change towards localization. These results are complemented by Nakazima test simulations where similar observations are made.

3.1. Introduction

Process design for functional yet lightweight components requires an accurate description of the material behavior during deformation in order to fully exploit the potential of materials and processes. The finite-element-based modeling has proven to be an efficient way to predict the material and structural behavior and is nowadays standard in industrial practice. However, the applicability and benefits of simulation strongly depends on the accuracy of the underlying constitutive material model. With regard to complex forming simulations, the efficient modeling of sheet metals is of special interest. There exists a number of phenomenological models, e.g., accounting for isotropic and kinematic hardening, which accurately describe the material behavior of sheet metals under uniaxial deformation conditions. However, as stated by Wagoner et al. [323], the deformation in real forming processes involves a number of strain path changes requiring special attention which is more complex than a uniaxial strain or stress state. Therefore more complicated models are required to accurately model the loading-path dependent behavior of sheet metals in forming simulations. In this regard, the present or emergent underlying microstructure plays a crucial role. Physical based models are developed accounting for microstructural changes during complex deformation states, in particular orthogonal loading-path changes [298, 181, 254]. These, still phenomenological models, are often based on the evolution and distortion of one or two yield surfaces [173, 35]. A particular class of material models, interesting for this work, model the loading path dependent microstructure changes with one yield surface determined by an evolving anisotropy tensor [90, 181, 77, 245, 40, 36, 49].

Of particular interest for the design and optimization of forming processes is the formability limit[1]. Following the definition of Banabic [24], the formability describes the capability of a material to undergo plastic deformation to a given shape without defects. The probably mostly used theory is based on the early work by Marciniak and Kuczyński [201], where on basis of a geometrical inhomogeneity (e.g., thickness variation in a distinct region), the onset of strain localization, representing the initiation point of failure or necking, is obtained. The model by Marciniak and Kuczyński has been widely applied as well as modified to improve its applicability [133, 227, 150, 101, 152, 151, 193]. In addition to process parameters, formability inevitably depends on the material properties. For instance, in associative plasticity yield locus curvature affects the formability limits of the material. The over-stiffness of the associative J_2 plasticity theory in prediction of plastic instabilities under distinctly nonproportional stress histories is well known [303]. Tvergaard [303] shows that a better agreement with the experimental necking strains is obtained using pure kinematic hardening in which the yield surface curvature remains constant. The reason is linked to the yield surface curvature, which is reduced in isotropic hardening. In crystal plasticity the overall yield surface forms as an envelope of individual glide yield surfaces. Vertices and corners then naturally arise at the loading point due to sliding on favorably oriented glide planes. Unlike smooth yield theories, where a tangential component of the stress loading $d\boldsymbol{\sigma}_{\text{tangent}}$ does not cause a plastic flow, plastic flow occurs in vertex theories. For a given finite, nonproportional stress change, more strain change occurs for a yield surface with high curvature at the loading point than that occurs for the yield surface with lower curvature. A demonstration of the yield loci evolution for various plastic hardening models are given in Figure 3.1.
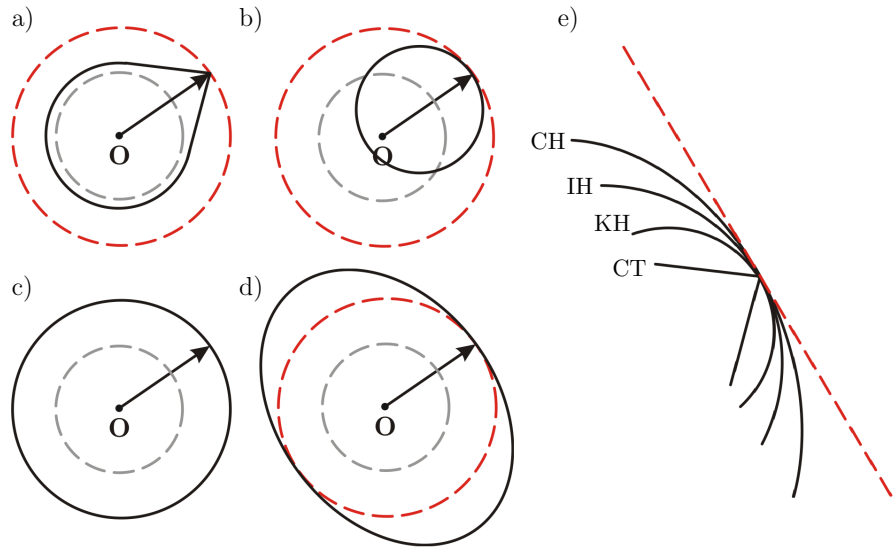
Figure 3.1.: A schematic depiction of yield locus evolution with different continuum theories: (a) corner theory (CT), (b) kinematic hardening (KH), (c) isotropic hardening (IH), (d) cross hardening (CH). (e) closer look at the yield locus curvature at the point of loading. As seen from corner theories to cross hardening the yield locus curvature systematically decreases. Gray dashed circles represent initial yield loci. Red dashed circles represent reference isotropic hardening yield loci. Red dashed line represents the limit $\rho \to \infty$ where ρ is the radius of curvature.

---

[1]Different types of forming limit diagrams exist, depending on the stress procedure [149, 201, 105, 227] and on the measure of limiting strain measures, e.g., necking or fracture.

As illustrated in Figure 3.1, cross hardening results in reduced yield locus curvature. This macroscopic response of the polycrystal is physically linked to the evolution of dislocation microstructure during plastic deformation [181]. For IF (interstitial free) steels, e.g., DC06, a cellular structure is formed by dislocations accumulating at cell boundaries under monotonic loading paths. In subsequent orthogonal paths, these dislocations structures act as obstacles for newly activated slip systems resulting in latent resistance to yielding and the hardening rate increase is named as cross hardening [49]. Contrary to Tvergaard's observations, which suggests a requirement for yield locus curvature increase in order to meet experimental necking strains, Levkovitch and Svendsen's cross-hardening model [181] signals an additional stiffness over the associative J_2 plasticity theory. Apart from the yield surface curvature, the strain rate sensitivity of the material strongly influences the formability as well. The studies [132, 103, 133] show that already a small strain-rate sensitivity shift the forming limit to larger strains which lead to better accordance with experiments. Inal et al. [136] employed a rate-sensitive polycrystal plasticity model to obtain FLDs based on the Marciniak-Kuczyński approach. Although the model allows the investigation of the strain-rate sensitivity, this study concentrates on the differences between face-centered-cubic (fcc) and body-centered-cubic (bcc) type slip systems. For fcc type materials a lower forming limit curvature is obtained due to a sharper yield locus compared to bcc type materials. Additionally, it is shown that texture evolution has a negligible effect. The study of Zhang et al. [353] clearly reveals that the formability is increasing for a rate-sensitive material, however, that the forming speed does not influence the material formability for the same rate-sensitive material. In a subsequent study of the same authors [354] two different approaches, one theoretical based on the Marciniak-Kuczyński model and one numerical based on the Marciniak test, are investigated with regard to strain hardening as well as strain rate sensitivity. An increasing formability is observed for an increase of both mechanisms.

With these motivations, in this study quantification of the gained stiffness with the change of the yield surface curvature is aimed at by investigating the stabilizing effect of the cross hardening on the flow localization predictions, a topic which is not documented in the literature so far. To this end, a reduced plane-stress viscoplastic formulation of Levkovitch-Svendsen's cross-hardening model is developed for thin shells and implemented as a user defined material subroutine into ABAQUS. Verification of the code is realized for finite-strain normal and small-strain shear loading scenarios for which analytical derivations are made available (see also [282]). The first quadrant of the forming limit diagram is numerically produced using a two-dimensional finite element model with a spatially correlated random defect distribution in the form of a reduction in yield strength reproducing the classical results by Marciniak and Kuczyński [201] (see also [227]). Additionally, the forming limit capabilities of the material are analyzed based on the Nakazima test [226]. These demonstrate the enhanced formability of the material with decreasing yield locus curvature with cross hardening relative to the classical J_2 flow theory.

3.2. Theory

3.2.1. Material Model - Tensor Notation

Considering small deformations, let the total strain tensor $\boldsymbol{\varepsilon} = 1/2 \left[\mathbf{Grad}\, \boldsymbol{u} + [\mathbf{Grad}\, \boldsymbol{u}]^\top \right]$ be additively split into elastic $\boldsymbol{\varepsilon}^e$ and plastic $\boldsymbol{\varepsilon}^p$ parts with $\boldsymbol{u}$ denoting the displacement vector. The stress $\boldsymbol{\sigma}$ is then computed from the stored elastic strain energy density $W = \frac{1}{2} \left[\boldsymbol{\varepsilon} - \boldsymbol{\varepsilon}^p \right] : \boldsymbol{\mathcal{C}}^e :$

$[\boldsymbol{\varepsilon} - \boldsymbol{\varepsilon}^p]$ viz.

$$\boldsymbol{\sigma} = \frac{\partial W(\boldsymbol{\varepsilon} - \boldsymbol{\varepsilon}^p)}{\partial \boldsymbol{\varepsilon}} = \boldsymbol{\mathcal{C}}^e : [\boldsymbol{\varepsilon} - \boldsymbol{\varepsilon}^p] \, , \tag{3.2.1}$$

where $\boldsymbol{\mathcal{C}}^e$ denotes the elastic constitutive tensor with

$$\boldsymbol{\mathcal{C}}^e := \frac{\partial^2 W(\boldsymbol{\varepsilon} - \boldsymbol{\varepsilon}^p)}{\partial \boldsymbol{\varepsilon}^2} = K \, \mathbf{1} \otimes \mathbf{1} + 2\mu \, \boldsymbol{\mathcal{I}}^{\text{dev}} = \text{constant}. \tag{3.2.2}$$

K represents the bulk modulus whereas μ is the shear modulus. $\boldsymbol{\mathcal{I}}^{\text{dev}}$ is the deviatoric part of the fourth-order symmetric identity tensor, $\boldsymbol{\mathcal{I}}^{\text{sym}} = 1/2\,[\mathbf{1}\overline{\otimes}\mathbf{1} + \mathbf{1}\underline{\otimes}\mathbf{1}]$, with $\boldsymbol{\mathcal{I}}^{\text{dev}} = \boldsymbol{\mathcal{I}}^{\text{sym}} - 1/3\,[\mathbf{1}\otimes\mathbf{1}]$. The flow stress of the material $\sigma_y\,(e^p, \dot{e}^p)$ depends on the equivalent plastic strain e^p and its rate $\dot{e}^p$. The contributions $h_y\,(e^p)$ and $r_y\,(\dot{e}^p)$ which are respectively associated with strain hardening and strain rate hardening are multiplied to give the total hardening following a Johnson–Cook type formulation [142]:

$$\sigma_y\,(e^p, \dot{e}^p) = h_y\,(e^p)\, r_y\,(\dot{e}^p) \, . \tag{3.2.3}$$

The multiplicative strain $h_y\,(e^p)$ and strain rate $r_y\,(\dot{e}^p)$ hardening components are defined as

$$\begin{aligned} h_y\,(e^p) &:= \sigma_\infty - [\sigma_\infty - \sigma_{y0}] \exp\left(-m\,[e^p]^n\right), \\ r_y\,(\dot{e}^p) &:= 1 + c\log\left(\dot{e}^p/\dot{e}^p_0\right), \end{aligned} \tag{3.2.4}$$

with σ_{y0}, σ_∞, c, n, m and $\dot{e}^p_0$ denoting material parameters. A single-surface elastic domain in the stress space

$$\mathbb{E}_{\boldsymbol{\sigma}} = \{[\boldsymbol{\sigma}, \boldsymbol{\chi}, \boldsymbol{\mathcal{H}}, e^p, \dot{e}^p] \in \mathbb{S} \times \mathbb{S} \times \mathbb{B} \times \mathbb{R}^+ \times \mathbb{R}^+ : \phi^p(\boldsymbol{\sigma}, \boldsymbol{\chi}, \boldsymbol{\mathcal{H}}, e^p, \dot{e}^p) \leq 0\} \, , \tag{3.2.5}$$

with the flow potential

$$\phi^p(\boldsymbol{\sigma}, \boldsymbol{\chi}, \boldsymbol{\mathcal{H}}, e^p, \dot{e}^p) = \sqrt{[\boldsymbol{\sigma} - \boldsymbol{\chi}] : [\boldsymbol{\mathcal{A}} + \boldsymbol{\mathcal{H}}] : [\boldsymbol{\sigma} - \boldsymbol{\chi}]} - \sigma_y\,(e^p, \dot{e}^p) \tag{3.2.6}$$

accounts for combined effects of isotropic, kinematic as well as cross hardening. Here, $\mathbb{S}$ denotes the vector space of symmetric second-order tensors with $\dim(\mathbb{S}) = 6$. Letting $\mathbb{D}$ denote the vector space of symmetric (major and minor) fourth-order tensors and $\dim(\mathbb{D}) = 21$ with $\mathcal{F}_{ijkl} = \mathcal{F}_{jikl} = \mathcal{F}_{ijlk} = \mathcal{F}_{klij}$ for $\boldsymbol{\mathcal{F}} \in \mathbb{D}$, the vector space of symmetric fourth-order tensors which are also deviatoric projections is represented by $\mathbb{B}$ with $\dim(\mathbb{B}) = 15$ with $\mathcal{F}'_{iikl} = 0$ for $\boldsymbol{\mathcal{F}}' \in \mathbb{B}$. While $\boldsymbol{\chi}$ denotes the back-stress controlling the translation of the yield surface, the fourth-order structural tensors (constant) $\boldsymbol{\mathcal{A}}$ and (nonconstant) $\boldsymbol{\mathcal{H}}$ are associated with its initial and evolving form, respectively. The current visco-plastic formulation is referred to as a consistency type visco-plastic formulation, see, e.g., [326], hence during fully developed plastic flow the consistency condition is satisfied, i.e., $\phi^p = 0$.

The plastic flow rule is assumed to be associative and hence it reads

$$\dot{\boldsymbol{\varepsilon}}^p = \dot{e}^p \frac{\partial \phi^p}{\partial \boldsymbol{\sigma}} \, . \tag{3.2.7}$$

The kinematic hardening evolution is modeled with a variant of the Armstrong–Frederick form via

$$\dot{\boldsymbol{\chi}} = c_x\, \dot{e}^p\, [s_x \boldsymbol{n}^p - \boldsymbol{\chi}] \, , \tag{3.2.8}$$

where c_x and s_x are associated with the saturation rate and magnitude with the back-stress tensor $\boldsymbol{\chi}$. Here, $\boldsymbol{n}^p$ denotes the direction of plastic flow with $\boldsymbol{n}^p = \dot{\boldsymbol{\varepsilon}}^p / |\dot{\boldsymbol{\varepsilon}}^p|$. A generalized plastic work equivalence defines the equivalent plastic strain rate via

$$\dot{e}^p = \frac{[\boldsymbol{\sigma} - \boldsymbol{\chi}] : \dot{\boldsymbol{\varepsilon}}^p}{\sigma_y} \,. \tag{3.2.9}$$

The shape change of the yield surface is controlled by using the projections of $\boldsymbol{\mathcal{H}}$ parallel ($\boldsymbol{\mathcal{H}}^d$) and orthogonal ($\boldsymbol{\mathcal{H}}^l$) to $\boldsymbol{n}^p$ in the rate expression of $\boldsymbol{\mathcal{H}}$ viz.

$$\dot{\boldsymbol{\mathcal{H}}}/\dot{e}^p = c_d \left[s_d \, \boldsymbol{n}^p \otimes \boldsymbol{n}^p - \boldsymbol{\mathcal{H}}^d \right] + c_l \left[s_l \left[\boldsymbol{\mathcal{I}}^{\text{dev}} - \boldsymbol{n}^p \otimes \boldsymbol{n}^p \right] - \boldsymbol{\mathcal{H}}^l \right] \,, \tag{3.2.10}$$

where

$$\boldsymbol{\mathcal{H}}^d = [\boldsymbol{n}^p : \boldsymbol{\mathcal{H}} : \boldsymbol{n}^p] \, [\boldsymbol{n}^p \otimes \boldsymbol{n}^p] \quad \text{and} \quad \boldsymbol{\mathcal{H}}^l = \boldsymbol{\mathcal{H}} - \boldsymbol{\mathcal{H}}^d \,. \tag{3.2.11}$$

The former accounts for growth due to dynamic and the latter due to latent hardening effects. Here, c_d and s_d represent the saturation rate and magnitude associated with $\boldsymbol{\mathcal{H}}^d$, respectively. Analogously, c_l and s_l are the saturation rate and magnitude associated with $\boldsymbol{\mathcal{H}}^l$. For the sake of completeness, Kuhn-Tucker loading/unloading (complementarity) conditions read

$$\dot{e}^p \geq 0, \ \phi^p(\boldsymbol{\sigma}, \boldsymbol{\chi}, \boldsymbol{\mathcal{H}}, e^p, \dot{e}^p) \leq 0, \ \dot{e}^p \phi^p(\boldsymbol{\sigma}, \boldsymbol{\chi}, \boldsymbol{\mathcal{H}}, e^p, \dot{e}^p) = 0 \,, \tag{3.2.12}$$

and the consistency condition is given as

$$\dot{e}^p \dot{\phi}^p(\boldsymbol{\sigma}, \boldsymbol{\chi}, \boldsymbol{\mathcal{H}}, e^p, \dot{e}^p) = 0 \,. \tag{3.2.13}$$

3.3. Reduced Plane-Stress Formulation - Vector Notation

In this part, constrained plane-stress equations are presented in the sense that the plane-stress condition is automatically enforced. To this end, the plane-stress subspace $\widehat{\mathbb{S}} \subset \mathbb{S}$ is defined as

$$\widehat{\mathbb{S}} := \{ \boldsymbol{\sigma} \in \mathbb{S} : \sigma_{13} = \sigma_{23} = \sigma_{33} \equiv 0 \} \,, \tag{3.3.1}$$

with $\dim(\widehat{\mathbb{S}}) = 3$. In addition, the subspace of deviatoric symmetric second-order tensors $\widehat{\mathbb{S}}^{\text{dev}} \subset \mathbb{S}$ with $\dim(\widehat{\mathbb{S}}^{\text{dev}}) = 3$ is defined as

$$\widehat{\mathbb{S}}^{\text{dev}} := \{ \boldsymbol{\sigma} \in \mathbb{S} : \sigma_{13} = \sigma_{23} \equiv 0, \operatorname{tr}(\boldsymbol{\sigma}) \equiv 0 \} \,. \tag{3.3.2}$$

In reduced plane-stress space implementation, 3×1 vectors and 3×3 matrices are used for the representation of symmetric second-order tensors and fourth-order tensors with at least minor-symmetries. The vector form of the reduced plane-stress space representation of the stress tensor $\widehat{\boldsymbol{\sigma}}$ reads $\widehat{\boldsymbol{\sigma}} = \left[\sigma_{11}, \sigma_{22}, \sqrt{2}\sigma_{12} \right]^\top$. The mapping $\widehat{\boldsymbol{\mathcal{I}}}^{\text{dev}} : \widehat{\mathbb{S}} \to \widehat{\mathbb{S}}^{\text{dev}}$ links the stress tensor $\widehat{\boldsymbol{\sigma}} \in \widehat{\mathbb{S}}$ and its deviator $\operatorname{dev}(\widehat{\boldsymbol{\sigma}}) \in \widehat{\mathbb{S}}^{\text{dev}}$ with $\operatorname{dev}(\widehat{\boldsymbol{\sigma}}) = \widehat{\boldsymbol{\mathcal{I}}}^{\text{dev}} \cdot \widehat{\boldsymbol{\sigma}}$ where

$$\widehat{\boldsymbol{\mathcal{I}}}^{\text{dev}} = \frac{1}{3} \begin{bmatrix} 2 & -1 & 0 \\ & 2 & 0 \\ \text{sym.} & & 3 \end{bmatrix} \,. \tag{3.3.3}$$

Note that $\widehat{\boldsymbol{\mathcal{I}}}^{\text{dev}} \neq [\widehat{\boldsymbol{\mathcal{I}}}^{\text{dev}}]^n$ for $n > 1$ and $\widehat{\boldsymbol{\mathcal{I}}}^{\text{dev}}$ is invertable, i.e., $\det(\widehat{\boldsymbol{\mathcal{I}}}^{\text{dev}}) \neq 0$. Let $\widehat{\boldsymbol{\varepsilon}} \in \mathbb{S}$ denote the strain vector which only collects the in-plane components with $\widehat{\boldsymbol{\varepsilon}} = \left[\varepsilon_{11}, \varepsilon_{22}, \sqrt{2}\varepsilon_{12} \right]^\top$.

Additivity of the total strain tensor into elastic $\widehat{\varepsilon}^e$ and plastic $\widehat{\varepsilon}^p$ parts viz. $\widehat{\varepsilon} = \widehat{\varepsilon}^e + \widehat{\varepsilon}^p$ is assumed. For both $\widehat{\varepsilon}^e$ and plastic $\widehat{\varepsilon}^p$ the same stencil applies. The rate of stress tensor is then computed by $\dot{\widehat{\sigma}} = \widehat{\mathcal{C}}^e \cdot \dot{\widehat{\varepsilon}}^e$ where for the plane-stress case $\widehat{\mathcal{C}}^e$ reads

$$\widehat{\mathcal{C}}^e = \frac{E}{1-\nu^2} \begin{bmatrix} 1 & \nu & 0 \\ & 1 & 0 \\ \text{sym.} & & 1-\nu \end{bmatrix}. \tag{3.3.4}$$

$\widehat{\chi} = \begin{bmatrix} \chi_{11}, \chi_{22}, \sqrt{2}\chi_{12} \end{bmatrix}^\top$ constitutes the vector representation for the kinematic hardening stress-like tensor $\widehat{\chi} \in \mathbb{S}^{\text{dev}}$. The definition $\widehat{\xi} := \widehat{\sigma} - \overline{\chi}$ is introduced, noting that $\overline{\chi} = [\widehat{\mathcal{I}}^{\text{dev}}]^{-1} \cdot \widehat{\chi} \in \widehat{\mathbb{S}}$. Accordingly, the plastic flow potential ϕ^p which accounts for isotropic-, kinematic- and cross-hardening is given as

$$\phi^p := \sqrt{\widehat{\xi} \cdot [\widehat{\mathcal{A}} + \widehat{\mathcal{H}}] \cdot \widehat{\xi}} - \sigma_y(e^p, \dot{e}^p) \leq 0. \tag{3.3.5}$$

In above, $\widehat{\mathcal{A}}$ and $\widehat{\mathcal{H}}$ denote the reduced plane-stress versions of the initial Hill-48-type [122] and the evolving 3×3 flow anisotropy matrices, respectively, with

$$\widehat{\mathcal{A}} = \begin{bmatrix} \mathcal{A}_{1111} & \mathcal{A}_{1122} & \sqrt{2}\mathcal{A}_{1112} \\ & \mathcal{A}_{2222} & \sqrt{2}\mathcal{A}_{2212} \\ \text{sym.} & & 2\mathcal{A}_{1212} \end{bmatrix} \text{ and } \widehat{\mathcal{H}} = \begin{bmatrix} \mathcal{H}_{1111} & \mathcal{H}_{1122} & \sqrt{2}\mathcal{H}_{1112} \\ & \mathcal{H}_{2222} & \sqrt{2}\mathcal{H}_{2212} \\ \text{sym.} & & 2\mathcal{H}_{1212} \end{bmatrix}. \tag{3.3.6}$$

This notation leads to the following matrix form of the Hill-48-type structural tensor

$$\widehat{\mathcal{A}} = \begin{bmatrix} G+H & -H & 0 \\ & F+H & 0 \\ \text{sym.} & & N \end{bmatrix}, \tag{3.3.7}$$

where F, G, H and N are parameters associated with plastic anisotropy which are related to the Lankford's coefficients r_0, r_{45} and r_{90} with

$$F = \frac{r_0}{r_{90}[1+r_0]}, \quad G = \frac{1}{[1+r_0]}, \quad H = \frac{r_0}{[1+r_0]}, \quad N = \frac{1}{2}\frac{[r_0+r_{90}][1+2r_{45}]}{r_{90}[1+r_0]}. \tag{3.3.8}$$

In reduced plane-stress space, the vector norm of deviatoric tensors should be treated with care due to possible nonzero out-of-plane components. For the reduced deviatoric $\widehat{\varepsilon}^p$ the following identities hold for the quadratic forms in between the tensor and vector notations

$$\varepsilon^p : \varepsilon^p = \overline{\varepsilon}^p \cdot \widehat{\mathcal{I}}^{\text{dev}} \cdot \overline{\varepsilon}^p = \widehat{\varepsilon}^p \cdot [\widehat{\mathcal{I}}^{\text{dev}}]^{-1} \cdot \widehat{\varepsilon}^p \quad \text{and} \quad n^p : \mathcal{H} : n^p = \overline{n}^p \cdot \widehat{\mathcal{H}} \cdot \overline{n}^p, \tag{3.3.9}$$

where $\overline{\varepsilon}^p = [\widehat{\mathcal{I}}^{\text{dev}}]^{-1} \cdot \widehat{\varepsilon}^p$ and $\overline{n}^p = [\widehat{\mathcal{I}}^{\text{dev}}]^{-1} \cdot \widehat{n}^p$. The reduced evolution equation of the flow anisotropy tensor reads

$$\dot{\widehat{\mathcal{H}}}/\dot{e}^p = c_d[s_d \, \widehat{n}^p \otimes \widehat{n}^p - \widehat{\mathcal{H}}^d] + c_l[s_l[\widehat{\mathcal{I}}^{\text{dev}} - \widehat{n}^p \otimes \widehat{n}^p] - \widehat{\mathcal{H}}^l], \tag{3.3.10}$$

with

$$\widehat{n}^p \otimes \widehat{n}^p = \begin{bmatrix} n_{11}^p n_{11}^p & n_{11}^p n_{22}^p & \sqrt{2}n_{11}^p n_{12}^p \\ & n_{22}^p n_{22}^p & \sqrt{2}n_{22}^p n_{12}^p \\ \text{sym.} & & 2n_{12}^p n_{12}^p \end{bmatrix}, \tag{3.3.11}$$

where

$$\widehat{\mathcal{H}}^d = [\overline{n}^p \cdot \widehat{\mathcal{H}} \cdot \overline{n}^p] [\widehat{n}^p \otimes \widehat{n}^p] \quad \text{and} \quad \widehat{\mathcal{H}}^l = \widehat{\mathcal{H}} - \widehat{\mathcal{H}}^d. \tag{3.3.12}$$

In Figure 3.2 the evolution of the yield loci for various strain paths for an initially isotropic material are given using the presented theory for the case of plane-stress. In this analysis any further hardening source except latent hardening are switched off. It is clearly seen that for each case the yield locus curvature at the point of loading decreases. This behavior is contrary to what is generally observed in metallic materials showing vertex formation, which gives relatively reduced formability limits [292, 219, 218]. In the subsequent pages the influence of this curvature decrease on material stability is investigated making use of basic formability tests.
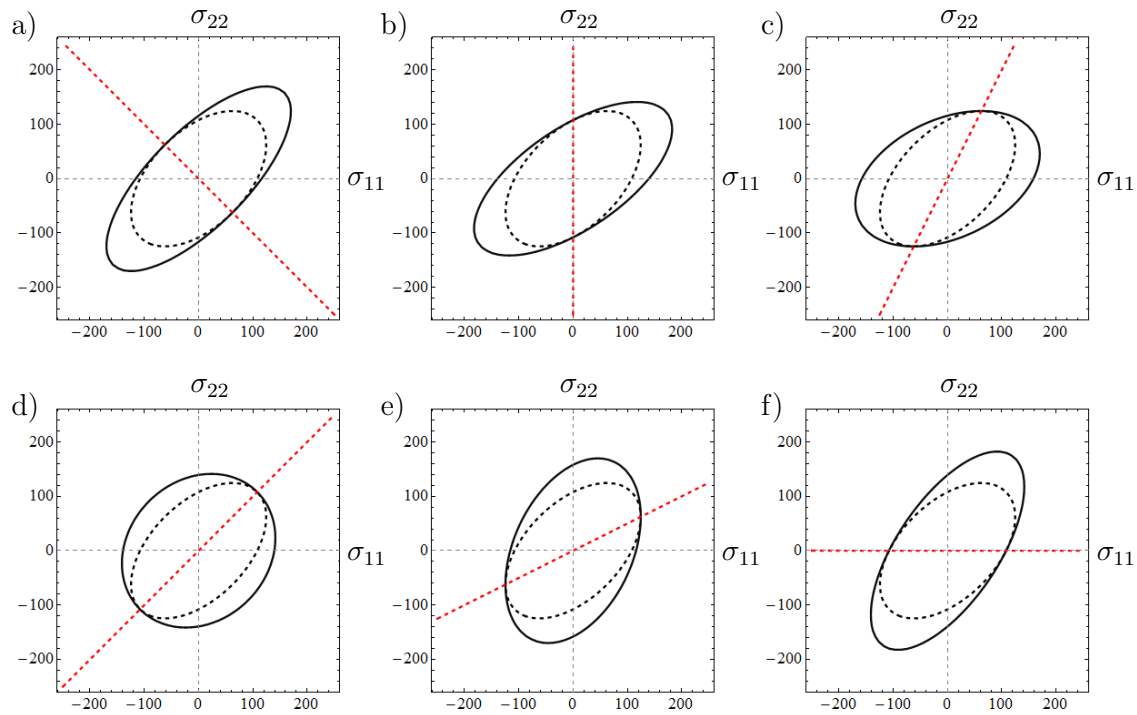
Figure 3.2.: Plane-stress yield loci evolution for various loading paths. Dashed curves refer to the initial yield loci whereas black curves refer to the current one after deformation under a linear strain (stress) path marked by the dashed red line; (a) pure shear, (b) uniaxial tension-compression, (c) plane strain tension-compression, (d) equibiaxial tension-compression, (e) plane strain tension-compression, (f) uniaxial tension-compression. In all cases the yield locus curvature at the point of loading decreases. This is governed principally by the rotation and the aspect ratio change of the representing ellipses. For the pure shear and equibiaxial stress paths, no rotation of the ellipse axes takes place.

3.4. Algorithmic Formulation and Verification of the Implementation

In this part, the return mapping algorithm used to define the state variables at the end of loading step $n + 1$, that is $[\bullet]^{\langle n+1 \rangle}$, using the state variables at the end of loading step n, that is $[\bullet]^{\langle n \rangle}$, through a strain driven framework using a cutting plane algorithm is summarized [239]. To this end, the flow potential is linearize around the current values of variables viz.

$$\dot{\phi}^p_{\langle k+1 \rangle} \simeq \dot{\phi}^p_{\langle k \rangle} + \widehat{\boldsymbol{r}}_{\langle k \rangle} \cdot \delta \widehat{\boldsymbol{\sigma}}_{\langle k \rangle} + \overline{\boldsymbol{s}}_{\langle k \rangle} \cdot \delta \overline{\boldsymbol{\chi}}_{\langle k \rangle} + \widehat{\boldsymbol{\mathcal{D}}}_{\langle k \rangle} : \delta \widehat{\boldsymbol{\mathcal{H}}}_{\langle k \rangle} + \varsigma_{\langle k \rangle} \delta e^p_{\langle k \rangle} + \vartheta_{\langle k \rangle} \delta \dot{e}^p_{\langle k \rangle} \,, \tag{3.4.1}$$

with k denoting the iteration number and $\widehat{\boldsymbol{r}} = \partial \phi^p / \partial \widehat{\boldsymbol{\sigma}}$, $\overline{\boldsymbol{s}} = \partial \phi^p / \partial \overline{\boldsymbol{\chi}}$, $\widehat{\boldsymbol{\mathcal{D}}} = \partial \phi^p / \partial \widehat{\boldsymbol{\mathcal{H}}}$, $\varsigma = \partial \phi^p / \partial e^p$ and $\vartheta = \partial \phi^p / \partial \dot{e}^p$ where

$$\sigma_y \, \widehat{\boldsymbol{r}} = [\widehat{\boldsymbol{\mathcal{A}}} + \widehat{\boldsymbol{\mathcal{H}}}] \cdot \widehat{\boldsymbol{\xi}} \,, \tag{3.4.2}$$

$$\overline{\boldsymbol{s}} = -\widehat{\boldsymbol{r}} \,, \tag{3.4.3}$$

$$\sigma_y \, \widehat{\boldsymbol{\mathcal{D}}} = [\widehat{\boldsymbol{\mathcal{I}}}^{\mathrm{dev}} \cdot \widehat{\boldsymbol{\xi}}] \otimes [\widehat{\boldsymbol{\mathcal{I}}}^{\mathrm{dev}} \cdot \widehat{\boldsymbol{\xi}}] = [\mathrm{dev}(\widehat{\boldsymbol{\sigma}}) - \widehat{\boldsymbol{\chi}}] \otimes [\mathrm{dev}(\widehat{\boldsymbol{\sigma}}) - \widehat{\boldsymbol{\chi}}] \,, \tag{3.4.4}$$

$$\varsigma = -h'_y r_y \,, \tag{3.4.5}$$

$$\vartheta = -h_y r'_y \,. \tag{3.4.6}$$

Using $\widehat{\boldsymbol{n}}_{\langle k \rangle} = \widehat{\boldsymbol{r}}_{\langle k \rangle} / \sqrt{\widehat{\boldsymbol{r}}_{\langle k \rangle} \cdot [\widehat{\boldsymbol{\mathcal{I}}}^{\mathrm{dev}}]^{-1} \cdot \widehat{\boldsymbol{r}}_{\langle k \rangle}}$, the increments within iterations read

$$\delta \widehat{\boldsymbol{\sigma}}_{\langle k \rangle} / \delta e^p_{\langle k \rangle} = -\widehat{\boldsymbol{\mathcal{C}}}^e \cdot \widehat{\boldsymbol{r}}_{\langle k \rangle} \,, \tag{3.4.7}$$

$$\delta \overline{\boldsymbol{\chi}}_{\langle k \rangle} / \delta e^p_{\langle k \rangle} = c_x [\widehat{\boldsymbol{\mathcal{I}}}^{\mathrm{dev}}]^{-1} \cdot [s_x \widehat{\boldsymbol{n}}^p_{\langle k \rangle} - \widehat{\boldsymbol{\chi}}_{\langle k \rangle}] \,, \tag{3.4.8}$$

$$\delta \widehat{\boldsymbol{\mathcal{H}}}_{\langle k \rangle} / \delta e^p_{\langle k \rangle} = c_d \left[s_d \widehat{\boldsymbol{n}}^p_{\langle k \rangle} \otimes \widehat{\boldsymbol{n}}^p_{\langle k \rangle} - \widehat{\boldsymbol{\mathcal{H}}}^d_{\langle k \rangle} \right] + c_l \left[s_l \left[\widehat{\boldsymbol{\mathcal{I}}}^{\mathrm{dev}} - \widehat{\boldsymbol{n}}^p_{\langle k \rangle} \otimes \widehat{\boldsymbol{n}}^p_{\langle k \rangle} \right] - \widehat{\boldsymbol{\mathcal{H}}}^l_{\langle k \rangle} \right] \,, \tag{3.4.9}$$

$$\delta \dot{e}^p_{\langle k \rangle} / \delta e^p_{\langle k \rangle} \simeq 1/\Delta t \,. \tag{3.4.10}$$

Iterations are started by defining $[\bullet]_{\langle 0 \rangle} := [\bullet]^{\langle n \rangle}$. Using the notation $\widehat{\boldsymbol{g}}_{\langle k \rangle} := c_x [s_x \widehat{\boldsymbol{n}}^p_{\langle k \rangle} - \widehat{\boldsymbol{\chi}}_{\langle k \rangle}]$ and $\widehat{\boldsymbol{\mathcal{Y}}}_{\langle k \rangle} := \delta \widehat{\boldsymbol{\mathcal{H}}}_{\langle k \rangle} / [\delta e^p_{\langle k \rangle} \sigma_{y \langle k \rangle}]$ the increment of equivalent plastic strain is computed at each iteration by

$$\delta e^p_{\langle k \rangle} = \frac{\dot{\phi}^p_{\langle k \rangle}}{\widehat{\boldsymbol{r}}_{\langle k \rangle} \cdot \widehat{\boldsymbol{\mathcal{C}}}^e \cdot \widehat{\boldsymbol{r}}_{\langle k \rangle} + \widehat{\boldsymbol{r}}_{\langle k \rangle} \cdot [\widehat{\boldsymbol{\mathcal{I}}}^{\mathrm{dev}}]^{-1} \cdot \widehat{\boldsymbol{g}}_{\langle k \rangle} - \widehat{\boldsymbol{\mathcal{D}}}_{\langle k \rangle} : \widehat{\boldsymbol{\mathcal{Y}}}_{\langle k \rangle} - \varsigma_{\langle k \rangle} - \vartheta_{\langle k \rangle}/\Delta t} \,. \tag{3.4.11}$$

Iterations are continued to update the state variables using $[\bullet]_{\langle k+1 \rangle} = [\bullet]_{\langle k \rangle} + \delta [\bullet]_{\langle k \rangle}$ until $\phi^p \leq$ TOL. The converged state gives the solution at the end of the loading step $n + 1$ with $[\bullet]^{\langle n+1 \rangle} = [\bullet]_{\langle k+1 \rangle}$ where the increments read $\Delta [\bullet] = [\bullet]^{\langle n+1 \rangle} - [\bullet]^{\langle n \rangle}$. The out-of-plane strain increment is then defined using $\Delta \widehat{\varepsilon}_{33} \equiv \Delta \widehat{\varepsilon}^e_{33} + \Delta \widehat{\varepsilon}^p_{33}$ and $\Delta \widehat{\boldsymbol{\varepsilon}}^p = \Delta e^p \, \widehat{\boldsymbol{r}}$ viz.

$$\Delta \widehat{\varepsilon}^e_{33} = -\frac{\nu}{1 - \nu} [\Delta \widehat{\varepsilon}^e_{11} + \Delta \widehat{\varepsilon}^e_{22}] \,, \text{ and } \Delta \widehat{\varepsilon}^p_{33} = -[\Delta \widehat{\varepsilon}^p_{11} + \Delta \widehat{\varepsilon}^p_{22}] \,. \tag{3.4.12}$$

Here ν denotes elastic Poisson's ratio. The developed algorithm is implemented as a VUMAT user defined material subroutine in ABAQUS. A comparison of the implementation via Voigt and Mandel vector notation are given in Appendix 3.A. Appendix 3.B presents the extension to finite strains of the presented small strain theory.

3.4.1. Verification of the Implementation

The implementation is verified using two problems: finite strain in-plane loading with non-rotating principal axes of deformation and small strain in-plane shear loading. The numerical solutions with single element tests are compared with fully analytical derivations which appear in the literature for the first time.

3.4.1.1. Finite Strain In-Plane Loading with Non-rotating Axes of Deformation

Rigid plasticity is assumed with $[\varepsilon_{11}, \varepsilon_{22}, \varepsilon_{33}]^\top \simeq [\varepsilon_{11}^p, \varepsilon_{22}^p, \varepsilon_{33}^p]^\top$. Strain controlled loading is applied where the in-plane strains in $x-$ and $y-$directions are defined and the out-of-plane strain is found using the other two using the assumptions of isochoric plastic flow. Only strictly proportional strain paths are considered, that is $\alpha = d\varepsilon_{11}/d\varepsilon_{22} = \varepsilon_{11}/\varepsilon_{22}$. Hence, the total strain vector $\boldsymbol{\varepsilon}$ reads $\boldsymbol{\varepsilon} = [\alpha, 1, -1 - \alpha]^\top$. The mentioned in-plane loading condition with non-rotating axis of deformation allows an immediate integration of the structural tensor to give the following normal components for $s_d = 0$ (see [282] for more details)

$$\mathcal{H}_{1111}\left(\gamma\right) = s_l f_{c_l} \left[\frac{2}{3} - \frac{\alpha^2}{2[1 + \alpha + \alpha^2]}\right], \tag{3.4.13}$$

$$\mathcal{H}_{1122}\left(\gamma\right) = s_l f_{c_l} \left[-\frac{1}{3} - \frac{\alpha}{2[1 + \alpha + \alpha^2]}\right], \tag{3.4.14}$$

$$\mathcal{H}_{2222}\left(\gamma\right) = s_l f_{c_l} \left[\frac{2}{3} - \frac{1}{2[1 + \alpha + \alpha^2]}\right], \tag{3.4.15}$$

where $f_{c_l}(\gamma) = 1 - \exp(-c_l\,\gamma)$. In this $xy-$plane loading, the shear component H_{1212} also evolves with

$$\mathcal{H}_{1212}\left(\gamma\right) = \frac{s_l}{2}\left[1 - \exp\left(-c_l\gamma\right)\right], \tag{3.4.16}$$

for $s_d = 0$. A comparison of the analytical derivation and the numerical result of a single element test is given in Figure 3.3 where a perfect agreement is observed.

3.4.1.2. Small Strain In-Plane Shear Loading

Assuming small shear strains in the $xy-$plane, the only nonzero strain components become $\varepsilon_{12}^p = \varepsilon_{21}^p$. This allows deriving the following expression for H_{1212} for $s_d \neq 0$ through integration

$$\mathcal{H}_{1212}\left(\gamma\right) = \frac{s_d}{2}\left[1 - \exp\left(-c_d\gamma\right)\right]. \tag{3.4.17}$$

A perfect agreement is observed for the comparison of the analytical derivation and the numerical result of a single element test in Figure 3.3.
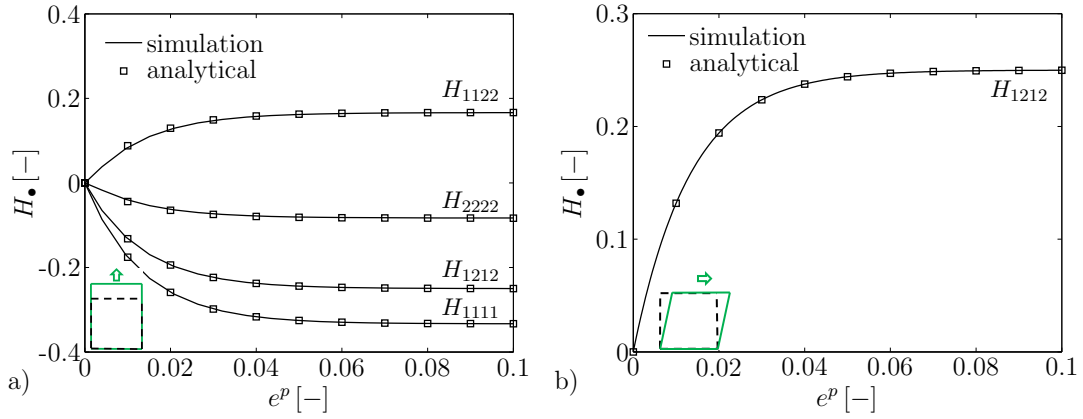
Figure 3.3.: Comparison of analytical and numerical results for the evolving structural tensor $\mathcal{H}$ components for (a) normal loading case with finite strain assumption, (b) shear loading case with small strain assumption. Both the normal loading and shear loading cases used parameters are listed in Table 8.3 with one exception that in the shear test $s_d = 0.5$ is used.

3.5.   Applications - Formability Analyses

In this section the formability prediction of cross hardening plasticity in comparison to non-cross hardening material models is presented. The section starts with a Marciniak-Kuczyński-type of analyses where a biaxial loading of a defected rectangular plate is analyzed under various strain paths to form the first quadrant of the forming limit diagram. Unlike conventional Marciniak-Kuczyński test which uses an oriented groove in the model, randomly distributed and spatially correlated defects are considered to trigger localization. The second application problem consists of the Nakazima test where a sheet with various cut geometries is stretched with a punch moving perpendicular to the plane of the sheet. Both formability analyses are realized using the finite element method. Both analyses show that with the decrease of yield locus curvature, cross hardening plasticity predicts a later localization and therefore an increase in formability.

In the analyses, the parameter set listed in Table 8.3 is used unless otherwise stated. In order to purely concentrate on the cross hardening effects, the rate parameter is chosen to yield vanishing rate dependence. With selecting Lankford's coefficients as $r_0 = r_{45} = r_{90} = 1$ initial plastic isotropy is assumed.

Table 3.1.: Material parameters, representing approximately steel.

Parameter	Symbol	Value	Dimension
Elastic constants	μ	69.6	[GPa]
	K	150.8	[GPa]
Isotropic hardening constants	σ_{y0}	132.2	[MPa]
	σ_{∞}	324.0	[MPa]
	m	6.6	[−]
	n	1	[−]
	$r_y\left(\dot{e}^p\right)$	1	[−]
Kinematic hardening constants	s_x	56.0	[MPa]
	c_x	33.1	[−]
Lankford's coeffcients	r_0	1	[−]
	r_{45}	1	[−]
	r_{90}	1	[−]
Cross hardening constants	s_d	0.0	[−]
	c_d	23.9	[−]
	s_l	−0.9	[−]
	c_l	87.3	[−]

3.5.1.   Marciniak-Kuczyński test simulations

The formability of the metallic sheets is determined by a localized through-thickness neck formation along a zero-extension direction which is often preceded by a diffuse neck. For the loading states involving two positive in-plane strains, however, no zero extension direction exists. Based on experimental results regarding strain localization, it was concluded by Marciniak and Kuczyński [201] that failure or necking is mostly initiated by geometrical or structural inhomogeneities. Hence, for the localization to develop in the first quadrant of the forming limit diagram, presence of imperfections was postulated to be responsible in Marciniak-Kuczyński
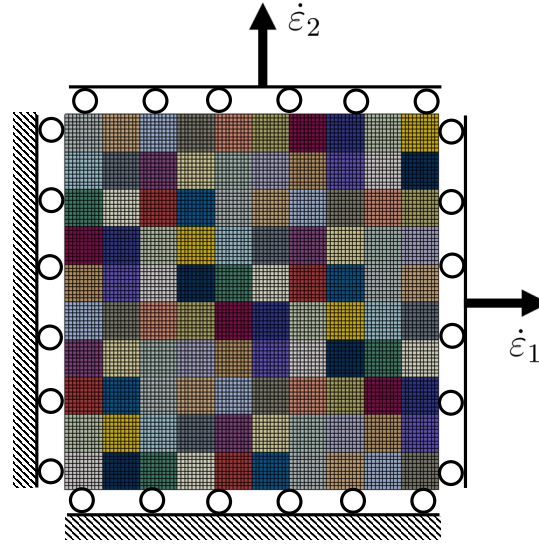
Figure 3.4.: Finite element analysis of the Marciniak-Kuczyński test: Simulation set-up representing the metal sheet/plate, a 2-dimensional $[0, L] \times [0, L]$ domain. True strain rates ($\dot{\varepsilon}_1$, $\dot{\varepsilon}_2$) are applied to load the plate under biaxial in-plane loading conditions. The strain rates are adjusted according to the investigated strain paths. The sample is subdivided into 100 cells with aspect ratio of 1:1. For each of these cells the average major, minor and equivalent plastic strain rates ($\dot{\varepsilon}_2$, $\dot{\varepsilon}_1$, $\dot{e}_p$) are calculated which are used for evaluation of the different formability criteria.

theory. The original Marciniak-Kuczyński analysis is, in order to allow fast analytical or semi-analytical solutions, based on two simplifying assumptions: 1) The defect considered is infinite in length. 2) Boundary conditions are assigned considering constant bulk stress paths [322]. A joint use of the finite element method with stochastically generated material defect distribution makes it possible to avoid these over-simplifications, hence allow a more realistic production of the forming limit diagrams. Figure 3.4.(a) shows the simulation set-up for the Marciniak-Kuczyński test. The plate is loaded under biaxial in-plane loading conditions considering totally six true strain (rate) ratios $\dot{\varepsilon}_2/\dot{\varepsilon}_1 \in \{0, 0.2, 0.4, 0.6, 0.8, 1.0\}$ which allows plotting forming limit diagram points corresponding to the first quadrant ($\dot{\varepsilon}_2$ serves as major strain rate.). For post processing reasons the specimen is subdivided into 10×10 different cells with aspect ratio $1 : 1$. The chosen discretization and subdivision prevent any sensitivity of the FEM results (see [227]).

In the model proposed by Marciniak and co-workers [201, 202], a thickness variation in a distinct region as geometrical inhomogeneity is introduced. The necking or failure behavior is analyzed on basis of the principal strains in these two regions of different thicknesses of the specimen subjected to a biaxial stress state. Using finite element analysis, Narasimhan and Wagoner [227] suggested three simple criteria to identify the point of failure of such specimens to determine the formability capabilities of the material on basis of the ratio of the major or minor principal strain rates or the effective strain rates of both regions. A random initial yield stress distribution is accounted for with a given correlation where the total yield stress distribution function is assumed to be

$$\sigma_{y0}(\boldsymbol{r}) = \sigma_{y0,u} + \sigma \, \widetilde{X}_{\boldsymbol{r}} \,, \tag{3.5.1}$$

where σ is the standard deviation of the yield stress which is superimposed over the base uniform yield stress distribution $\sigma_{y0,u}$. $\{\widetilde{X}_{\boldsymbol{r}}\}$ represents a stationary Gaussian random field with zero

mean and unit variance generated on each of the grid points $\{(i,j)/n, i = 0, 1, \ldots, n-1, j = 0, 1, \ldots, n-1\}$ corresponding to a Gaussian covariance function of the form

$$\mathrm{Cov}(\widetilde{X}_{\boldsymbol{r}}, \widetilde{X}_{\boldsymbol{s}}) = \phi(\boldsymbol{r} - \boldsymbol{s}) = \exp\left(\frac{-|\boldsymbol{r} - \boldsymbol{s}|^2}{L_c^2}\right). \tag{3.5.2}$$

Here, $\boldsymbol{r}$ and $\boldsymbol{s}$ represent position vectors with $|\boldsymbol{r} - \boldsymbol{s}|^2 = [r_1 - s_1]^2 + [r_2 - s_2]^2$ and with L_c corresponding to the (isotropic) correlation length. Using $L_c = L/10$, 12 realizations of the stationary Gaussian random field $\{\widetilde{X}_{\boldsymbol{r}}\}$ with $\mathcal{N}[0,1]$ are produced as shown in Figure 3.5. The statistics of each realization is given in Table 3.2. Details of the method of generation the random field distribution with a given correlation are given in the Appendices.
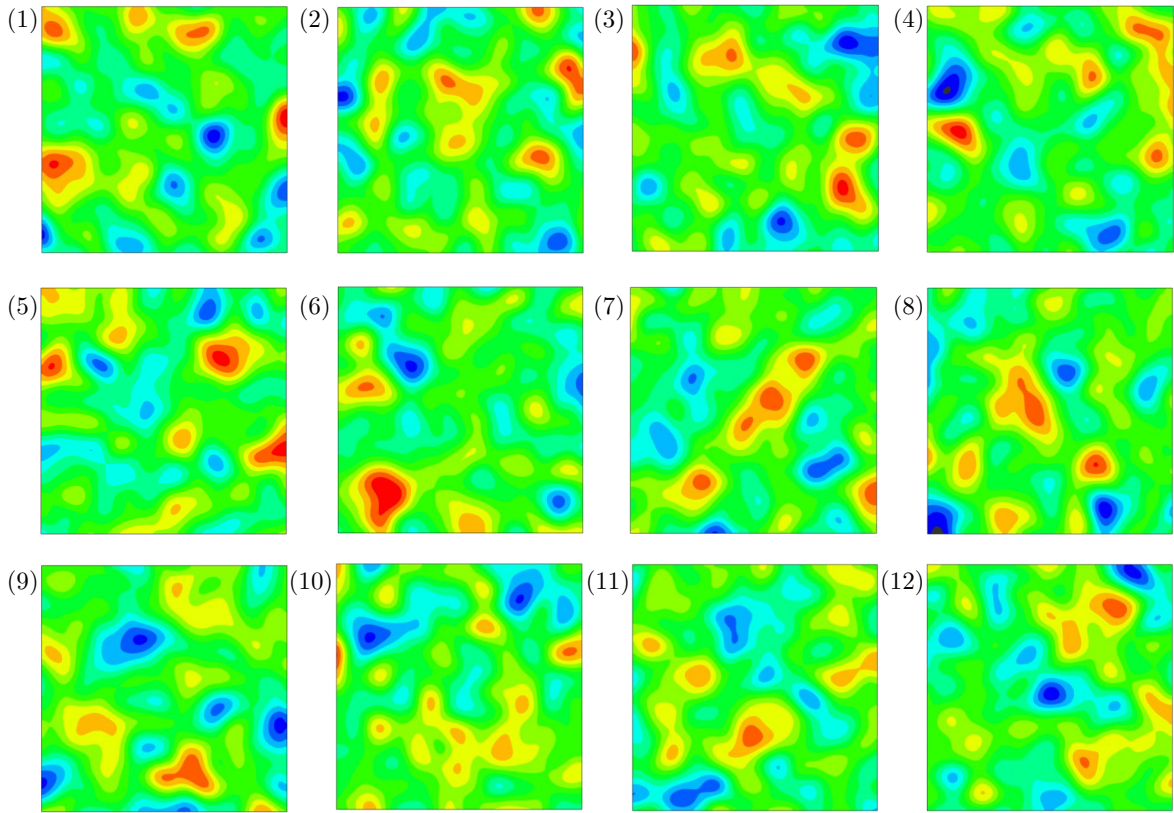
Figure 3.5.: 12 realizations of the stationary Gaussian random field $\{\widetilde{X}_{\boldsymbol{r}}\}$ with $\mathcal{N}[0,1]$, i.e., zero mean and unit variance. Correlation length of $L_c = L/10$ for the 2-dimensional $[0,L] \times [0,L]$ domain. (max,min)=(3.25, −3.25). Yield stress distributions are then computed using $\sigma_{y0}(\boldsymbol{r}) = \sigma_{y0,u} + \sigma\, \widetilde{X}_{\boldsymbol{r}}$, Equation (3.5.1), with $\sigma_{y0,u} = 132.19$ MPa and $\sigma = 2.5\% \times \sigma_{y0,u} \simeq 3.305$ MPa as the standard deviation of the yield stress distribution. The statistics of each realization are given in Table 3.2.

The previous described discretization into cells of the finite element model (see Figure 3.4.(b) is advantageous for the post-calculation of an appropriate failure criteria in stochastic simulations as the results no longer depend on the choice of one specific element for the evaluation of the failure criteria. For the following criteria, the different strain rates are averaged for each cell. Following Narasimhan and Wagoner[227], three criteria on basis of different strain rates are adopted. Additionally a criterion on basis of the stress is introduced. The first criterion, the

Table 3.2.: Statistics of each realization shown in Figure 3.5.

ID	mean	std.dev.=[variance]$^{1/2}$
1	0.0041	0.9873
2	−0.0107	0.9908
3	−0.0010	1.0122
4	−0.0018	1.0105
5	0.0077	0.1003
6	0.0104	0.9869
7	0.0101	0.9888
8	0.0159	1.0075
9	−0.0006	1.0153
10	0.0244	0.9778
11	−0.0119	0.9873
12	−0.0209	1.0027

major strain rate criterion $c_{\dot{\varepsilon}_2}$,

$$c_{\dot{\varepsilon}_2} = \frac{\text{largest major strain rate } (\dot{\varepsilon}_2) \text{ in one cell}}{\text{smallest major strain rate } (\dot{\varepsilon}_2) \text{ in one cell}} \geq 10 = c_{\dot{\varepsilon}_2,\text{threshold}}\,, \qquad (3.5.3)$$

calculates the ratio of largest major strain rate to smallest major strain rate in one of the different cells. As strain localization occurs very localized in one or only a few cells, the largest major strain rate is present in the cell of localization. This is usually happening in the weakest point of the sheet, here determined by the lowest yield strength within the specimen. On the other hand, a strain rate similar to the smallest strain rate is found in the remaining cells. As soon as a characteristic threshold $c_{\dot{\varepsilon}_2,\text{threshold}}$ is reached, the point of flow localization can be identified. The second criterion, the minor strain criterion $c_{\dot{\varepsilon}_1}$, reads as:

$$c_{\dot{\varepsilon}_1} = \frac{\text{largest minor strain rate } (\dot{\varepsilon}_1) \text{ in one cell}}{\text{smallest minor strain rate } (\dot{\varepsilon}_1) \text{ in one cell}} \geq 10 = c_{\dot{\varepsilon}_1,\text{threshold}}\,. \qquad (3.5.4)$$

This criterion fails under plane strain loading as $\dot{\varepsilon}_{1,\text{min}} = 0$. The third strain rate criterion $(c_{\dot{e}^p})$ is based on the equivalent plastic strain rate:

$$c_{\dot{e}^p} = \frac{\text{largest equivalent plastic strain rate } (\dot{e}^p) \text{ in one cell}}{\text{smallest equivalent plastic strain rate } (\dot{e}^p) \text{ in one cell}} \geq 4 = c_{\dot{e}^p,\text{threshold}}\,. \qquad (3.5.5)$$

As noted by [227], these three criteria show typically little variance of identifying the corresponding strains at strain localization. In addition to these three criteria, a new effective stress criterion, c_σ, is proposed which does not require local information of the structure, rather the information at the boundary. This criterion reads:

$$c_\sigma = \text{true effective stress}\left(\sqrt{\sigma_1^2 + \sigma_2^2}\right) \leq c_{\sigma,\text{threshold}} = 0.98\,\sigma_{\text{max}} \quad \text{and} \quad \dot{\sigma} \leq 0\,. \qquad (3.5.6)$$

It identifies the strain localization on basis of a negative stress rate in combination with a reduction of the stress by a certain percentage, here 2%, from its maximum value.

Calculations with the 12 realizations of the stationary Gaussian random field $\{\widetilde{X}_r\}$ with $\mathcal{N}[0,1]$ as shown in Figure 3.5 were performed for each of the strain ratios for the cross-hardening plasticity model. Figures 3.6 and 3.7 show, for a selected random initial yield stress distribution, the evolution of localized equivalent plastic strains under two strain paths: plane strain tension and equibiaxial tension. Both localization patterns are strongly influenced by the underlying initial yield stress distribution. In both cases the deformation bands initiate at points where the hardening source is exhausted. These correspond to regions with relatively lower initial yield stresses, the so-called defected regions. The responses for both strain paths show different characteristics. In plane strain tension, localization initiates at much earlier strains and the band develops orthogonal to the loading direction. Since localized neck occurs along a zero extension direction, this shows that in plane strain tension no path change occurs in the band during loading. Hence, in absence of loading path change, there is no effect of yield locus curvature on the localization. In the biaxial loading case, this is not the case. Prior to localized necking, the loading path is characterized by two positive in-plane strains. During neck development, there occurs a continuous strain path change from equibiaxial to plane strain to create a zero extension direction along the localization band. For an associated plastic flow, the local curvature of the yield locus at the loading point, thus, affects the response of the sheet. For lower local curvature due to cross hardening plasticity then leads to a more stable material response where the rotation of the normal becomes relatively harder. This observation is valid for all biaxial tensile loading paths with $\dot{\varepsilon}_2/\dot{\varepsilon}_1 > 0$. Moreover, as compared to the plane strain loading path the point of localization initiation is delayed. The final pattern does not emerge as a single band which traverses the whole domain but rather branches into secondary bands.
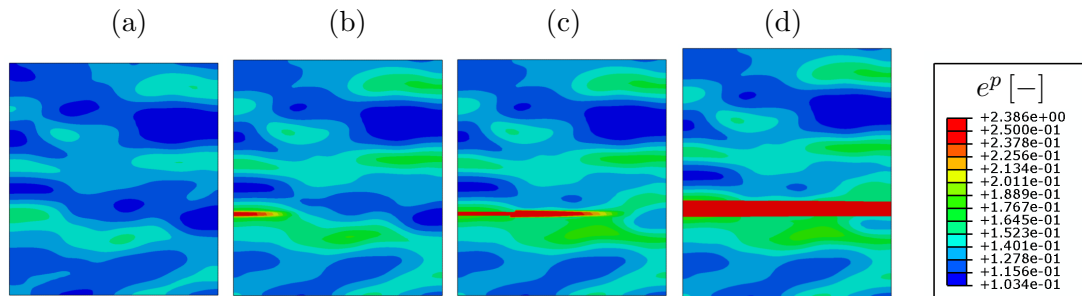
Figure 3.6.: Marciniak-Kuczyński test simulations, cross-hardening plasticity model: Evolution of localized plastic strain e^p in metal sheet with random defect distribution realization 5 (see Figure 3.5) at strains (a) $\varepsilon_2 = 0.116$, (b) $\varepsilon_2 = 0.127$, (c) $\varepsilon_2 = 0.133$, (d) $\varepsilon_2 = 0.191$, under plane strain loading. In the plane strain loading condition the band emerges orthogonal to the loading direction.

The response of the different criteria, normalized w.r.t. to the corresponding threshold value is shown in Figure 3.8. As for plane strain loading, the minor strain criterion fails as expected. All remaining three criteria predict a fairly similar value for the localization strain ε_2. For equibiaxial stretching, the equivalent strain rate predicts localization as first, followed by the major strain rate criteria and minor strain rate criterion. The stress criteria detects the localization at last. However, the differences are still rather small, all four criteria are acceptable for the identification of the material formability. In the following, the results are shown for the equivalent plastic strain rate criterion $c_{\dot{e}^p}$.

Figure 3.9 summarizes emerging localization patterns for different loading conditions. Due to the stochastic defect distribution, the resulting localization patterns are complex as the nucleation
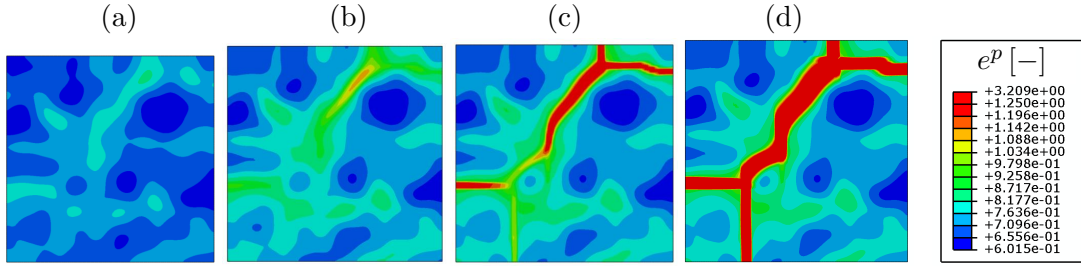
Figure 3.7.: Marciniak-Kuczyński test simulations, cross-hardening plasticity model: Evolution of localized equivalent plastic strain e^p in metal sheet with random defect distribution realization 5 (see Figure 3.5) at strains (a) $\varepsilon_2 = 0.405$, (b) $\varepsilon_2 = 0.462$, (c) $\varepsilon_2 = 0.477$, (d) $\varepsilon_2 = 0.507$, under equibiaxial stretching. In the equibiaxial loading condition, a diagonal band initiation is followed by band branching/merging. Considerably higher strain values at localization are observed as compared to plane strain loading.
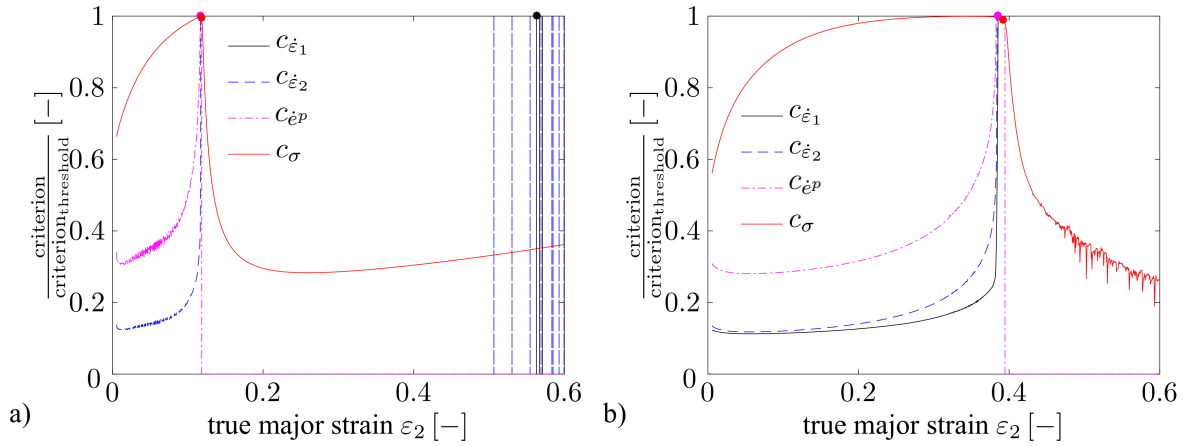
Figure 3.8.: Marciniak-Kuczyński test simulations, cross-hardening plasticity model: Normalized prediction of material formability by major strain rate criterion ($c_{\dot{\varepsilon}_2}$), minor strain rate criterion ($c_{\dot{\varepsilon}_1}$), equivalent plastic strain rate criterion $c_{\dot{e}^p}$ and stress criterion c_σ for (a) plane strain loading and (b) equibiaxial stretching. All criteria are normalized by its corresponding threshold value $c_{\bullet,threshold}$. The minor strain criterion fails for plane strain loading. Otherwise, all four criteria predict a similar formability.

might simultaneously occur at several positions in the specimen. The figures clearly show the relative localization tolerance of the plate to the applied loading path: least formability is observed in the plane strain loading case whereas most formability is recorded for the case of equibiaxial loading. Also, as anticipated, in the absence of loading path change in the band, there is no effect of yield locus curvature on the localization for plane strain loading case. Thus, in plane strain loading path, identical responses for the models with and without cross hardening are recorded.

The resulting first quadrant of the forming limit diagram obtained from the Marciniak-Kuczyński test for different simulation cases are displayed in Figure 3.10. Results for cross hardening plasticity and non-cross hardening material models are shown for 12 realizations for each loading path. In total, the figure includes the results of $12 \times 6 \times 2 = 144$ simulations. A critical amount of localization needs to be recorded in the stochastic simulations before the criteria detect the material formability limit. The results with cross-hardening (cross) and non-cross-hardening
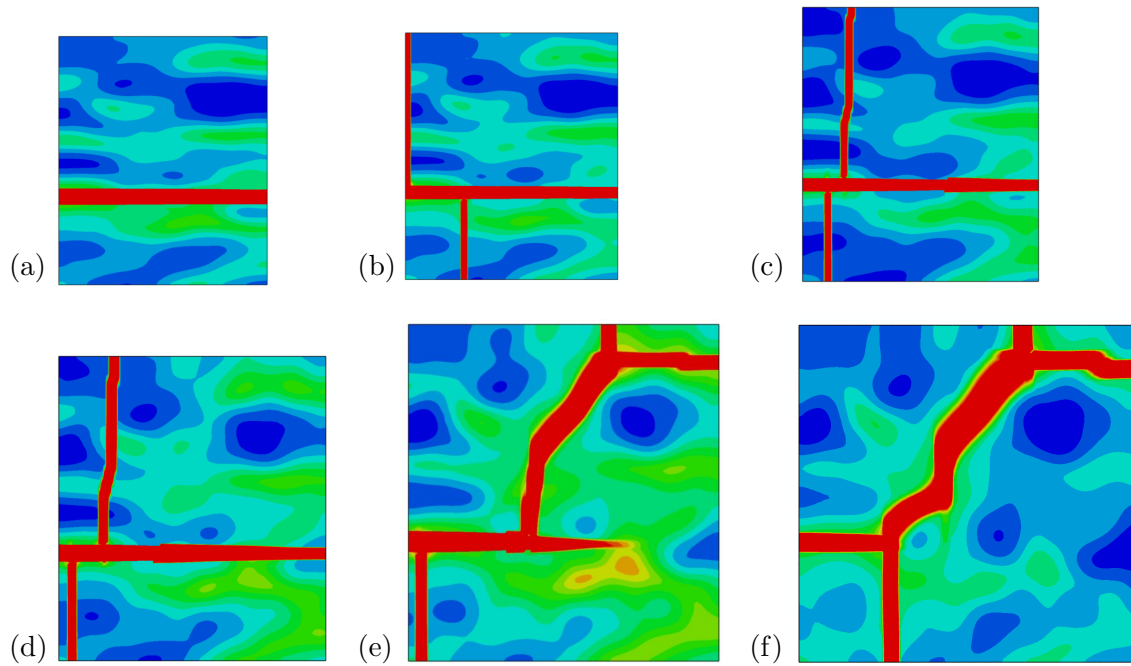
Figure 3.9.: Marciniak-Kuczyński test simulations, cross-hardening plasticity model: Final plastic strain e^p localization patterns in metal sheet with random defect distribution realization 5 (see Figure 3.5) under various loading conditions: (a) Strain ratio of $\dot{\varepsilon}_2/\dot{\varepsilon}_1 = 0$ at $\varepsilon_2 = 0.191$; (b) Strain ratio of $\dot{\varepsilon}_2/\dot{\varepsilon}_1 = 0.2$, at $\varepsilon_2 = 0.209$; (c) Strain ratio of $\dot{\varepsilon}_2/\dot{\varepsilon}_1 = 0.4$, at $\varepsilon_2 = 0.284$; (d) Strain ratio of $\dot{\varepsilon}_2/\dot{\varepsilon}_1 = 0.6$, at $\varepsilon_2 = 0.391$; (e) Strain ratio of $\dot{\varepsilon}_2/\dot{\varepsilon}_1 = 0.8$, at $\varepsilon_2 = 0.484$; (f) Strain ratio of $\dot{\varepsilon}_2/\dot{\varepsilon}_1 = 1.0$, at $\varepsilon_2 = 0.507$. The results show the effect of the stochastic distribution of defects. With increasing strain rate ratio, the formability increases.

(non-cross) material models have overlaps due to the effect of varying defect sizes in different realizations, however, the mean curves show a clear separation. For the plane strain path, both models predict the same formability as anticipated. For all other strain paths, the results demonstrate the improved formability due to cross-hardening. The explanation is the local curvature of the yield locus at the loading point whose decrease impedes the rotation of the normal for associated plastic flow and thus increases the stability. Figure 3.10 shows that for all biaxial tensile loading paths with $\dot{\varepsilon}_2/\dot{\varepsilon}_1 > 0$ this observation preserves validity where the curvature effect of the cross hardening plasticity gets more pronounced as the ratio $\dot{\varepsilon}_2/\dot{\varepsilon}_1 \leq 1$ gets higher.
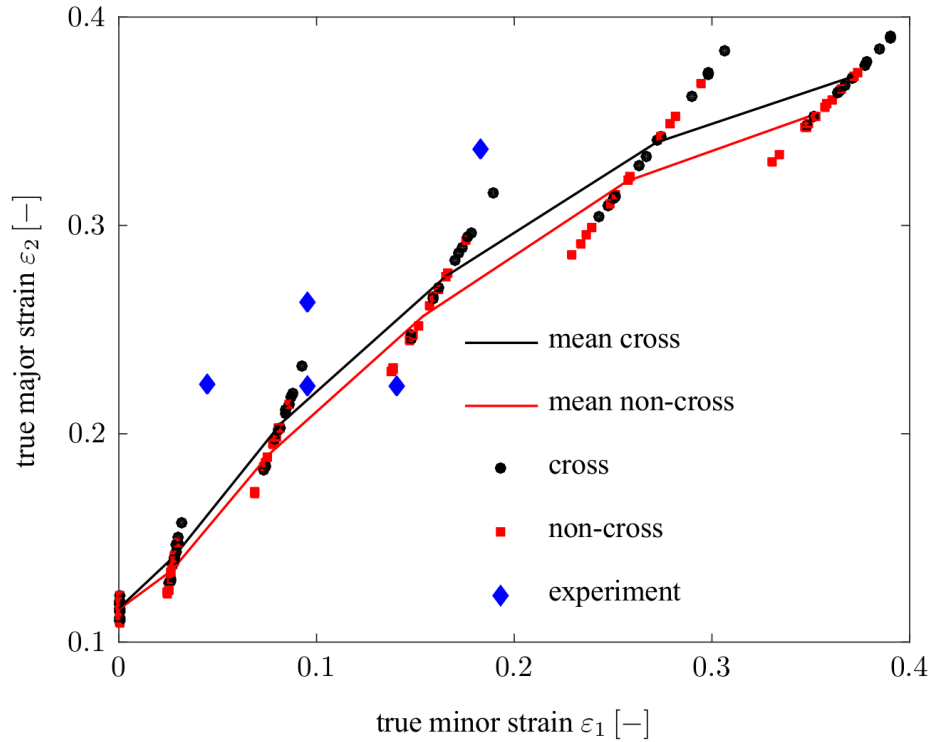
Figure 3.10.: Marciniak-Kuczyński test simulations: First quadrant of forming limit diagram for Marciniak-Kuczyński test with stochastic distribution of defects (12 distributions for each loading path) with cross-hardening (cross) as well as without cross-hardening plasticity model (non-cross). The markers (black circles and red squares) show the obtained single values on the forming limit diagram curve in the different stochastic simulations. The scattering is increasing from plane strain tension to equibiaxial stretching for both model responses where the direction of the scattering is related to the loading path only. The mean curve represents the average of all stochastic simulations. For a stochastic distribution a critical amount of local localization has to be present in one cell before these are recognized globally as formability limit. The simulated strains of the forming limit diagram are compared with experimental results for IF tailor welded blanks from [264] indicating that the numerical results are at the correct order of formability of such steels.

3.5.2. Nakazima Test Simulations

As a second application problem, Nakazima tests are performed to identify the formability of the material for different stress states [226]. The test set-up is similar to deep-drawing where the metal sheet is deformed using a hemispherical punch moving perpendicular to the plane of the sheet. Different stress states are achieved by using metal sheets with different cut geometries. The geometry of the metal sheet is shown in Figure 3.11a) where circles of different radii are cut from the entire blank leading to strongly waisted blanks (see Figure 3.12). Depending on the cutting radius, loading conditions reaching from a equibiaxial stretching to a uniaxial tensile loading are achievable.
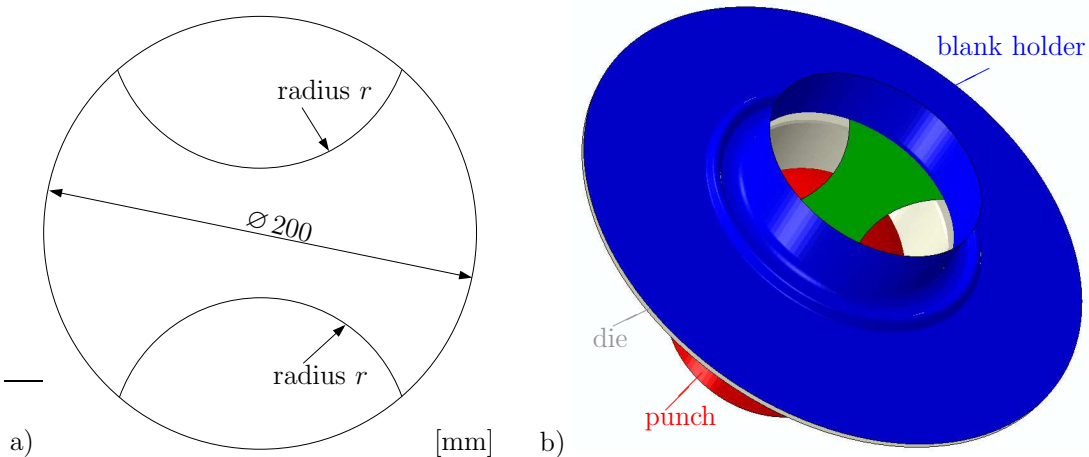
Figure 3.11.: Nakazima test simulations: (a) Geometry of the sheet. From the circular blank, radii of different radius r are cut out. Different radii are used to achieve different stress states. (b) Complete simulation set-up of Nakazima Test, involving hemispherical punch, blank holder and die. The contact between punch and blank is assumed to be as frictionless where the contact between blank and die as well as blank holder is modeled via Coulomb friction with a friction coefficient $\mu = 0.1$. In a first step, the blank holder is pressed against the die to clamp the blank between die and blank holder. In the next step, the punch moves perpendicular to the blank plane at a constant velocity.

The full simulation set-up is illustrated in Figure 3.11.(b). The contact conditions play a crucial role in the Nakazima test. Coulomb friction with a friction coefficient $\mu = 0.1$ is assumed between blank and die as well as blank and blank holder where the contact between punch and blank is modeled frictionless to minimize the influence on the formability prediction. The sliding motion of the sheet is prevented using a draw-bead which is located at $R = 66$ mm and which has a radius of $r_\mathrm{d} = 1.5$ mm. The simulation consists of two consecutive steps. First, the blank is clamped by pressing the blank holder against the die. Afterwards, the punch moves at a constant velocity perpendicular to the blank plane. The investigated specimen geometries with its mesh discretizations are illustrated in Figure 3.12. The specimen with $r = 0$ mm represents a equibiaxial loading case where for $r = 85$ mm a uniaxial tensile loading is achieved. Since uniformity of the emerging fields is not the case, there is no need for an additional localization triggering mechanism, hence material parameters are assumed to be uniformly distributed. Thus, no additional defects are present in the metal sheet.

Figure 3.13 exemplary shows the distribution of equivalent plastic strain after strain localization

$r = 0\,\mathrm{mm}$ $\qquad\qquad$ $r = 45\,\mathrm{mm}$ $\qquad\qquad$ $r = 65\,\mathrm{mm}$ $\qquad\qquad$ $r = 85\,\mathrm{mm}$
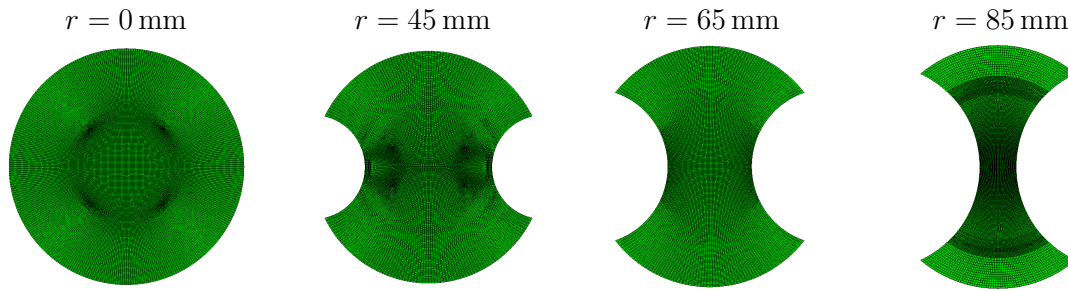
Figure 3.12.: Nakazima test simulations: Mesh discretization of sheets with different cut geometries used in the Nakazima test simulations. The full blank represents equibiaxial loading case where the most waisted blank is representative for simple tensile loading.

$u = 46.2\,\mathrm{mm}$ $\qquad\qquad\qquad\qquad$ $u = 31.4\,\mathrm{mm}$

a) $\qquad\qquad\qquad\qquad\qquad\qquad$ b)

$u = 25.9\,\mathrm{mm}$ $\qquad\qquad\qquad\qquad$ $u = 23.9\,\mathrm{mm}$

c) $\qquad\qquad\qquad\qquad\qquad\qquad$ d)
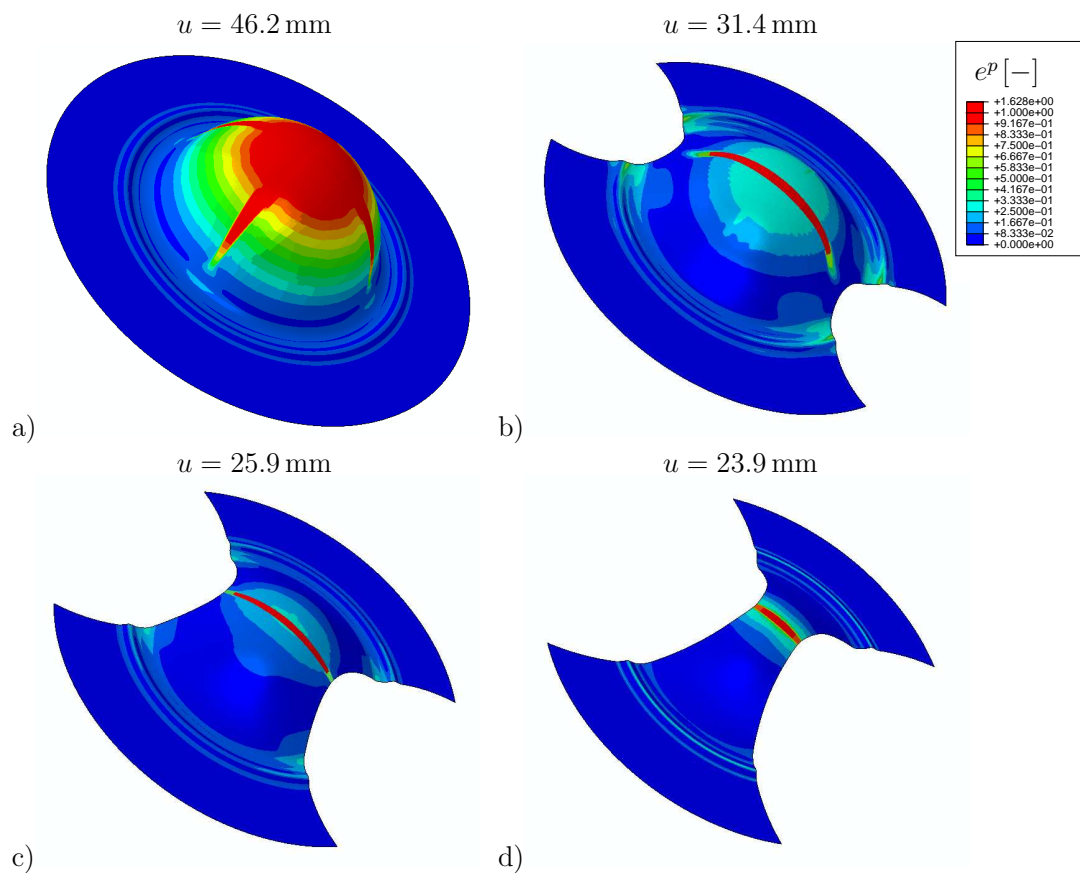
Figure 3.13.: Nakazima test simulations: Distribution of equivalent plastic strain for sheets with different cut geometries. The distribution of the plastic strain e^p shows the fully developed localization patterns which form depending on the stress stage/loading path invoked by the cut geometries. A more uniaxial loading stage (d) results in an earlier localization. The force drop in the simulation, indicating the formability capabilities, is observed at an earlier displacement.

occurred in the different investigated specimens. The different loading cases are clearly captured by the localization patterns. As expected, the reduction of material and more uniaxial loading leads to an earlier localization phenomena at the center region of the specimen.

To analyze the behavior of the different specimens and material models (cross-hardening vs.
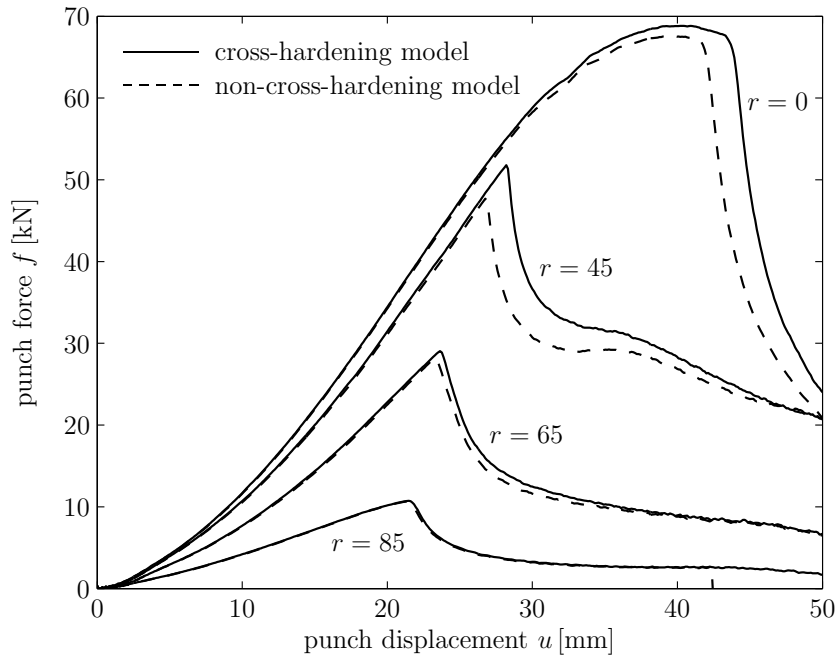
Figure 3.14.: Nakazima test simulations: Punch force f vs. punch displacement u for four different cut geometries with radii r (see Figure 3.12). The force and displacement are only representing the component in vertical direction, perpendicular to the plane of the sheet. The force drop indicates the start of localization and the corresponding strain represents the formability limit. For uniaxial tensile loading, both material models predict the same behavior, as cross-hardening is not influencing yield surface curvature in this loading direction.

non-cross-hardening model) quantitatively, Figure 3.14 displays the punch force over the punch displacement of the different simulation cases. Strain localization goes along with the decrease of the required punch force in loading direction. The punch force increases with decreasing cutting radius r as well as localization occurs at a larger displacement. The difference between both material models is significant for smaller cutting radii where the cross-hardening model predicts a significant improved formability. For $r = 85$ mm no difference is notable which perfectly fits with the theoretical expectation. As seen already from the Marciniak-Kuczyński results (see Figure 3.10), for plane strain loading no deviation between both material models is notable as the yield curvature is the same for this point of loading (see results in Soyarslan et al. [282] as well). The case of uniaxial tension is located in the second quadrant of the forming limit diagram for which both models are predicting identical values as cross-hardening is only relevant for loading paths orthogonal to the primary loading direction due to the evolving dislocation structure perpendicular to the loading (latent hardening). As the biaxiality of the loading increases the difference in the formability predictions increases which is visible in the Nakazima test simulations as well.

3.6. Conclusion

In this chapter the role of reduction in the yield locus curvature associated with cross hardening on the shape of the forming limit diagrams in the first quadrant is investigated. For this purpose, Levkovitch-Svendsen's cross-hardening model is used [181] with an assumption of initial material isotropy. A reduced plane-stress formulation is developed and implemented as a user defined

material subroutine into Abaqus. The implementation is verified for finite-strain normal and small-strain shear loading scenarios for which analytical derivations are presented. The formability analyses use finite element models of the stochastic Marciniak-Kuczyński and Nakazima tests. As anticipated, decrease of the yield locus curvature with cross hardening relative to the classical J_2 flow theory results in an enhanced formability of the material. More specifically, observed major and minor strains at localization in the Marciniak-Kuczyński tests are higher in the first quadrant except for the plane strain path where there is no path change on the course of localization. For the Nakazima tests, recorded punch displacements at maximum recorded punch forces, which could be identified as the point of localization, are higher with cross hardening plasticity as compared to J_2 flow theory. This strongly hints towards a significant increase of formability for cross hardening steel sheets in process chains.

3.A. Voigt and Mandel Vector Notations - A Comparison

In Chapter 1, and [49], the Voigt notation was introduced in formulation of the framework. Voigt notation vectorizes strain-like and stress-like tensors differently. Vector forms of strain-like tensors use the stencil $\begin{bmatrix} 1 & | & 2 \end{bmatrix}^\top$ whereas for stress-like tensors the stencil $\begin{bmatrix} 1 & | & 1 \end{bmatrix}^\top$ is used. Relating strain-like and stress-like vectors, as in the case of Armstrong-Frederick-type rate form, then requires a transformation operator $\mathcal{Q}$ which for the case of 3D reads

$$\mathcal{Q} = \frac{1}{2} \begin{bmatrix} 2 & 0 & 0 & 0 & 0 & 0 \\ & 2 & 0 & 0 & 0 & 0 \\ & & 2 & 0 & 0 & 0 \\ & & & 1 & 0 & 0 \\ & & & & 1 & 0 \\ \text{sym.} & & & & & 1 \end{bmatrix}. \tag{3.A.1}$$

Similar to vectors, the matrix forms of the fourth-order tensors used in the quadratic forms $\boldsymbol{x} : \boldsymbol{\mathcal{C}} : \boldsymbol{x}$ differ. If $\boldsymbol{x}$ is of type strain, the matrix form of $\boldsymbol{\mathcal{C}}$ uses the stencil $\left[\begin{array}{c|c} 1 & 1 \\ \hline 1 & 1 \end{array} \right]$. Otherwise $\left[\begin{array}{c|c} 1 & 2 \\ \hline 2 & 4 \end{array} \right]$ is used.

In this chapter the Mandel notation is utilized since it allows a more elegant and transparent scheme through a unique mapping in between vector and tensor forms. The most important point is that one does not have to distinguish in between the strain-like and stress-like variables since in the current formulation both uses the stencil $\begin{bmatrix} 1 & | & \sqrt{2} \end{bmatrix}^\top$. This is especially important where rates of strain-like variables are functions of stress-like variables, e.g., as in the case of the Armstrong-Frederic evolution equation for the kinematic hardening strain-like variable. Coming to the matrix notation for fourth-order tensors one has to use a single stencil $\left[\begin{array}{c|c} 1 & \sqrt{2} \\ \hline \sqrt{2} & 2 \end{array} \right]$. This gives a direct consequence where the current notation does not require additional operators such as $\mathcal{Q}$.

3.B. Extension to Finite Strains

Let $\boldsymbol{X}$ and $\boldsymbol{x} := \boldsymbol{\varphi}(\boldsymbol{X}, t)$ denote the particle positions at the reference (undeformed) configuration Ω_0 and current (deformed) configuration Ω respectively. $\boldsymbol{F} := \partial_{\boldsymbol{X}} \boldsymbol{\varphi}(\boldsymbol{X}, t)$ defines the

deformation gradient of the nonlinear map $\boldsymbol{\varphi} : \Omega_0 \times \mathbb{R} \to \mathbb{R}^3$ with $\det \boldsymbol{F} > 0$. Any infinitesimal material vector $d\boldsymbol{X}$ at the reference configuration is transformed to its final setting $d\boldsymbol{x}$ at the current configuration via $d\boldsymbol{x} := \boldsymbol{F} \cdot d\boldsymbol{X}$. Let $\boldsymbol{l} := \dot{\boldsymbol{F}} \cdot \boldsymbol{F}^{-1} = \partial_{\boldsymbol{x}} \boldsymbol{v}$ denote the spatial velocity gradient with $\boldsymbol{v} = \dot{\boldsymbol{x}}$. The symmetric part of $\boldsymbol{l}$ gives the spatial rate of deformation tensor $\boldsymbol{d} := \text{sym}\,(\boldsymbol{l})$. The following rate additive split is assumed

$$\boldsymbol{d} = \boldsymbol{d}^e + \boldsymbol{d}^p \,, \tag{3.B.1}$$

with $\boldsymbol{d}^e := \text{sym}\,(\boldsymbol{l}^e)$, $\boldsymbol{d}^p := \text{sym}\,(\boldsymbol{l}^p)$. This forms the basis of hypoelastic-plastic formulations which rely on certain objective rates of the selected stress measures. ABAQUS/VUMAT convention uses the Green–Naghdi–McInnis rate of the Cauchy (true) stress $\boldsymbol{\sigma}$ which requires the rotationally neutralized rate of deformation tensor $\dot{\tilde{\boldsymbol{\varepsilon}}}$ which is defined as

$$\dot{\tilde{\boldsymbol{\varepsilon}}} = \boldsymbol{R}^\top \cdot [\boldsymbol{d}^e + \boldsymbol{d}^p] \cdot \boldsymbol{R} = \dot{\tilde{\boldsymbol{\varepsilon}}}^e + \dot{\tilde{\boldsymbol{\varepsilon}}}^p \,, \tag{3.B.2}$$

with $\dot{\tilde{\boldsymbol{\varepsilon}}}^e := \boldsymbol{R}^\top \cdot \boldsymbol{d}^e \cdot \boldsymbol{R}$, $\dot{\tilde{\boldsymbol{\varepsilon}}}^p := \boldsymbol{R}^\top \cdot \boldsymbol{d}^p \cdot \boldsymbol{R}$. Here, $\boldsymbol{R}$ denotes the rotation tensor, carried out by the polar decomposition of the deformation gradient, $\boldsymbol{F} := \boldsymbol{R} \cdot \boldsymbol{U}$, with $\boldsymbol{U}$ representing the symmetric right stretch tensor. Similarly, a pull back operation on the Cauchy (true) stress tensor $\boldsymbol{\sigma}$ with the rotation tensor gives its rotationally neutralized counterpart viz $\tilde{\boldsymbol{\sigma}} := \boldsymbol{R}^\top \cdot \boldsymbol{\sigma} \cdot \boldsymbol{R}$ whose material time derivative $\dot{\tilde{\boldsymbol{\sigma}}}$ can be objectively integrated. Hence, the finite strain extension of the presented framework is realized using the replacements $\dot{\boldsymbol{\sigma}} \rightsquigarrow \dot{\tilde{\boldsymbol{\sigma}}}$ and $\dot{\boldsymbol{\varepsilon}} \rightsquigarrow \dot{\tilde{\boldsymbol{\varepsilon}}}$ and representing the expressions at the rotationally neutralized configuration.

3.C. Correlated Random Field Generation

In development of the correlated random fields, the method of circular embedding is used closely following the work of Kroese and Botev [158] and the MATLAB code listed therein is adapted. For the sake of completeness, the method is summarized in the following. For further details, the reader is referred to the work of [158] and the references therein. A random field is a spatial stochastic process which consists of a collection of random variables $\{X_{\boldsymbol{r}}, \, \boldsymbol{r} \in D\}$ where $D \subset \mathbb{R}^d$ represents a d-dimensional domain and $X_{\boldsymbol{r}}$ is a random quantity associated with a spatial position $\boldsymbol{r}$. In the current case only 2-dimensional domains are of interest, that is $D \subset \mathbb{R}^2$. The set of possible values of $X_{\boldsymbol{r}}$ is called the state space of the spatial process. A discrete number of material points is considered in the domain which are assigned a continuous material property, hence this stands for a process with a discrete index set and a continuous state space. It is assumed that the random field $\{\widetilde{X}_{\boldsymbol{r}}, \, \boldsymbol{r} \in \mathbb{R}^2\}$ is Gaussian such that the multivariate normal vector $\boldsymbol{X}$ has the property $\boldsymbol{X} = [\widetilde{X}_1, \widetilde{X}_2, \ldots, \widetilde{X}_n]^\top = [\widetilde{X}_{\boldsymbol{r}_1}, \widetilde{X}_{\boldsymbol{r}_2}, \ldots, \widetilde{X}_{\boldsymbol{r}_n}]^\top \sim \mathcal{N}(\boldsymbol{\mu}, \boldsymbol{\Sigma})$ where $\boldsymbol{\mu}$ and $\boldsymbol{\Sigma}$ denote expectation vector and covariance matrix, respectively. The Gaussian random field is determined completely by its expectation function $\widetilde{\boldsymbol{\mu}}_{\boldsymbol{r}} = \mathbb{E}\widetilde{X}_{\boldsymbol{r}}$ and covariance function $\widetilde{\boldsymbol{\Sigma}}_{\boldsymbol{r},\boldsymbol{s}} = \text{Cov}(\widetilde{X}_{\boldsymbol{r}}, \widetilde{X}_{\boldsymbol{s}})$ with $\boldsymbol{r}, \boldsymbol{s} \in D$. With the stationarity of the Gaussian process, one has a constant $\mathbb{E}\widetilde{X}_{\boldsymbol{r}}$ and invariant $\text{Cov}(\widetilde{X}_{\boldsymbol{r}}, \widetilde{X}_{\boldsymbol{s}})$ under translations, with $\text{Cov}(\widetilde{X}_{\boldsymbol{r}+\boldsymbol{d}}, \widetilde{X}_{\boldsymbol{s}+\boldsymbol{d}}) = \text{Cov}(\widetilde{X}_{\boldsymbol{r}}, \widetilde{X}_{\boldsymbol{s}})$ for an arbitrary vector $\boldsymbol{d}$.

A zero-mean stationary Gaussian random field $\{\widetilde{X}_{\boldsymbol{r}}\}$ is generated on each of the grid points $\{(i,j)/n, i = 0, 1, \ldots, n-1, j = 0, 1, \ldots, n-1\}$ corresponding to a Gaussian covariance function of the form

$$\text{Cov}(\widetilde{X}_{\boldsymbol{r}}, \widetilde{X}_{\boldsymbol{s}}) = \phi(\boldsymbol{r} - \boldsymbol{s}) = \exp\left(\frac{-|\boldsymbol{r} - \boldsymbol{s}|^2}{L_c^2}\right) \,, \tag{3.C.1}$$

where $|\boldsymbol{r} - \boldsymbol{s}|^2 = [r_1 - s_1]^2 + [r_2 - s_2]^2$ and L_c corresponds to the correlation length. Thus, the process is also isotropic, i.e. it does not depend on the selected orientation. Over the grid, the values of the Gaussian process are gathered in an $n^2 \times 1$ column vector $\boldsymbol{X}$. The covariance matrix $\Omega_{ij} = \phi(\boldsymbol{r}_i - \boldsymbol{s}_j)$, $i, j = 1, 2, \ldots n^2$ has a symmetric block-Toeplitz[2] structure and $\boldsymbol{\Omega}$ is uniquely characterized by its first block row $[\boldsymbol{R}_1, \boldsymbol{R}_2, \ldots, \boldsymbol{R}_n]$ where each block is an $n \times n$ Toeplitz matrix, which is not necessarily symmetric. Each $\boldsymbol{R}_k$ is embedded in the upper left corner of the circulant matrix $\boldsymbol{C}_k$. The entries of the the first block row $[\boldsymbol{C}_1, \boldsymbol{C}_2, \ldots, \boldsymbol{C}_n, \boldsymbol{C}_n^\top, \boldsymbol{C}_{n-1}^\top, \ldots, \boldsymbol{C}_2^\top]$ of the $[2n-1]^2 \times [2n-1]^2$ block circulant matrix $\boldsymbol{\Sigma}$ are stored in a $[2n-1] \times [2n-1]$ matrix $\boldsymbol{G}$.

After completing the embedding in block circulant matrix it is diagonalized with $\boldsymbol{\Sigma} = \boldsymbol{P}^\star \cdot \mathrm{diag}(\boldsymbol{\gamma}) \cdot \boldsymbol{P}$, where $\boldsymbol{P}$ is the $[2n-1]^2 \times [2n-1]^2$ two-dimensional discrete Fourier transform matrix with $\boldsymbol{P} = \boldsymbol{F} \otimes \boldsymbol{F}$, where $F_{jk} = \exp(-2\pi \mathrm{i} jk/n)/\sqrt{n}$ with $j, k = 0, 1, \ldots, n-1$. $[\bullet]^\star$ represents the complex conjugate transpose of $[\bullet]$. Ordering the eigenvalue vector $\boldsymbol{\gamma} = [\gamma_1, \gamma_2, \ldots, \gamma_{[2n-1]^2}]$ one reaches a $[2n-1] \times [2n-1]$ matrix $\boldsymbol{\Gamma}$ which is the (appropriately scaled) two-dimensional Fast Fourier Transform (FFT2) of $\boldsymbol{G}$. Denoting the component-wise square root operation with $\sqrt{[\bullet]}$, one defines the matrix $\boldsymbol{B} = \boldsymbol{P}^\star \cdot \mathrm{diag}(\sqrt{\boldsymbol{\gamma}})$ where $\boldsymbol{\Sigma} = \boldsymbol{B}^\star \cdot \boldsymbol{B}$.

Finally, letting the components $\underline{Z}_{jk} = U_{jk} + \mathrm{i}\, V_{jk}$ where $U_{jk}, V_{jk} \sim \mathcal{N}(0,1)$ make up the $[2n-1] \times [2n-1]$ complex Gaussian matrix $\underline{\boldsymbol{Z}}$, one reaches reach realizations of a correlated stationary Gaussian field on the grid through the first $n \times n$ sub-blocks of the real and the imaginary parts of the FFT2 of the array $\sqrt{\boldsymbol{\Gamma}} \odot \underline{\boldsymbol{Z}}$ where $\odot$ represents element by element multiplication.

---

[2]If its components along each diagonal are the same, an $N \times N$ matrix is referred to as Toeplitz.

4. A Directional Modification of the Levkovitch–Svendsen Cross–Hardening Model Based on the Stress Deviator

In the original Levkovitch–Svendsen cross–hardening model parallel and orthogonal projections required for the yield surface evolution with respective dynamic and latent hardening effects are associated with the unit plastic flow direction $\boldsymbol{n}_p = \dot{\boldsymbol{\varepsilon}}_p / |\dot{\boldsymbol{\varepsilon}}_p|$. This chapter gives a detailed investigation regarding the consequences and proposes the use of the so–called radial direction $\boldsymbol{n}_s = [\boldsymbol{S} - \boldsymbol{X}]/|\boldsymbol{S} - \boldsymbol{X}|$ instead where $\boldsymbol{S} = \mathrm{dev}(\boldsymbol{\sigma})$. It is shown that for an initially plastically anisotropic material under load paths with proportional stresses the original model brings a continuous directional change in the plastic strains. Eventually, even if the dynamic hardening component is bypassed, the material model predicts additional strengthening in loading direction due to latent hardening. In this undesired response, the broken coaxiality of the stress deviator and plastic strain rate tensor with initial anisotropy is the cause. This entanglement of isotropic/kinematic hardening and latent hardening creates difficulties – especially in the parameter identification even for the simplest uniaxial loading. The introduced modification to the model remedies this undesired feature and, hence, makes it possible to isolate the hardening sourced during parameter identification stage. The discussions are supported by analytically and numerically derived yield loci for various scenarios. The analytical studies allow definition of critical material parameter limits for the latent hardening parameter s_l in terms of the initial anisotropy and the constant stress deviator ratio.

4.1. Introduction

The macroscopic material behavior of crystalline solids is strongly related to a present or emergent underlying microstructure. The microstructure itself is a result of different physical mechanisms at lower length scales. As the level of deformation gets large enough, microstructural defects are permanently reconfigured to some characteristic dislocation patterns, i.e., labyrinth-type dislocation structure [141] or dislocation cell structures [293], to name but a few. As the attention in this chapter is restricted to phenomenological plasticity models which are applicable to forming processes, the evolution of the microstructure is accounted for by an evolving anisotropy tensor of the material [90, 324, 245, 269, 40, 49]. One aspect of this anisotropy is the appearance of cross–hardening effects for orthogonal loading-path changes [58].

Let $\Phi = \sqrt{[\boldsymbol{\sigma} - \boldsymbol{X}]^\top \boldsymbol{\mathcal{B}} [\boldsymbol{\sigma} - \boldsymbol{X}]} - h(\gamma) \leq 0$ denote the flow potential with γ representing the equivalent plastic strain and $h(\gamma)$ the associated flow stress. $\boldsymbol{\mathcal{B}} = \boldsymbol{\mathcal{A}} + \boldsymbol{\mathcal{H}}$ is the structural tensor where the additive component $\boldsymbol{\mathcal{A}}$ encapsulates material's inherent anisotropy, whereas $\boldsymbol{\mathcal{H}}$, the anisotropy induced by plastic flow with the initial value $\boldsymbol{\mathcal{H}}_0 = \boldsymbol{\mathcal{O}}$ for the loading time $t = 0$. Hence, along with these definitions, it is assumed that $\dot{\boldsymbol{\mathcal{A}}} = \boldsymbol{\mathcal{O}}$, $\dot{\boldsymbol{\mathcal{H}}} \neq \boldsymbol{\mathcal{O}}$ where $\boldsymbol{\mathcal{O}}$

represents the fourth-order zero tensor. In associated plasticity theory, the direction of plastic flow coincides with the normal to the yield locus at the point of loading as defined by $\boldsymbol{n}_p = \dot{\boldsymbol{\varepsilon}}_p / |\dot{\boldsymbol{\varepsilon}}_p| = \partial_{\boldsymbol{\sigma}}\Phi / |\partial_{\boldsymbol{\sigma}}\Phi| = \boldsymbol{\mathcal{B}}[\boldsymbol{\sigma} - \boldsymbol{X}] / |\boldsymbol{\mathcal{B}}[\boldsymbol{\sigma} - \boldsymbol{X}]|$, where $\dot{\boldsymbol{\varepsilon}}_p$ denotes the plastic strain rate tensor. Additionally, one may define a so–called radial direction $\boldsymbol{n}_s = [\boldsymbol{S} - \boldsymbol{X}] / |\boldsymbol{S} - \boldsymbol{X}|$ as a normalized difference of the stress deviator $\boldsymbol{S} = \mathrm{dev}(\boldsymbol{\sigma})$ and the back stress tensor $\boldsymbol{X}$. In Levkovitch–Svendsen cross–hardening model [181] parallel and orthogonal projections used in definition of $\dot{\boldsymbol{\mathcal{H}}}$ with respective dynamic and latent hardening effects require a certain direction. In retrospect, the original model formulation of Levkovitch–Svendsen [181] as well as the subsequent model formulations and extensions [41, 313, 77, 269, 40, 49], this direction is selected as the plastic flow direction $\boldsymbol{n}_p$. One exception in this context is the work by Pietryga et al. [245], where the evolution of the original anisotropic flow tensor is formulated based on the radial direction $\boldsymbol{n}_s$. However, the authors name this direction as the plastic flow direction without pointing out its difference from the previous model formulations as well as the consequences of such a usage.

In this chapter, restricting the current analysis to the Levkovitch–Svendsen model, the consequences of the use of these two distinct directions in the definition of the evolution of the fourth-order structural tensor $\boldsymbol{\mathcal{H}}$ is investigated for materials with initial plastic anisotropy. This analysis reveals a drawback, hereby named as the hardening entanglement, in the original model formulation based on the direction of plastic flow $\boldsymbol{n}_p$. For an initially plastically anisotropic material under loading paths with proportional stresses, the original model brings a continuous directional change in the rate of plastic strain tensor, hence, in the associated normal $\boldsymbol{n}_p$. Eventually, even if the dynamic hardening component is bypassed, the material model predicts additional hardening in loading direction. Under uniaxial stresses, as a consequence, a continuous change in the Lankford's coefficient r_0 is observed. Here, the broken coaxiality in between $\boldsymbol{n}_p$ and $\boldsymbol{n}_s$ is the cause. Note that only for the case of von Mises isotropic plasticity one has $\boldsymbol{n}_p \equiv \boldsymbol{n}_s$. This entanglement of isotropic/kinematic hardening and latent hardening creates difficulties – especially in the parameter identification even for the simplest uniaxial loading by precluding the isolation of the hardening sources. It is shown that the proposed modification by using the radial direction $\boldsymbol{n}_s$ remedies these undesired features and support this statement by analytical as well as numerical examples.

4.2. Generalization of Levkovitch–Svendsen Evolving Yield Locus

Assuming that the initial orthotropy axes are aligned with the loading directions, the principal axes of deformation do not rotate and in order to simplify the context the influence of the backstress is neglected. Thus, the Levkovitch–Svendsen yield locus reads

$$\Phi = \sqrt{\boldsymbol{\sigma}^\top \boldsymbol{\mathcal{B}} \boldsymbol{\sigma}} - h(\gamma) \leq 0 \,. \tag{4.2.1}$$

In absence of shear components, $\boldsymbol{\sigma}$ is regarded as a 3×1 vector with $\boldsymbol{\sigma} = (\sigma_{11}, \sigma_{22}, \sigma_{33})^\top$ aligned with principal axes. Here, a simple isotropic hardening function is assumed of the form

$$h(\gamma) = \sigma_\infty - [\sigma_\infty - \sigma_{y0}]\exp(-m\,\gamma)\,, \tag{4.2.2}$$

where σ_{y0} and σ_∞ denotes the initial and saturated yield stresses, respectively, and m represents the saturation rate. Moreover, $\boldsymbol{\mathcal{B}} = \boldsymbol{\mathcal{A}} + \boldsymbol{\mathcal{H}}$. Here both $\boldsymbol{\mathcal{A}}$ and $\boldsymbol{\mathcal{H}}$ represent 3×3 matrices with the former being the Hill'48-type structural matrix. For $\dot{\boldsymbol{\mathcal{H}}}$ the following generalization is proposed

$$\dot{\boldsymbol{\mathcal{H}}} = \dot{\gamma} c_d \left[s_d \boldsymbol{\mathcal{N}}_g - \boldsymbol{\mathcal{H}}_d \right] + \dot{\gamma} c_l \left\{ s_l \left[\boldsymbol{\mathcal{I}}^{\mathrm{dev}} - \boldsymbol{\mathcal{N}}_g \right] - \left[\boldsymbol{\mathcal{H}} - \boldsymbol{\mathcal{H}}_d \right] \right\}\,, \tag{4.2.3}$$

where $\boldsymbol{\mathcal{N}}_g := \boldsymbol{n}_g \otimes \boldsymbol{n}_g$ with $\boldsymbol{n}_g$ defining the unit tensor used for parallel and orthogonal projections. The term generalization is used, since unlike Levkovitch –Svendsen original model which fixes $\boldsymbol{n}_g$ as the unit direction of plastic flow with $\boldsymbol{n}_g \equiv \boldsymbol{n}_p$, a specific choice for $\boldsymbol{n}_g$ is not specified. $\boldsymbol{\mathcal{I}}^{\mathrm{dev}}$ is the 3×3 matrix representation (considering the normal components only) of the fourth-order deviatoric projection (idempotent), that is $[\boldsymbol{\mathcal{I}}^{\mathrm{dev}}]^n = \boldsymbol{\mathcal{I}}^{\mathrm{dev}}$ for $n \geq 1$ with

$$\boldsymbol{\mathcal{I}}^{\mathrm{dev}} = \frac{1}{3} \begin{pmatrix} 2 & -1 & -1 \\ -1 & 2 & -1 \\ -1 & -1 & 2 \end{pmatrix}, \tag{4.2.4}$$

and $\boldsymbol{\mathcal{H}}_d$ is defined by

$$\boldsymbol{\mathcal{H}}_d = \left[\boldsymbol{n}_g^\top \boldsymbol{\mathcal{H}} \, \boldsymbol{n}_g \right] \boldsymbol{n}_g \otimes \boldsymbol{n}_g. \tag{4.2.5}$$

An immediate integration of Equation (4.2.3) is possible for constant $\boldsymbol{n}_g$, thus constant $\boldsymbol{\mathcal{N}}_g$, no matter which direction it represents, giving an additive form $\boldsymbol{\mathcal{H}} = \boldsymbol{\mathcal{H}}_d + \boldsymbol{\mathcal{H}}_l$ where [1]

$$\boldsymbol{\mathcal{H}}_d = s_d f_{c_d}(\gamma) \boldsymbol{\mathcal{N}}_g \quad \text{and} \quad \boldsymbol{\mathcal{H}}_l = s_l f_{c_l}(\gamma) \left[\boldsymbol{\mathcal{I}}^{\mathrm{dev}} - \boldsymbol{\mathcal{N}}_g \right], \tag{4.2.6}$$

where the following abbreviations are used

$$f_{c_l}(\gamma) = 1 - \exp(-c_l \gamma) \quad \text{and} \quad f_{c_d}(\gamma) = 1 - \exp(-c_d \gamma). \tag{4.2.7}$$

Here, c_d and s_d denote the saturation rate and magnitude associated with the dynamic part $\boldsymbol{\mathcal{H}}_d$, where c_l and s_l are the saturation rate and magnitude associated with the latent part $\boldsymbol{\mathcal{H}}_l := \boldsymbol{\mathcal{H}} - \boldsymbol{\mathcal{H}}_d$, respectively[2]. $\boldsymbol{\mathcal{H}}_d$ accounts for the strength of the dislocation structures associated with the slip systems which are currently active whereas the strength of the dislocation structures of currently inactive slip systems is encapsulated in $\boldsymbol{\mathcal{H}}_l$. Hence, for $s_d = 0$ until a load path change occurs one expects that the material response will be dictated purely by isotropic hardening. For $\gamma = 0$ one has $\boldsymbol{\mathcal{H}}_0 = \boldsymbol{\mathcal{O}}$ as required.

Assumption of plane stress state lets one deal with only 2×1 and 2×2 sub-vectors and sub-matrices denoted as $(\widehat{\bullet})$ in the following. Additionally, a plane stress investigation allows a straightforward geometric interpretation. Eventually, the reduced plane stress version of Equation (4.2.1) reads

$$\widehat{\Phi} = \sqrt{\widehat{\boldsymbol{\sigma}}^\top \widehat{\boldsymbol{\mathcal{B}}} \, \widehat{\boldsymbol{\sigma}}} - h(\gamma) \leq 0, \tag{4.2.8}$$

with $\widehat{\boldsymbol{\mathcal{B}}} = \widehat{\boldsymbol{\mathcal{A}}} + \widehat{\boldsymbol{\mathcal{H}}}$ and the reduced stress vector $\widehat{\boldsymbol{\sigma}} = (\sigma_{11}, \sigma_{22})^\top$.

Coming to $\widehat{\boldsymbol{\mathcal{A}}}$, assuming Hill'48-type flow potential, one has

$$\widehat{\boldsymbol{\mathcal{A}}} = \begin{pmatrix} G_\natural + H_\natural = 1 & -H_\natural \\ -H_\natural & F_\natural + H_\natural \end{pmatrix}, \tag{4.2.9}$$

where $F_\natural$, $G_\natural$ and $H_\natural$ are non-negative, non-dimensional material parameters. Hence, Equation (4.2.9) together with Equation (4.2.13) gives $\widehat{\boldsymbol{\mathcal{B}}}(\gamma) = \widehat{\boldsymbol{\mathcal{A}}} + \widehat{\boldsymbol{\mathcal{H}}}(\gamma)$.

---

[1] In the presence of kinematic hardening evolving in direction of plastic flow $\boldsymbol{n}_p$, $\boldsymbol{n}_s$ is not constant in general.
[2] Both $\boldsymbol{\mathcal{H}}_d$ and $\boldsymbol{\mathcal{H}}_l$ have distortional effects which cannot be represented by isotropic or kinematic hardening.

4.2.1. The Case for Proportional Strain Path with $n_g \equiv n_p = \dot{\varepsilon}_p / |\dot{\varepsilon}_p|$ with Plane Stress State

In this part, the generalized direction is specified as $\boldsymbol{n}_g \equiv \boldsymbol{n}_p$. The integration for $\widehat{\mathcal{H}}(\gamma)$ computed for the generalized form of the plastic flow potential which leaves the choice $\boldsymbol{n}_g$ free is valid for $\boldsymbol{n}_p$ as well, provided that $\boldsymbol{n}_p$ is constant. Hence, rigid plasticity is assumed with $(E_{p,11}, E_{p,22}, E_{p,33}) \rightarrow (E_{11}, E_{22}, E_{33})$. Strain controlled loading is applied where in–plane strains in $x-$ and $y-$directions are defined and out–of–plane strain is found using the other two using the isochoric plastic flow condition. Moreover, strictly proportional strain paths are considered: $\alpha_E = dE_{11}/dE_{22} = E_{11}/E_{22}$. With these assumptions, the total strain vector $\boldsymbol{\varepsilon}$ and its normal $\boldsymbol{n}_p$, respectively, read

$$\boldsymbol{\varepsilon} = E_{22} \begin{pmatrix} \alpha_E \\ 1 \\ -[1+\alpha_E] \end{pmatrix} \quad \text{and} \quad \boldsymbol{n}_p = \frac{1}{\sqrt{2[1+\alpha_E+\alpha_E^2]}} \begin{pmatrix} \alpha_E \\ 1 \\ -[1+\alpha_E] \end{pmatrix}. \tag{4.2.10}$$

This lets one compute $\boldsymbol{\mathcal{N}}_g = \boldsymbol{\mathcal{N}}_p = \boldsymbol{n}_p \otimes \boldsymbol{n}_p$ as

$$\boldsymbol{\mathcal{N}}_p = \frac{1}{2[1+\alpha_E+\alpha_E^2]} \begin{pmatrix} \alpha_E^2 & \alpha_E & -\alpha_E[1+\alpha_E] \\ \alpha_E & 1 & -[1+\alpha_E] \\ -\alpha_E[1+\alpha_E] & -[1+\alpha_E] & [1+\alpha_E]^2 \end{pmatrix}. \tag{4.2.11}$$

Collecting the terms and reducing to 2×2 sub-matrices of $\boldsymbol{\mathcal{N}}_p$ and $\boldsymbol{\mathcal{I}}^{\text{dev}}$, respectively, the evolving structural matrix in Equation (4.2.6) as a function of the equivalent plastic strain γ reads

$$\begin{aligned} \widehat{\mathcal{H}}(\gamma) = \frac{s_d f_{c_d}(\gamma)}{2[1+\alpha_E+\alpha_E^2]} & \begin{pmatrix} \alpha_E^2 & \alpha_E \\ \alpha_E & 1 \end{pmatrix} \\ + s_l f_{c_l}(\gamma) & \begin{pmatrix} \dfrac{2}{3} - \dfrac{\alpha_E^2}{2[1+\alpha_E+\alpha_E^2]} & -\dfrac{1}{3} - \dfrac{\alpha_E}{2[1+\alpha_E+\alpha_E^2]} \\ -\dfrac{1}{3} - \dfrac{\alpha_E}{2[1+\alpha_E+\alpha_E^2]} & \dfrac{2}{3} - \dfrac{1}{2[1+\alpha_E+\alpha_E^2]} \end{pmatrix}. \end{aligned} \tag{4.2.12}$$

Now, assuming that only the latent part of the cross–hardening is active with $s_d = 0$ one obtains

$$\widehat{\mathcal{H}}(\gamma) = s_l f_{c_l}(\gamma) \begin{pmatrix} \dfrac{2}{3} - \dfrac{\alpha_E^2}{2[1+\alpha_E+\alpha_E^2]} & -\dfrac{1}{3} - \dfrac{\alpha_E}{2[1+\alpha_E+\alpha_E^2]} \\ -\dfrac{1}{3} - \dfrac{\alpha_E}{2[1+\alpha_E+\alpha_E^2]} & \dfrac{2}{3} - \dfrac{1}{2[1+\alpha_E+\alpha_E^2]} \end{pmatrix}. \tag{4.2.13}$$

For large plastic deformation, i.e., $\gamma \rightarrow \infty$ one has[3] $f_{c_l}(\gamma) \rightarrow 1$. Hence

$$\widehat{\mathcal{H}}(\gamma) \rightarrow s_l \begin{pmatrix} \dfrac{2}{3} - \dfrac{\alpha_E^2}{2[1+\alpha_E+\alpha_E^2]} & -\dfrac{1}{3} - \dfrac{\alpha_E}{2[1+\alpha_E+\alpha_E^2]} \\ -\dfrac{1}{3} - \dfrac{\alpha_E}{2[1+\alpha_E+\alpha_E^2]} & \dfrac{2}{3} - \dfrac{1}{2[1+\alpha_E+\alpha_E^2]} \end{pmatrix} \quad \text{as } \gamma \rightarrow \infty. \tag{4.2.14}$$

4.2.2. The Case for Proportional Stress Path with $n_g \equiv n_s = S/|S|$ with Plane Stress State

In this part, the generalized direction is specified as $\boldsymbol{n}_g \equiv \boldsymbol{n}_s$. The integration for $\widehat{\mathcal{H}}(\gamma)$ computed for the generalized form of the plastic flow potential which leaves the choice $\boldsymbol{n}_g$ free is valid for

---

[3]Although not used here one also has $f_{c_d}(\gamma) \rightarrow 1$ for $\gamma \rightarrow \infty$.

n_s as well, provided that n_s is constant. Hence, stress controlled loading is applied where the in–plane stresses in $x-$ and $y-$directions are defined and the out–of–plane stress vanishes with the plane stress assumption $\sigma_{33} = 0$. Moreover, strictly proportional stress paths are considered $\beta = \sigma_{11}/\sigma_{22}$. Now, to catch accordance with previously derived forms for the deviatoric stress tensor component ratio, use is made of $\alpha_S = S_{11}/S_{22} = [2\,\beta - 1]/[2 - \beta]$. Thus, following similar steps as previous, for the current case Equation (4.2.12) holds by simply replacing α_E with α_S

$$\widehat{\mathcal{H}}(\gamma) = \frac{s_d f_{c_d}(\gamma)}{2[1 + \alpha_E + \alpha_E^2]} \begin{pmatrix} \alpha_S^2 & \alpha_S \\ \alpha_S & 1 \end{pmatrix}$$
$$+ s_l f_{c_l}(\gamma) \begin{pmatrix} \dfrac{2}{3} - \dfrac{\alpha_S^2}{2[1 + \alpha_S + \alpha_S^2]} & -\dfrac{1}{3} - \dfrac{\alpha_S}{2[1 + \alpha_S + \alpha_S^2]} \\ -\dfrac{1}{3} - \dfrac{\alpha_S}{2[1 + \alpha_S + \alpha_S^2]} & \dfrac{2}{3} - \dfrac{1}{2[1 + \alpha_S + \alpha_S^2]} \end{pmatrix}, \tag{4.2.15}$$

where for $s_d = 0$ one obtains

$$\widehat{\mathcal{H}}(\gamma) = s_l f_{c_l}(\gamma) \begin{pmatrix} \dfrac{2}{3} - \dfrac{\alpha_S^2}{2[1 + \alpha_S + \alpha_S^2]} & -\dfrac{1}{3} - \dfrac{\alpha_S}{2[1 + \alpha_S + \alpha_S^2]} \\ -\dfrac{1}{3} - \dfrac{\alpha_S}{2[1 + \alpha_S + \alpha_S^2]} & \dfrac{2}{3} - \dfrac{1}{2[1 + \alpha_S + \alpha_S^2]} \end{pmatrix}. \tag{4.2.16}$$

4.2.3. Discussion: Simple Tension Test

Simple tension test is one of the fundamental materials science tests where a sample is extended slowly under a uniaxial state of stress. For a test conducted in $x-$direction the only nonzero component of the stress tensor is σ_1. Assume that for $t > 0$, one has the symmetric cross–hardening structural tensor as

$$\widehat{\mathcal{H}}(\gamma) = \begin{pmatrix} \widehat{\mathcal{H}}_{11} & \widehat{\mathcal{H}}_{12} \\ \widehat{\mathcal{H}}_{12} & \widehat{\mathcal{H}}_{22} \end{pmatrix}. \tag{4.2.17}$$

Substituting Equation (4.2.17) and $\widehat{\sigma} = (\sigma_1, 0)^\top$ in the expression

$$\sqrt{\widehat{\sigma}^\top \widehat{\mathcal{B}} \widehat{\sigma}} = \sqrt{\widehat{\sigma}^\top \widehat{\mathcal{A}} \widehat{\sigma} + \widehat{\sigma}^\top \widehat{\mathcal{H}}(\gamma) \widehat{\sigma}}$$

and using Equation (4.2.9), for the fully developed plastic flow reads

$$\sqrt{\widehat{\sigma}^\top \widehat{\mathcal{B}} \widehat{\sigma}} = \sqrt{G_\natural + H_\natural + \widehat{\mathcal{H}}_{11}}\, \sigma_1 = \sqrt{1 + \widehat{\mathcal{H}}_{11}}\, \sigma_1 = h(\gamma). \tag{4.2.18}$$

Using the flow rule $\dot{\varepsilon}_p = \dot{\gamma}\, \widehat{\mathcal{B}} \widehat{\sigma}/\sqrt{\widehat{\sigma}^\top \widehat{\mathcal{B}} \widehat{\sigma}}$ and making necessary substitutions render

$$\begin{pmatrix} \dot{\varepsilon}_{p,11} \\ \dot{\varepsilon}_{p,22} \end{pmatrix} = \dot{\gamma}\, \frac{1}{\sqrt{1 + \widehat{\mathcal{H}}_{11}}} \begin{pmatrix} 1 + \widehat{\mathcal{H}}_{11} \\ -H_\natural + \widehat{\mathcal{H}}_{12} \end{pmatrix}, \tag{4.2.19}$$

with $G_\natural + H_\natural = 1$. The Lankford's coefficient r_0 is computed using the plastic incompressibility condition $\dot{\varepsilon}_{p,11} + \dot{\varepsilon}_{p,22} + \dot{\varepsilon}_{p,33} = 0$ viz.

$$r_0 = \frac{\dot{\varepsilon}_{p,22}}{\dot{\varepsilon}_{p,33}} = \frac{\dot{\varepsilon}_{p,22}}{-[\dot{\varepsilon}_{p,11} + \dot{\varepsilon}_{p,22}]} = \frac{H_\natural - \widehat{\mathcal{H}}_{12}}{G_\natural + \widehat{\mathcal{H}}_{11} + \widehat{\mathcal{H}}_{12}}. \tag{4.2.20}$$

Equations (4.2.18) and (4.2.20) show that the stress response as well as r_0 depends on the cross hardening structural tensor components $\widehat{\mathcal{H}}_{11}$ and $\widehat{\mathcal{H}}_{12}$. If only latent hardening effects are considered by omitting the dynamic hardening contribution with $s_d = 0$, one should expect that these dependencies vanish in the active loading path. This is only possible by satisfying $\widehat{\mathcal{H}}_{11} = \widehat{\mathcal{H}}_{12} = 0$.

Indeed the analyzed test corresponds to a proportional stress path with $\alpha_S = -2$. Hence, exploiting the invariance of $\boldsymbol{n}_s$, $\boldsymbol{n}_g \equiv \boldsymbol{n}_s$ is used and the substitution $\alpha_S = -2$ into the right–hand side of Equation (4.2.16) is applied

$$\widehat{\mathcal{H}}(\gamma) = s_l f_{c_l}(\gamma) \begin{pmatrix} 0 & 0 \\ 0 & \xi(\gamma) \end{pmatrix} \quad \text{with} \quad \xi(\gamma) = \frac{1}{2} s_l \, f_{c_l}(\gamma). \tag{4.2.21}$$

satisfies the desired condition $\widehat{\mathcal{H}}_{11} = \widehat{\mathcal{H}}_{12} = 0$ and in view of Equations (4.2.18) and (4.2.20) gives

$$\sigma_1 = h(\gamma) \quad \text{and} \quad r_0 = \frac{H_\natural}{G_\natural}. \tag{4.2.22}$$

Thus, for $\boldsymbol{n}_g \equiv \boldsymbol{n}_s$ the hardening entanglement in loading direction is not observed and the invariance of r_0 is guaranteed. This is not the case, however, if one uses $\boldsymbol{n}_g \equiv \boldsymbol{n}_p$ for the same loading path for an initially anisotropic material. First of all, due to initial anisotropy $\boldsymbol{n}_p \neq \boldsymbol{n}_s$ and with constant evolution of $\widehat{\mathcal{H}}$, the invariance of $\boldsymbol{n}_p$ is lost. Hence, the main assumption rendering the integration in Equation (4.2.12) is not satisfied. Under these circumstances the non-vanishing $\widehat{\mathcal{H}}_{11}$ and $\widehat{\mathcal{H}}_{12}$ components result in hardening entanglement as well as variation of r_0, see Figure 4.1. As a direct effect, this creates difficulties in the identification of hardening parameters since a clear isolation of the hardening sources is not possible.
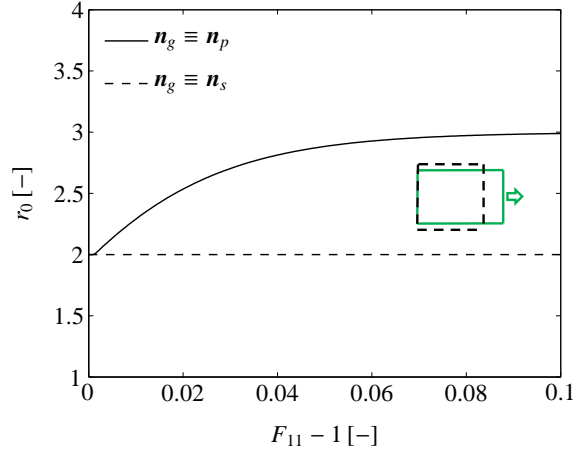
Figure 4.1.: Numerically obtained Lankford's coefficient r_0 for plastic flow direction $\boldsymbol{n}_g \equiv \boldsymbol{n}_p$, including cross-hardening effects and no kinematic hardening in a uniaxial tensile test. The Figure shows the change of the Lankford coefficient r_0 with loading. For the model $\boldsymbol{n}_g \equiv \boldsymbol{n}_s$, the Lankford coefficient is constant $r_0 = 2$ as analytically shown as well, see Equation(4.2.22). The results are obtained with the material parameters listed in Table 4.1, omitting kinematic hardening.

Extending the discussion to biaxial states of stress, one has $\beta = \sigma_{11}/\sigma_{22}$ hence $\boldsymbol{n}_g \equiv \boldsymbol{n}_s$. The loading direction in stress space is defined with the unit vector $\boldsymbol{v} = (v_1, v_2)^\top$ with $v_1 = \beta/\sqrt{1+\beta^2}$ and $v_2 = 1/\sqrt{1+\beta^2}$. Rotating $\widehat{\mathcal{H}}$ in Equation (4.2.16) with $\widehat{\mathcal{H}}^{\boldsymbol{v}}(\gamma) = \boldsymbol{\mathcal{R}} \, \widehat{\mathcal{H}} \, \boldsymbol{\mathcal{R}}^\top$

renders

$$\widehat{\mathcal{H}}^{\boldsymbol{v}}(\gamma) = \begin{pmatrix} 0 & 0 \\ 0 & \xi(\gamma) \end{pmatrix} \quad \text{with} \quad \xi(\gamma) = s_l\, f_{c_l}(\gamma) \left[\frac{5}{6} + \frac{\alpha_S}{2[1 + \alpha_S + \alpha_S^2]} \right], \tag{4.2.23}$$

where

$$\mathcal{R} = \begin{pmatrix} v_1 & v_2 \\ -v_2 & v_1 \end{pmatrix}. \tag{4.2.24}$$

In view of previous discussions this shows that the modification correctly inhibits any additional hardening component in direction of loading, which is the main premise of the cross–hardening model where the dynamic loading effects are bypassed. Again, this observation is not possible, in general, for $\boldsymbol{n}_g \equiv \boldsymbol{n}_p$.

4.2.4. The Case for $\boldsymbol{n}_g \equiv \boldsymbol{n}_p$ and $\boldsymbol{n}_g \equiv \boldsymbol{n}_s$ with Plane Stress State Including Kinematic Hardening

In the presence of kinematic hardening, the Levkovitch–Svendsen yield locus is given as

$$\Phi = \sqrt{[\boldsymbol{\sigma} - \boldsymbol{X}]^\top \boldsymbol{\mathcal{B}} [\boldsymbol{\sigma} - \boldsymbol{X}]} - h(\gamma) \leq 0. \tag{4.2.25}$$

Here, $\boldsymbol{X}$ denotes the back stress which is modeled via a variant of the Armstrong-Frederick form

$$\dot{\boldsymbol{X}} = \dot{\gamma}\, c_x \left[s_x \boldsymbol{n}_k - \boldsymbol{X} \right], \tag{4.2.26}$$

where $\boldsymbol{n}_k$ denotes the unit normal direction of the kinematic hardening evolution. The material parameters c_x and s_x denote the saturation rate and magnitude of the back stress $\boldsymbol{X}$, respectively. In the original model formulation, kinematic hardening is evolving in direction of plastic flow $\boldsymbol{n}_k \equiv \boldsymbol{n}_p$. Again, in absence of shear components, the back stress tensor can be given as vector in the form $\boldsymbol{X} = (X_{11}, X_{22}, X_{33})^\top$ aligned with principal axes. The reduced plane stress version of Equation (4.2.8) reads

$$\widehat{\Phi} = \sqrt{[\widehat{\boldsymbol{\sigma}} - [\widehat{\boldsymbol{\mathcal{I}}}^{\text{dev}}]^{-1}\widehat{\boldsymbol{X}}]^\top \widehat{\boldsymbol{\mathcal{B}}} [\widehat{\boldsymbol{\sigma}} - [\widehat{\boldsymbol{\mathcal{I}}}^{\text{dev}}]^{-1}\widehat{\boldsymbol{X}}]} - h(\gamma) \leq 0. \tag{4.2.27}$$

Here, the back stress is given in the 2×1 reduced vector form as $\widehat{\boldsymbol{X}} = (X_{11}, X_{22})^\top$ and the following definition is used

$$\widehat{\boldsymbol{\mathcal{I}}}^{\text{dev}} = \frac{1}{3} \begin{pmatrix} 2 & -1 \\ -1 & 2 \end{pmatrix} \quad \text{with} \quad [\widehat{\boldsymbol{\mathcal{I}}}^{\text{dev}}]^{-1} = \begin{pmatrix} 2 & 1 \\ 1 & 2 \end{pmatrix}. \tag{4.2.28}$$

For proportional strain paths the invariance of $\boldsymbol{n}_p$ allows the integration of $\dot{\mathcal{H}}$ as in Equation (4.2.3). Hence, the results of Section 4.2.1 with $\boldsymbol{n}_g \equiv \boldsymbol{n}_p$ even hold if kinematic hardening is accounted for. The situation for the model based on the radial direction (stress deviator) $\boldsymbol{n}_g \equiv \boldsymbol{n}_s := [\boldsymbol{S} - \boldsymbol{X}]/|\boldsymbol{S} - \boldsymbol{X}|$ is different, however, as the direction $\boldsymbol{n}_s$ can no longer be assumed as constant as soon as kinematic hardening evolves in direction of plastic flow. Figure 4.2 displays the results of a numerical analysis giving the ratio of the normal direction components in a uniaxial tensile test under plane stress conditions [4]. As anticipated the variations of $n_{g,11}/n_{g,22}$ for $\boldsymbol{n}_g \equiv \boldsymbol{n}_p\,,\boldsymbol{n}_k \equiv \boldsymbol{n}_p$ and $\boldsymbol{n}_g \equiv \boldsymbol{n}_s\,,\boldsymbol{n}_k \equiv \boldsymbol{n}_p$ render a maximum rate at the beginning of the loading path and ceases with the saturation of kinematic and cross hardening contributions,

---

[4]Note that for this loading conditions, the model based on $\boldsymbol{n}_g \equiv \boldsymbol{n}_p$ is not integrable since the normal is not constant for this loading situation, see Figure 4.2.
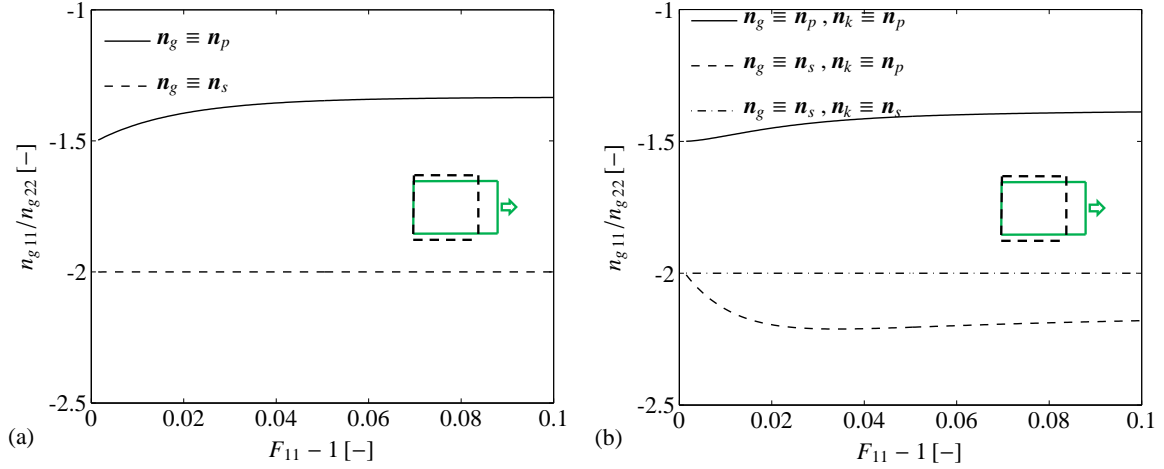
Figure 4.2.: Analysis of the ratio of the normal direction components $n_{g,11}/n_{g,22}$, including cross–hardening effects and (a) no kinematic hardening as well as (b) kinematic hardening in a uniaxial tensile test. The Figure shows the evolution of the plastic flow normal ratio $n_{p,11}/n_{p,22} = E_{p,11}/E_{p,22}$ in the original model formulation in comparison to the deviatoric stress ratio in the two model extensions $n_{s,11}/n_{s,22} = [S_{11} - X_{11}]/[S_{22} - X_{22}]$. In (b) the effect of kinematic hardening is shown for $\boldsymbol{n}_g \equiv \boldsymbol{n}_k \equiv \boldsymbol{n}_p$ and $\boldsymbol{n}_g \equiv \boldsymbol{n}_s$ with $\boldsymbol{n}_k \equiv \boldsymbol{n}_p$ and $\boldsymbol{n}_g \equiv \boldsymbol{n}_s$ with $\boldsymbol{n}_k \equiv \boldsymbol{n}_s$, respectively. The results are obtained with the material parameters listed in Table 4.1.

which, for the latter model takes place more quickly. Due to kinematic hardening in direction of plastic flow $\boldsymbol{n}_k \equiv \boldsymbol{n}_p$, the normal $\boldsymbol{n}_s$ is no longer constant in general which violates the fundamental assumption of the analytical solution. That is, the hardening entanglement problem remains. Nevertheless, the current numerical investigations show that the stress response difference between the analysis for a combined kinematic-isotropic hardening material with and without latent hardening for the simple tension test is marginal for kinematic hardening parameters within reasonable intervals of common engineering practice. This is mainly due to the relative magnitude of the back stress as compared to the total stress as well as its saturation rate.

This observed problem in the model ($\boldsymbol{n}_g \equiv \boldsymbol{n}_s$, $\boldsymbol{n}_k \equiv \boldsymbol{n}_p$) could be remedied by introducing another modification in the model which is formulating kinematic hardening with $\boldsymbol{n}_k \equiv \boldsymbol{n}_s$, i.e., letting the kinematic hardening evolution in the radial direction. This extension of the original model formulation leads to invariance of the normal $\boldsymbol{n}_s$ justified by the constant ratio $n_{g,11}/n_{g,22}$ in Figure 4.2 allowing an exact integration $\dot{\mathcal{H}}$ in Equation (4.2.3) with $\boldsymbol{n}_g \equiv \boldsymbol{n}_s$. Eventually, the problems pertaining to the hardening entanglement, although small, are resolved. In the following, in order to gain further insight regarding the model behavior, the consequences of the choice the selected normal in definition of the structural tensor evolution associated with selected material parameters are numerically investigated.

4.3.   Further Numerical Results

To extend the current discussion further numerical examples are presented for typical loading situations used in parameter identification. All simulations are performed under plane stress conditions. First, results are presented for the case without kinematic hardening, followed by an illustration of the effect of kinematic hardening on the cross–hardening behavior. The material

parameters used in this study are summarized in Table 4.1. All numerical results are carried out with an initially anisotropic yield locus as in view of the previous discussions for initial isotropic behavior no differences in the model formulations are observable.

Table 4.1.: Material parameters, representing approximately steel.

Parameter	Symbol	Value	Dimension
Elastic constants	E	210	[GPa]
	ν	0.3	[−]
Lankford's Coefficients	r_0	2.0	[−]
	r_{45}	1.5	[−]
	r_{90}	2.5	[−]
isotropic hardening constants	σ_{y0}	250.0	[MPa]
	σ_{∞}	500.0	[MPa]
	m	10	[−]
Kinematic hardening constants	s_x	100.0	[MPa]
	c_x	75.0	[MPa]
Cross hardening constants	s_d	0.0	[−]
	c_d	75.0	[−]
	s_l	−0.5	[−]
	c_l	75.0	[−]

4.3.1. Examples Neglecting Kinematic Hardening

The first numerical example considers plane strain tension loading, Figure 4.3(a). Although this situation represents a proportional loading path, the result based on the plastic flow normal $\boldsymbol{n}_g \equiv \boldsymbol{n}_p$ shows a notable difference to the results without evolving cross–hardening. In contrast, the original approach based on the radial direction $\boldsymbol{n}_g \equiv \boldsymbol{n}_s$ predicts identical response under proportional loading as without cross–hardening. In the situation of an orthogonal load path change, the models based on $\boldsymbol{n}_p$ as well as $\boldsymbol{n}_s$ shows a nearly identical stress overshoot due to latent hardening contribution. This clearly reveals, that the model change to $\boldsymbol{n}_g \equiv \boldsymbol{n}_s$ still maps the required cross–hardening behavior as experimentally observed [see, e.g., 58, 315, 324], and it additionally heals the artificial offset in the stress response for proportional loading paths.

The stress offset can be interpreted from an analysis of the yield loci after plane strain tensile loading, Figure 4.4. The model based on the plastic flow normal $\boldsymbol{n}_g \equiv \boldsymbol{n}_p$ leads to a distortion of the yield locus as desired but additionally to a shift of the loading point. Therefore, the stress–strain behaviors are not identical for the case with and without cross–hardening. The model based on the stress deviator $\boldsymbol{n}_g = \boldsymbol{n}_s$ equivalently distorts the yield locus, however, without shifting the point of loading. For an initially isotropic yield locus, both models predict the same response.

Next, the loading situation of uniaxial tension is analyzed numerically, Figure 4.5. As analytically already shown for this specific loading condition, the model based on the plastic flow normal $\boldsymbol{n}_g \equiv \boldsymbol{n}_p$ predicts a higher stress level as without cross–hardening. The loading conditions lead to a strong stretch of the initially anisotropic yield loci, Figure 4.6. Here, differences of the yield loci are notable, leading to different loading points in stress space afterwards. Additionally, for $\boldsymbol{n}_g = \boldsymbol{n}_s$ the primary axis of the ellipse seems to be rotating more, Figure 4.6(b).
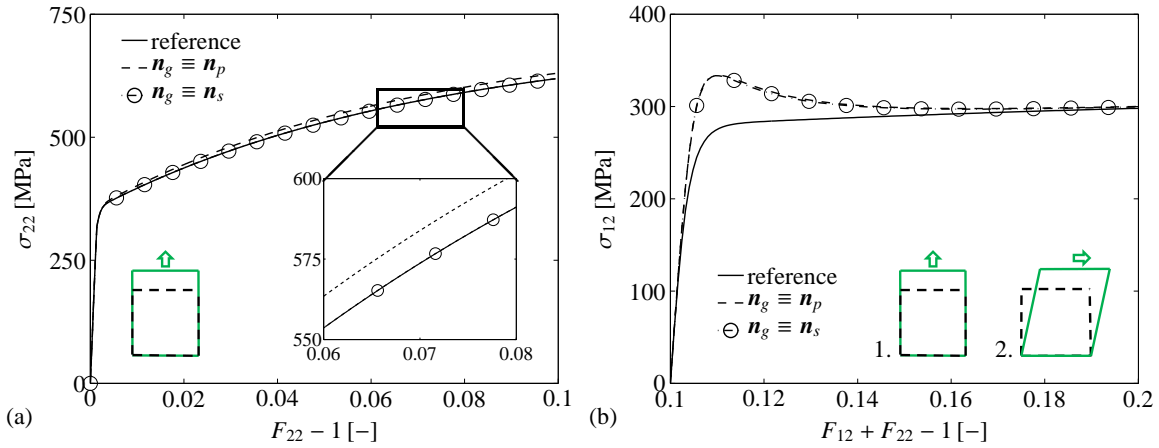
Figure 4.3.: Comparison of two model responses under (a) proportional (plane strain tension) and (b) non-proportional loading paths (plane strain tension followed by shear) neglecting kinematic hardening. The reference solution represents the solution obtained for isotropic hardening only (this reference solution is identical for both models). For the model $\boldsymbol{n}_g \equiv \boldsymbol{n}_s$ an identical response to the reference solution is observed under plane strain loading conditions as latent– hardening does affect the material response. For $\boldsymbol{n}_g \equiv \boldsymbol{n}_p$ a deviation is observed. Both models show a stress overshoot in the subsequent shear loading due to cross–hardening. The stress level is slightly lower for $\boldsymbol{n}_g \equiv \boldsymbol{n}_s$ as for $\boldsymbol{n}_g \equiv \boldsymbol{n}_p$ where additional dynamic hardening is occurring in the proportional loading path.
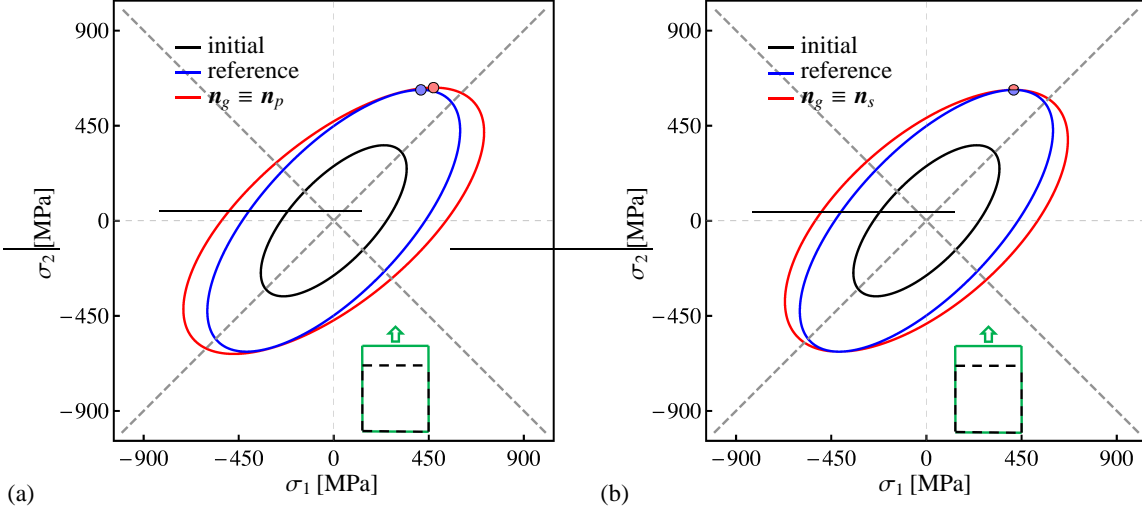
Figure 4.4.: Yield loci before as well as after a plane strain tensile test at $F_{22} - 1 = 0.1$, neglecting kinematic hardening. The initial yield locus has the form of Hill'48. The reference solution represents the solution obtained for isotropic hardening only. The model responses, based (a) on the plastic flow direction $\boldsymbol{n}_g \equiv \boldsymbol{n}_p$ and (b) on the stress deviator normal relatively to the center $\boldsymbol{n}_g \equiv \boldsymbol{n}_s$, are shown. The point of loading at $F_{22} - 1 = 0.1$ is additionally presented, which clearly shows the difference between the models for a proportional loading path.

4.3.2. Examples Including Kinematic Hardening

As mentioned earlier the consideration of kinematic hardening leads to an additional difficulty for $\boldsymbol{n}_g \equiv \boldsymbol{n}_s$. This section aims at investigating the consequences of selecting $\boldsymbol{n}_g \equiv \boldsymbol{n}_p$, $\boldsymbol{n}_k \equiv \boldsymbol{n}_p$,
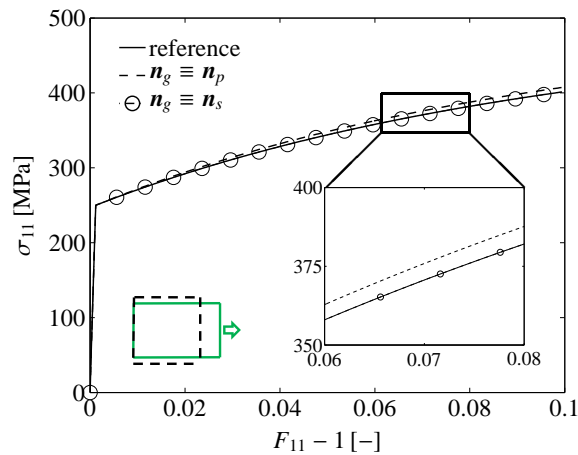
Figure 4.5.: Comparison of model responses under uniaxial tensile loading, neglecting kinematic hardening. The reference solution represents the solution obtained for isotropic hardening only. For the model based on the stress deviator $\boldsymbol{n}_g \equiv \boldsymbol{n}_s$ an identical response to the reference solution is observed, for the original model formulation based on the plastic flow normal $\boldsymbol{n}_g \equiv \boldsymbol{n}_p$ a deviation is observed. For an initially isotropic yield locus, both model predictions are identical to the reference solution.
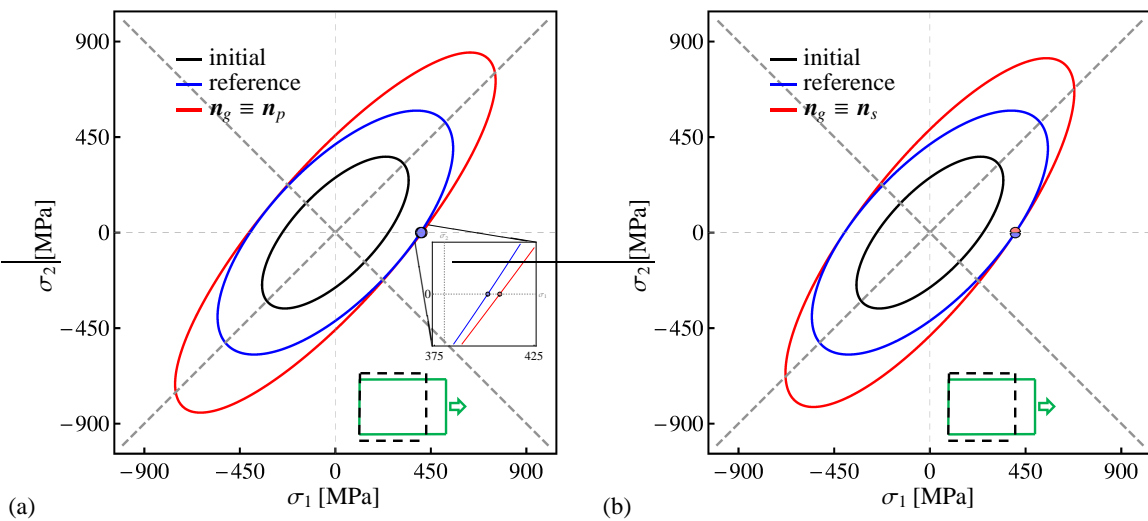
Figure 4.6.: Yield loci initially as well as after uniaxial tensile loading at $F_{11}-1 = 0.1$, neglecting kinematic hardening. The initial yield locus has the form of Hill'48. The reference solution represents the solution obtained for isotropic hardening only. The model responses, based (a) on the plastic flow direction $\boldsymbol{n}_g \equiv \boldsymbol{n}_p$ and (b) on the stress deviator normal relatively to the center $\boldsymbol{n}_g \equiv \boldsymbol{n}_s$, are shown. The point of loading at $F_{11} - 1 = 0.1$ is additionally presented. The original formulation based on the plastic flow direction shows a more extreme expansion of the yield locus which is reduced by the adjusted formulation based on the stress deviator.

$\boldsymbol{n}_g \equiv \boldsymbol{n}_s$, $\boldsymbol{n}_k \equiv \boldsymbol{n}_p$ as well as $\boldsymbol{n}_g \equiv \boldsymbol{n}_s$, $\boldsymbol{n}_k \equiv \boldsymbol{n}_s$ as the proposed remedy. Figure 4.7 displays the yield loci the models render once loaded under uniaxial stress. The shift of the center of the yield locus due to kinematic hardening in loading direction is clearly observed for all three models. The models based on the stress deviator ($\boldsymbol{n}_g \equiv \boldsymbol{n}_s$) exhibit an additional rotation to the present stretching of the yield locus. Here, the model based on the kinematic hardening with

$n_k \equiv n_s = [S - X]/|S - X|$ features a stretching between the other two models. At loading point $F_{11} - 1 = 0.1$, this model predicts a slightly lower stress level compared to the other one, Figure 4.8(a). Numerically, the reference solution without cross–hardening for the kinematic hardening model based on the plastic flow direction ($n_k \equiv n_p$) possesses a sufficiently close response to the second model ($n_g \equiv n_s, n_k \equiv n_p$). Although small, a stress offset is measured whereas this gap is completely avoided by the third model ($n_g \equiv n_s, n_k \equiv n_s$) [5]. For the case of plane strain loading, a similar behavior is seen.
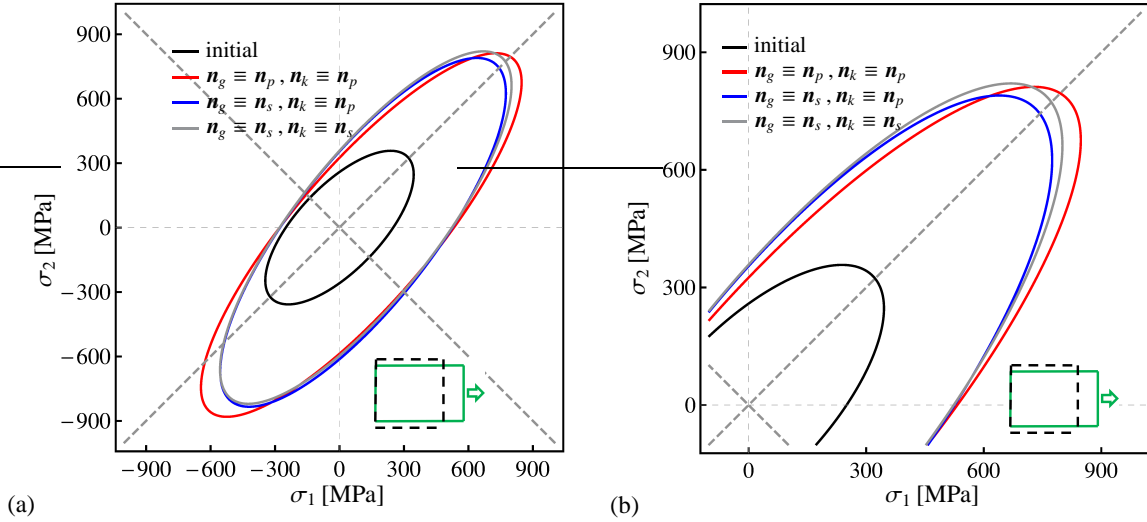
Figure 4.7.: Yield loci before as well as after uniaxial tensile loading for three different model formulations including kinematic hardening are shown at $F_{11} - 1 = 0.1$. The model responses are based on the plastic flow direction $n_g \equiv n_p$ where kinematic hardening evolves in direction of plastic flow as well $n_k \equiv n_p$. Furthermore, models based on the stress deviator normal relatively to the center $n_g \equiv n_s$ where (i) kinematic hardening is still in direction of plastic flow $n_k \equiv n_p$ and (ii) kinematic hardening is in radial direction $n_k \equiv n_s$. (a) Full yield loci clearly show the shift of the center due to kinematic hardening; (b) detailed view of the first quadrant.

Figure 4.8(b) shows the stress response after an orthogonal loading path change. The results indicate even in the present of kinematic hardening that no (significant) differences in the cross–hardening behavior are present between all three model formulations. In summary, the numerical results with kinematic hardening confirm the previous implications.

4.4. Conclusion

Within this chapter the consequences of the use of the radial direction $n_s = [S - X]/|S - X|$ in the evolution of the cross–hardening tensor in the Levkovitch–Svendsen model is discussed. In the original model parallel and orthogonal projections are based on the unit plastic flow direction $n_p = \dot{\varepsilon}_p/|\dot{\varepsilon}_p|$. For initially anisotropic plasticity under proportional loading, even in the absence of dynamic hardening with properly modified parameters the original model shows additional strength gain in direction of the active loading path. This phenomenon is called as the hardening entanglement in the current work. This effect is due to a continuous directional change in the

---

[5]In comparison to the solution without cross–hardening for the kinematic hardening model based on the stress deviator ($n_k \equiv n_s$).
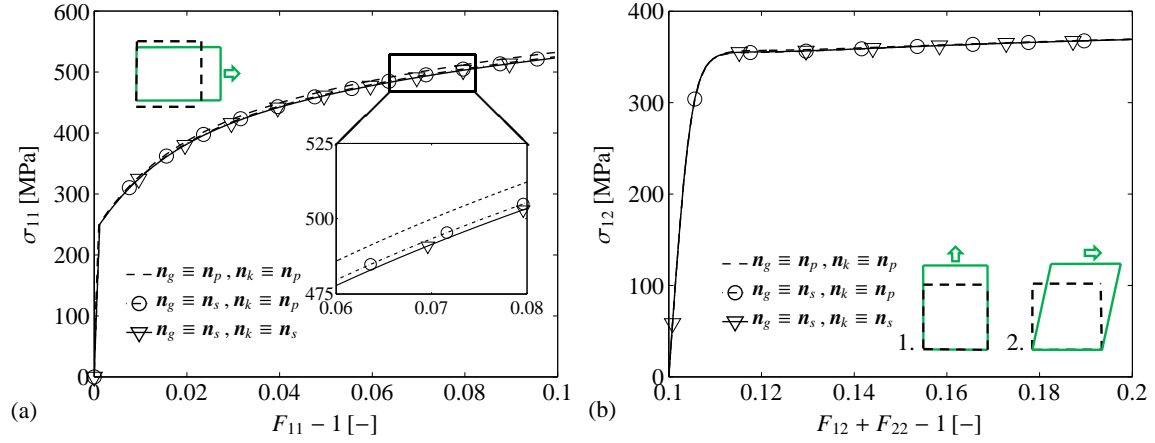
Figure 4.8.: Comparison of the three model responses under (a) uniaxial loading and (b) non-proportional loading path (plane strain tension followed by shear) including kinematic hardening. All models show nearly identical cross–hardening behavior after the load path change. Under uniaxial tensile loading, differences are observed between the models. For the model based on the plastic flow direction $\boldsymbol{n}_g \equiv \boldsymbol{n}_p$ these are identical to the case without kinematic hardening (see Figure 4.5). Furthermore, the models based on the stress deviator $\boldsymbol{n}_g \equiv \boldsymbol{n}_s$, although for $\boldsymbol{n}_k = \boldsymbol{n}_p$ an improvement is observed, only for the model including kinematic hardening in direction of the stress deviator $\boldsymbol{n}_k = \boldsymbol{n}_s$ an exactly identical result to the case without cross–hardening is obtained. Due to the different models for kinematic hardening, both models based on the stress deviator show a stress difference as well. Relatively less pronounced softening region in the shear stress response as compared to Figure 4.3 is due to rapid strengthening with kinematic hardening.

plastic strains during the loading path which does not comply with the stress direction in the presence of inherent material anisotropy. Supported by analytically and numerically handled results, it is shown that this hardening entanglement, which affects especially the parameter identification by precluding a clear identification of the hardening sources, is bypassed by using the radial direction $\boldsymbol{n}_s$ rather than plastic flow direction $\boldsymbol{n}_p$.

4.A. Loss of Ellipticity of the Yield Locus

The stretching and, therefore, the aspect ratio of the yield loci, strongly depends on the choice of material parameters. For the current model, this is analyzed based on the cross–hardening saturation magnitude s_l, Figure 4.9. For moderate values of s_l, the yield loci in both models show a reasonable expansion. However, for larger absolute values of s_l, the yield loci tend to loose ellipticity. This effect happens at a higher value for the model based on the stress deviator normal $\boldsymbol{n}_g = \boldsymbol{n}_s$. This shows that the model improvement, $\boldsymbol{n}_g \equiv \boldsymbol{n}_s$, solves not only the difficulty in identification processes of the material parameters, it additionally stabilizes the material response against loss of ellipticity.

Using Equations (4.2.9) and (4.2.14), it is possible to find rigorous bounds for s_l, say s_l^{critical}, associated with the model with $\boldsymbol{n}_g \equiv \boldsymbol{n}_s$, for which the yield locus for the projected plane stress state looses ellipticity with $\det(\widehat{\boldsymbol{\mathcal{B}}}(\gamma)) = \det(\widehat{\boldsymbol{\mathcal{A}}} + \widehat{\boldsymbol{\mathcal{H}}}(\gamma)) = 0$, that is if $\widehat{\boldsymbol{\mathcal{A}}} + \widehat{\boldsymbol{\mathcal{H}}}(\gamma)$ ceases to be positive definite for $\gamma \to \infty$. The analyses show that for the case of anisotropy the critical bound for s_l^{critical} depends on Hill's anisotropy parameters as well as loading path applied encapsulated
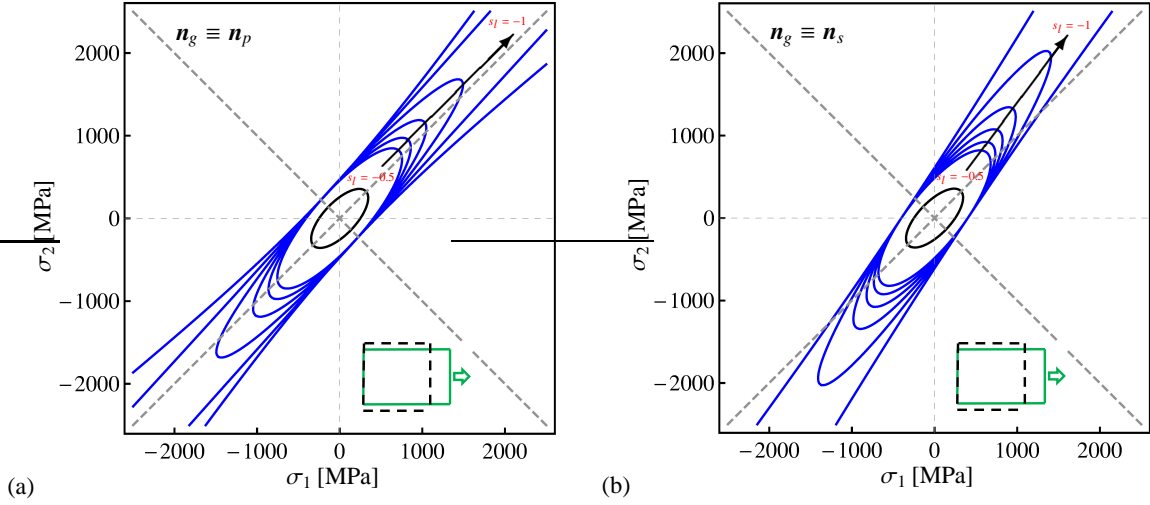
Figure 4.9.: Yield loci before as well as after uniaxial tensile loading at $F_{11} - 1 = 0.1$ for different values of the cross–hardening saturation magnitude s_l, neglecting kinematic hardening. Both models show for high values of s_l an extreme (unrealistic) expansion of the yield loci. The (a) original model based on the plastic flow direction ($\boldsymbol{n}_p$) loses ellipticity at lower s_l values than (b) the one on the stress deviator ($\boldsymbol{n}_s$).

in $\alpha_S = S_{11}/S_{22}$ with the expression

$$s_l^{\text{critical}} = -\frac{6[1 + \alpha_S + \alpha_S^2][F_\sharp G_\sharp + F_\sharp H_\sharp + G_\sharp H_\sharp]}{F_\sharp[4 + 4\alpha_S + \alpha_S^2] + G_\sharp[1 + 4\alpha_S + 4\alpha_S^2] + H_\sharp[1 - 2\alpha_S + \alpha_S^2]}, \tag{4.A.1}$$

Figure 4.10 depicts the variation of s_l^{critical} for the given set of anisotropy parameters in Table 4.1. It is noteworthy that for the case of isotropy, that is $F_\sharp = G_\sharp = H_\sharp = 1/2$, s_l^{critical} simplifies to $s_l^{\text{critical}} = -3/2$. Hence, its dependence on the loading path vanishes. For a given loading path, as long as s_l is chosen to obey $|s_l| < |s_l^{\text{critical}}|$ any loss of ellipticity is avoided.

4.B.   Determination of the Continuum Elastoplastic Moduli

Small strains are assumed with the use of tensor notation rather than vector notation. In order to define the continuum elasto-plastic moduli first one has to take the rate of the yield function which is written in classical form, in absence of kinematic hardening, as $\Phi(\boldsymbol{\sigma}, \boldsymbol{\mathcal{B}}, q) = \sqrt{\boldsymbol{\sigma} : \boldsymbol{\mathcal{B}} : \boldsymbol{\sigma}} - \sigma_{y,11}$, where $\boldsymbol{\mathcal{B}} = \boldsymbol{\mathcal{A}} + \boldsymbol{\mathcal{H}}$, $\sigma_{y,11} = \sigma_{0,11} + q$ with q representing the isotropic hardening stress like variable and $\sigma_{0,11}$ representing the initial yield stress in the direction of loading. Now, let $\dot{\Phi} = 0$ with

$$\dot{\Phi} = \frac{\partial \Phi}{\partial \boldsymbol{\sigma}} : \dot{\boldsymbol{\sigma}} + \frac{\partial \Phi}{\partial \boldsymbol{\mathcal{H}}} :: \dot{\boldsymbol{\mathcal{H}}} + \frac{\partial \Phi}{\partial q} \dot{q} = 0 \,. \tag{4.B.1}$$

Here :: represents the fourth-order contraction product where for two fourth-order tensors $\boldsymbol{\mathcal{E}}$ and $\boldsymbol{\mathcal{F}}$ one has $\boldsymbol{\mathcal{E}} :: \boldsymbol{\mathcal{F}} = \mathcal{E}_{ijkl}\mathcal{F}_{ijkl}$. Except for the standard derivatives with respect to the zeroth- and the second-order tensors, the linearization of the yield function involves derivatives with respect to the fourth-order structural tensor $\boldsymbol{\mathcal{H}}$. Now, since

$$\Phi = \sqrt{\boldsymbol{\sigma} : [\boldsymbol{\mathcal{A}} + \boldsymbol{\mathcal{H}}] : \boldsymbol{\sigma}} - [\sigma_0 + q] = 0 \,, \tag{4.B.2}$$
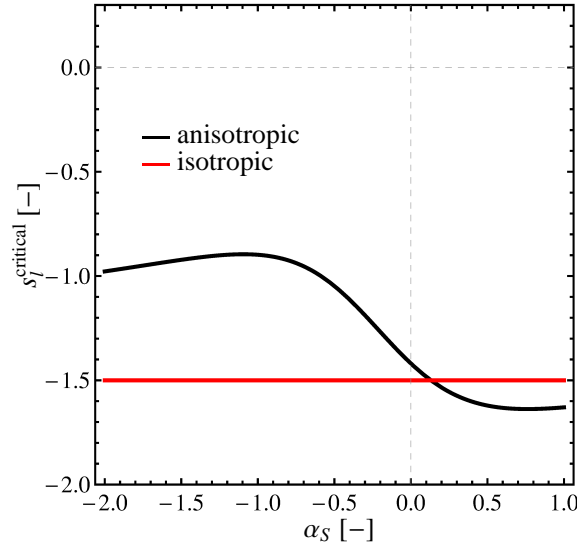
Figure 4.10.: $s_l^{critical}$ which gives $\det(\widehat{\boldsymbol{B}}(\gamma)) = 0$ for $\gamma \to \infty$ according to the parameter set given in Table 4.1 for the conditions of initial isotropy and anisotropy for $\boldsymbol{n}_g \equiv \boldsymbol{n}_s$. As seen for isotropy $s_l^{critical} = -3/2$ is invariant whereas for the case of anisotropy it varies with α_S according to Equation (4.A.1).

the derivative $\partial\Phi/\partial\boldsymbol{\mathcal{H}}$ can be represented in indicial notation as $\partial\Phi/\partial\mathcal{H}_{mnpq}$ with

$$\frac{\partial\Phi}{\partial\mathcal{H}_{mnpq}} = \frac{1}{2}\frac{1}{\sqrt{\sigma_{ij}\left[\mathcal{A}_{ijkl} + \mathcal{H}_{ijkl}\right]\sigma_{kl}}}\sigma_{ij}\frac{\partial\mathcal{H}_{ijkl}}{\partial\mathcal{H}_{mnpq}}\sigma_{kl}\,. \tag{4.B.3}$$

Noting that

$$\frac{\partial\mathcal{H}_{ijkl}}{\partial\mathcal{H}_{mnpq}} = \mathscr{I}_{ijklmnpq}^{\mathrm{sS,dev}}\,, \tag{4.B.4}$$

where the details are given in Section 4.C, and

$$\sigma_{ij}\mathscr{I}_{ijklmnpq}^{\mathrm{sS,dev}}\sigma_{kl} = \sigma_{mn}^{\mathrm{dev}}\sigma_{pq}^{\mathrm{dev}}\,, \tag{4.B.5}$$

where $\boldsymbol{\sigma}^{\mathrm{dev}} = \mathrm{dev}(\boldsymbol{\sigma})$ one obtains

$$\frac{\partial\Phi}{\partial\boldsymbol{\mathcal{H}}} = \frac{1}{2}\frac{\boldsymbol{\sigma}^{\mathrm{dev}} \otimes \boldsymbol{\sigma}^{\mathrm{dev}}}{\sqrt{\boldsymbol{\sigma} : [\boldsymbol{\mathcal{A}} + \boldsymbol{\mathcal{H}}] : \boldsymbol{\sigma}}}\,. \tag{4.B.6}$$

Now, using $\dot{\boldsymbol{\sigma}} = \boldsymbol{\mathcal{C}}^e : [\dot{\boldsymbol{\varepsilon}} - \dot{\boldsymbol{\varepsilon}}_p]$ and $\boldsymbol{r}_p = \partial\Phi/\partial\boldsymbol{\sigma}$ with

$$\boldsymbol{r}_p = \frac{\boldsymbol{\mathcal{B}} : \boldsymbol{\sigma}}{\sqrt{\boldsymbol{\sigma} : \boldsymbol{\mathcal{B}} : \boldsymbol{\sigma}}} = \frac{\boldsymbol{\mathcal{B}} : \boldsymbol{\sigma}}{\sigma_{y,11}}\,, \tag{4.B.7}$$

the associated flow rule reads $\dot{\boldsymbol{\varepsilon}}_p = \dot{\gamma}\,\boldsymbol{r}_p$. Hence one obtains

$$\frac{\partial\Phi}{\partial\boldsymbol{\sigma}} : \dot{\boldsymbol{\sigma}} = \boldsymbol{r}_p : \boldsymbol{\mathcal{C}}^e : \dot{\boldsymbol{\varepsilon}} - \dot{\gamma}\,\boldsymbol{r}_p : \boldsymbol{\mathcal{C}}^e : \boldsymbol{r}_p\,. \tag{4.B.8}$$

Coming to the derivative with respect to the structural tensor, using the condition of fully developed plastic flow with $\sigma_{y,11} = \sqrt{\boldsymbol{\sigma} : \boldsymbol{\mathcal{B}} : \boldsymbol{\sigma}}$ and with above definitions leading to $[\boldsymbol{\sigma}^{\mathrm{dev}} \otimes \boldsymbol{\sigma}^{\mathrm{dev}}] :: \dot{\boldsymbol{\mathcal{H}}} = \boldsymbol{\sigma}^{\mathrm{dev}} : \dot{\boldsymbol{\mathcal{H}}} : \boldsymbol{\sigma}^{\mathrm{dev}}$ one has

$$\frac{\partial\Phi}{\partial\boldsymbol{\mathcal{H}}} :: \dot{\boldsymbol{\mathcal{H}}} = \frac{1}{2}\frac{\boldsymbol{\sigma}^{\mathrm{dev}} : \dot{\boldsymbol{\mathcal{H}}} : \boldsymbol{\sigma}^{\mathrm{dev}}}{\sigma_{y,11}}\,. \tag{4.B.9}$$

Using the solution for the rate of the structural tensor for linear stress paths one has

$$\dot{\boldsymbol{\mathcal{H}}}/\dot{\gamma} = c_l s_l g_{c_l} \boldsymbol{\mathcal{I}}^{\text{dev}} + [c_d s_d g_{c_d} - c_l s_l g_{c_l}] \boldsymbol{N}_{\boldsymbol{\sigma}^{\text{dev}}} \otimes \boldsymbol{N}_{\boldsymbol{\sigma}^{\text{dev}}} \,. \tag{4.B.10}$$

Substituting this back into (4.B.9) and noting that $\boldsymbol{\sigma}^{\text{dev}} : \boldsymbol{\mathcal{I}}^{\text{dev}} : \boldsymbol{\sigma}^{\text{dev}} = \boldsymbol{\sigma}^{\text{dev}} : \boldsymbol{\sigma}^{\text{dev}} = |\boldsymbol{\sigma}^{\text{dev}}|^2$ and $\boldsymbol{\sigma}^{\text{dev}} : \boldsymbol{N}_{\boldsymbol{\sigma}^{\text{dev}}} = \boldsymbol{N}_{\boldsymbol{\sigma}^{\text{dev}}} : \boldsymbol{\sigma}^{\text{dev}} = |\boldsymbol{\sigma}^{\text{dev}}|$ one obtains

$$\frac{\partial \Phi}{\partial \boldsymbol{\mathcal{H}}} :: \dot{\boldsymbol{\mathcal{H}}} = \dot{\gamma} \frac{1}{2\sigma_{y,11}} \left[c_l s_l g_{c_l} |\boldsymbol{\sigma}^{\text{dev}}|^2 + [c_d s_d g_{c_d} - c_l s_l g_{c_l}] |\boldsymbol{\sigma}^{\text{dev}}|^2 \right] \,. \tag{4.B.11}$$

Rearranging the terms one reaches

$$\frac{\partial \Phi}{\partial \boldsymbol{\mathcal{H}}} :: \dot{\boldsymbol{\mathcal{H}}} = \dot{\gamma} \frac{c_d s_d g_{c_d} |\boldsymbol{\sigma}^{\text{dev}}|^2}{2\sigma_{y,11}} \,. \tag{4.B.12}$$

Finally,

$$\frac{\partial \Phi}{\partial q} \dot{q} = -\dot{\gamma} f_{,q}^2 q' = -\dot{\gamma} q' \,. \tag{4.B.13}$$

Collecting all terms one has

$$\dot{\Phi} = \boldsymbol{r}_p : \boldsymbol{\mathcal{C}}^e : \dot{\boldsymbol{\varepsilon}} - \dot{\gamma} \, \boldsymbol{r}_p : \boldsymbol{\mathcal{C}}^e : \boldsymbol{r}_p + \dot{\gamma} \frac{c_d s_d g_{c_d} |\boldsymbol{\sigma}^{\text{dev}}|^2}{2\sigma_{y,11}} - \dot{\gamma} q' = 0 \,. \tag{4.B.14}$$

Hence the plastic multiplier is

$$\dot{\gamma} = \frac{\boldsymbol{r}_p : \boldsymbol{\mathcal{C}}^e : \dot{\boldsymbol{\varepsilon}}}{\boldsymbol{r}_p : \boldsymbol{\mathcal{C}}^e : \boldsymbol{r}_p + q' - \dfrac{c_d s_d g_{c_d} |\boldsymbol{\sigma}^{\text{dev}}|^2}{2\sigma_{y,11}}} \,. \tag{4.B.15}$$

Substituting this expression into the stress rate relation $\dot{\boldsymbol{\sigma}} = \boldsymbol{\mathcal{C}}^e : [\dot{\boldsymbol{\varepsilon}} - \dot{\boldsymbol{\varepsilon}}_p] = \boldsymbol{\mathcal{C}}^e : [\dot{\boldsymbol{\varepsilon}} - \dot{\gamma} \boldsymbol{r}_p]$ one obtains

$$\dot{\boldsymbol{\sigma}} = \boldsymbol{\mathcal{C}}^e : \left[\dot{\boldsymbol{\varepsilon}} - \frac{\boldsymbol{r}_p : \boldsymbol{\mathcal{C}}^e : \dot{\boldsymbol{\varepsilon}}}{\boldsymbol{r}_p : \boldsymbol{\mathcal{C}}^e : \boldsymbol{r}_p + q' - \dfrac{c_d s_d g_{c_d} |\boldsymbol{\sigma}^{\text{dev}}|^2}{2\sigma_{y,11}}} \boldsymbol{r}_p \right] \,. \tag{4.B.16}$$

This can be rearranged to give $\dot{\boldsymbol{\sigma}} = \boldsymbol{\mathcal{C}}^{ep} : \dot{\boldsymbol{\varepsilon}}$ with

$$\boldsymbol{\mathcal{C}}^{ep} = \boldsymbol{\mathcal{C}}^e - \frac{\boldsymbol{r}_p : \boldsymbol{\mathcal{C}}^e \otimes \boldsymbol{\mathcal{C}}^e : \boldsymbol{r}_p}{\boldsymbol{r}_p : \boldsymbol{\mathcal{C}}^e : \boldsymbol{r}_p + q' - \dfrac{c_d s_d g_{c_d} |\boldsymbol{\sigma}^{\text{dev}}|^2}{2\sigma_{y,11}}} \,. \tag{4.B.17}$$

In the absence of dynamic hardening, as it is usually used in the literature, one has

$$\boldsymbol{\mathcal{C}}^{ep} = \boldsymbol{\mathcal{C}}^e - \frac{\boldsymbol{r}_p : \boldsymbol{\mathcal{C}}^e \otimes \boldsymbol{\mathcal{C}}^e : \boldsymbol{r}_p}{\boldsymbol{r}_p : \boldsymbol{\mathcal{C}}^e : \boldsymbol{r}_p + q'} \,. \tag{4.B.18}$$

4.C.   Eighth-Order Identity Tensors

For a fourth-order tensor $\mathcal{A}$ the self-derivative $\partial \mathcal{A}/\partial \mathcal{A}$ gives the following eighth-order identity tensor $\boldsymbol{\mathscr{I}} = \mathscr{I}_{ijklmnpq} \boldsymbol{\varepsilon}_i \otimes \boldsymbol{\varepsilon}_j \otimes \boldsymbol{\varepsilon}_k \otimes \boldsymbol{\varepsilon}_l \otimes \boldsymbol{\varepsilon}_m \otimes \boldsymbol{\varepsilon}_n \otimes \boldsymbol{\varepsilon}_p \otimes \boldsymbol{\varepsilon}_q$ with

$$\mathscr{I}_{ijklmnpq} = \delta_{im} \delta_{jn} \delta_{kp} \delta_{lq} \,. \tag{4.C.1}$$

If $\mathcal{A}$ has major but no minor symmetry, that is if $\mathcal{A}_{ijkl} = \mathcal{A}_{klij}$, the self-derivative gives $\partial\boldsymbol{\mathcal{A}}/\partial\boldsymbol{\mathcal{A}} = \boldsymbol{\mathscr{I}}^{\mathrm{S}}$ with

$$\mathscr{I}^{\mathrm{S}}_{ijklmnpq} = \frac{1}{2}\left[\delta_{im}\delta_{jn}\delta_{kp}\delta_{lq} + \delta_{km}\delta_{ln}\delta_{ip}\delta_{jq}\right] . \tag{4.C.2}$$

If $\mathcal{A}$ has minor but no major symmetry, that is if $\mathcal{A}_{ijkl} = \mathcal{A}_{jikl} = \mathcal{A}_{ijlk} = \mathcal{A}_{jilk}$, the self-derivative gives $\partial\boldsymbol{\mathcal{A}}/\partial\boldsymbol{\mathcal{A}} = \boldsymbol{\mathscr{I}}^{\mathrm{s}}$ with

$$\mathscr{I}^{\mathrm{s}}_{ijklmnpq} = \frac{1}{4}\left[\delta_{im}\delta_{jn}\delta_{kp}\delta_{lq} + \delta_{jm}\delta_{in}\delta_{kp}\delta_{lq} + \delta_{im}\delta_{jn}\delta_{lp}\delta_{kq} + \delta_{jm}\delta_{in}\delta_{lp}\delta_{kq}\right] . \tag{4.C.3}$$

Now, if $\mathcal{A}$ has super-symmetry, that is it has both major and minor symmetries, with $\mathcal{A}_{ijkl} = \mathcal{A}_{jikl} = \mathcal{A}_{ijlk} = \mathcal{A}_{jilk} = \mathcal{A}_{klij} = \mathcal{A}_{klji} = \mathcal{A}_{lkij} = \mathcal{A}_{lkji}$, the self-derivative gives $\partial\boldsymbol{\mathcal{A}}/\partial\boldsymbol{\mathcal{A}} = \boldsymbol{\mathscr{I}}^{\mathrm{sS}}$ with

$$\mathscr{I}^{\mathrm{sS}}_{ijklmnpq} = \frac{1}{8}\left[\begin{array}{c}\delta_{im}\delta_{jn}\delta_{kp}\delta_{lq} + \delta_{jm}\delta_{in}\delta_{kp}\delta_{lq} + \delta_{im}\delta_{jn}\delta_{lp}\delta_{kq} + \delta_{jm}\delta_{in}\delta_{lp}\delta_{kq} \\ +\delta_{km}\delta_{ln}\delta_{ip}\delta_{jq} + \delta_{lm}\delta_{kn}\delta_{ip}\delta_{jq} + \delta_{km}\delta_{ln}\delta_{jp}\delta_{iq} + \delta_{lm}\delta_{kn}\delta_{jp}\delta_{iq}\end{array}\right] . \tag{4.C.4}$$

Finally, if in addition to super-symmetry $\boldsymbol{\mathcal{A}}$ is deviatoric, that is $A_{iikl} = A_{ijkk} = 0$ the self-derivative gives $\partial\boldsymbol{\mathcal{A}}/\partial\boldsymbol{\mathcal{A}} = \boldsymbol{\mathscr{I}}^{\mathrm{sS,dev}}$ with

$$\begin{aligned}\mathscr{I}^{\mathrm{sS,dev}}_{ijklmnpq} = {}& \frac{1}{8}\left[\begin{array}{c}\delta_{im}\delta_{jn}\delta_{kp}\delta_{lq} + \delta_{im}\delta_{jn}\delta_{lp}\delta_{kq} + \delta_{jm}\delta_{in}\delta_{kp}\delta_{lq} + \delta_{jm}\delta_{in}\delta_{lp}\delta_{kq} \\ +\delta_{km}\delta_{ln}\delta_{ip}\delta_{jq} + \delta_{km}\delta_{ln}\delta_{jp}\delta_{iq} + \delta_{lm}\delta_{kn}\delta_{ip}\delta_{jq} + \delta_{lm}\delta_{kn}\delta_{jp}\delta_{iq}\end{array}\right] \\ & - \frac{1}{12}\left[\begin{array}{c}\delta_{kl}\delta_{im}\delta_{jn}\delta_{pq} + \delta_{kl}\delta_{jm}\delta_{in}\delta_{pq} + \delta_{ij}\delta_{kp}\delta_{lq}\delta_{nm} + \delta_{ij}\delta_{lp}\delta_{kq}\delta_{nm} \\ +\delta_{ij}\delta_{km}\delta_{ln}\delta_{pq} + \delta_{ij}\delta_{lm}\delta_{kn}\delta_{pq} + \delta_{kl}\delta_{ip}\delta_{jq}\delta_{mn} + \delta_{kl}\delta_{jp}\delta_{iq}\delta_{mn}\end{array}\right] \\ & + \frac{1}{9}\left[\delta_{ij}\delta_{kl}\delta_{mn}\delta_{pq}\right] .\end{aligned} \tag{4.C.5}$$

Part II.

Damage Driven Localization and Fracture

5. A combined experimental-numerical investigation of ductile fracture in bending of a class of ferritic-martensitic steel

In this chapter, a combined experimental-numerical study on fracture initiation at the convex surface and its propagation during bending of a class of ferritic-martensitic steel are presented. On the experimental side, so-called free bending experiments are conducted on DP1000 steel sheets until fracture, realizing optical and scanning electron microscopy analyses on the post mortem specimens for fracture characterization. A blended Mode I - Mode II fracture pattern, which is driven by cavitation at non-metallic inclusions as well as martensitic islands and resultant softening-based intense strain localization, is observed. Phenomena like crack zig-zagging and crack alternation at the bend apex along the bending axis are introduced and discussed. On the numerical side, based on this physical motivation, the process is simulated in 2D plane strain and 3D, using Gurson's dilatant plasticity model with a recent shear modification, strain-based void nucleation, and coalescence effects. The effect of certain material parameters (initial porosity, damage at coalescence and failure, shear modification term, etc.), plane strain constraint and mesh size on the localization and the fracture behavior are investigated in detail.

5.1. Introduction

In metallic materials, the localization into deformation bands, as a precursor to fracture, is sourced from two strongly microstructure-dependent constitutive features, (1) path dependence of strain hardening and (2) softening mechanism, [16]. The former is caused by destabilizing effects of the existence of a vertex or a region of sharp curvature at the loading point of the yield surface, which are implied by the stiffness reduction with respect to non-proportional load increments, [16, 47]. Such vertex formations are natural outcomes of the underlying physics of single crystals with the existence of discrete slip systems and accordingly resolved shear stresses. The latter may be due to the effect of temperature on mechanical properties, see e.g. [179], or progressive material deterioration due to cavitation, i.e. nucleation, growth, and coalescence of micro-voids, see e.g. [340, 228, 265] also [305].

Experiments reveal that fracture development in bending of modern alloys and polycrystals usually occurs with intense strain localization starting at the free convex surface, which is preceded by orange peels and gradually growing undulations parallel to the bend axis, [8, 266, 85, 185]. Numerical studies invariably use the finite element method in investigations on bendability. In accordance with the mentioned constitutive strain localization sources, previous numerical studies on bending will be classified under the following categories:

- Path-Dependent Strain Hardening,

Table 5.1.: *Studies on localization and fracture in bending of metallic sheets.*

ID	Reference	Model	Material	Crack Prop.
1.	TVERGAARD [1981]	GTN	Al 6000	✓
2.	TRIANTAFYLLIDIS ET AL. [1982]	Corner Theory	Hypothetical	-
3.	TVERGAARD [1987]	GTN+Kin. Hard.	Hypothetical	-
4.	BECKER [1992]	Crystal Plasticity	Polycrystal Al	✓
5.	KURODA & TVERGAARD [2001]	Non-associative Flow	Hypothetical	-
6.	DAO & LIE [2001]	Crystal Plasticity	Hypothetical	-
7.	HAMBLI ET AL. [2003]	CDM	Hypothetical	-
8.	LIEVERS ET AL. [2003a]	GTN+Kin. Hard.	AA6111	-
9.	LIEVERS ET AL. [2003b]	GTN+Kin. Hard.	Hypothetical	✓
10.	HAMBLI ET AL. [2004]	CDM	0.6% C-Steel	✓
11.	WISSELINK & HUETINK [2007]	Nonlocal CDM	Hypothetical	✓
12.	WISSELINK & HUETINK [2008]	Nonlocal CDM	Al 6016	✓
13.	XUE & WIERZBICKI [2008]	CDM	Al 2014-T351	✓
14.	LE MAOUT ET AL. [2009]	GTN	Al 6000	✓
15.	KIM ET AL. [2010]	Thermal Softening	DP 780	-
16.	BETTAIEB ET AL. [2010]	GTN+Kin. Hard.	DP 600	-

- Softening,

- Combined Path-Dependent Strain Hardening and Softening,

with a brief summary of approaches is given below. For convenience reasons, these studies are also listed in historical order in Table 5.1.

[47] investigates pure bending of a polycrystalline sheet using a slip-based Taylor-like polycrystal model. The effect of inherent inhomogeneity with incompatibility of neighboring grains by different sets of crystal orientations at each grain and its effect on the shear band initiation at the free surface and its propagation toward the neutral axis is studied. Using a crystal plasticity-based model, [85] investigate the localization and fracture initiation (generally in a transgranular fashion) during bending of aluminum alloy sheets. Like in [301, 47, 161] the localizations are observed at both convex and concave surfaces. It is shown that without constituent particles intense shear bands initiate from wave bottoms whereas a localization in the form of shear bending can start beneath the free surface with the inhomogeneity effect of second-phase particles. The most important factors affecting bending of aluminum sheets are found to be strain hardening, texture, second phase particle position, and distribution, where high strain hardening is found to reduce the susceptibility to localization. Finally, using a generalized Taylor type polycrystal model, bending localizations are modeled in [161]. In [301] localization and shear band development in pure bending of elastoplastic solids with sharp and blunt vertices is studied using the J_2 corner theory presented in [74]. Wavelength imperfections are applied which focus on the deformation into shear bands starting from the free surface. It is notable that initial localizations are captured in the concave surface rather than the convex one in this study. Finally, in [160] plane strain bending localizations with a material model involving non-associative plastic flow as given in [159] is presented.

Coming to softening-based models, in [153] thermo-mechanical coupling is used to model draw-bending where adiabatic thermal softening acts as the localization agent, with the condition of a maximum tensile force, i.e. $dF = 0$, being set as the condition of localization. This study does

not investigate crack modes and crack patterns.

Damage softening is taken into account through internal variables which phenomenologically reflect the stiffness and strength loss of the matter, as in the case of Continuum Damage Mechanics (CDM) models, or via dilatancy of macroscopic plasticity and cavitation, as in the case of Gurson's plasticity.

Starting with the former, using a (gradient type) nonlocally enhanced CDM model, [330] and [331] present mesh objective softening-induced strain localization (where bifurcation into two crossing shear bands occurs) and crack trajectories in bending. The effect of pre-strain is investigated where the prestrained specimens are shown to fail earlier, [331]. [339] investigates the bendability of 2024-T351 Al alloys using a phenomenological model where the plane strain (shear) effects are involved through the utilization of load angle dependence. For sheets having different width-thickness-ratios it is experimentally and numerically shown that cracks start with shear localization at the central zone with the plane strain constraint. [115] uses a Lemaitre type CDM model for the L-bending process with plane strain assumption. Unlike in previously mentioned studies damage development is seen at both convex and concave sides of the bend at the same orders of magnitude. These questionable results stem from the utilized tension-compression invariant damage growth formulation which does not involve quasi-unilateral effects. This study does not involve localization due to a relatively coarse adapted mesh which acts as a length scale. Identical comments apply to [116] in which another CDM model with the damage evolution relying on equivalent plastic strain and its rate is used to evaluate bending defects. Since this study focuses on a variant of Gurson's plasticity, theoretical details of the CDM models are beyond the current scope. Interested readers can refer to the texts of [175, 177] for fundamentals or the manuscripts, and [63, 64, 56, 210, 57, 248, 288, 287, 19] and more recently [100] for certain developed advanced finite strain frameworks and various applications.

Coming to the latter, [305] investigates shear band localization in pure bending with cavitation under the effect of surface waviness and material inhomogeneity through concentrated local sub-surface void nucleating particles. In the progressively cavitating model localization occurs faster at the apex of the bend as opposed to [301] since the void growth is hindered on the compressive side of the neutral axis. Without specific reference to localization modes or fracture patterns, [198] investigates a hemming process for 6000 series aluminum alloys using Gurson's damage model with Hill'48-type plastic anisotropy.

For the combined effects of path-dependent strain hardening and cavitation [307] constitutes an example where shear cracks developed from void sheets inside the localization bands are modeled with Gurson's porous plasticity which gives account for progressive cavitation with combined effects of kinematic and isotropic hardening on the yield surface curvature following [209]. Kinematic hardening, by introducing an increased curvature compared to a merely isotropic hardening one, adds imperfection sensitivity to the constitutive model due to slight additional load path changes.The degree of non-uniformity of the strain field by an enforcement of the surface waviness causes a shear band formation at the wave bottoms. As noted by [307], the results admit a length-scale where strong mesh-dependence is due. For smaller element sizes narrower yet earlier localization bands are carried out. [185] studies bendability of AA6111 sheets for different Fe concentrations using Gurson's model with isotropic and kinematic hardening effects where the surface roughness effect is also investigated. Together with an alternative formulation of kinematic hardening [186] investigates the localization in bending using Gurson's damage model on the same problem example as [307]. A systematic sensitivity analysis is

followed through many material parameters related to yield surface curvature, material gradient, and failure mode. Again, it is also shown that geometric imperfections amplify the strain gradients and act as strain concentrators. Finally, [51], using Gurson's damage model with kinematic hardening effects and Thomason type void coalescence developed in [54], study bending fractures by means of finite element analyses, also studying the effect of geometric imperfections.

This study aims at presenting a combined experimental and numerical analysis on bending of a class of ferritic-martensitic steel. Ferritic-martensitic steels are commonly utilized in automotive industry due to their lightweight characteristics and good stretching performance. However, their formability is limited by fracture originating from voidage with growth and the coalescence of micro-voids which nucleate with decohesion at matrix non-metallic inclusions ($\sim$5-30 microns in diameter) or ferrite-martensite interfaces as well as inclusions or dispersed martensite particle ($\sim$0.5 microns in diameter) cracking. This cavitation history strongly depends on the stress state during plastic flow. The triaxial tensile (compressive) stress states give account for exponential void growth (shrinkage), whereas void sheeting, void nucleation, void distortion and void interaction with material rotation promotes a degradation of stiffness and strength under the shear stress states.

On the experimental part, a fractography analysis of a set of DP1000 steel sheets which are bent until fracture with the free bending process is presented. At certain loading levels Light Optical Microscopy (LOM) investigations are realized on the convex surface of the bend in order to capture surface undulations which, as aforementioned, motivate strain localization throughout the rest of the loading. Similar mechanisms until incipient fracture at the wave bottom, observed by [8] and [266], are captured for this class of advanced high strength steels as well. Once the apex of the bent and cracked specimens is investigated it is seen that the crack follows alternate patterns which are discontinuous on the bending axis. Such a pattern which cannot be captured in a plane strain analysis is linked to local material inhomogeneities throughout the bending axis. Coming to the fracture patterns at planes orthogonal to the bend axis, the observations invariably show crack initiation with an angle to the maximum tensile loading direction which holds the sign of a developed shear localization at the incipient fracture. It is observed that the cracks tend to evolve following a zig-zag pattern in the form of periodic ridges and valleys, which are characteristic for fracture surfaces separated by homogeneous micro-void fracture, [46]. An elucidation of this phenomenon based on different sources is given. In order to clarify the mode of the fracture, SEM analyses are conducted focusing on post-mortem fractured surfaces. Considerable evidence for cavitation, as a sign of void sheeting and resulting localization, is observed where the parabolic dimples, taking into account the macroscopic loading conditions, give a sign of a blended condition of the transgranular fracture of Mode I and Mode II (using the elastic fracture mechanics notion), with a domination of Mode II.

On the numerical part, bending is simulated using 2D plane strain and 3D finite element models which aim at capturing not only initial localization into shear bands at the convex free surface, but also the crack propagation and the crack path. For this purpose, a finite strain hypoelastic-plasticity framework with Gurson's porous model including a recent shear modification, [224], is developed and algorithmic steps for local integrations, which use a class of cutting plane algorithms, [239], are derived. Since DP1000 shows a relatively weak anisotropy due to rolling, this study is limited to the plastic isotropy. To this end, the derivations are implemented as a VUMAT subroutine for ABAQUS/EXPLICIT. The current motivation regarding the selection of a porous plasticity model, where softening is the prime localization source, stems from the aforementioned experimental evidence of cavitation on fracture surfaces. With this model, in

accordance with [305] and [307], the localization is captured on the convex surface of the bend under tension since the concave surface does not give account for void growth due to compressive hydrostatic stress. It should be noted that without sufficient softening a localization pattern cannot be captured according to [339]. Under generalized plane strain conditions (pure shear plus hydrostatic stress) materials are more susceptible to fracturing compared to generalized compressive or tensile stress states on the Π plane, i.e. for equal pressure values, [339]. This experimental fact is resolved by [339] by making use of Lode parameter dependence, which distinguishes generalized plane strain states from axisymmetric stress states, of void growth in Gurson's damage model. [224]uses a third invariant of the deviatoric Cauchy (true) stress tensor for this purpose. A number of sensitivity analyses based on mesh size and damage-related material parameters are presented. It is observed that selected mesh size acts as a length scale and manipulates localization time and width, in accordance with the findings of [307]. Moreover, it is shown that a small damage threshold for fracture results in a fracture pattern orthogonal to the principal tensile stress direction which occurs prior to shear band development resembling a brittle cleavage type separation, see also [185]. Regarding the crack pattern, zig-zagging is qualitatively captured which, on numerical grounds, is attributed to the combined effect of macroscopic loading conditions and the shear band crossing, where the physical motivations are attributed to different phenomena.

5.2. Shear Enhanced GTN Damage Model

For the hydrostatic stress-independent classical von Mises plasticity one has $\Phi^p = \Phi^p(\text{dev}(\boldsymbol{\sigma}), e^p)$, with e^p denoting the equivalent plastic strain. The current formulation is based on the Gurson's generic scalar valued isotropic yield function, [110], taking as a basis the response of a representative volume element containing a matrix of an incompressible ideal plasticity and a spherical void whose homogenization results in a macroscopically compressible plasticity model. Assuming σ_y and e^p denote the virgin yield stress and the equivalent plastic strain of the undamaged material matrix with

$$\sigma_y = \sigma_0 + q(e^p)\,, \tag{5.2.1}$$

where $q(e^p)$ represents the matrix material hardening function. Allowing f to represent the void volume fraction, one has $\Phi^p = \Phi^p(\text{dev}(\boldsymbol{\sigma}), \text{tr}(\boldsymbol{\sigma}), f, e^p)$ with

$$\Phi^p = \left[\frac{\sigma_{eq}}{\sigma_y}\right]^2 + 2q_1 f^* \cosh\left(\frac{3}{2}\frac{q_2 \sigma_m}{\sigma_y}\right) - [1 + q_3 f^{*2}] = 0\,, \tag{5.2.2}$$

where $\sigma_{eq} = \sigma_{eq}(\text{dev}(\boldsymbol{\sigma}))$ is the (macroscopic) equivalent von Mises stress, a function of Cauchy stress tensor, $\boldsymbol{\sigma}$. q_1, q_2, and q_3 are the material parameters, see e.g. [304] and [306]. For $q_1 = q_2 = q_3 = 1$ Gurson's original model, [110], is recovered. For $q_1 = q_3 = 0$ the porous structure is lost, e.g. the pressure dependence is precluded and conventional isochoric-isotropic plasticity is recovered. f^* denotes the modified void volume fraction, giving account for the accelerating effects of the void coalescence, [308],

$$f^* = \begin{cases} f & f \leq f_c\,, \\ f_c + \dfrac{f_u^* - f_c}{f_f - f_c}\,[f - f_c] & f > f_c\,. \end{cases} \tag{5.2.3}$$

Here, f_c is the critical void volume fraction at incipient coalescence. f_f is the fraction at failure. The material parameter f_u^* is defined by $f_u^* = 1/q_1$. The coalescence phase can be linked to an effective plastic strain rate, as seen in [240]. A Thomason type void coalescence is used in [54].

The plastic strain rate follows a conventional normality postulate,

$$\dot{\boldsymbol{\varepsilon}}^p = \dot{\gamma} \partial_{\boldsymbol{\sigma}} \Phi^p \,, \tag{5.2.4}$$

where $\dot{\gamma}$ is the plastic multiplier which is computed by the consistency condition. The hydrostatic stress-dependent yield function dictates a non-vanishing trace of $\dot{\boldsymbol{\varepsilon}}^p$, i.e. $\mathrm{tr}(\dot{\boldsymbol{\varepsilon}}^p) \neq 0$. The rate $\dot{e}^p$ is defined by the following generalized plastic work equivalence relation via $[1-f]\sigma_y \dot{e}^p = \boldsymbol{\sigma} : \dot{\boldsymbol{\varepsilon}}^p$

$$\dot{e}^p = \frac{\boldsymbol{\sigma} : \dot{\boldsymbol{\varepsilon}}^p}{[1-f]\sigma_y} \,. \tag{5.2.5}$$

The void volume fraction is assumed to evolve in two phases, namely nucleation and growth, where the resulting form reads

$$\dot{f} = \dot{f}^n + \dot{f}^g \,, \tag{5.2.6}$$

with the superscripts; n and g stand for nucleation and growth, respectively. The void volume fraction due to nucleation depends on the equivalent plastic strain by

$$\dot{f}^n = A_N \dot{e}^p \quad \text{with} \quad A_N = A_N(e^p) = \frac{f_N}{S_N \sqrt{2\pi}} \exp\left(-\frac{[e^p - e_N^p]^2}{2[S_N]^2}\right) \,, \tag{5.2.7}$$

where f_N and S_N are the nucleated void volume fraction and Gaussian standard deviation, respectively. e_N^p denotes the mean equivalent plastic strain at the incipient nucleation. f_N, S_N and e_N^p are typical material parameters. In the classical Gurson's damage model the time rate of change of void volume fraction due to void growth is linked to the plastic dilatation under hydrostatic stress using $\dot{f}^g = \dot{f}_{\mathrm{normal}}^g$ where

$$\dot{f}_{\mathrm{normal}}^g = [1-f]\mathrm{tr}(\dot{\boldsymbol{\varepsilon}}^p) \,. \tag{5.2.8}$$

Unless the mean stress is positive, this expression does not predict any damage development, subsequent localization with softening and fracture which is not in correlation with the experimental findings reported in e.g. [29] and [39]. [224] modified $\dot{f}^g$ to give account for fracture for low and negative stress triaxialities to give $\dot{f}^g = \dot{f}_{\mathrm{normal}}^g + \dot{f}_{\mathrm{shear}}^g$. Here, $\dot{f}_{\mathrm{shear}}^g$ relates to the effect of shear in damage growth and is defined as the following form scaled by the material parameter k_w

$$\dot{f}_{\mathrm{shear}}^g = k_w f\, w\,(\mathrm{dev}(\boldsymbol{\sigma})) \frac{\dot{\boldsymbol{\varepsilon}}^p : \mathrm{dev}(\boldsymbol{\sigma})}{\sigma_{eq}} \,. \tag{5.2.9}$$

Accordingly, besides the exponential dependence of the void growth on triaxiality, softening and localization with mechanisms such as void distortion and void interaction with material rotation under shear is taken into account. A simple illustration of these two distinct stress state dependent microstructural mechanisms is given in Figure 5.1. Note that although in the original Gurson's damage model f corresponds to a micro-mechanical variable, i.e. an average volumetric fraction of voids reflecting configurational changes, in the current extension it is a purely phenomenological one since f_{shear}^g does not denote an actual void growth but a qualitative indicator of the weakening under shear. To emphasize this fact, in the following pages, f and regarding components will be named as *damage* rather than void volume fraction.

The modification of [224] proposes the dependence of void growth on the third invariant of the deviatoric stress tensor, which distinguishes the axisymmetric stress states from generalized plane strain states. The scalar valued tensor function $w\,(\mathrm{dev}(\boldsymbol{\sigma}))$ is defined as

$$w\,(\mathrm{dev}(\boldsymbol{\sigma})) = 1 - \left[\frac{27 J_3}{2\sigma_{eq}^3}\right]^2 \,, \tag{5.2.10}$$

(a) Void growth under hydro-static stress state.

(b) Void distortion and inter-void linking with material rotation under shear stress state.
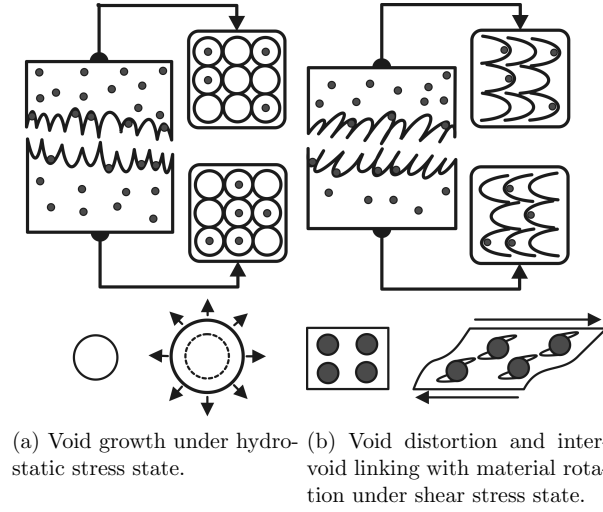
Figure 5.1.: Damage development under different stress states and characteristic fracture surface evidences.

where $J_3 = [1/3][\text{dev}(\boldsymbol{\sigma})]_{ij}[\text{dev}(\boldsymbol{\sigma})]_{jk}[\text{dev}(\boldsymbol{\sigma})]_{ki}$ is the third invariant of the deviatoric stress tensor. For all axisymmetric stress states (which include the hydrostatic stress states) w vanishes where the classical Gurson's model is recovered. Depending on the relative success of classical Gurson's model for modeling localization and fracture under moderate to high stress triaxialities [232] and [233] introduced a triaxiality-dependent correction to w as follows,

$$w = \chi(\eta) \times w(\text{dev}(\boldsymbol{\sigma})), \text{ where } \chi(\eta) = \begin{cases} 1 & \text{for} \quad \eta < \eta_1\,, \\ \dfrac{\eta - \eta_2}{\eta_1 - \eta_2} & \text{for} \quad \eta_1 < \eta < \eta_2\,, \\ 0 & \text{for} \quad \eta > \eta_2\,, \end{cases} \quad (5.2.11)$$

where the correction applies only for the triaxiality values over η_1. From η_1 to η_2 the shear damage effect is linearly reduced whereas after η_2 it is completely eliminated. [232] proposes two possible correction intervals, (η_1, η_2), as $(0, 0.5)$ and $(0.2, 0.7)$. It should be noted that both shear modifications of [224] and correction terms of [232] have strong effects on the evaluation of damage accumulation in plane strain bending. Following [224] for plane strain states, where $\eta \simeq 0.577$, shear damage growth to is fully active since $w \simeq 1$. With the presented corrections, for the interval $(0, 0.5)$, one has $w = 0$ and for $(0.2, 0.7)$ one has $w \simeq 0.244$. For the former case shear modification is completely suppressed, whereas for the latter case it is reduced nearly to one fourth. As noted earlier due to the hydrostatic stress dependence of the yield function as opposed to the Levy-Mises flow rule current framework results in a dilatant plastic flow. Accordingly the stress triaxiality ratio is not necessarily constant for constant strain paths where deviations depend mainly on the level of porosity and hydrostatic stress. Since for the high strength steel sheets initial porosity is considerably small, deviation of the stress triaxiality under constant strain paths (in which damage development is due) become dominant only at latter stages of loading.

This concludes the theoretical background regarding the shear modified Gurson's damage model.

Eventually, the complete set of equations to be solved reads

$$\left.\begin{aligned}
\dot{\boldsymbol{\varepsilon}} &= \dot{\boldsymbol{\varepsilon}}^e + \dot{\boldsymbol{\varepsilon}}^p\,, \\
\dot{\boldsymbol{\sigma}} &= \boldsymbol{\mathcal{C}}^e : \dot{\boldsymbol{\varepsilon}}^e\,, \\
\dot{\boldsymbol{\varepsilon}}^p &= \dot{\gamma}\partial_{\boldsymbol{\sigma}}\Phi^p\,, \\
\dot{e}^p &= \dot{\gamma}\boldsymbol{\eta} : \partial_{\boldsymbol{\sigma}}\Phi^p, \\
\dot{f} &= \dot{\gamma}\left[A_N\boldsymbol{\eta} + \boldsymbol{B}_G\right] : \partial_{\boldsymbol{\sigma}}\Phi^p\,.
\end{aligned}\right\} \tag{5.2.12}$$

Here, $\boldsymbol{\eta} := \boldsymbol{\sigma}/[[1-f]\sigma_y]$. In above the evolution of void growth is shortly represented as

$$\dot{f}^g = \boldsymbol{B}_G : \dot{\boldsymbol{\varepsilon}}^p\,, \tag{5.2.13}$$

where the second-order operator, $\boldsymbol{B}_G = \boldsymbol{B}_G(f, \mathrm{dev}(\boldsymbol{\sigma}))$, is defined as

$$\boldsymbol{B}_G = [1-f]\mathbf{1} + k_w f \frac{w\left(\mathrm{dev}(\boldsymbol{\sigma})\right)}{\sigma_{eq}}\mathrm{dev}(\boldsymbol{\sigma})\,. \tag{5.2.14}$$

Using the definition of the plastic flow one can add up the damage contributions to end up with the following expression

$$\dot{f} = \dot{\gamma}\left[A_N\frac{\boldsymbol{\sigma}}{[1-f]\sigma_y} + \boldsymbol{B}_G\right] : \partial_{\boldsymbol{\sigma}}\Phi^p. \tag{5.2.15}$$

An algorithmic treatment of the given framework is enclosed in the appendices.

5.3. Experiments

Free bending (or air bending) is a widely used brakebending operation where the blank is supported at the outer edges without being forced into a female cavity (as opposed to die bending). Thus, the bending angle is determined by the ramstroke, not by the die shape, see [157]. This reduces the force demand for forming. However, at the same time it gives rise to free surface cracks and, if not, to relatively high springback. An analysis of springback is beyond the aim of this study. In the following, first the chemical composition and the microstructure of the utilized material are given. Then, the experimental setup and outcomes of the tests are explained.

5.3.1. Chemical Composition and Microstructure Observation of DP1000 Steel

The investigated sheet material used within the scope of this chapter is a cold-rolled ferritic-martensitic steel, so-called DP1000. In order to figure out the chemical compositions, a chemical analysis with Optical Emission Spectroscopy (OES) is carried out. The results are summarized in Table 5.2.

Table 5.2.: Chemical composition for DP1000 in wt%.

C	Si	Mn	P	S	Cr	Ni	Al	Co
0.161	0.499	1.546	0.011	0.002	0.44	0.035	0.043	0.016

The slag morphology as well as the amount and the size of slag inclusions were assessed using the slag inclusion evaluation method. Important information regarding inclusion quantity and size is depicted in Figure 5.2.

Sum of drawn inclusion length [mm]	=	230.7
Total number of inclusions	=	56.0
Number of inclusions / mm^2	=	22.8
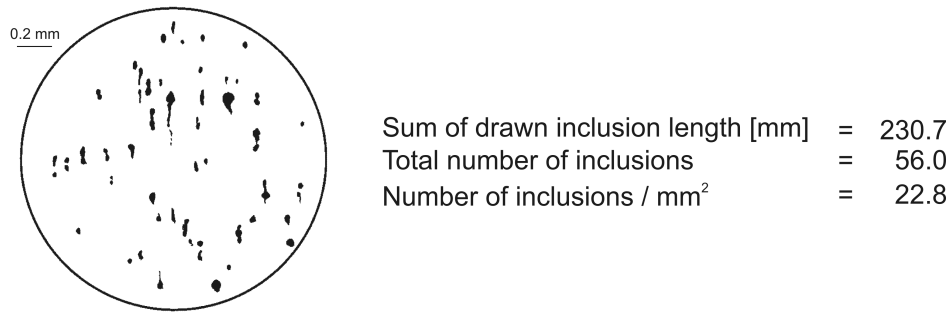
Figure 5.2.: Slag assessment of DP1000.

Energy dispersive spectrometry analysis showed that the inclusions consisted mainly of manganese sulfide or calcium aluminate. Despite the fact that the cracks usually initiate near complex macro slag, in this case manganese sulfide or calcium aluminate, the martensitic islands act as potential microvoid initiation zones, respectively. Especially for ferritic-martensitic steels consisting of relatively brittle martensite surrounded by ductile ferrite, this idea gains more importance.

5.3.2. Experimental Setup

Air bending tests are realized on universal testing machine, type Zwick 250. With reference to Figure 5.3, the radii of the punch, r_p, and the dies, r_d, are 1 mm, whereas the die width, d_d, is 24 mm. The sheet has a length of 100 mm, b, a width of 50 mm, w, and a thickness of 1.55 mm t. The punch moves downwards while the dies are stationary.
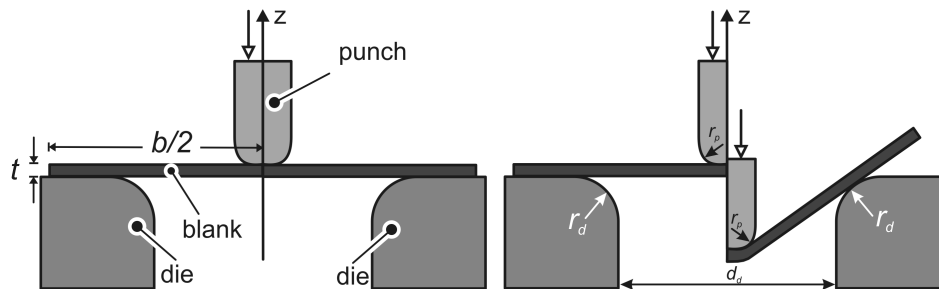
Figure 5.3.: Essential geometrical dimensions of the bending problem.

As noted in [2, pp. 403–415], bending occurs at plane strain conditions at $w/t > 8$, where $\epsilon_2 = 0$ and $\sigma_2/\sigma_1 = 0.5$. If $w/t < 8$, bending occurs under plane stress conditions with $\sigma_2/\sigma_1 < 0.5$ and plasticity occurs in all principal directions. For the former bend ductility is independent of the width-to-thickness ratio, whereas for the latter, bend ductility strongly depends on this ratio as given in Figure 5.4. Generally, tests are performed in width-to-thickness ratios larger than 8 to 1. In the current case the width-to-thickness ratio is $w/t = 35.48 > 8$, where the plane strain assumption is validated.

5.3.3. Observations at Macroscale

The experiments carried out until a fracture on the convex surface of the specimen was observed. The emanation of cracks is observed at the central portions where the plane strain effect is higher

(a) Stress and strain nota- (b) Fracture strain (at the convex surface) versus width-to-
tion for the problem.   thickness ratio, (w/t).
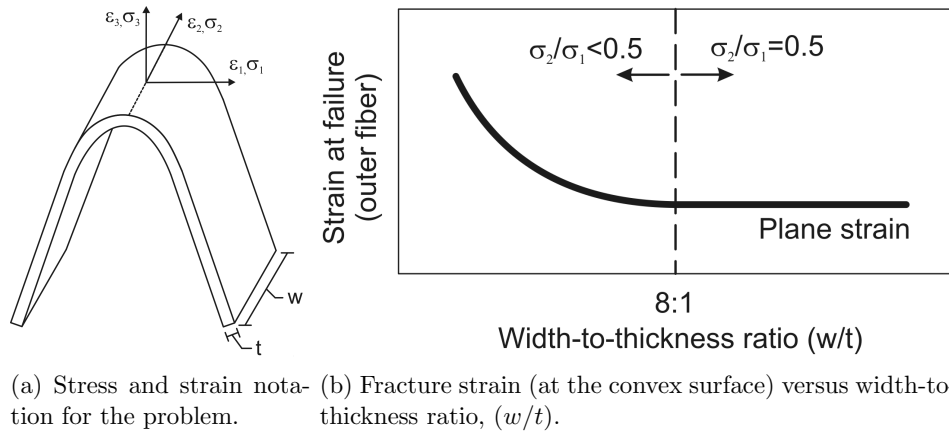
Figure 5.4.: Problem of bendability (adapted from [2, pp. 403–415]).

rather than at the edges in accordance with the definitions given in [2, pp. 403–415]. Figure 5.5
show bent specimens at different stages of the ram-stroke.

(a) 80°   (b) 90°   (c) 100°   (d) 110°
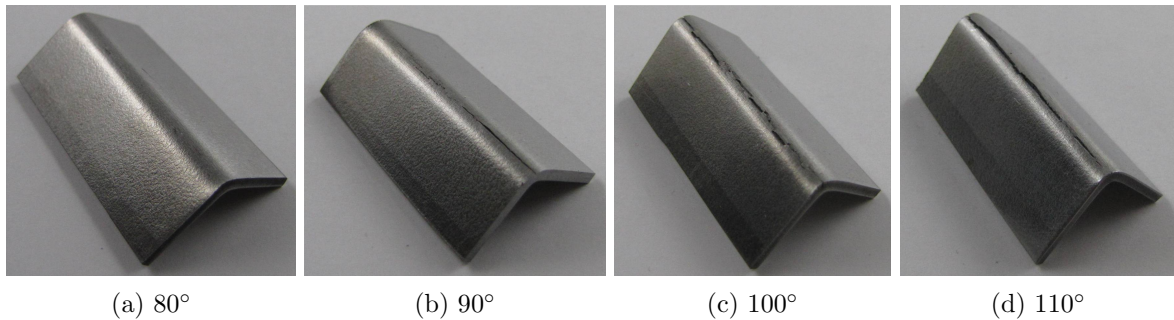
Figure 5.5.: Bent specimens for different levels of deformation measured in terms of bending
angle.

According to the test evaluation procedure presented in [2, pp. 403–415], surface examinations
for cracks are conducted on the convex surface with magnifications up to 20X where surface
wrinkles or orange peeling are not considered as unacceptable defects. Figure 5.6 shows the
stages of cracking at the apex of the bend. With a growing extent of deformation orange peels
and accompanying slight surface waviness (so-called undulation) is observed on the outer surface
in the bending zone in the form of bulges and dents (or extrusions and intrusions). As explained
in [85], these grooves increase the strain and plastic flow inhomogeneity at the micrometer scale
and the deformation is confined to narrow localized slip bands. In general, these slip bands,
act as sources of extrusions and intrusions when intersect a free surface. Cracks emanate from
intrusions, which is in correlation with the observations made in bending where the intruded
portions of undulations (or waviness) are the crack emanation zones.

These outcomes are in accordance with those obtained by [266], where observed phenomena
of bending defects in AA5754 Al alloys for low and high Fe content are listed as: 1) Strain
localization at various length scales, 2) Undulations at the surface, 3) Damage acceleration in
localization bands in Fe rich microstructures, which are linked to surface grooves and fracture
occurs inclined to the surface. The sequence and relation of these events are linked to a second
phase particle content (Fe), where the degree of material inhomogeneity and spacing of particles
gain importance. Accordingly, small interparticle spacing in high Fe alloys promotes the linking

(a)   (b)   (c)   (d)
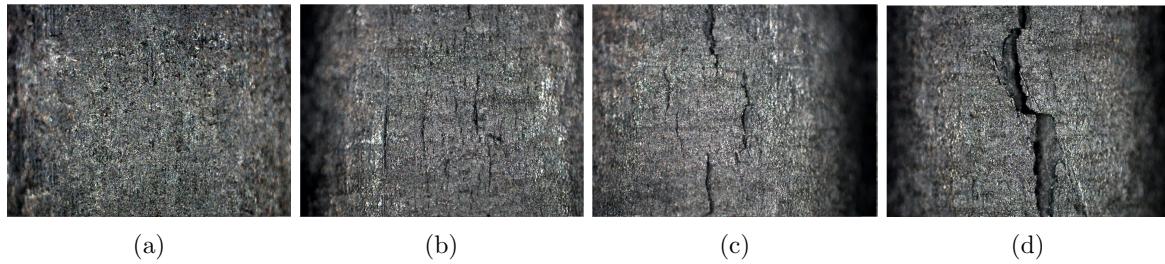
Figure 5.6.: Development of surface undulations by the extent of deformation.

of voids where the failure occurs in the form of void sheeting. It is shown that high Fe alloys show lower bendability. Cavity formation in the particles interacting with slip lines under the influence of shearing is clearly shown by SEM images. It is also shown that the prestrained materials show lower strain hardening rates, under loading due to their decreased hardening capacity; thus, undulations and associated localizations occur earlier, which initiates a softening effect again. [185] investigate the bendability of AA6111 sheets for different Fe concentrations using a combined experimental numerical procedure.

Crack alternation at the bend apex is shown in Figure 5.7. As will be further clarified by means of a section analysis and post-mortem surface fractographs, phenomena like alternating cracks at the apex along the central bending line, incipient cracks under free surface, crack trajectories, i.e. the size and orientation of crack tip evolution are strongly linked to the local material inhomogeneities. The observations show that the cracks tend to alternate from one localization band to another under the effect of cavitation, i.e. inclusion type, size, shape, and distribution. Once the local inhomogeneities are insufficient, the post-mortem fracture surfaces show less clues regarding parabolic dimples, which shows that plastic slip mechanisms dominate compared to void sheet mechanisms. Thus, the cracks alternate from a less critical localization condition to a more critical one, following maximum damage paths, comparable with the observations of [266] where it is detected that damage accelerates in localization bands in inclusion rich (Fe) microstructures.
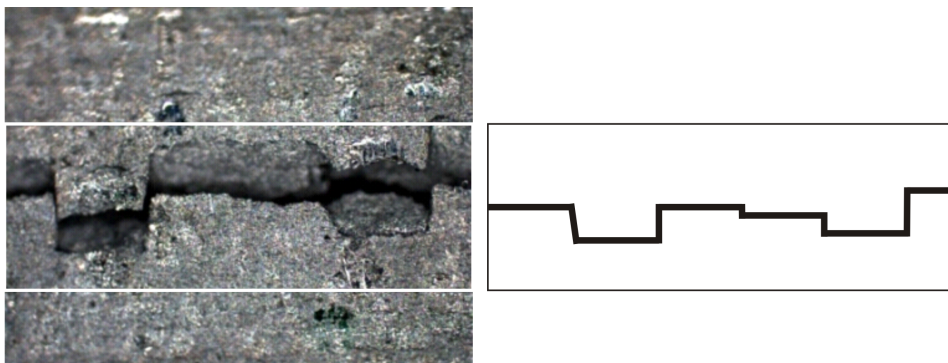
Figure 5.7.: Crack alternation along the bending axis at the bend apex.

Once the crack paths at random sections orthogonal to the bending axis, as seen in Figure 5.8, are analyzed, three characteristics are observed: 1) It can be noted that when the bending axis is orthogonal to the rolling direction cracking at the outer fiber occurs later than in transverse direction due to elongated inclusions, also noted in [213, p. 233]. 2) The cracks emanate from the free surface along the slip bands with maximum plastic straining at an angle of approximately

45° to the principal stress direction which is due to the tension of the outermost fiber. This structure is compatible with a combined Mode I Mode II fracture where the opening and shearing modes act. 3) After the cracks have reached a certain length they change direction to form a zig-zag pattern.
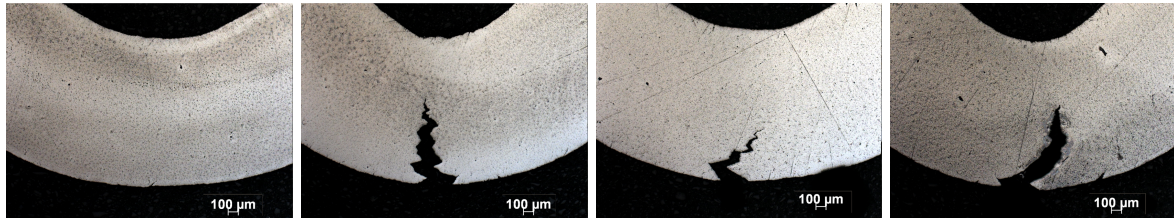
(a) Bending axis orthogonal to rolling axis, bending angle 90°. (b) Bending axis orthogonal to rolling axis, bending angle 110°. (c) Bending axis parallel to rolling axis, bending angle 90°. (d) Bending axis parallel to rolling axis, bending angle 110°.

Figure 5.8.: Observed crack patterns on the bend section.

For a transgranular brittle fracture a slight zig-zag pattern can be handled with the crack arrest at grain boundaries where the preferred splitting plane from grain to grain may differ in orientation, resulting in faceted fracture surfaces. For the current ductile pattern this may be attributed to a blending of two alternative mechanisms:

[60, p. 13] links this behavior to the bimodal particle distributions. Localized deformations in the form of shear bands occur between large particles which generally break or get loose earlier to form widely spaced holes in the vicinity of the crack tip. These join up by void linking and shearing through micro-void coalescence in smaller secondary particles. Accordingly, the crack changes direction in between the large particles. Due to this mechanism, the fracture surface includes both the dimples of smaller and larger particles.

According to [11], any crack subjected to Mode I loading tends to propagate through the preferred path of void coalescence which is the maximum plastic strain i.e. plastic localization path at 45° to the principal tensile stress. This determines the crack direction at the local level, whereas the global constraints tend to hold the crack on the plane orthogonal to the maximum stress. The resulting conciliatory path has a zig-zag pattern. These observations are in accordance with similar ideas proposed in [46] which, while investigating zig-zag ductile fracture patterns in the form of periodic ridges and valleys, link the size of ridges and valleys to fracture toughness.

Finally, the average punch force-punch displacement curve is given in Figure 5.9 since the material does not have strong anisotropy, [100]. No large gap in between the level of maximum forces for specimens bent at different orientations (0° and 90°) with respect to their rolling directions is observed. Comparisons with the simulations are stated in the following sections.

5.3.4. Observations at Microscale

Surface fractography is a powerful tool when determining the character and type of fracture. In the following, post-mortem surface fractography analyses by SEM with different magnifications as evidence for ductile fracturing mechanisms which occur under the influence of intense localization with void sheeting are summarized.
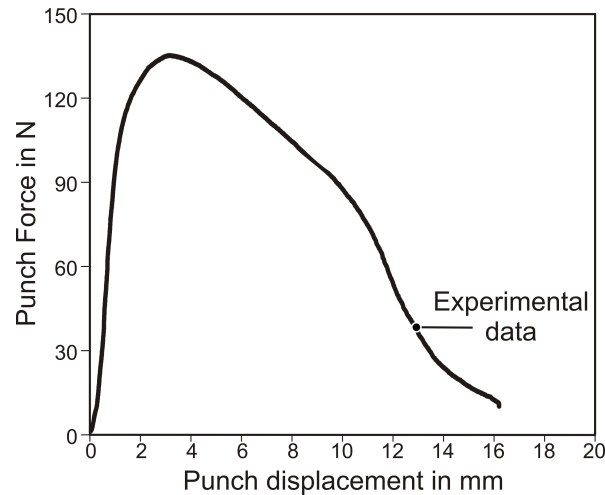
Figure 5.9.: Experimentally handled load-displacement curve for the punch.

Figure 5.10.(a) shows the region where the SEM analyses are conducted. The upper free surface shows the apex of the bend. In general, the dimple formations at the fracture surface constitute a clear sign for the ductility of fracture. However, the surface features are relatively complicated, so the analysis is divided into certain regions. Two regions are mainly concentrated on, where Figure 5.10.(b) (namely region A2) shows the fracture surface in the vicinity of crack emanation at the free surface at the bending apex and Figure 5.10.(c) (namely region A6) shows a relatively inner region closer to the neutral axis of the bend.

(a) Region A1   (b) Region A2   (c) Region A6
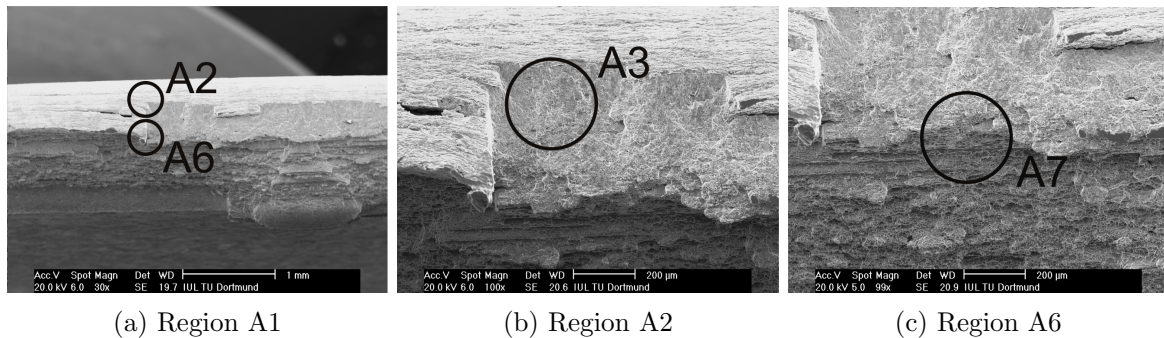
Figure 5.10.: SEM fractographs from fracture surfaces, Part I.

Region A3 is divided into two finer scale regions, namely region A4 and A5, for dimple pattern observations, as seen in Figure 5.11. Region A5 is closer to the crack alternation zone, whereas region A4 is relatively remote from this region. A5 shows relatively flat surface characteristics where the shearing direction is slightly oriented towards to a possible effect of crack alternation. As opposed, region A4 includes more obvious dimples forming a relatively rough surface where the shear loading has, as expected, a vertical direction. In both A4 and A5 the type of dimples is parabolic which shows the slantness of the fracture surface, see e.g. [129, p. 238], where the Mode II fracture is dominates among a blended Mode I and Mode II type fracture. The local change of fracture surface characteristics, such as increased surface flatness and reduced parabolic dimples in the vicinity of crack alternation, might be responsible for the crack's bifurcation into a less

stiff or more developed localization band.

(a) Region A3   (b) Region A4   (c) Region A5
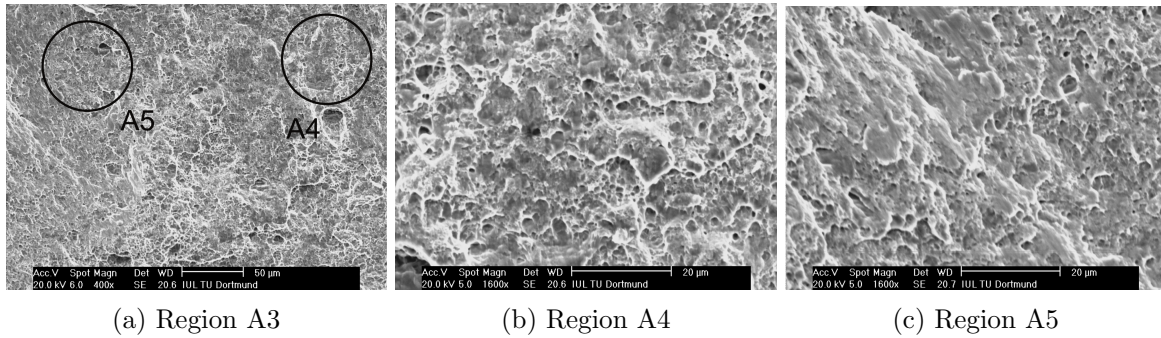
Figure 5.11.: SEM fractographs from fracture surfaces, Part II.

Figure 5.12 shows the surface features observed in region A6 with a finer scale SEM fracto-
graph, which gives A7, and a further refined region A8. These coincide with the region where
crack zig-zagging occurs. An evident observation is the relatively coarse surface characteristics
compared to region A2. In region A7 the dimples are more remarkable and a blend of larger
and smaller dimples is observed. As seen in more detail in region A8, the dimple types are still
parabolic. Again, the shear loading is dominant and the direction of loading is apparent from
the fractographs.

(a) Region A3   (b) Region A4   (c) Region A5
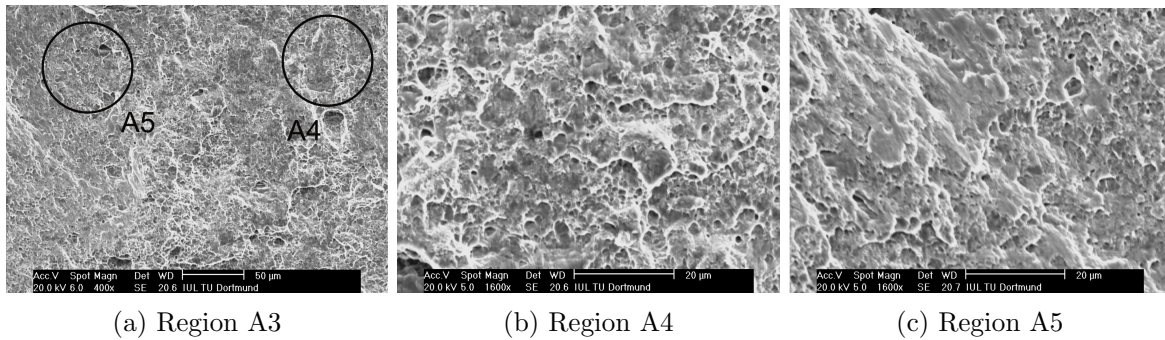
Figure 5.12.: SEM fractographs from fracture surfaces, Part III.

5.4. Simulations

The presented theoretical framework is implemented into VUMAT subroutines for ABAQUS/EXPLICIT
where the algorithmic forms can be found in the appendices. Simulations are conducted in both
2D plane strain and 3D with double precision. A solution of quasi-static problems with a
dynamic-explicit solution procedure generally involves a very large number of time steps. In or-
der to reduce the computational cost, mass scaling is applied with a target time step of 2.5×10^{-7}
over the whole analysis. Based on the statics of all elements the mean stable time increment
estimate without mass scaling is 3×10^{-9} . Accordingly, the mass scaling applied corresponds
to nearly 10^4. On this rather conservative selection local integration method based on cutting
plane algorithms was also conclusive. The material has a modulus of elasticity, E, of $E =$210000
MPa and the Poisson's ratio, ν, is $\nu = 0.3$. The hardening curve is constructed by fitting data
until the necking point and using extrapolation for the the post-neck. The extrapolated flow

curve is given in Figure 5.13. The anisotropy due to the rolling process is not taken into account.

It is desirable that a chemical analysis and/or quantitative metallography is used in order to estimate the initial porosity where constituents dominating the ductile fracture mechanism by acting as damage nucleation sites are taken into account, [138]. The Franklin's formula, [93], serves as an estimate for f_0 where manganese sulphide inclusions are the critical particles in fracture:

$$f_0 = \frac{0.054\sqrt{d_x d_y}}{d_z} \left[S\,(\%) - \frac{0.001}{Mn\,(\%)} \right] , \qquad (5.4.1)$$

where d_x, d_y, and d_z denote average inclusion diameters in the respective directions. $S\,(\%)$ and $Mn\,(\%)$ represents the weight percentages of sulphide and manganese in the matrix. Details on the usage of this relation can be found in [93]. Since this form relies on the quantitative metallography of materials where manganese sulphide inclusions dominate the fracture, a modification for the case of advanced high strength steels (DP, CP, and TRIP) is required implying a combined effect of inclusions and secondary phases on fracture. In DP steels hard martensitic islands have $5 - 20$ vol% which controls the ultimate tensile strength. Typical compositions of cold-rolled DP steels involve (wt.%) 0.08-0.15% C, 1.6-2.2% Mn, 0.4% (Cr+Mo), [213, p. 590]. So this procedure is not followed.
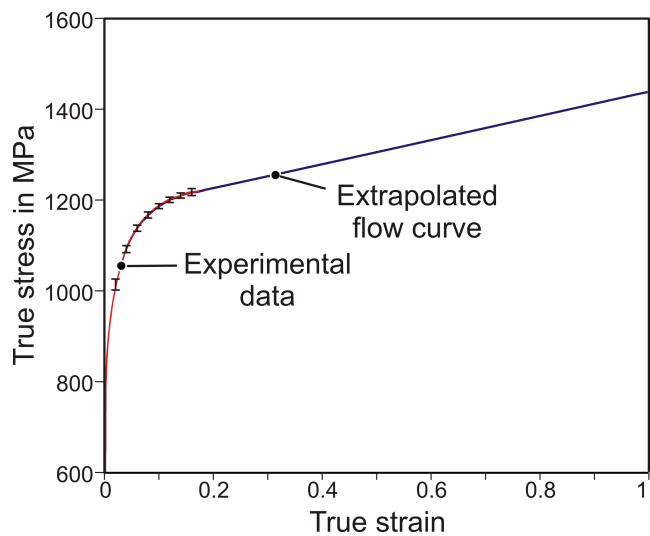
Figure 5.13.: Flow curve for DP1000.

In this class of steels the void nucleation depends on the non-metallic inclusions ($\sim$5-30 microns in diameter) as well as dispersed martensite particles ($\sim$0.5 microns in diameter), see e.g. [295]. Accordingly, the orders of magnitudes of respective particle sizes differ. The volume fraction shows an opposing trend where non-metallic inclusions constitute $0.01 - 0.05$ vol%, whereas martensitic islands reach $5 - 20$ vol%. Experimental investigations of [251] show that void nucleation at inclusions, either with particle cracking or inclusion-matrix decohesion, occurs at relatively low strains ($\sim$0.2) due to pre-existing cracks and weakly bonded interfaces. In comparison, the void nucleation strain is higher ($\sim$0.9) due to a relative coherence of the ferrite-martensite interface at martensite particles. It is noted that the fracture is controlled by growth and coalescence of martensitic void nucleation sources which is attributed to the higher volumetric fraction of martensite compared to non-metallic inclusions.

For the base shear enhanced Gurson parameters reported values in the literature are followed where in the analysis the effect of variations of certain ones are also investigated. These are summarized in Table 5.3. The parameters q_1, q_2, q_3 are chosen following [304] and [306]. [233] and [51] use similar parameters for the Gurson's damage model for DP600 and DP1000, respectively. f_c and f_F are selected following [12], [62], [225]. k_w is selected as 2 which lies in the proposed range for structural alloys, $1 < k_w < 3$, [224]. Selected f_0 is also due to [51]. For f_0, f_c, f_F and k_w a parametric study is also followed to investigate their relative effects on localization

and fracture.

Table 5.3.: Base Gurson's parameters for DP1000.

$q_1 = 1/f_U^*$	q_2	q_3	f_0	f_N	s_N	ϵ_N	f_c	f_F	k_w
1.500	1.000	2.250	0.002	0.020	0.110	0.350	0.150	0.250	2.000

5.4.1.   2D Plane Strain Models

Plane strain state is assumed. The dies and the punch are modeled as rigid curves, whereas the blank is modeled as a deformable body, as seen in Figure 5.14. In the following, a set of sensitivity analyses which investigate the effect of process parameters on localization, crack pattern, and load-displacement curves are summarized.
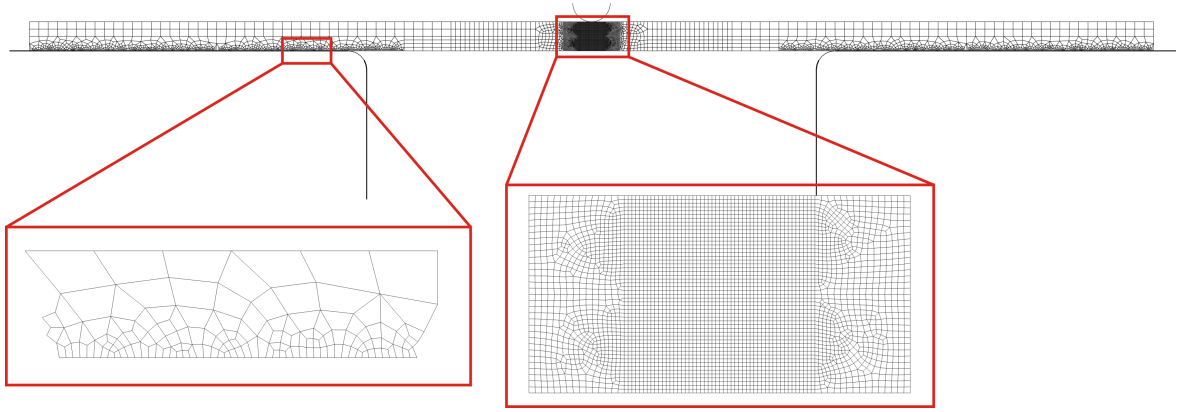
Figure 5.14.: 2D plane strain model for free bending.

5.4.1.1.   The Effect of Mesh Size

Capturing correct deformation and localization patterns requires fine meshes as noted by [48], on modeling cup-cone fracture mode in axisymmetric tension, see also [308]. In bending, highly inhomogeneous plastic flow localization is observed at micrometer scales until crack occurrence. In order to capture the size of localization or the physical crack size, the presented studies start with testing three different mesh refinement levels at the bend region which are 0.04 mm, 0.03 mm and 0.02 mm, see in Figures 5.15.(a), (b) and (c), respectively, for the selection of a proper mesh size at the bending region. The total number of elements is, as a consequence, 5265, 7017 and 10767, respectively, using CPE4R, i.e. 4-node bilinear plane strain quadrilateral, reduced integration elements with hourglass control. It is noteworthy to say that once insufficiently refined meshes are supplied, the physically observed inclined localizations and cracks are not captured properly. The mesh is also refined in the contact regions in the vicinity of the dies for a smooth node to surface contact treatment. Otherwise large scatters on the punch force-displacement diagram can be observed.

Resultant damage distributions prior to crack occurrence are given in Figure 5.16. The mesh dependence of localization is seen in the plots where the localization bands occur with an orientation of approximately 45° with respect to the principal stress direction. The time of localization, number of localization bands, and the damage intensities within the bands differ for each mesh.

(a) l_{elem}=0.04 mm.   (b) l_{elem}=0.03 mm.   (c) l_{elem}=0.02 mm.
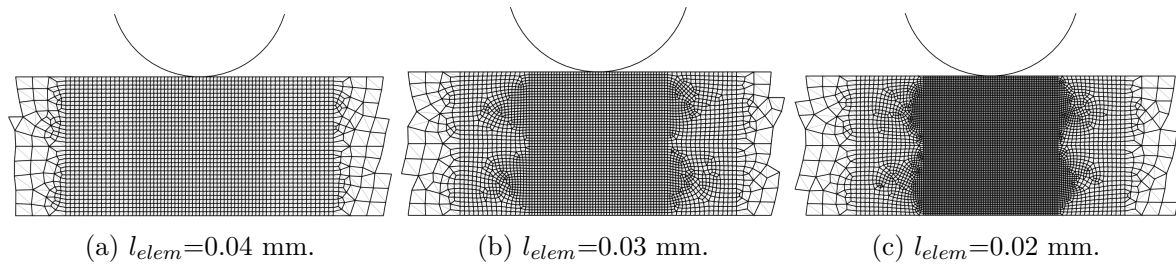
Figure 5.15.: Mesh refinement in the bending region for the 2D model.

As noted by [307], the results admit a length scale where a strong mesh dependence occurs. For smaller element sizes narrower localization bands are carried out. Moreover, the localization occurs earlier. A finite band width is enforced in materials by involving of inherent length scales, such as grain, inclusion, or void size. A natural length scale which limits the banding is not supplied in conventional continuum mechanics formulations. In finite element simulations, when not explicitly involved, the element size acts as a length scale. Accordingly, a general trend in literature is to use the mesh size as a material parameter and to fix it during the material characterization phase. More general methods, named nonlocal approaches, involve an explicit definition of the length scale, which falls beyond the aim of this study.

(a) l_{elem}=0.04 mm.   (b) l_{elem}=0.03 mm.   (c) l_{elem}=0.02 mm.
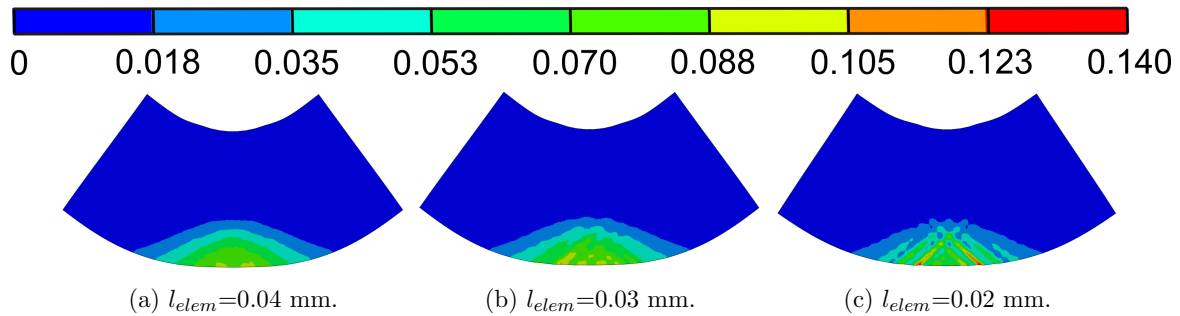
Figure 5.16.: The effect of mesh size on damage localization, punch displacement=10.2 mm.

The cracks are modeled using element deletion technique which serves as a standard procedure of ABAQUS/EXPLICIT. Accordingly, the reduced integration elements, whose Gauss point's damage value reaches f_f, are excluded from the computational stack. Element deletion technique is also used in [330] and [331]. Similar methods are used in [306], [307], and [186] where a final fracture is created by a progressive stiffness and strength degradation, the so-called crack smearing technique. Resultant cracks, which occur with bifurcation into one of the developed bands, are given in Figure 5.17 for identical punch displacements. The size of the cracks change with the mesh size. For the mesh with 0.04 mm element size the crack is not developed yet due to an insufficient damage development, whereas for 0.02 mm element size the crack initiates. For both 0.03 mm and 0.02 mm meshes the cracks change direction after a certain crack length. Although this is attributed to different micro-mechanical phenomena, as explained earlier, in the simulations the results can be ascribed to overlapping localization patterns and macroscopic loading conditions which force the cracks to stay on the symmetry axis.

The punch force-displacement curves are given in Figure 5.18. The points of steep decrease at the load levels are the incipient cracking points. In accordance with the localization analysis the loss of load carrying capacity is first observed in the model with the finest mesh. Prior to this cracking point no remarkable difference is observed in the load displacement diagrams. This

(a) l_{elem}=0.04 mm.   (b) l_{elem}=0.03 mm.   (c) l_{elem}=0.02 mm.
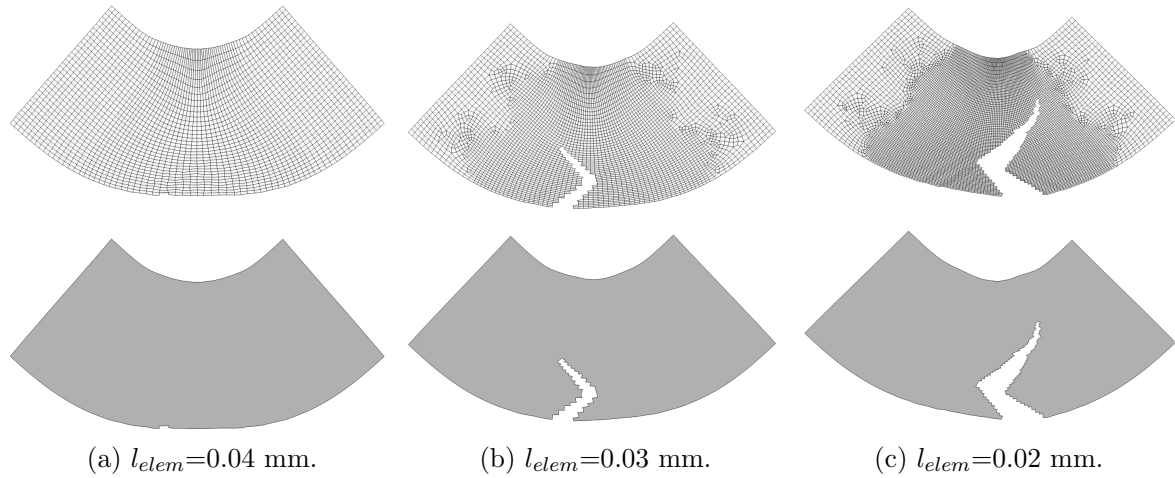
Figure 5.17.: The effect of mesh size on fracture pattern, punch displacement=13 mm.

may be attributed to the fact that until the fracture occurrence with localization the damage values reached are relatively small in magnitude and the damage spread only appears as a small scale phenomenon. Eventually, its distribution throughout the section of interest is limited in both intensity and extent.
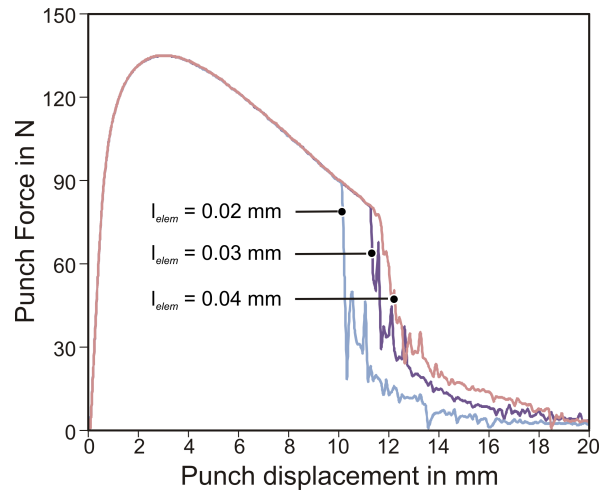
Figure 5.18.: The effect of mesh size on force-displacement curves.

The damage over the bend region, which reaches a maximum at the convex surface to create localization, is formed by three contributions, namely void nucleation, damage growth due to triaxiality, and damage growth due to shear. Figure 5.19 shows the individual distributions of these components for the analysis with 0.030 mm mesh size at an intermediate analysis step. Since void nucleation is assumed not to occur under negative hydrostatic stress states it acts only at the tensile portion below the neutral axis. On the convex surface however at this level of deformation all void nucleation source, which is 0.020, is reached. Coming to damage growth, a maximum growth at the convex surface is observed, as anticipated. On the concave surface damage reduction (in classical terminology this corresponds to void shrinkage) is observed with an absolute maximum value in the region which is in contact with the punch.

Figure 5.20 shows that damage growth due to shear is in the same order of magnitude as the

(a) f^n.   (b) f^g.   (c) f^g.
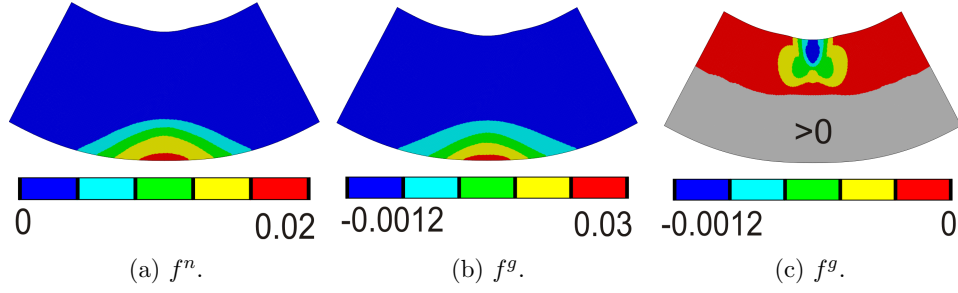
Figure 5.19.: Individual contributions of damage components in the bend region, punch displacement=8 mm.

damage growth due to triaxiality at the convex face. This is primarily due to the previously mentioned plane strain constraint which supplies $w \simeq 1$. A relatively large triaxiality ratio $\eta \simeq 0.577$ creates the hydrostatic stress-dependent void growth. Although damage growth due to shear occurs at the concave face and above the neutral axis it does not suffice to overcome damage reduction due to a compressive hydrostatic stress state to give $f^g < 0$. Under these conditions, a ductile damage mechanism with growth of voids is not possible at the concave surface, which is in correlation with the proposed fracture cut-off triaxiality as $\eta = -1/3$, [30], since at the concave free surface, plane strain compression results in $\eta \simeq -0.577$ whereas under the punch this reduces further due to compressive contact loads.

(a) f^g_{shr}.   (b) f^g_{shr}.   (c) f^g_{hyd}.   (d) f^g_{hyd}.
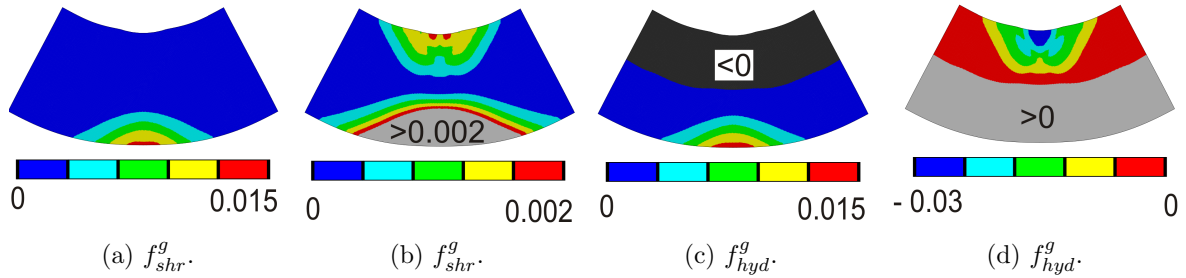
Figure 5.20.: Individual contributions of damage growth components at the bend region, punch displacement=8 mm. As respectively seen in (c) and (d) there is negative damage growth (i.e. damage reduction) above neutral axis and positive damage growth below neutral axis.

The authors' experience shows that once the initial porosity is taken as $f_0 = 0$ the compressive region above the neutral axis experiences no damage evolution, although shear damage growth might be expected due to the underlying physical mechanisms. This stems from the combined conditions where 1) the void nucleation requires a positive hydrostatic stress state, 2) already precluded damage reduction (void shrinkage) with completely eliminated porosity, and 3) the necessity of shear damage growth for an initial damage, which is seen from its evolutionary equation. Once an initial non-zero porosity is supplied, the current formulation gives rise to both void shrinkage due to negative triaxiality and damage growth due to shear. The summation of the damage growth rate may be negative, as it is seen in the current problem, depending on the loading conditions which will be a statement of void shrinkage beyond initial porosity. With an alternative formulation, [53] proposes the following modified potential

$$\widehat{\Phi}^p = \left[\frac{\sigma_{eq}}{\sigma_y}\right]^2 + 2q_1 f^* \cosh\left(\theta\frac{3}{2}\frac{q_2\sigma_m}{\sigma_y}\right) - [1 + q_3 f^{*2}] = 0, \qquad (5.4.2)$$

where

$$\theta = \begin{cases} 1 & \text{if } f^g > 0 \text{ or } \sigma_m \geq 0 \,, \\ 0 & \text{if } f^g = 0 \,, \end{cases} \tag{5.4.3}$$

which supplies $f^g \geq 0$ even for negative hydrostatic stresses. This approach, also used by [51], clearly hinders void shrinkage beyond initial porosity. This, of course, affects the damage evolution at the concave free surface of the bend and the compressive region above the natural axis.

5.4.1.2. The Effect of k_w

For the following studies, the mesh size is selected to be 0.03 mm due to the correlation in between experimentally and numerically captured fracture time and size as well as the computational cost. Figure 5.21 shows the damage distributions and deformation localization patterns for various k_w values. At identical step sizes, loss of adequate softening results in no localization for $k_w = 0$ and $k_w = 1$. In the current simulations a sufficient damage accumulation for localization with softening is around %10-%15. For $k_w = 2$ and $k_w = 3$ one observes well-developed deformation bands.

0   0.018   0.035   0.053   0.070   0.088   0.105   0.123   0.140

(a) k_w=0.   (b) k_w=1.   (c) k_w=2.   (d) k_w=3.
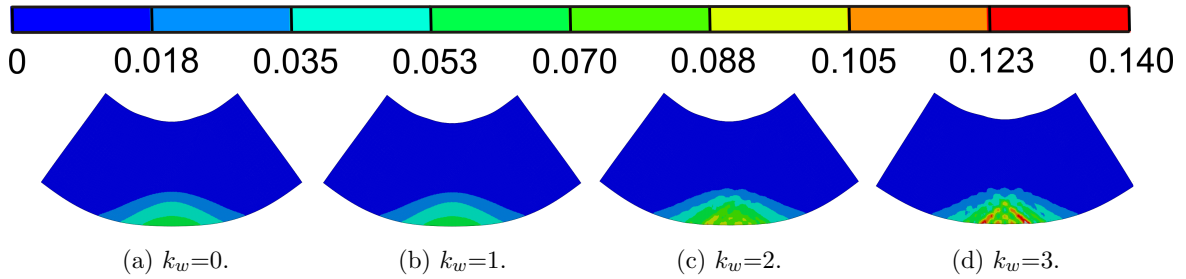
Figure 5.21.: The effect of mesh size on damage localization, punch displacement=10.2 mm.

Figure 5.22 gives crack paths for an identical ram stroke. For $k_w = 0$ and $k_w = 1$ no cracks are developed yet. For $k_w = 2$ and $k_w = 3$ there are crack occurrences when the crack size depends on k_w. This is anticipated since k_w controls the damage accumulation till fracture. Crack kinking is observed in both of the cases as well for which similar comments made for the mesh size effect apply.

(a) k_w=0.   (b) k_w=1.   (c) k_w=2.   (d) k_w=3.
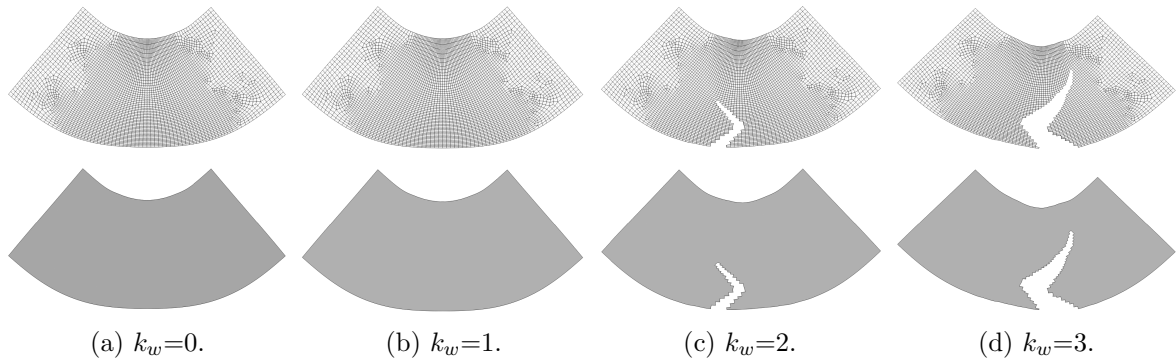
Figure 5.22.: The effect of k_w on fracture pattern, punch displacement=13 mm.

The punch force-displacement curves are given in Figure 5.23. As it can be seen the earliest loss of load carrying capacity is observed for $k_w = 3$, whereas for $k_w = 0$ and $k_w = 1$ no steep

decrease arises since no crack occurrence is captured within the selected loading interval. There is only a slight difference between the curves with different k_w values.
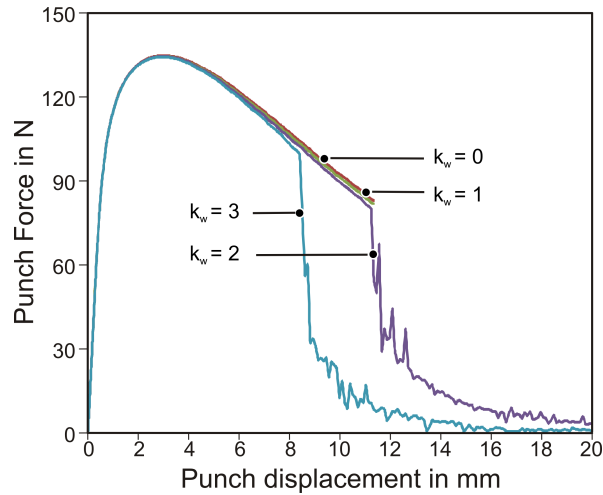
Figure 5.23.: The effect of k_w on force-displacement curves.

A comparison of the force-displacement curves for $k_w = 2$ and $k_w = 3$ with experimental data is given in Figure 5.24. The simulation results agree qualitatively with the experimentally investigated ones for $k_w = 2$. The unloading portions in the plane strain analysis give a steeper drop compared to the experimental results in which the overall section is not cracked, but the crack gradually propagates from the central plane strain regions to the edges. Further comments on this issue are included in the 3D model simulations section.
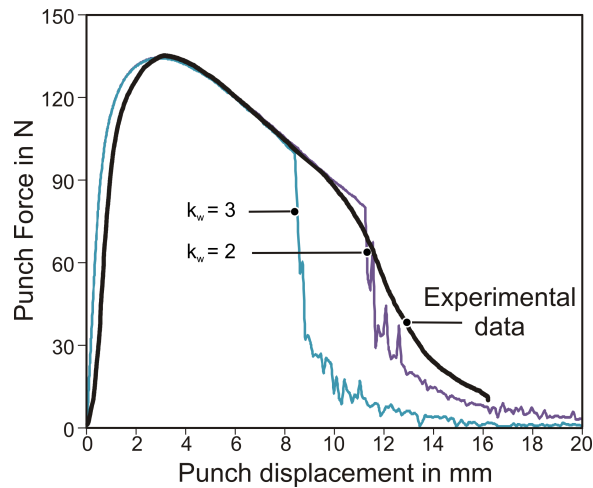
Figure 5.24.: Comparison of experimental and numerical (2D plane strain) force-displacement curves.

5.4.1.3. The Effects of f_0, f_c, and f_f

A set of analyses is run for different values of f_0, f_c, and f_f. The results are summarized in Figure 5.25. In correlation with the findings of [186] inclined crack patterns are only considered when the incipient crack is accompanied by a localization band. As seen in Figure 5.25.(c) and

(d), once the critical limit for coalescence and final fracture is kept too low, the crack emanates at the center and propagates orthogonal to the maximum principal stress direction as it is in the case of tensile stress controlled cleavage-type brittle fracture. However, in the current case plastic flow is the driving mechanism together with tensile stress, although the fracture occurs at relatively smaller fracture strains. Figures 5.25.(a), (b), (e) and (f) show the effect of initial void volume fraction on the final fracture patterns for the same punch displacement where f_c and f_f are kept constant. As seen large f_0 gives account for an accelerated damage development at successive loading stages which finally results in earlier fracture. Additionally, it can be seen that in general the crack experiences at least one kink and changes direction.

(a) f_0=0, f_c=0.08, f_f=0.15.   (b) f_0=0.01, f_c=0.15, f_f=0.25.   (c) f_0=0.002, f_c=0.01, f_f=0.02.

(d) f_0=0.002, f_c=0.04, f_f=0.05.   (e) f_0=0.02, f_c=0.15, f_f=0.25.   (f) f_0=0.05, f_c=0.15, f_f=0.25.
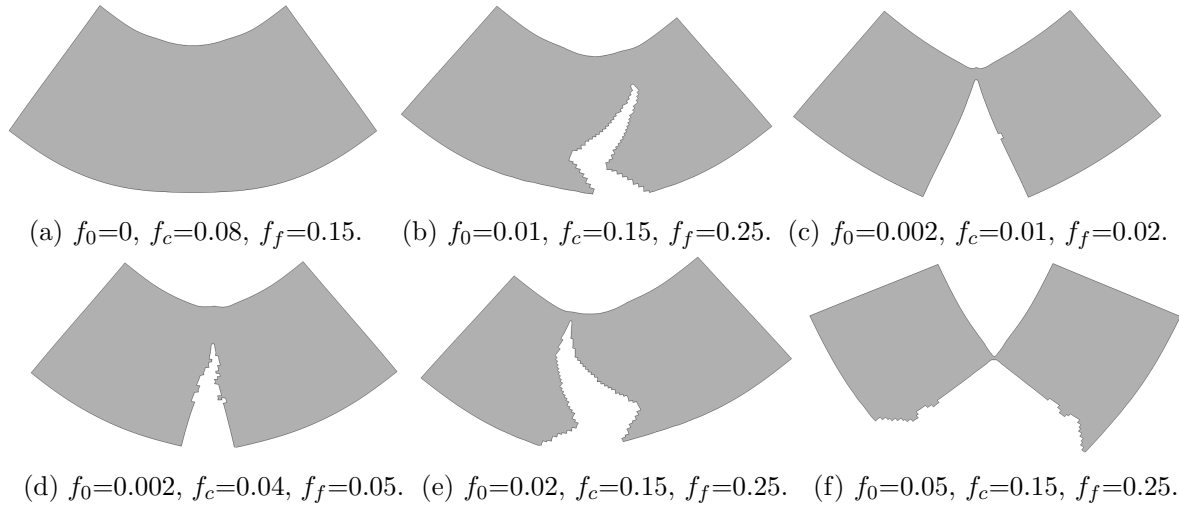
Figure 5.25.: The effect of process parameters on final fracture patterns, punch displacement=11 mm.

5.4.1.4.   The Effect of Nielsen and Tvergaard's Modification

Plane strain state dominates the current bending problem for the selected width-to-thickness ratio. As mentioned before, under these conditions the shear damage effect is fully involved since $w \simeq 1$, although triaxiality, $\eta \simeq 0.577$, is not low. With the motivation that the original Gurson's damage model works sufficiently well for moderate to high stress triaxialities [233] introduce an additional triaxiality-dependent scaling parameter for the shear modification which is given in Equation (5.2.11). In this part of the study, the effect of this correction is presented, selecting the triaxiality correction interval as $(\eta_1, \eta_2) = (0.2, 0.7)$ which is one of the proposed intervals in [233]. As aforementioned for the other proposed interval, i.e. $(\eta_1, \eta_2) = (0, 0.5)$, shear modification will be completely suppressed for the current problem.

Figure 5.26 represents the extent of modification for the bending problem. As an inherent property the region above the neutral axis experiences negative triaxialities in bending, i.e. $\eta < 0$. This region is not effected by shear correction, which can be seen in Figure 5.26.(c) where the correction factor is $\chi(\eta) = 1$. Coming to the tensile zone, although for Nahshon and Hutchinson's original form, $w \simeq 1$ dominates the section, depending on the gradual increase of triaxiality towards the convex surface where it has a value of $\eta \simeq 0.577$ due to plane strain tension conditions w gradually drops down to $w \simeq 0.244.$, its minimum value occurring at the free surface.

(a) w for Nahshon and Hutchinson.

(b) w for Nielsen and Tvergaard's correction with $(\eta_1, \eta_2) = (0.2, 0.7)$.

(c) Correction factor, $\chi(\eta)$.
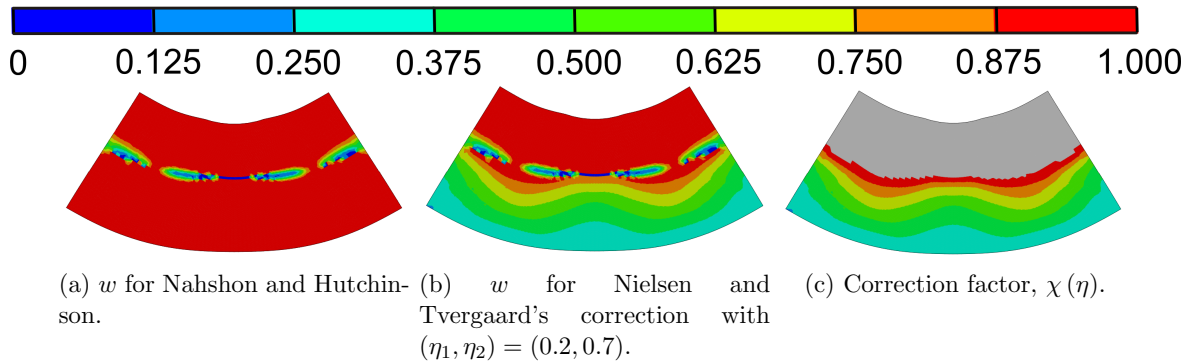
Figure 5.26.: Effect of Nielsen and Tvergaard's modification on w, punch displacement=10 mm.

In order to support the picture given in the previous paragraph, Figure 5.27 shows the evolution of triaxiality over the section in the bend zone at different time steps. The triaxiality distribution over the section is close to being axi-symmetric at the initial deformation levels, whereas with the extent of deformation it involves waviness. It should be noted that the process is not a pure bending process. Above the neutral axis, negative hydrostatic stress develops which suppresses the correction effect, as seen in Figure 5.26.

(a) Punch displacement=3.0 mm.

(b) Punch displacement=6.0 mm.

(c) Punch displacement=8.0 mm.
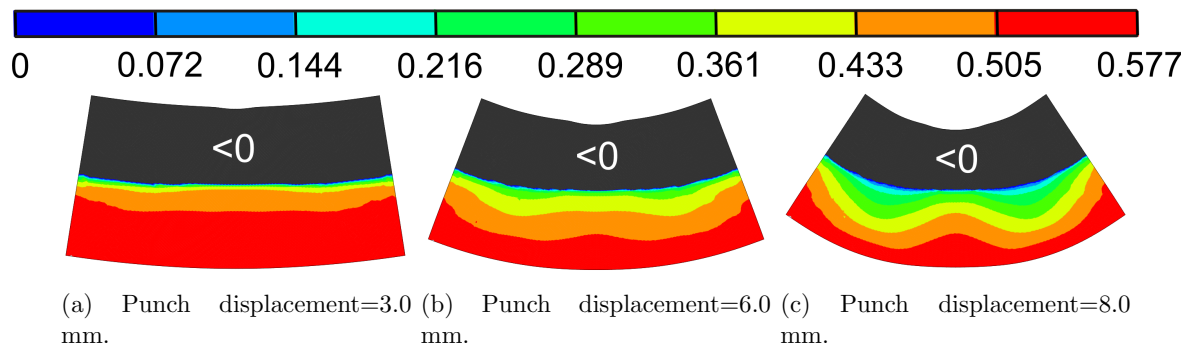
Figure 5.27.: The positive portion of the triaxiality distribution over the section at the bending zone.

This modification has crucial effects on the localization behavior. Since the intensity of shear-driven damage growth drops down to a quarter of its initial value, localization does not occur in the strain range of interest. Eventually, since a developed deformation band cannot be handled, using Nielsen and Tvergaard's correction together with the selected parameter set, one cannot observe crack occurrence. These results are summarized in Figure 5.28.

5.4.2. 3D Model

The dies and the punch are modeled as rigid surfaces, whereas the blank is modeled as a deformable body. The dies and punch radius is 1 mm. The sheet has a length of 100 mm, a width of 50 mm, and a thickness of 1.55 mm. For a reduction in computation time, half of the sheet is modeled exploiting one symmetry plane. In Figure 5.29 free surface of the cross section belongs to the symmetry plane, which is also shown in Figure 5.31. Mesh selection is done following the outputs of the 2D analysis. Accordingly, a 0.030 mm element size at the section bending zone is selected where the element has a relatively large aspect ratio throughout

(a) Deformed mesh.   (b) Total damage, f.
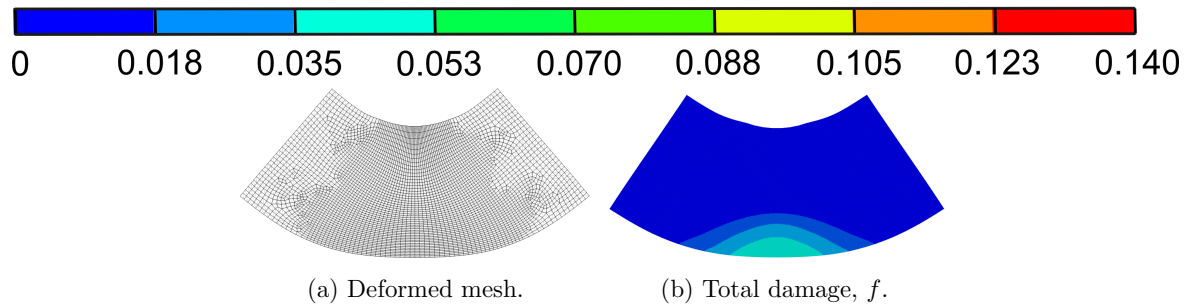
Figure 5.28.: Effect of Nielsen and Tvergaard's approach on damage accumulations, punch displacement=8 mm, (a) Deformed mesh, (b) Total damage, f.

the width for computational reasons. In the die contact regions the mesh is relatively coarse compared to the 2D analysis in order to reduce time for computations. For the blank 108000 C3D8R 8-node linear brick elements with reduced integration and hourglass control are used.

5.4.2.1. Simulation Results

Figure 5.30 gives damage accumulation and consequent localization bands prior to crack occurrence. In accordance with the ASM Handbook remarks and Figure 5.4, strong plane strain constraint forces incipient localization at the symmetry plane. At the edges a plane strain constraint is no longer valid and the stress mode changes to a plane stress one at the surfaces and a uniaxial one at the vertices where the η and w values reduce compared to the central portions. A gradual increase in the developed damage from the edges to the interior is seen which reaches an approximately steady state after nearly three to four thickness distance from the edges. Besides, damage distribution covers a wider area at the symmetry plane as compared to the relatively narrow distribution at the edges. Accordingly, deformation bands at the symmetry plane diffuses approaching to the edges for the same loading step. An anticlastic deformation pattern is also observed due to fibers under compression and tension at the opposing sides of the neutral axis.

The final fracture pattern is given in Figure 5.31. Following the localization, an inclined crack having an orientation of approx 45° with respect to the tensile stress direction starts from the central line and propagates towards the edges. The crack direction change is clearly seen which occurs approximately at the same distance as the plane strain analysis results. The reduction of band sizes is just a consequence of this mechanism. Clearly, the crack alternation cannot be modeled in the current case. However, once an inhomogeneously distributed initial porosity is implemented, such path alternations can be anticipated due to local heterogeneity effects. Besides the effects of random porosity distribution, those of width to thickness ratio of the sheet and the strain history effects on the edge fractures are of specific importance within the reach of 3D models in bending.

As seen in Figure 5.32, the load-displacement curves do not follow a sharp decrease due to gradual cracking towards the bending axis and a redistribution of load carrying capacity of the sheet. As noted before, cracks in the bent region emanate at the center and propagate to the sides. Thus, unlike plane strain simulations, the load carrying capacity progressively drops down. On the contrary, in plane strain simulations the section's load carrying capacity reduces with the occurrence of the first crack where the plane of interest represents the through-thickness plane. Accordingly, the plane strain analysis computes a steep drop of the punch force-displacement
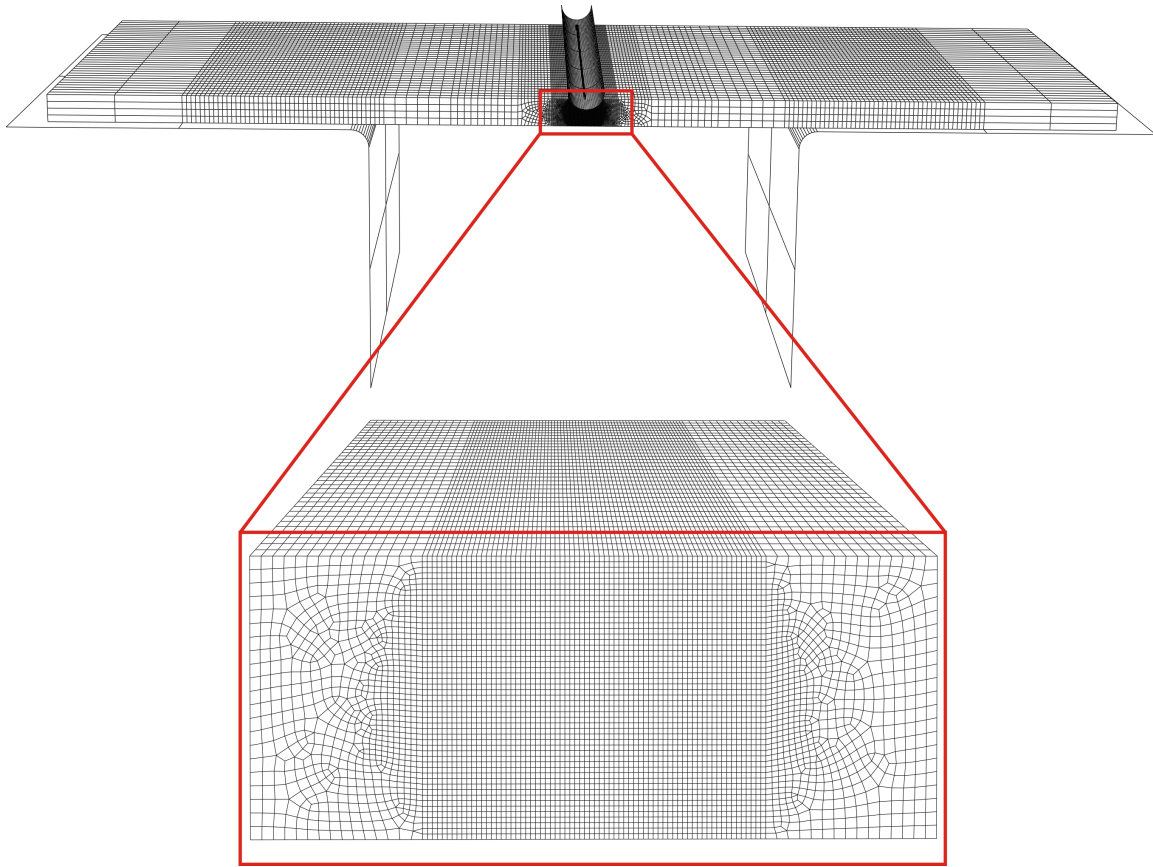
Figure 5.29.: 3D model for free bending. Enlarged section belongs to the plane of symmetry.

diagram. Another remark can be made on the scatters at the post-peak portion of the load-displacement curve. Unlike in the 2D analysis, these scatters are larger due to the relatively coarser mesh resolution in the contact region.

5.5.   Conclusion and Outlook

A detailed experimental numerical investigation of fracturing of DP1000 class advanced high strength steel under bending conditions is presented. Optical microscopy applied to the bend apex and cracked section and scanning electron microscopy applied to fracture surfaces show that the incipient fracture is mainly caused by cavitation and void shearing motivated strain localization. This ductile fracture mode is of a blended Mode I Mode II type. Characteristic steps such as nucleation and growth of undulations are recorded. Observations at the bend apex and various bending sections reveal that the cracks tends to alternate patterns where a shift from one localization band to another one is due. These are attributed to the local material inhomogeneities as well as general equilibrium requirements.

Based on these experimental evidences in the numerical analyses, Gurson's porous plasticity model is selected with recent enhancements to encounter shear-dominated failure modes. Simulations are conducted in both 2D plane strain and 3D. It is shown that 2D plane strain assumption sufficiently reflects the 3D response thanks to the sufficiently large width to thickness ratio. A detailed parameter sensitivity analysis is conducted where the effects of mesh size, shear dam-
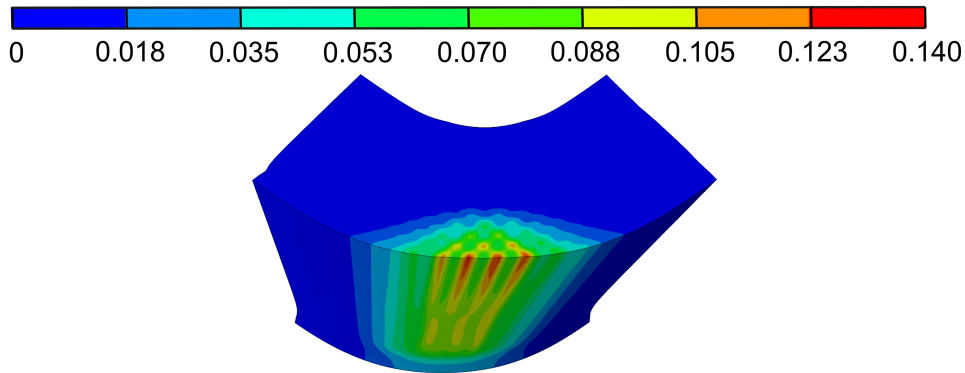
Figure 5.30.: Damage accumulation and localization at the plane of symmetry and the apex, punch displacement=12.2 mm.

(a) Punch displacement=13.0 mm.   (b) Punch displacement=13.6 mm.
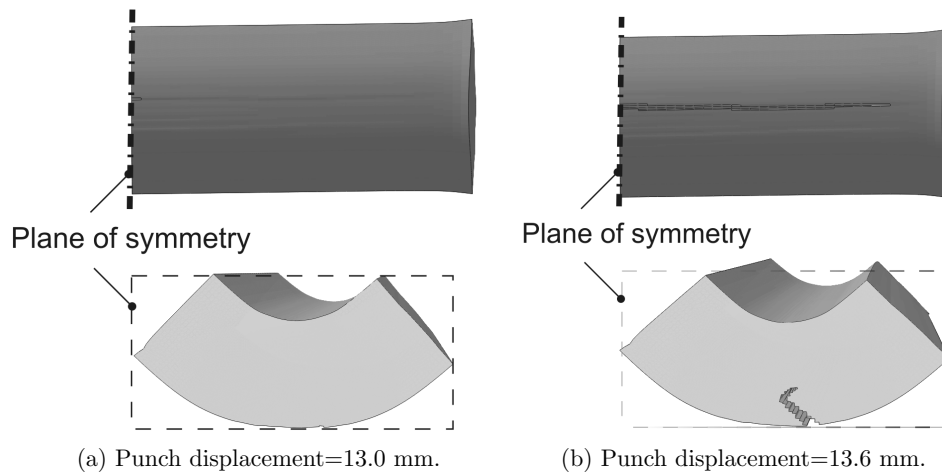
Figure 5.31.: Crack initiation and propagation from the central plane at the apex in 3D simulations. Top figures show the apex of the bend and bottom figures show the crack formation at the plane of symmetry.

age parameter, initial, critical and fracture porosities and finally the Nielsen and Tvergaard's modification on the localization and fracture patters are investigated. It is shown that the size of the localization band is controlled by the selected mesh size which acts as an additional material parameter due to softening material response. Since the regularization of this inherent mesh size dependence is beyond the aim of this study, based on the observed localization and fracture sizes, a computationally reasonable mesh size is selected for the further sensitivity analysis. It is concluded that different variants of shear modification of Gurson's porous plasticity has direct consequences on the damage accumulation and localization deformations. This is due to the plane strain constraint inherent to the problem which indeed includes moderate triaxiality accumulation, which is around 0.577. Coming to the effect of initial porosity, critical and fracture damage values it is shown that relatively small critical damage and fracture damage parameters supply cleavage like vertical fracture patterns due to insufficient damage accumulation to localization emanation.
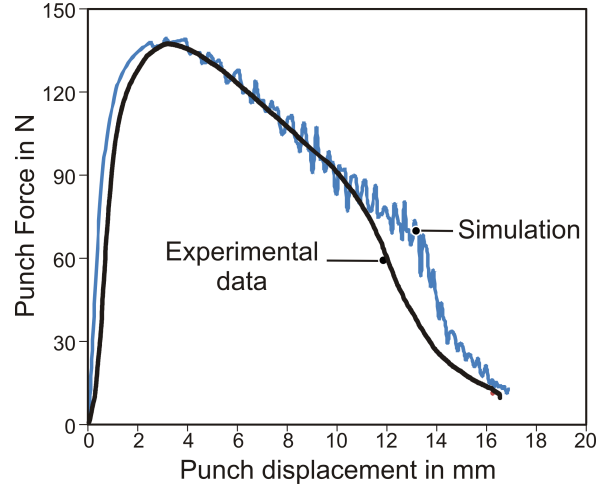
Figure 5.32.: Comparison of experimental and numerical (3D) load-displacement curves.

5.A. Hypoelastic-Plasticity

To set the stage, particle positions at the reference (undeformed), Ω_0 , and current (deformed) configurations, Ω, respectively are denoted by $\boldsymbol{X}$ and $\boldsymbol{x} := \varphi(\boldsymbol{X},t)$ and $\boldsymbol{F} := \partial_{\boldsymbol{X}}\boldsymbol{x}$ define the deformation gradient of the nonlinear map $\varphi : \Omega_0 \times \mathbb{R} \to \mathbb{R}^3$. Any infinitesimal material vector $d\boldsymbol{X}$ at the reference configuration is transformed to its final setting $d\boldsymbol{x}$ at the current configuration via

$$d\boldsymbol{x} := \boldsymbol{F} \cdot d\boldsymbol{X} \,. \tag{5.A.1}$$

Small strain plasticity is based on the additivity of the total strain tensor into elastic and plastic portions where the computation of the stress tensor utilizes a conventional elastic stress definition. In the finite strain regimes, however, the following rate additive form[1] is postulated,

$$\boldsymbol{d} = \boldsymbol{d}^e + \boldsymbol{d}^p \,. \tag{5.A.2}$$

This forms the basis of hypoelastic-plastic formulations which rely on certain objective rates of the selected stress measures. ABAQUS/VUMAT convention is based on a corotational formulation where corotated rate of deformation tensor $\widehat{\boldsymbol{d}}$ is defined as

$$\widehat{\boldsymbol{d}} = \boldsymbol{R}^\top \cdot [\boldsymbol{d}^e + \boldsymbol{d}^p] \cdot \boldsymbol{R} = \widehat{\boldsymbol{d}}^e + \widehat{\boldsymbol{d}}^p \,, \tag{5.A.3}$$

with $\widehat{\boldsymbol{d}}^e = \boldsymbol{R}^\top \cdot \boldsymbol{d}^e \cdot \boldsymbol{R}$ and $\widehat{\boldsymbol{d}}^p = \boldsymbol{R}^\top \cdot \boldsymbol{d}^p \cdot \boldsymbol{R}$. $\boldsymbol{R}$ denotes the rotation tensor, carried out by the polar decomposition of the deformation gradient, $\boldsymbol{F} := \boldsymbol{R} \cdot \boldsymbol{U}$, with $\boldsymbol{U}$ representing the symmetric right stretch tensor. Similarly, a pull back operation on $\boldsymbol{\sigma}$ with the rotation tensor gives the corotated Cauchy stress tensor, $\widehat{\boldsymbol{\sigma}}$,

$$\widehat{\boldsymbol{\sigma}} = \boldsymbol{R}^\top \cdot \boldsymbol{\sigma} \cdot \boldsymbol{R} \,, \tag{5.A.4}$$

whose material time derivative, $\dot{\widehat{\boldsymbol{\sigma}}}$, can be objectively integrated. Together with the definition of hardening one has

$$\left. \begin{aligned} \dot{\widehat{\boldsymbol{\sigma}}} &= \boldsymbol{\mathcal{C}}^e : \widehat{\boldsymbol{d}}^e \,, \\ q(\alpha) &= K\alpha + [Y^\infty - Y^0][1 - \exp(-\delta\alpha)] \,, \end{aligned} \right\} \tag{5.A.5}$$

---

[1]Further details of this split were represented in Chapter 1.

where $\boldsymbol{\mathcal{C}}^e$ denotes the elastic constitutive tensor with

$$\boldsymbol{\mathcal{C}}^e = K\left[\mathbf{1} \otimes \mathbf{1}\right] + 2\mu\,\boldsymbol{\mathcal{I}}^{\mathrm{dev}}\,, \tag{5.A.6}$$

in which K denotes the bulk modulus and μ the shear modulus. $\boldsymbol{\mathcal{I}}^{\mathrm{dev}} = \boldsymbol{\mathcal{I}}^{\mathrm{sym}} - 1/3\left[\mathbf{1} \otimes \mathbf{1}\right]$ is the deviatoric part of the fourth-order symmetric identity tensor, $\boldsymbol{\mathcal{I}}^{\mathrm{sym}} = 1/2\left[\mathbf{1}\overline{\otimes}\mathbf{1} + \mathbf{1}\underline{\otimes}\mathbf{1}\right]$.

5.B.   Numerical Implementation of GTN Model

Letting $\widehat{\Phi}^p$ represent the yield function defined on corotational stress space with

$$\widehat{\Phi}^p = \widehat{\Phi}^p(\mathrm{dev}(\widehat{\boldsymbol{\sigma}}), \mathrm{tr}(\widehat{\boldsymbol{\sigma}}), f, e^p)\,,$$

complete set of equations to be solved can be collected as follows,

$$\left.\begin{aligned}
\widehat{\boldsymbol{d}} &= \widehat{\boldsymbol{d}}^e + \widehat{\boldsymbol{d}}^p \neq \mathbf{0}\,,\\
\dot{\widehat{\boldsymbol{\sigma}}} &= \boldsymbol{\mathcal{C}}^e : \widehat{\boldsymbol{d}}^e\,,\\
\widehat{\boldsymbol{d}}^p &= \dot{\gamma}\partial_{\widehat{\boldsymbol{\sigma}}}\widehat{\Phi}^p\,,\\
\dot{e}^p &= \dot{\gamma}\widehat{\boldsymbol{\eta}} : \partial_{\widehat{\boldsymbol{\sigma}}}\widehat{\Phi}^p\,,\\
\dot{f} &= \dot{\gamma}[A_N\widehat{\boldsymbol{\eta}} + \widehat{\boldsymbol{B}}_G] : \partial_{\widehat{\boldsymbol{\sigma}}}\widehat{\Phi}^p\,,
\end{aligned}\right\} \tag{5.B.1}$$

where $\widehat{\boldsymbol{\eta}} := \widehat{\boldsymbol{\sigma}}/[(1-f)\sigma_y]$. The rotated second-order operator, $\widehat{\boldsymbol{B}}_G$, is defined as

$$\widehat{\boldsymbol{B}}_G = \widehat{\boldsymbol{B}}_G(f, \mathrm{dev}[\widehat{\boldsymbol{\sigma}}]) = [1-f]\mathbf{1} + k_w f \frac{w\left(\mathrm{dev}\left(\widehat{\boldsymbol{\sigma}}\right)\right)}{\sigma_{eq}}\mathrm{dev}(\widehat{\boldsymbol{\sigma}})\,. \tag{5.B.2}$$

The algorithms utilized in this study fall in the class of cutting plane algorithms. The methods rely on the elastic predictor plastic corrector type operator split. It is assumed that for a typical time step $\Delta t = t_{n+1} - t_n$ the solution at t_n is known as $\{\widehat{\boldsymbol{\sigma}}_n, e_n^p, f_n\}$ and the solution at t_{n+1} is sought for as $\{\widehat{\boldsymbol{\sigma}}_{n+1}, e_{n+1}^p, f_{n+1}\}$. Following abbreviations will be utilized in the formulations for brevity reasons,

$$\widehat{\boldsymbol{r}} := \partial_{\widehat{\boldsymbol{\sigma}}}\widehat{\Phi}^p, \quad \xi := \partial_{e^p}\widehat{\Phi}^p, \quad \varsigma := \partial_f\widehat{\Phi}^p\,. \tag{5.B.3}$$

Overall equations will be solved with the operator-split methodology given in Table 5.4.

Table 5.4.: Elastic predictor-plastic corrector type operator split.

Total		Elastic predictor		Plastic corrector
$\left\{\begin{aligned}\widehat{\boldsymbol{d}} &= \widehat{\boldsymbol{d}}^e + \widehat{\boldsymbol{d}}^p \neq \mathbf{0}\,,\\ \dot{\widehat{\boldsymbol{\sigma}}} &= \boldsymbol{\mathcal{C}}^e : \widehat{\boldsymbol{d}}^e\,,\\ \widehat{\boldsymbol{d}}^p &\neq \mathbf{0}\,,\\ \dot{e}^p &\neq 0\,,\\ \dot{f} &\neq 0\,.\end{aligned}\right\}$	$=$	$\left\{\begin{aligned}\widehat{\boldsymbol{d}} &= \widehat{\boldsymbol{d}}^e + \widehat{\boldsymbol{d}}^p \neq \mathbf{0},\\ \dot{\widehat{\boldsymbol{\sigma}}} &= \boldsymbol{\mathcal{C}}^e : \widehat{\boldsymbol{d}}\,,\\ \widehat{\boldsymbol{d}}^p &= \mathbf{0}\,,\\ \dot{e}^p &= 0\,,\\ \dot{f} &= 0\,.\end{aligned}\right\}$	$+$	$\left\{\begin{aligned}\widehat{\boldsymbol{d}} &= \widehat{\boldsymbol{d}}^e + \widehat{\boldsymbol{d}}^p = \mathbf{0}\,,\\ \dot{\widehat{\boldsymbol{\sigma}}} &= -\boldsymbol{\mathcal{C}}^e : \widehat{\boldsymbol{d}}^p\,,\\ \widehat{\boldsymbol{d}}^p &= \dot{\gamma}\partial_{\widehat{\boldsymbol{\sigma}}}\widehat{\Phi}^p\,,\\ \dot{e}^p &= \dot{\gamma}\widehat{\boldsymbol{\eta}} : \partial_{\widehat{\boldsymbol{\sigma}}}\widehat{\Phi}^p\,,\\ \dot{f} &= \dot{\gamma}(A_N\widehat{\boldsymbol{\eta}} + \widehat{\boldsymbol{B}}_G) : \partial_{\widehat{\boldsymbol{\sigma}}}\widehat{\Phi}^p\,.\end{aligned}\right\}$

Elastic Prediction. The elastic prediction for the corotated Cauchy stress $\widehat{\boldsymbol{\sigma}}_{n+1}^{\mathrm{trial}}$ reads

$$\widehat{\boldsymbol{\sigma}}_{n+1}^{\mathrm{trial}} = \widehat{\boldsymbol{\sigma}}_n + \Delta t\,\dot{\widehat{\boldsymbol{\sigma}}}_{n+1}^{\mathrm{trial}}\,, \tag{5.B.4}$$

which relies on integration at the corotational configuration using

$$\dot{\widehat{\boldsymbol{\sigma}}}_{n+1}^{\mathrm{trial}} = \lambda\,\mathrm{tr}(\widehat{\boldsymbol{d}}_{n+1}^{e,\mathrm{trial}})\mathbf{1} + 2\mu\,\widehat{\boldsymbol{d}}_{n+1}^{e,\mathrm{trial}}\,, \tag{5.B.5}$$

with

$$\widehat{\boldsymbol{d}}_{n+1}^{e,\text{trial}} = \widehat{\boldsymbol{d}}_{n+1}\,, \quad e_{n+1}^{p,\text{trial}} = e_n^p\,, \quad f_{n+1}^{\text{trial}} = f_n\,. \tag{5.B.6}$$

Within the time step the elastic or plastic character of the status is checked by inserting the trial stress into the yield function,

$$\widehat{\Phi}_{n+1}^{p,\text{trial}} = \widehat{\Phi}^p(\text{dev}(\widehat{\boldsymbol{\sigma}}_{n+1}^{\text{trial}}), \text{tr}(\widehat{\boldsymbol{\sigma}}_{n+1}^{\text{trial}}),\ f_{n+1}^{\text{trial}}, e_{n+1}^{p,\text{trial}}), \begin{cases} \leq 0 \Longrightarrow \text{elastic}\,, \\ > 0 \Longrightarrow \text{plastic/damage}\,. \end{cases} \tag{5.B.7}$$

Once $\widehat{\Phi}_{n+1}^{p,\text{trial}} \leq 0$ is satisfied, an elastic state at t_{n+1} is defined and the trial values come out to be admissible which do not require any correction. Otherwise, a plastic correction state, named return mapping, is realized to fulfill the yield condition.

Plastic Correction - Cutting Plane Algorithms. For the plastic correction with $\widehat{\boldsymbol{d}} = \boldsymbol{0}$, one has $\dot{\widehat{\boldsymbol{\sigma}}} = -\dot{\gamma}\, \boldsymbol{\mathcal{C}}^e : \partial_{\widehat{\boldsymbol{\sigma}}} \widehat{\Phi}^p$. This supplies

$$\left. \begin{array}{l} \partial_{\dot{\gamma}}[\dot{\widehat{\boldsymbol{\sigma}}}] = -\boldsymbol{\mathcal{C}}^e : \partial_{\widehat{\boldsymbol{\sigma}}} \widehat{\Phi}^p\,, \\ \partial_{\dot{\gamma}}[\dot{e}^p] = \widehat{\boldsymbol{\eta}} : \partial_{\widehat{\boldsymbol{\sigma}}} \widehat{\Phi}^p\,, \\ \partial_{\dot{\gamma}}[\dot{f}] = [A_N \widehat{\boldsymbol{\eta}} + \widehat{\boldsymbol{B}}_G] : \partial_{\widehat{\boldsymbol{\sigma}}} \widehat{\Phi}^p\,. \end{array} \right\} \tag{5.B.8}$$

The algorithm utilized in the following falls in the class of cutting plane algorithms, [239], taking advantage of the great generality and implementation convenience proposed. Linearizing the yield function around the current values of variables, calling

$$\widehat{\Phi}_{n+1}^{p\langle i+1 \rangle} = \widehat{\Phi}^p(\text{dev}(\widehat{\boldsymbol{\sigma}}_{n+1}^{\langle i+1 \rangle}), \text{tr}(\widehat{\boldsymbol{\sigma}}_{n+1}^{\langle i+1 \rangle}), f_{n+1}^{\langle i+1 \rangle}, e_{n+1}^{p,\langle i+1 \rangle})\,,$$

one has,

$$\widehat{\Phi}_{n+1}^{p\langle i+1 \rangle} \simeq \widehat{\Phi}_{n+1}^{p\langle i \rangle} + \widehat{\boldsymbol{r}}_{n+1}^{\langle i \rangle} : [\widehat{\boldsymbol{\sigma}}_{n+1}^{\langle i+1 \rangle} - \widehat{\boldsymbol{\sigma}}_{n+1}^{\langle i \rangle}] + \xi_{n+1}^{\langle i \rangle}[e_{n+1}^{p\langle i+1 \rangle} - e_{n+1}^{p\langle i \rangle}] + \varsigma_{n+1}^{\langle i \rangle}[f_{n+1}^{\langle i+1 \rangle} - f_{n+1}^{\langle i \rangle}]\,, \tag{5.B.9}$$

The increments read,

$$\left. \begin{array}{l} \widehat{\boldsymbol{\sigma}}_{n+1}^{\langle i+1 \rangle} - \widehat{\boldsymbol{\sigma}}_{n+1}^{\langle i \rangle} = -\delta\gamma_{n+1}^{\langle i \rangle} \boldsymbol{\mathcal{C}}^e : \widehat{\boldsymbol{r}}_{n+1}^{\langle i \rangle}\,, \\ e_{n+1}^{p\langle i+1 \rangle} - e_{n+1}^{p\langle i \rangle} = \delta\gamma_{n+1}^{\langle i \rangle} \widehat{\boldsymbol{\eta}}_{n+1}^{\langle i \rangle} : \widehat{\boldsymbol{r}}_{n+1}^{\langle i \rangle}\,, \\ f_{n+1}^{\langle i+1 \rangle} - f_{n+1}^{\langle i \rangle} = \delta\gamma_{n+1}^{\langle i \rangle}[A_{N,n+1}^{\langle i \rangle} \widehat{\boldsymbol{\eta}}_{n+1}^{\langle i \rangle} + \widehat{\boldsymbol{B}}_{G,n+1}^{\langle i \rangle}] : \widehat{\boldsymbol{r}}_{n+1}^{\langle i \rangle}\,. \end{array} \right\} \tag{5.B.10}$$

The incremental plasticity parameter $\delta\gamma_{n+1}^{\langle i \rangle}$ is computed using

$$\delta\gamma_{n+1}^{\langle i \rangle} = \frac{\widehat{\Phi}_{n+1}^{p\langle i \rangle}}{\widehat{\boldsymbol{r}}_{n+1}^{\langle i \rangle} : \boldsymbol{\mathcal{C}}^e : \widehat{\boldsymbol{r}}_{n+1}^{\langle i \rangle} - \xi_{n+1}^{\langle i \rangle} \widehat{\boldsymbol{\eta}}_{n+1}^{\langle i \rangle} : \widehat{\boldsymbol{r}}_{n+1}^{\langle i \rangle} - \varsigma_{n+1}^{\langle i \rangle}[A_{N,n+1}^{\langle i \rangle} \widehat{\boldsymbol{\eta}}_{n+1}^{\langle i \rangle} + \widehat{\boldsymbol{B}}_{G,n+1}^{\langle i \rangle}] : \widehat{\boldsymbol{r}}_{n+1}^{\langle i \rangle}}\,. \tag{5.B.11}$$

This is used in the computation of the new variable updates and the total plasticity parameter $\Delta\gamma$ at the step end through iterations $\Delta\gamma_{n+1}^{\langle i+1 \rangle} = \Delta\gamma_{n+1}^{\langle i \rangle} + \delta\gamma_{n+1}^{\langle i \rangle}$ with $\Delta\gamma_{n+1}^{\langle 0 \rangle} = 0$. For the update of damage components $\Delta f_{n+1}^{\langle i \rangle} = \Delta f_{n,n+1}^{\langle i \rangle} + \Delta f_{g,n+1}^{\langle i \rangle}$ one has

$$\left. \begin{array}{l} \Delta f_{n,n+1}^{\langle i \rangle} = \delta\gamma_{n+1}^{\langle i \rangle} A_{N,n+1}^{\langle i \rangle} \widehat{\boldsymbol{\eta}}_{n+1}^{\langle i \rangle} : \widehat{\boldsymbol{r}}_{n+1}^{\langle i \rangle}\,, \\ \Delta f_{g,n+1}^{\langle i \rangle} = \delta\gamma_{n+1}^{\langle i \rangle} \widehat{\boldsymbol{B}}_{G,n+1}^{\langle i \rangle} : \widehat{\boldsymbol{r}}_{n+1}^{\langle i \rangle}\,. \end{array} \right\} \tag{5.B.12}$$

Iterations are continued until $\widehat{\Phi}^p(\widehat{\boldsymbol{\sigma}}_{n+1}^{\langle i+1 \rangle}, e_{n+1}^{p\langle i+1 \rangle}, f_{n+1}^{\langle i+1 \rangle}) \leq$ TOL. Finally, the converged corotational stress tensor $\widehat{\boldsymbol{\sigma}}_{n+1}$ should be rotated back to the current configuration using $\boldsymbol{\sigma}_{n+1} =$

$\boldsymbol{R}_{n+1} \cdot \widehat{\boldsymbol{\sigma}}_{n+1} \cdot \boldsymbol{R}_{n+1}^{\top}$[2]. As remarked in [239], above algorithm merely requires essential response function derivations. That is, unlike closest point projection type algorithms, this method does not require a derivation of the Hessian of the yield function. However, as noted in [273, p. 252], unlike closest point projection algorithms significant errors may be introduced for large time steps. Thus, the method should better be used only with explicit transient simulations, where the Courant stability condition severely limits the allowable time steps.

---

[2]In Vumat implementation, it should be noted that pre- and post- corotational transformations of tensors are automatically handled by Abaqus.

6. Ductile Fracture under Large-scale Yielding Conditions: Experimental and Computational Study of the Small Punch

In this chapter, a unified experimental-numerical study on ductile fracture initiation and propagation during small punch testing is presented. Tests are carried out at room temperature with unnotched disks of different thicknesses where large-scale yielding prevails. For thinner specimens fracture occurs with severe necking under membrane tension whereas for thicker ones a through thickness shearing mode prevails which changes the crack orientation relative to the loading direction. Numerical studies involve finite element simulations using a shear modified Gurson-Tvergaard-Needleman porous plasticity model with an integral-type nonlocal formulation. The predicted punch load-displacement curves and deformed profiles are in good agreement with the experimental results.

6.1. Introduction

Small punch testing is used at high homologous temperatures for investigation of creep properties such as rupture time and minimum creep rate or at low homologous temperatures for investigation of fracture properties such as yield stress, ultimate stress or fracture toughness. The test requires smaller specimen sizes as compared to standard mechanical tests, hence it allows investigations of regions with gradients properly, such as heat affected zones [107, 108]. Due to its small size the test is almost non-destructive. Thus it eliminates the need for repairing the component after sample removal, which is another advantage of the small punch (SP) test compared to the standard tests. During a small punch test the sample deforms by different deformation mechanisms initially by elastic and plastic bending and followed by membrane stretching. Hence, a rather complex multiaxial stress state, evolving with puncher displacement, occurs inside the sample. The sample thickness closely affects the occurrence of these deformation modes. If the thickness is increased then shearing mode becomes more dominant as compared to membrane stretching. In a recent work [281], the authors applied GTN/RKR (Ritchie-Knott-Rice) approach to plain and notched SP disks for a wide temperature range. The current study aims at a detailed investigation of deformation mechanisms including crack initiation and propagation at room temperature small punch test of P91 steels exploiting the effect of disk thickness. To this end, the problem is studied by experimental and numerical analyses in order to:

- further exploit multiaxial SP testing for numerical model validation,
- consolidate the parameter identification through application of the model to a wide range of disk thicknesses,

- elucidate the effects of shear and initial porosity on damage progression and failure,

- derive robust predictions for the yield stress (YS) and ultimate tensile stress (UTS) for future applications.

On the experimental side small punch tests are carried out using disks of 8 mm diameter and varying thicknesses from 0.2 to 1 mm up to complete fracture. At all thicknesses, due to lack of notch large scale yielding conditions prevail (at least before intense localization with voidage) and the observed consequent fracture mode is ductile. For smaller thicknesses the fracture is led by diffuse necking followed by an intense localization throughout the section. For larger thicknesses on the other hand an initial diffuse necking pattern is not observed since shear deformation prevails rather than membrane stretching. Unlike a simple tension test where the cracks start inside the specimen, the crack initiates from the bottom surface at a distance where thinning takes place. From the recorded force displacement curves it is seen that with increasing thickness the fracture occurs at larger punch displacements. Scanning electron microscope (SEM) studies of the fracture surfaces show signs of a mixed mode I (normal) mode II (shear) fracture with relatively flat dimple walls elongated along the fracture surface. Fracture is primarily due to voidage nucleated at $M_{23}C_6$ carbides and/or MX precipitates coalesced under severe shearing.

On the numerical side, finite element simulations are carried out for the given thickness range. To this end a shear modified GTN model with strain hardening and strain rate hardening is implemented to model the ductile fracture based on void nucleation, growth and coalescence. The origin of the model goes back to Gurson [110] and later modifications were introduced by Tvergaard and Needleman to better account for cavity growth [304, 306, 308]. More recently, a shear modification has been proposed in [224] to accommodate softening by inter-void linking under low stress triaxiality conditions which is not accounted for in the original formulation. Pathological mesh sensitivity pertaining to softening is remedied by an integral-type nonlocal formulation applied to each additive void volume fraction rate component similar to [229]. This formulation requires a characteristic length hence allowing incorporating the size effect in the model. This model is implemented as a VUMAT user defined material subroutine for ABAQUS/EXPLICIT. Prior to applications to the small punch test, the implementation is validated using single element tests under dilatation and simple shear conditions for which analytical solutions exist. The effectiveness of the implemented delocalization scheme is also demonstrated by plane strain tensile tests with different mesh sizes. These studies are followed by small punch simulations with 2D axisymmetric models. Model parameters for P91 steel including the associated length scale are identified using quantitative metallurgy as well as inverse methods relying on experimentally determined force-displacement curves. A good agreement of not only the force-displacement curves but also the deformed profiles of the failed samples in between the numerically and experimentally determined results was obtained. A parameter sensitivity analysis is also conducted where the influence of shear damage parameter k_w and the initial porosity f_0 are investigated. Since the gradient of solution dependent fields are relatively low during the tests in these investigations, the effect of nonlocal regularisation is not observed until the onset of localization. It is believed that the nonlocal modeling framework developed will be helpful to further analyze the effects of strain rate, specimen size, puncher head geometries and especially notched specimens where higher gradients of field variables could prevail.

6.2. Theory

6.2.1. Fundamental Kinematical Assumptions and Hypoelastic Plasticity

Let $\boldsymbol{F} := \partial_{\boldsymbol{X}}\boldsymbol{x}$ define the deformation gradient of the nonlinear map $\boldsymbol{\varphi} : \Omega_0 \times \mathbb{R} \to \mathbb{R}^3$ where $\boldsymbol{X}$ and $\boldsymbol{x} := \boldsymbol{\varphi}(\boldsymbol{X}, t)$ denote the particle positions at the reference (undeformed) configuration Ω_0 and current (deformed) configuration Ω respectively. Then $\boldsymbol{l} := \dot{\boldsymbol{F}} \cdot \boldsymbol{F}^{-1} = \partial_{\boldsymbol{x}}\boldsymbol{v}$ denotes the spatial velocity gradient, with $\boldsymbol{v} = \dot{\boldsymbol{x}}$. An additive split of $\boldsymbol{d} := \mathrm{sym}\,(\boldsymbol{l})$ into elastic and plastic parts is hypothesised to reach

$$\boldsymbol{d} = \boldsymbol{d}^e + \boldsymbol{d}^p. \tag{6.2.1}$$

One then introduces the rotationally neutralized rate of deformation tensor $\dot{\boldsymbol{\epsilon}}$ defined as

$$\dot{\boldsymbol{\epsilon}} = \dot{\boldsymbol{\epsilon}}^e + \dot{\boldsymbol{\epsilon}}^p, \tag{6.2.2}$$

with $\dot{\boldsymbol{\epsilon}}^e := \boldsymbol{R}^\top \cdot \boldsymbol{d}^e \cdot \boldsymbol{R}$ and $\dot{\boldsymbol{\epsilon}}^p := \boldsymbol{R}^\top \cdot \boldsymbol{d}^p \cdot \boldsymbol{R}$. Here, $\boldsymbol{R}$ is the rotation tensor found through the polar decomposition of the deformation gradient with $\boldsymbol{F} = \boldsymbol{R} \cdot \boldsymbol{U}$. Similarly, a pull back operation on the Cauchy stress tensor $\boldsymbol{\sigma}$ with the rotation tensor gives its rotationally neutralized counterpart viz $\widehat{\boldsymbol{\sigma}} := \boldsymbol{R}^\top \cdot \boldsymbol{\sigma} \cdot \boldsymbol{R}$ whose material time derivative $\dot{\widehat{\boldsymbol{\sigma}}}$ is postulated to obey the following hypoelastic relation

$$\dot{\widehat{\boldsymbol{\sigma}}} = \boldsymbol{\mathcal{C}}^e : \dot{\boldsymbol{\epsilon}}^e, \tag{6.2.3}$$

with $\boldsymbol{\mathcal{C}}^e := [K - 2\mu/3]\,[\mathbf{1} \otimes \mathbf{1}] + \mu\,[\mathbf{1}\overline{\otimes}\mathbf{1} + \mathbf{1}\underline{\otimes}\mathbf{1}]$ where K and μ denote the bulk and the shear modulus, respectively.

6.2.2. Shear Modified GTN Porous Plasticity - Local Formulation

The model used here is Gurson's dilatant plasticity model [110], which is extended by parameters q_1, q_2 and q_3 in [304, 306] to account for a better agreement with the numerical analyses of various void distributions, and by the bilinear function $f^*(f)$ in [308] to account for rapid void coalescence prior to failure. The hydrostatic stress dependent flow potential Φ^p is then formulated as

$$\Phi^p = \left[\frac{\sigma_{eq}}{\sigma_y}\right]^2 + 2q_1 f^* \cosh\left(\frac{3}{2}\frac{q_2 \sigma_m}{\sigma_y}\right) - \left[1 + q_3 f^{*2}\right] = 0. \tag{6.2.4}$$

with

$$f^*(f) = \begin{cases} f & f \leq f_c, \\ f_c + [f_u^* - f_c]\,[f - f_c]\,/\,[f_f - f_c] & f > f_c. \end{cases} \tag{6.2.5}$$

where f is the void volume fraction, σ_{eq} is the (macroscopic) equivalent von Mises stress and q_1, q_2 and q_3 are material parameters. f_c denotes the critical void volume fraction at incipient coalescence, f_f the fraction at failure and $f_u^* = 1/q_1$.

The viscoplastic hardening of the material matrix is described by σ_y which accounts for strain and strain rate dependence. Hence, letting e^p denote the equivalent plastic strain and $\dot{e}^p$ its rate, the following multiplicative form is assumed

$$\sigma_y\left(e^p, \dot{e}^p, \theta\right) = h_y\left(e^p\right) r_y\left(\dot{e}^p\right), \tag{6.2.6}$$

where h_y and r_y respectively denote the functions of strain hardening and strain rate hardening

$$\left. \begin{aligned} h_y\left(e^p\right) &= \begin{cases} \sigma_{y0} + h_0 e^p, & e^p \leq e_0^p, \\ h_1 e^p + \sigma_{y\infty} - [\sigma_{y\infty} - \sigma_{y1}]\exp(-m[e^p]^n), & e^p > e_0^p, \end{cases} \\ r_y\left(\dot{e}^p\right) &= 1 + C \log\left(\dot{e}^p/\dot{e}_0^p\right), \end{aligned} \right\} \tag{6.2.7}$$

where σ_{y0}, σ_{y1}, $\sigma_{y\infty}$, h_0, h_1, m, n and e_0^p are plastic strain hardening parameters. C and $\dot{e}_0^p$, on the other hand, are parameters controlling the rate dependence.

Associated plastic flow rule gives the plastic rate of deformation tensor at the rotationally neutralized configuration as

$$\dot{\hat{\boldsymbol{\epsilon}}}^p = \dot{\gamma}\partial_{\hat{\boldsymbol{\sigma}}}\Phi^p\,, \tag{6.2.8}$$

where $\dot{\gamma}$ denotes the plastic multiplier. The equivalent plastic strain rate, using the plastic work equivalence with $[1-f]\,\sigma_y\dot{e}^p = \hat{\boldsymbol{\sigma}} : \dot{\hat{\boldsymbol{\epsilon}}}^p$, reads

$$\dot{e}^p = \frac{\hat{\boldsymbol{\sigma}} : \dot{\hat{\boldsymbol{\epsilon}}}^p}{[1-f]\,\sigma_y}\,. \tag{6.2.9}$$

The void volume fraction evolution involves nucleation and growth. The rate of the total void volume fraction is formulated additively in terms of void nucleation rate $\dot{f}^n$ and void growth rate $\dot{f}^g$

$$\dot{f} = \dot{f}^n + \dot{f}^g. \tag{6.2.10}$$

For $\dot{f}^n$ a strain dependent void nucleation is assumed [75]

$$\dot{f}^n = A_N\dot{e}^p \text{ where } A_N = A_N\left(e^p\right) = \frac{f_N}{S_N\sqrt{2\pi}}\exp\left(-\frac{\left[e^p - e_N^p\right]^2}{2\left[S_N\right]^2}\right)\,, \tag{6.2.11}$$

where e_N^p and S_N respectively denote the mean equivalent plastic strain at the incipient nucleation and its standard deviation. f_N denotes the total source for void volume fraction of nucleation.

$\dot{f}^g$ is further split into two parts, namely normal $\dot{f}^g_{\text{normal}}$ and shear $\dot{f}^g_{\text{shear}}$, [224]

$$\dot{f}^g = \dot{f}^g_{\text{normal}} + \dot{f}^g_{\text{shear}}\,, \tag{6.2.12}$$

where $\dot{f}^g_{\text{normal}}$ accounts for the void growth under hydrostatic stresses whose formulation simply uses the mass conservation viz.

$$\dot{f}^g_{\text{normal}} = [1-f]\,\text{tr}(\dot{\hat{\boldsymbol{\epsilon}}}^p)\,, \tag{6.2.13}$$

whereas $\dot{f}^g_{\text{shear}}$ accounts for softening effects associated with void distortion and void interaction with material rotation under shear stress states where

$$\dot{f}^g_{\text{shear}} = k_w f\, w(\text{dev}\hat{\boldsymbol{\sigma}})\frac{\dot{\hat{\boldsymbol{\epsilon}}}^p : \text{dev}\,\hat{\boldsymbol{\sigma}}}{\sigma_{eq}}\,. \tag{6.2.14}$$

Here, k_w is a material parameter with a suggested interval $0 \leq k_w \leq 3$, [224]. $w(\text{dev}\,\hat{\boldsymbol{\sigma}}) = 1 - \left[27J_3/2\sigma_{eq}^3\right]^2$ with $0 \leq w \leq 1$ distinguishes the states of axisymmetric stress from those of generalized shear on the $\Pi-$plane. Here, $w = 0$ through $J_3 = \pm[2/27]\sigma_{eq}^3$ for all axisymmetric stress states, whereas $w = 1$ through $J_3 = 0$ for the states of generalized shear. This modification due to [224] is motivated by the reported experimental evidence for low triaxiality fracture development in, e.g., [29] and [39], for which the original GTN model falls short in predictive capability.

The fracture responses for the shear modified Gurson model are given in Figure 6.1 for linear and uniform strain paths. As the figure clearly depicts the monotonic dependence of the

fracture strain on the stress triaxiality is suppressed for $k_w \neq 0$. Further, there occurs considerable shrinkage in the admissible range of deformation for generalized plane strain paths, i.e., pure shear and plane strain loading paths with vanishing stress triaxiality ratio $\sigma_m/\sigma_y \to 0$. On the other hand, strain paths associated with the axisymmetric stress states, i.e., uniaxial and biaxial loading paths respectively with $\sigma_m/\sigma_y = 1/3$ and $\sigma_m/\sigma_y = 2/3$, are not affected by the shear correction since for these paths the shear fracture controlling parameter $w(\mathrm{dev}\,\widehat{\boldsymbol{\sigma}})$ becomes zero with vanishing third invariant of the deviatoric stress tensor: $J_3 = 0$. An application of the model to the problem of severe plastic localization bands initiated at free surfaces during free bending is given in [280].
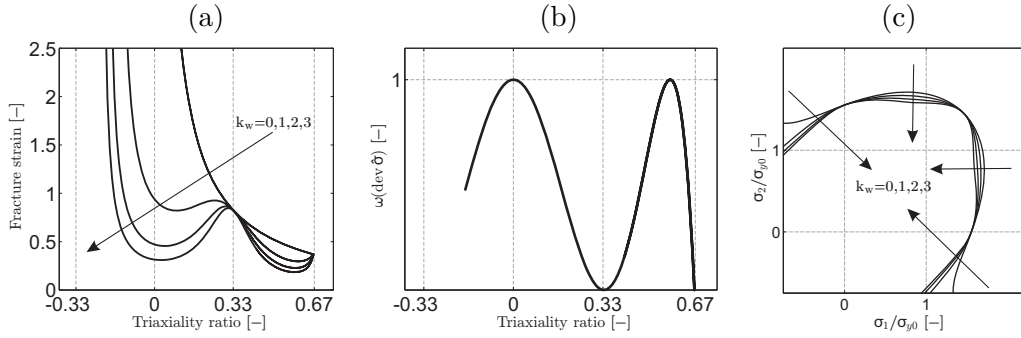
Figure 6.1.: Isochronous fracture surfaces at planar strain and stress spaces for the shear enhanced Gurson's model for linear (uniform) in plane stress paths with linear hardening matrix.

6.2.2.1. Integral-Type Nonlocal Extension

The motivation behind integral-type nonlocal formulations is twofold. On the mechanical side, with micro-void and micro-crack interactions being their micromechanical motivation, integral-type nonlocal formulations constitute distributed damage models[1] capable of reproducing size effects. In view of finite element analysis with damage models, they remedy the pathological mesh dependence of the local solution where the size of the process zone and associated energy dissipation per unit volume is dictated by the discretization. With this motivation, in the current study an integral-type nonlocal formulation is adopted which relies on the following delocalization operation

$$v_{\mathrm{nonlocal}}\left(\boldsymbol{x}\right) = \int_V \widetilde{\omega}\left(\boldsymbol{x}, \boldsymbol{y}\right) v\left(\boldsymbol{y}\right) \mathrm{d}V\left(\boldsymbol{y}\right). \tag{6.2.15}$$

Here $\boldsymbol{y}$ represents the location vector and V the volume at the current coordinates. If $\omega\left(\boldsymbol{x}, \boldsymbol{y}\right)$ denotes the bell-shaped nonlocal weight function

$$\omega\left(\boldsymbol{x}, \boldsymbol{y}\right) = \begin{cases} \left[1 - |\boldsymbol{x} - \boldsymbol{y}|^2/R^2\right]^2 & \text{if } |\boldsymbol{x} - \boldsymbol{y}| \leq R, \\ 0 & \text{otherwise}, \end{cases} \tag{6.2.16}$$

the normalized weight function $\widetilde{\omega}\left(\boldsymbol{x}, \boldsymbol{y}\right)$, which remedies any inconsistency pertaining to the unrestricted averaging domains extending over the problem boundary, reads

$$\widetilde{\omega}\left(\boldsymbol{x}, \boldsymbol{y}\right) = \frac{\omega\left(\boldsymbol{x}, \boldsymbol{y}\right)}{\int_V \omega\left(\boldsymbol{x}, \boldsymbol{y}\right) \mathrm{d}V\left(\boldsymbol{y}\right)}. \tag{6.2.17}$$

---

[1]Other powerful models in this context are gradient localization limiters.

As long as the boundaries are not violated $\int_V \omega\left(\boldsymbol{x}, \boldsymbol{y}\right) \mathrm{d}V\left(\boldsymbol{y}\right)$ is a constant. R in (6.2.16) denotes the interaction radius which constitutes the characteristic length. For $R \to 0$ a local formulation is recovered. In practical applications, R is related to the material microstructure, e.g., four times void size or half void spacing for ductile fracture mechanism [309]. Delocalization could be applied either directly to the kinematic fields; see, e.g., [352], or to the damage variables which control softening, see, e.g., [246], [169], [309] and [229]. In the current study, delocalization of each additive rate component of the void volume fraction is applied. Hence, v in (8.2.20) is substituted by the damage rate component as follows

$$
\left.\begin{array}{rcl}
\dot{f}^n_{\text{nonlocal}}\left(\boldsymbol{x}\right) & = & \int_V \widetilde{\omega}\left(\boldsymbol{x}, \boldsymbol{y}\right) \dot{f}^n\left(\boldsymbol{y}\right) \mathrm{d}V\left(\boldsymbol{y}\right) , \\
\dot{f}^g_{\text{normal, nonlocal}}\left(\boldsymbol{x}\right) & = & \int_V \widetilde{\omega}\left(\boldsymbol{x}, \boldsymbol{y}\right) \dot{f}^g_{\text{normal}}\left(\boldsymbol{y}\right) \mathrm{d}V\left(\boldsymbol{y}\right) , \\
\dot{f}^g_{\text{shear, nonlocal}}\left(\boldsymbol{x}\right) & = & \int_V \widetilde{\omega}\left(\boldsymbol{x}, \boldsymbol{y}\right) \dot{f}^g_{\text{shear}}\left(\boldsymbol{y}\right) \mathrm{d}V\left(\boldsymbol{y}\right) ,
\end{array}\right\} \tag{6.2.18}
$$

which finally adds up to the total nonlocal porosity rate $\dot{f}_{\text{nonlocal}}$, viz.

$$
\dot{f}_{\text{nonlocal}} = \dot{f}^n_{\text{nonlocal}} + \dot{f}^g_{\text{normal, nonlocal}} + \dot{f}^g_{\text{shear, nonlocal}}. \tag{6.2.19}
$$

One notes that for spatially uniform porosity rate distributions delocalization is not effective. Hence, local and nonlocal theories differ only if field gradients exist. The material model is implemented as a VUMAT material subroutine for ABAQUS/EXPLICIT. The algorithmic details are given in the appendices.

6.3.   Experiments

6.3.1.   Material Employed

The material used in this study is modified P91 which has a tempered martensitic microstructure. An optical image revealing the microstructure is given in Figure 6.2. The prior austenite grain size was approximately 14-25 μm. The chemical composition of the material is (wt%) 0.10 C, 0.27 Si, 0.53 Mn, 0.007 P, 0.01 S, 8.76 Cr, 0.91 Mo, 0.2 V, 0.35 Ni, 0.04 Nb, 0.038 N. Conventional disk shaped SP specimens with a diameter of 8 mm and initial thickness in the range of 0.2 to 1 mm were used. Attention was paid not to violate the tolerances stated for disk thicknesses ($\pm 1\%$ of nominal thickness) during the polishing process.
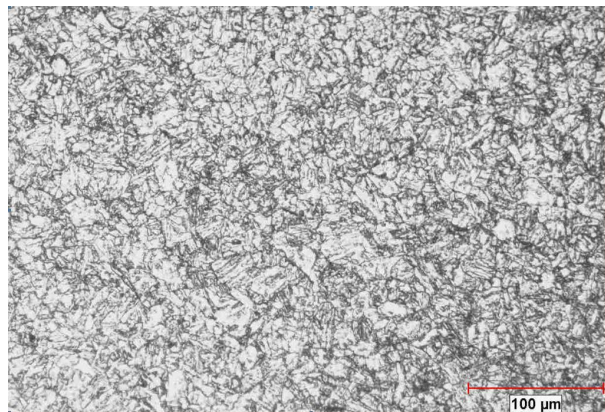
Figure 6.2.: Optical micrograph of the tempered martensitic structure of P91 steel.

6.3.2. Experimental Setup

Small punch tests were performed using the experimental setup in Figure 6.3. The major components of the set up are a specimen holder to ensure the tight clamping of the SP disk, a puncher with a hemispherical head of 2.5 mm diameter for the central loading of the disk and two Linear Variable Displacement Transducers (LVDT) to measure the displacement of the puncher. The SP specimens were circumferentially clamped to prevent slippage of the SP specimen during the test. The aperture of the receiving die was 4 mm in diameter with an edge chamfer of 0.2 mm. The crosshead displacement rate was 0.005 mm/s. All the tests were carried out at room temperature (25°C) in accordance with the Code of Practice for Small Punch Testing [69]. The typical output from an SP test is a force-displacement curve.
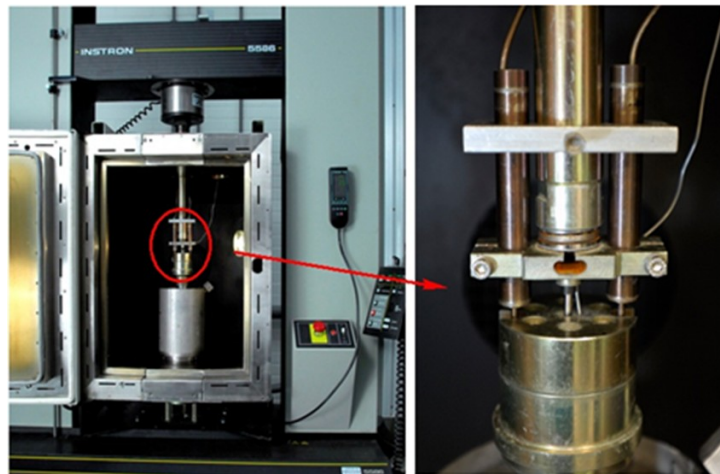
Figure 6.3.: Experimental setup for small punch testing.

6.3.3. Crack Propagation and Fracture Surfaces

During SP testing at room temperature, the fracture is ductile and proceeded by uniform necking. The crack initiates from the bottom surface at a distance where necking takes place. Then it propagates in direction of the maximum equivalent plastic strain through the thickness and follows a circumferential path along this necking region [197] and [112]. This is valid regardless of disk thickness.

For most metals, voids nucleate from inclusions and secondary phase particles by particle cracking or interface decohesion with increasing plastic strain. If particles are not large like MnS inclusions, the voids nucleate by debonding of the particle-matrix interface and grow with the plastic deformation in the matrix. The resulting fracture surface exhibits a dimpled structure with many microvoids. In Figure 6.4 the fracture surface of the SP disk with 0.5 mm thickness is presented. This image reveals a dimpled fracture surface consisting of high density of small microvoids and lower density of relatively large and deep ones. The approximate distance between the large dimples was found to be 30-35 μm whereas the distance was 2-5 μm for the small dimples. The initiation of small microvoids is attributed to MX precipitates distributed in the matrix which are higher in density. The larger microvoids presumably are initiated by larger $M_{23}C_6$ carbides which are mainly precipitated on the grain and lath boundaries. The alignment of the dimple walls shows that fracture does not take place with void growth under Mode I, in which one would expect dimple wall elongation orthogonal to the surface, but a mixed Mode I

and Mode II, where shearing is incorporated. The shearing direction acutely angled with the vertical is distinguishable from the fractograph of Figure 6.4.
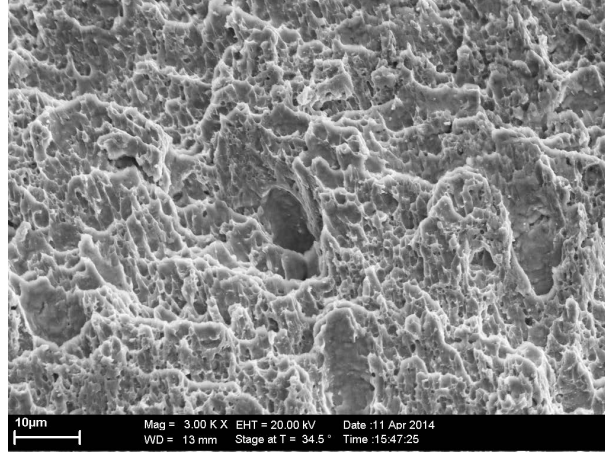
Figure 6.4.: Fracture surface of the unnotched 0.5mm thick SP disk showing the dimpled structure.

6.4.   Material Parameters for P91 Steel

The elastic bulk modulus of P91 at room temperature is $K = 175000$ MPa and the shear modulus is $G = 80769$ MPa. The isotropic plastic hardening parameters are given in Table 6.1. Since no rate sensitivity is observed for P91 in the conditions of interest, the corresponding parameters are arranged to suppress the rate effect.

Table 6.1.: Flow curve data of P91 at room temperature.

σ_{y0} [MPa]	σ_{y1} [MPa]	$\sigma_{y\infty}$ [MPa]	h_0 [MPa]	h_1 [MPa]	m [-]	n [-]	e_0^p [-]
520	376	831	123.31	75	6.14	0.541	0.006

Letting d_x, d_y, and d_z denote average inclusion diameters in the respective directions and S(%) and Mn(%) represent the weight percentages of sulphide and manganese in the matrix, respectively, the initial porosity can be estimated using quantitative metallography from Franklin's formula [93]

$$f_0 = \frac{0.054\sqrt{d_x d_y}}{d_z}\left[\text{S}\,(\%) - \frac{0.001}{\text{Mn}\,(\%)}\right]. \tag{6.4.1}$$

Assuming approximately spherical inclusions ($d_x = d_y = d_z$), the initial porosity is calculated as $f_0 = 0.00044$, based on the previously given chemical properties of P91. A higher value of f_0 was suggested ($f_0 = 0.002$) in [345] thus in further sections the effect of f_0 on simulation results was investigated by using $f_0 = 0.00044$ and $f_0 = 0.002$. The parameters $q_1 = 1.5$, $q_2 = 1$, $q_3 = q_1^2$ of the extended Gurson model are chosen following [304] and [306]. Motivated by the fact that the volume fraction of the segregated inclusions f_N is within a narrow band of 0.01 to 0.03 the parameters controlling void nucleation are chosen as $f_N = 0.02$, $\epsilon_N = 0.3$ and $S_N = 0.1$ [5, 6]. The proposed range of k_w for structural alloys is reported as $0 < k_w < 3$, see, e.g., [224]. In the current study $k_w = 0$ gives the best results for the predicted fracture strains. Nevertheless, a sensitivity analysis is performed investigating the effect of k_w for various disk thicknesses.

Pertaining to the void coalescence and final fracture, the European Structural Integrity Society round robin [1] recommends the slope of the tail of the bilinear coalescence function (6) as 4. For the final void volume fraction at failure different references give different results, e.g., [172] takes $f_f = 0.25$ in accordance with [62] whereas $f_f = 0.2$ is used in [5, 6, 334, 336], where the last two studies refer to steel A533 B. Based on the room temperature parameter fitting studies for P91 steels the coalescence and failure porosity are taken as $f_c = 0.1$ and $f_f = 0.25$.

When applying a nonlocal regularisation to local formulation of porous plasticity, introduction of a characteristic length scale is necessary. This length scale has been related to a physical quantity such as (four times) void size or (half) void spacing for ductile fracture mechanism [309]. If two populations of second phase particles are present, which is the case for P91, one should select the population which is dominant in crack initiation and propagation. While Xia and Shih observed that large inclusions constitute the main contribution to void formation while small inclusions only assist the hole link-up [335]. Thus, they selected the length scale as the mean spacing between voids nucleated by large inclusions. As seen from the fracture surface in Figure 6.4, the small voids nucleated by MX precipitates are dominating in quantity and the mean distance between them ranges from 1.5 to 2.5 μm. On the other hand, the distance between large voids nucleated by $M_{23}C_6$ precipitates are between 20 and 30 μm. Regarding the two studies mentioned, $R = 5$ μm is used as an average value considering the two population of precipitates. This value is also validated by the simulations.

6.5. Simulations

2D axisymmetric simulations with CAX4R reduced integration elements for room temperature are conducted in ABAQUS/EXPLICIT with double precision. A solution of quasi-static problems with a dynamic-explicit solution procedure generally involves a very large number of time steps. In order to reduce the computational cost, mass scaling is applied with a target time step of 10^{-3} s over the whole analysis which lasts for 150 s. This supplies acceleration of the simulations without changing the actual time scale of the process which can affect the other time dependent phenomena such as viscosity or heat transfer. The dies and the punch are modeled as rigid bodies and the disk as a deformable body. The interaction in-between the rigid and deformable bodies is assumed to be constant with a dynamic friction coefficient chosen as $\mu = 0.25$, which is taken to be temperature independent.

The mesh used for 0.5 mm thickness is given in Figure 6.5. The number of elements for each model is given in Table 6.2. When using an integral-type nonlocal formulation, the element size should be below the used characteristic length. For $R = 5$ μm which is selected depending on the microstructure of P91, this requirement puts severe restrictions on the selected mesh size. In order to reduce the computational time non-uniform meshing was used for the model: refined mesh at the crack location, coarse mesh at the clamped part. Initially, a uniform coarse mesh is applied which enabled us to identify the approximate crack location then refined meshing is applied to this region of interest.

Crack propagation is modeled using an element erosion technique where the elements with Gauss points whose damage reaches the corresponding failure thresholds are removed from the computational stack. Although the applied nonlocal formulation removes the mesh dependence of the field distributions to an extent, for the crack propagation this could be limited. Hence, since element erosion is used, the direction of the crack and the crack propagation size are controlled by the mesh. Once biased and/or coarse mesh is used, predicted crack paths will be
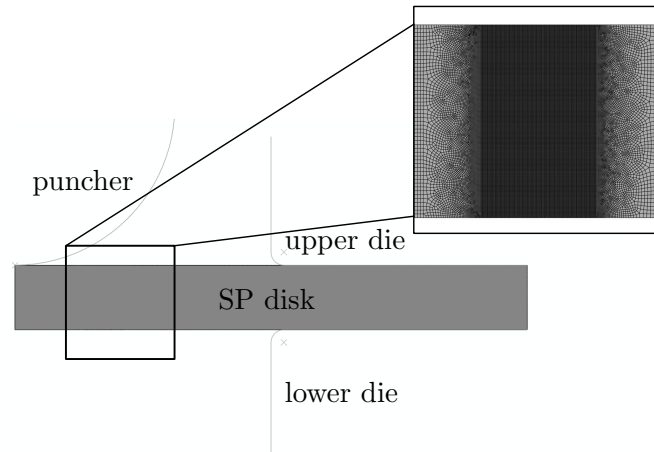
Figure 6.5.: Axisymmetric finite element model and the mesh used for 0.5 mm thick disk (min. element size: 1.5×2.5 µm, number of elements: 59143).The same meshing pattern was applied to the disks with other thicknesses.

Table 6.2.: Number of elements used in the finite element models of the small punch tests with different specimen thicknesses.

Model	1.5µm×2.5µm mesh	2.5µm×2.5µm mesh
0.2 mm	41504	28744
0.3 mm	49351	35505
0.5 mm	59140	45254
0.7 mm	78120	58859
0.8 mm	89442	67132
1 mm	111479	84034

inevitably poor. In this study sufficiently small sized elements with irregular distributions are used. The irregularity of the mesh created by the advancing front quad method accounts for the microstructural heterogeneity. With the same motivation the number of elements within the effective radius of each element vary spatially. During SP test as the puncher deforms the SP specimen, multi-axial stress and strain fields occur which evolve with time. Various deformation stages take place, respectively, elastic bending, plastic bending and membrane stretching and eventually crack initiation and failure of the specimen.

The von Mises stress plots (Figure 6.6) of the SP disk with 0.5 mm thickness reveals that with the onset of contact between the puncher and the disk, high stresses occur underneath the contact region and this zone expands with the contact region till the crack initiation. Due to high stresses developed along with the contact, plastic deformation takes place underneath the contact region at the beginning of the test. As the puncher continues to deform the disk, maximum plastic deformation moves to the bottom surface and localizes in this region where crack initiates.

The deformation modes are intimately dependent on the specimen thickness. For thinner specimens, considerable thickness change and stretching occurs during the test until fracture. On the other hand, indentation caused by the localized plastic yielding underneath the puncher gets more pronounced with increasing thickness. This is revealed by the plastic strain plots of 0.2, 0.5 and 1 mm disks at the initial stage (at displacement ∼0.08 mm and 0.3 mm) of the test. The plastically deformed region under the contact area is more pronounced for the 1 mm thick disk
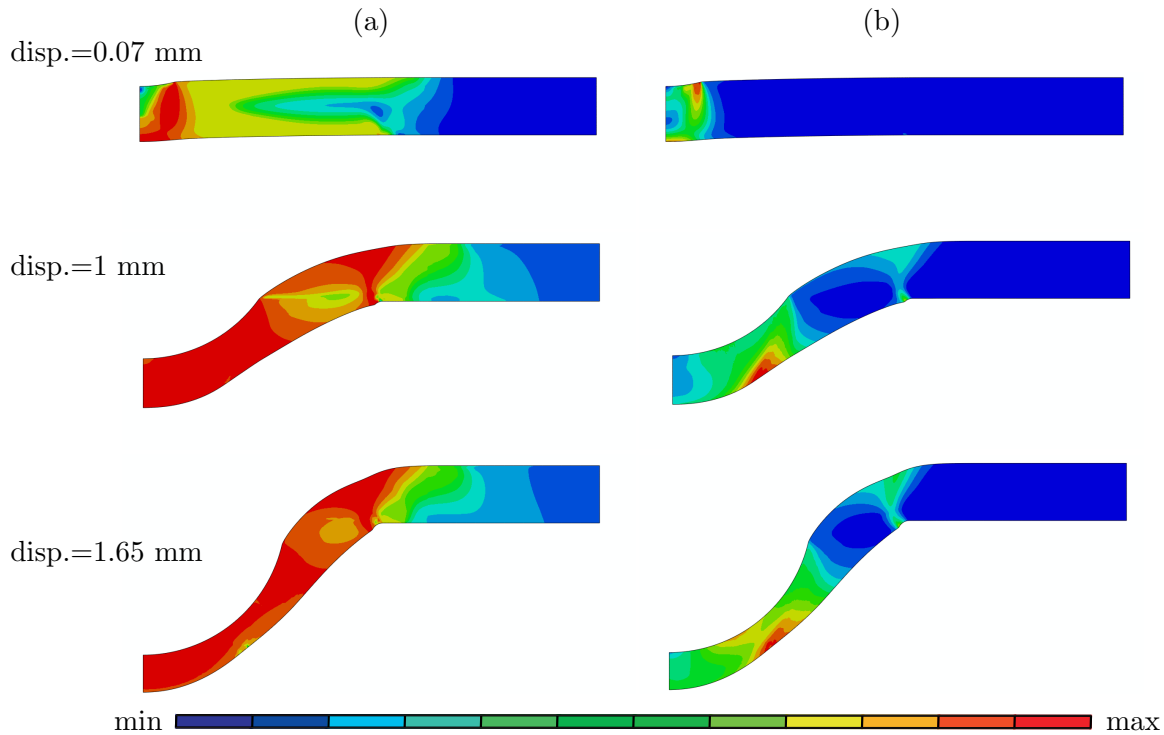
Figure 6.6.: (a) von Mises stress and (b) plastic strain plots of SP disk with 0.5 mm thickness at various displacements: 0.77 mm ((a) [max 7.69×10^2; min 0], (b) [max 1.24×10^{-1}; min 0], 1 mm ((a) [max 8.56×10^2; min 0], (b) [max 6.83×10^{-1}; min 0] and 1.65 mm ((a) [max 8.71×10^2; min 0], (b) [max 1.12; min 0]).

compared to the thinner disks of 0.2 and 0.5 mm. As the puncher further penetrates through the disk, the plastically strained region for the 1 mm disk expands in the upper surface and moves away from the center whereas for 0.2 mm and 0.5 mm it localizes at the bottom surface.

In order to make further evaluations to reveal the influence of the disk thickness, the von Mises stress, plastic strain and pressure plots of 0.2, 0.5 and 1 mm thick disks prior to crack initiation are demonstrated in Figure 6.8. For all thicknesses, maximum plastic strain occurs at the bottom surface of the disk where tensile stresses prevail and promote voidage. For the 1 mm disk there is also a highly strained region at the upper side close to the clamped region which occurs under the combined influence of tension and shear. Again for all thicknesses, the crack initiation starts from the bottom surface where plastic strain is maximum. Practically, the whole unclamped part of the disk exhibits the high stresses with a slight decrease at the crack initiation location for all thicknesses. If the hydrostatic stresses are compared (which is the negative of the pressure plotted in Figure 6.8(c), it is seen that for all thicknesses the unclamped region is under positive hydrostatic stress except the zone underneath puncher for 1 mm. As the thickness gets smaller, the distribution of the hydrostatic stress becomes more uniform through the thickness. Obviously, this has direct consequences on the void nucleation and growth.

Figure 6.9 depicts the damage fields: f, f^n, f^g. Since in this figure k_w is taken as 0, there is no damage growth due to shear. Hence, f is equal to the summation of f_0, f^n and f^g. When pressure plots in Figure 6.8c are taken into account, one can see that just before crack initiation, nucleation mostly reaches its maximum value of 0.02 at the region under positive hydrostatic stress. Hence, with plastification all the void nucleation sources are exhausted where the distribution is rather uniform over the positive hydrostatic stress region. With thinner
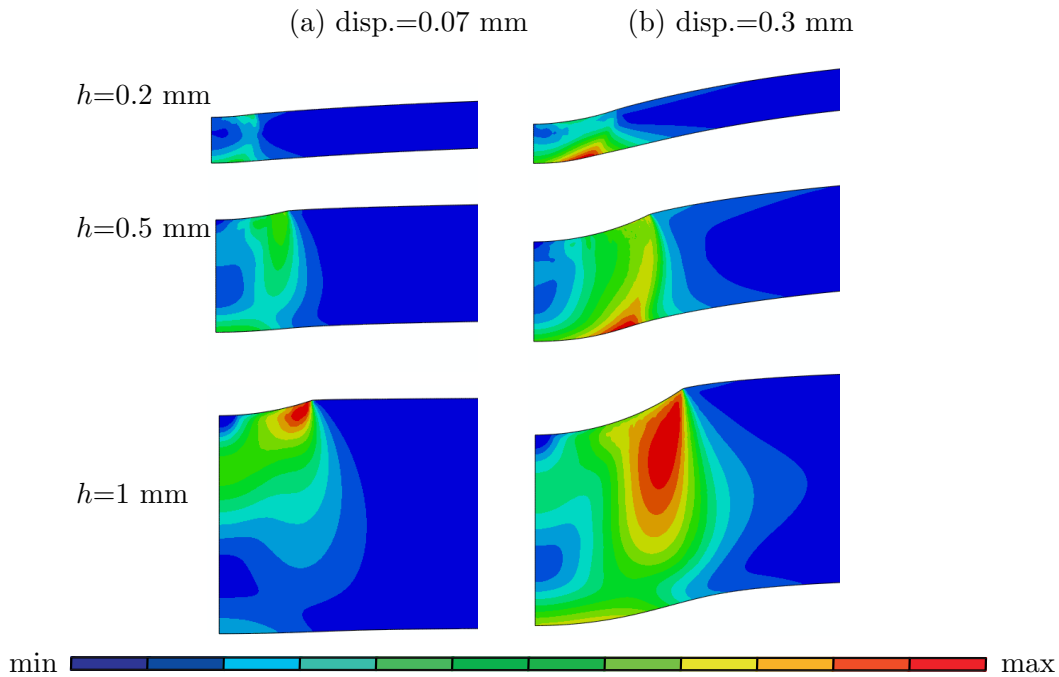
Figure 6.7.: Plastic indentation underneath the puncher at the initial stage of the test according to disk thicknesses: at disp=0.07 mm for h=0.2, 0.5 and 1 mm [max 1.98×10^{-1}; min 0], at disp=0.3 mm for h=0.2 mm [max 2.11×10^{-1}; min 0], for h=0.5 mm [max 2.64×10^{-1}; min 0] and for h=1 mm [max 3.03×10^{-1}; min 0].

specimens the source of positive hydrostatic stresses is the stretching behavior thus underneath the punch also there is considerable nucleation. This is not the case for increased thicknesses where under the punch since the indentation mode is dominant, high compressive stresses with this confinement allows neither nucleation nor positive growth. f^g_{normal} also occurs in the region where positive hydrostatic stress prevails and has its maximum value where plastic strain is also maximal. For the disk with 1 mm thickness, the zone underneath the contact region where hydrostatic stress is negative f^g is also negative. Thus, in this zone void shrinkage takes place instead of void growth.

For all thicknesses, the crack initiates from the highest strained location underneath the puncher at the bottom surface and propagates upwards as shown in Figure 6.10, where plots of plastic strain are given in various stages of crack propagation for disks with thickness of 0.2 mm, 0.5 mm and 1 mm. This reveals the ductile crack propagation in the direction of the maximum plastic strain. Virtually maximum plastic strain occurs in the path due to localization of voidage and the crack simply follows this path since the main controlling variable for the crack path is the porosity. For the 0.2 mm disk, the final crack has an inclined path whereas for 0.5 mm disk the crack also starts with an inclined path but then kinks away almost half way. Similar kinking was also observed for this disk in the optical image of the section (see Figure 6.16(c). As to the 1 mm disk, the crack initiating at the bottom side propagates vertically inside the shear band. Although there is a highly strained region at the upper side of the disk, both the maximum strain and damage localization occur at the bottom side where the crack initiates. In general it can be stated that for thinner specimens the crack propagation direction is less inclined whereas for the thick ones, vertical crack propagation takes place. It is also seen that for the thin specimens relatively uniform fields are observed which is not the case for the thick ones.
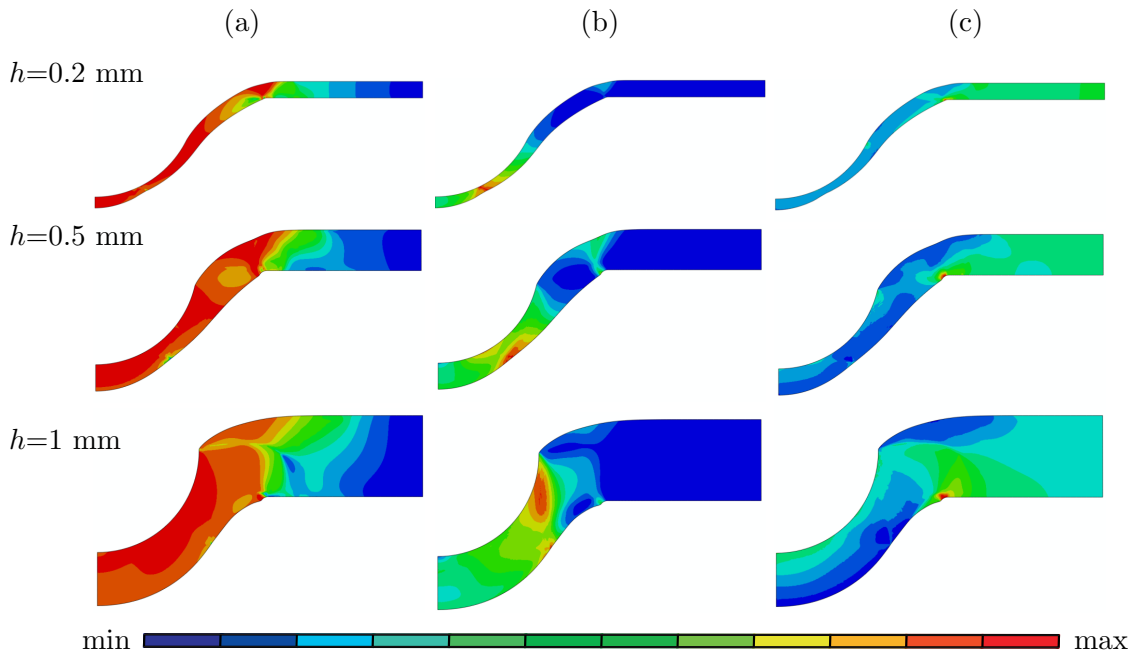
Figure 6.8.: Field distributions before crack initiation: (a) von Mises Stress, (b) plastic strain and (c) pressure for disks with 0.2 mm, 0.5 mm and 1 mm thickness: for h=0.2 mm (a) [max 8.30×10^2; min 1.18×10^2], (b) [max 1.10; min 0], (c) [max 1.33×10^3; min -8.87×10^2], for h=0.5 mm (a) [max 8.70×10^2; min 6.68×10^1], (b) [max 1.14; min 0], (c) [max 1.49×10^3; min -7.22×10^2], and for h=1 mm (a) [max 9.13×10^2; min 2.18×10^1], (b) [max 1.20; min 0], (c) [max 1.39×10^3; min -6.21×10^2].

The effect of shear softening due to void distortion and inter-void linking is investigated by using different values of the parameter k_w : $k_w = 0$ representing no shear influence and $k_w = 1$. These values were investigated for the two extreme thickness values: 0.2 mm and 1 mm. As concluded from Figure 6.11 increasing k_w values results in an earlier loss of load carrying capacity, and thus, a decrease in the recorded displacements at incipient fracture. As anticipated, in the thinner disks the membrane stretching mode of deformation governs while shear effects are much less important. Accordingly, with an increase of thickness shear effects govern and as a consequence, the shear extension in the GTN model results in a considerable reduction in the materials ductility.

In Figure 6.12 the damage distribution plot at a displacement of 0.7 mm reveals how the k_w parameter influences the total damage development in a 1 mm thick disk. In agreement with abovementioned observations, with the increase of k_w from 0 to 1, the maximum damage value increases by 28% at the same displacement.

The effect of f_0 on force-displacement curves is investigated by taking f_0 as 0.002 from [1] and 0.00044 which was calculated from Franklin's formula. As anticipated, increased value of f_0 results in earlier fracture, while the hardening part of the curve is almost not affected (see Figure 6.13(a)). In Figure 6.14 the damage development of a 0.5 mm thick disk prior to crack initiation for $f_0 = 0.002$ and $f_0 = 0.00044$ are presented showing that with higher initial porosity the damage accumulation also increases.

In conclusion when the shear extension was utilized, a premature fracture occurred, so the k_w parameter had to be taken as 0 to achieve agreement with experimental results. As to the initial porosity, whilst the effect on force-displacement curves was not so prominent, the $f_0 = 0.00044$
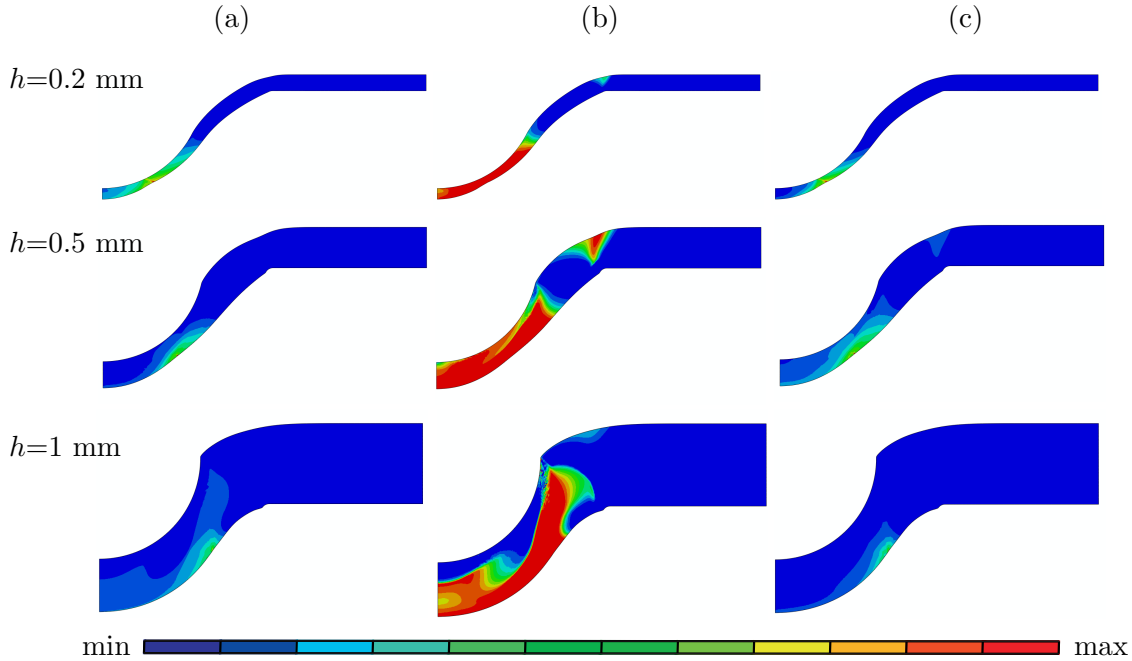
Figure 6.9.: Damage plots (a) f (b) f^n (c) f^g of disks with 0.2 mm , 0.5 mm and 1 mm thickness before crack initiation: for h=0.2 mm (a) [max 1.29×10^{-1}; min 2.30×10^{-4}],(b) [max 2.00×10^{-2}; min 0],(c) [max 1.08×10^{-1}; min -2.10×10^{-4}], for h=0.5 mm (a) [max 1.92×10^{-1}; min 3.43×10^{-5}],(b) [max 2.00×10^{-2}; min 0],(c) [max 1.72×10^{-1}; min -5.96×10^{-4}], and for h=1 mm (a) [max 2.02×10^{-1}; min 6.21×10^{-5}],(b) [max 2.00×10^{-2}; min 0],(c) [max 1.81×10^{-1}; min -5.90×10^{-3}].

as calculated from Franklin's formula gave closer agreement with the experimental curve.

6.5.1. Comparison with Experimentally Determined Results

In Figure 6.15 the numerical and experimental load-displacement curves of SP disks are compared. Experimentally two to three tests were carried out for each thickness. For comparison with the numerical curves, averages of experimental load-displacement curves were used. The results show a very good agreement between numerical and experimental curves especially in terms of hardening. The maximum strengths are slightly underestimated for disks with 0.7 mm, 0.8 mm and 1 mm thickness. Generally speaking, the calculated curves exhibited a steeper force drop compared to the experiments due to axisymmetry assumption in the simulations which prevails in both localization and fracture behaviour. It should be noted that for the selected sample size, shape, loading conditions and selected mesh size/length scale ratio both local and nonlocal formulation estimations were similar in both force displacement paths, i.e., energy dissipation during fracture, and fracture patterns which is attributed to the milder stress and strain gradients. Considering the severe change in element aspect ratios under stretching during small punch test simulation, only nonlocal formulations supply spatially invariant material length. With this property, the developed framework constitutes a unified modeling environment for problems involving sharp notches where high stress gradients are evident or problems with smaller specimen sizes where size effects will govern.

In Figure 6.16 a comparison of the deformed profiles obtained from optical microscopy observations (left) and simulations (right) is given. The fractured SP disks are sectioned by a precision cutter and images are obtained by an optical microscope. Both crack locations and the paths
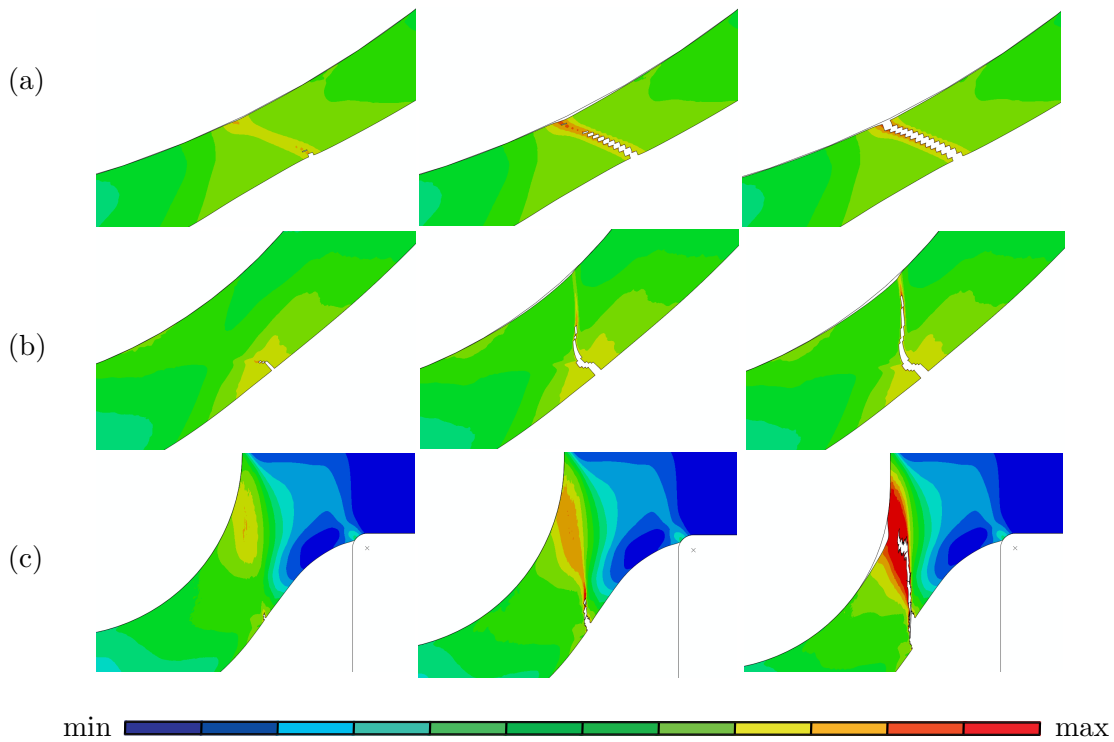
Figure 6.10.: Initiation and propagation of the crack along the maximum plastic strain for disks with thicknesses of (a) 0.2 mm (b) 0.5 mm (c) 1 mm. For all cases min=0, max=1.5.
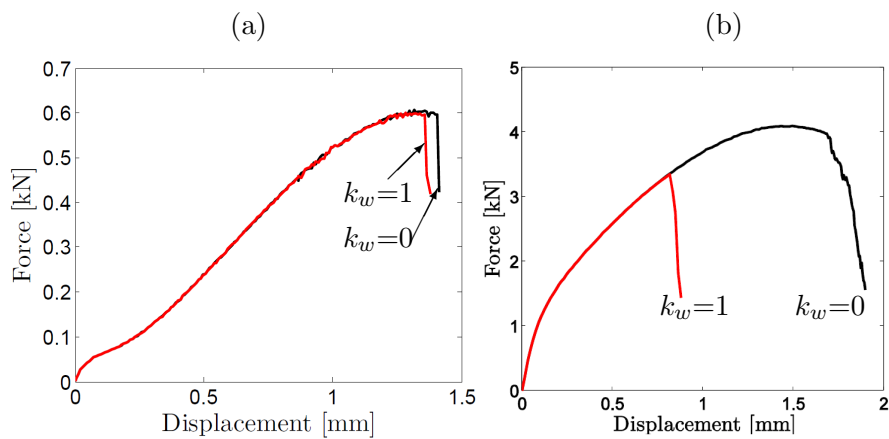
Figure 6.11.: Effect of shear parameter, k_w on force-displacement curves: disk thickness of (a) 0.2 mm and (b) 1 mm for values of k_w=0 and k_w=1.

of the cracks of the numerical results are found to be in good agreement with the experimental ones. It is noted both from FE results and optical images that the location of crack initiation slightly moves further away from the center of the disk with increasing thickness.

In 3D, the crack follows approximately a circular path along the maximum plastic strain contour for all thicknesses (see Figure 6.17) which complies with the axisymmetry assumption applied in the present modeling.
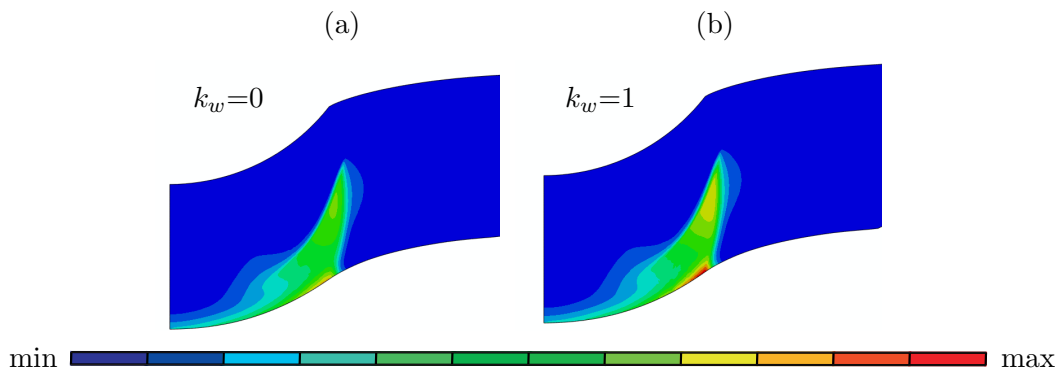
Figure 6.12.: Damage development for a disk of 1 mm thickness at a displacement of 0.7 mm for (a) $k_w = 0$ and (b) $k_w = 1$: [max 2.02×10^{-1}; min 6.21×10^{-5}].
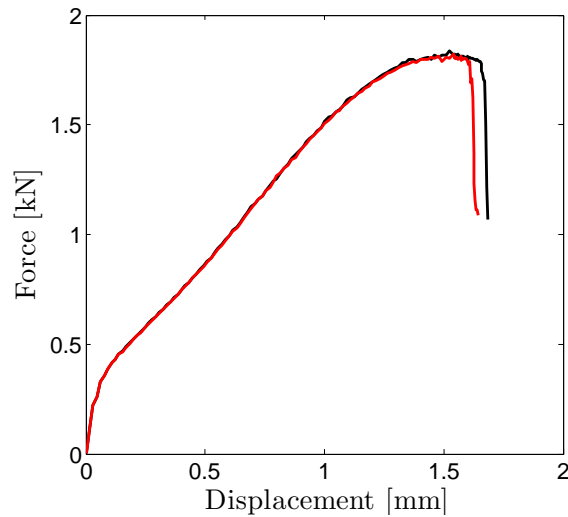
Figure 6.13.: Effect of initial porosity f_0 on force-displacement curves of 0.5 mm disk. The red curve represents $f_0 = 0.002$ whereas the black curve represents $f_0 = 0.00044$.
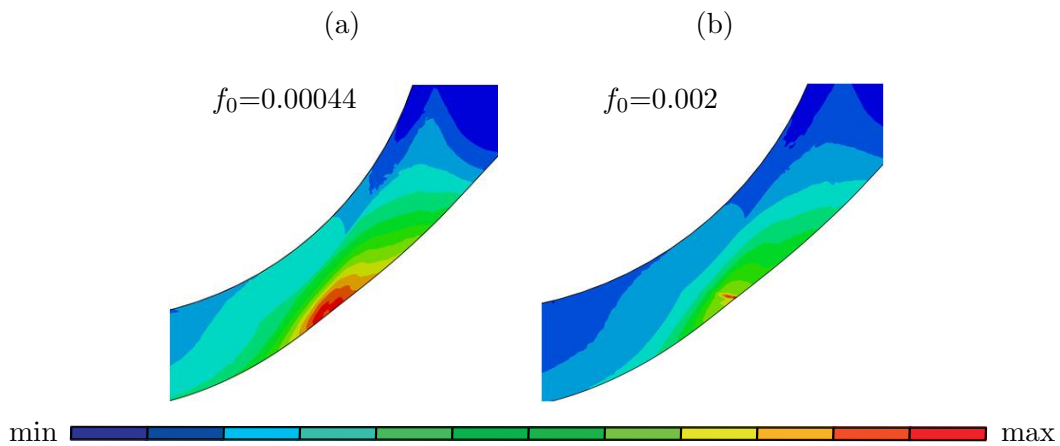
Figure 6.14.: Damage development for (a) $f_0 = 0.002$ [max 1.08×10^{-1}; min 3.44×10^{-5}] (b) $f_0 = 0.00044$ [max 1.81×10^{-1}; min 1.51×10^{-4}] at punch displacement of 1.6 mm.
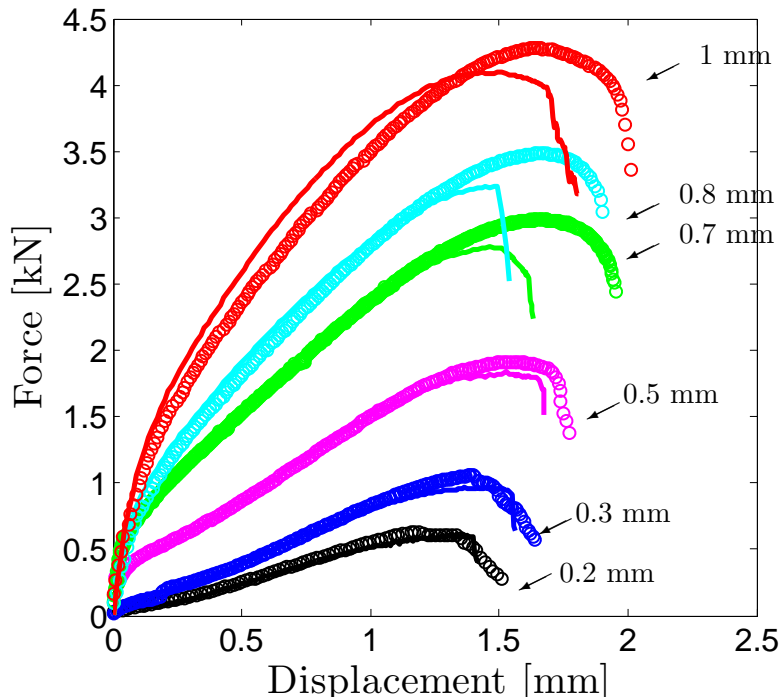
Figure 6.15.: Comparison of experimental and numerical force-displacement curves of disks of varying thicknesses. Discrete circles represent the experimental data and the solid lines represent the simulations.

6.6. Conclusion and Outlook

In this chapter, a combined experimental and numerical investigation of deformation and fracture during room temperature small punch tests of P91 steel disks has been presented. To this end tests were conducted on disks with different thicknesses. A void driven ductile fracture mode is recorded for all cases which is preceded by a diffuse necking with membrane stretching followed by a localized deformation for smaller thicknesses and shear localization for larger ones.

On the numerical side a rate dependent porous-plastic constitutive model with a non-local extension is established to predict the deformation and fracture behavior of P91 steel during small punch testing. The nonlocal formulation allows a natural control of the localization size through incorporating a material length parameter relating to the inter-particle spacing. With the developed framework besides a detailed full field investigation of the deformation process in the small punch test, parameter sensitivity analyses are also realized. The set of material parameters were identified through a combined quantitative metallurgical and inverse mechanical analysis by comparison of the numerical and experimental force-displacement curves. The accuracy of the simulation results with the identified parameters were assessed by comparing experimental and numerical force-displacement curves as well as the deformed sections of disks obtained from FE and optical images. A good agreement is captured between the experimentally and numerically determined force-displacement curves as well as the deformed sections at fracture.
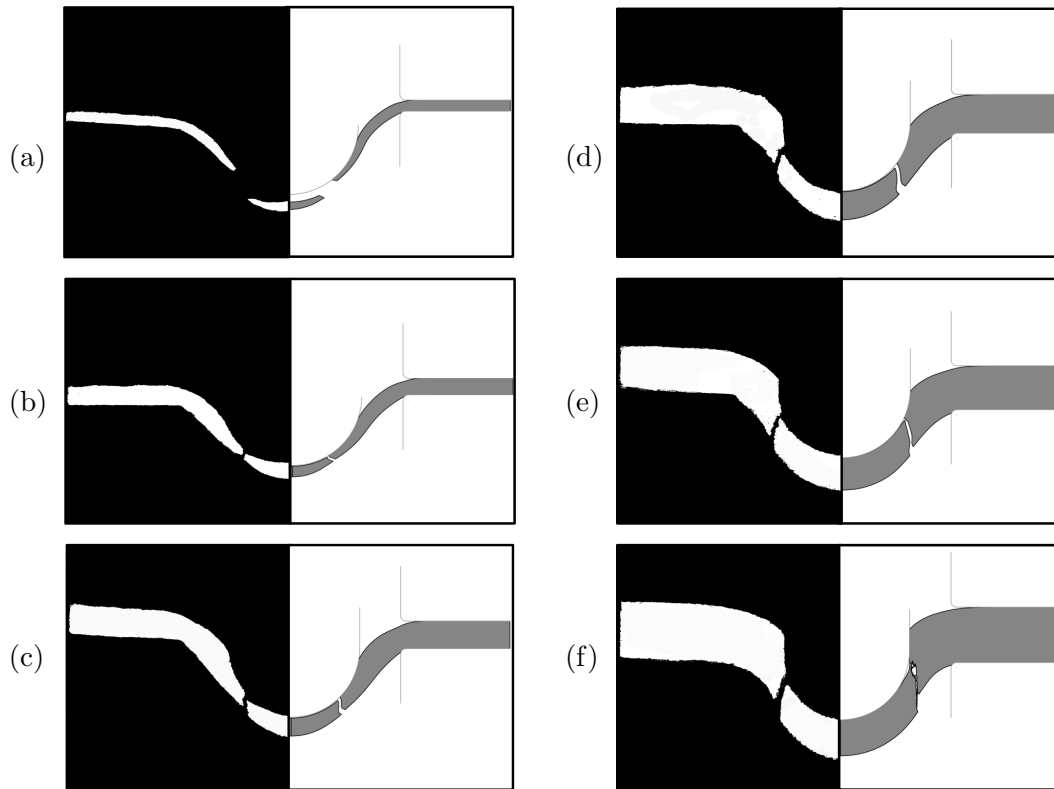
Figure 6.16.: Comparison of experimental (left) and numerical (right) deformed sections of SP disks of varying thickness: (a) h=0.2 mm, (b) h=0.3 mm, (c) h=0.5 mm, (d) h=0.7 mm, (e) h=0.8 mm, (f) h=1 mm.
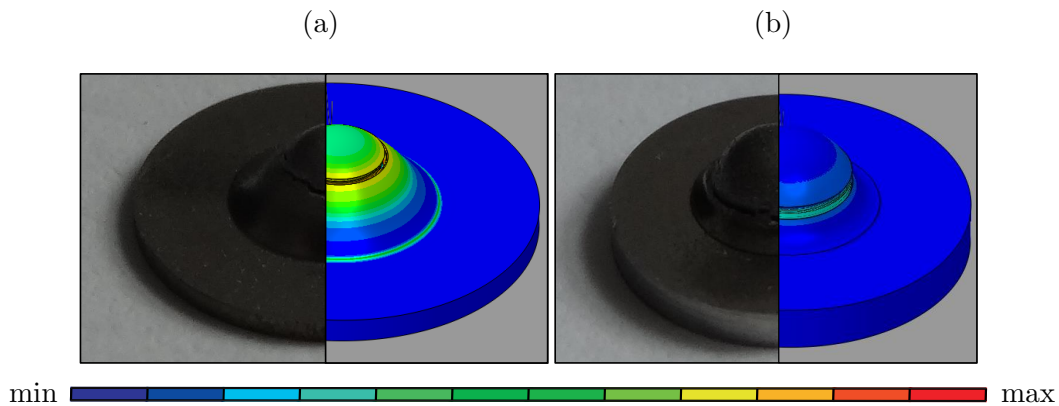
Figure 6.17.: Circular crack path of disks with thicknesses of (a) 0.5 mm (b) 1 mm: optical images on the left and simulation on the right.

The parameter sensitivity analysis conducted for the shear damage parameter k_w shows that increasing values of k_w result in earlier fracture and this effect got more pronounced with increasing disk thickness due to the influence of shear. To a lesser extent initial porosity, f_0, also affected the force-displacement curves in the same way since with higher values of f_0 the damage development was higher. Finally, it was found that for the selected sample size, shape, loading conditions and length scale both local and nonlocal formulation estimations were similar in both fracture pattern and energy dissipation during fracture which was attributed to the milder stress

and strain gradients unlike a case where a notch is present. Still the developed framework allows modeling ductile fracture in the presence of sharp stress gradients driven by, e.g., notches. The model was also found to be efficient in predicting the deformed geometry: necking patterns, crack initiation location and the crack propagation paths by comparing the sections of the failed samples obtained through simulations and optical microscopy.

6.A.   Numerical Implementation

The complete set of equations to be solved can be reiterated as follows,

$$
\left.
\begin{aligned}
\dot{\widehat{\boldsymbol{\epsilon}}}^e &= \dot{\widehat{\boldsymbol{\epsilon}}} - \dot{\widehat{\boldsymbol{\epsilon}}}^p \,, \\
\dot{\widehat{\boldsymbol{\epsilon}}}^p &= \dot{\gamma}\partial_{\widehat{\boldsymbol{\sigma}}}\Phi^p \,, \\
\dot{\widehat{\boldsymbol{\sigma}}} &= \mathcal{C}^e : \dot{\widehat{\boldsymbol{\epsilon}}}^e \,, \\
\dot{e}^p &= \dot{\gamma}\boldsymbol{\eta} : \partial_{\widehat{\boldsymbol{\sigma}}}\Phi^p \,, \\
\dot{f} &= \dot{\gamma}\left[A_N\boldsymbol{\eta} + \boldsymbol{B}_G\right] : \partial_{\widehat{\boldsymbol{\sigma}}}\Phi^p \,.
\end{aligned}
\right\}
\tag{6.A.1}
$$

$\boldsymbol{\eta} := \widehat{\boldsymbol{\sigma}}/\left[\left[1 - f\right]\sigma_y\right]$ and $\boldsymbol{B}_G = \boldsymbol{B}_G\left(f, \operatorname{dev}\widehat{\boldsymbol{\sigma}}\right)$ is defined as

$$
\boldsymbol{B}_G := \left[1 - f\right]\mathbf{1} + k_w f\frac{w\left(\operatorname{dev}\widehat{\boldsymbol{\sigma}}\right)}{\sigma_{eq}}\operatorname{dev}\widehat{\boldsymbol{\sigma}} \,.
\tag{6.A.2}
$$

For solving Equations (8.A.1), an elastic predictor$-$plastic corrector type of algorithm is used. Letting $\Delta\left(\bullet\right) = \Delta t \times \left(\dot{\bullet}\right)$, the subscript $n+1$ denote the (unknown) step at time t_{n+1} and n denote the (known) step at time t_n, the solution $\left\{\widehat{\boldsymbol{\sigma}}_{n+1}, e^p_{n+1}, f_{n+1}\right\}$ is sought for the given $\left\{\widehat{\boldsymbol{\sigma}}_n, e^p_n, f_n\right\}$ and the strain increment $\Delta\widehat{\boldsymbol{\epsilon}}$ with $\Delta t = t_{n+1} - t_n$. The corresponding operator-split is summarized in Table 6.3.

Table 6.3.: Elastic predictor$-$plastic corrector type operator split.

Total		Elastic predictor		Plastic corrector
$\left\{\begin{aligned}\Delta\widehat{\boldsymbol{\epsilon}} &\neq \mathbf{0} \\ \Delta\widehat{\boldsymbol{\epsilon}}^p &\neq \mathbf{0} \\ \Delta\widehat{\boldsymbol{\sigma}} &\neq \mathbf{0} \\ \Delta e^p &\neq 0 \\ \Delta f &\neq 0\end{aligned}\right.$	$=$	$\left\{\begin{aligned}\Delta\widehat{\boldsymbol{\epsilon}} &\neq \mathbf{0} \\ \Delta\widehat{\boldsymbol{\epsilon}}^p &= \mathbf{0} \\ \Delta\widehat{\boldsymbol{\sigma}} &= \mathcal{C}^e : \Delta\widehat{\boldsymbol{\epsilon}} \\ \Delta e^p &= 0 \\ \Delta f &= 0\end{aligned}\right.$	$+$	$\left\{\begin{aligned}\Delta\widehat{\boldsymbol{\epsilon}} &= \mathbf{0} \\ \Delta\widehat{\boldsymbol{\epsilon}}^p &\neq \mathbf{0} \\ \Delta\widehat{\boldsymbol{\sigma}} &= -\mathcal{C}^e : \Delta\widehat{\boldsymbol{\epsilon}}^p \\ \Delta e^p &\neq 0 \\ \Delta f &\neq 0\end{aligned}\right\}.$

Elastic Predictor. Here, a *trial* step is realized assuming the strain increment $\Delta\widehat{\boldsymbol{\epsilon}}$ is purely elastic. Once the corresponding value of the flow potential $\Phi^{p,trial}_{n+1}$ is smaller than zero, i.e. $\Phi^{p,trial}_{n+1} < 0$, the trial step is assumed to be correct, otherwise a plastic correction is required.

Plastic Corrector. The semi-implicit plastic corrector algorithm relies on exploitation of the first order Taylor series expansion of the yield potential around a known step $\langle i\rangle$

$$
\Phi^{p\langle i+1\rangle}_{n+1} \simeq \Phi^{p\langle i\rangle}_{n+1} + \boldsymbol{r}^{\langle i\rangle}_{n+1} : \delta\widehat{\boldsymbol{\sigma}}^{\langle i\rangle}_{n+1} + \xi^{\langle i\rangle}_{n+1}\delta e^{p\langle i\rangle}_{n+1} + \varsigma^{\langle i\rangle}_{n+1}\delta f^{\langle i\rangle}_{n+1} + \varpi^{\langle i\rangle}_{n+1}\delta\dot{e}^{p,\langle i\rangle}_{n+1} \,,
\tag{6.A.3}
$$

where

$$
\left.
\begin{aligned}
\boldsymbol{r} &:= \partial_{\widehat{\boldsymbol{\sigma}}}\Phi^p &&= \partial_{\sigma_{eq}}\Phi^p\partial_{\widehat{\boldsymbol{\sigma}}}\sigma_{eq} + \partial_{\sigma_m}\Phi^p\partial_{\widehat{\boldsymbol{\sigma}}}\sigma_m \,, \\
\xi &:= \partial_{e^p}\Phi^p &&= \partial_{\sigma_y}\Phi^p\partial_{e^p}\sigma_y \,, \\
\varsigma &:= \partial_f\Phi^p &&= 2q_1\cosh\left(\left[3/2\right]\left[q_2\sigma_m/\sigma_y\right]\right) - 2fq_3 \,, \\
\varpi &:= \partial_{\dot{e}^p}\Phi^p &&= \partial_{\sigma_y}\Phi^p\partial_{\dot{e}}\sigma_y \,.
\end{aligned}
\right\}
\tag{6.A.4}
$$

The increments $\delta\left(\bullet\right)^{\langle i\rangle} = \left(\bullet\right)^{\langle i+1\rangle} - \left(\bullet\right)^{\langle i\rangle}$ in (8.A.3) read

$$
\left.
\begin{aligned}
\delta\widehat{\boldsymbol{\sigma}}_{n+1}^{\langle i\rangle} &= -\delta\gamma_{n+1}^{\langle i\rangle}\mathcal{C}^e : \boldsymbol{r}_{n+1}^{\langle i\rangle}\,, \\
\delta e_{n+1}^{p\langle i\rangle} &= \delta\gamma_{n+1}^{\langle i\rangle}\boldsymbol{\eta}_{n+1}^{\langle i\rangle} : \boldsymbol{r}_{n+1}^{\langle i\rangle}\,, \\
\delta f_{n+1}^{\langle i\rangle} &= \delta\gamma_{n+1}^{\langle i\rangle}\left[A_{N,n+1}^{\langle i\rangle}\boldsymbol{\eta}_{n+1}^{\langle i\rangle} + \boldsymbol{B}_{G,n+1}^{\langle i\rangle}\right] : \boldsymbol{r}_{n+1}^{\langle i\rangle}\,, \\
\delta\dot{e}_{n+1}^{p,\langle i\rangle} &= \delta e_{n+1}^{p\langle i\rangle}/\Delta t\,.
\end{aligned}
\right\}
\qquad (6.A.5)
$$

Using the condition $\Phi_{n+1}^{p\langle i+1\rangle} = 0$ as required, and substituting (8.A.3) into the right-hand side of (8.A.5) which allows factoring out the incremental plasticity parameter, one finds $\delta\gamma_{n+1}^{\langle i\rangle}$ as

$$
\delta\gamma_{n+1}^{\langle i\rangle} = \frac{\Phi_{n+1}^{p\langle i\rangle}}{\boldsymbol{r}_{n+1}^{\langle i\rangle} : \mathcal{C}^e : \boldsymbol{r}_{n+1}^{\langle i\rangle} + \boldsymbol{r}_{n+1}^{\langle i\rangle} : \boldsymbol{D}_{n+1}^{\langle i\rangle}}\,,
\qquad (6.A.6)
$$

where

$$
\boldsymbol{D}_{n+1}^{\langle i\rangle} = \left[\xi_{n+1}^{\langle i\rangle} + \frac{\varpi_{n+1}^{\langle i\rangle}}{\Delta t}\right]\boldsymbol{\eta}_{n+1}^{\langle i\rangle} + \varsigma_{n+1}^{\langle i\rangle}\left[A_{N,n+1}^{\langle i\rangle}\boldsymbol{\eta}_{n+1}^{\langle i\rangle} + \boldsymbol{B}_{G,n+1}^{\langle i\rangle}\right]\,.
\qquad (6.A.7)
$$

The iterations are started with an initial guess of plastic multiplier $\Delta\gamma_{n+1}^{\langle 0\rangle}$. This depends on the rate dependence of hardening which is assumed to vanish for $\dot{e}^p < \dot{e}_0^p$, that is $r_y = 1$ as $\dot{e}^p < \dot{e}_0^p$. Consequent numerical difficulty pertaining to the hardening discontinuity is remedied following in the lines of [351]. Consequently, once $\Phi^p\left(\Delta t \times \dot{e}_0^p\right) > 0$ the initial guess of $\Delta\gamma_{n+1}^{\langle 0\rangle} = \Delta t \times \dot{e}_0^p$, otherwise $\Delta\gamma_{n+1}^{\langle 0\rangle} = 0$ is used. State variable updates $\left(\bullet\right)^{\langle i+1\rangle} = \left(\bullet\right)^{\langle i\rangle} + \delta\left(\bullet\right)^{\langle i\rangle}$ are continued throughout the iterations $\langle i\rangle$ for the computed increment of the plastic multiplier in (8.A.6), until $\Phi_{n+1}^{p\langle i+1\rangle} \simeq 0$ with a desired accuracy. The stress tensor is then rotated back to the current coordinates viz $\boldsymbol{\sigma}_{n+1} = \boldsymbol{R}_{n+1} \cdot \widehat{\boldsymbol{\sigma}}_{n+1} \cdot \boldsymbol{R}_{n+1}^{\top}$.

6.B.   Verification of Implementation through Benchmark Problems

The verification of the implementation is done using the benchmark studies presented in [225], where the problems involve uniform field tests conducted on a single finite element with side length of 1 mm. The first problem uses Gurson's model without shear extension which agrees with the solution of the current framework for $k_w=0$. The second problem compares numerical solutions with analytically handled results for different k_w values.

6.B.1.   Dilatation

Dilatation in three directions is supplied by loading three faces of a cube by 0.01 m/s in normal direction while the other three faces are let stationary. In addition, all faces are given expansion free boundary conditions. The elastic material parameters are selected as $E = 200$ GPa and $\nu =0.3$. The elastic limit of the matrix material is defined by $\sigma_{y0} = 200$ MPa. A power law function $\sigma_y\left[Ee^p/\sigma_y\right]^n$ with $n = 0.1$ is supplied as the flow curve. Extended Gurson's model parameters are selected as $q_1 = q_2 = q_3 = 1$. The initial void volume fraction is taken as $f_0 = 0.005$. Strain dependent void nucleation parameters are taken as $e_N = 0.3$, $S_N = 0.1$ and $f_N = 0.04$. Coalescence parameters are chosen to be $f_c = 0.15$ and $f_f = 0.25$. To create a comparison basis with the ABAQUS implementation where shear extension does not exist, the shear parameter is set as $k_w = 0$. In Figure 6.18, comparisons are presented between ABAQUS

built-in Gurson model (Keyword `*Porous Plasticity`) and current VUMAT implementation using the same input parameters. The results for the modified and original Gurson models are identical for uniform expansion as the figures reveal.
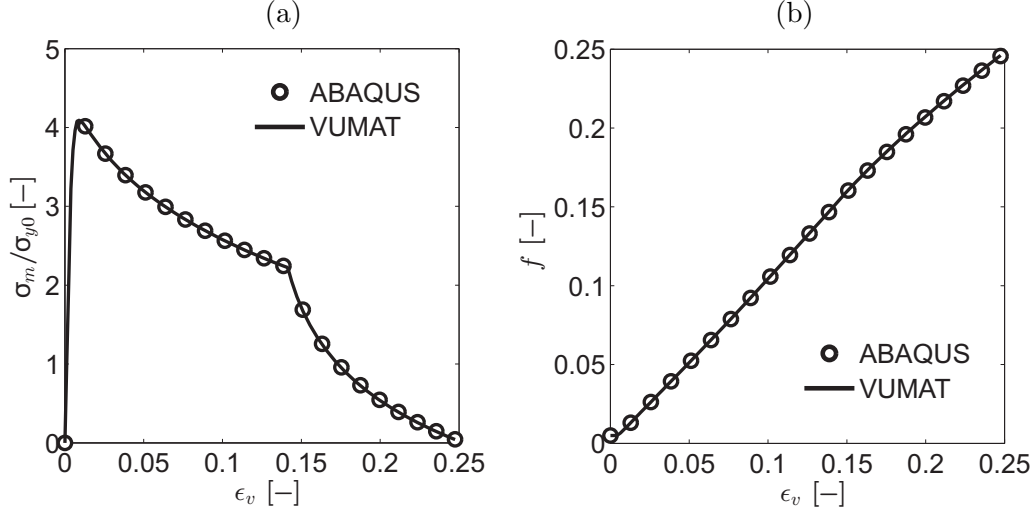
Figure 6.18.: ABAQUS *built-in model and* VUMAT *implementation comparisons for (a)* σ_m/σ_{y0}, *(b) void volume fraction histories during the dilatational loading.*

6.B.2. Simple Shear

This problem is executed by excluding void nucleation and growth due to triaxiality and coalescence acceleration to facilitate a comparison with the following analytical solutions for f and σ_{eq} which neglect elasticity for simple shear in $(\boldsymbol{e}_1, \boldsymbol{e}_3)$ plane [225]

$$f = f_0 \exp\left(k_w e^p\right) \ \ \text{and} \ \ \frac{\sigma_{eq}}{\sigma_{y0}} = \left[\frac{E e^p}{\sigma_Y}\right]^n \left[1 - f_0 \exp\left(k_w e^p\right)\right]. \tag{6.B.1}$$

The rest of the material parameters selected are identical to the previous problem. Simple shearing is supplied by loading one face with 0.01 m/s to obtain $\boldsymbol{\sigma} = \tau\left[\boldsymbol{e}_1 \otimes \boldsymbol{e}_3 + \boldsymbol{e}_3 \otimes \boldsymbol{e}_1\right]$. As given in Figure 6.19 the resulting curves from the VUMAT implementations are in complete agreement with those of the analytical solution. As a conclusion, for $k_w > 0$ damage growth under shear stresses becomes exponential and increasing k_w reduces the localization and fracture strains that could be reached. For $k_w = 0$ conventional Gurson's model response is carried out without an explicit dependence on shear.

6.C. Analysis of the Effectiveness of Delocalization

In order to verify the regularisation property of the developed nonlocal framework, plane strain tensile tests on imperfect models are realized. The imperfections are introduced as a smoothly distributed width change by 98% to the initially square domains with edges of 1 mm. Three cases with different element sizes $h = 0.05$ mm, $h = 0.025$ mm and $h = 0.0125$ mm are run. Thermal effects as an additional source of softening are switched off. The analysis is conducted for the ductile interaction radius of $R = 0$, which corresponds to the local analysis, and for $R = 0.15$ mm. As the contour plots for porosity development at the deformed configuration
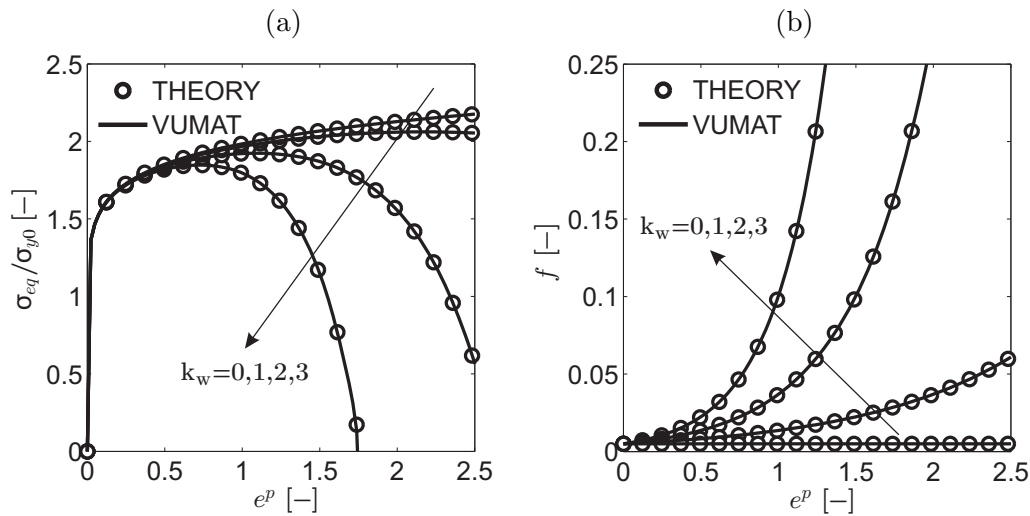
Figure 6.19.: Analytical solution and VUMAT *implementation comparisons for (a)* σ_{eq}/σ_{y0}, *(b) Void volume fraction histories during the shear loading.*

given in Figure 6.20 suggests, for the local analysis strong mesh dependence occurs as the mesh is refined a continuous reduction of the localization size results even at relatively low amounts of voidage which shows a clear loss of uniqueness. On the simulation results accounting for nonlocality however, it is seen that the localization band width as well as the magnitude of the maximum observed porosity could be kept constant. This verifies the desired delocalization and regularisation property of the developed framework.
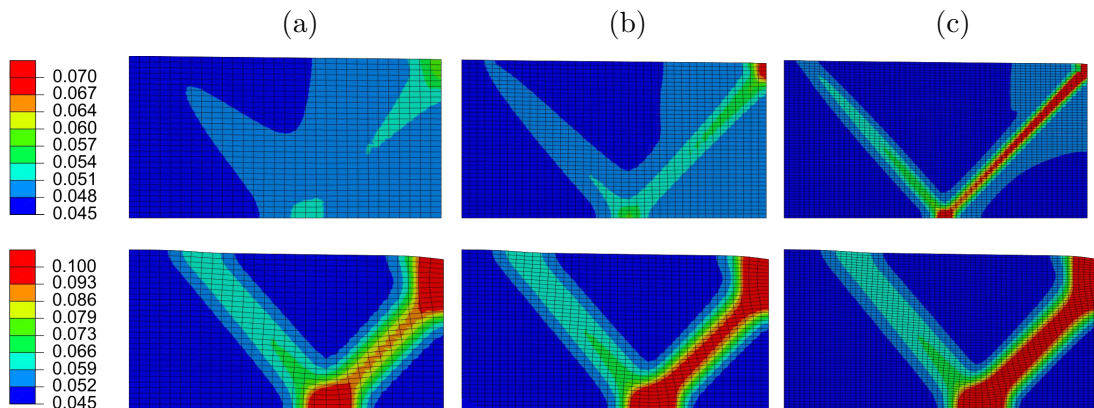
Figure 6.20.: Total damage contours and localization patterns for local (top) and nonlocal (bottom) formulations for three different element sizes, (a) 0.05 mm, (b) 0.025 mm and (c) 0.0125 mm. The rows differ in investigated time steps since they represent different formulations whereas the columns do not.

7. Variants of Lemaitre's Damage Model and Their Use in Formability Prediction of Metallic Materials

In this chapter, taking Lemaitre's damage model [J. Lemaitre, *A Course on Damage Mechanics*, Springer Verlag, (1996)] as the point of departure, two successive enhancements to meet the requirements of formability prediction for today's modern steels are presented. The first extension is a quasi-unilateral damage evolution which, after a spectral decomposition of the stress tensor, scales the elastic energy release rate due to compressive principal stress components. The second one is inspired by a recent multiplicative modification of triaxiality dependent Oyane's fracture criterion with a shear stress dependent term, following [Y. Lou, H. Huh, S. Lim, K. Pack, *International Journal of Solids and Structures* 49, 3605–3615 (2012)]. For plane stress states, the former modification allows, besides correcting the pathological symmetry of the fracture strain with respect to vanishing stress triaxiality ratio, i.e. $\eta = 0$, hindering fracture under uniaxial compression since the altered fracture strain curve shows an asymptotic behavior at $\eta = -1/3$. Depending on the selected parameters, the latter modification permits one to further modify this curve to give account for two local minima in the vicinity of generalized shear points within the triaxiality interval $[-1/3, 2/3]$. From a formability prediction perspective, as a consequence of the former modification, premature failure prediction of the conventional Lemaitre's damage model in many compression dominated metal forming operations is remedied. The latter modification permits modeling shear dominated fracture. Moreover, for each variant, closed form expressions for the isochronous fracture surfaces associated with linear strain paths are derived and resulting surface plots at various spaces are compared. It is shown that only shear modification together with quasi-unilateral enhancement lets model show enough flexibility during parameter calibration for the experimental data. Handled calibrations are compared with those of the existing fracture criteria frequently used in the literature to highlight relative strengths of the current proposal. Finally, the models are implemented as user subroutines for Abaqus/Explicit and used in prediction of initiation and propagation of cracks for a series of deep-drawing punch tests. A good agreement with the outputs reported in the literature is observed in terms of the shear damage occurrence zones as well as corresponding punch force-displacement diagrams.

7.1. Introduction

Although not all metal forming defects result from fracture, oftentimes the formability of metallic materials is hindered by localization of deformation into narrow bands and subsequent fracture. The sources of localization are classified under two groups, such as path-dependent strain hardening and softening [16], where a blend of these can also arise if conditions are met. While path dependent hardening occurs due to a sharp curvature of the yield locus [16], softening takes the

root either from thermal or mechanical grounds [179, 340].

In order to circumvent localization as a precursor to fracture, the metal forming community mostly calls upon the forming limit curves. These experimentally or analytically handled curves define the boundary setting apart safe and unsafe in the space of stress, strain or selected process parameters. Although being very practical, these approaches are not generalizable (e.g., not transferable from sheet to bulk metal forming) and fail to supply accurate predictions for conditions involving non-proportional strain paths and strain histories (e.g., hole expansion test), less ductile materials (e.g., advanced high strength steels), intense shear localization (e.g., blanking) and through thickness stress and strain gradients (e.g., bending). Moreover, these concepts only qualify in the context of forming design, thus, product property prediction, service life and crashworthiness analyses fall beyond their reach.

Advanced constitutive models which monitor local microstructure development and, thus, naturally account for path dependent hardening and softening at a material point on the course of deformation appear to be strong alternatives. Development of such models helps, in a unified manner, in the understanding and the resolution of above mentioned obstacles in forming analysis and design. However, this is not a trivial task for ductile fracture. For today's technological steels, strength enhancement is supplied through hindering dislocation motion via introducing inclusions, solid solutions and additional phases into the material matrix. For such materials the fracture process is a void driven mechanism with nucleation, growth and coalescence phases. Even if the material does not involve any secondary phases, dislocation pile-ups can act as void nucleation zones [111]. In metal forming practice the site of ductile fracture is not known ab initio. It can happen in many locations simultaneously, if far apart, accompanied by considerable micro-structural rotation and plastic flow. Besides, the fracture can happen under a wide range of hydrostatic stresses [17].

Contrary to the mentioned difficulties, there are constitutive approaches in the literature for the purpose of quantitative modeling of ductile damage and fracture. This study is limited to Lemaitre's damage model, which constitutes one of the widely used continuum damage mechanics approaches. In what follows, the presentation starts with the derivation of the conventional Lemaitre's damage model according to the internal variable of thermodynamics. Following the approach of [175], the effective stress argument of [145] and [255] is used, as well as the strain equivalence principle with the concrete definition as phrased in [175]. After creating an uncoupled version of this form, it is shown that this form has critical shortcomings in estimation of the time and the zone of ductile failure in forming processes which fall out of the tensile forming class according to the classification of DIN8582. Building upon this basis two successive empirical enhancements are presented each of which introduces just a single additional material parameter. The initial formerly known improvement prevents the fracture strains under the compressive stresses from being underestimated whereas the novel one aims at improving the fracture strain estimates under generalized shear stress states. The limitations and the predictive capabilities of the base model and the models with introduced enhancements are critically assessed within the context of metal forming practice. These are complemented by the analyses of the geometry of the analytically developed isochronous fracture surfaces and curves at various spaces of stress and strain components for 3D and 2D plane-stress conditions. A point which has not been studied so far in such detail in the literature, to the authors' knowledge.

7.2. Theory

7.2.1. Lemaitre's Damage Model Coupled to Isotropic Hardening Plasticity - Theory of State Kinetic Coupling

Let the particles labeled with $\boldsymbol{X}$ in the reference configuration be mapped to their actual position $\boldsymbol{x}$ by the nonlinear deformation map $\boldsymbol{x} = \boldsymbol{\varphi}(\boldsymbol{X})$. Now, $\boldsymbol{F} = \partial_{\boldsymbol{X}}\boldsymbol{\varphi}$ with $J = \det\boldsymbol{F} > 0$ defines the deformation gradient which is multiplicatively decomposed into an elastic and plastic part via $\boldsymbol{F} = \boldsymbol{F}^e \cdot \boldsymbol{F}^p$. Then, the elastic Finger tensor is defined at the spatial configuration as $\boldsymbol{b}^e = \boldsymbol{F}^e \cdot [\boldsymbol{F}^e]^\top$ whose material time derivative reads $\dot{\boldsymbol{b}}^e = \boldsymbol{F} \cdot [[\dot{\boldsymbol{C}^p}]^{-1}] \cdot \boldsymbol{F}^\top + \boldsymbol{l} \cdot \boldsymbol{b}^e + \boldsymbol{b}^e \cdot \boldsymbol{l}^\top$ where $\boldsymbol{C}^p = [\boldsymbol{F}^p]^\top \cdot \boldsymbol{F}^p$ is the plastic Cauchy-Green tensor in the reference configuration and $\boldsymbol{l} = \dot{\boldsymbol{F}} \cdot \boldsymbol{F}^{-1}$ represents the spatial velocity gradient which is decomposed additively into symmetric $\boldsymbol{d} = \mathrm{sym}(\boldsymbol{l})$ and skewsymmetric $\boldsymbol{w} = \mathrm{skw}(\boldsymbol{l})$ parts, which are respectively named as the rate of deformation tensor and the spin tensor, with $\boldsymbol{l} = \boldsymbol{d} + \boldsymbol{w}$.

Now, following Lemaitre [176], let $\boldsymbol{\chi}$ and $\boldsymbol{\varsigma}$ denote the vectors of all strain like variables and their associated dual variables, respectively. Thermodynamic stability of the state is ensured by the postulated Helmholtz free energy Ψ concave with respect to the temperature T and convex with respect to its other arguments. With the assumption of purely mechanical theory a specific choice for $\Psi = \Psi(\boldsymbol{\chi})$ giving account for the fact that the plastic strain variations do not alter the stored (reversible) energy with $\boldsymbol{\chi} = [\boldsymbol{b}^e, \alpha^p, D]^\top$ reads,

$$\Psi = \Psi(\boldsymbol{b}^e, \alpha^p, D), \tag{7.2.1}$$

where α^p denotes the isotropic hardening strain-like variable. D represents the scalar damage variable, i.e., the phenomenological construct which holds a measure of homogenized microvoids and microcracks in the material. The limits $D = 0$ (undamaged material) and $D = 1$ (rupture) form the mathematical bounds of D as $D \in [0,1]$. The second law of thermodynamics dictates a non-negative dissipation Ω,

$$0 \leq \Omega = \boldsymbol{\tau} : \boldsymbol{d} - \dot{\Psi}, \tag{7.2.2}$$

where $\boldsymbol{\tau} = J\boldsymbol{\sigma}$ is the Kirchhhoff (weighted Cauchy) stress tensor with $\boldsymbol{\sigma}$ denoting the (true) Cauchy stress tensor. Arbitrariness of $\boldsymbol{l}$ leads to $\boldsymbol{\tau} = 2\partial_{\boldsymbol{b}^e}\Psi \cdot \boldsymbol{b}^e$. Hence, the complete state equations for $\boldsymbol{\varsigma} = [\boldsymbol{\tau}, q, Y]^\top$ read

$$\left. \begin{array}{rcl} \boldsymbol{\tau} &=& 2\partial_{\boldsymbol{b}^e}\Psi(\boldsymbol{b}^e, \alpha^p, D) \cdot \boldsymbol{b}^e, \\ q &=& \partial_{\alpha^p}\Psi(\boldsymbol{b}^e, \alpha^p, D), \\ Y &=& \partial_D\Psi(\boldsymbol{b}^e, \alpha^p, D), \end{array} \right\} \tag{7.2.3}$$

where q denotes the isotropic hardening stress-like variable. Y represents the dual variable for damage. Substitution of the state equations back in Equation (7.2.2), the mechanical part of the reduced dissipation inequality Ω^m is carried out,

$$0 \leq \Omega^m = -\boldsymbol{\tau} : \left[\frac{1}{2}\boldsymbol{F} \cdot [[\dot{\boldsymbol{C}^p}]^{-1}] \cdot \boldsymbol{F}^\top \cdot [\boldsymbol{b}^e]^{-1} \right] - q\dot{\alpha}^p - Y\dot{D}. \tag{7.2.4}$$

The thermodynamic admissibility of the evolutionary equations for $\dot{\boldsymbol{\chi}}$ are satisfied by postulating a dissipation potential $\Phi = \Phi(\boldsymbol{\varsigma}; \boldsymbol{\chi})$. Assuming, $\Phi = \Phi(\boldsymbol{\tau}, q, Y; D)$, and applying the generalized normality rule, one has

$$\left. \begin{array}{rcl} \frac{1}{2}\boldsymbol{F} \cdot [[\dot{\boldsymbol{C}^p}]^{-1}] \cdot \boldsymbol{F}^\top \cdot [\boldsymbol{b}^e]^{-1} &=& -\dot{\gamma}\,\partial_{\boldsymbol{\tau}}\Phi(\boldsymbol{\tau}, q, Y; D), \\ \dot{\alpha}^p &=& -\dot{\gamma}\,\partial_q\Phi(\boldsymbol{\tau}, q, Y; D), \\ \dot{D} &=& -\dot{\gamma}\,\partial_Y\Phi(\boldsymbol{\tau}, q, Y; D), \end{array} \right\} \tag{7.2.5}$$

where $\dot{\gamma}$ is the so-called plastic multiplier. Explicit forms of the state and evolution equations require specification of the potentials Φ and Ω. The total Helmholtz free energy is additively decomposed into elastic Ψ^e and plastic Ψ^p parts as follows,

$$\Psi(\boldsymbol{b}^e, \alpha^p, D) = \Psi^e(\boldsymbol{b}^e, D) + \Psi^p(\alpha^p) . \tag{7.2.6}$$

Following [175] the state coupling with isotropic elasticity and damage is governed using the damage dependent elastic free energy $\Psi^e(\boldsymbol{b}^e, D) = [1 - D]\tilde{\Psi}^e(\boldsymbol{b}^e)$ where the effective elastic free energy $\tilde{\Psi}^e$ is additively decomposed into volumetric $\tilde{\Psi}^{e,\mathrm{vol}}$ and deviatoric $\tilde{\Psi}^{e,\mathrm{dev}}$ parts with $\tilde{\Psi}^e = \tilde{\Psi}^{e,\mathrm{vol}} + \tilde{\Psi}^{e,\mathrm{dev}}$ where

$$\left. \begin{aligned} \tilde{\Psi}^{e,\mathrm{vol}}(\boldsymbol{b}^e) &= \frac{1}{2}\kappa \left[\log(J^e)\right]^2 , \\ \tilde{\Psi}^{e,\mathrm{dev}}(\boldsymbol{b}^e) &= \mu \left[\frac{1}{2}\log(\widehat{\boldsymbol{b}}^e)\right] : \left[\frac{1}{2}\log(\widehat{\boldsymbol{b}}^e)\right] , \end{aligned} \right\} \tag{7.2.7}$$

where κ and μ respectively denote the bulk and the shear moduli. J^e denotes the elastic Jacobi determinant and $\widehat{\boldsymbol{b}}^e := J^{-2/3}\boldsymbol{b}^e$ represents the isochoric elastic Finger tensor. $\Psi^p(\alpha^p)$ represents the plastic free energy for isotropic hardening with

$$\Psi^p(\alpha^p) = \frac{C}{n+1} \left[[\alpha^p + \alpha_0^p]^{n+1} - [\alpha_0^p]^{n+1} \right] - \tau_0 \alpha^p , \tag{7.2.8}$$

where α_0^p, C, n and τ_0 are material parameters. Now, letting $\boldsymbol{e}^e = [1/2]\log(\boldsymbol{b}^e)$ denote the elastic spatial logarithmic strain tensor with $\mathrm{tr}(\boldsymbol{e}^e) = \log(J^e)$ and $\mathrm{dev}(\boldsymbol{e}^e) = \boldsymbol{e}^e - [1/3]\mathrm{tr}(\boldsymbol{e}^e)\boldsymbol{1} = [1/2]\log(\widehat{\boldsymbol{b}}^e)$ and substituting Equations (7.2.7) and (7.2.8) into Equation (7.2.3) the state equations for the dual internal variables are found

$$\left. \begin{aligned} \boldsymbol{\tau} &= [1 - D] \left[\kappa \, \mathrm{tr}(\boldsymbol{e}^e)\boldsymbol{1} + 2\mu \, \mathrm{dev}(\boldsymbol{e}^e) \right] , \\ q &= C[\alpha^p + \alpha_0^p]^n - \tau_0 , \\ Y &= -\frac{1}{2}\kappa \left[\mathrm{tr}(\boldsymbol{e}^e)\right]^2 - \mu \left[\mathrm{dev}(\boldsymbol{e}^e) : \mathrm{dev}(\boldsymbol{e}^e)\right] . \end{aligned} \right\} \tag{7.2.9}$$

In applications, it is more convenient to represent Y in terms of the stress components

$$Y = -\frac{1}{2[1 - D]^2} \left[\frac{1}{9\kappa} \left[\mathrm{tr}(\boldsymbol{\tau})\right]^2 + \frac{1}{2\mu} \left[\boldsymbol{s} : \boldsymbol{s}\right] \right] , \tag{7.2.10}$$

with the Kirchhoff stress deviator $\boldsymbol{s} := \mathrm{dev}(\boldsymbol{\tau})$, which is modified to give

$$Y = -\frac{1}{4\mu[1 - D]^2} \left[[\boldsymbol{\tau} : \boldsymbol{\tau}] + \frac{2\mu - 3\kappa}{9\kappa} \left[\mathrm{tr}(\boldsymbol{\tau})\right]^2 \right] . \tag{7.2.11}$$

For the dissipation potential Φ an additive decomposition into plastic $\Phi^{p,\mathrm{flow}}$ and damage Φ^d parts are postulated viz.

$$\Phi = \Phi^{p,\mathrm{flow}}(\boldsymbol{\tau}, q; D) + \Phi^d(Y; D) , \tag{7.2.12}$$

where $\Phi^{p,\mathrm{flow}} \leq 0$ is the yield potential which characterizes the elastic domain and sets the stage for kinematic coupling between plasticity and damage with

$$\Phi^{p,\mathrm{flow}}(\boldsymbol{\tau}, q; D) = \tilde{\tau}_{\mathrm{vMises}} - [\tau_0 + q] . \tag{7.2.13}$$

Defining $\tilde{\boldsymbol{\tau}} = \boldsymbol{\tau}/[1 - D]$ as the effective stress tensor, $\tilde{\tau}_{\mathrm{vMises}} = \sqrt{3/2 \left[\tilde{\boldsymbol{s}} : \tilde{\boldsymbol{s}}\right]}$ represents the effective von Mises equivalent stress with $\tilde{\boldsymbol{s}} = \mathrm{dev}(\tilde{\boldsymbol{\tau}})$. Hence, τ_0 corresponds to the initial yield stress.

For the isotropic damage, the following damage dissipation potential is used [175]

$$\Phi^d = \frac{S}{m+1} \left\langle \frac{-Y-Y_0}{S} \right\rangle^{m+1} \frac{1}{[1-D]^\beta} \, . \tag{7.2.14}$$

where S, m, Y_0 and β are regarding material parameters.

Substituting Equations (7.2.13) and (7.2.14) into Equation (7.2.5) the evolution equations are derived,

$$\left. \begin{aligned} \frac{1}{2} \boldsymbol{F} \cdot [[\boldsymbol{C}^{\dot{p}}]^{-1}] \cdot [\boldsymbol{F}]^\top \cdot [\boldsymbol{b}^e]^{-1} &= \dot{\gamma} \frac{1}{[1-D]} \frac{3}{2} \frac{\tilde{\boldsymbol{s}}}{\tilde{\tau}_{\text{vMises}}} \, , \\ \dot{\alpha}^p &= \dot{\gamma} \, , \\ \dot{D} &= \dot{\gamma} \left\langle \frac{-Y-Y_0}{S} \right\rangle^m \frac{1}{[1-D]^\beta} \, . \end{aligned} \right\} \tag{7.2.15}$$

With the yield function given in Equation (7.2.13), Equations (7.2.9) and (7.2.15) form the complete mathematical description of the material model.

7.3.   Model L1: A Lemaitre Model Based Fracture Criterion

In this section, a Lemaitre model based fracture criterion, i.e., an uncoupled version of Lemaitre's model will be developed. Hence, the state coupling of damage and elasticity, also the kinematic coupling damage and plasticity is ignored. Thus the concept of effective stress is not required any more and the von Mises equivalent stress is defined as $\tau_{\text{vMises}} = \sqrt{3/2 \, [\boldsymbol{s} : \boldsymbol{s}]}$. With this reduction α^p represents the equivalent plastic strain. Denoting the yield stress as $\tau_y := \tau_0 + q$ the state and the evolution equations in Equations (7.2.9) and (7.2.15) reduce to

$$\left. \begin{aligned} \boldsymbol{\tau} &= \kappa \operatorname{tr}(\boldsymbol{e}^e)\boldsymbol{1} + 2\mu \operatorname{dev}(\boldsymbol{e}^e) \, , \\ \tau_y &= C[\alpha^p + \alpha_0^p]^n \, , \end{aligned} \right\} \tag{7.3.1}$$

and

$$\frac{1}{2} \boldsymbol{F} \cdot [[\boldsymbol{C}^{\dot{p}}]^{-1}] \cdot \boldsymbol{F}^\top \cdot [\boldsymbol{b}^e]^{-1} = \dot{\alpha}^p \frac{3}{2} \frac{\boldsymbol{s}}{\tau_{\text{vMises}}} \, , \tag{7.3.2}$$

where for the fully developed plastic flow $\tau_y = \tau_{\text{vMises}}$. The damage evolution in Equation (7.2.15) is rewritten

$$\dot{D} = \dot{\alpha}^p \left\langle \frac{-Y-Y_0}{S} \right\rangle^m \frac{1}{[1-D]^\beta} \, . \tag{7.3.3}$$

Equation (7.3.3) is integrated to give

$$D = \int \omega\left(\boldsymbol{\tau}, D\right) \dot{\alpha}^p dt \, , \tag{7.3.4}$$

where using Equation (7.3.3) and the integrand for Lemaitre based fracture criterion $\omega(\boldsymbol{\tau}, D)$ for $Y_0 = 0$ reads

$$\omega\left(\boldsymbol{\tau}, D\right) = \left[\frac{\check{Y}}{S} \right]^m \frac{1}{[1-D]^\beta} \, . \tag{7.3.5}$$

for $Y \geq 0$. In the current form Y is the following modified form of Equation (7.2.11)

$$\check{Y} = \frac{1}{4\mu} \left[[\boldsymbol{\tau} : \boldsymbol{\tau}] + \frac{2\mu - 3\kappa}{9\kappa} [\operatorname{tr}(\boldsymbol{\tau})]^2 \right] \, . \tag{7.3.6}$$

It is assumed that once the explicit integration for D in Equation (7.3.4) reaches the damage at fracture D_f, the material fails without any progressive softening accounted for.

In demonstration of the behavior of any fracture model, it is convenient to analyze the isochronous fracture surfaces drawn in different spaces such as the stress triaxiality ratio η and the Lode parameter θ, $\overline{\theta}$ or L space (η, θ), $(\eta, \overline{\theta})$ or (η, L), the principal stress space (τ_1, τ_2, τ_3), the principal strain and pressure space (e_1^p, e_2^p, e_3^p, p); see, e.g., [192, 29, 339] among others where the definitions of these components and their interrelations are given in 7.A. In order to accomplish this analytically three important ingredients are required, non-rotating principal axes of deformation, proportional strain paths and rigid plasticity.

Non-rotating principal axes of deformation. As explained in 7.B, with the non-rotating axes of deformation one has the following flow rule in terms of the rate of logarithmic plastic strain $\dot{e}^p$

$$\dot{e}^p = \dot{\alpha}^p \frac{3}{2} \frac{s}{\tau_{\text{vMises}}} \,, \tag{7.3.7}$$

where $\text{tr}(\dot{e}^p) = 0$. The flow rule or plastic stress-strain relations in Equations (7.3.1) and (7.B.8) are Prandtl-Reuss relations. If written in terms of total strain rates $\dot{e}$, Levy-Mises relations are obtained.

Proportional strain paths. For isotropic plasticity with proportional strain paths the ratio $s_\nu / \tau_{\text{vMises}}$ is constant[1] for $\nu = 1, 2, 3$. Hence, using the flow rule in Equation (7.3.2) and the identity for the equivalent plastic strain rate $\dot{\alpha}^p = \sqrt{2/3 \, \dot{e}^p : \dot{e}^p}$ which is valid for isotropic plasticity, and an immediate integration gives the total principal plastic strains

$$e_\nu^p = \alpha^p \frac{3}{2} \frac{s_\nu}{\tau_{\text{vMises}}} \text{ for } \nu = 1, 2, 3 \,, \tag{7.3.8}$$

where $\tau_{\text{vMises}} = \tau_y = C[\alpha^p + \alpha_0^p]^n$ with

$$\alpha^p = \sqrt{2/3 \left[[e_1^p]^2 + [e_2^p]^2 + [e_3^p]^2 \right]} \,. \tag{7.3.9}$$

Equation (7.3.8), due to Hencky [120], allows relating current state of stress with plastic strains independent of the history of loading. Hence, total or deformation theory of plasticity as a specific case of the incremental or flow theories is carried out for the case of proportional loading.

Rigid plasticity. This point is important for successive developments where the assumption for small elastic strains as compared to the plastic ones is used. Hence, for rigid plasticity assumption one has $e^p \simeq e$. With this assumption together with plastic incompressibility one has $J = J^p = 1$, hence there is no distinction between the Kirchhoff and Cauchy stress tensor. Consequently, for the rest of the chapter σ is used as the main stress measure.

In the following the isochronous fracture surface, say $g = 0$, is presented interchangeably in the

---

[1]Note that for proportional strain paths for isotropic plasticity one has the principal strain rate ratios equal to the deviatoric stress ratios, i.e., $\dot{e}_2^p / \dot{e}_1^p = s_2/s_1 = \beta$, where β denotes the constant loading ratio. Hence, letting $s_2 = \beta s_1$, the traceless property of the deviatoric stress tensor will yield $s_3 = -[1 + \beta]s_1$. Moreover, the equivalent von Mises stress description gives $\tau_{\text{vMises}} = \sqrt{[3/2] [s_1^2 + s_2^2 + s_3^2]} = s_1 \sqrt{3 [1 + \beta + \beta^2]}$. Thus, $s_1/\tau_{\text{vMises}} = 1/\sqrt{3 [1 + \beta + \beta^2]}$ is constant. Hence is $s_1/[C[\alpha^p + \alpha_0^p]^n]$ for fully developed plastic flow.

spaces, $(\eta, \theta, \alpha_f^p)$, $(\eta, \overline{\theta}, \alpha_f^p)$, (η, L, α_f^p), $(\sigma_1, \sigma_2, \sigma_3)$, (e_1^p, e_2^p, e_3^p, p) using corresponding parametrizations. With an abuse of notation, these representations are respectively denoted by $g(\eta, \theta, \alpha_f^p)$, $g(\eta, \overline{\theta}, \alpha_f^p)$, $g(\eta, L, \alpha_f^p)$, $g(\sigma_1, \sigma_2, \sigma_3)$ and $g(e_1^p, e_2^p, e_3^p, p)$. The same notation applies to any reparametrization of a function.

7.3.1. Isochronous Fracture Surface Representations at Various Spaces

For subsequent developments, it is sensible to reiterate the damage driving force in Equation (7.2.11) in terms of principal Cauchy stresses σ_ν for $\nu = 1, 2, 3$

$$\check{Y} = \frac{1}{4\mu} \left[\left[\sigma_1^2 + \sigma_2^2 + \sigma_3^2 \right] + \left[\frac{2\mu}{\kappa} - 3 \right] p^2 \right] , \qquad (7.3.10)$$

where $p = \mathrm{tr}(\boldsymbol{\sigma})/3 = [\sigma_1 + \sigma_2 + \sigma_3]/3$ represents the hydrostatic stress. In the following, the fracture surface plots are studied based on hypothetical material parameters for (uniform) radial stress paths.

7.3.1.1. Representations in $(\eta, \theta, \alpha_f^p)$, $(\eta, \overline{\theta}, \alpha_f^p)$ and (η, L, α_f^p)

With these definitions, the damage driving force in Equation (7.3.10) is reiterated which proves useful for latter developments

$$\check{Y} = \frac{1}{4\mu} \left[C[\alpha^p + \alpha_0^p]^n \right]^2 f(\eta, \theta) , \qquad (7.3.11)$$

with the plastic flow condition $C[\alpha^p + \alpha_0^p]^n = \sigma_{\mathrm{vMises}}$ and

$$f(\eta, \theta) := \sum_{\nu=1}^{3} \left[\eta + \frac{2}{3} \cos \left(\frac{2[\nu-1]}{3}\pi - \theta \right) \right]^2 + \left[\frac{2\mu}{\kappa} - 3 \right] \eta^2 . \qquad (7.3.12)$$

Then, for the standard model following simplification applies

$$\sum_{\nu=1}^{3} \left[\eta + \frac{2}{3} \cos \left(\frac{2[\nu-1]}{3}\pi - \theta \right) \right]^2 = \frac{2}{3} + 3\eta^2 . \qquad (7.3.13)$$

Hence,

$$f(\eta, \theta) = \frac{2}{3} + \frac{2\mu}{\kappa}\eta^2 . \qquad (7.3.14)$$

That is, in the conventional Lemaitre model, the damage driving force has no Lode parameter dependence.

Coming to the damage integration, one has

$$dD = d\alpha^p \left[\frac{\check{Y}}{S} \right]^m \frac{1}{[1-D]^\beta} . \qquad (7.3.15)$$

Substituting Equation (7.3.11) into the right-hand side of Equation (7.3.15), rearranging for the use of separation of variables during integration and using the condition that triaxiality and the

Lode parameter is constant thanks to the radial loading paths, one can take $f(\eta, \theta)$ out of the integral and reach

$$\int_0^{D_f} [1 - D]^\beta \, dD = \left[\frac{C^2 f(\eta, \theta)}{4\mu S} \right]^m \int_0^{\alpha_f^p} [\alpha^p + \alpha_0^p]^{2mn} d\alpha^p, \tag{7.3.16}$$

where α_f^p and D_f are equivalent plastic strain and damage at fracture. For $D_f \leq 1$, one has

$$\frac{\left[1 - [1 - D_f]^{\beta+1} \right]}{[\beta + 1]} = \left[\frac{C^2 f(\eta, \theta)}{4\mu S} \right]^m \frac{[\alpha_f^p + \alpha_0^p]^{2mn+1}}{[2mn + 1]}, \tag{7.3.17}$$

where the fracture strain is computed as

$$\alpha_f^p = \left[[2mn + 1] \left[\frac{4\mu S}{C^2 f(\eta, \theta)} \right]^m \frac{\left[1 - [1 - D_f]^{\beta+1} \right]}{[\beta + 1]} \right]^{\frac{1}{2mn+1}} - \alpha_0^p. \tag{7.3.18}$$

Now for $D_f = 1$, which is the theoretical damage threshold for coupled damage models, one reaches

$$\alpha_f^p = B \left[f(\eta, \theta) \right]^{\frac{-m}{2mn+1}} - \alpha_0^p, \tag{7.3.19}$$

using the following notation

$$B = \left[\frac{[2mn + 1]}{[\beta + 1]} \left[\frac{4\mu S}{C^2} \right]^m \right]^{\frac{1}{2mn+1}}. \tag{7.3.20}$$

Substituting Equation (7.3.14) into the right-hand side of Equation (7.3.19)

$$\alpha_f^p = \alpha_f^p(\eta, \theta) = B \left[\frac{2}{3} + \frac{2\mu}{\kappa} \eta^2 \right]^{\frac{-m}{2mn+1}} - \alpha_0^p. \tag{7.3.21}$$

Since an explicit Lode parameter dependence does not exist, identical contour plots are due for $\alpha_f^p(\eta, \theta)$, $\alpha_f^p(\eta, \overline{\theta})$ and $\alpha_f^p(\eta, L)$ as given in Figure 7.1. The maximum equivalent strain to fracture occurs under pure shear stress conditions, whereas it symmetrically decreases further away from this point. Corresponding fracture surfaces are $g(\eta, \theta, \alpha_f^p) = 0$, $g(\eta, \overline{\theta}, \alpha_f^p) = 0$ and $g(\eta, L, \alpha_f^p) = 0$ with $g(\eta, \theta, \alpha_f^p) = \alpha_f^p - \alpha_f^p(\eta, \theta)$, $g(\eta, \overline{\theta}, \alpha_f^p) = \alpha_f^p - \alpha_f^p(\eta, \overline{\theta})$ and $g(\eta, L, \alpha_f^p) = \alpha_f^p - \alpha_f^p(\eta, L)$, respectively.

7.3.1.2. Representation in $(\sigma_1, \sigma_2, \sigma_3)$ and (e_1^p, e_2^p, e_3^p, p)

The representation of the fracture surface in terms of $(\sigma_1, \sigma_2, \sigma_3)$ requires corresponding representations of f and α_f^p. Using Equation (7.3.14) and $\eta = p/\sigma_{\text{vMises}}$

$$f(\sigma_1, \sigma_2, \sigma_3) = \frac{2}{3} + \frac{2\mu}{\kappa} \left[\frac{p(\sigma_1, \sigma_2, \sigma_3)}{\sigma_{\text{vMises}}(\sigma_1, \sigma_2, \sigma_3)} \right]^2. \tag{7.3.22}$$

whereas

$$\sigma_{\text{vMises}}(\sigma_1, \sigma_2, \sigma_3) = \sqrt{\frac{[\sigma_1 - \sigma_2]^2 + [\sigma_2 - \sigma_3]^2 + [\sigma_3 - \sigma_1]^2}{2}}. \tag{7.3.23}$$
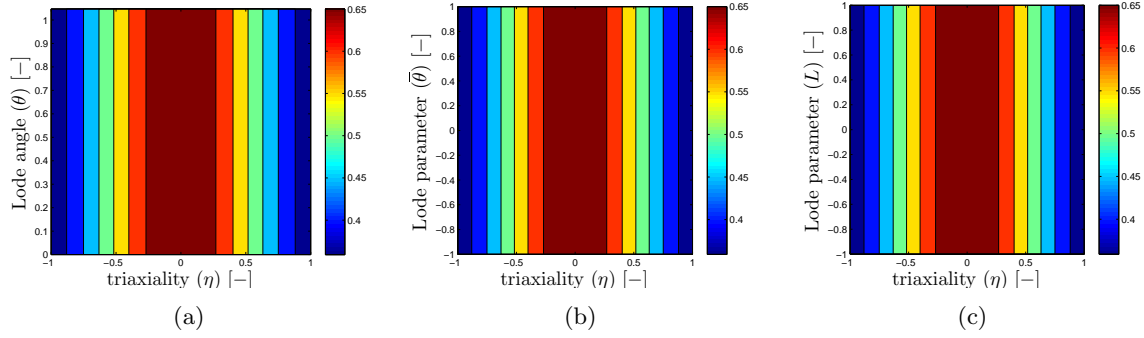
Figure 7.1.: *Equivalent fracture strain α_f^p contours for the damage criterion based on original Lemaitre's damage model. Plots are given on spaces (a) (η, θ), (b) $(\eta, \overline{\theta})$ and (c) (η, L). Selected parameters are $\mu = 80769.2$ MPa, $\kappa = 175000$ MPa, $\beta = 1$, $m = 1$, $S = 0.5$ MPa, $C = 500$ MPa, $\alpha_0^p = 0.001$, $n = 0.15$.*

Finally,

$$\alpha_f^p(\sigma_1, \sigma_2, \sigma_3) = \left[\frac{\sigma_{\mathrm{vMises}}(\sigma_1, \sigma_2, \sigma_3)}{C} \right]^{\frac{1}{n}} - \alpha_0^p. \tag{7.3.24}$$

Hence, using Equations (7.3.22) and (7.3.24) the fracture surface $g(\sigma_1, \sigma_2, \sigma_3) = 0$ is determined

$$g(\sigma_1, \sigma_2, \sigma_3) = \left[\frac{\sigma_{\mathrm{vMises}}(\sigma_1, \sigma_2, \sigma_3)}{C} \right]^{\frac{1}{n}} - B f(\sigma_1, \sigma_2, \sigma_3)^{\frac{-m}{2mn+1}} - \alpha_0^p. \tag{7.3.25}$$
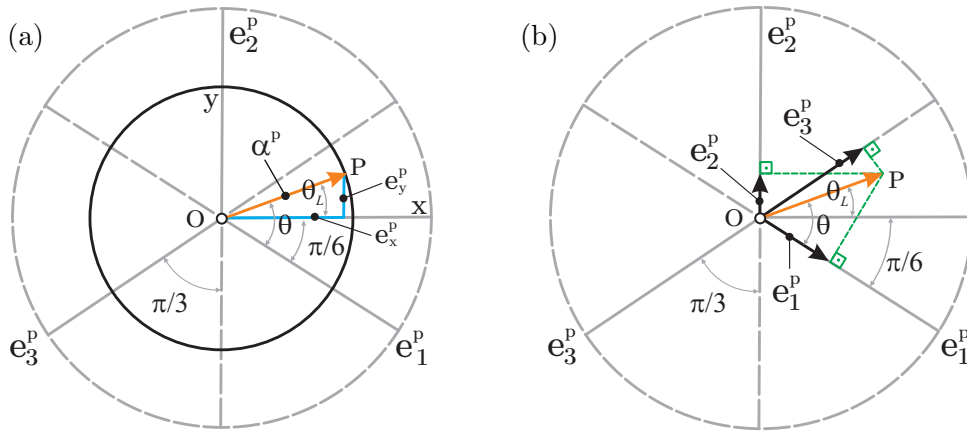
Figure 7.2.: *Geometrical representation of the Lode angle θ, α and (a) von Mises yield locus on the deviatoric-strain plane and (b) the principal deviatoric stress components (e_1^p, e_2^p, e_3^p) of point P on the deviatoric-strain plane, note that $e_1^p + e_2^p + e_3^p = 0$, i.e. linear dependence. Note that for 3-dimensional representations of the fracture locus in (e_1^p, e_2^p, e_3^p, p) the transformation of (e_1^p, e_2^p, e_3^p) to (e_x^p, e_y^p) is required.*

Likewise, the representation of the fracture surface in terms of (e_1^p, e_2^p, e_3^p, p) as given in Figure 7.2 requires corresponding representations of f and α_f^p. For the former, the substitution of $\sigma_{\mathrm{vMises}}(e_1^p, e_2^p, e_3^p) = C[\alpha_f^p(e_1^p, e_2^p, e_3^p) + \alpha_0^p]^n$ into Equation (7.3.22) is realized to give

$$f(e_1^p, e_2^p, e_3^p, p) = \frac{2}{3} + \frac{2\mu}{\kappa} \left[\frac{p}{\sigma_{\mathrm{vMises}}(e_1^p, e_2^p, e_3^p)} \right]^2, \tag{7.3.26}$$

where for $\alpha_f^p = \alpha_f^p(e_1^p, e_2^p, e_3^p)$ Equation (7.3.9) is used. The consequent representation of the function denoting the fracture surface is

$$g(e_1^p, e_2^p, e_3^p, p) = \alpha_f^p(e_1^p, e_2^p, e_3^p) - B \left[\frac{2}{3} + \frac{2\mu}{\kappa} \left[\frac{p}{\sigma_{\text{vMises}}(e_1^p, e_2^p, e_3^p)} \right]^2 \right]^{\frac{-m}{2mn+1}} . \qquad (7.3.27)$$

The sketch of the fracture surface represented by Equation (7.3.27) on the space (e_1^p, e_2^p, e_3^p, p) is given in Figure 7.3(b). The derivations in construction of the plot in Figure 7.3(b) uses

$$\left. \begin{array}{rcl} e_1^p & = & \frac{1}{2}\left[\sqrt{3}e_x^p - e_y^p\right] , \\ e_2^p & = & e_y^p, \\ e_3^p & = & \frac{1}{2}\left[-\sqrt{3}e_x^p - e_y^p\right] . \end{array} \right\} \qquad (7.3.28)$$

with $e_3^p = -e_1^p - e_2^p$. Hence, the triangular coordinates (e_1^p, e_2^p, e_3^p) are transformed to the Cartesian coordinates (e_x^p, e_y^p). Using Equation (7.3.25), the sketch of the isochronous fracture surface in the principal stress space $(\sigma_1, \sigma_2, \sigma_3)$ is given in Figure 7.3(a). Similarly, using Equation (7.3.27) with the transformations given in Equation (7.3.28) and the axis normal to the (e_x^p, e_y^p)−plane as the pressure axis, the fracture surface plot is realized as given in Figure 7.3(b). It is seen that both the stress and strain space plots has the circular sections; hence, the independence from the Lode parameter is also graphically seen. Also the symmetry with respect to the Π plane, that is the plane with zero triaxiality, is obvious from both of the plots in stress and strain spaces. As $p \to \pm\infty$ the fracture locus converges to the von Mises type cylindrical yield surface. For very high values of positive hydrostatic pressure decohesion may precede plastic flow, thus, direct extrapolation of the plastic response might become at stake. Hence, the ductile character of fracture. This is remedied in the literature following Galileo hypothesis, i.e. hypothesis of critical stress, by proposing cut-offs for the normal stress magnitudes which results in sharpened pencil-like fracture surfaces. It should be noted that in the current chapter assumptions of this kind are not used.

(a)   (b)
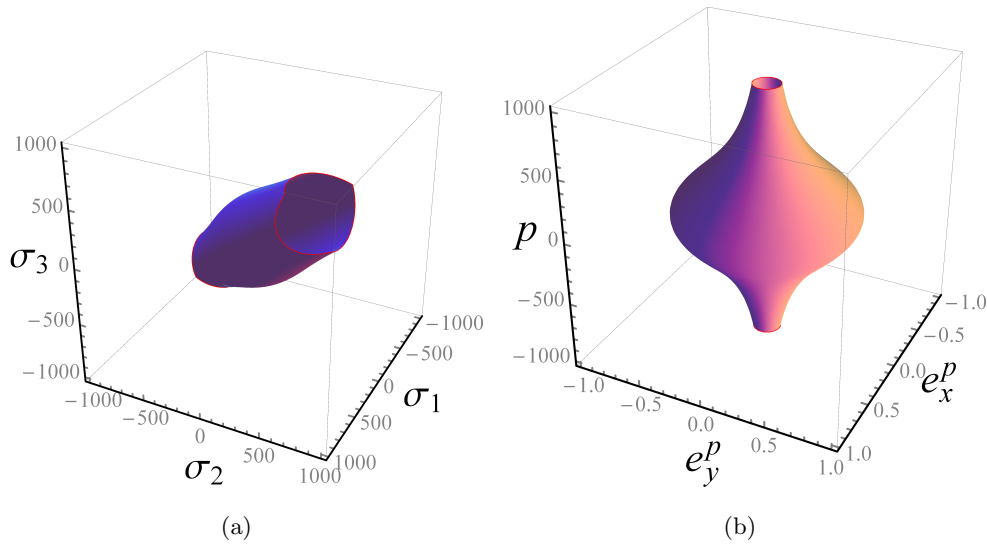
Figure 7.3.: Isochronous fracture surfaces on (a) $(\sigma_1, \sigma_2, \sigma_3)$ in MPa, (b) (e_1^p, e_2^p, e_3^p) space for the damage criterion based on the quasi-unilateral modification of the Lemaitre's damage model. Selected parameters are $\mu = 80769.2$ MPa, $\kappa = 175000$ MPa, $\beta = 1$, $m = 1$, $S = 0.5$ MPa, $C = 500$ MPa, $\alpha_0^p = 0.001$, $n = 0.15$.

Figure 7.4 depicts the sections of the fracture surfaces plotted on the triangular plastic strain coordinates. Circular sections mentioned for Figure 7.3 can be clearly seen. Also in agreement with the observations on Figure 7.3 uniform shrinkage of the fracture surface by increasing positive hydrostatic stresses or decreasing negative hydrostatic stresses symmetrically with respect to the zero hydrostatic stress plane is seen.
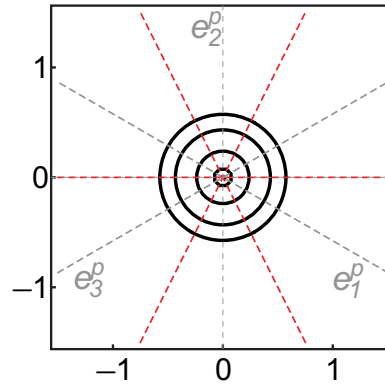
Figure 7.4.: Fracture loci projected on the (deviatoric) plastic strain plane from outer to inner $p = 0, 250, 500, 1000$ MPa and equivalently $p = 0, -250, -500, -1000$ MPa. Selected parameters are $\mu = 80769.2$ MPa, $\kappa = 175000$ MPa, $\beta = 1$, $m = 1$, $S = 0.5$ MPa, $C = 500$ MPa, $\alpha_0^p = 0.001$, $n = 0.15$.

7.3.1.3. State of Plane Stress and Planar Plots for the Fracture Loci

Equation (7.3.21) gives the stress triaxiality ratio dependence under the state of plane stress states as well. For the representation in (σ_1, σ_2), it is sufficient to modify Equation (7.3.25) with $\sigma_3 = 0$. For the representation in (e_1^p, e_2^p), $s_3 = -p$ is used and Equation (7.3.8) to obtain

$$\eta = \frac{p}{\sigma_{\text{vMises}}} = -\frac{s_3}{\sigma_y} = -\frac{2}{3}\frac{e_3^p}{\alpha^p} \, . \tag{7.3.29}$$

Substituting Equation (7.3.29) into the right-hand side of Equation (7.3.27) with the plastic incompressibility condition $e_3^p = -e_1^p - e_2^p$ allows one reach the planar fracture locus. Figure 7.5 shows the fracture loci corresponding to the conventional Lemaitre damage model drawn at triaxiality, equivalent plastic strain, principal stress and principal strain spaces with the given derivations. In all similar subsequent figures, the pairs (σ_1, σ_2) and (e_1^p, e_2^p) respectively denote the in-plane principal stress and strain components, which are not necessarily ordered. At the first glance, a marked fallacy occurs in the symmetry of the fracture behavior with respect to the pure shear line, i.e., $\eta = 0$, i.e., in the triaxiality space. On the stress and the strain spaces a two-fold symmetry with respect to the pure shear and equi-biaxial stress (or strain) lines is observed. The symmetry with respect to the equi-biaxial stress (or strain) lines is a natural outcome of the material isotropy. This means that the fracture strain is affected only by the magnitude of the components of the pairs (σ_1, σ_2) and (e_1^p, e_2^p) but not by their signs. In other words, tensile and compressive character of the stress components is immaterial. At the extremes, this is a declaration of equivalence of a tensile-tensile equi-biaxial stress state with a compressive-compressive one, with equal equivalent stresses, as the strain to fracture is concerned. Once the void dynamics is taken into account this is not plausible. The voids tend

to exponentially grow under tensile hydrostatic stresses whereas shrink under compressive ones. Thus, compressive stress states promote material ductility and eventually formability; see, e.g., [59, 253, 286].

(a)   (b)   (c)
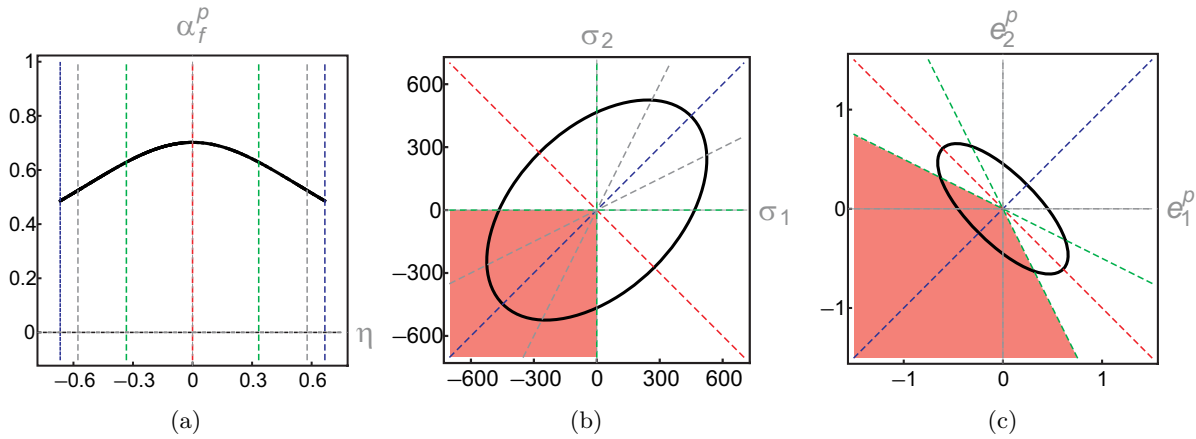
Figure 7.5.: Fracture loci drawn at (a) triaxiality equivalent fracture strain, (b) principal stress and (c) principal strain spaces for conventional Lemaitre's damage model for plane stress state. Inconsistencies are marked with red over the plots at various spaces. Selected parameters are $\mu = 80769.2$ MPa, $\kappa = 175000$ MPa, $\beta = 1$, $m = 1$, $S = 0.5$ MPa, $C = 500$ MPa, $\alpha_0^p = 0.001$, $n = 0.15$.

In order to assess the implications in metal forming practice, it is sensible to review the stress state based forming process classification, according to DIN8582, given in Figure 7.6. The red framed process groups involve at least one compressive principal stress components. Accordingly, one would expect that, for these processes, the predictions of the Lemaitre's model in its conventional form will be incorrect regarding not only the zone but also the time of fracture. Same comments are valid for strain paths involving cyclic tensile-compressive load reversals. This inherently involves the problem of the transferability of the identified damage parameters. Regarding the service life of the product, one should recall that the crashworthiness analyses are almost always dominated by compressive stresses.
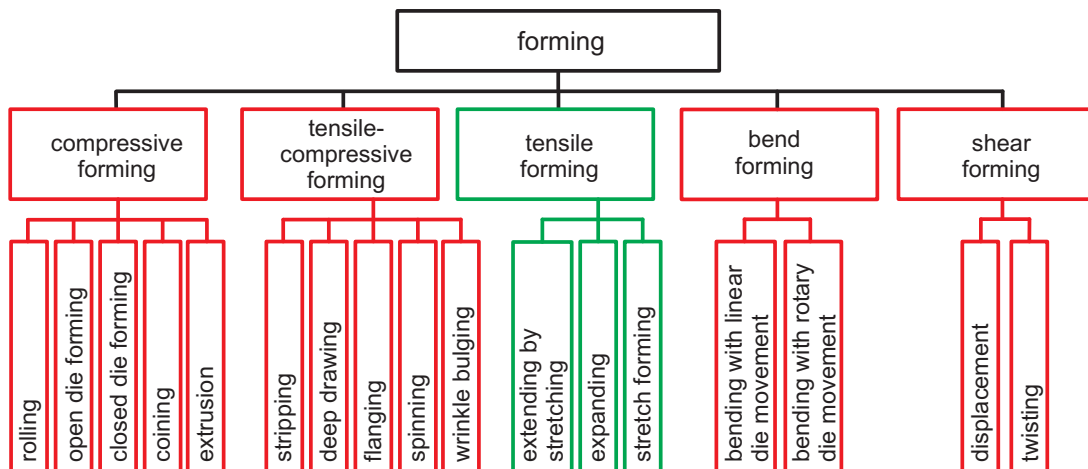
Figure 7.6.: Classification of forming processes according to DIN8582. Red framed process subclasses constitute the ones for which the conventional Lemaitre's damage model falls short.

Accordingly, the underlined problems considerably confine the use of conventional Lemaitre's damage model to the tensile forming process analyses. These are inevitably complemented by damage characterization tests which are also of tensile character only as seen in countless studies in the literature.

7.4. Model L2: Extension to Quasi-Unilateral Damage Evolution

It is possible to cure this pathological symmetry with respect to the pure shear stress state by modifying the damage driving force $\check{Y}$ in Equation (7.3.10) as follows

$$
\begin{aligned}
\check{Y}^{\oplus} = {}& \frac{1}{4\mu} \left[\left[\langle \sigma_1 \rangle^2 + \langle \sigma_2 \rangle^2 + \langle \sigma_3 \rangle^2 \right] + \left[\frac{2\mu}{\kappa} - 3 \right] \langle p \rangle^2 \right] , \\
& + \frac{h}{4\mu} \left[\left[\langle -\sigma_1 \rangle^2 + \langle -\sigma_2 \rangle^2 + \langle -\sigma_3 \rangle^2 \right] + \left[\frac{2\mu}{\kappa} - 3 \right] \langle -p \rangle^2 \right] .
\end{aligned}
\tag{7.4.1}
$$

In this modification, due to [166], the quasi-unilateral damage evolution parameter $h \in [0, 1]$ acts as a weighting factor which scales the energetic contribution of the compressive principal stresses and the hydrostatic stress. Accordingly, for only the tensile principal and hydrostatic stress components contribute to damage development whereas the conventional Lemaitre based fracture criterion given in Equation (7.3.10) is recovered for $h = 1$.

7.4.1. Isochronous Fracture Surface Representations at Various Spaces

7.4.1.1. Representations in $(\eta, \theta, \alpha_f^p)$, $(\eta, \overline{\theta}, \alpha_f^p)$ and (η, L, α_f^p)

Following similar steps as before while using the quasi-unilateral enhancement in Equation (7.4.1) results in the following modified form of Equation (7.3.19)

$$
\alpha_f^p = B \left[f^{\oplus}(\eta, \theta) \right]^{\frac{-m}{2mn+1}} - \alpha_0^p ,
\tag{7.4.2}
$$

with

$$
f^{\oplus}(\eta, \theta) = f^+(\eta, \theta) + h f^-(\eta, \theta) ,
\tag{7.4.3}
$$

where $f^+(\eta, \theta)$ and $= f^-(\eta, \theta)$ are defined using Equation (7.A.3) and Equation (7.3.11) together with Equation (7.4.1)

$$
\left.
\begin{aligned}
f^+(\eta, \theta) &= \sum_{\nu=1}^{3} \left\langle \eta + \frac{2}{3} \cos\left(\frac{2(\nu-1)}{3}\pi - \theta \right) \right\rangle^2 + \left[\frac{2\mu}{\kappa} - 3 \right] \langle \eta \rangle^2 , \\
f^-(\eta, \theta) &= \sum_{\nu=1}^{3} \left\langle -\eta - \frac{2}{3} \cos\left(\frac{2(\nu-1)}{3}\pi - \theta \right) \right\rangle^2 + \left[\frac{2\mu}{\kappa} - 3 \right] \langle -\eta \rangle^2 .
\end{aligned}
\right\}
\tag{7.4.4}
$$

Representation in $(\eta, \overline{\theta})$ and (η, L) requires corresponding substitutions with Equation (7.A.1) and Equation (7.A.7) into the right-hand side of Equation (7.4.1), respectively. The plot of these α_f^p contours for a set of selected parameters in the spaces of (η, θ), $(\eta, \overline{\theta})$ and (η, L) are given in Figure 7.7. Once compared to Figure 7.1 unlike the conventional Lemaitre based fracture strain, which boils down to a mere stress triaxiality ratio dependent expression given in Equation (7.3.21), Equation (7.4.3) accounts for the Lode angle dependence as well. For $h = 0.2$, it is seen that there occurs a steep increase of the fracture strain towards the uniaxial compression point as anticipated.

(a)   (b)   (c)
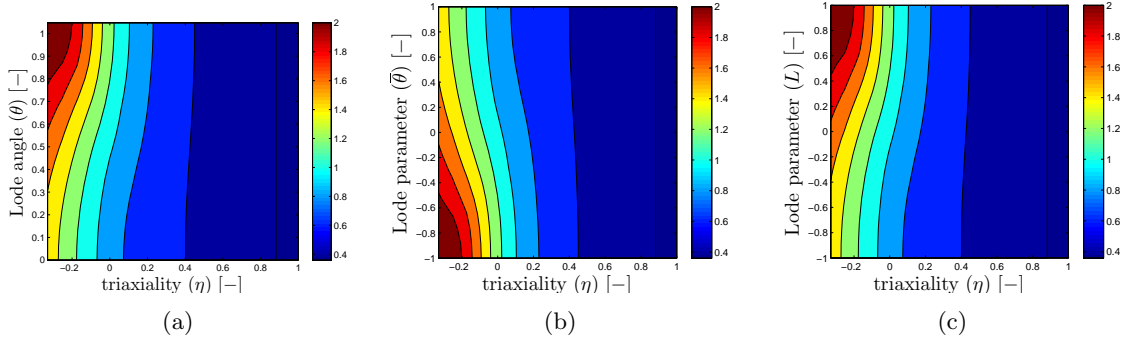
Figure 7.7.: Equivalent fracture strain α_f^p contours for the damage criterion based on the quasi-unilateral modification of the Lemaitre's damage model. Plots are given on spaces (a) (η, θ), (b) $(\eta, \bar{\theta})$ and (c) (η, L). Selected parameters are $\mu = 80769.2$ MPa, $\kappa = 175000$ MPa, $\beta = 1$, $m = 1$, $S = 0.5$ MPa, $C = 500$ MPa, $\alpha_0^p = 0.001$, $n = 0.15$, $h = 0.2$.

7.4.1.2. Representation in $(\sigma_1, \sigma_2, \sigma_3)$ and (e_1^p, e_2^p, e_3^p, p)

In order to represent the fracture surface for criterion with the quasi-unilateral enhancement in terms of the triad $(\sigma_1, \sigma_2, \sigma_3)$, one starts with using Equation (7.3.11) to reach

$$f^{\oplus}(\sigma_1, \sigma_2, \sigma_3) = 4\mu \frac{\check{Y}^{\oplus}(\sigma_1, \sigma_2, \sigma_3)}{[\sigma_{\text{vMises}}(\sigma_1, \sigma_2, \sigma_3)]^2} \, , \tag{7.4.5}$$

where for $\check{Y}^{\oplus}(\sigma_1, \sigma_2, \sigma_3)$ Equation (7.4.1) is used. Hence, replacing f in Equation (7.3.25) with the enhanced $f^{\otimes}(\eta, \theta)$, one reaches the function $g^{\oplus} = 0$ representing the fracture surface for the quasi-unilateral enhancement

$$g^{\oplus}(\sigma_1, \sigma_2, \sigma_3) = \left[\frac{\sigma_{\text{vMises}}(\sigma_1, \sigma_2, \sigma_3)}{C} \right]^{\frac{1}{n}} - Bf^{\oplus}(\sigma_1, \sigma_2, \sigma_3)^{\frac{-m}{2mn+1}} - \alpha_0^p \, . \tag{7.4.6}$$

Now, using $\sigma_\nu / \sigma_{\text{vMises}} = \eta + s_\nu / \sigma_{\text{vMises}}$ with Equation (7.3.8) to give $s_\nu / \sigma_{\text{vMises}} = [2/3][e_\nu^p / \alpha^p]$ for $\nu = 1, 2, 3$

$$\left. \begin{aligned} f^+(e_1^p, e_2^p, e_3^p, p) &= \frac{1}{[\sigma_{\text{vMises}}(e_1^p, e_2^p, e_3^p)]^2} \left[\sum_{\nu=1}^3 \left\langle p + \frac{2}{3} \frac{e_\nu^p}{\alpha^p(e_1^p, e_2^p, e_3^p)} \right\rangle^2 + \left[\frac{2\mu}{\kappa} - 3 \right] \langle p \rangle^2 \right] , \\ f^-(e_1^p, e_2^p, e_3^p, p) &= \frac{1}{[\sigma_{\text{vMises}}(e_1^p, e_2^p, e_3^p)]^2} \left[\sum_{\nu=1}^3 \left\langle -p - \frac{2}{3} \frac{e_\nu^p}{\alpha^p(e_1^p, e_2^p, e_3^p)} \right\rangle^2 + \left[\frac{2\mu}{\kappa} - 3 \right] \langle -p \rangle^2 \right] . \end{aligned} \right\} \tag{7.4.7}$$

Thus, letting $f^{\oplus}(e_1^p, e_2^p, e_3^p, p) = f^+(e_1^p, e_2^p, e_3^p, p) + hf^-(e_1^p, e_2^p, e_3^p, p)$ the consequent representation of the function denoting the fracture surface is

$$g^{\oplus}(e_1^p, e_2^p, e_3^p, p) = \alpha_f^p(e_1^p, e_2^p, e_3^p) - Bf^{\oplus}(e_1^p, e_2^p, e_3^p, p)^{\frac{-m}{2mn+1}} - \alpha_0^p \, . \tag{7.4.8}$$

The plot of the fracture envelope in principal stress space $(\sigma_1, \sigma_2, \sigma_3)$ is given in Figure 7.8(a). Using the triangular to Cartesian coordinate transformation as done previously, the plot of the fracture surface in the space (e_1^p, e_2^p, e_3^p, p) is realized as given in Figure 7.8(b). One should note that in the current correction h also controls the symmetry with respect to the Lode parameter. If $h = 1$ complete symmetry is due whereas otherwise the symmetry is lost. This time as $p \to -\infty$ the fracture surface expands indefinitely wheres for $p \to \infty$ it converges again to the von Mises type cylindrical yield surface no matter what the value of h is.

(a)

(b)
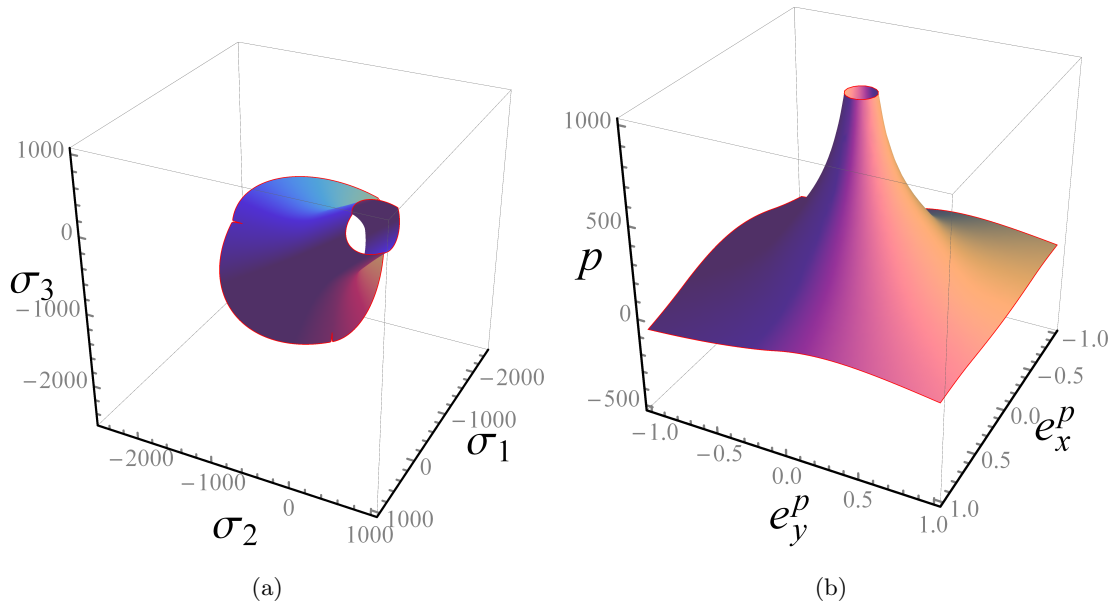
Figure 7.8.: Isochronous fracture surfaces on (a) $(\sigma_1, \sigma_2, \sigma_3)$ in MPa, (b) (e_1^p, e_2^p, e_3^p) space for the damage criterion based on the quasi-unilateral modification of the Lemaitre's damage model. Selected parameters are $\mu = 80769.2$ MPa, $\kappa = 175000$ MPa, $\beta = 1$, $m = 1$, $S = 0.5$ MPa, $C = 500$ MPa, $\alpha_0^p = 0.001$, $n = 0.15$, $h = 0$.

For a more detailed analysis, Figure 7.9 depicts the sections of the fracture surfaces plotted on the triangular plastic strain coordinates. A comparison with Figure 7.4 shows that as anticipated the quasi-unilateral damage evolution introduces a (generalized) tension-compression asymmetry to the fracture response. For the selected range of parameters it is shown that the section does not necessarily represent a convex shape and as h increases the concavity also increases. Although still the shapes preserve three direct (rotational) symmetries through 0, $\pi/3$ and $2\pi/3$ and three reflectional symmetries through the axes representing axisymmetric stress states, the Lode parameter dependence added through the introduction of the parameter h is obvious as also seen in the analytical expressions.
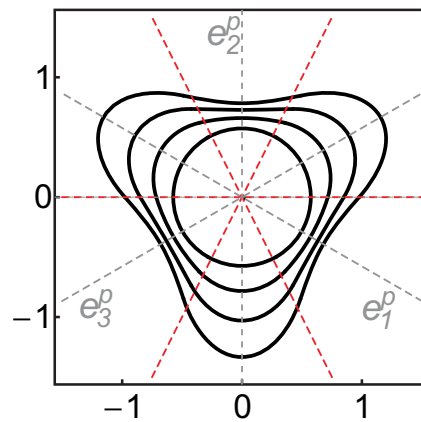
Figure 7.9.: Fracture loci projected on the (deviatoric) plastic strain plane for $p = 0$, from outer to inner $h = 0, 0.2, 0.5, 1$. Selected parameters are $\mu = 80769.2$ MPa, $\kappa = 175000$ MPa, $\beta = 1$, $m = 1$, $S = 0.5$ MPa, $C = 500$ MPa, $\alpha_0^p = 0.001$, $n = 0.15$.

7.4.1.3. State of Plane Stress and Planar Plots for the Fracture Loci

For the state of plane stress, the stress triaxiality ratio is linked to the Lode angle θ with the following expression

$$\theta = \frac{4}{3}\pi - \arccos\left(-\frac{3}{2}\eta\right) . \tag{7.4.9}$$

Hence using Equation (7.4.9), it is possible to represent the fracture surface merely in terms of triaxiality ratio. For the representations in (σ_1, σ_2) and (e_1^p, e_2^p) same methodology given in the previous section applies. Eventually, corresponding fracture loci are plotted as given in Figure 7.10 in triaxiality, equivalent plastic strain, principal stress and principal strain spaces. In Figure 7.10, the curves in black represent the loci for $h = 0$ whereas the gray coloured regions represent the area that can be filled for $0 < h < 1$. As seen, for $h = 0$ the symmetry of the fracture loci with respect to the pure shear line is amended and for the uniaxial compression, i.e. $\eta = -1/3$, the fracture loci show an asymptotic behavior. This behavior, however for the plane stress state, is in correlation with the studies in the literature which state that ductile fracture never occurs under the triaxiality ratios smaller than that of the uniaxial compression i.e. $\eta \leq -1/3$; for a recent study, see, e.g., [192]. As anticipated from the formulation, for all biaxial stretching states, i.e., the stress states taking place at the first quadrant of the principal plane-stress space with $\eta \geq 1/3$, there is no distinction between the predictions of the current modification and the conventional Lemaitre's model.
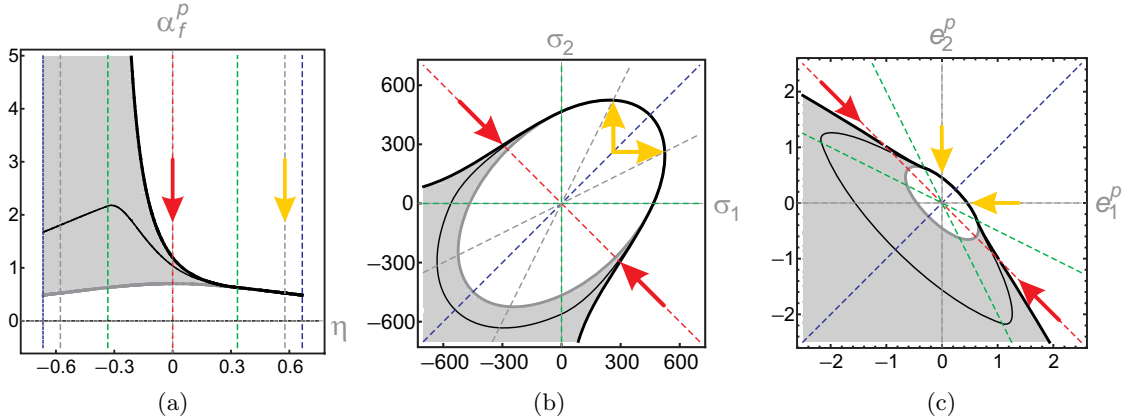
Figure 7.10.: Fracture loci drawn at (a) triaxiality equivalent fracture strain, (b) principal stress and (c) principal strain spaces for Lemaitre's damage model with quasi-unilateral damage growth for plane stress state. Curves are given for different choices of h. h = 1 (thick gray curves), h = 0.2 (thin black curves) and h = 0 (thick black curves). Gray coloured regions stand for 0 < h < 1. Inconsistencies are marked with red and yellow arrows. Selected parameters are μ = 80769.2 MPa, κ = 175000 MPa, β = 1, m = 1, S = 0.5 MPa, C = 500 MPa, α₀ᵖ = 0.001, n = 0.15.

The results presented show relative superiority of the modification with quasi-unilateral damage evolution as compared to the conventional Lemaitre model. However, once today's state of the art research regarding low and negative triaxiality fracture is concerned, there is still room for further developments. Pioneering studies on certain aluminum alloys by Wierzbicki and colleagues questioned the monotonic dependence of the fracture strain on the triaxiality ratio as predicted by the fracture criteria relying on void growth computations, as in the case of [259], or porous plasticity models, as in the case of [111, 110]; see, e.g., [29]. According to these findings,

low and negative triaxiality as well as plane strain regimes are prone to so-called shear fracture[2]. As a consequence, new damage models, or the modifications introduced to the existing ones, besides the stress triaxiality ratio, devise an additional stress dependent parameter in the damage evolution equation as a measure to distinguish axisymmetric stress states from the generalized shear stress states. For this purpose Lode parameter, the third invariant of the deviatoric stress tensor J_3 or the maximum shear stress are used[3]; see, e.g., [29]. Once the fracture loci in these studies are observed, it is seen that the produced curves account for two local minima in the vicinity of generalized shear stress points within the interval $\eta \in [-1/3, 2/3]$ for plane stress states. Taking this behavior as a basis of comparison, one realizes that the current enhancement falls short in its mathematical flexibility to supply a reduced fracture strain at the plane strain valley, i.e., the vicinity of $\eta = 1/\sqrt{3}$, as compared to the biaxial strain state. On Figure 7.10 this weakness is shown with yellow arrows. Once the pure shear stress point is concerned, i.e., $\eta = 0$, reduction of the fracture equivalent plastic strain is possible by using $0 < h < 1$ at the expense of violating the standpoint which disclaims fracture occurrence for $\eta \leq -1/\sqrt{3}$. On Figure 7.10 pure shear points are marked with red arrows.

Since in sheet metal forming practice the admissible triaxiality interval is limited by the sheet geometry as well as buckling the concept of shear fracture gains additional importance. [4] Mainly two characteristic maximum shear stress states can be defined on a thin sheet. As shown on the rectangular deep drawing process in Figure 7.11, in-plane maximum shear is due in drawing region[5] where the pure shear stress state takes place with $\eta \sim 0$. Out-of-plane maximum shear takes place in bending region where plane strain stress state is observed with $\eta \sim 1/\sqrt{3}$. Depending on this characterization, the former condition, i.e., maximum in-plane shear, stands for the pure shear stress state and represented by the yellow arrows on Figure 7.10, whereas red arrows represent, the latter plane strain condition, i.e., maximum out-of-plane shear.

---

[2]This point needs a clarification based on the void dynamics, i.e. from a micromechanical point of view. Under the effect of the hydrostatic stresses the voids grow. Under shear stress state, although an actual growth of the existing voids is not due, two mechanisms can be effective. First one is the destabilizing effects of inter-void linking with material rotation under shear and eventual void interaction. The second one is the nucleation of new voids around secondary phases with inclusion matrix separation; see, e.g., [224]. Mostly a forming process involves mixed stress states blending hydrostatic and shear stresses.

[3]In various models proposed in the literature Lode parameter dependence is accounted for in the yield function, see, e.g., [20] or more recently [66]. Here, the size of the yield surface is controlled by the the hydrostatic pressure whereas the its shape by the Lode angle. In the current study any dependence of the yield stress on the hydrostatic pressure and Lode parameter dependence is not assumed.

[4]In sheet metal forming analysis thin shell elements with vanishing out of plane stresses, i.e. plane stress state, are used which results in a triaxiality ratio confined to $\eta \in [-1/3, 2/3]$. Due to lack of the out-of-plane stress component, such elements show premature necking and fracture under normal loadings. Accordingly, fracture analysis with thin shell elements is not suggested. Nevertheless, it should be noted that, any free surface fracture either in bulk or sheet metal forming occurs under plane stress conditions.

[5]For high strength steels, shear fracture occurrence in the drawing region is shown in, e.g., [183] among others.
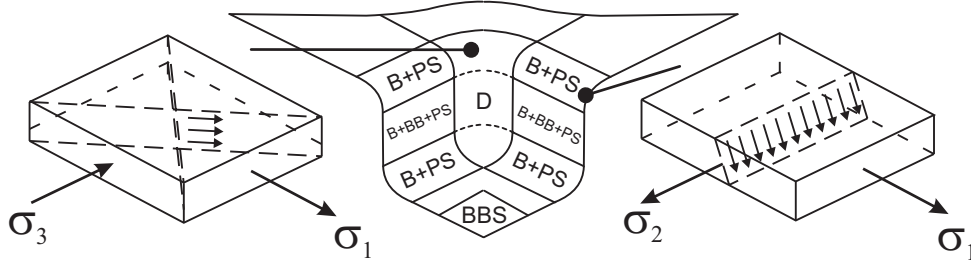
Figure 7.11.: In plane (left) and out of plane (right) shear stress states in deep drawing as a sheet metal forming process. The letters on the drawn sheet denote the following: B: Bending, BB: Bending Back, PS: Plane Strain, BBS: Balanced Biaxial Stretching, D: Drawing. Adapted from [312].

7.5. Model L3: Extension to Shear Modification

This leads to the next enhancement which follows in the lines of empirical multiplicative[6] modification of the Oyane's fracture criterion, [241] by [192]. Accordingly, using the definition of maximum shear stress $\tau_{\max}$ the damage rate is modified by a factor which represents the shear correction exponent

$$\dot{D} = \dot{\alpha}^p \left[\frac{2\tau_{\max}}{\sigma_{\text{vMises}}}\right]^\delta \left[\frac{\check{Y}^\oplus}{S}\right]^m \frac{1}{[1-D]^\beta} . \tag{7.5.1}$$

In Equation (7.5.1) the exponent δ represents the shear damage parameter. For $\delta = 0$ Lemaitre's damage model with quasi-unilateral enhancement is recovered. For integration, one starts by substituting Equation (7.A.3) into $\tau_{\max} = [\sigma_1 - \sigma_3]/2$ with $\sigma_1 > \sigma_2 > \sigma_3$ which gives

$$\tau_{\max} = \frac{1}{2}\left[\sigma_{\text{vMises}}\left[\eta + \frac{2}{3}\cos(\theta)\right] - \sigma_{\text{vMises}}\left[\eta + \frac{2}{3}\cos\left(\frac{4}{3}\pi - \theta\right)\right]\right] . \tag{7.5.2}$$

Normalization with respect to the von Mises equivalent stress gives the following non-dimensional expression used in Equation (7.5.1)

$$h(\theta) = \frac{2\tau_{\max}}{\sigma_{\text{vMises}}} = \frac{2}{3}\left[\cos(\theta) - \cos\left(\frac{4}{3}\pi - \theta\right)\right] . \tag{7.5.3}$$

7.5.1. Isochronous Fracture Surface Representations at Various Spaces

7.5.1.1. Representations in $(\eta, \theta, \alpha_f^p)$, $(\eta, \overline{\theta}, \alpha_f^p)$ and (η, L, α_f^p)

Since $h(\theta)$ in Equation (7.5.3) is constant during radial loading paths, it leads to the following immediate integration

$$\alpha_f^p = B\left[h(\theta)^\delta f^\oplus(\eta, \theta)^m\right]^{\frac{-1}{2mn+1}} - \alpha_0^p . \tag{7.5.4}$$

---

[6]On the contrary, an additive modification is introduced to the void growth expression in the Gurson's model by [224]. Unlike original Gurson's model, this modification is not micromechanical but rather phenomenological. In the same sense, unlike original Lemaitre's damage model, the current extension is empirical and does not follow the formal steps of internal variables of thermodynamics. Recently, other multiplicative shear modifications for the Lemaitre model proposing a Lode parameter dependent dissipation potential is given in [67] also in [195]. Both works propose a Lode parameter dependent damage rate form following the formal steps of internal variable thermodynamics drived from a Lode parameter dependent damage dissipation potential.

Like in the previous model, representations in $(\eta, \overline{\theta})$ and (η, L) follow standard substitutions which have to be considered for the function $h(\theta)$ also. For $\delta = 3$ and $h = 0$ the plot of α_f^p contours for in the space of (η, θ), $(\eta, \overline{\theta})$ and (η, L) are given in Figure 7.12. As compared to Figure 7.7 it is seen that $h(\theta)$ with the selected δ controls the curvature in θ direction. Once $h = 1$, this outcome is completely symmetric with respect to $\theta = \pi/6$, or equivalently with respect to $\overline{\theta} = L = 0$.
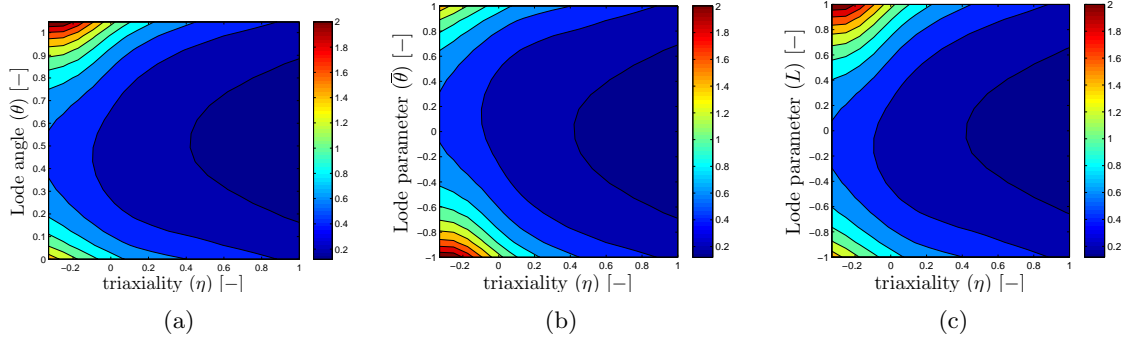
Figure 7.12.: Equivalent fracture strain α_f^p contours for the damage criterion based on the shear and quasi-unilateral modification of the Lemaitre's damage model. Plots are given on (a) (η, θ), (b) $(\eta, \overline{\theta})$ and (c) (η, L). Selected parameters are $\mu = 80769.2$ MPa, $\kappa = 175000$ MPa, $\beta = 1$, $m = 1$, $S = 0.5$ MPa, $C = 500$ MPa, $\alpha_0^p = 0.001$, $n = 0.15$, $h = 0.2$, $\delta = 10$.

7.5.1.2. Representation in $(\sigma_1, \sigma_2, \sigma_3)$ and (e_1^p, e_2^p, e_3^p)

$g^{\odot} = 0$ representing the fracture surface for the shear and quasi-unilateral enhancement in terms of stress principals read

$$g^{\odot}(\sigma_1, \sigma_2, \sigma_3) = \left[\frac{\sigma_{\mathrm{vMises}}(\sigma_1, \sigma_2, \sigma_3)}{C} \right]^{\frac{1}{n}} - B \left[h(\sigma_1, \sigma_2, \sigma_3)^{\delta} f^{\oplus}(\sigma_1, \sigma_2, \sigma_3) \right]^{\frac{-m}{2mn+1}} - \alpha_0^p, \quad (7.5.5)$$

where for $h(\sigma_1, \sigma_2, \sigma_3)$ the following is used

$$h(\sigma_1, \sigma_2, \sigma_3) = \frac{\sigma_1 - \sigma_3}{\sigma_{\mathrm{vMises}}(\sigma_1, \sigma_2, \sigma_3)} . \quad (7.5.6)$$

Coming to the representation $g^{\odot}(e_1^p, e_2^p, e_3^p, p)$ one has

$$g^{\odot}(e_1^p, e_2^p, e_3^p, p) = \alpha_f^p(e_1^p, e_2^p, e_3^p) - B \left[h(e_1^p, e_2^p, e_3^p)^{\delta} f^{\oplus}(e_1^p, e_2^p, e_3^p, p) \right]^{\frac{-m}{2mn+1}} - \alpha_0^p. \quad (7.5.7)$$

Here, using $[\sigma_1 - \sigma_3] = [s_1 - s_3]$ and $s_\nu/\sigma_{\mathrm{vMises}} = [2/3][e_\nu^p/\alpha^p]$ for $\nu = 1, 2, 3$

$$h(e_1^p, e_2^p, e_3^p) = \frac{2}{3} \frac{e_1 - e_3}{\alpha^p(e_1^p, e_2^p, e_3^p)} , \quad (7.5.8)$$

with $e_1^p \geq e_2^p \geq e_3^p$. Corresponding plots of the isochronous fracture surfaces in principal stress space $(\sigma_1, \sigma_2, \sigma_3)$ and in the space of (e_1^p, e_2^p, e_3^p, p) are respectively given in Figures 7.13(a) and 7.13(b). As seen this time instead of a complete smoothness the fracture surface involves kinks through the planes representing axisymmetric loading points with corresponding shrinkage at the generalized shear stress planes. As before as $p \to -\infty$ the fracture surface expands indefinitely
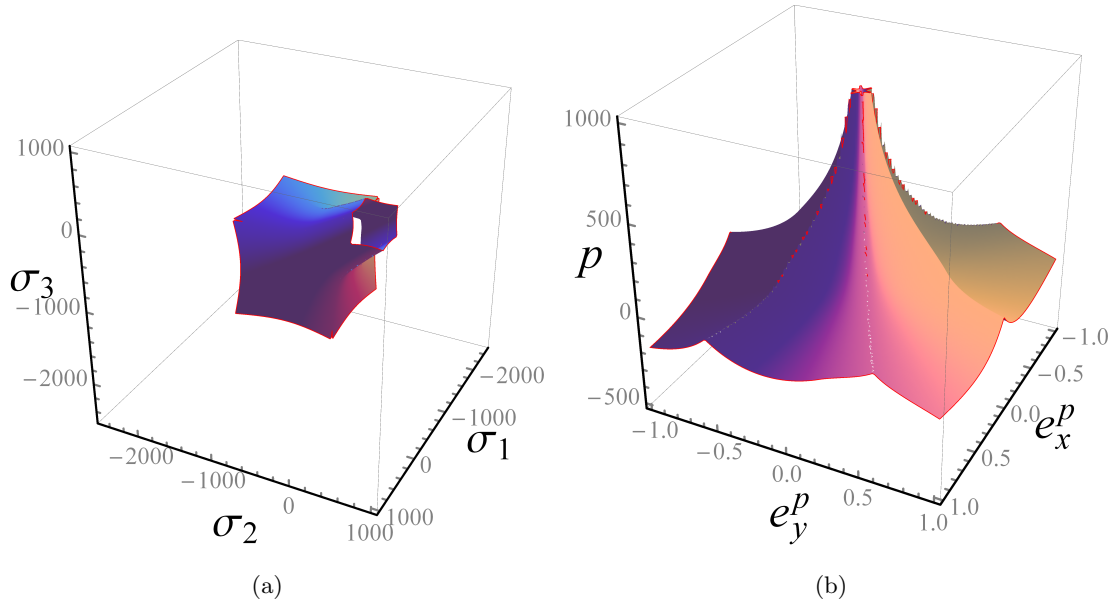
Figure 7.13.: *Isochronous fracture surfaces on (a) $(\sigma_1, \sigma_2, \sigma_3)$ in MPa, (b) (e_1^p, e_2^p, e_3^p) space for the damage criterion based on the shear and quasi-unilateral modification of the Lemaitre's damage model. Selected parameters are $\mu = 80769.2$ MPa, $\kappa = 175000$ MPa, $\beta = 1$, $m = 1$, $S = 0.5$ MPa, $C = 500$ MPa, $\alpha_0^p = 0.001$, $n = 0.15$, $h = 0$, $\delta = 10$.*

whereas for $p \to \infty$ it converges again to the von Mises type cylindrical yield surface no matter what the value of h or δ is.

Figure 7.14 depicts the sections of the fracture surfaces plotted on the triangular plastic strain coordinates with variations of δ for $h = 1$ (left) and $h = 0$ (right). In both of the cases δ introduces a considerable shrinkage depending on the its magnitude in the fracture loci for the generalized shear loading paths. A noteworthy fact is that the fracture strains for the axisymmetric stress axes do not alter by this change. For $h = 1$, with $\delta > 0$ the fracture loci has six direct (rotational) and six indirect (reflective) symmetries whereas for $h < 1$ these reduce to three direct and three indirect ones. The fracture loci for $h = 1$ are comparable to those carried out with the Lode parameter dependent models given in, e.g., [339].

7.5.1.3. State of Plane Stress and Planar Plots for the Fracture Loci

Fracture loci regarding the final enhancement are given in Figure 7.15 for two different δ values. In the given curves $h = 0$ is used. It is observed that, on the triaxiality space the fracture strains become critical as δ is increased at the shear and the plane strain regions. On the other hand, the uniaxial and the biaxial tensile points with $\eta = 1/3$ and $\eta = 2/3$, respectively, are not affected from this modification. For the uniaxial compression, i.e., $\eta = -1/3$, the fracture curves preserve their asymptotic behavior. It should be noted that for $h > 0$ the fracture loci in the triaxiality range $-1/3 \leq \eta \leq 1/3$ can be modeled additionally. This would lead to a finite fracture strain at uniaxial compression but on the other hand to more flexibility in fitting experimental results and in modifying the minimum of the fracture curve in the pure stress area. In both the principal stress and the principal strain plots one can see the shrinkage of the fracture loci at the generalized shear stress regions accounting for non-convex fracture surfaces. Note that unlike yield loci the fracture loci do not necessarily admit convexity. The principal
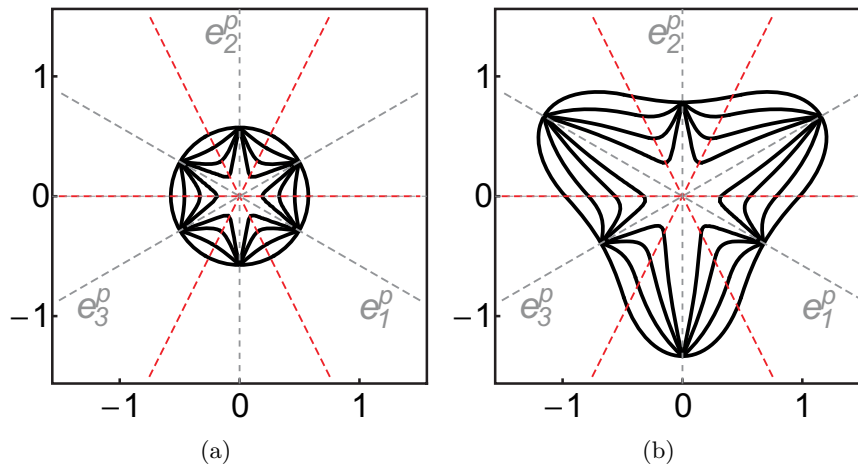
Figure 7.14.: Fracture loci projected on the (deviatoric) plastic strain plane for (a) $h = 1$, $p = 0$, from outer to inner $\delta = 0, 2, 5, 10$, (b) $h = 0$, $p = 0$, from outer to inner $\delta = 0, 2, 5, 10$. Selected parameters are $\mu = 80769.2$ MPa, $\kappa = 175000$ MPa, $\beta = 1$, $m = 1$, $S = 0.5$ MPa, $C = 500$ MPa, $\alpha_0^p = 0.001$, $n = 0.15$.

in-plane strain space plot shows that, with the shrinkage at the plane strain region, the fracture locus resembles a forming limit curve, in the range covered from equi-biaxial stress state to uniaxial stress state. Approaching towards the pure shear point the shear fracture risk adds an additional critical branching which is not seen in the forming limit curves. This pattern is in accordance with the findings of [183] constitutes a critical superiority of the proposed model as compared to forming limit curve based analyses which fall short in modeling shear failure. Unlike Nahshon and Hutchinson's additive modification, [224], the current multiplicative one is incapable of supplying a local minimum fracture strain at the pure shear point in the interval $-1/3 \leq \eta \leq 1/3$. The reasons become clear once the behavior of the factor $2\tau_{\max}/\sigma_{\text{vMises}}$ is investigated. As seen the current model gives comparable results with the ones proposed in the literature.

Figure 7.16 shows the plot of the factor $2\tau_{\max}/\sigma_{\text{vMises}}$ with respect to the triaxiality. As seen, for generalized shear stress states, i.e., for $\eta = 0$ and $\eta = 1/\sqrt{3}$, at which shear fracture is critical, this ratio reaches its maxima. This information combined with the symmetry of the $2\tau_{\max}/\sigma_{\text{vMises}}$ plot in the interval $-1/3 \leq \eta \leq 1/3$ clearly shows why a local minimum fracture strain at the pure shear point, i.e., $h = 0$, in the interval $-1/3 \leq \eta \leq 1/3$ is not possible. Coming to the axi-symmetric stress states, i.e., $\eta = -1/3$, $\eta = 1/3$ and $\eta = 2/3$, this ratio gives $2\tau_{\max}/\sigma_{\text{vMises}} = 1$ thus it has no effect on the damage rate. This explains why the fracture points for the uniaxial and the biaxial stress states are not altered by this modification.

7.6. Applications

7.6.1. Model L2 and the Secondary Tensile Stresses

Secondary tensile stresses are principal stresses of unintended tensile character during fully developed plastic flow which can exhaust the formability of the material considerably. Mannesmann effect with the formation of a cavity along the longitudinal axis in bars subjected to radial compression in metalworking operations [102], alligatoring defect encountered in hot or cold rolling
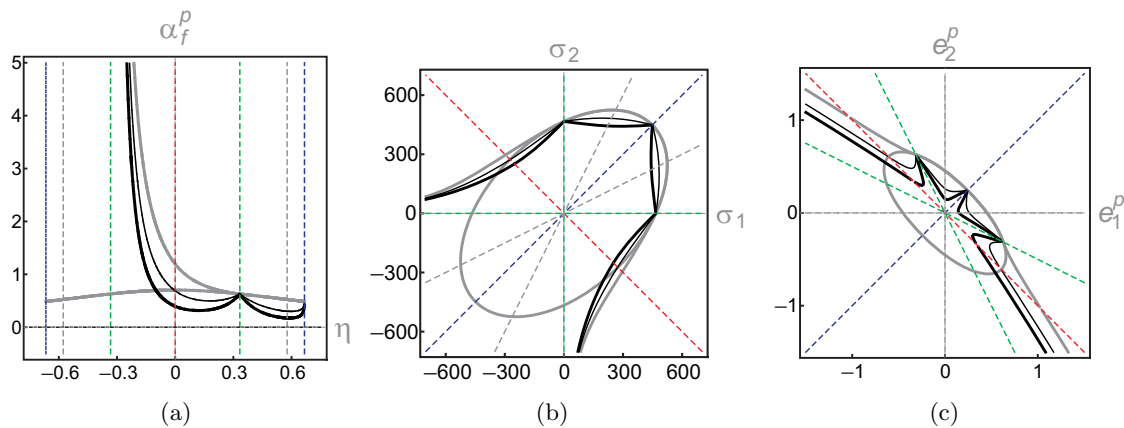
Figure 7.15.: *Fracture loci drawn at (a) triaxiality equivalent fracture strain, (b) principal stress and (c) principal strain spaces for Lemaitre's damage model with shear modification as well as quasi-unilateral damage growth for plane stress state. The results are given for different choices of $\delta = 0$ (thick gray curves), $\delta = 5$ (thin black curves) and $\delta = 10$ (thick black curves). Selected parameters are $\mu = 80769.2$ MPa, $\kappa = 175000$ MPa, $\beta = 1$, $m = 1$, $S = 0.5$ MPa, $C = 500$ MPa, $\alpha_0^p = 0.001$, $n = 0.15$, $h = 0$.*
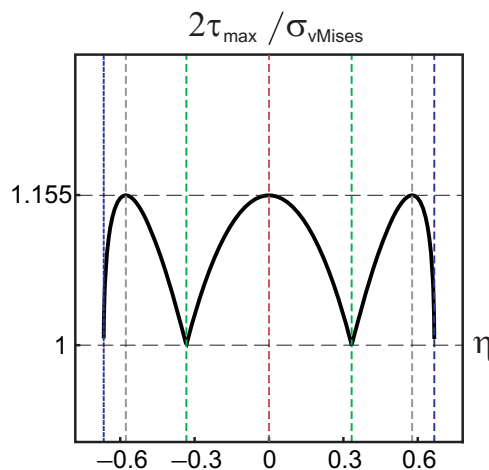
Figure 7.16.: *Triaxiality dependence of the ratio $2\sigma_{max}/\sigma_{vMises}$ for plane stress state.*

practice where a slab or rod splits into two halves on a plane parallel to the rolling plane [155], and chevron cracks, which are central cracks occurring at the longitudinal axis of the extruded specimens [288], constitute some important examples.

Figure 7.17, illustrating the damage contours computed for two extremes of h, i.e., for $h = 0$ and $h = 1$, for four deformation processes, shows the influence of using quasi-unilateral modification in the damage analysis. In upsetting of a tapered strip and extrusion of a billet, let alone the intensities, which are not given over the figures for the sake of brevity, the damage development zones completely differ. For the upsetting process, taking the point of the maximum damage development as the incipient fracture spot, for $h = 0$ one predicts a surface crack, whereas for $h = 1$ an internal crack is expected. For the extrusion processes strikingly an opposing observation is due, i.e., surface and internal cracks are predicted with $h = 1$ and $h = 0$, respectively. Both upsetting and extrusion processes involve the so-called secondary tensile stresses. Although the

globally applied external loading is compressive, local tensile stresses occur inevitably during the deformation. For the upsetting test, this happens at the bulging zone, whereas for the extrusion at the area reduction zone. The damage development lead by the secondary tensile stresses meeting the plastic flow at the area reduction zone can cause characteristic internal cracks whose internal character makes it hard to detect; see, e.g., [288, 287]. For free bending process, both for $h = 1$ and $h = 0$ one predicts the free surface cracks at the bending zone, however this time the former estimates the concave whereas the latter the convex surface of the bend for the fracture to emanate. Once the void dynamics is concerned, fracturing above the neutral axis, where the plane strain compression is due, is highly unlikely. Thus latter prediction is plausible and in qualitative correlation with the experimental findings given in [280]. A noteworthy fact is that, the notched tensile test is not affected by h. As a direct consequence, with quasi-unilateral enhancement, the damage parameter identification is incomplete using merely tensile tests. For definition of , one should conduct tests at which at least one principal stress component at the critical zone of fracture becomes compressive. For this purpose shear tests can be realized. With the assumption of isotropy and small strains, in a simple (in-plane) shear loading, the planar principal stress components have the same magnitude as the shear stress, however with opposing signs due to the deviatoric stress state. Besides, the ratio of enhanced and conventional damage conjugate variable becomes $Y^+/Y = [1 + h]/2$.
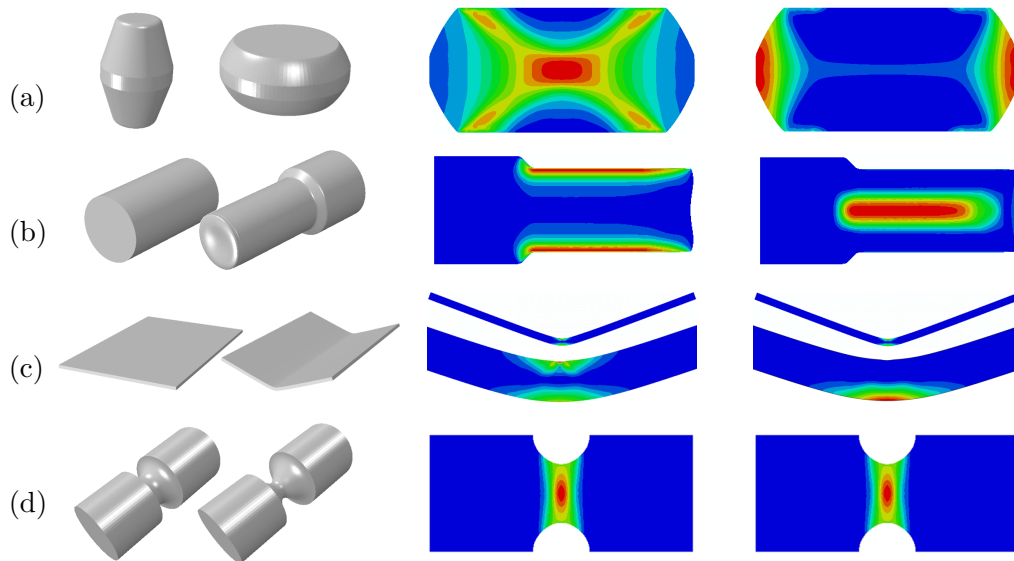
Figure 7.17.: Damage contour plots for $h = 1$ (results given on the left of figure couples) and $h = 0$ (results given on the right of figure couples) for various deformation process simulations: (a) tapered strip upsetting, (b) axisymmetric bar extrusion, (c) plate bending, (d) tension of an axisymmetric notched bar. Red color denotes the maximum where the maximum is not necessarily identical for all processes. For a more information on (a), (c) and (d) the reader is referred to [287].

7.6.2. Model L3 and Experimental Validation

In this section two parameter identification applications to the material fracture data from the literature are presented. The first one, [30], includes a data set handled for a wide range of data set for 2024-T351 aluminum. For the second one, [21], the data is supplied for steel sheets of TRIP690 provided by ThyssenKrupp Steel, under plane stress conditions, also reported in [183].

For comparison purposes, the calibrations are realized for the three proposed variants of the Lemaitre based fracture criteria as well as for a set of selected fracture criteria frequently used in the literature which are given below and the results are discussed.

Rice–Tracey (RT). Being among the earliest fracture criteria, [259] model considers the growth of a spherical void in a cubic cell under remote loading field. The Lode angle parameter-independent equivalent (plastic) fracture strain, α_f^p, of Rice and Tracey damage model is derived as a function of only η as

$$\alpha_f^p\left(\eta,\overline{\theta}\right) = c_1 + c_2 e^{-c_3\eta}. \tag{7.6.1}$$

Cockcroft–Latham (CL). The model of [78] constitutes an energy-based ductile fracture criterion considering a critical threshold for the plastic work done by the maximum tensile principal stress. Corresponding equivalent fracture strain, φ_f, which is a function of both η and $\overline{\theta}$, reads

$$\alpha_f^p\left(\eta,\overline{\theta}\right) = \frac{C_{\mathrm{CL}}}{\eta + \frac{2}{3}\cos\left(\frac{\pi}{6}\left[1 - \overline{\theta}\right]\right)}. \tag{7.6.2}$$

The Pressure-Modified Maximum Shear (PMMS). Being among the models proposed by the MIT Crashworthiness Lab., this damage model is an extension of the maximum shear stress model by accounting for the effect of stress triaxiality ratio. Corresponding equivalent fracture strain, α_f^p, which is a function of both η and $\overline{\theta}$, reads

$$\alpha_f^p\left(\eta,\overline{\theta}\right) = \left[\frac{C}{c_2}\left[c_1\eta + \frac{\sqrt{3}}{3}\cos\left(\frac{\overline{\theta}\pi}{6}\right)\right]\right]^{-\frac{1}{n}}. \tag{7.6.3}$$

Note that above closed form is made possible assuming a power type hardening, $\sigma_{\mathrm{vMises}} = C\alpha_n^p$.

Modified Mohr–Coulomb (MMC). The closed form solution for the equivalent fracture strain for the empirical modified Mohr–Coulomb fracture criterion [183] assumes a power type hardening, $\sigma_{\mathrm{vMises}} = C[\alpha^p]^n$, and results in the following function of both η and $\overline{\theta}$

$$\begin{aligned}\alpha_f^p\left(\eta,\overline{\theta}\right) = \Bigg[\frac{C}{c_2}\Bigg[&c_3 + \frac{\sqrt{3}}{2 - \sqrt{3}}\left[1 - c_3\right]\left[\sec\left(\frac{\overline{\theta}\pi}{6}\right) - 1\right]\Bigg] \times\\ &\left[\sqrt{\frac{1 + c_1^2}{3}}\cos\left(\frac{\overline{\theta}\pi}{6}\right) + c_1\left[\eta + \frac{1}{3}\sin\left(\frac{\overline{\theta}\pi}{6}\right)\right]\right]\Bigg]^{-\frac{1}{n}}.\end{aligned} \tag{7.6.4}$$

As seen, apart from the hardening variables, this model requires three parameters.

Lou–Huh (LH). This phenomenological model, developed by [192], considers of damage evolution motivated by the micro-mechanical phenomena of void nucleation, growth and coalescence. The growth of voids is accounted for materializing the stress triaxiality whereas the effects of void coalescence are incorporated by normalized maximum shear stress. The equivalent plastic strain, as a measure of material flow, besides scaling both of the void growth and coalescence, gives account for continuous nucleation of voids. In its original setting, the model reads

$$\alpha_f^p = C_{\mathrm{LH}}\left[\frac{2\tau_{\max}}{\sigma_{\mathrm{vMises}}}\right]^{-a}\left[\frac{\langle 1 + 3\eta\rangle}{2}\right]^{-b}, \tag{7.6.5}$$

where C_{LH}, a and b are material parameters. Corresponding equivalent fracture strain α_f^p which is a function of both η and $\bar{\theta}$, reads

$$\alpha_f^p\left(\eta, \bar{\theta}\right) = C_{\mathrm{LH}} \left[\frac{2}{\sqrt{3}} \cos\left(\frac{\bar{\theta}\pi}{6}\right)\right]^{-a} \left[\frac{\langle 1 + 3\eta \rangle}{2}\right]^{-b}. \tag{7.6.6}$$

One should note that the closed form expression for Lou–Huh fracture criterion does not explicitly depend on the functional form of the flow curve. This property makes the model more flexible since sticking to the power form can be highly limiting. Hence the model can be used for materials showing hardening regimes other than power type hardening.

7.6.2.1. Calibration of The Model Parameters for Bao and Wierzbicki [2005]

In this first calibration example, the collection of fracture experiments composed of 15 types of tests conducted for a wide range of stress triaxiality and Lode parameter for 2024-T351 aluminum alloy as reported in [30] is used. For Al2024 the shear modulus is $\mu = 27857.1$ MPa and the bulk modulus is $\kappa = 72647.1$ MPa. The plastic hardening of the material is calibrated using upsetting tests for a power hardening rule where the parameters are found to be $C = 740$ MPa, $\alpha_0^n = 0$ and $n = 0.15$. The equivalent plastic strains at fracture are reported in terms of the average triaxiality and Lode parameter, $(\eta_{\mathrm{ave}}, \bar{\theta}_{\mathrm{ave}})$ where $(\bullet)_{\mathrm{ave}} = \left[\int_0^{\alpha_f^p} (\bullet) d\alpha^p\right]/\alpha_f^p$, as given in Table 7.1. For more details of the tests, the reader is referred to [30].

Table 7.1.: The fracture test results for Al2024-T351 adapted from [30].

ID	Description	η_{ave}	$\bar{\theta}_{\mathrm{ave}}$	α_f^p
1.	Smooth round bar, tension	0.4014	0.9992	0.4687
2.	Round large notched bar, tension	0.6264	0.9992	0.2830
3.	Round small notched bar, tension	0.9274	0.9984	0.1665
4.	Flat grooved, tension	0.6030	0.0754	0.2100
5.	Cylinder, aspect ratio of 0.5, compression	−0.2780	−0.8215	0.4505
6.	Cylinder, aspect ratio of 0.8, compression	−0.2339	−0.6809	0.3800
7.	Cylinder, aspect ratio of 1.0, compression	−0.2326	−0.6794	0.3563
8.	Cylinder, aspect ratio of 1.5, compression	−0.2235	−0.6521	0.3410
9.	Round notched, compression	−0.2476	−0.7141	0.6217
10.	Simple shear	0.0124	0.0355	0.2107
11.	Combination of shear and tension	0.1173	0.3381	0.2613
12.	Plate with a circular hole	0.3431	0.9661	0.3099
13.	Dog-bone specimen, tension	0.3570	0.9182	0.4798
14.	Pipe, tension	0.3557	0.9286	0.3255
15.	Solid square bar, tension	0.3687	0.9992	0.3551

`NonlinearModelFit` function of MATHEMATICA is used to fit[7] the fracture surfaces of damage models to the data listed in Table 7.2. The results are given in Table 7.1. Here $\sum \mathrm{Res.}^2$ stands for

---

[7] Since the plasticity parameters are those reported in the original work, one is left with identifying just the fracture parameters. Since the fracture criteria has no effect on the elastoplastic response, every experiment in Table 7.1 represents a single input, that is the equivalent plastic strain to fracture at computed average triaxiality and Lode parameter. Once the number of experiments is less than the number of ductile fracture model parameters to be identified the system is underdetermined and it is not possible to define a unique set of parameters. On the contrary, in the case where the number of parameters is smaller than the experimental fracture points the system is called overdetermined for which the method of least squares is a standard approach

the sum of squared residuals and R^2 the coefficient of determination. From this table it can be seen that models L3 shows the best fitting properties. It is followed by PMMS and MMC. Except for the LH model Lemaitre mod II, and Cao's modification require power type hardening curve description. The single parameter CL shows the poorest performance in this calibration study mainly due to the sensitivity of the material fracture to the Lode angle parameter. It is notable that L3 has considerable improvement over L2 and L1 which shows that the modifications show desired flexibility.

Table 7.2.: Determined parameters of the selected fracture criteria for Al2024-T351.

Model	Parameters	$\sum$Res.^{2}	R^2
L3	$\beta = 2.2616$; $m = 2.0345$; $S = 2.6024$;	0.0867	0.9571
	$h = 0.7477$; $\delta = 8.5562$		
PMMS	$c_1 = 0.0728$; $c_2 = 339.435$;	0.0942	0.9533
MMC (Reprocessed)	$c_1 = 0.0453$; $c_2 = 334.82$; $c_3 = 0.9663$	0.0953	0.9528
LH	$a = 3.5593$; $b = 0.2166$; $C_{LH} = 0.3599$	0.1099	0.9456
MMC (Published)	$c_1 = 0.03451$; $c_2 = 338.6$; $c_3 = 1$	0.1272	0.9370
L2	$\beta = 2.7978$; $m = 0.1072$; $S = 7.9433$; $h = 0$	0.1483	0.9266
RT	$c_1 = 0$; $c_2 = 0.3752$; $c_3 = 0.4601$	0.1510	0.9252
L1	$\beta = 3.4246$; $m = 1.1771$; $S = 3.1088$	0.1660	0.9178
CL	$C_{CL} = 0.0783$	0.7329	0.6371

Figure 7.18 depicts the fracture surface plots and their comparison with the experimental fracture points. The gained additional curvature in $\bar{\theta}$ direction of L3 is clear as compared to L1. Although an explicit $\bar{\theta}$ dependence is not accounted for, L2 also shows a variation in this direction with $h = 0$ in accordance with previous comments. Among the selected models only L1 and RT are independent of $\bar{\theta}$ as the figures also depict. $h \neq 0$ in L3 results in a saddle geometry with slight bending. Hence, this identification process result does not impose a negative triaxiality cut-off for ductile fracture.

7.6.2.2. Calibration of The Model Parameters for Bai and Wierzbicki [2010]

In this example the material studied falls under the group of Advanced High Strength Steels. As a product of ThyssenKrupp Steel Europe AG, the sheets are cold rolled Retained Austenite Steel where the minimum tensile strenght is 690MPa, hence TRIP690. Since the tests are realized on the sheets the tests are reported as to correspond to the plane stress condition. Anisotropy of the material in both plasticity and fracture is reported as negligible which makes it possible to use the current modeling framework. For TRIP690 the shear modulus is $\mu = 80769.2$ MPa and the bulk modulus is $\kappa = 175000$ MPa. For the plastic hardening of the material a power hardening rule is used with $C = 1275.9$ MPa, $\alpha_0^n = 0$ and $n = 0.2655$. The material is assumed to behave isotropically for both the plasticity and fracture. For fracture calibration, tests are conducted on five types of specimens: dog-bone specimen, flat specimen with cutouts, punch

---

in regression analysis. The current least squares problem fall into the category of nonlinear least squares since the residuals are non-linear in unknowns. Unlike the linear least-squares problem which admits a closed-form solution, the non-linear problem is usually solved iteratively. In nonlinear least squares, multiple minima can occur which have equal values of the objective function. That is, uniqueness of the solution is not guaranteed. Also (false) local minima can occur when the objective function value is greater than its value at the global minimum. The iterations should be started with widely differing initial estimates of the parameters, to be certain that the minimum found is the global minimum. If identical parameter set is converged regardless of starting point, it is likely to be the global minimum. This way is taken in the current identification studies.
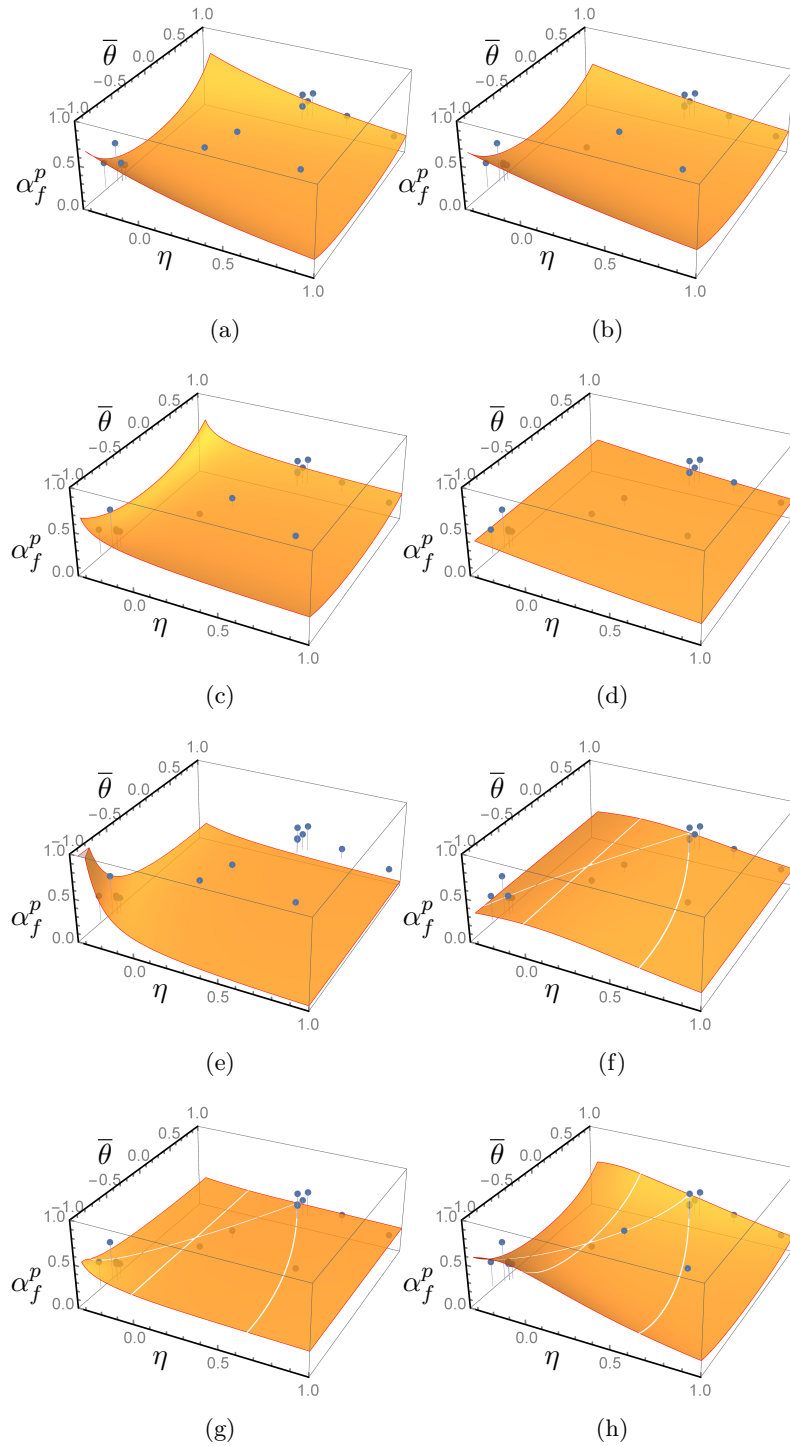
Figure 7.18.: Fracture surface plots and their comparison with the experimental fracture points for (a) PMMS, (b) MMC, (c) HL, (d) RT, (e) CL, (f) L1, (g) L2, (h) L3.

test, butterfly specimen in tension and butterfly specimen in simple shear. The fracture strains are computed using finite element analysis with shell elements and like in the previous example represented in terms of the average triaxiality and Lode parameter, $(\eta_{\text{ave}}, \overline{\theta}_{\text{ave}})$, values given in Table 7.3. For more details of the tests reader is referred to [183] and [21].

Table 7.3.: The fracture test results for TRIP690 adapted from [21].

ID	Description	η_{ave}	$\overline{\theta}_{\mathrm{ave}}$	α_f^p
1.	Dog-bone, tension	0.379	1.0	0.751
2.	Flat specimen with cutouts, tension	0.472	0.496	0.394
3.	Disk specimen, equi-biaxial tension	0.667	−0.921	0.950
4.	Butterfly specimen, tension	0.577	0	0.460
5.	Butterfly specimen, simple shear	0	0	0.645

A summary of the fit to the fracture surfaces of damage models to the data listed in Table 7.3 is given in Table 7.4. This time MMC, [21], shows the best performance. L3 and LH follows with good fitting properties. CL shows the poorest performance in this calibration as well. As before L3 has considerable improvement over L2 and L1 for which identical parameters are found. This is mainly due to the fact that the crack closure parameter is effective only for $\eta < 1/3$ which excludes the majority of the points. Also the experimentally recorded early shear fracture does not allow use of $h < 1$, at least in absence of the shear modification.

Table 7.4.: Determined parameters of the selected fracture criteria for TRIP690.

Model	Parameters	$\sum\mathrm{Res.}^2$	R^2
MMC (Reprocessed)	$c_1 = 0.1361$; $c_2 = 709.894$; $c_3 = 1.0679$	0.0503	0.9777
MMC (Published)	$c_1 = 0.12$; $c_2 = 720$; $c_3 = 1.095$	0.0694	0.9692
L3	$\beta = 1.0849$; $m = 0.2132$; $S = 37.5554$;	0.0833	0.9630
	$h = 0$; $\delta = 4.5788$		
LH	$a = 3.9606$; $b = 0.1581$; $C_{\mathrm{LH}} = 0.8794$	0.0862	0.9617
PMMS	$c_1 = 0$; $c_2 = 612.319$;	0.0908	0.9597
RT	$c_1 = 0$; $c_2 = 0.6305$; $c_3 = 0$	0.2018	0.9103
L1, L2	$\beta = 1$; $m = 0.0757$; $S = 50$; $h = 1$	0.2049	0.9089
CL	$C_{\mathrm{CL}} = 0.5473$	0.3257	0.8552

A 2D plot of the fracture criteria in η space is possible assuming plane stress conditions. For the case of plane stress state one has a direct relation between $\overline{\theta}$ and the triaxiality η as

$$\overline{\theta} = 1 - \frac{2}{\pi} \arccos\left(-\frac{27}{2}\eta\left[\eta^2 - \frac{1}{3}\right]\right). \tag{7.6.7}$$

In Figure 13.14 the equivalent fracture strain is given in the triaxiality space within the range of $-\frac{1}{3} \leq \eta \leq \frac{2}{3}$ for all used fracture criteria. The experimental points are also shown as red dots. Except for CL, RT and L1 and L2, it can be said that the rest four curves show considerably close trends altough their formulations are completely different. With the parameter identification for L3 in plane stress space, $h = 0$ imposes $-1/3$ as the negative triaxiality cut-off for ductile fracture.

7.6.2.3. Fracture Development During Rectangular Deep Drawing of a TRIP690 Sheet

In this part an application of the shear modified Lemaitre model to a rectangular deep drawing simulation including shear fracture, which was reported in [284], is shown. To this end, the model is implemented as a VUSDFLD routine into ABAQUS/EXPLICIT. The calibrated model parameters are those listed in Table 7.4, however with slight modifications since β is kept constant as $\beta = 1$ to give $m = 0.2132$; $S = 30.93$; $h = 0$; $\delta = 4.579$. In Figure 13.14 the
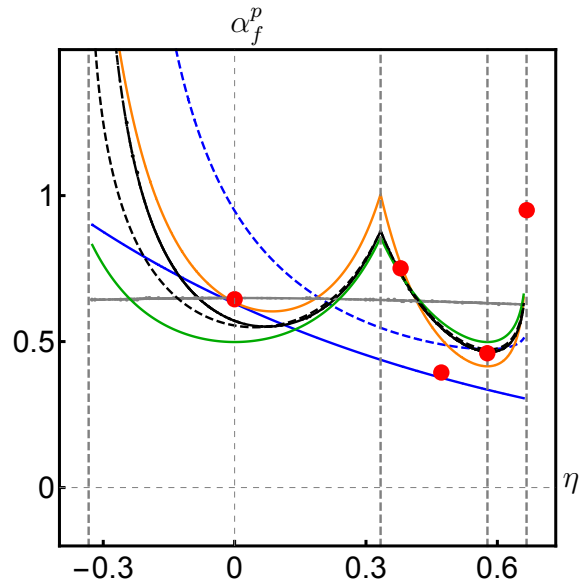
Figure 7.19.: Plot of the fracture locus for TRIP690 for the eight fracture criteria represented at the triaxiality (η) space for plane stress conditions for the identified parameters. Color mapping follows: $\{CL \rightarrow Dashed\ Blue\}$, $\{RT \rightarrow Blue\}$, $\{MMC \rightarrow Orange\}$, $\{PMMS \rightarrow Green\}$, $\{LH \rightarrow Dashed\ Black\}$, $\{L1,\ L2 \rightarrow Gray\}$, $\{L3 \rightarrow Black\}$.

equivalent fracture strain is given in the triaxiality space within the range of $-\frac{1}{3} \leq \eta \leq \frac{2}{3}$ for the modified Lemaitre fracture criterion with the new parameter set. The experimental points are also shown as red dots. As seen, even with new parameter set, Lemaitre model modification II shows a good agreement with the experimental data.
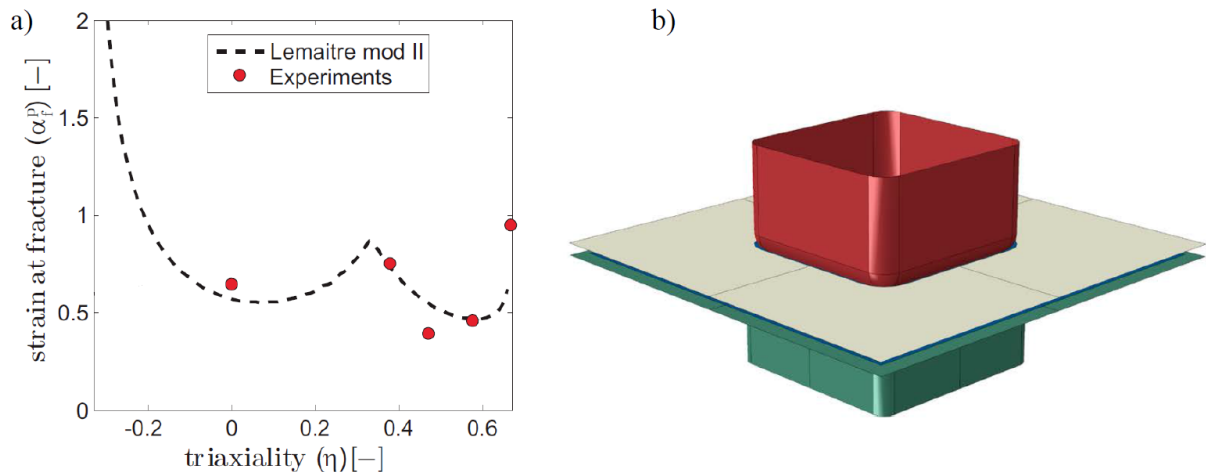
Figure 7.20.: (a) Plot of the fracture locus for TRIP690 for the best four fracture criteria represented at the triaxiality (η) space for plane stress conditions for the identified parameters. (b) The finite element model setup of the rectangular deep drawing test.

In Figure 7.21 it is shown that maximum damage indicator takes place in the drawing region where cracking occurs under in-plane maximum shear stresses using the model with both enhancements. Corresponding force-displacement diagram given in the same figure shows that there is a good agreement between the punch force displacement diagrams handled in the simulations and experiments reported in [184].
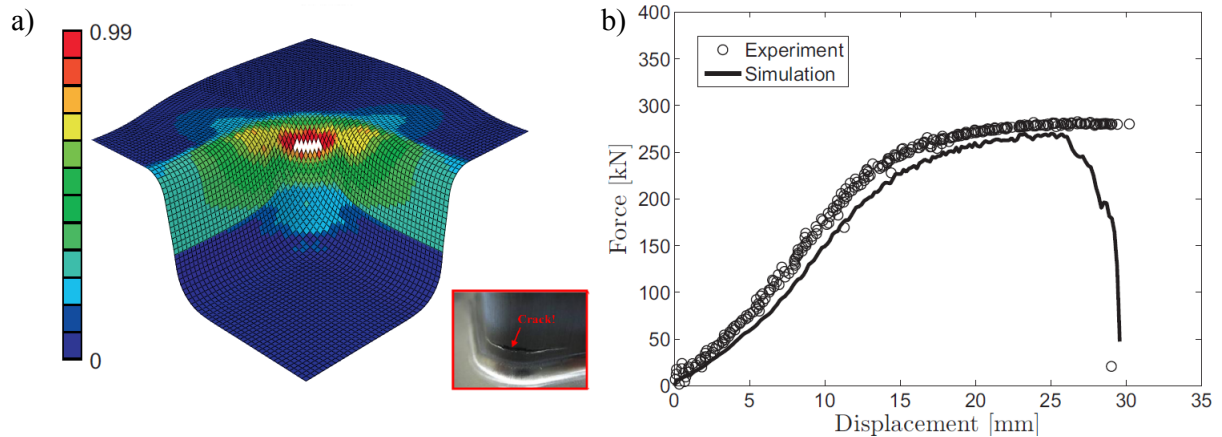
Figure 7.21.: (a) Damage distribution and crack formation in the drawing region due to shear damage accumulation. The small figure shows experimentally determined shear cracks in the same region during rectangular deep drawing of TRIP690 [184]. (b) The comparison of the simulation result with the experimentally determined [184] punch force-displacement diagram.

7.7.   Conclusions and Outlook

Building upon the classical Lemaitre's damage model, two rather empirical enhancements with the least number of material parameters are presented. The former is the already known quasi-unilateral damage evolution. This enhancement relies on a weighted damage evolution for the compressive principal stress components which is overestimated by the conventional model. The latter is a novel suggestion to remedy shear fracture. Although the conventional Lemaitre's damage model is derived following internal variable of thermodynamics the enhancements do not follow these formal steps. The limitations and the predictive capabilities of the models are critically assessed within the context of metal forming practice. The blend of quasi-unilateral and shear modification seems to give promising results as the experimental calibration studies with comparison to other existing models show, with the assumption of proportional strain paths. Obviously, once nonproportional loading with tension-compression path changes are considered, the developed model, especially with the quasi-unilateral modification, allows a better modeling by potentially reducing the damage development under compression. Still, a detailed analysis of the model performance requires further experimental and numerical studies. Other noteworthy directions are considering coupling with elastoplasticity and plastic and damage anisotropy.

7.A.   Stress States

A point on von Mises yield locus can be represented in terms of different parameterizations the straightforward one being with the Cartesian coordinates $(\sigma_1, \sigma_2, \sigma_3)$ of the Haigh-Westergaard stress space. A particularly useful parametrization is with the cylindrical polar coordinates (r, θ, η). As depicted in Figure 7.22, $r = \sqrt{2/3}\,\sigma_{\text{vMises}}$ represents the radius of the circle and the Lode angle $0 \leq \theta \leq \pi/3$ is measured from the axis representing axisymmetric tension[8]. For this range the stress principals are ordered $\sigma_1 \geq \sigma_2 \geq \sigma_3$. $\eta := p/\sigma_{\text{vMises}}$ is the stress triaxiality ratio as the coordinate normal to the deviatoric plane.

---

[8]As Figure 7.22 shows, the current notation differs from the general notation of the Lode angle θ_L by $\pi/6$ that is $\theta_L = \theta - \pi/6$ where $\theta_L = \arctan\left(\frac{1}{\sqrt{3}}\left[\frac{2\sigma_2 - \sigma_1 - \sigma_3}{\sigma_1 - \sigma_3}\right]\right)$.
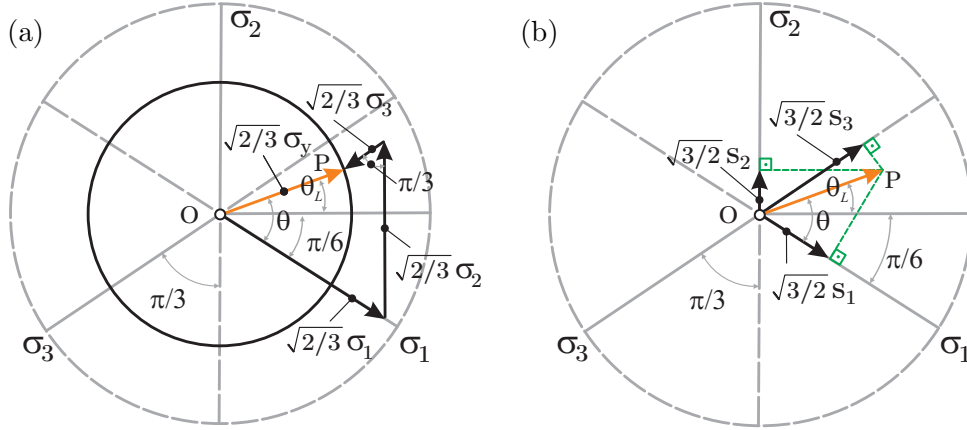
Figure 7.22.: Geometrical representation of the Lode angle θ, $\sigma_y = \sigma_{vMises}$ and (a) projections of the von Mises yield locus as well as of point P on the (deviatoric-stress) $\Pi-$plane and with corresponding projected stress components $(\sigma_1, \sigma_2, \sigma_3)$ and (b) the principal deviatoric stress components (s_1, s_2, s_3) of point P on the $\Pi-$plane, note that $s_1 + s_2 + s_3 = 0$.

Normalization of the Lode angle gives $\bar{\theta}$ with the range $-1 \leq \bar{\theta} \leq 1$

$$\bar{\theta} = 1 - \frac{6\theta}{\pi} \,. \tag{7.A.1}$$

In the light of these definitions, using Figure 7.22 and using the even function property $\cos(\theta) = \cos(-\theta)$ principal deviatoric Cauchy stress components s_A read

$$s_\nu = \frac{2}{3}\sigma_{vMises} \cos\left(\frac{2[\nu-1]}{3}\pi - \theta\right) \text{ for } \nu = 1, 2, 3 \,, \tag{7.A.2}$$

with $\cos(-\theta) + \cos([2/3]\pi - \theta) + \cos([4/3]\pi - \theta)$ vanishing identically. The principal Cauchy stress components using $\sigma_\nu = s_\nu + p$ and the definition of the stress triaxiality ratio $\eta := p/\sigma_{vMises}$ read

$$\sigma_\nu = \sigma_{vMises} \left[\eta + \frac{2}{3}\cos\left(\frac{2[\nu-1]}{3}\pi - \theta\right)\right] \text{ for } \nu = 1, 2, 3 \,. \tag{7.A.3}$$

σ_ν can also be represented in terms of $\bar{\theta}$ by the substitution of Equation (7.A.1) into Equation (7.A.3) with $\sin(\pi + \theta) = -\sin(\theta)$

$$\sigma_\nu = \sigma_{vMises} \left[\eta + \frac{2}{3}\sin\left(\frac{[2\nu-1]}{3}\pi + \frac{\pi}{6}\bar{\theta}\right)\right] \text{ for } \nu = 1, 2, 3 \,. \tag{7.A.4}$$

Another notation for the Lode parameter is $-1 \leq L \leq 1$ with

$$L = \frac{2\sigma_2 - \sigma_1 - \sigma_3}{\sigma_1 - \sigma_3} \,. \tag{7.A.5}$$

Indeed Equation (7.A.5) is the originally form which appears in [321]. With the ordered set of principal stresses $\sigma_1 \geq \sigma_2 \geq \sigma_3$, the definition of a shear state of stress can also be most naturally done through normalized maximum shear stress, $2[\tau_{max}/\sigma_{vMises}]$ where $\tau_{max} = [1/2][\sigma_1 - \sigma_3]$. Note that for pure hydrostatic stress states $2[\tau_{max}/\sigma_{vMises}]$ vanishes whereas for uniaxial tension and compression $2[\tau_{max}/\sigma_{vMises}]$ has the value of 1 and -1 respectively. Coming to a simple shear stress state one has $2[\tau_{max}/\sigma_{vMises}] = 2/\sqrt{3}$. $2[\tau_{max}/\sigma_{vMises}]$ could be linked to L using

$$\frac{2\tau_{max}}{\sigma_{vMises}} = \frac{2}{\sqrt{L^2 + 3}} \,. \tag{7.A.6}$$

Finally, the following relation bridges the gap between θ and L and allows us to form representations in terms of the pair (η, θ) consistently

$$L = \sqrt{3} \tan \left(\theta - \frac{\pi}{6} \right) . \qquad (7.A.7)$$

Using Equation (7.A.5) one has, [192]

$$\sigma_\nu = \sigma_{\text{vMises}} \left[\eta + \frac{2L + 3\,[2 - \nu] - 3L\,[2 - \nu]^2}{3\sqrt{L^2 + 3}} \right] \quad \text{for } \nu = 1, 2, 3 . \qquad (7.A.8)$$

Eventually, defined parameters can be given as follows for ten conventional test specimens for fracture calibration following [20]. In the table, for the expressions of η for the notched round bars under tension or compression R stands for the radius of a notch and r is the radius of a round bar at the notch. For the flat grooved plates under tension R stands for the radius of the groove and t is the thickness of a flat grooved plate at the groove.

Table 7.5.: Analytical expressions representing the ideal state of stress for ten conventional fracture calibration specimens (adapted from [20]).

ID	Type of the specimen	η	θ	$\bar{\theta}$	L
1.	Smooth round bar, tension	$1/3$	0	1	-1
2.	Notched round bars, tension, [59]	$1/3 + \sqrt{2} \log(1 + r/[2R])$	0	1	-1
3.	Plastic plane strain, tension	$1/\sqrt{3}$	$\pi/6$	0	0
4.	Flat grooved plates, tension, [28]	$1/\sqrt{3}[1 + 2\log(1 + t/[4R])]$	$\pi/6$	0	0
5.	Torsion or shear	0	$\pi/6$	0	0
6.	Cylinders, compression	$-1/3$	$\pi/3$	-1	1
7.	Equi-biaxial plane stress tension	$2/3$	$\pi/3$	-1	1
8.	Equi-biaxial plane stress compression	$-2/3$	0	1	-1
9.	Plastic plane strain, compression	$-1/\sqrt{3}$	$\pi/6$	0	0
10.	Notched round bars, compression	$-1/3 - \sqrt{2} \log(1 + r/[2R])$	$\pi/3$	-1	1

7.B. Non-rotating Principal Axes of Deformation

Let $(\boldsymbol{N}_1, \boldsymbol{N}_2, \boldsymbol{N}_3)$ and $(\boldsymbol{n}_1, \boldsymbol{n}_2, \boldsymbol{n}_3)$ respectively denote the orthogonal material and spatial unit vector triads. Then the two-point tensor $\boldsymbol{F}$ is represented as $\boldsymbol{F} = \sum_{\nu=1}^{3} \lambda_\nu \, \boldsymbol{n}_\nu \otimes \boldsymbol{N}_\nu$ whereas the spatial tensor $\boldsymbol{b} = \sum_{\nu=1}^{3} \lambda_\nu^2 \, \boldsymbol{n}_\nu \otimes \boldsymbol{n}_\nu$ and the material tensor $\boldsymbol{C} = \sum_{\nu=1}^{3} \lambda_\nu^2 \, \boldsymbol{N}_\nu \otimes \boldsymbol{N}_\nu$. The two-point rotation tensor $\boldsymbol{R}$ which is found using the polar decomposition of the deformation gradient with $\boldsymbol{F} = \boldsymbol{R} \cdot \boldsymbol{U}$ transforms the material vector triad into the spatial vector triad viz $\boldsymbol{n}_\nu = \boldsymbol{R} \cdot \boldsymbol{N}_\nu$ where $\boldsymbol{U} = \boldsymbol{C}^{[1/2]} = \sum_{\nu=1}^{3} \lambda_\nu \, \boldsymbol{N}_\nu \otimes \boldsymbol{N}_\nu$. denotes the material stretch tensor. Now, for the deformation modes with non-rotating principal vector triad one has $\boldsymbol{R} = \boldsymbol{1}$. Hence, considering the principal axes of deformation parallel to the orthogonal unit vectors of the Cartesian axes $(\boldsymbol{a}_1, \boldsymbol{a}_2, \boldsymbol{a}_3)$ one has $\boldsymbol{n}_\nu = \boldsymbol{N}_\nu = \boldsymbol{a}_\nu$ for $\nu = 1, 2, 3$ where $\boldsymbol{a}_1 = (1, 0, 0)^\top$, $\boldsymbol{a}_2 = (0, 1, 0)^\top$ and $\boldsymbol{a}_3 = (0, 0, 1)^\top$. Thus, the total stretch components λ_ν are defined as the multiplication of the elastic λ_ν^e and plastic λ_ν^p stretches $\lambda_\nu = \lambda_\nu^e \lambda_\nu^p$ for $\nu = 1, 2, 3$ and the following matrix representations are made possible

$$\boldsymbol{F} = \begin{pmatrix} \lambda_1^e \lambda_1^p & 0 & 0 \\ 0 & \lambda_2^e \lambda_2^p & 0 \\ 0 & 0 & \lambda_3^e \lambda_3^p \end{pmatrix} \text{ where } \boldsymbol{F}^e = \begin{pmatrix} \lambda_1^e & 0 & 0 \\ 0 & \lambda_2^e & 0 \\ 0 & 0 & \lambda_3^e \end{pmatrix} \text{ and } \boldsymbol{F}^p = \begin{pmatrix} \lambda_1^p & 0 & 0 \\ 0 & \lambda_2^p & 0 \\ 0 & 0 & \lambda_3^p \end{pmatrix} .$$

$$(7.B.1)$$

Since with this assumption $\boldsymbol{F}^{\top} \cdot \boldsymbol{F} \equiv \boldsymbol{F} \cdot \boldsymbol{F}^{\top}$, one has

$$
\boldsymbol{b} \equiv \boldsymbol{C} = \begin{pmatrix} [\lambda_1^e \lambda_1^p]^2 & 0 & 0 \\ 0 & [\lambda_2^e \lambda_2^p]^2 & 0 \\ 0 & 0 & [\lambda_3^e \lambda_3^p]^2 \end{pmatrix} . \tag{7.B.2}
$$

Also $\boldsymbol{b}^e$ and $[\boldsymbol{b}^e]^{-1}$ read

$$
\boldsymbol{b}^e = \begin{pmatrix} [\lambda_1^e]^2 & 0 & 0 \\ 0 & [\lambda_2^e]^2 & 0 \\ 0 & 0 & [\lambda_3^e]^2 \end{pmatrix} \text{ and } [\boldsymbol{b}^e]^{-1} = \begin{pmatrix} 1/[\lambda_1^e]^2 & 0 & 0 \\ 0 & 1/[\lambda_2^e]^2 & 0 \\ 0 & 0 & 1/[\lambda_3^e]^2 \end{pmatrix} . \tag{7.B.3}
$$

Similarly, $\boldsymbol{C}^p$ and $[\boldsymbol{C}^p]^{-1}$ are derived as

$$
\boldsymbol{C}^p = \begin{pmatrix} [\lambda_1^p]^2 & 0 & 0 \\ 0 & [\lambda_2^p]^2 & 0 \\ 0 & 0 & [\lambda_3^p]^2 \end{pmatrix} \text{ and } [\boldsymbol{C}^p]^{-1} = \begin{pmatrix} 1/[\lambda_1^p]^2 & 0 & 0 \\ 0 & 1/[\lambda_2^p]^2 & 0 \\ 0 & 0 & 1/[\lambda_3^p]^2 \end{pmatrix} . \tag{7.B.4}
$$

Hence, one has

$$
-\frac{1}{2} \boldsymbol{F} \cdot [[\boldsymbol{C}^p]^{-1}]^{\dot{}} \cdot [\boldsymbol{F}]^{\top} \cdot [\boldsymbol{b}^e]^{-1} = \begin{pmatrix} \dot{\lambda}_1^p/\lambda_1^p & 0 & 0 \\ 0 & \dot{\lambda}_2^p/\lambda_2^p & 0 \\ 0 & 0 & \dot{\lambda}_3^p/\lambda_3^p \end{pmatrix} . \tag{7.B.5}
$$

The condition of non-rotating principal axes also sets the stage for the additive decomposition of the spatial logarithmic strain tensor $\boldsymbol{e} = 1/2 \log(\boldsymbol{b})$ into elastic $\boldsymbol{e}^e$ and plastic $\boldsymbol{e}^p$ parts with $\boldsymbol{e} = \boldsymbol{e}^e + \boldsymbol{e}^p$ where

$$
\boldsymbol{e}^e = \begin{pmatrix} \log(\lambda_1^e) & 0 & 0 \\ 0 & \log(\lambda_2^e) & 0 \\ 0 & 0 & \log(\lambda_3^e) \end{pmatrix} \text{ and } \boldsymbol{e}^p = \begin{pmatrix} \log(\lambda_1^p) & 0 & 0 \\ 0 & \log(\lambda_2^p) & 0 \\ 0 & 0 & \log(\lambda_3^p) \end{pmatrix} . \tag{7.B.6}
$$

Taking the material time derivative supplies the rate additive form $\dot{\boldsymbol{e}} = \dot{\boldsymbol{e}}^e + \dot{\boldsymbol{e}}^p$. Using $\boldsymbol{l} = \boldsymbol{d} + \boldsymbol{w}$ with the rate of deformation tensor $\boldsymbol{d} = \operatorname{sym}(\boldsymbol{l})$ and the spin tensor $\boldsymbol{w} = \operatorname{skw}(\boldsymbol{l})$, for current conditions one has $\boldsymbol{w} = \boldsymbol{0}$. Hence, one has $\dot{\boldsymbol{e}} = \boldsymbol{d}$

$$
\dot{\boldsymbol{e}} = \begin{pmatrix} \dot{\lambda}_1/\lambda_1 & 0 & 0 \\ 0 & \dot{\lambda}_2/\lambda_2 & 0 \\ 0 & 0 & \dot{\lambda}_3/\lambda_3 \end{pmatrix} . \tag{7.B.7}
$$

With $\boldsymbol{d} = \boldsymbol{d}^e + \boldsymbol{d}^p$ also $\boldsymbol{d}^e = \dot{\boldsymbol{e}}^e$ and $\boldsymbol{d}^p = \dot{\boldsymbol{e}}^p$ one reaches

$$
\dot{\boldsymbol{e}}^p = -\frac{1}{2} \boldsymbol{F} \cdot [[\boldsymbol{C}^p]^{-1}]^{\dot{}} \cdot \boldsymbol{F}^{\top} \cdot [\boldsymbol{b}^e]^{-1} = \dot{\alpha}^p \frac{3}{2} \frac{\boldsymbol{s}}{\sigma_{\text{vMises}}} . \tag{7.B.8}
$$

Part III.

Temperature Effects on Damage Driven Localization and Fracture

8. Modeling of Fracture in Small Punch Tests for Small- and Large-Scale Yielding Conditions at Various Temperatures

In this chapter, a systematic numerical study on temperature dependent fracture mode change in small punch tests is presented. Following Needleman-Tvergaard [Needleman and Tvergaard, *Int. J. Frac.*, **101**, 73, (2000)], the material is modeled as thermo-inelastic, where the ductile fracture mode, by void nucleation, growth and coalescence is accounted for by Gurson's porous metal plasticity [Gurson, *J. Engng. Mater. Tech.*, **99**, 2, (1977)]. The brittle fracture mode by cleavage is accounted for by Ritchie–Knott–Rice's deterministic maximum principal stress criterion [Ritchie, Knott and Rice, *J. Mech. Phys. Solids*, **21**, 395, (1973)]. The well-known problem of mesh dependence associated with softening material behavior is remedied by using an integral type nonlocal formulation similar to that presented in [Tvergaard and Needleman, *Int. J. Solids Structures*, **32**, 1063, (1995)]. Two length scales are incorporated into the constitutive relations: The ductile fracture length scale is based on the average inclusion distance and associated with the nonlocal evolution equation for the porosity. The brittle fracture length scale is based on the average grain size and associated with the material region at which the maximum principal stress is averaged out. The material model is used to simulate small punch tests at $-196°$C, $-158°$C and $25°$C of notched and unnotched specimens of P91 steel representative for small- and large-scale yielding conditions, respectively. The simulated fracture modes and patterns show a very good agreement with experiments: for $-196°$C brittle fracture propagating normal to the maximum (tensile) principal stress prevails. For $25°$C ductile fracture is governed by shear localization with voidage. The simulations also show that the deformation energy is considerably higher for the upper shelf tests compared to the lower shelf tests.

8.1. Introduction

The ductile–brittle transition, typically seen in bcc and hcp metals, involves a change of fracture mode as a function of test temperature and/or loading rate. Brittle fracture occurs by cleavage along specific crystallographic planes at lower temperatures, associated with the lower shelf in deformation energy, whereas ductile fracture goes along with progressive cavitation until void coalescence at higher temperatures, associated with the upper shelf. The temperature at which the prevailing mode of failure changes from brittle to ductile is named ductile–brittle transition temperature.

At a finer scale this transition is explained by minute energetic requirements for the evolution of the defect structure. Once certain conditions are met, brittle propagation of a sharp crack front with free surface development and atomic bond rupture is favored over dislocation emission and/or mobility and concomitant crack tip blunting. Brittle fracture is referred to as a

low energy fracture, whereas ductile fracture is a high energy fracture since the overall process zone is larger due to crack blunting and plastic zone development. Ductile fracture by void growth occurs under relatively large strains as compared to brittle fracture in which the driving mechanism is the critical stress over the cleavage grain (see, e.g., [230]). As the flow stress is temperature and rate dependent, large stresses needed for brittle fracture are achieved only for low temperatures and/or high strain rates; otherwise ductile fracture at high strains is observed.

In the present chapter, the ductile–brittle transition at the macroscale in small punch tests is modeled at various temperatures. Small punch testing was first developed in the early 1980's for determining the post irradiation mechanical properties including ductile–brittle transition temperature [196]. The method possesses great advantage over the conventional Charpy test due to the small amount of material needed. Small punch specimens are usually disk-shaped with thicknesses in the range of $0.25 - 0.5$ mm and diameters of $3 - 10$ mm. Therefore, the test is virtually non-destructive, and samples can even be extracted from big components in service. Owing to this reduced material requirement, small punch testing is also applied when sampling volume is limited, for instance, to the heat affected zone of a weldment [107]. In previous works, it was reported that the transition temperatures determined by small punch tests were considerably lower than the ones determined by Charpy tests [22, 234, 112, 355]. A linear correlation between the small punch transition temperature and the conventional ductile–brittle transition temperature was proposed in the European Code of Practice of small punch testing [69]. Possible reasons for the discrepancy were attributed to the stress triaxiality, size and strain rate effects.

Despite the wide range of literature on the transition temperature as determined by small punch testing, there has been no attempt to assess the ductile and brittle crack patterns as well as the transition temperature in a unified numerical framework. Following the lines of Needleman and Tvergaard [230], a temperature coupled Gurson-Tvergaard-Needleman porous metal visco-plasticity is used for modeling the ductile fracture involving progressive cavitation with the recent shear modification by [224]. The brittle fracture is modeled deterministically following the Ritchie–Knott–Rice (RKR) model [260]. The motivation for the selection of a porous metal plasticity model stems from the experimental evidence of cavitation on fracture surfaces. Physically, ductile and brittle fracture are nonlocal processes with interacting sources of disorder at various length scales. Thus, a nonlocal formulation is required with incorporation of length scales. Through that an accurate control of the size of the localization zone (important in consideration of the size effects) on the course of deformation is supplied. In addition, the problem of pathological mesh dependence of the numerical simulations is removed.

The model is validated by comparisons between the numerical analysis and experimental results obtained at -196°C, -158°C and 25°C. Notched and unnotched specimen geometries are simulated corresponding to the small- and large-scale yielding conditions, respectively. The experimental evaluation of the $J - R$ (J resistance) curves for P91 shows that the transition temperature is around -150°C based on experimental and numerical load-displacement curves as well as optical and SEM images revealing the crack patterns and fracture surface morphologies. It is shown that, as anticipated, for both notched and unnotched tests ductile fracture at the upper shelf follows the plastic localization bands whose sizes are of the order of magnitude of the utilized length scale. This amounts to a mixed Mode I Mode II fracture. Brittle cracks propagate under Mode I conditions in the direction normal to the maximum principal stress, with small-scale yielding prevailing at the crack tip. This is in agreement with the experimental observation of cleavage facets orthogonal to the maximum principal stress direction.

The role of stress gradients in identifying the length scale and critical fracture threshold associated with brittle fracture is investigated by comparing simulation results for the notched and the unnotched specimens. The simultaneous consideration of the notched and unnotched cases considerably narrows down the ranges of admissible material parameters associated with the Ritchie–Rice–Knott criterion.

The effect of temperature is investigated by isothermal analyses with various ambient temperatures. The model developed will be helpful to further analyze the effects of strain rate, specimen size, different notch and puncher head geometries, etc., on the transition temperature. Owing to its multi-axiality and loading history, the small punch test is most sensitive as a model validation tool which is why the present application of a numerical modeling scheme to small punch testing constitutes a novel approach.

8.2. Theory

8.2.1. Hypoelastic-plastic Model

Let $\boldsymbol{X}$ and $\boldsymbol{x} := \boldsymbol{\varphi}(\boldsymbol{X}, t)$ denote the particle positions in the reference (undeformed) configuration $\mathcal{B}_0$ and current (deformed) configuration $\mathcal{B}$, respectively. $\boldsymbol{F} := \partial_{\boldsymbol{X}} \boldsymbol{x}$ defines the deformation gradient of the nonlinear motion map $\boldsymbol{\varphi} : \mathcal{B}_0 \times \mathbb{R}^{\geq 0} \to \mathbb{R}^3$. Let $\boldsymbol{l} := \dot{\boldsymbol{F}} \cdot \boldsymbol{F}^{-1} = \partial_{\boldsymbol{x}} \boldsymbol{v}$ denote the velocity gradient, with $\boldsymbol{v} = \dot{\boldsymbol{x}}$. Splitting $\boldsymbol{l}$ into its symmetric $\boldsymbol{d} := \operatorname{sym}(\boldsymbol{l})$ and skewsymmetric $\boldsymbol{w} := \operatorname{skw}(\boldsymbol{l})$ parts via $\boldsymbol{l} = \boldsymbol{d} + \boldsymbol{w}$ where $\boldsymbol{d}$ denotes the rate of deformation tensor the following additive decomposition of $\boldsymbol{d}$ is postulated

$$ \boldsymbol{d} = \boldsymbol{d}_\mathrm{e} + \boldsymbol{d}_\mathrm{p} + \boldsymbol{d}_\Theta \,, \tag{8.2.1} $$

with $\boldsymbol{d}_\mathrm{e}$, $\boldsymbol{d}_\mathrm{p}$ and $\boldsymbol{d}_\Theta$ representing its elastic, plastic and thermal parts, respectively. This forms the basis of hypoelastic-plastic formulations which rely on certain objective rates of the selected stress measures. The Green–Naghdi–McInnis rate of the Cauchy (true) stresses is used which requires the rotationally neutralized rate of the deformation tensor $\dot{\hat{\boldsymbol{\epsilon}}}$ defined as

$$ \dot{\hat{\boldsymbol{\epsilon}}} = \boldsymbol{R}^\top \cdot [\boldsymbol{d}_\mathrm{e} + \boldsymbol{d}_\mathrm{p} + \boldsymbol{d}_\Theta] \cdot \boldsymbol{R} = \dot{\hat{\boldsymbol{\epsilon}}}_\mathrm{e} + \dot{\hat{\boldsymbol{\epsilon}}}_\mathrm{p} + \dot{\hat{\boldsymbol{\epsilon}}}_\Theta \,, \tag{8.2.2} $$

with $\dot{\hat{\boldsymbol{\epsilon}}}_\mathrm{e} := \boldsymbol{R}^\top \cdot \boldsymbol{d}_\mathrm{e} \cdot \boldsymbol{R}$, $\dot{\hat{\boldsymbol{\epsilon}}}_\mathrm{p} := \boldsymbol{R}^\top \cdot \boldsymbol{d}_\mathrm{p} \cdot \boldsymbol{R}$ and $\dot{\hat{\boldsymbol{\epsilon}}}_\Theta := \boldsymbol{R}^\top \cdot \boldsymbol{d}_\Theta \cdot \boldsymbol{R} = \boldsymbol{d}_\Theta$. Here, $\boldsymbol{R}$ denotes the rotation tensor, carried out by the polar decomposition of the deformation gradient $\boldsymbol{F} = \boldsymbol{R} \cdot \boldsymbol{U}$, with $\boldsymbol{U}$ representing the symmetric right stretch tensor. Similarly, a pull back operation on the Cauchy stress tensor $\boldsymbol{\sigma}$ with the rotation tensor gives its rotationally neutralized counterpart: $\widehat{\boldsymbol{\sigma}} := \boldsymbol{R}^\top \cdot \boldsymbol{\sigma} \cdot \boldsymbol{R}$. Its material time derivative $\dot{\widehat{\boldsymbol{\sigma}}}$ can be objectively integrated. Using the thermo-elastic constitutive relations one has

$$ \dot{\widehat{\boldsymbol{\sigma}}} = \boldsymbol{\mathcal{C}}_\mathrm{e} : \left[\dot{\hat{\boldsymbol{\epsilon}}} - \dot{\hat{\boldsymbol{\epsilon}}}_\mathrm{p} - \dot{\hat{\boldsymbol{\epsilon}}}_\Theta \right] = \boldsymbol{\mathcal{C}}_\mathrm{e} : \dot{\hat{\boldsymbol{\epsilon}}}_\mathrm{e} \,, \tag{8.2.3} $$

where $\boldsymbol{\mathcal{C}}_\mathrm{e}$ denotes the elastic constitutive tensor with, for isotropic materials,

$$ \boldsymbol{\mathcal{C}}_\mathrm{e} := \frac{\nu E}{[1+\nu][1-2\nu]} \left[\mathbf{1} \otimes \mathbf{1} \right] + \frac{E}{2[1+\nu]} \left[\mathbf{1} \overline{\otimes} \mathbf{1} + \mathbf{1} \underline{\otimes} \mathbf{1} \right] \,. \tag{8.2.4} $$

E and ν denote Young's modulus and Poisson's ratio, respectively. Moreover,

$$ \dot{\hat{\boldsymbol{\epsilon}}}_\Theta = \boldsymbol{d}_\Theta = \alpha_\Theta \dot{\Theta} \mathbf{1} \,, \tag{8.2.5} $$

where α_Θ denotes the thermal expansion coefficient and Θ the temperature.

8.2.2. Model for Ductile Fracture - Gurson's Porous Plasticity - Local Formulation

The ductile fracture mode by progressive cavitation of a porous solid with a void volume fraction f is based on Gurson's dilatant plasticity model [110]. The model is extended by parameters q_1, q_2 and q_3 in [304, 306] to achieve better agreement with numerical analyses of unit cells, and by the bilinear function $f^*(f)$ in [308] to account for rapid void coalescence prior to failure. The hydrostatic stress dependent flow potential Φ_p is then formulated as

$$\Phi_\mathrm{p} = \left[\frac{\sigma_\mathrm{eq}}{\sigma_\mathrm{y}}\right]^2 + 2q_1 f^* \cosh\left(\frac{3}{2}\frac{q_2\sigma_\mathrm{m}}{\sigma_\mathrm{y}}\right) - \left[1 + q_3 f^{*2}\right] \leq 0 \,. \tag{8.2.6}$$

$\sigma_\mathrm{eq} = 3/2\,\mathrm{dev}(\widehat{\boldsymbol{\sigma}}) : \mathrm{dev}(\widehat{\boldsymbol{\sigma}})$ is the equivalent von Mises stress, $\sigma_\mathrm{m} = \mathrm{tr}(\widehat{\boldsymbol{\sigma}})/3$ is the hydrostatic stress and q_1, q_2 and q_3 are material parameters[1]. When f_c denotes the critical void volume fraction at incipient coalescence, f_F the fraction at failure and the material parameter $f_\mathrm{u}^* = 1/q_1$, the bilinear function $f^*(f)$ is defined as[2]

$$f^*(f) = \begin{cases} f & f \leq f_\mathrm{c}\,, \\ f_\mathrm{c} + [f_\mathrm{u}^* - f_\mathrm{c}]\,[f - f_\mathrm{c}]\,/\,[f_\mathrm{F} - f_\mathrm{c}] & f > f_\mathrm{c}\,. \end{cases} \tag{8.2.7}$$

The thermo-visco-plastic hardening of the material matrix is described by the flow stress σ_y which accounts for strain, strain rate and temperature dependences. Hence, letting e_p denote the equivalent plastic strain and $\dot{e}_\mathrm{p}$ its rate, a Johnson–Cook type multiplicative form is assumed

$$\sigma_\mathrm{y}\left(e_\mathrm{p}, \dot{e}_\mathrm{p}, \Theta\right) = h_\mathrm{y}\left(e_\mathrm{p}\right) r_\mathrm{y}\left(\dot{e}_\mathrm{p}\right) t_\mathrm{y}\left(\Theta\right) \,, \tag{8.2.8}$$

where h_y, r_y and t_y denote the functions of strain hardening, strain rate hardening and thermal softening which are defined as

$$\begin{aligned} h_y\left(e_\mathrm{p}\right) &= \sigma_\mathrm{y0} + Be_\mathrm{p}^n\,, \\ r_y\left(\dot{e}_\mathrm{p}\right) &= 1 + C\log\left(\dot{e}_\mathrm{p}/\dot{e}_\mathrm{p0}\right)\,, \\ t_y\left(\Theta\right) &= 1 - \Omega^m\,, \end{aligned} \tag{8.2.9}$$

where σ_y0 is the initial yield stress. The strain hardening is controlled by B and n, whereas strain rate and temperature dependence of hardening are controlled by C and m, respectively. The reference strain rate is denoted by $\dot{e}_\mathrm{p0}$.

$$\Omega = \left[\Theta - \Theta_\mathrm{ref}\right] / \left[\Theta_\mathrm{melt} - \Theta_\mathrm{ref}\right] \,, \tag{8.2.10}$$

is the homologous temperature with Θ_ref and Θ_melt representing the reference and the melting temperatures, respectively.

Using the normality postulate, the plastic part of the rate of deformation tensor at the rotationally neutralized configuration is defined as

$$\dot{\widehat{\boldsymbol{\epsilon}}}_\mathrm{p} = \dot{\gamma}\partial_{\widehat{\boldsymbol{\sigma}}}\Phi_\mathrm{p} \,, \tag{8.2.11}$$

which is not traceless due to the hydrostatic stress dependence of Φ_p. Here, $\dot{\gamma}$ denotes the plastic multiplier[3].

---

[1] The plastic potential reduces to that of Gurson's original proposal for $q_1 = q_2 = q_3 = 1$, and to that of von Mises isochoric plasticity for $q_1 = q_3 = 0$.

[2] As $f \to f_\mathrm{F}$, $f^* \to f_\mathrm{u}^*$ and the material loses its load carrying capacity which defines ductile fracture.

[3] The eventual framework is a consistency type rather than an over-stress type, see, e.g., [326]. That is, the computation of the plastic multiplier $\dot{\gamma}$ exploits the consistency condition viz. $\dot{\Phi}_\mathrm{p} = 0$.

According to the plastic work equivalence $[1 - f]\, \sigma_\mathrm{y} \dot{e}_\mathrm{p} = \widehat{\boldsymbol{\sigma}} : \dot{\widehat{\boldsymbol{\epsilon}}}_\mathrm{p}$, the equivalent plastic strain rate reads

$$\dot{e}_\mathrm{p} = \frac{\widehat{\boldsymbol{\sigma}} : \dot{\widehat{\boldsymbol{\epsilon}}}_\mathrm{p}}{[1 - f]\, \sigma_\mathrm{y}}. \tag{8.2.12}$$

The kinetic evolution of the void volume fraction involves nucleation and growth taking place during fully developed plastic flow. The time rate of change of the total void volume fraction is formulated additively in terms of void nucleation rate $\dot{f}_\mathrm{n}$ and void growth rate $\dot{f}_\mathrm{g}$

$$\dot{f} = \dot{f}_\mathrm{n} + \dot{f}_\mathrm{g}. \tag{8.2.13}$$

Assuming a strain dependent void nucleation [75], $\dot{f}_\mathrm{n}$ is written as

$$\dot{f}_\mathrm{n} = A_\mathrm{N} \dot{e}_\mathrm{p} \ \text{where} \ A_\mathrm{N} = A_\mathrm{N}\left(e_\mathrm{p}\right) = \frac{f_\mathrm{N}}{S_\mathrm{N} \sqrt{2\pi}} \exp\left(-\frac{[e_\mathrm{p} - e_\mathrm{p\,N}]^2}{2 S_\mathrm{N}^2}\right). \tag{8.2.14}$$

In Equation 8.2.14, $e_\mathrm{p\,N}$ and S_N denote the mean equivalent plastic strain at the incipient nucleation and its standard deviation, respectively. f_N denotes the total source of nucleation for the void volume fraction.

Following [224], $\dot{f}_\mathrm{g}$ is further split into

$$\dot{f}_\mathrm{g} = \dot{f}_\mathrm{g\,normal} + \dot{f}_\mathrm{g\,shear}, \tag{8.2.15}$$

with $\dot{f}_\mathrm{g\,normal}$ accounting for the void growth under hydrostatic stresses and reflecting mass conservation:

$$\dot{f}_\mathrm{g\,normal} = [1 - f]\, \mathrm{tr}\, \dot{\widehat{\boldsymbol{\epsilon}}}_\mathrm{p}. \tag{8.2.16}$$

$\dot{f}_\mathrm{g\,normal}$ alone falls short to predict fracture modes under low stress triaxiality ratios; see, e.g., experimental studies reported in [29] and [39]. Hence, $\dot{f}_\mathrm{g\,shear}$ is introduced to account qualitatively for the softening effects associated with void distortion, void interaction and with material rotation under shear stress states, see, e.g. [224]:

$$\dot{f}_\mathrm{g\,shear} = k_w f\, w(\mathrm{dev}\widehat{\boldsymbol{\sigma}}) \frac{\dot{\widehat{\boldsymbol{\epsilon}}}^p : \mathrm{dev}\,\widehat{\boldsymbol{\sigma}}}{\sigma_{eq}}. \tag{8.2.17}$$

where k_w is a material parameter with a suggested interval $0 \le k_\mathrm{w} \le 3$ [224] and $0 \le w \le 1$ is the function which distinguishes the states of axisymmetric stress from those of generalized shear, i.e., pure shear plus a hydrostatic stress:

$$w\left(\mathrm{dev}\,\widehat{\boldsymbol{\sigma}}\right) = 1 - \left[\frac{27}{2} \frac{J_3}{\sigma_\mathrm{eq}^3}\right]^2. \tag{8.2.18}$$

$J_3 = 1/3\,[\sigma_{ij} - \sigma_\mathrm{m}]\,[\sigma_{jk} - \sigma_\mathrm{m}]\,[\sigma_{ki} - \sigma_\mathrm{m}]$ is the third invariant of the deviatoric stress tensor. Note that $w = 0$ for all axisymmetric stress states, whereas $w = 1$ through $J_3 = 0$ for the states of generalized shear.

Finally, in absence of elastic-plastic heating related to latent elastic and inelastic structural changes or any heat source the temperature increase is due to the heat flux $\boldsymbol{q}$ and plastic dissipation including void nucleation and growth

$$\rho c_\mathrm{p} \dot{\Theta} = -\mathrm{div}\, \boldsymbol{q} + \chi \widehat{\boldsymbol{\sigma}} : \dot{\widehat{\boldsymbol{\epsilon}}}_\mathrm{p}. \tag{8.2.19}$$

ρ and c_p denote the density in the current configuration and the specific heat capacity. Fourier's law is assumed, $\boldsymbol{q} = -k\, \mathbf{grad}\,\Theta$, with k denoting the thermal conductivity. χ is the so-called Taylor–Quinney coefficient denoting the fraction of plastic work converted to heat [296].

8.2.2.1. Integral-Type Nonlocal Regularization

Numerical solutions for the local material models accounting for softening lose uniqueness and suffer from a pathological dependence on the applied discretization. Hence, a consistent regularization requires incorporation of a material length scale which controls the width of localization in the numerical solutions, as demonstrated by, e.g., [45].

The present analysis uses the nonlocal integral type[4] regularization scheme presented in [309] and [229], see also, e.g., [246], [169]. Let $\dot{f}(\boldsymbol{x})$ represent the local damage rate at point $\boldsymbol{x}$ defined at the current configuration. Its delocalization produces $\dot{f}_{\text{nonlocal}}$ at $\boldsymbol{x}$ according to

$$\dot{f}_{\text{nonlocal}}(\boldsymbol{x}) = \int_V \widetilde{\omega}_{\text{ductile}}(\boldsymbol{x}, \boldsymbol{y})\, \dot{f}(\boldsymbol{y})\, \mathrm{d}V(\boldsymbol{y})\,, \tag{8.2.20}$$

where $\boldsymbol{y}$ represents the location vector at current coordinates and V the volume at the current configuration. Let $\omega_{\text{ductile}}(\boldsymbol{x}, \boldsymbol{y})$ denote the bell shaped nonlocal weight function:

$$\omega_{\text{ductile}}(\boldsymbol{x}, \boldsymbol{y}) = \begin{cases} \left[1 - |\boldsymbol{x} - \boldsymbol{y}|^2 / R_{\text{ductile}}^2\right]^2 & \text{if } R_{\text{ductile}} \geq |\boldsymbol{x} - \boldsymbol{y}| \geq 0, \\ 0 & \text{if } R_{\text{ductile}} < |\boldsymbol{x} - \boldsymbol{y}|. \end{cases} \tag{8.2.21}$$

Here R_{ductile} denotes the ductile interaction radius, a parameter proportional to the material characteristic length associated with ductile fracture. The normalized weight function reads

$$\widetilde{\omega}_{\text{ductile}}(\boldsymbol{x}, \boldsymbol{y}) = \frac{\omega_{\text{ductile}}(\boldsymbol{x}, \boldsymbol{y})}{\int_V \omega_{\text{ductile}}(\boldsymbol{x}, \boldsymbol{y})\, \mathrm{d}V(\boldsymbol{y})}\,. \tag{8.2.22}$$

With $\widetilde{\omega}(\boldsymbol{x}, \boldsymbol{y})$ any inconsistency pertaining to unrestricted averaging domains extending over the problem boundary is remedied. As long as boundaries are not violated, $\int_V \omega_{\text{ductile}}(\boldsymbol{x}, \boldsymbol{y})\, \mathrm{d}V(\boldsymbol{y})$ is a constant. The local formulation is recovered for $R_{\text{ductile}} \to 0$, while for finite R_{ductile} the nonlocal formulation makes a difference in the presence of spatial gradients in the ductile damage variable.

8.2.3. Model for Brittle Fracture: The Ritchie–Knott–Rice Maximum Stress Criterion

There exist numerous approaches for modeling cleavage in metallic materials. Based on the Weibull weakest link theory, Beremin's statistical model reflects random nature of brittle fracture and incorporates the effect of plastic flow, see, e.g., [52], [223] or more recently [13]. So-called energy limiters, which, by enforcing saturation in the strain energy function automatically bound stresses in the constitutive equations, constitute another approach to brittle fracture [320]. Continuum damage mechanics models, within a thermodynamics of internal variables formalism, introduce scalar or tensorial damage variables and their conjugate variables which allows not only modeling of stiffness and strength degradation associated with brittle (as well as ductile) damage but also determination of associated inelastic dissipation, see, e.g., [175]. Recently, in order to model the brittle fracture phase in ductile-brittle fracture transition the authors proposed a blend of continuum damage mechanics and Gurson's plasticity, [289]. For additional recent developments in brittle fracture modeling and ductile-brittle fracture transition, the reader is refered to, e.g., [216], [88] and [134], among others. In the current study, following [230] and aiming at deterministic modeling of crack paths, the simple yet powerful Ritchie–Knott–Rice

---

[4]A gradient enhanced nonlocal formulation together with a Gurson-type plastic potential is used in, e.g., [189].

criterion is used for modeling brittle fracture, [260].

Let $\sigma_1(\boldsymbol{x})$ represent the local maximum principal stress at point $\boldsymbol{x}$ defined at the current configuration. Its delocalization reads

$$\sigma_{1,\text{nonlocal}}\left(\boldsymbol{x}\right) = \int_V \widetilde{\omega}_{\text{brittle}}\left(\boldsymbol{x},\boldsymbol{y}\right)\sigma_1\left(\boldsymbol{y}\right)\mathrm{d}V\left(\boldsymbol{y}\right), \tag{8.2.23}$$

where $\omega_{\text{brittle}}\left(\boldsymbol{x},\boldsymbol{y}\right)$ denotes the following nonlocal weight function:

$$\omega_{\text{brittle}}\left(\boldsymbol{x},\boldsymbol{y}\right) = \begin{cases} 1 & \text{if } R_{\text{brittle}} \geq |\boldsymbol{x}-\boldsymbol{y}| \geq 0, \\ 0 & \text{if } R_{\text{brittle}} < |\boldsymbol{x}-\boldsymbol{y}|. \end{cases} \tag{8.2.24}$$

Here R_{brittle} denotes the brittle interaction radius, defining characteristic length associated with brittle fracture. The normalized weight function reads

$$\widetilde{\omega}_{\text{brittle}}\left(\boldsymbol{x},\boldsymbol{y}\right) = \frac{\omega_{\text{brittle}}\left(\boldsymbol{x},\boldsymbol{y}\right)}{\int_V \omega_{\text{brittle}}\left(\boldsymbol{x},\boldsymbol{y}\right)\mathrm{d}V\left(\boldsymbol{y}\right)}. \tag{8.2.25}$$

According to the RKR criterion [260] once $\sigma_{1,\text{nonlocal}}\left(\boldsymbol{x}\right)$ reaches a critical value σ_c, brittle fracture results. The criterion can be formulated as

$$\sigma_{1,\text{nonlocal}} = \sigma_c. \tag{8.2.26}$$

Following [230], σ_c is independent of temperature and strain rate. R_{brittle} is linked to the size of the cleavage grain V_{cleavage}. Hence, the interaction radius of brittle fracture is larger than that of intragranular ductile fracture. One should note that the RKR criterion does not require plastic flow. By being non-cumulative, it is different from the nonlocal treatment of Gurson's model, as each integration associated with the time step is independent.

8.3. Experiments

In small punch fracture tests a non-deformable hemispherical puncher loads a rigidly clamped disk-shaped specimen at constant displacement rate deforming it through an aperture in the lower die. The specimen design recommended in the Code of Practice is a disk with diameter $d=8$ mm and thickness 0.5 mm [69]. During the test, the puncher force and the central disk deflection (or puncher displacement) are recorded. Small punch force-deflection (or displacement) curves are then used to estimate mechanical properties such as yield stress, ultimate tensile strength and ductile–brittle transition temperature.

8.3.1. Chemical Composition and Microstructure Observation of P91 Steel

In this study, a ferritic/martensitic P91 steel is used for small punch fracture tests over a wide temperature range. P91 is an advanced steel for high temperature applications, especially, in power plants where creep resistance is of importance. However, components may be exposed to loading at lower or intermediate temperatures as well. Thus, toughness and ductile–brittle transition temperature are important, particularly, if components are subjected to irradiation which deteriorates those properties. The chemical composition of the P91 steel is given in Table 8.1.

Table 8.1.: Chemical composition of P91 in wt%.

C	Si	Mn	P	S	Cr	Mo	V	Ni	Nb	N
0.10	0.27	0.53	0.007	0.01	8.76	0.91	0.2	0.35	0.04	0.038

The prevailing microstructure of P91 consists of tempered martensite (as shown in the optical micrograph in Figure 8.1) and secondary phases that precipitate on martensite lath, prior-austenite grain boundaries and in the ferrite matrix. Precipitates result from the tempering process which is applied to improve the ductility and toughness of the martensitic structure. $M_{23}C_6$ (M denotes Cr, Fe, or Mo) carbides mainly precipitate on prior-austenite grain boundaries, martensite lath and delta-ferrite boundaries whereas smaller MX (M denotes V or Nb, and X is C or N) particles precipitate in the matrix [156].
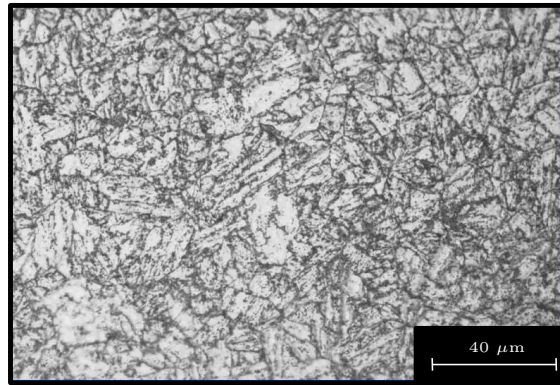
Figure 8.1.: Optical micrograph showing the tempered martensitic structure of P91 steel.

8.3.2. Experimental Setup

The small punch fracture tests were carried out according to the guidelines of the Code of Practice [69]. The specimen holder (see Figure 8.2(a)) consists of upper and lower dies between which the specimens were clamped firmly. The receiving aperture of the holder was 4 mm. The test rig was mounted in a universal testing machine equipped with an environmental chamber allowing temperature control from $-150°C$ to $+300°C$. The actual test temperature range was between $-196°C$ and $25°C$. To achieve the lowest test temperature $-196°C$, the specimen holder was immersed in a vessel (not shown in Figure 2(a)) filled with liquid nitrogen, while the environmental chamber remained idle. The temperature was measured by a Type T thermocouple with an accuracy of $\pm2°C$. Before starting a test, sufficient time was given to the system to reach thermal equilibrium, as verified by pre-tests with an additional thermocouple spot-welded to a dummy specimen. Two Class 2 linear variable displacement transducers mounted to the puncher rod measured the puncher displacement. The small punch disks were deformed under a constant velocity of the cross-head of 0.005 mm/s.

For all small punch tests, disks of 8 mm diameter were used: unnotched disks with 0.5 mm nominal thickness and notched disks with 1 mm thickness. The circular V notches which were produced by electrical discharge machining had a diameter of 2.5 mm, a notch tip radius of approximately 5 μm and different notch depths of 0.3, 0.4 and 0.5 mm (Figures 8.2.(b) and (c)).
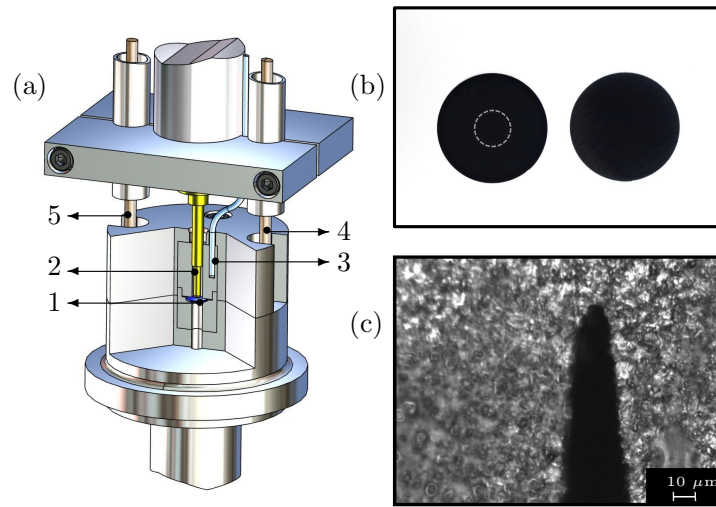
Figure 8.2.: Experimental equipment and specimens: (a) instrumented specimen holder of small punch fracture testing equipment (1: small punch disk, 2: hemispherical ended punch, 3: thermocouple, 4/5: LVDT); (b) small punch disks with a circular V notch (dotted circle represents the notch) and standard unnotched small punch disks; (c) cross-sectional view of notch tip.

8.3.3. Observations at Macroscale

With decreasing temperature reduced bulging and increased cleavage facets (i.e., decreasing amount of plastic deformation until failure) are noted from the overall appearance of the unnotched small punch disks (Figure 8.3.(a)–(c)). Figures 8.3(a)–(f) reveal the macroscopic crack patterns. At 25°C, where the material fails in a ductile manner, the crack pattern is circular. This fracture appearance is valid approximately till −100°C where the ductile–brittle transition regime starts. The crack initiates where necking takes place on the bottom surface, propagates through the thickness and follows a circumferential path along this necking region (Figures 8.3(a), (d), see also [197, 112]). In the transition region (Figure 8.3.(b), (e), test temperature −158°C) ductile and brittle features are observed to coexist. Radial cracks as indications of brittle behavior develop from the widely open semi-circular crack, see, e.g., [171, 117]. At −196°C, disks fail in an almost completely brittle mode with insignificant plastic deformation, exhibiting a more piecewise linear crack propagation path (Figure 8.3(c), (f)).

8.3.4. Observations at Microscale

The fracture mode at the upper shelf (from 25°C down to approximately −100°C) is completely ductile. The fracture surface features dimples and small microvoids (Figure 8.3(g)) which are dominant in number and nucleated by fine MX precipitates. Less frequent larger voids are nucleated by coarser $Mo_{23}C_6$ precipitates. In the transition region, both ductile and brittle fracture features consisting of transgranular cleavage facets co-exist (Figure 8.3(h)). The amount of ductile crack growth gradually decreases with decreasing temperature. At the lowest test temperature, −196°C, the fracture surfaces are almost completely brittle as depicted in Figure 8.3(i).

Figure 8.4 presents fractured notched disks tested at temperatures 25°C, −158°C and −196°C. On the right, the corresponding fracture surfaces are given. For 25°C, the surface is covered by microvoids. Ductile tearing ahead of the notch is revealed. For −158°C, the fracture surface is
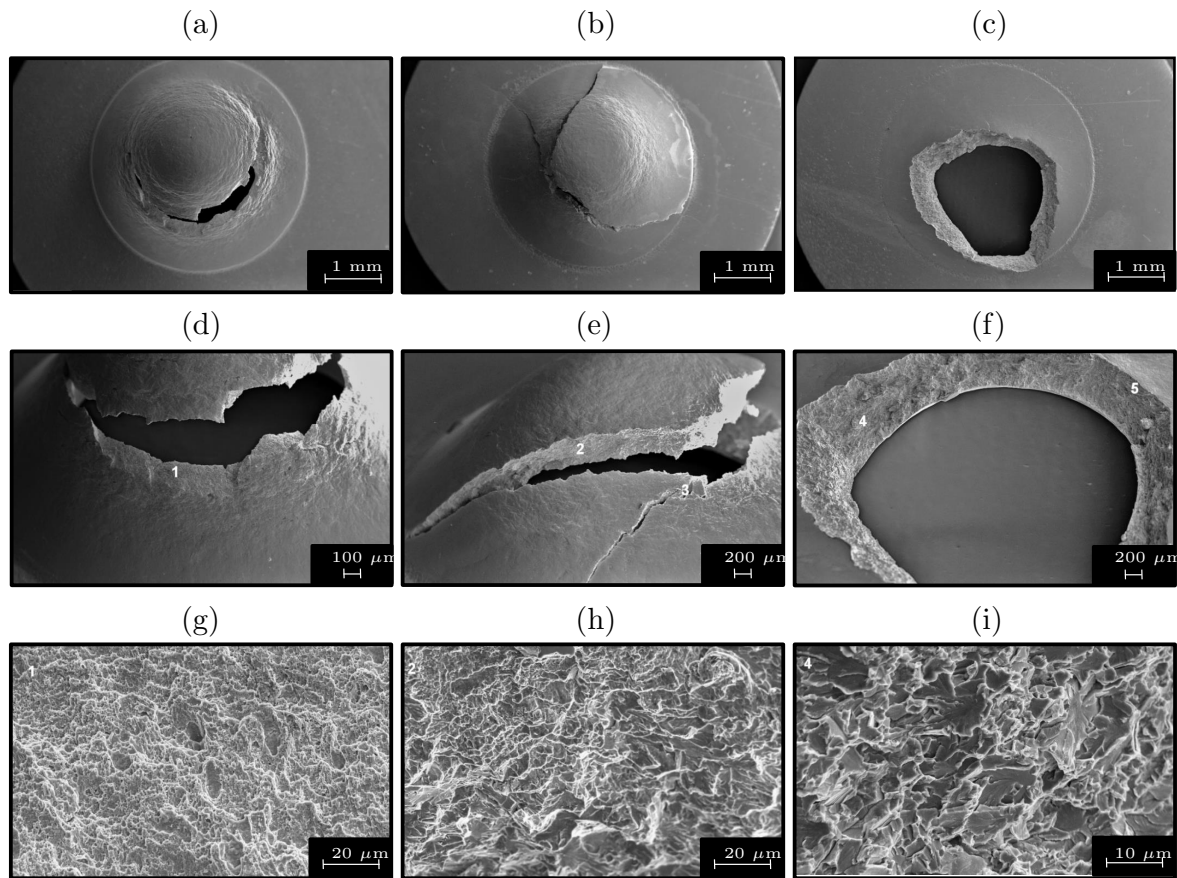
Figure 8.3.: Fracture appearance of failed unnotched small punch disks tested at different temperatures and the corresponding fracture surfaces: (a) 25°C, ductile failure with (d) presenting a close view and (g) its fracture surface; (b) −158°C, ductile to brittle transition region, with (e) presenting a close view and (h) its fracture surface; (c) −196°C, brittle failure, with (f) presenting a close view and (i) its fracture surface.

characteristic of quasi-cleaveage with tear ridges here and there which are the source of plastic deformation noted for this temperature. To observe the fracture surface of the −196°C specimen, the central bulged part was removed to get an SEM image of this zone. Cleavage facets confirmed the brittle fracture prevailing for this temperature.

8.3.5.   Crack Propagation Direction

As stated in [302], the radial symmetry of the notch promotes a plane strain condition. Owing to the small radius of the notch tip, high stress concentrations could be achieved so that the initiation of the crack was found to start from the notch tip.

SEM images of sections of small punch disks for different temperatures representative of the upper shelf, lower shelf and transition region were acquired to identify the crack propagation directions as given in Figure 8.5. For the ductile case (where void initiation and growth are controlled by plastic strain), the crack propagation was found to follow the direction of the notch along the maximum equivalent plastic strain. At 25°C, microvoids nucleated at MX and $Mo_{23}C_6$ in the vicinity of the notch tip grow and coalesce as the strain level increases. Subsequently,
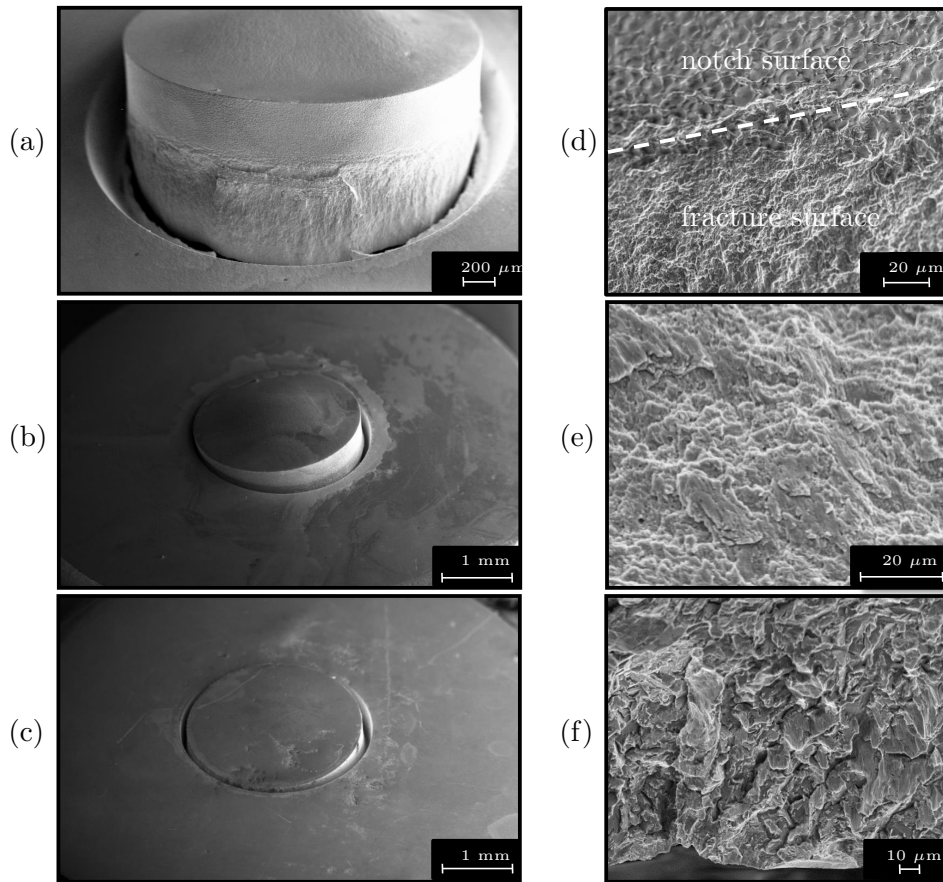
Figure 8.4.: Fracture appearance at the circular notch: small punch disks with notch depth of 0.5 mm tested at (a) $25°C$*, (b)* $-158°C$ *and (c)* $-196°C$ *and the corresponding fracture surfaces given in (d), (e) and (f), respectively. For the disk tested at* $25°C$ *dimples, and for the disk tested at* $-196°C$ *cleavage facets are visible.*

a continuous crack is formed leading to complete fracture. At $-196°C$, microcracks form due to cracking of larger $Mo_{23}C_6$ precipitates [72] in the highly stressed region close to the notch tip and propagate almost perpendicular to the maximum tensile stress. In the transition region both ductile and brittle fracture mechanisms compete, while the macrocrack follows an angle in between the ductile and brittle cases, closer to the brittle case.

Second phase particles which are responsible for void nucleation in ductile fracture mode act as microcrack initiators in the cleavage fracture mode. As schematically illustrated in Figure 8.6(a), ahead of the stress concentration provided by the notch, cracking of brittle second phase particles can take place and microcracks can propagate in the matrix. Cracks may get arrested at grain boundaries or in neighboring grains, if the driving stress is not high enough. Figure 8.6 illustrates possible scenarios. In Figure 8.6.(b) the secondary cracks around the main cleavage crack are visualized according to the sketch given in Figure 8.6(a). If these cracks are observed under higher magnification, different mechanisms can be identified. In Figure 8.6(c) a microcrack initiated from a secondary phase particle and got arrested in the same grain, whereas in (d) a microcrack is noted which propagated into the adjacent grains and got arrested at a grain boundary on one side, and in the matrix on the other side.
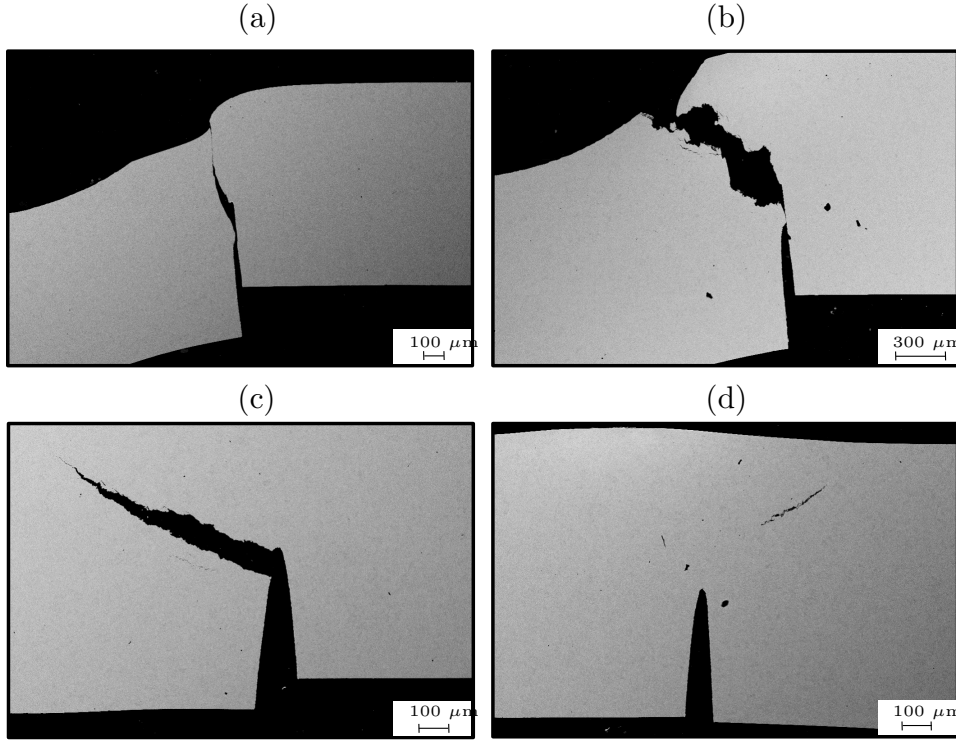
Figure 8.5.: SEM images of specimen sections of the notched small punch disks fractured at (a) 25°C, (b) −158°C and (c) −196°C showing the crack propagation direction from the notch tip, as well as (d) arrested secondary cracks away from the notch tip at −196°C [302].

8.4. Thermomechanical Material Parameters for P91 Steel

Isotropy in both elasticity and plasticity is assumed[5] since the disks were extracted from thick-walled pipes without significant texture. A temperature dependent modulus of elasticity is assumed, $E(\Theta) = -0.1127\,\Theta + 243.6$ in GPa with Θ in K (adapted from [300]). This corresponds to $E = 210$ GPa, $E = 230.6$ GPa and $E = 234.9$ GPa at 25°C, −158°C and −196°C, respectively. Poisson's ratio is $\nu = 0.3$ for all temperatures. The thermal expansion coefficient is $\alpha_\Theta = 1.3 \times 10^{-5}$ K^{-1}, the melting temperature and the reference temperature are $\Theta_{\mathrm{melt}} = 1717$ K and $\Theta_{\mathrm{ref}} = 298$ K, respectively. The specific heat capacity is $c_{\mathrm{p}} = 622$ m^{2}K^{-1}s^{-2} according to data supplied by the producer. Finally, the Taylor–Quinney coefficient is taken as $\chi = 0.9$.

The plastic hardening behavior is based on tensile tests conducted at constant engineering strain rate of 5×10^{-5} s^{-1}. The data up to maximum tensile force, i.e., the necking point, is used. A simple power-law hardening in the Johnson–Cook form turned out insufficient. Thus, the following function is adopted (cf. Equations 13 and 14)

$$h_y(e_{\mathrm{p}}) = \begin{cases} \sigma_{\mathrm{y0}} + h_0 e_{\mathrm{p}}, & e_{\mathrm{p}} \le e_{\mathrm{p0}}, \\ h_1 e_{\mathrm{p}} + \sigma_{\mathrm{y\infty}} - [\sigma_{\mathrm{y\infty}} - \sigma_{\mathrm{y1}}]\exp(-m e_{\mathrm{p}}^n), & e_{\mathrm{p}} > e_{\mathrm{p0}}, \end{cases} \tag{8.4.1}$$

where the associated parameters at room temperature have been identified as $h_0 = 123$ MPa, $h_1 = 75$ MPa, $\sigma_{\mathrm{y0}} = 520$ MPa, $\sigma_{\mathrm{y1}} = 376$ MPa, $\sigma_{\mathrm{y\infty}} = 831$ MPa, $m = 6.14$, $n = 0.541$ and $e_0^p = 0.006$. The experimentally determined data and fitted flow curve are shown in Figure 8.7.

---

[5]For convenience, Table 8.3 compiles the material parameters listed in this section.
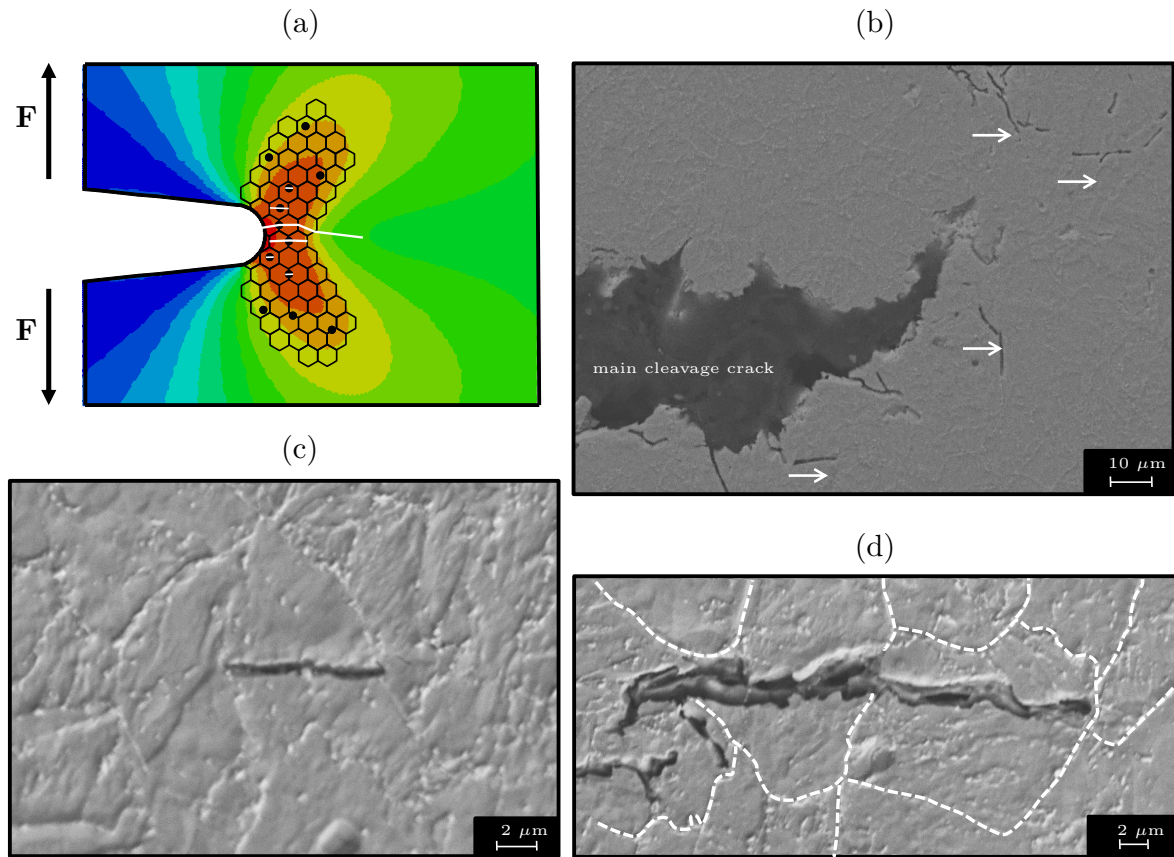
Figure 8.6.: Cleavage crack arrest: (a) Scheme showing the arrest mechanisms; (b) SEM image showing main cleavage crack and secondary cracks in its vicinity (observations performed on a notched disk tested at −196° C); (c) microcrack initiated at a precipitate inside the grain and arrested at grain boundaries; (d) higher magnification SEM image of a secondary crack arrested at a grain boundary and in the matrix (grain boundaries are highlighted).

The scaling factor $t_{\mathrm{y}}(\Theta)$ controls the temperature dependence of the flow curve and is given in terms of homologous temperature in Figure 8.8. Assessing the temperature dependence for a wide range of temperatures including cryogenic and elevated temperatures is not straightforward as, in the literature, either low or high temperatures are studied. In the current study, the temperature dependence of the flow curve was established by merging different results reported in the literature[6] and a best fit was used. It is seen that the distribution of the data required a function with an inflection point. Hence, the single curvature model of Johnson-Cook was not sufficient. The best fit was supplied by the fourth-order polynomial, $42.562\Omega^4 - 44.846\Omega^3 + 11.438\Omega^2 - 1.1021\Omega + 1$, where $\Omega = [\Theta - \Theta_{\mathrm{ref}}]/[\Theta_{\mathrm{melt}} - \Theta_{\mathrm{ref}}]$. The comparison of punch force−displacement simulations with the experiments at the three different temperatures (25°C, −158°C and −196°C) required a slight deviation from the best fit of tensile data, and led us to $t_{\mathrm{y}}(\Theta)$ equal to 1, 1.24 and 1.54 for 25°C, −158°C and −196°C, respectively. The corresponding points are marked as "used"in Figure 8.8. A rate dependence was not taken into account.

Following [304] and [306], the parameters of the extended Gurson model are chosen as $q_1 =$

---

[6]A non-dimensional ratio of the actual yield stress with respect to the one reported at room temperature (i.e., reference temperature of each study) is produced.
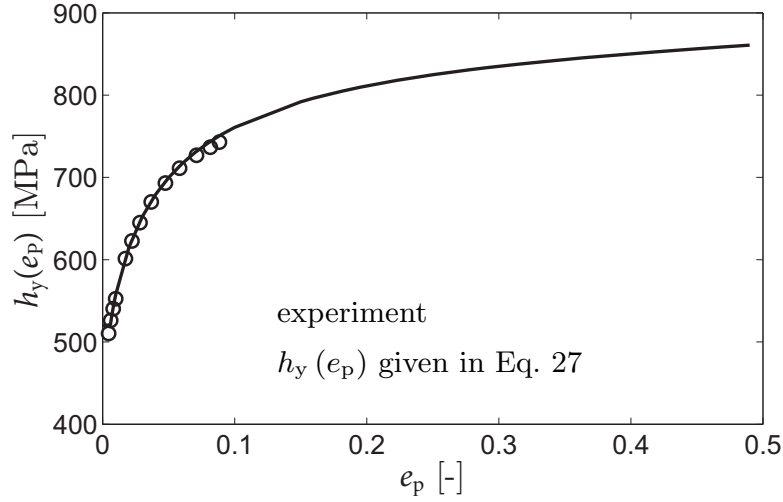
Figure 8.7.: Flow curve of P91 at room temperature. The circles represent experimentally recorded points prior to necking and the solid line is a plot of Equation (8.4.1) for the parameters given.
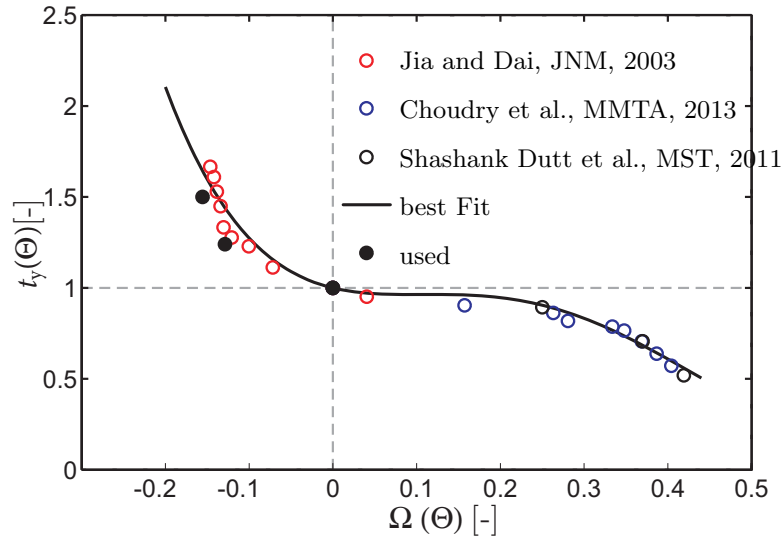
Figure 8.8.: Homologous temperature Ω dependence of the yield stress scaling parameter $t_y(\Theta)$ after processing three experimental sources as an initial guess for parameter identification. Comparisons based on force−displacement response of simulations with experiments of small punch tests at $25° C$, $-158° C$ and $-196° C$. Source 1 is the un-irradiated T91 from Figure 1 of [140], for temperatures smaller or slightly higher than room temperature. Source 2 is adopted from the true stress–true plastic strain data at various temperatures for 9Cr-1Mo steel tested at a strain rate of 3.16×10^{-4} s^{-1} from Figure 3 of [73] for temperatures equal or greater than room temperature. Finally, Source 3 represents data given in Table 1 of [268] which lists the tensile properties of P91 steel for temperatures equal or greater than room temperature.

$1.5 = 1/f_u^*$, $q_2 = 1$, $q_3 = q_1^2 = 2.25$. The initial void volume fraction[7] is selected as $f_0 = 0.00044$.

---

[7]Franklin's formula [93] serves as an estimate for the initial void volume fraction f_0

$$f_0 = \frac{0.054\sqrt{d_x d_y}}{d_z}\left[\mathrm{S}\,(\%) - \frac{0.001}{\mathrm{Mn}\,(\%)}\right].$$ (8.4.2)

The parameters associated with the nucleation mechanism $f_N = 0.02$, $\epsilon_N = 0.3$ and $S_N = 0.1$ are selected, following [5, 6] suggesting that the volume fraction of the segregated inclusions f_N is within a narrow band of 0.01 to 0.03.

Presented simulations of notched samples show that the notch induces a strong plane strain effect with w reaching 1 and increased triaxiality (Equation (8.2.18)). This amplifies the effect of the shear modification. As a consequence, incorporation of the shear modification results in simulated crack initiation significantly preceding the experimentally observed one. Hence, $k_w = 0$ is selected and the shear modification is suppressed for simplicity. By this choice the void nucleation rather than the void growth term incorporates the shear stress effects provided that hydrostatic stresses are positive. Regarding the uniqueness of the parameter choice, it is notable that it is also possible to arrive at reasonable fracture initiation strains with $k_w \neq 0$ and relaxed void nucleation and/or initial porosity data.

For the final void fraction at failure, different references give somewhat different results, e.g., [172] takes $f_F = 0.25$ in accordance with [62] whereas $f_F = 0.2$ is used in [334, 336, 5, 6], noting that the last two references study steel A533 B. In the present work coalescence and failure porosity were taken as $f_c = 0.1$ and $f_F = 0.25$. The so-called energetic length scale for ductile fracture has been suggested to be between four times the void size and half the void spacing, see [309]. If two populations of second phase particles are present, which is the case for P91, one should select the population which is dominant in crack initiation and propagation. In the fractographic images, fine dimples initiated by small MX particles are noticeable. This precipitate type prevails in quantity and is believed to play a significant role in the ductile fracture (Figure 8.3(g)) in addition to $M_{23}C_6$ precipitates. From the images the relevant length scale being of the order of the average distance between the MX and the $M_{23}C_6$ precipitates was identified as 2.5 μm to 5 μm and used to define the lower and upper bounds of R_{ductile}, respectively. These values pose restrictions in selecting the finite element mesh size which scales the computational cost. One could also use a local formulation where the mesh size constitutes the characteristic length. This was not pursued in the current study due to the need to vary the mesh size around the notch tip as well as the relatively large aspect ratio of the elements in this region.

According to the RKR cleavage model, cracks initiate if a critical stress is exceeded over a characteristic distance, associated with the grain size. As previously mentioned, P91 microstructure is composed of prior austenite grains which are subdivided into packets of fine martensite laths (Figure 8.9(a)). In order to reveal the microstructure and make prior austenite grain boundaries distinguishable, Vilela's reagent (1 g picric acid and 5 mL HCl in 100 mL ethanol) was used for etching. In Figure 8.9.(b) an SEM image of an etched sample is given. The two types of precipitates $M_{23}C_6$ (with M identified as Mo by EDX analysis) and MX are apparent in this image: $M_{23}C_6$ mostly in the prior austenite subgrain boundaries whereas MX distributed in the matrix. The grain size determined by the intercept method (ASTM E112) was found to be $14 - 25$ μm which is comparable with values reported in the literature. This was used to define lower and upper bounds of R_{brittle} as 7 μm and 12.5 μm. For the associated critical stress for brittle fracture, the present numerical computations suggested $\sigma_c = 2.83\sigma_{y0}$ and $\sigma_c = 2.55\sigma_{y0}$.

Here, d_x, d_y, and d_z denote average inclusion diameters in the respective directions. S% and Mn% represent the weight percentages of sulphur and manganese in the matrix, respectively. For $d_x = d_y = d_z$ and the chemical composition of P91 given in Table 8.1, one has $f_0 = 0.00044$. Although Franklin's formula is used for materials where manganese sulphide inclusions are the critical particles for fracture, it supplies a realistic initial value for porosity for the investigated material whose chemical content also involves S and Mn. Moreover, the authors' simulations on unnotched disks show that initial porosity estimates within $(0.0044, 0.002)$ resulted in only marginal differences in the computed failure times.

The latter yielded reasonable results if small-scale yielding conditions prevail. For unnotched small punch specimens, however, the former gave better results as large-scale yielding conditions have to be taken into account. No temperature dependence of σ_c was assumed.
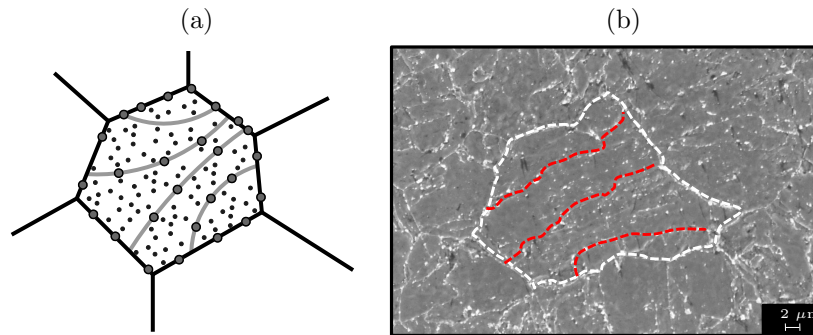
Figure 8.9.: (a) Scheme representing P91 microstructure, (b) SEM image of polished–etched sample revealing this structure.

8.5.   Simulations

2D axi-symmetric simulations with CAX4R reduced integration elements for temperatures of $-196°C$, $-158°C$ and $25°C$ were conducted in ABAQUS/EXPLICIT with double precision. The dies and the punch were modeled as rigid bodies and the disk as a deformable body. The interaction between the rigid and deformable bodies was assumed to be constant with a temperature independent friction coefficient chosen as $\mu = 0.25$. A solution of quasi-static problems with a dynamic-explicit solution procedure generally involves a large number of time steps due to the Courant stability condition. In order to reduce the computational cost, mass scaling was applied with a target time step of 10^{-3} s over the whole analysis which lasted 150 s. This supplies acceleration of the simulations without changing the actual time scale of the process affecting other time dependent phenomena such as viscosity or heat transfer.

The heat source is localized at the crack tip. However, since the loading rate is low, this concentration is effectively lost by diffusion, without significant effect on the material response. This is the case for ductile fracture with relatively low propagation rate as well as brittle fracture with high propagation rate but limited plastic flow and accompanying dissipation. Therefore, isothermal analysis for the three different temperatures is used.

Crack propagation was modeled using an element erosion technique whereby elements with Gauss points whose porosity and/or normalized RKR integral reach the corresponding failure thresholds are removed from the computational stack. Doing so within a nonlocal environment is possible in different ways as depicted in Figure 8.10 for brittle fracture. Without loss of generality, the same scenarios apply for ductile fracture as well. The first method consists in deleting the whole element set within the interaction radius once the central element's Gauss point becomes critical (ductile or brittle failure threshold reached), e.g., [230]. If the internal length associated with the failure mechanism is large, this can result in a violation of mass conservation. Alternatively, only the central element can be deleted. For virtually ductile crack extension this method is applied and only the single central element is eroded. For brittle fracture with a larger material length scale, however, current studies showed that this method results

in cleavage crack islands formed by eroded elements ahead of the crack tip. These crack islands can be seen as computational counterparts of arrested cracks around the crack tip, as found experimentally, which are then bridged either by ductile or brittle fracturing. Although simple, this method does not allow any control on the crack propagation direction. However, it is well known that the principal stress is effective in directing cleavage cracks. Thus, a new method was implemented: Once the central element's normalized RKR integral reached the corresponding failure threshold the element itself, as well as the elements whose Gauss points fell within a crack band thickness along the direction orthogonal to the maximum tensile principal stress, were deleted all together.

R radius of interaction for the brittle fracture (cleavage grain)

🟡 central Gauss point (GP)   🔴 deleted central GP

⚫ GPs in the interaction radius   ⚫ deleted GP in the interaction radius
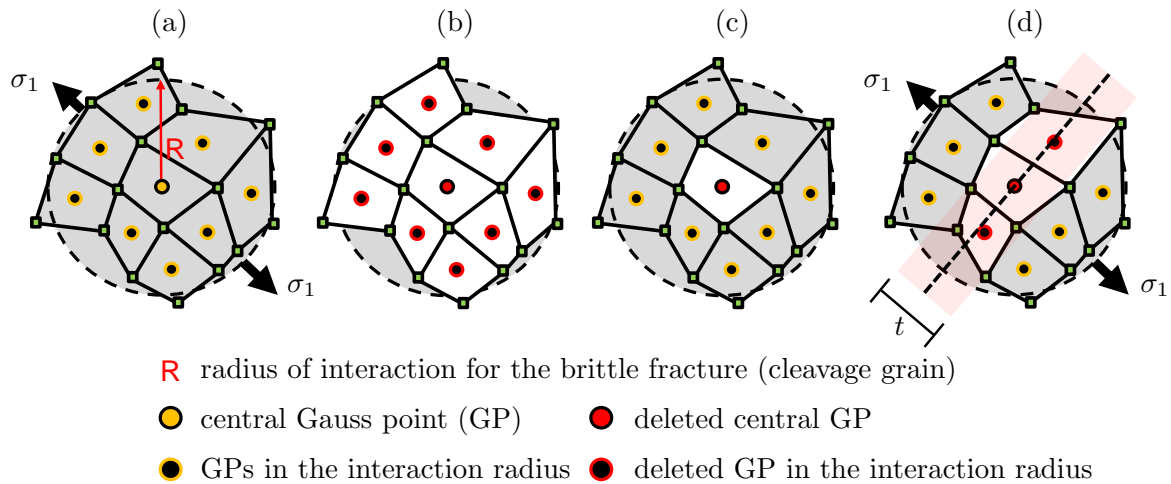
Figure 8.10.: Methods of virtual extension of cleavage cracks for the cleavage grain given in (a). (b) deletion of the whole cleavage grain, e.g., [230]. In this method many elements are deleted without any directional information on the crack formation. (c) Deletion of central element only: Only the central element is deleted once the criterion is satisfied. Again this method suffers from ignoring directional information for crack propagation. (d) Deletion of elements whose GPs fall into a band oriented in the direction orthogonal to the maximum tensile principal stress: Deletion band size t can be selected according to the finite element size. Hence, $\boldsymbol{x}_c$ is the position vector of the central GP and $\boldsymbol{x}$ is the position vector of the neighboring GP with respect to a common origin and $\boldsymbol{n}$ is the unit vector in direction of the maximum principal stress (belonging to the central element), then deletion is applied to elements for which $(\boldsymbol{x} - \boldsymbol{x}_c) \cdot \boldsymbol{n} \leq t/2$. It is observed that the fracture patterns for total deletion (b) and single deletion (c) resulted in fracture islands and largely deleted regions with considerable mass loss, respectively.

8.5.1. Small Scale Yielding Condition

This set of simulations concerns the notched small punch tests where the fracture, either ductile or brittle, emanates from the notch as a result of stress concentration. The upper limits of the brittle and ductile interaction radii are used with $R_{\mathrm{ductile}} = 5 \ \mu\mathrm{m}$ and $R_{\mathrm{brittle}} = 12.5 \ \mu\mathrm{m}$ with $\sigma_{\mathrm{c}} = 2.55\sigma_{\mathrm{y0}}$.

The mesh used in the simulations is given in Figure 8.11. Due to high stress gradients around the notch tip the finite element discretization requires special attention in that region. In the current study 2 μm mesh size allowed traversing the notch tip with sufficiently fine mesh for a

reasonable notch tip stress resolution[8]. This requires the application of a nonlocal theory, since the emerging element sizes are smaller than the interaction radius identified for ductile failure. Since the radius of interaction is 5 μm the utilized finite element sizes should be smaller than this to allow delocalization to be applied. Consequently, with the utilized mesh up to 230 elements in the vicinity and around 40 elements further away from the notch are supplied within a brittle interaction radius.

At the notch tip the Arbitrary Lagrangian Eulerian (ALE) remeshing[9] was utilized where VDISP subroutine interface allowed to track the corresponding element volumes. By morphing the mesh compatible with the underlying deformation this avoids otherwise extreme element distortion or aspect ratio change around the notch tip for the ductile fracture. Hence, smooth distributions of stress and strain fields are obtained which is conclusive in the damage development. Apart from the notch tip the mesh was created by the advancing front quad method. The number of elements within the effective radius of each element varied spatially. The size of the ALE region was determined by a trial and error analysis. Possible self-contact of the notch free surface was taken into account.

For $-196°$C, the main fracture mechanism is cleavage controlled by the stress over the cleavage grain. In order to shed light on the mechanism, the distribution of the Ritchie–Rice–Knott (RKR) integral normalized by σ_{y0} is investigated for various stages of loading (Figure 8.12).

In early stages of the process, the RKR integral has its maximum first on the symmetry axis on the convex surface of the bent region, say the tip of the dome, whose magnitude is far from critical. With further loading, the critical region is carried away from the center but still stays on the free surface. At a punch displacement of $u = 0.187$ mm till the crack initiation the maximum RKR integral is found on the left-hand side of the notch tip where hydrostatic stress is tensile. Taking into account the interaction radius for brittle fracture the visibility criterion (Figure 8.25) gives a reasonable distribution of the RKR integral over the region at the notch tip. Without visibility criterion the sign change of the maximum principal stresses at either side of the notch results in smaller values of the RKR integral at the fracture region around the notch. This unrealistic smoothing affects the threshold value for the RKR integral to be used. Situations with the maximum RKR integral being at the bottom of the disk can then occur at the instant of experimentally determined brittle fracture. Hence, the implementation of the visibility criterion seems to be crucial for the current application, where the interaction radius is larger than the notch radius.

The cleavage crack starts at the notch root where the RKR integral first reaches the threshold (Figure 8.13). Fast cleavage crack propagation follows until the complete separation and loss of load carrying capacity of the disk. Throughout the loading, the RKR integral maintains

---

[8]As noted in [223] and [230], for sufficiently smooth stress gradients the finite element size can be adapted to the grain size in order to circumvent an integration over a number of elements. However, for small–scale yielding conditions where a sharp notch or crack tip creates high stress gradients or for materials involving secondary microstructural mechanisms acting at a smaller scale, the maximum finite element sizes are limited by that smaller scale.

[9]ALE adaptive remeshing is used to remedy excessive distortion of the elements in the mesh at the notch vicinity. It consists of two fundamental steps: creation of a new mesh, and solution variable remapping with advection process. In order to preclude accumulation of numerical errors associated with solution mapping and delocalization operations and also keeping the computational cost to a reasonable limit, the number of ALE remeshing increments is kept minimum through a trial and error analyses. Accordingly the selected parameters are as follows: ALE remeshing frequency: 50 (typically 5–100 without Eulerian boundaries), remeshing sweeps per increment: 1 (default), Initial remeshing sweeps: default. The remaining ALE adaptive mesh controls are selected as the default values proposed, see, e.g., [3].
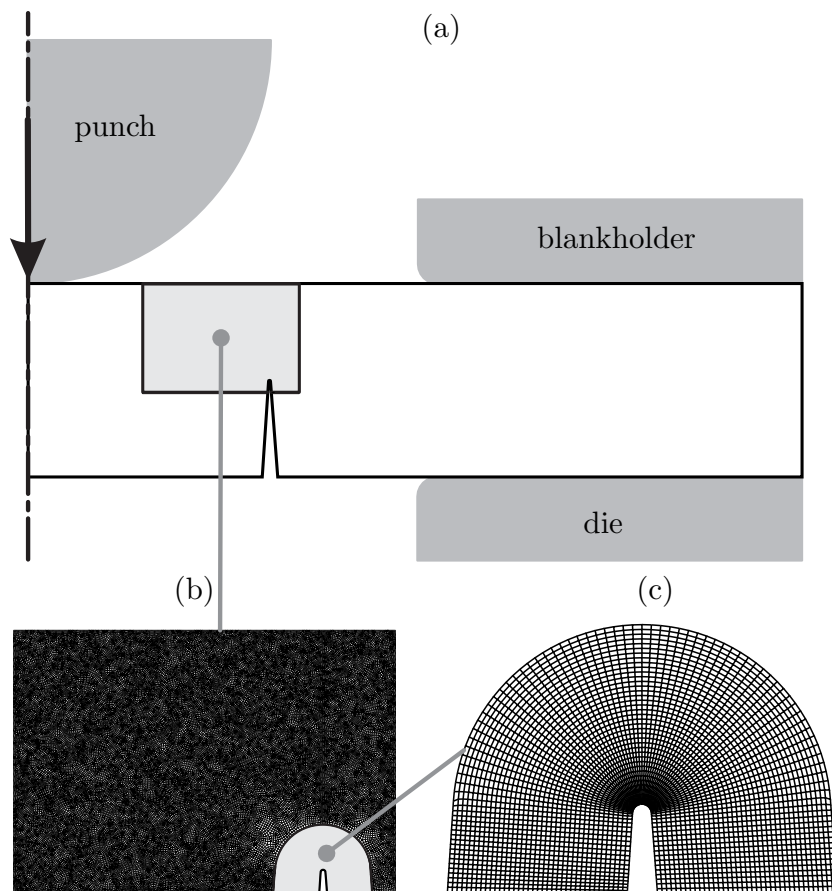
Figure 8.11.: (a) axisymmetric finite element model for the notched small punch test. In (b) and (c) the mesh design is depicted where the region in (c) corresponds to the ALE remeshing region.

the direction of the crack, while its maximum remains at the advancing crack tip. The crack propagation is not completely straight but slightly bent due to the redistribution of stresses induced by the continuous motion of the punch. This is in agreement with experimental findings, and it shows that the virtual crack propagation methodology is correctly taking into account the slight rotation of the maximum stress direction ahead of the advancing crack.

Figure 8.14 shows the distribution of various fields around the notch tip just before the initiation of brittle fracture at punch displacement u =0.23 mm. From (a) to (e), the fields are the normalized RKR integral, the normalized maximum principal stress, the vector distribution of the maximum and minimum principal stresses, the total void volume fraction and the von Mises stress, respectively. The RKR integral considerably smoothens the high gradients of the underlying principal stress field. As anticipated, the directions of the maximum (tensile) principal stress define the direction orthogonal to the crack propagation. Thus, fracture is of Mode I. The dominantly compressive (right) and tensile (left) stress fields separated by the notch are also apparent. The maximum void volume fraction, unlike the RKR integral, is located ahead of the notch tip which coincides with the given distribution of the von Mises stress. However, at this stage of loading its magnitude is far from being critical, in line with the brittle nature of fracture at $-196°$C.

For 25°C, ductile fracture is mainly controlled by plastic flow and hydrostatic stress with focus
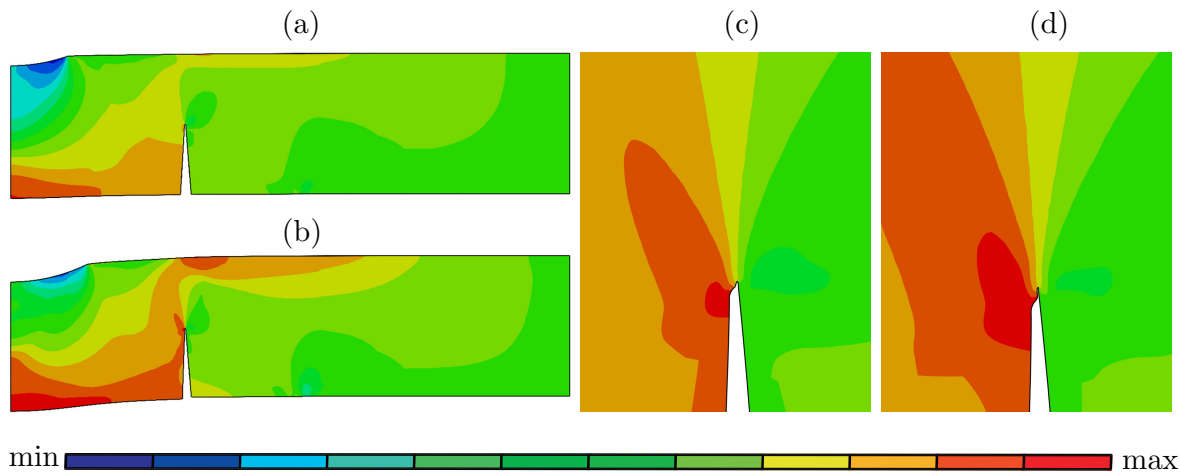
Figure 8.12.: RKR integral distribution (normalized with respect to σ_{y0}) at four stages of loading at $-196°C$. (a) punch displacement $u = 0.088$ mm, [max 2.075; min -3.185]; (b) punch displacement $u = 0.187$ mm, [max 2.324; min -2.664]; (c) punch displacement $u = 0.187$ mm, detail at notch, [max 2.324; min -2.664]; (d) punch displacement $u = 0.23$ mm, [max 2.535; min -2.739]. At punch displacement $u = 0.187$ mm the maximum occurs at the notch rather than the bottom for the first time.

now being on the distribution of the void volume fraction at various stages of loading (Figure 8.15). In the early stages of the process the void volume fraction has its maximum on the symmetry axis at the apex of the bend, however, with a magnitude far from the failure threshold. After a punch displacement of $u = 0.157$ mm till the incipient fracture, the maximum porosity is located ahead of the notch tip, however, slightly shifted to the left where the hydrostatic stress is tensile. As the punch travel continues its magnitude and extension get larger, while the porosity growth tends to align itself along the punch loading direction.

Figure 8.16 shows the crack propagation from its initiation to complete separation. In accordance with the distribution of the porosity, the crack propagates almost parallel to the punch loading direction after a slight inflection to the left at the initial stage. This pattern is in good agreement with experimental findings. The whole process is governed by ductile failure, in the sense that the element deletion proceeds according to the ductile fracture criterion. The speed of crack propagation is considerably lower than in the brittle case. The failure process is distributed over a longer time period with larger energy required. The initiation and propagation of the crack feature mixing of Mode I and Mode II, noting that during almost vertical propagation Mode II dominates.

Figure 8.17 displays various fields around the notch tip just before the initiation of ductile fracture at punch displacement $u = 0.405$ mm : normalized RKR integral, the normalized maximum principal stress, the vector distribution of the maximum and minimum principal stresses, the total void volume fraction and the von Mises stress, from (a) to (e), respectively. The normalized RKR integral is considerably smaller than the threshold. Similar to the findings for $-196°C$ it deviates from the normalized maximum principal stress due to the high stress gradients at the notch tip. The principal stress vectors are similar in direction to the ones for $-196°C$, however, with considerably reduced magnitudes. The temperature dependence of the yield stress causes plastic flow to take place at lower stress levels than for $-196°C$. Without brittle fracture intervening, the notch tip experiences sufficient deformation to accumulate a critical amount of porosity under tensile hydrostatic stresses. Moreover, the von Mises equivalent stress (as driving
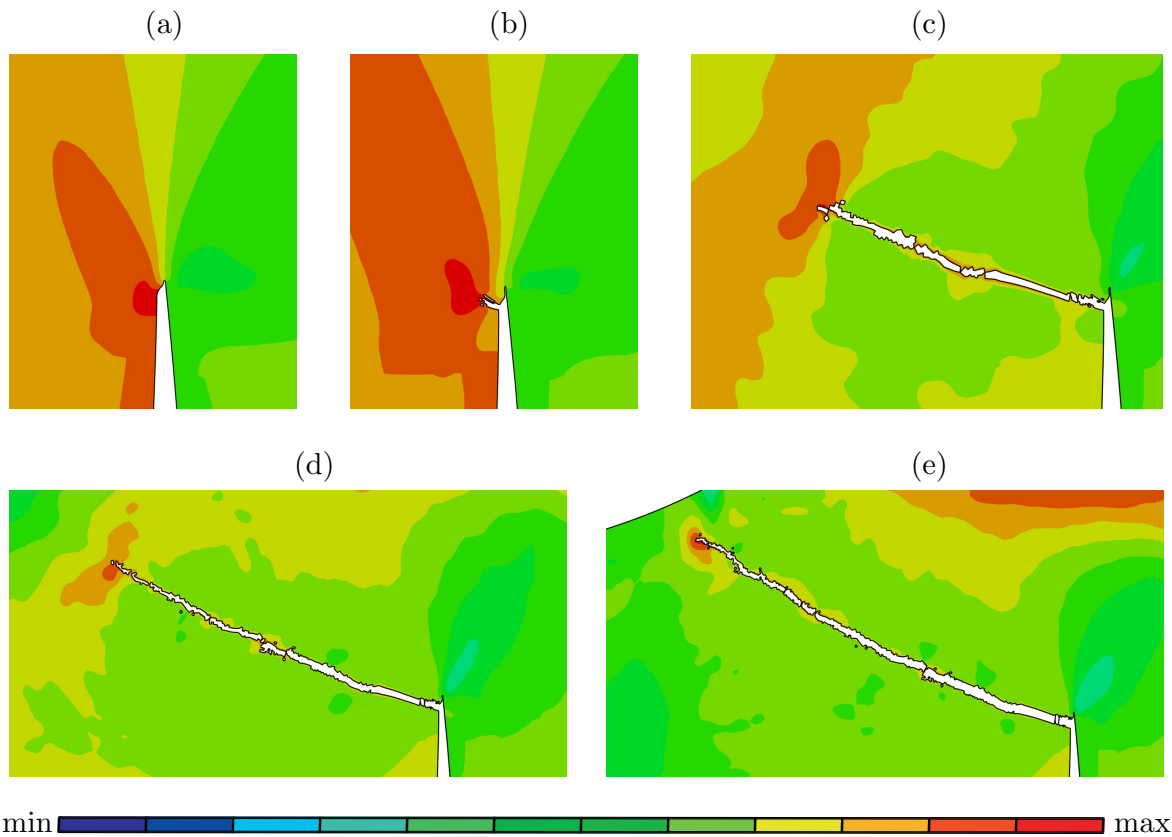
Figure 8.13.: *Initiation and evolution of the crack at different stages of loading at $-196°C$. RKR integral distribution (normalized with respect to σ_{y0}) at five different successive loading steps: (a) $u = 0.230$ mm [max 2.535; min -2.739]; (b) $u = 0.231$ mm [max 2.359; min -2.731]; (c) $u = 0.232$ mm [max 2.269; min -2.757]; (d) $u = 0.233$ mm [max 2.251; min -2.508]; (e) $u = 0.234$ mm [max 2.351; min -1.420].*
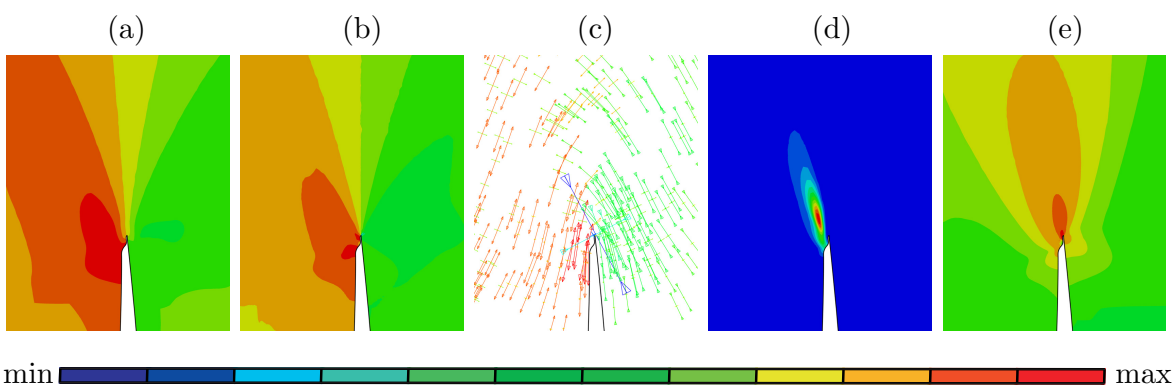
Figure 8.14.: *Different field distributions at punch displacement $u = 0.23$ mm for $-196°C$. (a) RKR integral distribution [max 2.535; min -2.739]; (b) maximum normalized principal stress distribution [max 3.086; min -4.056]; (c) in-plane principal stresses with associated directions [max=1605 MPa; min=-3631 MPa]; (d) total void volume fraction [max=0.013; min=3.679×10^{-7}]; (e) von Mises equivalent stress [max=1498 MPa; min=17.74 MPa].*
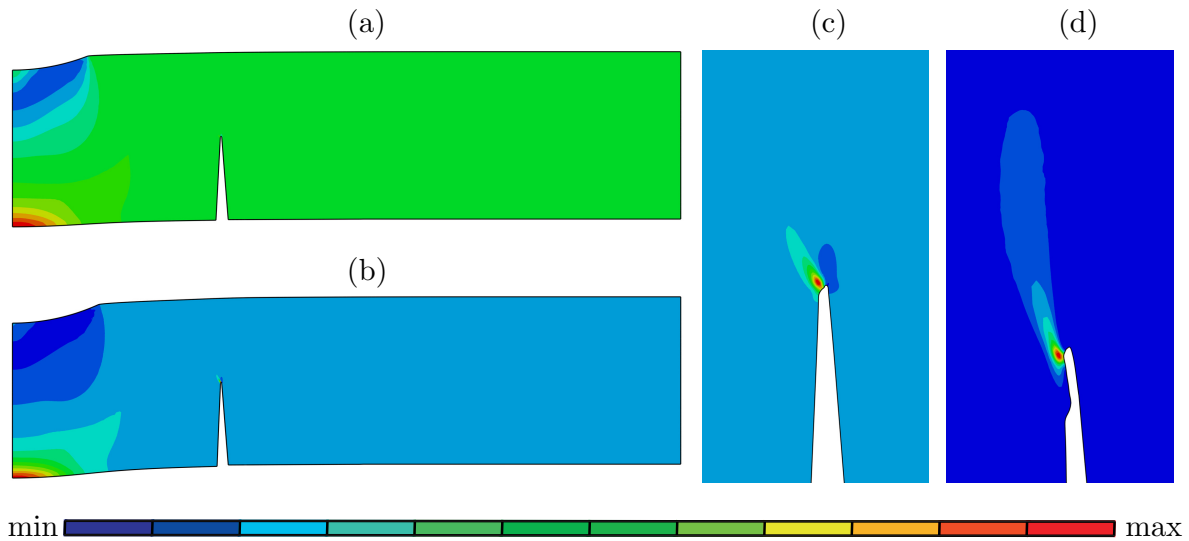
Figure 8.15.: Void volume fraction distribution at four different stages of loading at $25°C$. (a) punch displacement $u = 0.11$ mm, [max 9.294×10^{-4}]; (b) punch displacement $u = 0.157$ mm, [max 2.162×10^{-3}]; (c) punch displacement $u = 0.157$ mm, detail at notch, [max 2.162×10^{-3}]; (d) punch displacement $u = 0.405$ mm, [max 0.2186]. At punch displacement $u = 0.157$ mm the void density concentrates for the first time at the notch rather than the bottom. The minimum porosity is set to zero in all these contour plots.
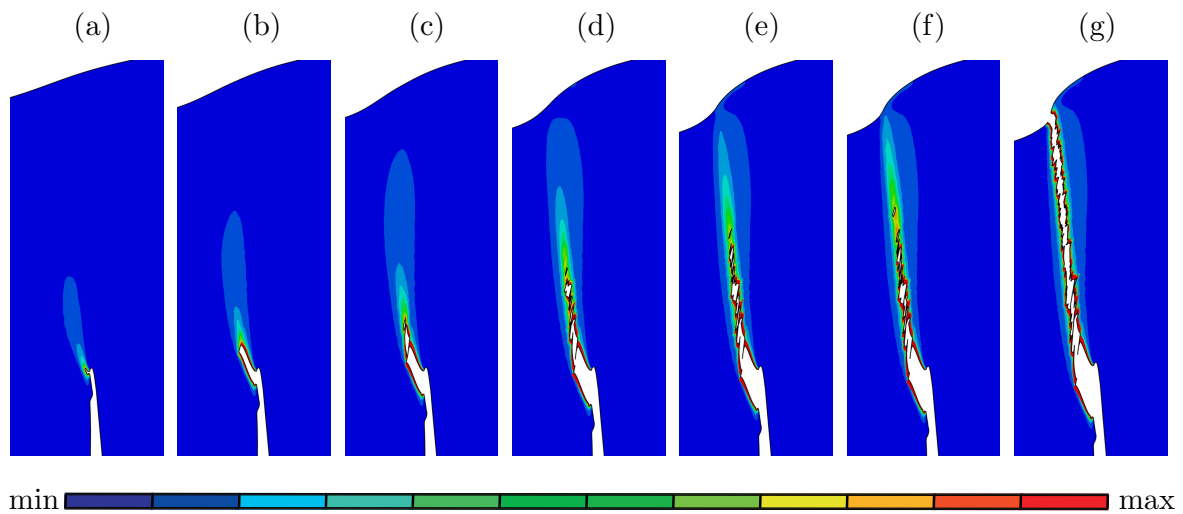
Figure 8.16.: Initiation and evolution of the crack at different stages of loading at $25°C$ evidenced by contours of void volume fraction. Maximum void volume fraction is naturally 0.25 and minimum is set to zero.

force for the plastic deformation) has its maximum ahead of the crack tip and the contours orient themselves along the vertical direction of punch travel.

For $-158°C$, fracture initiates at an intermediate punch travel $u = 0.23$ mm, however, with a brittle mode. Figure 8.18 displays the fields around the notch tip just before fracture initiation. While the accumulated porosity is higher than for $-196°C$ prior to fracture, it still remains below the coalescence void volume fraction. Thus, ductile fracture does not take place. The
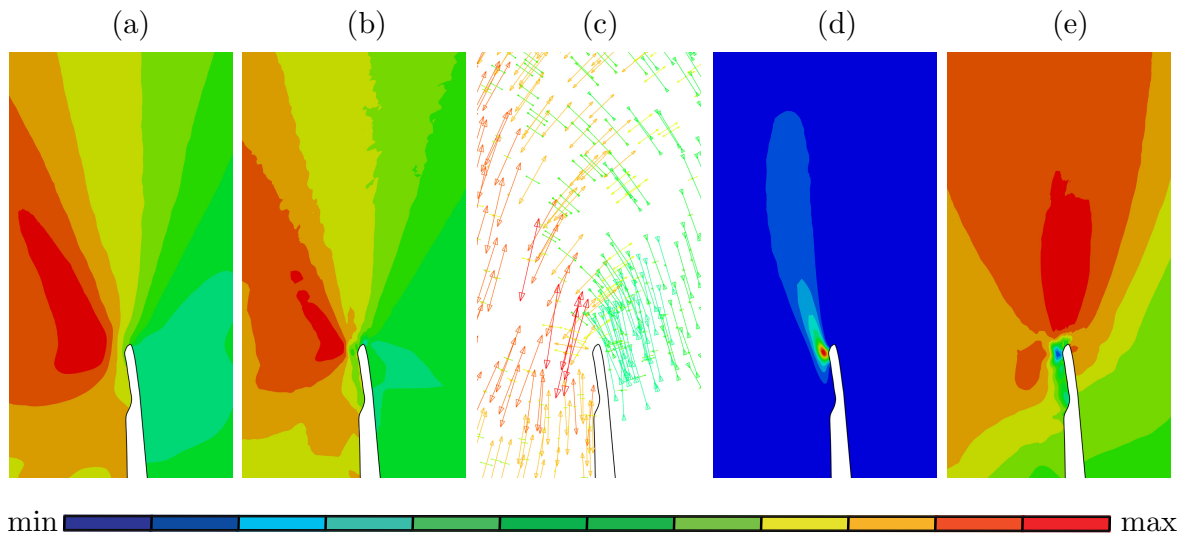
Figure 8.17.: Field distributions at punch displacement $u = 0.405$ mm for $25°C$. (a) RKR integral [max 2.271; min −1.719]; (b) maximum normalized principal stress [max 2.551; min −2.242]; (c) in-plane principal stresses with associated directions [max=1362 MPa; min=−2320 MPa]; (d) total void volume fraction [max=0.0219; min=6.830×10^{-5}]; (e) von Mises equivalent stress [max=926.6 MPa, min=22.42 MPa].

accumulation of sufficiently high stress levels requires more deformation though. Consequently, hardening takes place at the crack tip.
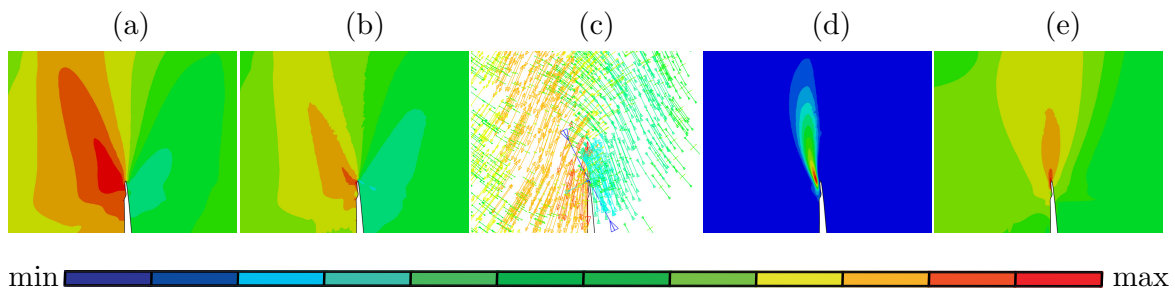
Figure 8.18.: Field distributions at punch displacement $u = 0.36$ mm for $−158°C$. (a) RKR integral [max 2.518; min −1.940]; (b) maximum normalized principal stress [max 3.395; min −2.324]; (c) in plane principal stresses with associated directions [max=1789 MPa; min=−2412 MPa]; (d) total void volume fraction [max=0.0406; min=3.934×10^{-5}]; (e) von Mises equivalent stress [max=1370 MPa, min=22.97 MPa].

A comparison of the crack patterns observed in simulations and experiments is given in Figure 8.19. Obviously, the crack patterns for both $25°C$ and $−196°C$ are in very good agreement. For $25°C$, besides the crack pattern itself, the similarity of the upper face curvatures of the disk is noteworthy. For $−196°C$, although the direction of the crack is well reproduced, axisymmetry conditions are not preserved during brittle fracture in the experiments. For $−158°C$ the fracture takes place much later than for $−196°C$. The fracture mode is predominantly brittle in the simulations, while the experimental findings show more mixing of ductile and brittle fracture. Also, it is seen that the steepness of the propagation direction decreases with decreasing temperature. For $−158°C$, the orientation of the crack lies in between those of $25°C$ and $−196°C$.
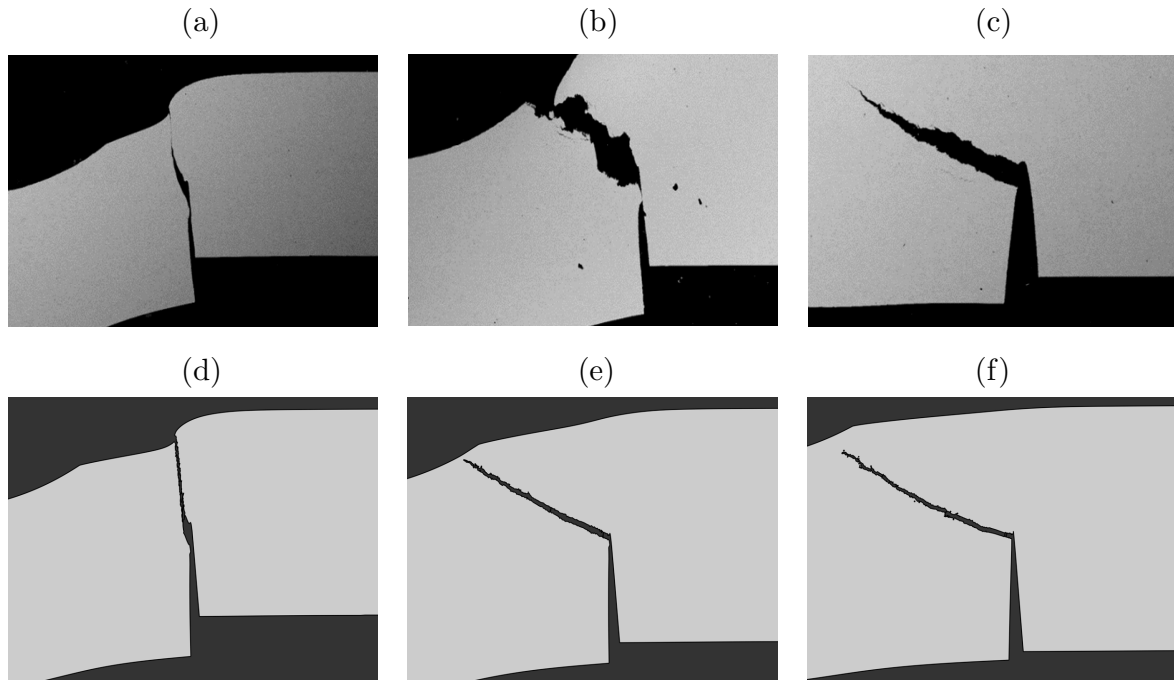
Figure 8.19.: Comparison of the crack patterns observed in simulations and experiments. (a) Experiment at 25° C (Simulation given in (d)); (b) Experiment at −158° C (Simulation given in (e)); (c) Experiment at −196° C (Simulation given in (f)).

Finally, a comparison of the punch force vs. displacement curves is given in Figure 8.20. A good agreement is observed throughout the elastic-plastic deformation phase. At −196°C, the fracture strains are also well captured. For 25°C, a slightly premature failure is obtained with a rather steep drop of the force response. For −158°C, although the displacement at fracture is close to the experimental ones, a more brittle mode of fracture results in a steeper drop of the force response compared to the experimental findings. This discrepancy is supposed to be emphasized by the fact that the axisymmetric 2D simulations cannot capture the distributed failure of the specimen along the circular notch as observed in 3D.

Small punch deformation energies up to fracture are obtained by integrating the total area under the load–displacement curves. According to the Code of Practice [69], a small punch disk is defined to fail when a 20% load drop after maximum load is reached. If deformation energies are plotted as a function of temperature, a sigmoidal increase is revealed similar to an impact energy vs. temperature graph of Charpy tests. For the experiments average deformation energies for −196°C, −158°C and 25°C are calculated to be 292 Nmm, 678 Nmm and 703 Nmm, respectively. For the simulations these are 340 Nmm, 549 Nmm and 619 Nmm, respectively. Hence, quantitatively the energy requirements until brittle or ductile fracture are well captured.

Simulations also allow quantification of the average crack tip speed during crack propagation. For −196°C, −158°C and 25°C, the average crack speeds turned out to be 1.42 mm/s, 1.06 mm/s and 0.037 mm/s, respectively, meaning that for −196°C the crack speed exceeded that of 25°C by approximately a factor of 40. The closeness of −196°C and −158°C crack speeds also points at the predominately brittle nature of fracture at −158°C.
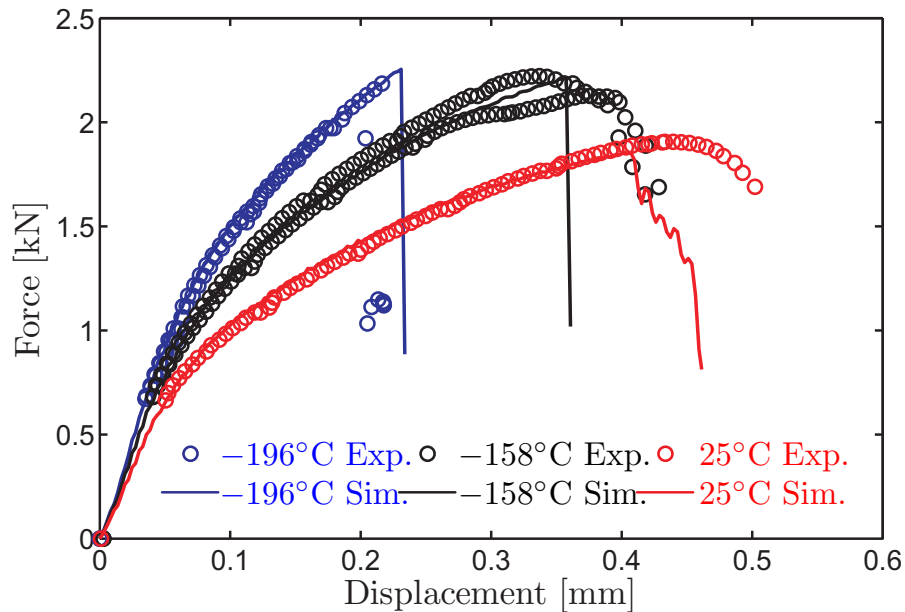
Figure 8.20.: Comparison of experimental and numerical punch force-displacement plots, with two repeat tests at the lower shelf ($-196°C$) and the transition region temperature ($-158°C$).

8.5.2. Small- and Large-Scale Yielding Conditions

The results in the previous section refer to small-scale yielding conditions, which work well for the notched specimens. The unnotched specimen simulations with the same interaction radius of 12.5 μm and $\sigma_c = 2.55\sigma_{y0}$ governing brittle fracture, however, showed premature fracturing, at about one fourth of the actual fracture displacement observed in the experiments. This is why a closer look at the role of this interaction radius is required.

For brittle interaction radii even larger than 12.5 μm, the nonlocal operator causes increasing levelling of the notch tip RKR field such that the disk bottom exhibits the maximum RKR integral in excess of the one at the notch tip. Besides being out of the predefined bounds for the brittle interaction radius as set by the microstructural observations, the use of a larger interaction radius makes it impossible to obtain the correct location of brittle fracture at the notch tip at reasonable punch displacements.

On the other hand, interaction radii smaller than 7 μm make the delocalized RKR integral get closer to the local. In absence of a stress concentrator in the unnotched case, the RKR integral cannot reach the threshold level, at least not at realistic strains as observed in the experiments. Hence, a set of values within the interval $[7\,\mu\text{m}, 12.5\,\mu\text{m}]$ should be used. However, unlike the previous approach, where, first the length scale and then the critical RKR threshold is defined. The length can be selected for the unnotched specimens after defining a critical fracture stress, because gradients are much less pronounced and, therefore, less affected by the selected length scale.

It is found that $R_{\text{brittle}} = 7.0\,\mu$m with $\sigma_c = 2.83\sigma_{y0}$ gave acceptable results for both the notched and unnotched cases in so far as brittle fracture onset could be predicted reasonably well. One should note that interaction radii within $[7\,\mu\text{m}, 12.5\,\mu\text{m}]$ did not affect the RKR integrals for the unnotched tests as much as for the notched ones. In order to be consistent with the previous

analysis, the ductile fracture parameter was also reduced to its lower limit, i.e., $R_{\text{ductile}} = 2.5$ μm. This corresponds to the smallest mesh size in the region with mesh refinement. Hence, at the notch tip the ductile damage delocalization applies for the finest elements. For the region away from the notch, fracture development is controlled by the mesh size, the smallest of which is equal to the interaction radius. Consistently also for the unnotched cases uniform 2.5 μm elements are used at crack regions.

The effect of the nonlocal operator on the resultant stress gradients is shown in Figure 8.21 where the normalized principal stress distributions before and after delocalization are depicted for the notched and the unnotched cases for $-196°$C and an interaction radius of 7 μm. At the notch tip, the stress field shows a steep gradient. The delocalization has a strong effect even for the relatively small interaction radius selected. On the other hand, for the unnotched specimen, the effect of delocalization is hardly distinguishable.
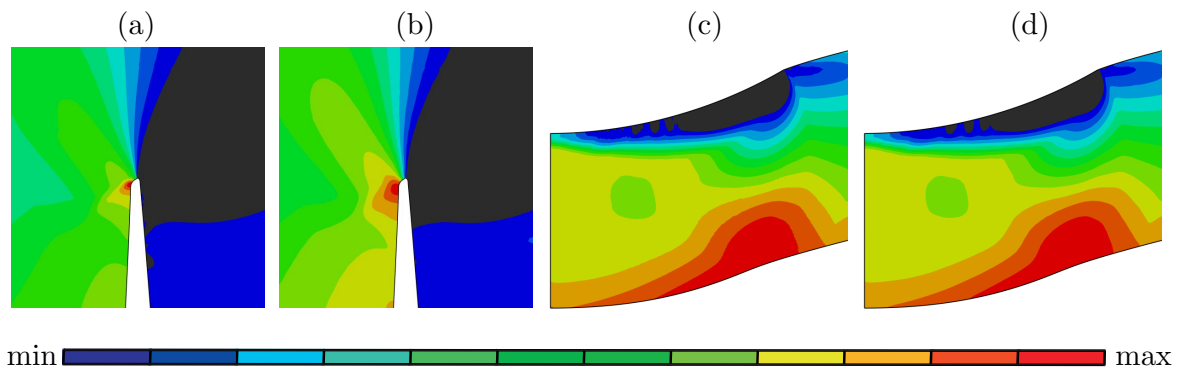
Figure 8.21.: Effect of gradients on nonlocal averaging for $-196°C$ and interaction radius of 7 μm. (a) notched model, before delocalization, maximum normalized principal stress distribution [max 2.742; min 0]; (b) notched model, after del., normalized RKR integral distribution [max 2.278; min 0]; (c) unnotched model, before del., maximum normalized principal stress distribution [max 2.744; min 0]; (d) unnotched model, after del., normalized RKR integral distribution [max 2.742; min 0].

Since the underlying mechanisms for the notched specimens are identical to those of the previous section, this part confines itself to giving the crack patterns for the unnotched tests for the three temperatures $-196°$C, $-158°$C and $25°$C as depicted in Figure 8.22. Large stresses needed for brittle fracture are achieved only at low temperatures. Otherwise, ductile fracture at high strains is observed. Similar to experimental findings, towards lower temperatures reduced bulging (i.e., decreasing amount of plastic deformation) is noted from the overall morphology of the fractured disks. In all cases the cracks start from the bottom surface of the disk and propagate towards the top face until complete separation. For $-196°$C, a linear crack orthogonal to the disk propagates along the direction of maximum in-plane stress. Hence, fracture is of brittle Mode I with the total deformation for fracture being considerably lower than at $-158°$C and $25°$C. For $25°$C, fracture takes place only after a considerable reduction in thickness in a ductile manner following a path parallel to the punch travel. For $-158°$C, on the other hand, a kink is observed when the initially vertical crack takes an inclined direction.

While ductile fracture shows a ring-shaped pattern in the experimental results, brittle fracture propagation is not fully axisymmetric unlike the basic assumption which the current 2D model is based on. A 3D model with random material property distributions and some inevitable

eccentricity of the puncher loading is expected to reproduce even better the fracture patterns. Nevertheless, the current modeling framework already provides various insights regarding the mechanisms of ductile and brittle fracture at much lower computational cost.
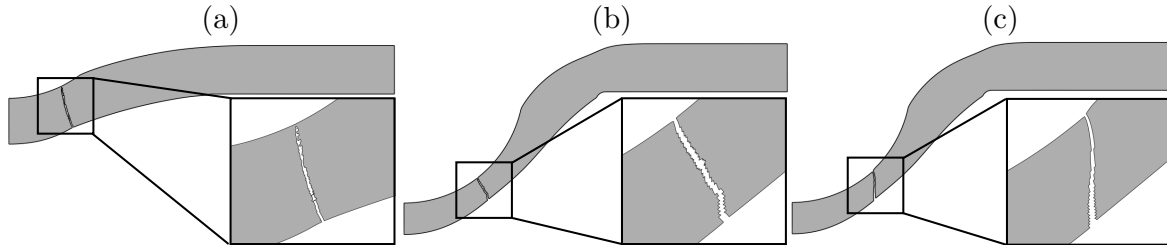
Figure 8.22.: Crack patterns for the unnotched disk test simulations. (a) $-196^\circ C$, (b) $-158^\circ C$ and (c) $25^\circ C$.

Figure 8.23 illustrates the crack development for -158°C and 25°C. In both cases, fracture starts with a severe strain localization due to void formation in a direction around 45° to the maximum principal stress direction. This ductile mode of fracture is preserved for 25°C until complete failure. However, for -158°C, a transition from initially ductile to brittle fracture is observed with a considerably higher RKR integral at the crack tip as compared to 25°C. This transition creates a kink when the crack abruptly deflects to follow the normal of the maximum principal stress. As seen in Figure 8.23(d) during the brittle cracking phase there is almost no void formation.
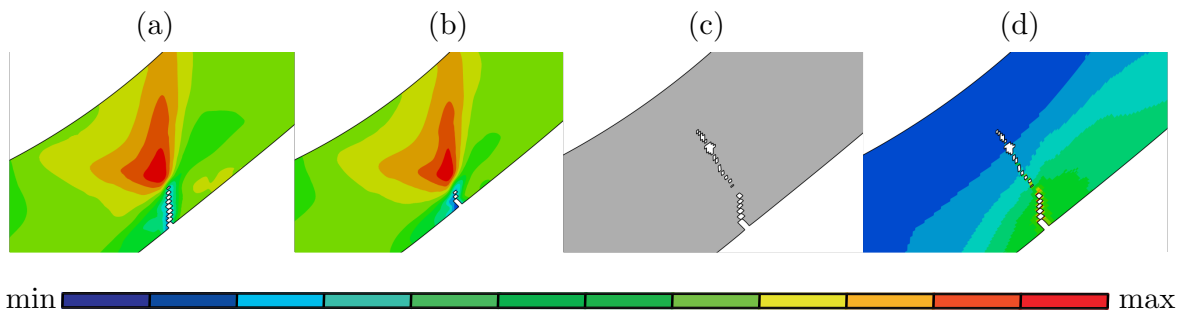
Figure 8.23.: (a) Normalized RKR integral distribution at $25^\circ C$ [max 2.294; min 0]; (b) the same for $-158^\circ C$ [max 2.784; min 0]; (c) transition from ductile to brittle fracture; (d) corresponding void volume fraction far below threshold.

The punch force vs. displacement curves are compared with the experimental ones in Figure 8.24. For -196°C, the force-displacement curves as well as displacement to fracture agree reasonably well with experimental results. For the unnotched tests, there is some overestimation of the fracture displacements for -158°C and 25°C. Both curves show steep drops as a result of abrupt fracturing. A possible way to better capture ductile fracture strains for different temperatures might consist in a temperature dependent modification of the void kinetics in addition to the temperature dependence of plastic flow. However, this is beyond the scope of the current study. For -158°C a significant divergence of the forces occurs after a punch displacement of about 0.7 mm. However, it is impossible to identify the source of this discrepancy on the base of a single experimental result.

The deformation energies for the unnotched tests computed for -196°C , -158°C and 25°C are 472 Nmm, 2497 Nmm and 2057 Nmm, respectively, while experimental values are 499

Nmm, 1819 Nmm and 1916 Nmm. For the simulations these are , respectively. The unnotched tests are seen to require considerably higher deformation energy until fracture. While the considerable differences in the energies required for brittle or ductile fracture are captured by the simulations, the energy required in the simulation at $-158°C$ is predicted to exceed that at room temperature. This relates to the delayed fracture for $-158°C$ as compared to the experimental findings.
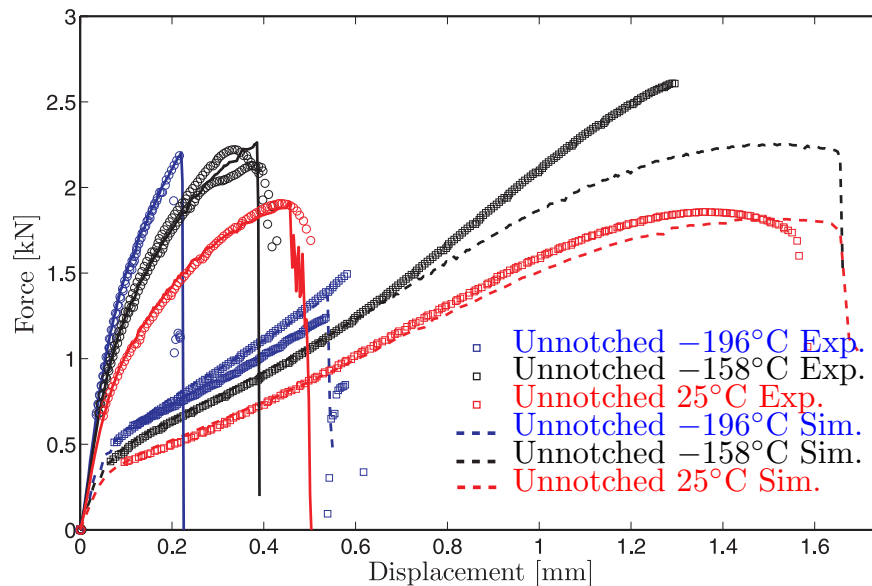
Figure 8.24.: Comparison of experimental and numerical punch force-displacement plots for notched and unnotched tests. The unmarked curves belong to the notched tests shown in Figure 8.20.

8.6.   Conclusion and Outlook

Notwithstanding various experimental studies regarding the ductile–brittle transistion temperature of small punch tests, there has been no attempt to estimate the transition temperature numerically. In this study, a unified thermo-plastic constitutive model combining the RKR brittle damage approach with Gurson's porous plasticity was therefore established to predict the temperature dependent fracture behavior of notched and unnotched small punch specimens. Associated length scales are taken into account for both the ductile and brittle modes of fracture. A detailed parameter identification has been carried out for the corresponding constitutive behaviors. The model was validated by comparing experimental and numerical load-displacement curves as well as optical and SEM images of the fractured disks revealing the crack patterns and fracture surface morphologies. The results provide new insight in the application of a non-local formulation of brittle fracture under small-scale (notched specimens) and large-scale yielding conditions (unnotched specimens). The model developed will be instrumental in the further analysis of the effects of strain rate, different notch and puncher head geometries on small punch transition temperature.

The application of the present numerical modeling scheme to small punch testing constitutes a novel approach which is expected to impact model validation and calibration in general: as a matter of fact, the small punch test is most sensitive as a model validation tool owing to its

multi-axiality and loading history. This is even more true as different specimen geometries – notched and unnotched – are considered. At the same time, from an experimental point of view it only requires tiny amounts of material and, therefore, is almost non-destructive. Further, specimens are easy (and cheap) to manufacture, and the experimental setup is comparatively simple.

8.A. Numerical Implementation

The ABAQUS implementation of the nonlocal framework is handled in two parts. In the first part a local return mapping algorithm is applied via the VUMAT subroutine interface. The void volume fraction increments and the maximum principal stresses are saved at the end of the time step. These are then used through the VUSDFLD subroutine for the computation of the nonlocal counterparts. At the beginning of the following time step, the local void volume fraction increments are replaced by their nonlocal counterparts.

8.A.1. Local Integration Algorithm

Due to the reasons given in Section 5, $\boldsymbol{q} = \boldsymbol{0}$ is assumed and the global heat flux problem is not solved. The remaining system could be solved locally assuming adiabatic conditions. For the sake of completeness, the adiabatic implementation is given. Isothermal conditions are met for $\chi = 0$. The complete set of equations reads:

$$\left.\begin{array}{rcl} \dot{\widehat{\boldsymbol{\epsilon}}}_{\mathrm{e}} & = & \dot{\widehat{\boldsymbol{\epsilon}}} - \dot{\widehat{\boldsymbol{\epsilon}}}_{\mathrm{p}} - \dot{\widehat{\boldsymbol{\epsilon}}}_{\Theta}\,, \\ \dot{\widehat{\boldsymbol{\epsilon}}}_{\mathrm{p}} & = & \dot{\gamma}\partial_{\widehat{\boldsymbol{\sigma}}}\Phi_{\mathrm{p}}\,, \\ \dot{\widehat{\boldsymbol{\epsilon}}}_{\Theta} & = & \alpha_{\Theta}\dot{\Theta}\boldsymbol{1}\,, \\ \dot{\widehat{\boldsymbol{\sigma}}} & = & \boldsymbol{\mathcal{C}}_{\mathrm{e}} : \dot{\widehat{\boldsymbol{\epsilon}}}_{\mathrm{e}}\,, \\ \dot{e}_{\mathrm{p}} & = & \dot{\gamma}\boldsymbol{\eta} : \partial_{\widehat{\boldsymbol{\sigma}}}\Phi_{\mathrm{p}}\,, \\ \dot{f} & = & \dot{\gamma}\left[A_{N}\boldsymbol{\eta} + \boldsymbol{B}_{G}\right] : \partial_{\widehat{\boldsymbol{\sigma}}}\Phi_{\mathrm{p}}\,, \\ \dot{\Theta} & = & \dot{\gamma}\left[\chi/\rho c_{\mathrm{p}}\right]\widehat{\boldsymbol{\sigma}} : \partial_{\widehat{\boldsymbol{\sigma}}}\Phi_{\mathrm{p}}\,. \end{array}\right\} \tag{8.A.1}$$

$\boldsymbol{\eta} := \widehat{\boldsymbol{\sigma}}/\left[\left[1 - f\right]\sigma_{\mathrm{y}}\right]$ and $\boldsymbol{B}_{G} = \boldsymbol{B}_{G}\left(f, \boldsymbol{\sigma}_{D}\right)$ is defined as

$$\boldsymbol{B}_{G} := \left[1 - f\right]\boldsymbol{1} + k_{w}f\frac{w\left(\widehat{\boldsymbol{\sigma}}_{D}\right)}{\sigma_{\mathrm{eq}}}\widehat{\boldsymbol{\sigma}}_{D}\,. \tag{8.A.2}$$

For solving Equations 8.A.1, an elastic predictor−thermo-plastic corrector type of algorithm is used. Letting $\Delta\left(\bullet\right) = \Delta t \times \left(\dot{\bullet}\right)$, the subscript $n+1$ denotes the (unknown) step at time t_{n+1} and n denotes the (known) step at time t_{n}, the solution $\{\widehat{\boldsymbol{\sigma}}_{n+1}, e_{\mathrm{p}\,n+1}, f_{n+1}, \Theta_{n+1}\}$ is sought for the given $\{\widehat{\boldsymbol{\sigma}}_{n}, e_{\mathrm{p}\,n}, f_{n}, \Theta_{n}\}$ and the strain increment $\Delta\widehat{\boldsymbol{\epsilon}}$ with $\Delta t = t_{n+1} - t_{n}$. The corresponding operator-split is summarized in Table 8.2.

Elastic Predictor. Here, a *trial* step is realized assuming that the strain increment $\Delta\widehat{\boldsymbol{\epsilon}}$ is purely elastic. Once the corresponding value of the flow potential is smaller than zero, i.e., $\Phi_{\mathrm{p},n+1,\mathrm{trial}} < 0$, the trial step is assumed to be correct, otherwise a thermo-plastic correction is required.

Thermo-Plastic Corrector. The semi-implicit thermo-plastic corrector algorithm relies on exploitation of the first-order Taylor series expansion of the yield potential around a known step

Table 8.2.: Elastic predictor−thermo-plastic corrector type operator split.

total				elastic predictor				thermo-plastic corrector		
$\Delta\widehat{\boldsymbol{\epsilon}}$	$\neq$	$\mathbf{0}$		$\Delta\widehat{\boldsymbol{\epsilon}}$	$\neq$	$\mathbf{0}$		$\Delta\widehat{\boldsymbol{\epsilon}}$	$=$	$\mathbf{0}$
$\Delta\widehat{\boldsymbol{\epsilon}}_{\mathrm{p}}$	$\neq$	$\mathbf{0}$		$\Delta\widehat{\boldsymbol{\epsilon}}_{\mathrm{p}}$	$=$	$\mathbf{0}$		$\Delta\widehat{\boldsymbol{\epsilon}}_{\mathrm{p}}$	$\neq$	$\mathbf{0}$
$\Delta\widehat{\boldsymbol{\epsilon}}_{\Theta}$	$\neq$	$\mathbf{0}$		$\Delta\widehat{\boldsymbol{\epsilon}}_{\Theta}$	$=$	$\mathbf{0}$		$\Delta\widehat{\boldsymbol{\epsilon}}_{\Theta}$	$\neq$	$\mathbf{0}$
$\Delta\widehat{\boldsymbol{\sigma}}$	$\neq$	$\mathbf{0}$	$=$	$\Delta\widehat{\boldsymbol{\sigma}}$	$=$	$\boldsymbol{\mathcal{C}}_{\mathrm{e}}:\Delta\widehat{\boldsymbol{\epsilon}}$	$+$	$\Delta\widehat{\boldsymbol{\sigma}}$	$=$	$-\boldsymbol{\mathcal{C}}_{\mathrm{e}}:[\Delta\widehat{\boldsymbol{\epsilon}}_{p}+\Delta\widehat{\boldsymbol{\epsilon}}_{\Theta}]$
Δe_{p}	$\neq$	0		Δe_{p}	$=$	0		Δe_{p}	$\neq$	0
Δf	$\neq$	0		Δf	$=$	0		Δf	$\neq$	0
$\Delta\Theta$	$\neq$	0		$\Delta\Theta$	$=$	0		$\Delta\Theta$	$\neq$	0

$\langle i\rangle$

$$
\Phi_{\mathrm{p},n+1,\langle i+1\rangle} \simeq \Phi_{\mathrm{p},n+1,\langle i\rangle} + \boldsymbol{r}_{n+1}^{\langle i\rangle} : \delta\widehat{\boldsymbol{\sigma}}_{n+1}^{\langle i\rangle} + \xi_{n+1}^{\langle i\rangle}\delta e_{\mathrm{p},n+1,\langle i\rangle} + \varsigma_{n+1}^{\langle i\rangle}\delta f_{n+1}^{\langle i\rangle}
$$
$$
+ \varpi_{n+1}^{\langle i\rangle}\delta\dot{e}_{\mathrm{p},n+1,\langle i\rangle} + \mu_{n+1}^{\langle i\rangle}\delta\Theta_{n+1}^{\langle i\rangle}\,, \tag{8.A.3}
$$

where

$$
\begin{aligned}
\boldsymbol{r} &:= \partial_{\widehat{\boldsymbol{\sigma}}}\Phi_{\mathrm{p}} &&= \partial_{\sigma_{\mathrm{eq}}}\Phi_{\mathrm{p}}\partial_{\widehat{\boldsymbol{\sigma}}}\sigma_{\mathrm{eq}} + \partial_{\sigma_{\mathrm{m}}}\Phi_{\mathrm{p}}\partial_{\widehat{\boldsymbol{\sigma}}}\sigma_{\mathrm{m}}\,, \\
\xi &:= \partial_{e_{\mathrm{p}}}\Phi_{\mathrm{p}} &&= \partial_{\sigma_{\mathrm{y}}}\Phi_{\mathrm{p}}\partial_{e_{\mathrm{p}}}\sigma_{\mathrm{y}}\,, \\
\varsigma &:= \partial_{f}\Phi_{\mathrm{p}} &&= 2q_1\cosh\left(3/2\left[q_2\sigma_{\mathrm{m}}/\sigma_{\mathrm{y}}\right]\right) - 2fq_3\,, \\
\varpi &:= \partial_{\dot{e}_{\mathrm{p}}}\Phi_{\mathrm{p}} &&= \partial_{\sigma_{\mathrm{y}}}\Phi_{\mathrm{p}}\partial_{\dot{e}_{\mathrm{p}}}\sigma_{\mathrm{y}}\,, \\
\mu &:= \partial_{\Theta}\Phi_{\mathrm{p}} &&= \partial_{\sigma_{\mathrm{y}}}\Phi_{\mathrm{p}}\partial_{\Theta}\sigma_{\mathrm{y}}\,.
\end{aligned} \tag{8.A.4}
$$

The increments $\delta\left(\bullet\right)^{\langle i\rangle} = \left(\bullet\right)^{\langle i+1\rangle} - \left(\bullet\right)^{\langle i\rangle}$ in Equation (8.A.3) read

$$
\begin{aligned}
\delta\widehat{\boldsymbol{\sigma}}_{n+1}^{\langle i\rangle} &= -\delta\gamma_{n+1}^{\langle i\rangle}\boldsymbol{\mathcal{C}}_{\mathrm{e}} : \left[\boldsymbol{r}_{n+1}^{\langle i\rangle} + \alpha_{\Theta}\chi/\left[\rho_0 c_{\mathrm{p}}\right]\left[\widehat{\boldsymbol{\sigma}}_{n+1}^{\langle i\rangle} : \boldsymbol{r}_{n+1}^{\langle i\rangle}\right]\mathbf{1}\right]\,, \\
\delta e_{\mathrm{p},n+1,\langle i\rangle} &= \delta\gamma_{n+1}^{\langle i\rangle}\boldsymbol{\eta}_{n+1}^{\langle i\rangle} : \boldsymbol{r}_{n+1}^{\langle i\rangle}\,, \\
\delta f_{n+1}^{\langle i\rangle} &= \delta\gamma_{n+1}^{\langle i\rangle}\left[A_{N,n+1}^{\langle i\rangle}\boldsymbol{\eta}_{n+1}^{\langle i\rangle} + \boldsymbol{B}_{G,n+1}^{\langle i\rangle}\right] : \boldsymbol{r}_{n+1}^{\langle i\rangle}\,, \\
\delta\dot{e}_{\mathrm{p},n+1,\langle i\rangle} &= \delta e_{\mathrm{p},n+1,\langle i\rangle}/\Delta t \\
\delta\Theta_{n+1}^{\langle i\rangle} &= \delta\gamma_{n+1}^{\langle i\rangle}\chi/\left[\rho_0 c_{\mathrm{p}}\right]\widehat{\boldsymbol{\sigma}}_{n+1}^{\langle i\rangle} : \boldsymbol{r}_{n+1}^{\langle i\rangle}\,.
\end{aligned} \tag{8.A.5}
$$

Using the condition $\Phi_{\mathrm{p},n+1,\langle i+1\rangle} = 0$ as required, and substituting Equation (8.A.3) into the right-hand side of Equation (8.A.5) which allows factoring out the incremental plasticity parameter, one finds $\delta\gamma_{n+1}^{\langle i\rangle}$ as

$$
\delta\gamma_{n+1}^{\langle i\rangle} = \frac{\Phi_{\mathrm{p},n+1,\langle i\rangle}}{\boldsymbol{r}_{n+1}^{\langle i\rangle} : \left[\boldsymbol{\mathcal{C}}_{\mathrm{e}} : \boldsymbol{A}_{n+1}^{\langle i\rangle} + \boldsymbol{D}_{n+1}^{\langle i\rangle}\right]}\,, \tag{8.A.6}
$$

where

$$
\boldsymbol{A}_{n+1}^{\langle i\rangle} = \boldsymbol{r}_{n+1}^{\langle i\rangle} + \alpha_{\Theta}\chi/\left[\rho_0 c_{\mathrm{p}}\right]\left[\widehat{\boldsymbol{\sigma}}_{n+1}^{\langle i\rangle} : \boldsymbol{r}_{n+1}^{\langle i\rangle}\right]\mathbf{1}\,, \tag{8.A.7}
$$

and

$$
\boldsymbol{D}_{n+1}^{\langle i\rangle} = \left[\xi_{n+1}^{\langle i\rangle} + \frac{\varpi_{n+1}^{\langle i\rangle}}{\Delta t}\right]\boldsymbol{\eta}_{n+1}^{\langle i\rangle} + \varsigma_{n+1}^{\langle i\rangle}\left[A_{N,n+1}^{\langle i\rangle}\boldsymbol{\eta}_{n+1}^{\langle i\rangle} + \boldsymbol{B}_{G,n+1}^{\langle i\rangle}\right] + \mu_{n+1}^{\langle i\rangle}\frac{\chi}{\rho_0 c_{\mathrm{p}}}\widehat{\boldsymbol{\sigma}}_{n+1}^{\langle i\rangle}\,. \tag{8.A.8}
$$

An initial guess of the plastic multiplier $\Delta\gamma_{n+1}^{\langle 0\rangle}$ is assigned while starting the iterations. This depends on the rate dependence of hardening which is assumed to vanish for $\dot{e}_{\mathrm{p}} < \dot{e}_{\mathrm{p0}}$, that is $r_{\mathrm{y}} = 1$ as $\dot{e}_{\mathrm{p}} < \dot{e}_{\mathrm{p0}}$. The consequent numerical difficulty pertaining to the hardening discontinuity is remedied following the lines of [351]. Consequently, once $\Phi_{\mathrm{p}}\left(\Delta t \times \dot{e}_{\mathrm{p0}}\right) > 0$ the initial guess

$\Delta\gamma_{n+1}^{\langle 0 \rangle} = \Delta t \times \dot{e}_{\mathrm{p0}}$, otherwise $\Delta\gamma_{n+1}^{\langle 0 \rangle} = 0$, is used. State variable updates $(\bullet)^{\langle i+1 \rangle} = (\bullet)^{\langle i \rangle} + \delta\,(\bullet)^{\langle i \rangle}$ are continued throughout the iterations $\langle i \rangle$ for the computed increment of the plastic multiplier in Equation (8.A.6), until $\Phi_{\mathrm{p},n+1,\langle i+1 \rangle} \simeq 0$ to a desired accuracy. The stress tensor is then rotated back to the current coordinates: $\boldsymbol{\sigma}_{n+1} = \boldsymbol{R}_{n+1} \cdot \widehat{\boldsymbol{\sigma}}_{n+1} \cdot \boldsymbol{R}_{n+1}^{\top}$.

8.A.2.   Nonlocal Averaging

The implementation of the nonlocal averaging is realized over the time discrete form of the void volume fraction rate and the principal stress components using the VUSDFLD subroutine interface of ABAQUS. The integration is supplied using Gaussian quadrature over the material points inside the nonlocal volume of interaction.

A drawback of the nonlocal averaging schemes is associated with the boundary nonconvexity. Nonconvexity can occur due to specimen geometry as well as newly produced surfaces from crack propagation. Such nonconvexities render the interaction among material points at opposing sides of the discontinuity questionable due to the long range interactions of the microcracks with each other related to the high scattering effects of the elastic waves. In order to circumvent this problem a visibility criterion, similar to the one presented in [50] within the context of meshless methods, is applied for both brittle and ductile damage processes. Accordingly, Gauss points blocked by the existence of a free surface either due to an extended crack or nonconvex boundary surface are excluded from the interaction vector of the receiver Gauss point even if they are within the interaction radius Equation (8.25).

■ element containing central Gauss point (GP)

■ elements with visible GPs in the interaction radius

■ elements with invisible GPs in the interaction radius

□ elements with GPs outside the interaction radius

□ deleted elements representing the crack
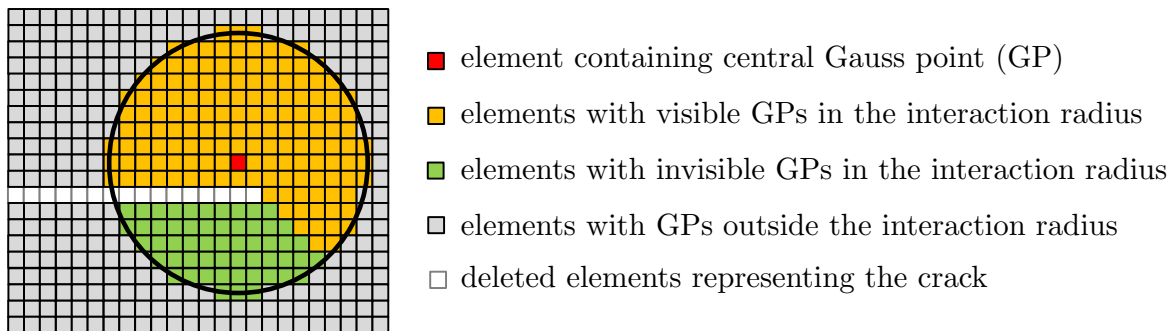
Figure 8.25.: A depiction of the visibility method implemented which is motivated by [50]. Besides the free surfaces produced by element deletion during virtual crack extension, without loss of generality the implementation is generalized to include any kind of nonconvexities in the problem boundary which naturally arises in the notched small punch test.

8.B.   Material Parameters

For convenience, Table 8.3 compiles the material parameters used.

Table 8.3.: Material parameters for small punch disks made of P91 steel. Values are given at
$\Theta = \{-196^\circ C, -158^\circ C, 25^\circ C\}$.

Parameter	Symbol	Value	Unit	Reference
Thermal expansion coef.	α_Θ	1.3×10^{-5}	K^{-1}	Equation (8.2.5)
Melting temperature	Θ_{melt}	1717	K	Equation (9.3.6)
Reference temperature	Θ_{ref}	298	K	Equation (9.3.6)
Specific heat capacity	c_{p}	622	$m^2 K^{-1} s^{-2}$	Equation (8.2.19)
Taylor–Quinney coef.	χ	0.9	$[-]$	Equation (8.2.19)
Density (initial)	ρ	7.85×10^{-9}	$\mathrm{t\,mm^{-3}}$	Equation (8.2.19)
Young's modulus	E	$\{234.9, 230.6, 210\}$	GPa	Equation (8.2.4)
Poisson's ratio	ν	0.3	$[-]$	Equation (8.2.4)
Plastic hardening	h_0	123	MPa	Equation (8.4.1)
	h_1	75	MPa	Equation (8.4.1)
	σ_{y0}	520	MPa	Equation (8.4.1)
	σ_{y1}	376	MPa	Equation (8.4.1)
	$\sigma_{\mathrm{y\infty}}$	831	MPa	Equation (8.4.1)
	m	6.14	$[-]$	Equation (8.4.1)
	n	0.541	$[-]$	Equation (8.4.1)
	e_{p0}	0.006	$[-]$	Equation (8.4.1)
Temperature effect	$t_{\mathrm{y}}(\Theta)$	$\{1.54, 1.24, 1\}$	$[-]$	Equation (8.2.8)
Strain rate effect	$r_{\mathrm{y}}(\dot{\epsilon}^p)$	1	$[-]$	Equation (8.2.8)
Nonlocal GTN model	$(q_1 = 1/f_{\mathrm{u}}^*, q_2, q_3)$	$(1.5, 1, 2.25)$	$[-]$	Equation (8.2.6)
	f_0	0.00044	$[-]$	Equation (8.4.2)
	f_{N}	0.02	$[-]$	Equation (8.2.14)
	ϵ_{N}	0.3	$[-]$	Equation (8.2.14)
	S_{N}	0.1	$[-]$	Equation (8.2.14)
	k_{w}	0	$[-]$	Equation (8.2.17)
	f_{c}	0.1	$[-]$	Equation (8.2.7)
	f_{F}	0.25	$[-]$	Equation (8.2.7)
	R_{ductile}	$[2.5, 5]$	μm	Equation (8.2.21)
Nonlocal RKR model*	σ_{c}	$[2.83\sigma_{\mathrm{y0}}, 2.55\sigma_{\mathrm{y0}}]$	MPa	Equation (8.2.26)
	R_{brittle}	$[7, 12.5]$	μm	Equation (8.2.24)

*For both the notched and unnotched cases the brittle fracture onset can be predicted reasonably well with $(\sigma_{\mathrm{c}}, R_{\mathrm{brittle}}) = (2.83\sigma_{\mathrm{y0}}, 7\ \mu\mathrm{m})$ for which $R_{\mathrm{ductile}} = 2.5\ \mu\mathrm{m} < R_{\mathrm{brittle}}$ can be selected.

9. Thermomechanical formulation of ductile damage coupled to nonlinear isotropic hardening and multiplicative viscoplasticity

In this chapter, a thermomechanical framework which makes use of the internal variable theory of thermodynamics for damage-coupled finite viscoplasticity with nonlinear isotropic hardening is presented. Damage evolution, being an irreversible process, generates heat. In addition to its direct effect on material's strength and stiffness, it causes deterioration of the heat conduction. The formulation, following the footsteps of [SIMO, J. C., MIEHE, CH. [1992]: "Associative coupled thermoplasticity at finite strains: Formulation, numerical analysis and implementation", *Computer Methods in Applied Mechanics and Engineering*, Vol. 98, 41–104.], introduces inelastic entropy as an additional state variable. Given a temperature dependent damage dissipation potential, it is shown that the evolution of inelastic entropy assumes a split form relating to plastic and damage parts, respectively. The solution of the thermomechanical problem is based on the so-called isothermal split. This allows the use of the model in 2D and 3D example problems involving geometrical imperfection triggered necking in an axisymmetric bar and thermally triggered necking of a 3D rectangular bar. The presented content constitutes an extended and more systematic treatment (both theoretically and numerically) of the framework that is presented in [278]. In the current treatment, viscosity is used not for regularization purpose but for characterizing physical rate effect which makes the treatment more transparent.

9.1. Introduction

Dissipated mechanical work produces heat which is conducted/convected over the problem domain. Complicated mutual interactions among fields act in a coupled problem of deformation and temperature. Without reckoning damage, one can consider a two sided coupling: the influence of the thermal field on the mechanical field (thermal expansion, temperature induced elastic softening with temperature dependence of elastic material properties, temperature induced plastic softening with yield locus shrinkage), the influence of the mechanical field on the thermal field (geometric coupling on heat flux, heat generation by plastic dissipation, structural elastic heating: the GOUGH-JOULE effect.)

Plasticity and damage are two path dependent irreversible dissipative deformation mechanisms that differ on micro-mechanical foundations. The former entails crystal slip through dislocation movements, while the latter involves the nucleation, growth and coalescence of micro-voids and/or micro-cracks. Hence, further conditions that must be analyzed in the presence of damage include: the action of damage on the other mechanical fields (damage induced elastic softening with deteriorated elastic stiffness, damage induced plastic softening with yield locus shrinkage), the influence of damage on the thermal field (heat generation by damage dissipation, damage

dependent heat flux), and the influence of the thermal field on damage (direct effect through temperature dependence of the damage dissipation functions, indirect effect through reconstruction of other damage driving mechanical fields, e.g., triaxiality).

Many studies on damage coupled finite plasticity, e.g., [274, 144, 291, 86, 167, 247], among others, are limited to purely isothermal conditions. Damage coupled finite strain thermoplastic frameworks utilizing GURSON and LEMAITRE damage models are presented in [84] and [263], respectively. More recently, a combination of Lemaitre and Gurson damage models, for modeling micro-void and/or micro-crack driven failure in metals at finite strains, is presented in [289]. None of the above mentioned works accounts for the effect of damage on heat conduction. However, micro-void and/or micro-crack nucleation, growth and coalescence creates a discontinuous porous medium for which the heat transfer is disturbed.

The current chapter aims to develop a thermodynamically consistent framework for damage coupled finite multiplicative thermoviscoplasticity. The framework for finite thermoplasticity is set forward along the same lines with [275] whereas the damage is formulated along with the effective stress concept, [145] and [255], with strain equivalence principle, [174]. Accordingly, using its extensive property, entropy is postulated to be decomposed into elastic and inelastic parts, where the latter is further additively partitioned into plastic and damage parts as a consequence of temperature dependent plastic and damage dissipation potentials. Hence this extends the theoretical framework postulated in [275]to consider not only the plastic structural changes due to dislocation and lattice defect motion but also the damage structural changes due to microvoid nucleation, growth and coalescence.

9.2. Mathematical Theory

9.2.1. Fundamental Kinematics

Let $\varphi(\boldsymbol{X}, t)$ denote the invertible nonlinear deformation map which maps points $\boldsymbol{X} \in \mathfrak{B}_0$ of the reference configuration $\mathfrak{B}_0$ onto points $\boldsymbol{x} \in \mathfrak{B}$ of the current configuration $\mathfrak{B}$ at time $t \in \mathbb{R}_+$ via $\boldsymbol{x} = \varphi(\boldsymbol{X}, t)$ with $\boldsymbol{X} = \varphi^{-1}(\boldsymbol{x}, t)$. Then $\boldsymbol{F}$ defines the deformation gradient and J its JACOBIAN determinant with

$$\boldsymbol{F} = \mathbf{Grad}\, \varphi(\boldsymbol{X}, t) \quad \text{and} \quad J := \det \boldsymbol{F} > 0\,, \tag{9.2.1}$$

where the latter is due to local impenetrability condition. The volume-preserving part of the deformation gradient is denoted by $\overline{\boldsymbol{F}}$ where

$$\overline{\boldsymbol{F}} := J^{-1/3} \boldsymbol{F} \quad \text{and} \quad \det \overline{\boldsymbol{F}} = 1\,. \tag{9.2.2}$$

The right $\boldsymbol{C}$ and left $\boldsymbol{b}$ CAUCHY-GREEN deformation tensors and their respective volume preserving counterparts $\overline{\boldsymbol{C}}$ and $\overline{\boldsymbol{b}}$ read

$$\boldsymbol{C} := \boldsymbol{F}^\top \cdot \boldsymbol{F}\,, \quad \overline{\boldsymbol{C}} := \overline{\boldsymbol{F}}^\top \cdot \overline{\boldsymbol{F}} = J^{-2/3} \boldsymbol{C} \quad \text{with} \quad \det \boldsymbol{C} = J^2 \quad \text{and} \quad \det \overline{\boldsymbol{C}} = 1\,, \tag{9.2.3}$$

$$\boldsymbol{b} := \boldsymbol{F} \cdot \boldsymbol{F}^\top\,, \quad \overline{\boldsymbol{b}} := \overline{\boldsymbol{F}} \cdot \overline{\boldsymbol{F}}^\top = J^{-2/3} \boldsymbol{b} \quad \text{with} \quad \det \boldsymbol{b} = J^2 \quad \text{and} \quad \det \overline{\boldsymbol{b}} = 1\,. \tag{9.2.4}$$

The following local multiplicative decomposition of the deformation gradient into elastic $\boldsymbol{F}^{\mathrm{e}}$ and viscoplastic $\boldsymbol{F}^{\mathrm{vp}}$ parts is used [[170]]

$$\boldsymbol{F} := \boldsymbol{F}^{\mathrm{e}} \cdot \boldsymbol{F}^{\mathrm{vp}} \quad \text{with} \quad J^{\mathrm{e}} := \det \boldsymbol{F}^{\mathrm{e}} \equiv J \quad \text{and} \quad J^{\mathrm{vp}} := \det \boldsymbol{F}^{\mathrm{vp}} = 1\,, \tag{9.2.5}$$

which exploits plastic incompressibility. Hence, the volume preserving parts of elastic and plastic parts of the deformation gradient are defined respectively as

$$\overline{\boldsymbol{F}^{\mathrm{e}}} := [J^{\mathrm{e}}]^{-1/3} \boldsymbol{F}^{\mathrm{e}} \quad \text{with} \quad \overline{\boldsymbol{F}^{\mathrm{vp}}} := [J^{\mathrm{vp}}]^{-1/3} \boldsymbol{F}^{\mathrm{vp}} \equiv \boldsymbol{F}^{\mathrm{vp}} \,. \tag{9.2.6}$$

The viscoplastic right CAUCHY-GREEN deformation tensor $\boldsymbol{C}^{\mathrm{vp}}$ and elastic left CAUCHY-GREEN deformation tensor $\boldsymbol{b}^{\mathrm{e}}$ read

$$\boldsymbol{C}^{\mathrm{vp}} := [\boldsymbol{F}^{\mathrm{vp}}]^{\top} \cdot \boldsymbol{F}^{\mathrm{vp}} \equiv \boldsymbol{F}^{-1} \cdot \boldsymbol{b}^{\mathrm{e}} \cdot [\boldsymbol{F}]^{-\top} \quad \text{and} \quad \boldsymbol{b}^{\mathrm{e}} := \boldsymbol{F}^{\mathrm{e}} \cdot [\boldsymbol{F}^{\mathrm{e}}]^{\top} \,. \tag{9.2.7}$$

The volume preserving counterparts $\overline{\boldsymbol{C}^{\mathrm{vp}}}$ and $\overline{\boldsymbol{b}^{\mathrm{e}}}$ can be given as

$$\overline{\boldsymbol{C}^{\mathrm{vp}}} := \overline{\boldsymbol{F}^{\mathrm{vp}}}^{\top} \cdot \overline{\boldsymbol{F}^{\mathrm{vp}}} \equiv \boldsymbol{C}^{\mathrm{vp}} \quad \text{and} \quad \overline{\boldsymbol{b}^{\mathrm{e}}} := \overline{\boldsymbol{F}^{\mathrm{e}}} \cdot \overline{\boldsymbol{F}^{\mathrm{e}}}^{\top} \equiv [J^{\mathrm{e}}]^{-2/3} \boldsymbol{b}^{\mathrm{e}} \,. \tag{9.2.8}$$

The spatial elastic logarithmic strains are denoted by $\boldsymbol{\epsilon}^{\mathrm{e}}$ with corresponding eigenvalues ϵ_A^{e} for $A = 1, 2, 3$. Let b_A^{e} for $A = 1, 2, 3$ denote the eigenvalues of $\boldsymbol{b}^{\mathrm{e}}$, the following connexions apply

$$\boldsymbol{\epsilon}^{\mathrm{e}} := 1/2 \log \boldsymbol{b}^{\mathrm{e}} \quad \text{and} \quad \epsilon_A^{\mathrm{e}} := \log \lambda_A^{\mathrm{e}} \quad \text{with} \quad \lambda_A^{\mathrm{e}} := \sqrt{b_A^{\mathrm{e}}} \quad \text{and} \quad \lambda_1^{\mathrm{e}} \lambda_2^{\mathrm{e}} \lambda_3^{\mathrm{e}} = J^{\mathrm{e}} \,, \tag{9.2.9}$$

$$\overline{\boldsymbol{\epsilon}^{\mathrm{e}}} := 1/2 \log \overline{\boldsymbol{b}^{\mathrm{e}}} \quad \text{and} \quad \overline{\epsilon_A^{\mathrm{e}}} := \log \overline{\lambda_A^{\mathrm{e}}} \quad \text{with} \quad \overline{\lambda_A^{\mathrm{e}}} := \sqrt{\overline{b_A^{\mathrm{e}}}} \quad \text{and} \quad \overline{\lambda_1^{\mathrm{e}}} \, \overline{\lambda_2^{\mathrm{e}}} \, \overline{\lambda_3^{\mathrm{e}}} = 1 \,. \tag{9.2.10}$$

Here, $\overline{\boldsymbol{\epsilon}^{\mathrm{e}}}$ denotes the volume preserving part of the spatial elastic logarithmic strains with corresponding eigenvalues $\overline{\epsilon_A^{\mathrm{e}}}$. Similarly, $\overline{b_A^{\mathrm{e}}}$ for $A = 1, 2, 3$ denote the eigenvalues of $\overline{\boldsymbol{b}^{\mathrm{e}}}$. λ_A^{e} for $A = 1, 2, 3$ are referred to as elastic principal stretches, whereas $\overline{\lambda_A^{\mathrm{e}}}$ their isochoric counterparts. Note that since

$$\operatorname{tr} \boldsymbol{\epsilon}^{\mathrm{e}} = \log \lambda_1^{\mathrm{e}} + \log \lambda_2^{\mathrm{e}} + \log \lambda_3^{\mathrm{e}} = \log(\lambda_1^{\mathrm{e}} \lambda_2^{\mathrm{e}} \lambda_3^{\mathrm{e}}) = \log J^{\mathrm{e}} \,, \tag{9.2.11}$$

$\operatorname{tr} \boldsymbol{\epsilon}^{\mathrm{e}}$ and $\log J^{\mathrm{e}}$ can be used interchangeably. Finally, the following identity applies

$$\overline{\boldsymbol{\epsilon}^{\mathrm{e}}} \equiv \operatorname{dev} \boldsymbol{\epsilon}^{\mathrm{e}} = \boldsymbol{\epsilon}^{\mathrm{e}} - \frac{1}{3} \log J^{\mathrm{e}} \, \mathbf{1} \,. \tag{9.2.12}$$

9.2.2. Extension of the Thermodynamic Approach Represented in [275]

Following the rational thermodynamics approach followed by [275], the internal energy per unit reference volume is represented by $e(\boldsymbol{F}^{\mathrm{e}}, \boldsymbol{\xi}, \eta^{\mathrm{e}})$. The elastic entropy η^{e} is associated with the lattice and the vector $\boldsymbol{\xi}$ of strain-like internal variables responsible for irreversible mechanisms. Utilizing its extensive property, an additively decoupled total entropy (per unit reference volume)

$$\eta = \eta^{\mathrm{e}} + \eta^{\mathrm{vpd}} \tag{9.2.13}$$

is postulated. η^{vpd} denotes the inelastic (configurational) entropy, linked to the dissipative mechanisms such as viscoplasticity, hardening and damage. An additive split $\eta^{\mathrm{vpd}} = \eta^{\mathrm{vp}} + \eta^{\mathrm{d}}$ follows as a consequence of associative evolutionary equations together with a temperature dependent damage dissipation potential. Here, η^{vp} is associated with irreversible time dependent plastic structural changes, such as dislocation motion and lattice defects whereas η^{d} is associated with dissipative micro-structural changes accompanied by nucleation, growth and coalescence of micro-voids and micro-cracks. By this way, the framework given in [275] is extended to account for damage induced effects.

$\boldsymbol{\xi} = [\alpha, D]^{\top}$ defines the vector of strain-like internal variables with $\alpha \in \mathbb{R}_+$ and $D \in [0, 1]$ which

relates to isotropic hardening and damage, respectively. Through the invariance requirements under arbitrary rigid body rotations on the intermediate configuration $e(\boldsymbol{F}^{\mathrm{e}}, \boldsymbol{\xi}, \eta^{\mathrm{e}}) \mapsto e(\boldsymbol{b}^{\mathrm{e}}, \boldsymbol{\xi}, \eta^{\mathrm{e}})$. Through a LEGENDRE transformation one obtains

$$e(\boldsymbol{b}^{\mathrm{e}}, \boldsymbol{\xi}, \eta^{\mathrm{e}}) = \Psi(\boldsymbol{b}^{\mathrm{e}}, \boldsymbol{\xi}, \Theta) + \Theta\eta^{\mathrm{e}}, \tag{9.2.14}$$

where $\Psi(\boldsymbol{b}^{\mathrm{e}}, \boldsymbol{\xi}, \Theta)$ represents the HELMHOLTZ free energy per unit reference volume, as a function of the absolute temperature $\Theta \in \mathbb{R}_+$. Additive decoupling of $\Psi(\boldsymbol{b}^{\mathrm{e}}, \boldsymbol{\xi}, \Theta)$ gives

$$\Psi(\boldsymbol{b}^{\mathrm{e}}, \boldsymbol{\xi}, \Theta) := \Psi^{\mathrm{e}}(\boldsymbol{b}^{\mathrm{e}}, D) + \Psi^{\Theta\mathrm{e}}(J^{\mathrm{e}}, \Theta, D) + \Psi^{\Theta}(\Theta) + \Psi^{\mathrm{vp}}(\alpha, \Theta). \tag{9.2.15}$$

Here, $\Psi^{\mathrm{e}}(\boldsymbol{b}^{\mathrm{e}}, D)$ represents the damage affected pure elastic free energy which is stored by the body and can be recovered in a purely mechanical process[1]. The thermodilatational potential $\Psi^{\Theta\mathrm{e}}(J^{\mathrm{e}}, \Theta, D)$ encapsulates the effect of damage on material's thermal expansion and it is associated with elastic structural entropy. $\Psi^{\Theta}(\Theta)$ is linked to the purely thermal entropy. $\Psi^{\mathrm{vp}}(\alpha, \Theta)$ stands for the viscoplastic free energy blocked in dislocations due to dislocation rearrangement. Following expressions relate the nominal and the effective[2] free energies

$$\Psi^{\mathrm{e}}(\boldsymbol{b}^{\mathrm{e}}, D) = [1 - D]\, \tilde{\Psi}^{\mathrm{e}}(\boldsymbol{b}^{\mathrm{e}}) \quad \text{and} \quad \Psi^{\Theta\mathrm{e}}(J^{\mathrm{e}}, \Theta, D) = [1 - D]\, \tilde{\Psi}^{\Theta\mathrm{e}}(J^{\mathrm{e}}, \Theta), \tag{9.2.16}$$

where $[\tilde{\bullet}] := [\bullet]\,/[1 - D]$.

State Equations   The second law of thermodynamics supplies the CLAUSIUS-DUHEM inequality

$$0 \le \Omega = \Omega_{\mathrm{conther}} + \Omega_{\mathrm{thermech}}, \tag{9.2.17}$$

where the respective dissipation expressions for the conductive thermal form and the local thermomechanical form per unit reference volume are denoted by $\Omega_{\mathrm{conther}}$ and $\Omega_{\mathrm{thermech}}$, with

$$\Omega_{\mathrm{conther}} := -\frac{1}{\Theta}\boldsymbol{q} \cdot \mathbf{grad}\,\Theta \quad \text{and} \quad \Omega_{\mathrm{thermech}} := \boldsymbol{\tau} : \boldsymbol{d} + \Theta\dot{\eta} - \dot{e}. \tag{9.2.18}$$

Here, $\boldsymbol{q}$ stands for the KIRCHHOFF-type heat flux, analogous with the KIRCHHOFF (weighted CAUCHY) stress tensor $\boldsymbol{\tau}$ which is the work conjugate of the spatial rate of deformation tensor $\boldsymbol{d} := \mathrm{sym}\,(\boldsymbol{l})$ with $\boldsymbol{l} := \dot{\boldsymbol{F}} \cdot \boldsymbol{F}^{-1}$ denoting the spatial velocity gradient. Inequality (9.2.17) can be split into two more restrictive inequalities viz.

$$\Omega_{\mathrm{conther}} \ge 0 \quad \text{and} \quad \Omega_{\mathrm{thermech}} \ge 0. \tag{9.2.19}$$

In view of Equation (9.2.18.1), satisfaction of $\Omega_{\mathrm{conther}} \ge 0$ merely depends upon an appropriately selected definition for $\boldsymbol{q}$. The latter inequality $\Omega_{\mathrm{thermech}} \ge 0$ requires more effort. Taking the material time derivative of the LEGENDRE transform given in Equation (9.2.14), $\dot{e} = \dot{\Psi} + \dot{\Theta}\eta^{\mathrm{e}} + \dot{\eta}^{\mathrm{e}}\Theta$, the latter inequality $\Omega_{\mathrm{thermech}} \ge 0$ can be represented as

$$0 \le \Omega_{\mathrm{thermech}} = \boldsymbol{\tau} : \boldsymbol{d} + \Theta\dot{\eta}^{\mathrm{vpd}} - \dot{\Psi} - \dot{\Theta}\eta^{\mathrm{e}}, \tag{9.2.20}$$

where $\dot{\eta}^{\mathrm{vpd}} := \dot{\eta} - \dot{\eta}^{\mathrm{e}}$. Computation of $\dot{\Psi}$ requires the chain rule

$$\dot{\Psi} = \frac{\partial \Psi}{\partial \boldsymbol{b}^{\mathrm{e}}} : \dot{\boldsymbol{b}}^{\mathrm{e}} + \frac{\partial \Psi}{\partial \boldsymbol{\xi}} \cdot \dot{\boldsymbol{\xi}} + \frac{\partial \Psi}{\partial \Theta}\dot{\Theta}, \tag{9.2.21}$$

---

[1]Although not pursued in the current study, a thermoplastic framework with temperature dependent elastic parameters can be found in [316].

[2]Effective quantities are defined relative to the fictitious undamaged material subscale. Nominal quantities, on the other hand, reflect the influence of damage through homogenization.

with

$$\dot{\boldsymbol{b}}^{\mathrm{e}} = \mathcal{L}_v \boldsymbol{b}^{\mathrm{e}} + \boldsymbol{l} \cdot \boldsymbol{b}^{\mathrm{e}} + \boldsymbol{b}^{\mathrm{e}} \cdot [\boldsymbol{l}]^{\top} \ . \tag{9.2.22}$$

Here, $\mathcal{L}_v(\bullet)$ stands for the objective LIE derivative of $(\bullet)$ via

$$\mathcal{L}_v \boldsymbol{b}^{\mathrm{e}} = \boldsymbol{F} \cdot \dot{\boldsymbol{G}}^{\mathrm{vp}} \cdot [\boldsymbol{F}]^{\top} \ , \tag{9.2.23}$$

where $\boldsymbol{G}^{\mathrm{vp}} := [\boldsymbol{C}^{\mathrm{vp}}]^{-1}$, [205]. Substituting Equations (9.2.21) and (9.2.22) into inequality (9.2.20) one finds

$$\begin{aligned} 0 \le \Omega_{\mathrm{thermech}} = {}&\left[\boldsymbol{\tau} - 2 \frac{\partial \Psi}{\partial \boldsymbol{b}^{\mathrm{e}}} \cdot \boldsymbol{b}^{\mathrm{e}} \right] : \boldsymbol{d} + 2 \frac{\partial \Psi}{\partial \boldsymbol{b}^{\mathrm{e}}} \cdot \boldsymbol{b}^{\mathrm{e}} : \left[-\frac{1}{2} \mathcal{L}_v \boldsymbol{b}^{\mathrm{e}} \cdot [\boldsymbol{b}^{\mathrm{e}}]^{-1} \right] + \Theta \dot{\eta}^{\mathrm{vpd}} \\ &+ \left[-\frac{\partial \Psi}{\partial \boldsymbol{\xi}} \right] \cdot \dot{\boldsymbol{\xi}} + \left[-\frac{\partial \Psi}{\partial \Theta} - \eta^{\mathrm{e}} \right] \dot{\Theta} \,. \end{aligned} \tag{9.2.24}$$

Inelastic rates, i.e. $-1/2\,\mathcal{L}_v \boldsymbol{b}^{\mathrm{e}} \cdot [\boldsymbol{b}^{\mathrm{e}}]^{-1}$, $\dot{\eta}^{\mathrm{vpd}}$ and $\dot{\boldsymbol{\xi}}$, tend to zero for any reversible process. Hence, following the arguments of [79], for inequality (9.2.24) to be valid for arbitrary reversible changes in the observable variables $\boldsymbol{d}$ and $\dot{\Theta}$, the first and the last terms on the right-hand side must independently vanish to give[3]

$$\boldsymbol{\tau} = 2 \frac{\partial \Psi}{\partial \boldsymbol{b}^{\mathrm{e}}} \cdot \boldsymbol{b}^{\mathrm{e}} = \frac{\partial \Psi}{\partial \boldsymbol{\epsilon}^{\mathrm{e}}} \quad \text{and} \quad \eta^{\mathrm{e}} = -\frac{\partial \Psi}{\partial \Theta} \,. \tag{9.2.25}$$

Hence, elastic entropy is the conjugate variable of the temperature. Analogically, one can devise

$$\boldsymbol{\varsigma} = -\frac{\partial \Psi}{\partial \boldsymbol{\xi}} \quad \Rightarrow \quad q = -\frac{\partial \Psi}{\partial \alpha} \quad \text{and} \quad Y^{\mathrm{d}} = -\frac{\partial \Psi}{\partial D} \,. \tag{9.2.26}$$

Here, $\boldsymbol{\varsigma}$ is the vector of stress-like internal variables which are dual to $\boldsymbol{\xi}$ with $\boldsymbol{\varsigma} = \left[q, Y^{\mathrm{d}} \right]^{\top}$. q is responsible for isotropic hardening in the form of yield locus expansion whereas Y^{d} is the thermodynamically formal damage conjugate variable. Additive decomposition of the potentials postulated in Equations (9.2.15) and (9.2.16) result in explicit representations for the state equations given in Equations (9.2.25)

$$\boldsymbol{\tau} = 2\left[1 - D\right] \left[\frac{\partial \tilde{\Psi}^{\mathrm{e}}}{\partial \boldsymbol{\epsilon}^{\mathrm{e}}} + \frac{\partial \tilde{\Psi}^{\Theta\mathrm{e}}}{\partial \boldsymbol{\epsilon}^{\mathrm{e}}} \right] \quad \text{and} \quad \eta^{\mathrm{e}} = -\left[1 - D\right] \frac{\partial \tilde{\Psi}^{\Theta\mathrm{e}}}{\partial \Theta} - \frac{\partial \Psi^{\Theta}}{\partial \Theta} - \frac{\partial \Psi^{\mathrm{vp}}}{\partial \Theta} \tag{9.2.27}$$

and in Equations (9.2.26)

$$q = -\frac{\partial \Psi^{\mathrm{vp}}}{\partial \alpha} \quad \text{and} \quad Y^{\mathrm{d}} = \tilde{\Psi}^{\mathrm{e}} + \tilde{\Psi}^{\Theta\mathrm{e}} \,. \tag{9.2.28}$$

The temperature dependent dilatational terms in KIRCHHOFF stress tensor definition are due to its dependence on $\tilde{\Psi}^{\Theta\mathrm{e}}$. Moreover, as opposed to the conventional LEMAITRE damage model the damage conjugate variable includes temperature dependent terms. As a consequence of the temperature dependence of the viscoplastic free energy[4], elastic entropy involves the term $\partial \Psi^{\mathrm{vp}}/\partial \Theta$.

---

[3]For Equation (9.2.25.1), one uses the chain rule of differentiation

$$\frac{\partial \Psi}{\partial \boldsymbol{b}^{\mathrm{e}}} = \frac{1}{2} \frac{\partial \Psi}{\partial \boldsymbol{\epsilon}^{\mathrm{e}}} : \frac{\partial \log(\boldsymbol{b}^{\mathrm{e}})}{\partial \boldsymbol{b}^{\mathrm{e}}} \quad \text{and} \quad \left[\frac{\partial \Psi}{\partial \boldsymbol{\epsilon}^{\mathrm{e}}} : \frac{\partial \log(\boldsymbol{b}^{\mathrm{e}})}{\partial \boldsymbol{b}^{\mathrm{e}}} \right] \cdot \boldsymbol{b}^{\mathrm{e}} = \frac{\partial \Psi}{\partial \boldsymbol{\epsilon}^{\mathrm{e}}} \,. $$

See, e.g., [87].

[4]In the work of [275] this kind of a coupling at the free energy level is bypassed in the theory, however, used in the application problems.

Evolution Equations   Substitution of Equations (9.2.25) and (9.2.26) back in inequality (9.2.24) with an explicit representation of the vectors $\boldsymbol{\xi}$ and $\boldsymbol{\varsigma}$ yields the following reduced dissipation inequality

$$0 \leq \Omega_{\text{thermech}} = \boldsymbol{\tau} : \left[-\frac{1}{2} \mathcal{L}_v \boldsymbol{b}^{\text{e}} \cdot [\boldsymbol{b}^{\text{e}}]^{-1} \right] + q\,\dot{\alpha} + Y^{\text{d}}\,\dot{D} + \Theta\dot{\eta}^{\text{vpd}} \,. \tag{9.2.29}$$

The local thermomechanical dissipation Ω_{thermech} can be split into thermal Ω_{ther} and mechanical Ω_{mech} parts [[79]] to give

$$0 \leq \Omega_{\text{thermech}} := \Omega_{\text{ther}} + \Omega_{\text{mech}} \,, \tag{9.2.30}$$

where

$$\Omega_{\text{ther}} := \Theta\dot{\eta}^{\text{vpd}} \quad \text{and} \quad \Omega_{\text{mech}} := \Omega_{\text{mech}}^{\text{vp}} + \Omega_{\text{mech}}^{\text{d}} \,, \tag{9.2.31}$$

with

$$\Omega_{\text{mech}}^{\text{vp}} = \boldsymbol{\tau} : \left[-\frac{1}{2} \mathcal{L}_v \boldsymbol{b}^{\text{e}} \cdot [\boldsymbol{b}^{\text{e}}]^{-1} \right] + q\,\dot{\alpha} \quad \text{and} \quad \Omega_{\text{mech}}^{\text{d}} = Y^{\text{d}}\,\dot{D} \,. \tag{9.2.32}$$

Similar to what is done for inequality (9.2.19) one can split inequality (9.2.31) into two stronger inequalities

$$\Omega_{\text{ther}} \geq 0 \quad \text{and} \quad \Omega_{\text{mech}} \geq 0 \,. \tag{9.2.33}$$

Hypothesis of generalized standard materials, which proposes the existence of normality rules, [207], is followed in definition of the evolution equations. For this purpose, an additively decoupled loading function Φ into a temperature dependent viscoplastic potential Φ^{vp} and a temperature dependent damage dissipation potential Φ^{d} is postulated

$$\Phi(\boldsymbol{\tau}, q, Y^{\text{d}}, \Theta, D) := \Phi^{\text{vp}}(\tilde{\boldsymbol{\tau}}, q, \Theta) + \Phi^{\text{d}}(Y^{\text{d}}, \Theta, D) \,. \tag{9.2.34}$$

The reason of formulating Φ^{vp} in terms of effective KIRCHHOFF stress tensor is due to the fact that viscoplastic flow is physically possible at the undamaged material subscale. Extending the standard normality rule and using Equation (9.2.34) the flow rule is computed viz.

$$-\frac{1}{2} \mathcal{L}_v \boldsymbol{b}^{\text{e}} \cdot [\boldsymbol{b}^{\text{e}}]^{-1} = \dot{\gamma} \frac{\partial \Phi}{\partial \boldsymbol{\tau}} \quad \Rightarrow \quad \mathcal{L}_v \boldsymbol{b}^{\text{e}} = -2 \frac{\dot{\gamma}}{1 - D} \frac{\partial \Phi^{\text{vp}}}{\partial \tilde{\boldsymbol{\tau}}} \cdot \boldsymbol{b}^{\text{e}} \,, \tag{9.2.35}$$

which is coaxial with the KIRCHHOFF stress due to isotropy. Here, $\dot{\gamma}$ represents the viscoplastic multiplier. The current approach generalizes the viscoplasticity of overstress-type[5] by considering all processes to be viscoplastic for stress states outside the thermoelastic domain, i.e., $\Phi^{\text{vp}} > 0$. Thermoelastic domain, on the other hand, is represented by $\Phi^{\text{vp}} < 0$. Accordingly, in spirit of PERZYNA the following is postulated[6]

$$\dot{\gamma} := \begin{cases} 0 & \Phi^{\text{vp}} \leq 0 \,, \\ \dfrac{1}{t_\star} f(\Phi^{\text{vp}}) & \Phi^{\text{vp}} > 0 \,, \end{cases} \tag{9.2.36}$$

where $t_\star$ is the characteristic relaxation time and the nondimensional function f is a monotonically increasing function of Φ^{vp} and it is required that $f(\Phi^{\text{vp}}) = 0$ for $\Phi^{\text{vp}} = 0$. As $t_\star \to 0$

---

[5]Viscosity has also a regularizing effect on the mesh dependence of the softening response. In context of damage-coupled plasticity, using PERZYNA-type rate dependence, single surface overstress-type viscous forms are utilized by [83] and [277] among others.

[6]On the contrary, rate independent theories do not allow the condition $\Phi^{\text{p}} > 0$. Thus, the definition of the plastic multiplier $\dot{\gamma}$ relies on the KUHN-TUCKER optimality conditions

$$\dot{\gamma} \geq 0 \,, \quad \Phi^{\text{p}}(\tilde{\boldsymbol{\tau}}, q, \Theta) \leq 0 \quad \text{and} \quad \dot{\gamma}\Phi^{\text{p}}(\tilde{\boldsymbol{\tau}}, q, \Theta) = 0 \,.$$

rate independent plasticity is recovered whereas $t_\star \to \infty$ represents the elastic theory since all inelastic processes cease to evolve. Also for zero elastic limit creep is carried out. Having $\dot{\gamma}$ defined, the rates of the scalar internal variables α, D and η^{vpd} read

$$\dot{\alpha} = \dot{\gamma}\, \frac{\partial \Phi}{\partial q}\,, \quad \dot{D} = \dot{\gamma}\, \frac{\partial \Phi}{\partial Y^{\mathrm{d}}} \quad \text{and} \quad \dot{\eta}^{\mathrm{vpd}} = \dot{\gamma}\, \frac{\partial \Phi}{\partial \Theta}\,. \tag{9.2.37}$$

In view of Equation (9.2.34), Equations (9.2.37) can be reiterated as

$$\dot{\alpha} = \dot{\gamma}\, \frac{\partial \Phi^{\mathrm{vp}}}{\partial q}\,, \quad \dot{D} = \dot{\gamma}\, \frac{\partial \Phi^{\mathrm{d}}}{\partial Y^{\mathrm{d}}} \quad \text{and} \quad \dot{\eta}^{\mathrm{vpd}} = \dot{\gamma}\, \frac{\partial \Phi^{\mathrm{vp}}}{\partial \Theta} + \dot{\gamma}\, \frac{\partial \Phi^{\mathrm{d}}}{\partial \Theta}\,. \tag{9.2.38}$$

In context of the maximum inelastic dissipation postulate, multi-surface damage-plasticity models which account for separate viscoplastic and damage multipliers (in form of LAGRANGE multipliers), damage evolution in absence of plastic flow is possible, [119]. In the current formulation, on the other hand, damage concurrently occurs with viscoplasticity since the growths of both α and D depend on the viscoplastic multiplier $\dot{\gamma}$ as the consequence of kinematic coupling between plasticity and damage. Such an application has proven convenient in ductile metal damage, where the dislocation pile-ups supply as a void nucleation source. This also postulates that the evolution of the inelastic entropy depends on both the viscoplasticity and the damage dissipation potentials, which is an extension to [275] where no damage mechanism is taken into account. One may represent the inelastic entropy production given in Equation (9.2.38.3) in an additive form in terms of viscoplastic and damage parts

$$\dot{\eta}^{\mathrm{vpd}} = \dot{\eta}^{\mathrm{vp}} + \dot{\eta}^{\mathrm{d}} \quad \text{with} \quad \dot{\eta}^{\mathrm{vp}} = \dot{\gamma}\, \frac{\partial \Phi^{\mathrm{vp}}}{\partial \Theta} \quad \text{and} \quad \dot{\eta}^{\mathrm{d}} = \dot{\gamma}\, \frac{\partial \Phi^{\mathrm{d}}}{\partial \Theta}\,. \tag{9.2.39}$$

Finally, for the temperature evolution equation, following [275], the local energy balance equation, i.e., the first law of thermodynamics, reads

$$-J \mathrm{div}\left(\frac{\boldsymbol{q}}{J} \right) + R = \dot{e} - \boldsymbol{\tau} : \boldsymbol{d}\,. \tag{9.2.40}$$

Here, R represents the heat source. In the first term on the left-hand side, $\boldsymbol{q}/J$ represents conversion of the heat flux from KIRCHHOFF- to CAUCHY-type whereas the factor J in front of $\mathrm{div}\left(\boldsymbol{q}/J \right)$ guarantees that the quantity is computed per unit reference volume. Using Equations (9.2.13), (9.2.20), (9.2.30) and (9.2.31.2) and the material time derivative of Equation (9.2.25.2) one carries out

$$\dot{e} - \boldsymbol{\tau} : \boldsymbol{d} = -\Omega_{\mathrm{mech}} + \Theta \left[\dot{\eta} - \dot{\eta}^{\mathrm{vpd}} \right] = -\Omega_{\mathrm{mech}} + \mathcal{H} + \dot{\Theta} c\,, \tag{9.2.41}$$

where $\mathcal{H}$ denotes the elastic-plastic-damage structural heating which is related to the latent elastic and inelastic structural changes and c denotes the heat capacity with

$$\mathcal{H} := -\Theta\, \frac{\partial \left(\boldsymbol{\tau} : \boldsymbol{d} - \Omega_{\mathrm{mech}} \right)}{\partial \Theta} \quad \text{and} \quad c := -\Theta\, \frac{\partial^2 \Psi}{\partial \Theta^2}\,. \tag{9.2.42}$$

Substituting Equation (9.2.41) into the right-hand side of Equation (9.2.40) and rearranging, one reaches the temperature evolution equation

$$c\dot{\Theta} = \Omega_{\mathrm{mech}} - \mathcal{H} - J \mathrm{div}\left(\frac{\boldsymbol{q}}{J} \right) + R\,. \tag{9.2.43}$$

Note that Equation (9.2.43) is in agreement with [275]. However, in the current context, Ω_{mech} inherently involves damage effects. Moreover, $\mathcal{H}$ is found as

$$\mathcal{H} = -\Theta \left[\frac{\partial}{\partial \Theta}\left(\frac{\partial \Psi}{\partial \boldsymbol{b}^{\mathrm{e}}} \right) : \dot{\boldsymbol{b}}^{\mathrm{e}} + \frac{\partial}{\partial \Theta}\left(\frac{\partial \Psi}{\partial \alpha} \right) \dot{\alpha} + \frac{\partial}{\partial \Theta}\left(\frac{\partial \Psi}{\partial D} \right) \dot{D} \right]\,. \tag{9.2.44}$$

9.3. Specification of Constitutive Functions for Metals

This part aims to derive the explicit representations of state laws and evolutionary equations through specification of the relevant potentials. For elasticity, a volumetric-isochoric split for the effective elastic potential is postulated,

$$\tilde{\Psi}^{\mathrm{e}}(\boldsymbol{b}^{\mathrm{e}}) = \tilde{\Psi}^{\mathrm{e}}_{\mathrm{vol}}(J^{\mathrm{e}}) + \tilde{\Psi}^{\mathrm{e}}_{\mathrm{iso}}(\overline{\boldsymbol{\epsilon}^{\mathrm{e}}}) \,. \tag{9.3.1}$$

where $\tilde{\Psi}^{\mathrm{e}}_{\mathrm{vol}}$ represents the volumetric part and $\tilde{\Psi}^{\mathrm{e}}_{\mathrm{iso}}$ the isochoric part. With the use of the principals of the tensor arguments in representation of the isotropic tensor functions one has $\tilde{\Psi}^{\mathrm{e}}_{\mathrm{iso}}(\overline{\boldsymbol{\epsilon}^{\mathrm{e}}}) \mapsto \tilde{\Psi}^{\mathrm{e}}_{\mathrm{iso}}(\overline{\epsilon^{\mathrm{e}}_A})$ for $A = 1, 2, 3$, and

$$\tilde{\Psi}^{\mathrm{e}}_{\mathrm{vol}}(J^{\mathrm{e}}) := \frac{1}{2} H \log^2 (J^{\mathrm{e}}) \quad \text{and} \quad \tilde{\Psi}^{\mathrm{e}}_{\mathrm{iso}}(\overline{\epsilon^{\mathrm{e}}_A}) := \mu \left[\overline{\epsilon}^{\mathrm{e}2}_1 + \overline{\epsilon}^{\mathrm{e}2}_2 + \overline{\epsilon}^{\mathrm{e}2}_3 \right] \,. \tag{9.3.2}$$

Here, H and μ denote the bulk and the shear modulus, respectively[7]. Denoting the linear coefficient of thermal expansion by α_Θ and the reference temperature by Θ_0 volumetric elastic deformation is associated with the thermal effects through the following effective thermodilatational potential, see, e.g., [114]

$$\tilde{\Psi}^{\Theta\mathrm{e}}(J^{\mathrm{e}}, \Theta) := -3 \, H \, \alpha_\Theta [\Theta - \Theta_0] \log (J^{\mathrm{e}}) \,. \tag{9.3.3}$$

A combined linear and saturation-type isotropic hardening potential with temperature dependence defines the plastic part Ψ^{vp}

$$\Psi^{\mathrm{vp}}(\alpha, \Theta) := \frac{1}{2} K(\Theta) \, \alpha^2 + [\tau_{y\infty}(\Theta) - \tau_{y0}(\Theta)] \left[\alpha - \frac{1 - \exp(-\delta\alpha)}{\delta} \right] \,. \tag{9.3.4}$$

Here, $K(\Theta)$ represents the temperature dependent linear hardening coefficient. τ_{y0} and $\tau_{y\infty}$ denote the initial and the saturation yield stress, respectively. δ is the hardening saturation exponent. One has $\Psi^{\mathrm{vp}}(\alpha, \Theta) \to 0$ for $\alpha \to 0$, as required. Defining functions $g_{\omega^{\mathrm{vp}}}(\Theta)$ and $g_{\omega^{\mathrm{d}}}(\Theta)$ as

$$g_{\omega^{\mathrm{vp}}}(\Theta) := 1 - [\Lambda(\Theta)]^{\omega^{\mathrm{vp}}} \quad \text{and} \quad g_{\omega^{\mathrm{d}}}(\Theta) := 1 - [\Lambda(\Theta)]^{\omega^{\mathrm{d}}} \,, \tag{9.3.5}$$

where ω^{vp} and ω^{d} denote the viscoplastic and damage thermal softening exponents, respectively, and $\Lambda(\Theta)$ represents the homologous temperature with

$$\Lambda(\Theta) = \frac{\Theta - \Theta_0}{\Theta_{\mathrm{melt}} - \Theta_0} \,, \tag{9.3.6}$$

where Θ_{melt} denotes the melting temperature, and using the notation $K_0 = K(\Theta_0)$, $\tau_{y0,0} = \tau_{y0}(\Theta_0)$ and $\tau_{y\infty,0} = \tau_{y\infty}(\Theta_0)$ one can adopt nonlinear thermoplasticity viz.

$$K(\Theta) := g_{\omega^{\mathrm{vp}}}(\Theta)K_0 \,, \quad \tau_{y0}(\Theta) := g_{\omega^{\mathrm{vp}}}(\Theta)\tau_{y0,0} \quad \text{and} \quad \tau_{y\infty}(\Theta) := g_{\omega^{\mathrm{vp}}}(\Theta)\tau_{y\infty,0} \,. \tag{9.3.7}$$

Finally, letting $-c_0 = \Theta \, \partial^2 \tilde{\Psi}^\Theta / \partial \Theta^2$ denote the temperature-independent heat capacity of the material at constant deformation, the following pure thermal potential is postulated

$$\Psi^\Theta(\Theta) := c_0 \left[[\Theta - \Theta_0] - \Theta \log \left(\frac{\Theta}{\Theta_0} \right) \right] \,, \tag{9.3.8}$$

---

[7]This quadratic form in terms of Hencky measure of elastic strains preserves validity for a large class of materials up to moderately large deformations, [328], but does not satisfy the polyconvexity condition, [187].

Hence, using Equation (9.3.1) with Equations (9.3.2), (9.3.3) and (9.3.4) along with Equation (9.2.42.2), heat capacity c reads

$$c = c_0 - \Theta g''_{\omega^{vp}} \Psi^{vp}(\alpha, \Theta_0),\tag{9.3.9}$$

where $g''_{\omega^{vp}} = \partial^2 g_{\omega^{vp}}/\partial\Theta^2$. Note that selecting $\omega^{vp} = 1$, i.e., linear temperature dependence of the isotropic hardening potential, Equation (9.3.9) reduces to $c \to c_0$ with $g''_{\omega^{vp}}\Psi^{vp} \to 0$.

The total KIRCHHOFF stress tensor can be decomposed additively into volumetric $p\mathbf{1}$ and deviatoric $\mathbf{s}$ parts to give $\boldsymbol{\tau} = p\mathbf{1} + \mathbf{s}$ where $p := 1/3\,\mathrm{tr}\,\boldsymbol{\tau}$ represents the mean stress and $\mathbf{s} := \mathrm{dev}\,\boldsymbol{\tau}$. Using the connexions $\tilde{p} = p/[1-D]$, $\tilde{\mathbf{s}} = \mathbf{s}/[1-D]$ and $\tilde{\boldsymbol{\tau}} = \boldsymbol{\tau}/[1-D]$ this amounts for $\tilde{\boldsymbol{\tau}} = \tilde{p}\mathbf{1} + \tilde{\mathbf{s}}$ where $\tilde{p}$ and $\tilde{\mathbf{s}}$ represent *effective* mean (KIRCHHOFF) stress and the deviatoric stress tensor, respectively. Substituting Equations (9.3.1) with (9.3.2) and (9.3.3) into Equation (9.2.25.1) and noting that $\partial J^e/\partial\boldsymbol{\epsilon}^e = \mathbf{1}$, $\tilde{p}$ and $\tilde{\mathbf{s}}$ are computed as[8]

$$\tilde{p} = H\log(J^e) - 3\,H\,\alpha_\Theta\,[\Theta - \Theta_0] \quad\text{and}\quad \tilde{\mathbf{s}} = 2\mu\,\bar{\boldsymbol{\epsilon}}^e.\tag{9.3.10}$$

Using Equations (9.2.28) along with Equations (9.3.1–9.3.4) gives the plastic isotropic hardening function q with temperature effects

$$q(\alpha, \Theta) = g_{\omega^{vp}}(\Theta)q(\alpha, \Theta_0) \quad\text{where}\quad q(\alpha, \Theta_0) = -K_0\,\alpha - [\tau_{y\infty,0} - \tau_{y0,0}]\,[1 - \exp(-\delta\alpha)]\tag{9.3.11}$$

and the damage conjugate variable Y^d associated with the temperature dependent total thermoelastic energy release rate

$$Y^d = \frac{1}{2}\,H\,[\log(J^e)]^2 + \mu\left[\overline{\epsilon}_1^{e2} + \overline{\epsilon}_2^{e2} + \overline{\epsilon}_3^{e2}\right] - 3\,H\,\alpha_\Theta[\Theta - \Theta_0]\log(J^e).\tag{9.3.12}$$

Finally, in view of Equation (9.2.25.2) together with Equations (9.3.3) and (9.3.4) one derives the following expression for η^e

$$\begin{aligned}
\eta^e = {}& [1 - D]\,3\,H\,\alpha_\Theta\log(J^e) + c_0\log\left(\frac{\Theta}{\Theta_0}\right)\\
& - g'_{\omega^{vp}}(\Theta)\left[\frac{1}{2}K_0\,\alpha^2 + [\tau_{y\infty,0} - \tau_{y0,0}]\left[\delta + \frac{\exp(-\delta\alpha)}{\delta}\right]\right].
\end{aligned}\tag{9.3.13}$$

where using Equations (9.3.5), $g'_{\omega^{vp}}(\Theta) = dg_{\omega^{vp}}(\Theta)/d\Theta$ and $g'_{\omega^d}(\Theta) = dg_{\omega^d}(\Theta)/d\Theta$ one has

$$g'_{\omega^{vp}}(\Theta) = -\frac{\omega^{vp}}{\Theta_{melt} - \Theta_0}\Lambda(\Theta)^{\omega^{vp}-1} \quad\text{and}\quad g'_{\omega^d}(\Theta) = -\frac{\omega^d}{\Theta_{melt} - \Theta_0}\Lambda(\Theta)^{\omega^d-1}.\tag{9.3.14}$$

Plastic incompressibility allows to represent the yield function Φ^{vp} in terms of the stress deviator, i.e., $\Phi^{vp}(\tilde{\boldsymbol{\tau}}, q; \Theta) \mapsto \Phi^{vp}(\tilde{\mathbf{s}}, q; \Theta)$. Plastic isotropy, on the other hand, concedes a representation in terms of effective deviatoric stress principals $\tilde{s}_A$ for $A = 1, 2, 3$ through $\Phi^{vp}(\tilde{\mathbf{s}}, q; \Theta) \mapsto \Phi^{vp}(\tilde{s}_A, q; \Theta)$ as in the case of Equation (9.3.2.2). Hence, using a J_2 theory for plasticity together with a four-parameter damage dissipation potential, see, e.g., [175], one has:

$$\Phi^{vp}(\tilde{s}_A, q, \Theta) := \left[\tilde{s}_1^2 + \tilde{s}_2^2 + \tilde{s}_3^2\right]^{1/2} - \sqrt{\frac{2}{3}}\,y(q, \Theta),\tag{9.3.15}$$

$$\Phi^d(Y^d, \Theta, D) := \frac{1}{s+1}\frac{a(\Theta)}{[1-D]^r}\left[\frac{\langle Y^d - Y_0^d\rangle}{a(\Theta)}\right]^{s+1}.\tag{9.3.16}$$

---

[8]Thanks to elastic isotropy, $\boldsymbol{\epsilon}^e$ and $\tilde{\mathbf{s}}$ are coaxial, and, thus share identical eigenbases: $\mathbf{m}^A = \boldsymbol{\nu}^A \otimes \boldsymbol{\nu}^A$, where $\boldsymbol{\nu}^A$ represents the corresponding eigenvectors with $A = 1, 2, 3$.

Here, $y(q, \Theta) = [\tau_{y0}(\Theta) - q(\alpha, \Theta)]$ represents the hardening/softening function with thermal coupling. In fact, $[\tilde{s}_1^2 + \tilde{s}_2^2 + \tilde{s}_3^2]^{1/2}$ corresponds to a norm of $\tilde{s}$ via $\|\tilde{s}\| := [\tilde{s}_1^2 + \tilde{s}_2^2 + \tilde{s}_3^2]^{1/2}$. Y_0^{d} represents the threshold for Y^{d} below which damage ceases to evolve. r, s and $a(\Theta)$ represent other damage related material parameters. Using Equation (9.3.5.2) with $a_0 = a(\Theta_0)$ a nonlinear temperature dependence is chosen for the damage parameter $a(\Theta)$ via

$$a(\Theta) = g_{\omega^{\mathrm{d}}}(\Theta)\, a_0 \,. \tag{9.3.17}$$

The choice of $f(\Phi^{\mathrm{vp}})$ is defined using a NORTON-type formulation viz.

$$f(\Phi^{\mathrm{vp}}) := \left[\frac{\Phi^{\mathrm{vp}}(\tilde{s}_A, q, \Theta)}{\kappa^{\mathrm{vp}}} \right]^{1/m} , \tag{9.3.18}$$

where κ^{vp} is the constant drag stress and m the viscoplastic exponent. In view of Equation (9.3.18), Equation (9.2.36) can be rewritten as

$$\dot{\gamma} = \frac{1}{t_\star} \left\langle \frac{\Phi^{\mathrm{vp}}(\tilde{s}_A, q, \Theta)}{\kappa^{\mathrm{vp}}} \right\rangle^{1/m} . \tag{9.3.19}$$

Exploiting the condition $n_A := s_A / \|s\| \equiv \partial \Phi^{\mathrm{vp}} / \partial \tilde{\tau}_A \equiv \tilde{s}_A / \|\tilde{s}\| =: \tilde{n}_A$ as well as the fact that the eigenbases for the nominal and effective stresses are equivalent, i.e., $\boldsymbol{\nu}^A \otimes \boldsymbol{\nu}^A \equiv \tilde{\boldsymbol{\nu}}^A \otimes \tilde{\boldsymbol{\nu}}^A$, and using Equation (9.2.35.2) with Equation (9.3.15), the viscoplastic flow rule is derived as

$$\frac{\partial \Phi^{\mathrm{vp}}}{\partial \tilde{\boldsymbol{\tau}}} = \sum_{A=1}^{3} n_A\, \boldsymbol{\nu}^A \otimes \boldsymbol{\nu}^A \quad \Rightarrow \quad \mathcal{L}_v \boldsymbol{b}^{\mathrm{e}} = -2\, \frac{\dot{\gamma}}{1-D} \left[\sum_{A=1}^{3} n_A\, \boldsymbol{\nu}^A \otimes \boldsymbol{\nu}^A \right] \cdot \boldsymbol{b}^{\mathrm{e}} \,. \tag{9.3.20}$$

Coming to the kinetic relations for the scalar strain-like variables α and D, using Equations (9.2.37) along with Equations (9.3.15) and (9.3.16) gives

$$\frac{\partial \Phi^{\mathrm{vp}}}{\partial q} = \sqrt{\frac{2}{3}} \quad \Rightarrow \quad \dot{\alpha} = \dot{\gamma}\sqrt{\frac{2}{3}}\,, \tag{9.3.21}$$

$$\frac{\partial \Phi^{\mathrm{d}}}{\partial Y^{\mathrm{d}}} = \frac{1}{[1-D]^r} \left[\frac{\langle Y^{\mathrm{d}} - Y_0^{\mathrm{d}} \rangle}{a(\Theta)} \right]^s \quad \Rightarrow \quad \dot{D} = \dot{\gamma}\frac{1}{[1-D]^r} \left[\frac{\langle Y^{\mathrm{d}} - Y_0^{\mathrm{d}} \rangle}{a(\Theta)} \right]^s . \tag{9.3.22}$$

Using Equation (9.5.17.1) with Equation (9.3.21), $\Omega_{\mathrm{mech}}^{\mathrm{vp}}$ yields

$$\Omega_{\mathrm{mech}}^{\mathrm{vp}} = \dot{\gamma} \left[\|\tilde{\boldsymbol{s}}\| + \sqrt{\frac{2}{3}} q(\alpha, \Theta) \right] . \tag{9.3.23}$$

Note that at the rate independent limit one has $\Omega_{\mathrm{mech}}^{\mathrm{vp}} = \dot{\gamma}\sqrt{2/3}\,\tau_{y0}(\Theta)$ with $\dot{\gamma}\Phi^{\mathrm{vp}} = 0$, in agreement with [275]. The details of this derivation are found in Appendix D. Via Equations (9.5.17.2) and (9.3.22) damage dissipation reads

$$\Omega_{\mathrm{mech}}^{\mathrm{d}} = \dot{\gamma}\, \frac{Y^{\mathrm{d}}}{[1-D]^r} \left[\frac{\langle Y^{\mathrm{d}} - Y_0^{\mathrm{d}} \rangle}{a(\Theta)} \right]^s . \tag{9.3.24}$$

Using Equation (9.2.31.1) along with Equations (9.3.23) and (9.3.24) the total mechanical dissipation Ω_{mech}, which constitutes the heat source and which is used in linearization of the weak form of the thermal problem, is derived as[9]

$$\Omega_{\mathrm{mech}} = \dot{\gamma} \left[\|\tilde{\boldsymbol{s}}\| + \sqrt{\frac{2}{3}} q(\alpha, \Theta) + \frac{Y^{\mathrm{d}}}{[1-D]^r} \left[\frac{\langle Y^{\mathrm{d}} - Y_0^{\mathrm{d}} \rangle}{a(\Theta)} \right]^s \right] . \tag{9.3.25}$$

---

[9]In general, $\Omega_{\mathrm{mech}}^{\mathrm{d}} \ll \Omega_{\mathrm{mech}}^{\mathrm{vp}}$ and one may ommit $\Omega_{\mathrm{mech}}^{\mathrm{d}}$ to reach $\Omega_{\mathrm{mech}} \simeq \Omega_{\mathrm{mech}}^{\mathrm{vp}}$.

Using Equation (9.2.39.2) the growth of the viscoplastic entropy is derived using $\dot{\eta}^{\mathrm{vp}} = \partial \Phi^{\mathrm{vp}}/\partial \Theta$ at constant $\tilde{s}_A$ for $A = 1, 2, 3$ and q as

$$\dot{\eta}^{\mathrm{vp}} = -\dot{\gamma}\,\sqrt{\frac{2}{3}}\,g'_{\omega^{\mathrm{vp}}}(\Theta)\,\tau_{y0,0}\,. \tag{9.3.26}$$

For the growth of the inelastic entropy associated with damage one reverts to Equation (9.2.39.3) and use $\dot{\eta}^{\mathrm{d}} = \partial \Phi^{\mathrm{d}}/\partial \Theta$ at constant D and Y to give

$$\dot{\eta}^{\mathrm{d}} = -\dot{\gamma}\,g'_{\omega^{\mathrm{d}}}(\Theta)\,a_0\,\frac{s}{s+1}\,\frac{1}{[1-D]^r}\left[\frac{\langle Y^{\mathrm{d}} - Y_0^{\mathrm{d}}\rangle}{a(\Theta)}\right]^{s+1}\,. \tag{9.3.27}$$

The second law of thermodynamics as given in Equation (9.2.33.2) places the restriction $\dot{\eta}^{\mathrm{vpd}} \geq 0$. Since the expressions in Equations (9.3.26) and (9.3.27) add up to the rate of total inelastic entropy production $\dot{\eta}^{\mathrm{vpd}}$ with Equation (9.2.39.1), one may suggest two stronger inequalities, such as $\dot{\eta}^{\mathrm{vp}} \geq 0$ and $\dot{\eta}^{\mathrm{d}} \geq 0$. The former is naturally satisfied, where in view of Equations (9.3.7) and (9.3.6) thermal softening of the yield stress is addressed. This condition, also named as the yield locus contraction with temperature, reflects the experimental evidences. The latter inequality, however, may put an over restriction on the material parameters.

Finally, coming to the time sensitive thermal dissipation analysis an isotropic EULERIAN FOURIER law for the *effective* KIRCHHOFF heat flux is assumed viz. [215]

$$\tilde{q} = -k\,\mathbf{grad}\,\Theta\,, \tag{9.3.28}$$

where $k > 0$ is the isotropic heat conduction coefficient in absence of damage effects. The *homogenized* flux in the interior of the body is assumed to read [95]

$$q = [1 - D]\,\tilde{q}\,. \tag{9.3.29}$$

With Equation (9.3.29), the negative effect of damage on the ability of the body to transfer thermal energy from one point to another in presence of temperature gradients is reflected via the factor $[1 - D]$. For a completely damaged material point (if $D \to 1$ one has $[1 - D]k \to 0$) no heat conduction takes place. Substituting Equations (9.3.29) in the conductive thermal dissipation inequality given in Equation (9.2.18.1) yields

$$\Omega_{\mathrm{conther}} = [1 - D]\,\frac{1}{\Theta}\,k\,\mathbf{grad}\,\Theta \cdot \mathbf{grad}\,\Theta \geq 0\,, \tag{9.3.30}$$

as required[10].

---

[10]Note that the expression for q can also be derived from the damage affected version of the so-called FOURIER dissipation potential Υ postulated per unit reference volume as

$$\Upsilon(\mathbf{grad}\,\Theta, D) = [1 - D]\,\tilde{\Upsilon}(\mathbf{grad}\,\Theta) \quad \text{and} \quad \tilde{\Upsilon}(\mathbf{grad}\,\Theta) = -\frac{1}{2}k\,\mathbf{grad}\,\Theta \cdot \mathbf{grad}\,\Theta\,,$$

with $q = \partial \Upsilon/\partial\,[\mathbf{grad}\,\Theta]$.

BOX 1. A summary of the proposed model for general 3D stress-state.

i. Multiplicative kinematics

$$\boldsymbol{F} = \boldsymbol{F}^{\mathrm{e}} \cdot \boldsymbol{F}^{\mathrm{vp}}\,.$$

ii. Thermoelastic stress-strain relationship

$$\boldsymbol{\tau} = [1 - D][\tilde{p}\boldsymbol{1} + \tilde{\boldsymbol{s}}]\,,$$

where

$$\tilde{p} = H\log(J^e) - 3H\,\alpha_\Theta\,[\Theta - \Theta_0] \quad \text{and} \quad \tilde{\boldsymbol{s}} = 2\mu\,\overline{\boldsymbol{\epsilon}}^{\,\mathrm{e}}\,.$$

iii. State laws for hardening and damage conjugate variables

$$q = -g_{\omega^{\mathrm{vp}}}(\Theta)\left[K_0\,\alpha + [\tau_{y\infty,0} - \tau_{y0,0}]\,[1 - \exp\left(-\delta\alpha\right)]\right]\,,$$

$$Y^{\mathrm{d}} = \frac{1}{2}\,H\,[\log\left(J^{\mathrm{e}}\right)]^2 + \mu\,\left[\overline{\epsilon}_1^{\mathrm{e}2} + \overline{\epsilon}_2^{\mathrm{e}2} + \overline{\epsilon}_3^{\mathrm{e}2}\right] - 3\,H\,\alpha_\Theta[\Theta - \Theta_0]\log\left(J^{\mathrm{e}}\right)\,.$$

iv. Thermoelastic domain in (principal) stress space (single surface)

$$\mathbb{E}_{\boldsymbol{\tau}} = \left\{[\tilde{s}_A, q, \Theta] \in \mathbb{R}^3 \times \mathbb{R}_- \times \mathbb{R}_+ : \Phi^{\mathrm{vp}}(\tilde{s}_A, q, \Theta) \leq 0\right\}\,,$$

where $A = 1, 2, 3$ and using $y(q, \Theta) = \tau_{y0}(\Theta) - q$

$$\Phi^{\mathrm{vp}}(\tilde{s}_A, q, \Theta) = \left[\tilde{s}_1^2 + \tilde{s}_2^2 + \tilde{s}_3^2\right]^{1/2} - \sqrt{\frac{2}{3}}\,y(q, \Theta)\,.$$

v. Associative flow rule (PERZYNA model)

$$-\frac{1}{2}\mathcal{L}_v\boldsymbol{b}^{\mathrm{e}} \cdot [\boldsymbol{b}^{\mathrm{e}}]^{-1} = \frac{\dot{\gamma}}{1 - D}\left[\sum_{A=1}^{3} n_A\,\boldsymbol{\nu}^A \otimes \boldsymbol{\nu}^A\right]\,,$$

where

$$\dot{\gamma} = \frac{1}{t_\star}\left\langle\frac{\Phi^{\mathrm{vp}}(\tilde{s}_A, q, \Theta)}{\kappa^{\mathrm{vp}}}\right\rangle^{1/m}\,, \quad \boldsymbol{s} = \sum_{A=1}^{3} s_A\,\boldsymbol{\nu}^A \otimes \boldsymbol{\nu}^A \quad \text{and} \quad n_A = \frac{s_A}{\|\boldsymbol{s}\|}\,.$$

vi. Evolution equations for hardening and damage

$$\dot{\alpha} = \dot{\gamma}\sqrt{\frac{2}{3}} \quad \text{and} \quad \dot{D} = \dot{\gamma}\frac{1}{[1 - D]^r}\left[\frac{\langle Y^{\mathrm{d}} - Y_0^{\mathrm{d}}\rangle}{a(\Theta)}\right]^s\,.$$

9.4. Numerical Implementation

9.4.1. Finite Element Formulation of the Coupled Initial Boundary Value Problem

Let $\boldsymbol{P} := \boldsymbol{\tau} \cdot \boldsymbol{F}^{-\top}$ stand for the first PIOLA-KIRCHHOFF stress and $\boldsymbol{Q} := \boldsymbol{q} \cdot \boldsymbol{F}^{-\top}$ for the heat flux of equivalent type, analogically. The primary unknowns of the thermomechanical problem $[\boldsymbol{u}, \boldsymbol{v}, \Theta]^{\top}$ with $\boldsymbol{u}$, $\boldsymbol{v}$ and Θ respectively denoting the displacement vector, velocity vector and temperature, are resolved at the global solution stage by considering the following coupled differential equation set constructed at the reference configuration

$$\left\{ \begin{array}{c} \dot{\boldsymbol{u}} - \boldsymbol{v} \\ \mathrm{Div}\boldsymbol{P} + \boldsymbol{\zeta}_0 - \rho_0\dot{\boldsymbol{v}} \\ c\dot{\Theta} - \Omega_{\mathrm{mech}} + \mathcal{H} + \mathrm{Div}\boldsymbol{Q} - R \end{array} \right\} = \boldsymbol{0} \,. \qquad (9.4.1)$$

Apart from the trivial velocity vector definition given in the first row in a residual setting, the second and third rows stand for the local equation of motion and the heat equation. $\dot{\boldsymbol{v}}$ is the acceleration vector and ρ_0 is the reference (initial) density which is linked to the mass density in current configuration ρ by $\rho_0 = J\rho$ with the balance of mass principle. $\boldsymbol{\zeta}_0$ denotes the body forces per unit underformed volume where it is linked to the body forces per unit deformed volume $\boldsymbol{\zeta}$ via $\boldsymbol{\zeta}_0 = J\boldsymbol{\zeta}$. The boundary conditions for the problem can be listed as follows

$$\begin{array}{llll} \boldsymbol{u} = \overline{\boldsymbol{u}} \text{ at } \partial\mathfrak{B}_0^{\boldsymbol{u}}, & \overline{\boldsymbol{T}} = \boldsymbol{P} \cdot N \text{ at } \partial\mathfrak{B}_0^{\boldsymbol{\sigma}}, & \partial\mathfrak{B}_0^{\boldsymbol{u}} \cap \partial\mathfrak{B}_0^{\boldsymbol{\sigma}} = \varnothing, & \partial\mathfrak{B}_0^{\boldsymbol{u}} \cup \partial\mathfrak{B}_0^{\boldsymbol{\sigma}} = \partial\mathfrak{B}_0 \,. \\ \Theta = \overline{\Theta} \text{ at } \partial\mathfrak{B}_0^{\Theta}, & \overline{\theta} = \boldsymbol{Q} \cdot N \text{ at } \partial\mathfrak{B}_0^{\boldsymbol{q}}, & \partial\mathfrak{B}_0^{\Theta} \cap \partial\mathfrak{B}_0^{\boldsymbol{q}} = \varnothing, & \partial\mathfrak{B}_0^{\Theta} \cup \partial\mathfrak{B}_0^{\boldsymbol{q}} = \partial\mathfrak{B}_0 \,. \end{array} \qquad (9.4.2)$$

Here, $\boldsymbol{N}$ is the outward unit normal to the boundary $\partial\mathfrak{B}_0$ in the reference configuration. $\partial\mathfrak{B}_0^{\boldsymbol{u}} \subset \partial\mathfrak{B}_0$ and $\partial\mathfrak{B}_0^{\Theta} \subset \partial\mathfrak{B}_0$ denote the parts of the boundary on which the DIRICHLET boundary conditions are specified with the prescribed displacements $\overline{\boldsymbol{u}}$ and temperatures $\overline{\Theta}$, respectively. With the prescribed tractions $\overline{\boldsymbol{T}}$ and heat flux $\overline{\theta}$ NEUMANN-type boundary conditions act the boundary parts $\partial\mathfrak{B}_0^{\boldsymbol{\sigma}} \subset \partial\mathfrak{B}_0$ and $\partial\mathfrak{B}_0^{\boldsymbol{q}} \subset \partial\mathfrak{B}_0$, respectively. The latter defines the heat flux entering the body through the boundary and its value can be assigned or defined by a convective or a radiation relation. In the current context, temperature increase is merely associated with the mechanical dissipation due to irreversible processes such as viscoplasticity and damage. Accordingly, the heat source and the temperature variations due to elastic loading are omitted, by canceling R and $\mathcal{H}$ respectively, to give $c\dot{\Theta} - \Omega_{\mathrm{mech}} + \mathrm{Div}\boldsymbol{Q} = 0$.

9.4.1.1. Staggered Solution Scheme

An isothermal staggered solution scheme is followed, where an isothermal mechanical step is followed by a thermal step on fixed configuration. With $\circ$ representing a *composition* Equation (9.4.1) can be decomposed into the following mechanical (left) and thermal (right) steps

$$\left[\left\{ \begin{array}{c} \dot{\boldsymbol{u}} - \boldsymbol{v} \\ \mathrm{Div}\boldsymbol{P} + \boldsymbol{\zeta}_0 \\ c\dot{\Theta} \end{array} \right\} = \boldsymbol{0} \right] \quad \circ \quad \left[\left\{ \begin{array}{c} \boldsymbol{v} \\ \dot{\boldsymbol{v}} \\ c\dot{\Theta} - \Omega_{\mathrm{mech}} + \mathrm{Div}\boldsymbol{Q} \end{array} \right\} = \boldsymbol{0} \right] \,. \qquad (9.4.3)$$

Mechanical Step. In this step, for any generic field $\boldsymbol{\chi}$ one has the following reduction of dependence $\boldsymbol{\chi}(\boldsymbol{\epsilon}, \Theta) \mapsto \boldsymbol{\chi}(\boldsymbol{\epsilon})$. The quasi-static limit is considered with $\rho_0 \to 0$. Corresponding mechanical weak statement for the residual $\mathrm{Div}\boldsymbol{P} + \boldsymbol{\zeta}_0$ is encapsulated in the following scalar

valued function $G_{\boldsymbol{\varphi}}(\boldsymbol{u}, \delta\boldsymbol{u})$ where $\delta\boldsymbol{u}$ denotes a sufficiently smooth virtual displacement field (defined in the reference configuration)

$$G_{\boldsymbol{\varphi}}(\boldsymbol{u}, \delta\boldsymbol{u}) := \int_{\mathfrak{B}_0} \delta\boldsymbol{u} \cdot [\mathrm{Div}\boldsymbol{P} + \boldsymbol{\zeta}_0]\, \mathrm{d}V = 0\,. \tag{9.4.4}$$

Noting that $\mathrm{Div}\,(\delta\boldsymbol{u} \cdot \boldsymbol{P}) = \mathbf{Grad}\,\delta\boldsymbol{u} : \boldsymbol{P} + \delta\boldsymbol{u} \cdot \mathrm{Div}\boldsymbol{P}$ and applying GAUSS theorem with $\overline{\boldsymbol{T}} = \boldsymbol{P} \cdot \boldsymbol{N}$ one reaches $\int_{\mathfrak{B}_0} \mathrm{Div}\,(\delta\boldsymbol{u} \cdot \boldsymbol{P})\, \mathrm{d}V = \int_{\partial\mathfrak{B}_0^{\sigma}} \overline{\boldsymbol{T}} \cdot \delta\boldsymbol{u}\, \mathrm{d}A$, since $\delta\boldsymbol{u} = \mathbf{0}$ at $\partial\mathfrak{B}_0^{\varphi} = \partial\mathfrak{B}_0 \backslash \partial\mathfrak{B}_0^{\sigma}$ where $\backslash$ denotes the *complement*. Consequently, the total mechanical virtual work expression in Equation (9.4.4) can be iterated as

$$G_{\boldsymbol{\varphi}}(\boldsymbol{u}, \delta\boldsymbol{u}) := G_{\boldsymbol{\varphi}}^{\mathrm{int}}(\boldsymbol{u}, \delta\boldsymbol{u}) - G_{\boldsymbol{\varphi}}^{\mathrm{ext}}(\boldsymbol{u}, \delta\boldsymbol{u}) = 0\,. \tag{9.4.5}$$

Here, the components $G_{\boldsymbol{\varphi}}^{\mathrm{int}}$ and $G_{\boldsymbol{\varphi}}^{\mathrm{ext}}$ represent internal and external parts of the mechanical virtual work, respectively. Using $\boldsymbol{P} := \boldsymbol{\tau} \cdot \boldsymbol{F}^{-\top}$ and the symmetry of $\boldsymbol{\tau}$ to give $\boldsymbol{P} : \mathbf{Grad}\,\delta\boldsymbol{u} = \boldsymbol{\tau} : \mathbf{grad}\,\delta\boldsymbol{u}$, these amount to

$$G_{\boldsymbol{\varphi}}^{\mathrm{int}}(\boldsymbol{u}, \delta\boldsymbol{u}) := \int_{\mathfrak{B}_0} \boldsymbol{\tau} : \mathbf{grad}\,\delta\boldsymbol{u}\, \mathrm{d}V \quad \text{and} \quad G_{\boldsymbol{\varphi}}^{\mathrm{ext}}(\boldsymbol{u}, \delta\boldsymbol{u}) := \int_{\partial\mathfrak{B}_0^{\sigma}} \overline{\boldsymbol{T}} \cdot \delta\boldsymbol{u}\, \mathrm{d}A + \int_{\mathfrak{B}_0} \boldsymbol{\zeta}_0 \cdot \delta\boldsymbol{u}\, \mathrm{d}V\,. \tag{9.4.6}$$

An iterative scheme based on NEWTON's method is used for the solution of problem (9.4.6) within the context of the finite element method. Accordingly, a sequence of consistently linearized problems is solved until the residual vanishes. To continue, the focus is set on the internal part of the mechanical virtual work. The time discrete form of internal virtual work given in Equation (9.4.6.1) reads

$$G_{\boldsymbol{\varphi}}^{\mathrm{int}}(\boldsymbol{u}_{n+1}^i, \delta\boldsymbol{u}) = \int_{\mathfrak{B}_0} \boldsymbol{\tau}_{n+1}^i : \mathbf{grad}\,\delta\boldsymbol{u}\, \mathrm{d}V\,. \tag{9.4.7}$$

Linearization of $G_{\boldsymbol{\varphi}}^{\mathrm{int}}$ given in Equation (9.4.7) in direction of the displacement increment $\Delta\boldsymbol{u}_{n+1}^i$ where i represents the iteration number, i.e., $DG_{\boldsymbol{\varphi}}^{\mathrm{int}}(\boldsymbol{u}_{n+1}^i, \delta\boldsymbol{u})[\Delta\boldsymbol{u}_{n+1}^i]$ leads to

$$DG_{\boldsymbol{\varphi}}^{\mathrm{int}}(\boldsymbol{u}_{n+1}^i, \delta\boldsymbol{u})[\Delta\boldsymbol{u}_{n+1}^i] := \left.\frac{\mathrm{d}}{\mathrm{d}\varepsilon}\right|_{\varepsilon=0} G_{\boldsymbol{\varphi}}^{\mathrm{int}}(\boldsymbol{u}_{n+1}^i + \varepsilon\Delta\boldsymbol{u}_{n+1}^i, \delta\boldsymbol{u})\,. \tag{9.4.8}$$

To save space, in the subsequent expressions, the superscripts i and the subscripts $n+1$ will be dropped. Note that the virtual displacements $\delta\boldsymbol{u}$ are not a function of the configuration however the operator $\mathbf{grad}$ is, with $\mathbf{grad}\,\delta\boldsymbol{u} = \mathbf{Grad}\,\delta\boldsymbol{u} \cdot \boldsymbol{F}^{-1}$. Using this substitution for $\mathbf{grad}\,\delta\boldsymbol{u}$ and interchanging differentiation and integration in Equation (9.4.8) one derives

$$DG_{\boldsymbol{\varphi}}^{\mathrm{int}}(\boldsymbol{u}, \delta\boldsymbol{u})[\Delta\boldsymbol{u}] = \int_{\mathfrak{B}_0} \left.\frac{\mathrm{d}}{\mathrm{d}\varepsilon}\right|_{\varepsilon=0} \left[\boldsymbol{\tau}(\boldsymbol{u} + \varepsilon\Delta\boldsymbol{u}) : \mathbf{Grad}\,\delta\boldsymbol{u} \cdot \boldsymbol{F}^{-1}(\boldsymbol{u} + \varepsilon\Delta\boldsymbol{u})\right]\, \mathrm{d}V\,. \tag{9.4.9}$$

Linearizations of $\boldsymbol{F}$, $\boldsymbol{F}^{\top}$ and $\boldsymbol{F}^{-1}$ respectively represented by $D\boldsymbol{F}(\boldsymbol{u})[\Delta\boldsymbol{u}]$, $D\boldsymbol{F}^{\top}(\boldsymbol{u})[\Delta\boldsymbol{u}]$ and $D\boldsymbol{F}^{-1}(\boldsymbol{u})[\Delta\boldsymbol{u}]$ prove useful for successive developments and read

$$\left.\frac{\mathrm{d}}{\mathrm{d}\varepsilon}\right|_{\varepsilon=0} \boldsymbol{F}(\boldsymbol{u} + \varepsilon\Delta\boldsymbol{u}) = \mathbf{grad}\,\Delta\boldsymbol{u} \cdot \boldsymbol{F}\,,$$

$$\left.\frac{\mathrm{d}}{\mathrm{d}\varepsilon}\right|_{\varepsilon=0} \boldsymbol{F}^{\top}(\boldsymbol{u} + \varepsilon\Delta\boldsymbol{u}) = \boldsymbol{F}^{\top} \cdot [\mathbf{grad}\,\Delta\boldsymbol{u}]^{\top}\,, \tag{9.4.10}$$

$$\left.\frac{\mathrm{d}}{\mathrm{d}\varepsilon}\right|_{\varepsilon=0} \boldsymbol{F}^{-1}(\boldsymbol{u} + \varepsilon\Delta\boldsymbol{u}) = -\boldsymbol{F}^{-1} \cdot \mathbf{grad}\,\Delta\boldsymbol{u}\,.$$

Using $\boldsymbol{\tau} := \boldsymbol{F} \cdot \boldsymbol{S} \cdot \boldsymbol{F}^{\top}$, where $\boldsymbol{S} = \boldsymbol{F}^{-1} \cdot \boldsymbol{\tau} \cdot \boldsymbol{F}^{-\top}$ denotes the second PIOLA–KIRCHHOFF stress tensor, together with $\boldsymbol{C} = \boldsymbol{F}^{\top} \cdot \boldsymbol{F}$ the linearization of $\boldsymbol{\tau}$, i.e., $D\boldsymbol{\tau}(\boldsymbol{u})[\Delta\boldsymbol{u}]$, reads

$$\left.\frac{\mathrm{d}}{\mathrm{d}\varepsilon}\right|_{\varepsilon=0} [\boldsymbol{\tau}(\boldsymbol{u} + \varepsilon\Delta\boldsymbol{u})] = 2\, \boldsymbol{F} \cdot \boldsymbol{F} \cdot \frac{\partial \boldsymbol{S}}{\partial \boldsymbol{C}} \cdot \boldsymbol{F}^{\top} \cdot \boldsymbol{F}^{\top} : \mathrm{sym}\,(\mathbf{grad}\,\Delta\boldsymbol{u}) + 2\mathbf{grad}\,\Delta\boldsymbol{u} \cdot \boldsymbol{\tau}\,. \quad (9.4.11)$$

Finally, using $J\,\mathbb{c}_{\mathrm{MM}} := 2\, \boldsymbol{F} \cdot \boldsymbol{F} \cdot [\partial \boldsymbol{S}/\partial \boldsymbol{C}] \cdot \boldsymbol{F}^{\top} \cdot \boldsymbol{F}^{\top}$ the linearized mechanical internal virtual work can be reiterated to give

$$\begin{aligned} DG_{\boldsymbol{\varphi}}^{\mathrm{int}}(\boldsymbol{u}, \delta\boldsymbol{u})[\Delta\boldsymbol{u}] &= \int_{\mathfrak{B}_0} \mathbf{grad}\,\delta\boldsymbol{u} : J\,\mathbb{c}_{\mathrm{MM}} : \mathrm{sym}(\mathbf{grad}\,\Delta\boldsymbol{u})\,\mathrm{d}V \\ &+ \int_{\mathfrak{B}_0} \mathbf{grad}\,\delta\boldsymbol{u} : [\mathbf{grad}\,\Delta\boldsymbol{u} \cdot \boldsymbol{\tau}]\,\mathrm{d}V\,. \end{aligned} \quad (9.4.12)$$

On the right-hand side, the first term is due to material stiffness and the second term is due to initial stress stiffness (or geometric stiffness). An explicit representation of $\boldsymbol{c}_{\mathrm{MM}}$ is given on the subsequent pages[11]. Together with the solution of this step, appropriate updates will be realized to give $[\boldsymbol{b}_n^{\mathrm{e}}, \boldsymbol{\xi}_n, \Theta_n] \mapsto [\breve{\boldsymbol{b}}_{n+1}^{\mathrm{e}}, \breve{\boldsymbol{\xi}}_{n+1}, \breve{\Theta}_{n+1}]$.

Thermal Step. In this step, for any generic field $\boldsymbol{\chi}$ one can have the following reduction of dependence $\boldsymbol{\chi}(\boldsymbol{\epsilon}, \Theta) \mapsto \boldsymbol{\chi}(\Theta)$. Thermal weak statement for the residual $c\dot{\Theta} - \Omega_{\mathrm{mech}} + \mathrm{Div}\boldsymbol{Q}$ is encapsulated in the following scalar valued function $G_{\Theta}(\Theta, \delta\Theta)$ where $\delta\Theta$ denotes a sufficiently smooth virtual temperature field defined in the reference configuration

$$G_{\Theta}(\Theta, \delta\Theta) := \int_{\mathfrak{B}_0} \delta\Theta \left[c\,\dot{\Theta} - \Omega_{\mathrm{mech}} + \mathrm{Div}\boldsymbol{Q}\right]\mathrm{d}V = 0\,. \quad (9.4.13)$$

Noting that $\mathrm{Div}\,(\delta\Theta\,\boldsymbol{Q}) = \mathbf{Grad}\,\delta\Theta \cdot \boldsymbol{Q} + \delta\Theta\,\mathrm{Div}\boldsymbol{Q}$ and applying GAUSS theorem with $\overline{\theta} = \boldsymbol{Q} \cdot \boldsymbol{N}$ one reaches $\int_{\mathfrak{B}_0} \mathrm{Div}\,(\delta\Theta\,\boldsymbol{Q})\,\mathrm{d}V = \int_{\partial\mathfrak{B}_0^q} \overline{\theta}\,\delta\Theta\,\mathrm{d}A$, since $\delta\Theta = 0$ at $\partial\mathfrak{B}_0^{\Theta} = \partial\mathfrak{B}_0 \backslash \partial\mathfrak{B}_0^q$. Consequently, the total virtual work expression in Equation (9.4.13) can be rewritten as

$$G_{\Theta}(\Theta, \delta\Theta) := G_{\Theta}^{\mathrm{int}}(\Theta, \delta\Theta) - G_{\Theta}^{\mathrm{ext}}(\Theta, \delta\Theta) = 0\,. \quad (9.4.14)$$

Here, the components $G_{\Theta}^{\mathrm{int}}$ and $G_{\Theta}^{\mathrm{ext}}$ represent internal and external part of the thermal virtual work, respectively. Using $\boldsymbol{Q} = \boldsymbol{q} \cdot \boldsymbol{F}^{-\top}$ to give $\mathbf{Grad}\,\delta\Theta \cdot \boldsymbol{Q} = -[1 - D]\,k\,\mathbf{grad}\,\delta\Theta \cdot \mathbf{grad}\,\Theta$ with FOURIER heat conduction relation, these amount to

$$\begin{aligned} G_{\Theta}^{\mathrm{int}}(\Theta, \delta\Theta) &:= \int_{\mathfrak{B}_0} \delta\Theta\,\Omega_{\mathrm{mech}}\,\mathrm{d}V - \int_{\mathfrak{B}_0} c\,\delta\Theta\,\dot{\Theta}\,\mathrm{d}V \\ &+ \int_{\mathfrak{B}_0} [1 - D]\,k\,\mathbf{grad}\,\delta\Theta \cdot \mathbf{grad}\,\Theta\,\mathrm{d}V\,, \\ G_{\Theta}^{\mathrm{ext}}(\Theta, \delta\Theta) &:= \int_{\partial\mathfrak{B}_0^q} \overline{\theta}\,\delta\Theta\,\mathrm{d}A\,. \end{aligned} \quad (9.4.15)$$

---

[11]The spatial constitutive tangent moduli $c_{\mathrm{MM},\,ijkl}$ can be computed with a push-forward transformation of LAGRANGIAN constitutive tangent moduli $\mathcal{C}_{IJKL}$ viz.

$$J\,c_{\mathrm{MM},\,ijkl} = F_{iI}\,F_{jJ}\,F_{kK}\,F_{lL}\,\mathcal{C}_{IJKL} \quad \text{with} \quad \mathcal{C}_{IJKL} = 2\frac{\partial S_{IJ}}{\partial C_{KL}}\,.$$

Similar to the mechanical step, the focus is set on the internal part of the thermal virtual work. The time discrete form of internal virtual work given in Equation(9.4.15.1) reads

$$
\begin{aligned}
G_\Theta^{\mathrm{int}}(\Theta_{n+1}^i, \delta\Theta) := & \int_{\mathfrak{B}_0} \delta\Theta\, \Omega_{\mathrm{mech},n+1}^i \,\mathrm{d}V - \int_{\mathfrak{B}_0} c_{n+1}^i\, \delta\Theta\, \frac{\Delta\Theta_{n+1}^i}{\Delta t}\,\mathrm{d}V \\
& + \int_{\mathfrak{B}_0} [1 - D_{n+1}^i]\, k\, \mathbf{grad}\,\delta\Theta \cdot \mathbf{grad}\,\Theta_{n+1}^i \,\mathrm{d}V\,.
\end{aligned}
\tag{9.4.16}
$$

Linearization of G_Θ^{int} in direction of the temperature increment $\Delta\Theta_{n+1}^i$, i.e., $DG_\Theta^{\mathrm{int}}(\Theta_{n+1}^i, \delta\Theta)[\Delta\Theta_{n+1}^i]$, leads to

$$
DG_\Theta^{\mathrm{int}}(\Theta_{n+1}^i, \delta\Theta)[\Delta\Theta] := \left.\frac{\mathrm{d}}{\mathrm{d}\varepsilon}\right|_{\varepsilon=0} G_\Theta^{\mathrm{int}}(\Theta_{n+1}^i + \varepsilon\Delta\Theta_{n+1}^i, \delta\Theta)\,.
\tag{9.4.17}
$$

Like before dropping the superscripts i and the subscripts $n+1$, the linearized thermal internal virtual work expression is given as

$$
\begin{aligned}
DG_\Theta^{\mathrm{int}}(\Theta, \delta\Theta)[\Delta\Theta] = & \int_{\mathfrak{B}_0} \delta\Theta\left[c_{\Theta\Theta} - \frac{\partial c}{\partial\Theta}\frac{\Delta\Theta}{\Delta t} - \frac{c}{\Delta t}\right]\Delta\Theta\,\mathrm{d}V \\
& + \int_{\mathfrak{B}_0} [1 - D]\, k\, \mathbf{grad}\,\delta\Theta \cdot \mathbf{grad}\,\Delta\Theta\,\mathrm{d}V \\
& - \int_{\mathfrak{B}_0} \frac{\partial D}{\partial\Theta}\Delta\Theta\, k\, \mathbf{grad}\,\delta\Theta \cdot \mathbf{grad}\,\Theta\,\mathrm{d}V\,.
\end{aligned}
\tag{9.4.18}
$$

Here, $c_{\Theta\Theta} := \partial\Omega_{\mathrm{mech}}/\partial\Theta$ represents the thermoinelastic modulus. At this step, the variable update $[\check{\boldsymbol{b}}_{n+1}^{\mathrm{e}}, \check{\boldsymbol{\xi}}_{n+1}, \check{\Theta}_{n+1}] \mapsto [\boldsymbol{b}_{n+1}^{\mathrm{e}}, \boldsymbol{\xi}_{n+1}, \Theta_{n+1}]$ is realized. Accordingly, temperature change induced by inelastic dissipative mechanisms such as plasticity and damage are taken into account as well as softening and expansion induced by temperature. Besides, heat conduction is affected by deformation and damage.

9.4.2. Return Mapping

Update of the state variables with local integration follows a two-step operator-split with a simultaneous plastic/damage correction for a given elastic prediction. Studying a strain driven process, one defines an elastic trial left CAUCHY-GREEN deformation tensor $\boldsymbol{b}^{\mathrm{e,\,tri}}$, making use of relative deformation gradient tensor at current step, i.e. $\boldsymbol{f} = \boldsymbol{F} \cdot \boldsymbol{F}_n^{-1}$, and elastic left CAUCHY-GREEN deformation tensor of the previous step, i.e., $\boldsymbol{b}_n^{\mathrm{e}}$, as follows

$$
\boldsymbol{b}^{\mathrm{e,\,tri}} = \boldsymbol{f} \cdot \boldsymbol{b}_n^{\mathrm{e}} \cdot \boldsymbol{f}^\top \quad \text{where} \quad \boldsymbol{b}^{\mathrm{e,\,tri}} = \sum_{A=1}^{3}\left[\lambda_A^{\mathrm{e,\,tri}}\right]^2 \boldsymbol{\nu}^{\mathrm{tri},\,A} \otimes \boldsymbol{\nu}^{\mathrm{tri},\,A}\,.
\tag{9.4.19}
$$

For the integration of flow rule given in Equation (9.3.20) exponential mapping approximation which exploits the coaxiality of the plastic flow and the elastic trial state is used. Accordingly, the following plastic-damage correction on trial elastic principal strains, where the strain corrections are in the form of the principal plastic strain increments $\Delta\epsilon_A^{\mathrm{vp}}$, is carried out

$$
\epsilon_A^{\mathrm{e}} = \epsilon_A^{\mathrm{e,\,tri}} - \Delta\epsilon_A^{\mathrm{vp}} \quad \text{where} \quad \Delta\epsilon_A^{\mathrm{vp}} = \frac{\Delta\gamma}{1 - D}\frac{\partial\Phi^{\mathrm{vp}}}{\partial\tilde{\tau}_A}\,,
\tag{9.4.20}
$$

with $\Delta\gamma = \Delta t\,\dot{\gamma}$. Using Equations (9.3.21) and (9.3.22) for $\dot{\alpha}$ and $\dot{D}$, the implicit backward-EULER method yields

$$
\alpha = \alpha_n + \sqrt{\frac{2}{3}}\Delta\gamma \quad \text{and} \quad D = D_n + \Delta\gamma\frac{1}{[1 - D]^r}\left[\frac{\langle Y^{\mathrm{d}} - Y_0^{\mathrm{d}}\rangle}{a(\Theta)}\right]^s\,.
\tag{9.4.21}
$$

Resultant viscoplastic/damage correction of principal KIRCHHOFF stresses yields

$$\tilde{\tau}_A = \tilde{\tau}_A^{\text{tri}} - 2\mu \frac{\Delta\gamma}{1-D} \, n_A \quad \text{with} \quad \tilde{\tau}_A^{\text{tri}} = \tilde{p} + \tilde{s}_A^{\text{tri}} \, . \tag{9.4.22}$$

Moreover, the viscoplastic potential at step $n+1$ reads

$$\Phi^{\text{vp}} := \|\tilde{s}\| - \sqrt{\frac{2}{3}} \, y \, (q, \Theta) \, . \tag{9.4.23}$$

Using Equation (9.3.25), the mechanical dissipation at step $n+1$ is defined as

$$\Omega_{\text{mech}} = \frac{\Delta\gamma}{\Delta t} \left[\|\tilde{s}\| + \sqrt{\frac{2}{3}} q(\alpha, \Theta) + \frac{Y^{\text{d}}}{[1-D]^r} \left[\frac{\langle Y^{\text{d}} - Y_0^{\text{d}} \rangle}{a(\Theta)} \right]^s \right] \, . \tag{9.4.24}$$

The backward-EULER method is applied for the integration of the components of the inelastic entropy. Accordingly, in view of Equation (9.3.26), the viscoplastic part reads

$$\eta^{\text{vp}} = \eta_n^{\text{vp}} - \Delta\gamma\sqrt{\frac{2}{3}} \, g'_{\omega^{\text{vp}}}(\Theta) \, \tau_{y0,0} \, . \tag{9.4.25}$$

Applying Equation (9.3.27) the damage entropy is integrated to read

$$\eta^{\text{d}} = \eta_n^{\text{d}} - \Delta\gamma g'_{\omega^{\text{d}}}(\Theta) \, a_0 \frac{s}{s+1} \frac{1}{[1-D]^r} \left[\frac{\langle Y^{\text{d}} - Y_0^{\text{d}} \rangle}{a(\Theta)} \right]^{s+1} \, . \tag{9.4.26}$$

Equations (9.4.25) and (9.4.26) add up to find $\eta^{\text{vpd}} = \eta^{\text{vp}} + \eta^{\text{d}}$. It is remarkable that the local integration expressions for η^{vp} and η^{d} have explicit representations in $\Delta\gamma$ and D. Thus, setting the inelastic entropy as an additional internal variable does not alter the local integration scheme and conventional finite thermoplastic algorithmic structure presented in [275], even for damage-coupled conditions.

9.4.2.1. Solution of Equations of Local Integration

Following [276], local governing equations collected so far can be reduced, particularly for the chosen yield criterion, making use of the substitution $\tilde{s}_A = \|\tilde{s}\| \, n_A$ and exploiting the condition of collinear flow and the trial KIRCHHOFF stress tensor, finally, representing the hardening/softening function definition in terms of the viscoplastic multiplier, to reach

$$\boldsymbol{r}(\boldsymbol{x}) = \left\{ \begin{array}{l} \sqrt{\dfrac{2}{3}} \left[\tau_{y0}(\Theta) - q(\alpha_n + \sqrt{\dfrac{2}{3}}\Delta\gamma, \Theta) \right] - \|\tilde{s}^{\text{tri}}\| + 2\mu\dfrac{\Delta\gamma}{1-D} + \kappa^{\text{vp}}\left[\dfrac{t_\star\Delta\gamma}{\Delta t}\right]^m \\[4mm] D - D_n - \Delta\gamma\dfrac{1}{[1-D]^r}\left[\dfrac{\langle Y^{\text{d}} - Y_0^{\text{d}} \rangle}{a(\Theta)}\right]^s \end{array} \right\}, \tag{9.4.27}$$

where $\boldsymbol{r} = \boldsymbol{r}(\boldsymbol{x}) = \boldsymbol{0}$. The array of unknowns is represented by $\boldsymbol{x} = [\Delta\gamma, D]^\top$. Equations (9.4.27) can be treated with the standard NEWTON-RAPHSON solution scheme. Accordingly, the linearized version of the equations is given as $\mathrm{d}\boldsymbol{r} = \boldsymbol{\Gamma}\cdot\mathrm{d}\boldsymbol{x}$, where $\boldsymbol{\Gamma}$ denotes the JACOBIAN of the system

$$\boldsymbol{\Gamma} = \left[\begin{array}{cc} \dfrac{\partial r_1}{\partial\Delta\gamma} & \dfrac{\partial r_1}{\partial D} \\[3mm] \dfrac{\partial r_2}{\partial\Delta\gamma} & \dfrac{\partial r_2}{\partial D} \end{array} \right], \tag{9.4.28}$$

where the component derivations are given in Appendix A. Using $\mathbf{\Gamma}^{-1} \cdot \mathrm{d}\boldsymbol{r} = \mathrm{d}\boldsymbol{x}$, the solution for $\boldsymbol{x}$, which constitutes the local return mapping realized at each GAUSS point, is found via the iterative scheme

$$\boldsymbol{x}^{(k+1)} = \boldsymbol{x}^{(k)} - \delta^{(k)} \left[\mathbf{\Gamma}^{(k)}\right]^{-1} \cdot \boldsymbol{r}^{(k)} \,, \tag{9.4.29}$$

where k represents the iteration number and $\delta^{(k)} \in (0, 1]$ is the proper line-search parameter.

9.4.3. Algorithmic Tangent Matrices

For the monolithic solution of the global equilibrium problem of coupled thermomechanical analysis, one has

$$\boldsymbol{r} = \boldsymbol{r}(\widehat{\boldsymbol{x}}) = \boldsymbol{0}; \quad \widehat{\boldsymbol{x}} = \left\{ \begin{array}{c} \epsilon_B \\ \Theta \\ \Delta\gamma \\ D \end{array} \right\} \quad \text{for } B = 1, 2, 3 \,, \tag{9.4.30}$$

where $\Delta\gamma = \Delta\gamma(\boldsymbol{\epsilon}, \Theta)$ and $D = D(\boldsymbol{\epsilon}, \Theta)$. A mechanical-thermal staggered approach introduces the following simplifications into the solution scheme.

Mechanical Step.   For the mechanical step $\boldsymbol{c}_{\mathrm{MM}}$ reads

$$\begin{aligned} J\mathbb{c}_{\mathrm{MM}} = & \sum_{A=1}^{3} \sum_{B=1}^{3} a_{AB}^{\mathrm{evpd}} \, \mathbf{\Lambda}^{\mathrm{tri},\, AABB} - \sum_{A=1}^{3} 2\tau_A \, \mathbf{\Lambda}^{\mathrm{tri},\, AAAA} \\ & + \sum_{A=1}^{3} \sum_{\substack{B=1 \\ A \neq B}}^{3} \vartheta_{AB} \left[\mathbf{\Lambda}^{\mathrm{tri},\, ABAB} + \mathbf{\Lambda}^{\mathrm{tri},\, ABBA} \right] . \end{aligned} \tag{9.4.31}$$

a_{AB}^{evpd} corresponds to the following 3×3 matrix

$$a_{AB}^{\mathrm{evpd}} = \frac{\partial \tau_A}{\partial \epsilon_B} \equiv \frac{\partial \tau_A}{\partial \epsilon_B^{\mathrm{e, tri}}} \,, \tag{9.4.32}$$

where the condition $\partial[\bullet]/\partial\epsilon_B \equiv \partial[\bullet]/\partial\epsilon_B^{\mathrm{e, tri}}$ is exploited. $\mathbf{\Lambda}^{ABCD}$ represents a fourth-order tensor with $\mathbf{\Lambda}^{ABCD} := \boldsymbol{\nu}^A \otimes \boldsymbol{\nu}^B \otimes \boldsymbol{\nu}^C \otimes \boldsymbol{\nu}^D$. The designation of ϑ_{AB} is given as[12]

$$\vartheta_{AB} = \frac{\tau_A \left[\lambda_B^{\mathrm{e, tri}}\right]^2 - \tau_B \left[\lambda_A^{\mathrm{e, tri}}\right]^2}{\left[\lambda_A^{\mathrm{e, tri}}\right]^2 - \left[\lambda_B^{\mathrm{e, tri}}\right]^2} \,. \tag{9.4.33}$$

Mechanical pass is realized under constant temperature, where $\Theta = \check{\Theta}$ which results in $\Delta\gamma = \Delta\gamma(\boldsymbol{\epsilon})|_{\Theta=\check{\Theta}}$ and $D = D(\boldsymbol{\epsilon})|_{\Theta=\check{\Theta}}$. For this stage

$$\boldsymbol{r} = \boldsymbol{r}(\widehat{\boldsymbol{x}}) = \boldsymbol{0} \quad \text{where} \quad \widehat{\boldsymbol{x}} = \left\{ \begin{array}{c} \epsilon_B \\ \Delta\gamma \\ D \end{array} \right\}\Bigg|_{\Theta=\check{\Theta}} . \tag{9.4.34}$$

---

[12]Equation (9.4.33) suffers from singularity or ill-conditioning for equal or nearly equal eigenvalues, respectively, where $\lambda_A^{\mathrm{e, tri}} - \lambda_B^{\mathrm{e, tri}} \to 0$. [235, pp. 338–341] includes an analytical treatment of such cases in the context of finite elasticity materializing L'HOSPITAL rule. In this work, a numerical perturbation as an efficient substitute for the L'HOSPITAL rule is used. Consequently, equal or numerically close eigenvalues with $\lambda_A^{\mathrm{e, tri}} \simeq \lambda_B^{\mathrm{e, tri}}$ are perturbed with a perturbation factor $\varepsilon^{\mathrm{per}} \ll 1$ ($\varepsilon^{\mathrm{per}} = 10^{-12}$ constitutes a reasonable choice) which gives $\lambda_A^{\mathrm{e, tri}} \mapsto [1 + \varepsilon^{\mathrm{per}}] \, \lambda_A^{\mathrm{e, tri}}$, $\lambda_B^{\mathrm{e, tri}} \mapsto [1 - \varepsilon^{\mathrm{per}}] \, \lambda_B^{\mathrm{e, tri}}$, and for volumetric consistency $\lambda_C^{\mathrm{e, tri}} \mapsto 1/\left[[1 + \varepsilon^{\mathrm{per}}] [1 - \varepsilon^{\mathrm{per}}]\right] \lambda_C^{\mathrm{e, tri}}$, [214].

Hence, the mechanical step in the staggered approach assumes

$$\boldsymbol{\tau}(\boldsymbol{\epsilon}, \Theta, \Delta\gamma\,(\boldsymbol{\epsilon}, \Theta), D(\boldsymbol{\epsilon}, \Theta)) \mapsto \boldsymbol{\tau}(\boldsymbol{\epsilon}, \Delta\gamma\,(\boldsymbol{\epsilon}), D(\boldsymbol{\epsilon}))|_{\Theta=\check{\Theta}} \; . \tag{9.4.35}$$

This allows the computation of a_{AB}^{evpd} through the chain rule

$$\frac{\partial\tau_A}{\partial\epsilon_B^{\mathrm{e,\,tri}}} = \frac{\partial\tau_A}{\partial\epsilon_B^{\mathrm{e,\,tri}}}\bigg|_{\Delta\gamma, D \rightsquigarrow \mathrm{const.}} + \frac{\partial\tau_A}{\partial\Delta\gamma}\frac{\mathrm{d}\Delta\gamma}{\mathrm{d}\epsilon_B^{\mathrm{e,\,tri}}} + \frac{\partial\tau_A}{\partial D}\frac{\mathrm{d}D}{\mathrm{d}\epsilon_B^{\mathrm{e,\,tri}}} \; , \tag{9.4.36}$$

where determination of $\mathrm{d}\Delta\gamma/\mathrm{d}\epsilon_B^{\mathrm{e,\,tri}}$ and $\mathrm{d}D/\mathrm{d}\epsilon_B^{\mathrm{e,\,tri}}$ requires the condition $\mathrm{d}\boldsymbol{r} = \boldsymbol{0}$ with

$$\left\{ \begin{array}{c} \dfrac{\mathrm{d}\Delta\gamma}{\mathrm{d}\epsilon_B} \\[2mm] \dfrac{\mathrm{d}D}{\mathrm{d}\epsilon_B} \end{array} \right\} = -\boldsymbol{\Gamma}^{-1} \cdot \left\{ \begin{array}{c} \dfrac{\partial r_1}{\partial\epsilon_B} \\[2mm] \dfrac{\partial r_2}{\partial\epsilon_B} \end{array} \right\} \tag{9.4.37}$$

with $\partial[\bullet]/\partial\epsilon_B \equiv \partial[\bullet]/\partial\epsilon_B^{\mathrm{e,\,tri}}$. The details of the derivations are given in Appendix B.

Thermal Step. Equation (9.4.24) is used in computation of the thermoinelastic coupling modulus $c_{\Theta\Theta}$ viz.

$$c_{\Theta\Theta} := \frac{\partial\Omega_{\mathrm{mech}}}{\partial\Theta} \; . \tag{9.4.38}$$

During thermal pass the configuration is held fixed $\epsilon_A = \check{\epsilon}_A$, which results in $\Delta\gamma = \Delta\gamma(\Theta)|_{\boldsymbol{\epsilon}=\check{\boldsymbol{\epsilon}}}$ and $D = D(\Theta)|_{\boldsymbol{\epsilon}=\check{\boldsymbol{\epsilon}}}$. Consequently, one has

$$\boldsymbol{r} = \boldsymbol{r}(\widehat{\boldsymbol{x}}) = \boldsymbol{0} \quad \text{where} \quad \widehat{\boldsymbol{x}} = \left\{ \begin{array}{c} \Theta \\ \Delta\gamma \\ D \end{array} \right\}\Bigg|_{\epsilon_A=\check{\epsilon}_A} \; . \tag{9.4.39}$$

Hence, analogous to mechanical step one has

$$\Omega_{\mathrm{mech}}(\boldsymbol{\epsilon}, \Theta, \Delta\gamma\,(\boldsymbol{\epsilon}, \Theta), D(\boldsymbol{\epsilon}, \Theta)) \mapsto \Omega_{\mathrm{mech}}(\Theta, \Delta\gamma\,(\Theta), D(\Theta))|_{\boldsymbol{\epsilon}=\check{\boldsymbol{\epsilon}}} \; . \tag{9.4.40}$$

This allows the computation of $c_{\Theta\Theta}$ with the following chain rule of differentiation

$$\frac{\partial\Omega_{\mathrm{mech}}}{\partial\Theta} = \frac{\partial\Omega_{\mathrm{mech}}}{\partial\Theta}\bigg|_{\Delta\gamma, D \rightsquigarrow \mathrm{const.}} + \frac{\partial\Omega_{\mathrm{mech}}}{\partial\Delta\gamma}\frac{\mathrm{d}\Delta\gamma}{\mathrm{d}\Theta} + \frac{\partial\Omega_{\mathrm{mech}}}{\partial D}\frac{\mathrm{d}D}{\mathrm{d}\Theta} \; . \tag{9.4.41}$$

where determination of $\mathrm{d}\Delta\gamma/\mathrm{d}\Theta$ and $\mathrm{d}D/\mathrm{d}\Theta$ requires the condition $\mathrm{d}\boldsymbol{r} = \boldsymbol{0}$ with

$$\left\{ \begin{array}{c} \dfrac{\mathrm{d}\Delta\gamma}{\mathrm{d}\Theta} \\[2mm] \dfrac{\mathrm{d}D}{\mathrm{d}\Theta} \end{array} \right\} = -\boldsymbol{\Gamma}^{-1} \cdot \left\{ \begin{array}{c} \dfrac{\partial r_1}{\partial\Theta} \\[2mm] \dfrac{\partial r_2}{\partial\Theta} \end{array} \right\} \; . \tag{9.4.42}$$

The details of the derivations are given in Appendix C. It should be noted that in both the mechanical pass and the thermal pass the internal variables are changing. The thermal part will be due only if there exists plastic flow and induced damage. This concludes the numerical setup.

Table 9.1.: Material parameters for a steel-like material at reference temperature.

Parameter	Symbol	Magnitude	Dimension
Referential density	ρ_0	7.8×10^{-9}	[Ns^2/mm^4]
Bulk modulus	H	164206.0	[MPa]
Shear modulus	μ	80193.8	[MPa]
Linear hardening	K_0	129.24	[MPa]
Flow stress	$\tau_{y,0}$	450.0	[MPa]
Saturation stress	$\tau_{y\infty,0}$	715.0	[MPa]
Saturation exponent	δ	16.93	[−]
Damage multiplier	a_0	5.0	[MPa]
Damage exponent 1	s	1.0	[−]
Damage exponent 2	r	2.0	[−]
Threshold for Y	Y_0^{d}	0	[MPa]
Rate exponent	m	1	[−]
Drag stress	κ^{vp}	100	[MPa]
Characteristic time	$t_\star$	1	[s]
Coefficient of thermal expansion	α_Θ	1.0×10^{-5}	[K^{-1}]
Specific heat capacity	c_s	0.46×10^9	[mm/s^{2}K]
Heat conductivity	k	45.0	[N/sK]
Plastic thermal softening	ω^{vp}	1	[−]
Damage thermal softening	ω^{d}	1	[−]
Reference temperature	Θ_0	293	[K]
Melting temperature	Θ_{melt}	1700	[K]

9.5. Application Problems

Preceding algorithmic resolutions are implemented as Abaqus subroutines where the implementation details are included in appendices. Material parameters used in the analyses are given in Table 9.1, where for mere thermoplasticity the damage deterioration effects are omitted. Two example problems consisting of necking of an axisymmetric bar and localization in a 3D rectangular bar are investigated.

9.5.1. Monotonic Uniaxial Tension

In this section, first a systematic reduction of the theory to uniaxial stress state is presented. Solution of the resultant reduced equation set allows conduction of some parametric studies which show predictive capabilities of the model. Let e_1, e_2 and e_3 denote orthogonal unit vectors associated with $x-$, $y-$ and $z-$directions. Tensile loading in $x-$direction is of interest, where the material motion is free in $y-$ and $z-$directions. This corresponds to a uniaxial state of stress and triaxial state of strain with

$$\boldsymbol{\tau} = \tau \boldsymbol{e}_1 \otimes \boldsymbol{e}_1 \quad \text{and} \quad \boldsymbol{F} = \lambda_1 \boldsymbol{e}_1 \otimes \boldsymbol{e}_1 + \lambda_2 [\boldsymbol{e}_2 \otimes \boldsymbol{e}_2 + \boldsymbol{e}_3 \otimes \boldsymbol{e}_3], \qquad (9.5.1)$$

where λ_1 and λ_2 represent principal stretches in $x-$ and $y-$ (equivalently $z-$) directions. With Equation (10.4.1.1) following equivalences hold

$$[s_1^2 + s_2^2 + s_3^2]^{1/2} = \sqrt{\frac{2}{3}}\tau \quad \text{and} \quad p = \frac{1}{3}\tau. \qquad (9.5.2)$$

Using Equation (10.4.1.2) the Jacobian of the deformation gradient becomes $J = \lambda_1 \lambda_2^2$. In analogy to Eq. (10.4.1.2), the elastic and viscoplastic parts of the deformation gradient can be given as

$$
\begin{aligned}
\boldsymbol{F}^{\mathrm{e}} &= \lambda_1^{\mathrm{e}} \boldsymbol{e}_1 \otimes \boldsymbol{e}_1 + \lambda_2^{\mathrm{e}} [\boldsymbol{e}_2 \otimes \boldsymbol{e}_2 + \boldsymbol{e}_3 \otimes \boldsymbol{e}_3] \,, \\
\boldsymbol{F}^{\mathrm{vp}} &= \lambda_1^{\mathrm{vp}} \boldsymbol{e}_1 \otimes \boldsymbol{e}_1 + \lambda_2^{\mathrm{vp}} [\boldsymbol{e}_2 \otimes \boldsymbol{e}_2 + \boldsymbol{e}_3 \otimes \boldsymbol{e}_3] \,.
\end{aligned}
\tag{9.5.3}
$$

where $J^{\mathrm{e}} = \det \boldsymbol{F}^{\mathrm{e}} = \lambda_1^{\mathrm{e}} [\lambda_2^{\mathrm{e}}]^2$ and $J^{\mathrm{vp}} = \det \boldsymbol{F}^{\mathrm{vp}} = \lambda_1^{\mathrm{vp}} [\lambda_2^{\mathrm{vp}}]^2$. Using $J^{\mathrm{vp}} = 1$, Equation (9.5.3.2) can be written as

$$
\boldsymbol{F}^{\mathrm{vp}} = \lambda_1^{\mathrm{vp}} \boldsymbol{e}_1 \otimes \boldsymbol{e}_1 + [\lambda_1^{\mathrm{vp}}]^{-1/2} [\boldsymbol{e}_2 \otimes \boldsymbol{e}_2 + \boldsymbol{e}_3 \otimes \boldsymbol{e}_3] \,.
\tag{9.5.4}
$$

Hence, the right CAUCHY-GREEN deformation tensor $\boldsymbol{C} = \boldsymbol{F}^{\top} \cdot \boldsymbol{F}$ computes

$$
\boldsymbol{C} = [\lambda_1^{\mathrm{e}}]^2 [\lambda_1^{\mathrm{vp}}]^2 \boldsymbol{e}_1 \otimes \boldsymbol{e}_1 + [\lambda_2^{\mathrm{e}}]^2 [\lambda_1^{\mathrm{vp}}]^{-1} [\boldsymbol{e}_2 \otimes \boldsymbol{e}_2 + \boldsymbol{e}_3 \otimes \boldsymbol{e}_3] \,.
\tag{9.5.5}
$$

Now, using the definition of the logarithmic strain $\boldsymbol{\epsilon} = 1/2 \log \boldsymbol{C}$ one reaches

$$
\boldsymbol{\epsilon} = \boldsymbol{\epsilon}^{\mathrm{e}} + \boldsymbol{\epsilon}^{\mathrm{vp}} \,,
\tag{9.5.6}
$$

where

$$
\begin{aligned}
\boldsymbol{\epsilon}^{\mathrm{e}} &= \log \lambda_1^{\mathrm{e}} \boldsymbol{e}_1 \otimes \boldsymbol{e}_1 + \log \lambda_2^{\mathrm{e}} [\boldsymbol{e}_2 \otimes \boldsymbol{e}_2 + \boldsymbol{e}_3 \otimes \boldsymbol{e}_3] \,, \\
\boldsymbol{\epsilon}^{\mathrm{vp}} &= \log \lambda_1^{\mathrm{vp}} \boldsymbol{e}_1 \otimes \boldsymbol{e}_1 - \frac{1}{2} \log \lambda_1^{\mathrm{vp}} [\boldsymbol{e}_2 \otimes \boldsymbol{e}_2 + \boldsymbol{e}_3 \otimes \boldsymbol{e}_3] \,.
\end{aligned}
\tag{9.5.7}
$$

Equation (10.4.5) encapsulates an additive decomposition in logarithmic strains carried out from a multiplicative decomposition of the deformation gradient. The thermoelastic stress definition given in Equation (9.3.10) and the vanishing stress components in $y-$ and $z-$directions reveal $\log \lambda_2^{\mathrm{e}} = -\nu \log \lambda_1^{\mathrm{e}} + \alpha_{\Theta} [1 + \nu][\Theta - \Theta_0]$. Hence, using the notation $\epsilon^{\mathrm{e}} = \log \lambda_1^{\mathrm{e}}$, $\epsilon^{\mathrm{p}} = \log \lambda_1^{\mathrm{p}}$ one has

$$
\begin{aligned}
\boldsymbol{\epsilon}^{\mathrm{e}} &= \epsilon^{\mathrm{e}} \boldsymbol{e}_1 \otimes \boldsymbol{e}_1 + [-\nu \epsilon^{\mathrm{e}} + \alpha_{\Theta} [1 + \nu][\Theta - \Theta_0]] [\boldsymbol{e}_2 \otimes \boldsymbol{e}_2 + \boldsymbol{e}_3 \otimes \boldsymbol{e}_3] \,, \\
\boldsymbol{\epsilon}^{\mathrm{vp}} &= \epsilon^{\mathrm{vp}} \boldsymbol{e}_1 \otimes \boldsymbol{e}_1 - \frac{1}{2} \epsilon^{\mathrm{vp}} [\boldsymbol{e}_2 \otimes \boldsymbol{e}_2 + \boldsymbol{e}_3 \otimes \boldsymbol{e}_3] \,.
\end{aligned}
\tag{9.5.8}
$$

Equation (9.5.8.1) lets one compute τ as

$$
\tau = [1 - D] \tilde{\tau} \quad \text{where} \quad \tilde{\tau} = E \left[\epsilon^{\mathrm{e}} - \alpha_{\Theta} [\Theta - \Theta_0] \right] \,.
\tag{9.5.9}
$$

and Y^{d}, using Equation (9.3.12), as

$$
Y^{\mathrm{d}} = \frac{1}{2} E [\epsilon^{\mathrm{e}}]^2 - E \epsilon^{\mathrm{e}} \alpha_{\Theta} [\Theta - \Theta_0] - 3 \kappa [1 + \nu][\alpha_{\Theta}]^2 [\Theta - \Theta_0]^2 \,.
\tag{9.5.10}
$$

Note that for the analyzed monotonic uniaxial tensile loading[13]

$$
\sum_{A=1}^{3} n_A \boldsymbol{\nu}^A \otimes \boldsymbol{\nu}^A = \sqrt{\frac{2}{3}} \, \boldsymbol{e}_1 \otimes \boldsymbol{e}_1 - \frac{1}{\sqrt{6}} [\boldsymbol{e}_2 \otimes \boldsymbol{e}_2 + \boldsymbol{e}_3 \otimes \boldsymbol{e}_3] \,.
\tag{9.5.11}
$$

Now, using $\boldsymbol{G} = [\boldsymbol{C}^{\mathrm{vp}}]^{-1}$ one reaches

$$
\begin{aligned}
\boldsymbol{b}^{\mathrm{e}} &= [\lambda_1^{\mathrm{e}}]^2 \boldsymbol{e}_1 \otimes \boldsymbol{e}_1 + [\lambda_2^{\mathrm{e}}]^2 [\boldsymbol{e}_2 \otimes \boldsymbol{e}_2 + \boldsymbol{e}_3 \otimes \boldsymbol{e}_3] \,, \\
\boldsymbol{C}^{\mathrm{vp}} &= [\lambda_1^{\mathrm{vp}}]^2 \boldsymbol{e}_1 \otimes \boldsymbol{e}_1 + [\lambda_1^{\mathrm{vp}}]^{-1} [\boldsymbol{e}_2 \otimes \boldsymbol{e}_2 + \boldsymbol{e}_3 \otimes \boldsymbol{e}_3] \,, \\
\boldsymbol{G}^{\mathrm{vp}} &= [\lambda_1^{\mathrm{vp}}]^{-2} \boldsymbol{e}_1 \otimes \boldsymbol{e}_1 + \lambda_1^{\mathrm{vp}} [\boldsymbol{e}_2 \otimes \boldsymbol{e}_2 + \boldsymbol{e}_3 \otimes \boldsymbol{e}_3] \,.
\end{aligned}
\tag{9.5.12}
$$

---

[13]In case of cyclic character this expression should be multiplied by sign(τ).

Hence $\dot{\boldsymbol{G}}$ reads

$$\dot{\boldsymbol{G}}^{\mathrm{vp}} = -2[\lambda_1^{\mathrm{vp}}]^{-3}\dot{\lambda}_1^{\mathrm{vp}}\boldsymbol{e}_1 \otimes \boldsymbol{e}_1 + \dot{\lambda}_1^{\mathrm{vp}}[\boldsymbol{e}_2 \otimes \boldsymbol{e}_2 + \boldsymbol{e}_3 \otimes \boldsymbol{e}_3]\,. \tag{9.5.13}$$

Now, noting that $\mathcal{L}_v\boldsymbol{b}^{\mathrm{e}} = \boldsymbol{F} \cdot \dot{\boldsymbol{G}}^{\mathrm{vp}} \cdot [\boldsymbol{F}]^\top$ one has

$$-\frac{1}{2}\mathcal{L}_v\boldsymbol{b}^{\mathrm{e}} \cdot [\boldsymbol{b}^{\mathrm{e}}]^{-1} = \frac{\dot{\lambda}_1^{\mathrm{vp}}}{\lambda_1^{\mathrm{vp}}}\,\boldsymbol{e}_1 \otimes \boldsymbol{e}_1 - \frac{1}{2}\frac{\dot{\lambda}_1^{\mathrm{vp}}}{\lambda_1^{\mathrm{vp}}}\,[\boldsymbol{e}_2 \otimes \boldsymbol{e}_2 + \boldsymbol{e}_3 \otimes \boldsymbol{e}_3] \equiv \dot{\boldsymbol{\epsilon}}^{\mathrm{vp}}\,. \tag{9.5.14}$$

Thus, using Equation (10.4.12) along with Equation (9.5.11) the flow rule given in Equation (9.3.20) can be reiterated as

$$\dot{\boldsymbol{\epsilon}}^{\mathrm{vp}} = \sqrt{\frac{2}{3}}\,\frac{\dot{\gamma}}{1-D}\,\boldsymbol{e}_1 \otimes \boldsymbol{e}_1 - \frac{1}{\sqrt{6}}\,\frac{\dot{\gamma}}{1-D}\,[\boldsymbol{e}_2 \otimes \boldsymbol{e}_2 + \boldsymbol{e}_3 \otimes \boldsymbol{e}_3]\,, \tag{9.5.15}$$

where

$$\dot{\epsilon}^{\mathrm{vp}} = \sqrt{\frac{2}{3}}\,\frac{\dot{\gamma}}{1-D}\,. \tag{9.5.16}$$

For convenience, the complete reformulation of the model under uniaxial tension is given in **BOX 2**.

BOX 2. A reduction of the proposed model for uniaxial stress-state and monotonic tension.

i. Additive kinematics

$$\epsilon = \epsilon^{\mathrm{e}} + \epsilon^{\mathrm{vp}}.$$

ii. Thermoelastic stress-strain relationship

$$\tau = [1 - D]\, \tilde{\tau} \quad \text{where} \quad \tilde{\tau} = E\left[\epsilon^{\mathrm{e}} - \alpha_\Theta[\Theta - \Theta_0]\right].$$

iii. State laws for hardening and damage conjugate variables

$$q = -g_{\omega^{\mathrm{vp}}}(\Theta)\left[K_0\,\alpha + [\tau_{y\infty,0} - \tau_{y0,0}]\left[1 - \exp\left(-\delta\alpha\right)\right]\right],$$

$$Y^{\mathrm{d}} = \frac{1}{2}E[\epsilon^{\mathrm{e}}]^2 - E\epsilon^{\mathrm{e}}\alpha_\Theta[\Theta - \Theta_0] - 3\kappa[1+\nu][\alpha_\Theta]^2[\Theta - \Theta_0]^2.$$

iv. Thermoelastic domain in stress space (single surface)

$$\mathbb{E}_\tau = \left\{[\tilde{\tau}, q, \Theta] \in \mathbb{R}_+ \times \mathbb{R}_- \times \mathbb{R}_+ : \Phi^{\mathrm{vp}}(\tilde{\tau}, q, \Theta) \le 0\right\},$$

where

$$\Phi^{\mathrm{vp}}(\tilde{\tau}, q, \Theta) = \sqrt{\frac{2}{3}}\left[\tilde{\tau} - y(q, \Theta)\right] \quad \text{with} \quad y(q, \Theta) = \tau_{y0}(\Theta) - q.$$

v. Associative flow rule (Perzyna model)

$$\dot{\epsilon}^{\mathrm{vp}} = \sqrt{\frac{2}{3}}\frac{\dot{\gamma}}{1 - D} \quad \text{where} \quad \dot{\gamma} = \frac{1}{t_\star}\left\langle \frac{\Phi^{\mathrm{vp}}(\tilde{\tau}, q, \Theta)}{\kappa^{\mathrm{vp}}}\right\rangle^{1/m}.$$

vi. Evolution equations for hardening and damage

$$\dot{\alpha} = \dot{\gamma}\sqrt{\frac{2}{3}} \quad \text{and} \quad \dot{D} = \dot{\gamma}\frac{1}{[1-D]^r}\left[\frac{\langle Y^{\mathrm{d}} - Y_0^{\mathrm{d}}\rangle}{a(\Theta)}\right]^s.$$

The derivations correspond to a single material point loaded under uniaxial stress state. Hence, there is no heat conduction. Any heat source, except for inelastic dissipation, is not accounted for. Hence heat source is composed of viscoplastic and damage dissipation which can be given using Equation (9.5.17.1) along with Equations (10.4.1) and (9.2.38.1) for the current uniaxial state of stress as

$$\Omega_{\mathrm{mech}}^{\mathrm{vp}} = \sqrt{\frac{2}{3}}\dot{\gamma}\left[\tilde{\tau} + q\right] \quad \text{and} \quad \Omega_{\mathrm{mech}}^{\mathrm{d}} = Y^{\mathrm{d}}\dot{D}. \tag{9.5.17}$$

Hence the temperature increase can be locally solved to give

$$\dot{\Theta} = \frac{1}{c}\Omega_{\mathrm{mech}} = \frac{\dot{\gamma}}{c}\left[\sqrt{\frac{2}{3}}\left[\tilde{\tau} + q\right] + \frac{Y^{\mathrm{d}}}{[1-D]^r}\left[\frac{\langle Y^{\mathrm{d}} - Y_0^{\mathrm{d}}\rangle}{a(\Theta)}\right]^s\right]. \tag{9.5.18}$$

Using $\dot{\gamma} = \sqrt{3/2}\,\dot{\alpha}$ the rate equations that needs to be solved can be given as follows

$$
\begin{aligned}
\dot{\alpha} &= \sqrt{\frac{2}{3}}\frac{1}{t_\star}\left\langle \frac{1}{\kappa^{\mathrm{vp}}}\sqrt{\frac{2}{3}}\left[\tilde{\tau}+q(\alpha,\Theta)-\tau_{y0}(\Theta)\right]\right\rangle^{1/m}, \\
\dot{\epsilon}^{\mathrm{vp}} &= \frac{\dot{\alpha}}{1-D}, \\
\dot{D} &= \sqrt{\frac{3}{2}}\frac{\dot{\alpha}}{[1-D]^r}\left[\frac{\langle Y^{\mathrm{d}}-Y_0^{\mathrm{d}}\rangle}{a(\Theta)}\right]^s, \\
\dot{\Theta} &= \frac{\dot{\alpha}}{c}\left[\tilde{\tau}+q(\alpha,\Theta)+\sqrt{\frac{3}{2}}\frac{Y^{\mathrm{d}}}{[1-D]^r}\left[\frac{\langle Y^{\mathrm{d}}-Y_0^{\mathrm{d}}\rangle}{a(\Theta)}\right]^s\right].
\end{aligned}
\tag{9.5.19}
$$

This system of ordinary differential equations are solved using RK4 method implemented in MATLAB where the iterations are run under a desired tolerance. The parameter set is identical to those listed in Table 9.1, except for the fact that $a_0 = 0.5$ MPa in order to increase rate of damage evolution. The results are compared with those of ABAQUS 3D single element under tension where the UMAT subroutine is devised. The results are collectively given in Figure 9.1 where the agreement between predictions constitutes a means of verification.

9.5.2. Necking of an Axisymmetric Bar

Necking of an axisymmetric bar is investigated in the context of damage-coupled thermoplastic framework. Contrary to the common idea, in the FE simulations with a typical free contracting (shear-free grip conditions) tensile test specimen of a certain gauge length, central refinement of the mesh does not suffice to transform the bifurcation problem, where the necking can emanate at any section, to a limit load problem. This is due to the fact that necking emanation requires the break up of the stress uniformity. For this purpose, two necking triggering methods widely used in the literature are the geometric imperfection method and the thermal triggering method. The former requires a reduction of the central area, linearly varied over the half-length as utilized in [291], [272] and [135], among others. In the latter, fixed temperature boundary conditions applied at both ends are utilized as a necking triggering mechanism, which was first studied by [333].

In this first example the former method of introduction of a geometrical imperfection at the center is used. Only a quarter of the specimen has been discretized by exploiting the symmetry of the problem. Figure 9.2 shows the geometrical setup and boundary conditions. In the geometrical imperfection method the radius of face B is selected as 98.2% of the radius of face A. The heat exchange at the surfaces of the specimen are neglected by assuming adiabatic thermal boundary conditions. A displacement controlled simulation is performed where the displacement Δu is assigned to face A as seen in Figure 9.2.(b) with a loading rate of 1 mm/s. The elements are assumed to have a reference absolute temperature of $\Theta_0 = 293$ K.

In order to evaluate the mesh dependence of the softening mechanism due to temperature and damage and the effect of viscosity 10×20, 20×40 and 40×80 meshes are used as shown in Figures 9.3.(a), (b) and (c), respectively. Here 10×20 refers to 10 elements in radial direction and 20 elements in longitudinal direction. The meshes are composed of element CAX4T, which is a 4-node axisymmetric thermally coupled quadrangular element with bilinear displacement and temperature interpolations. Besides rate independent limit with $\kappa^{\mathrm{vp}} = 0$, rate effects are
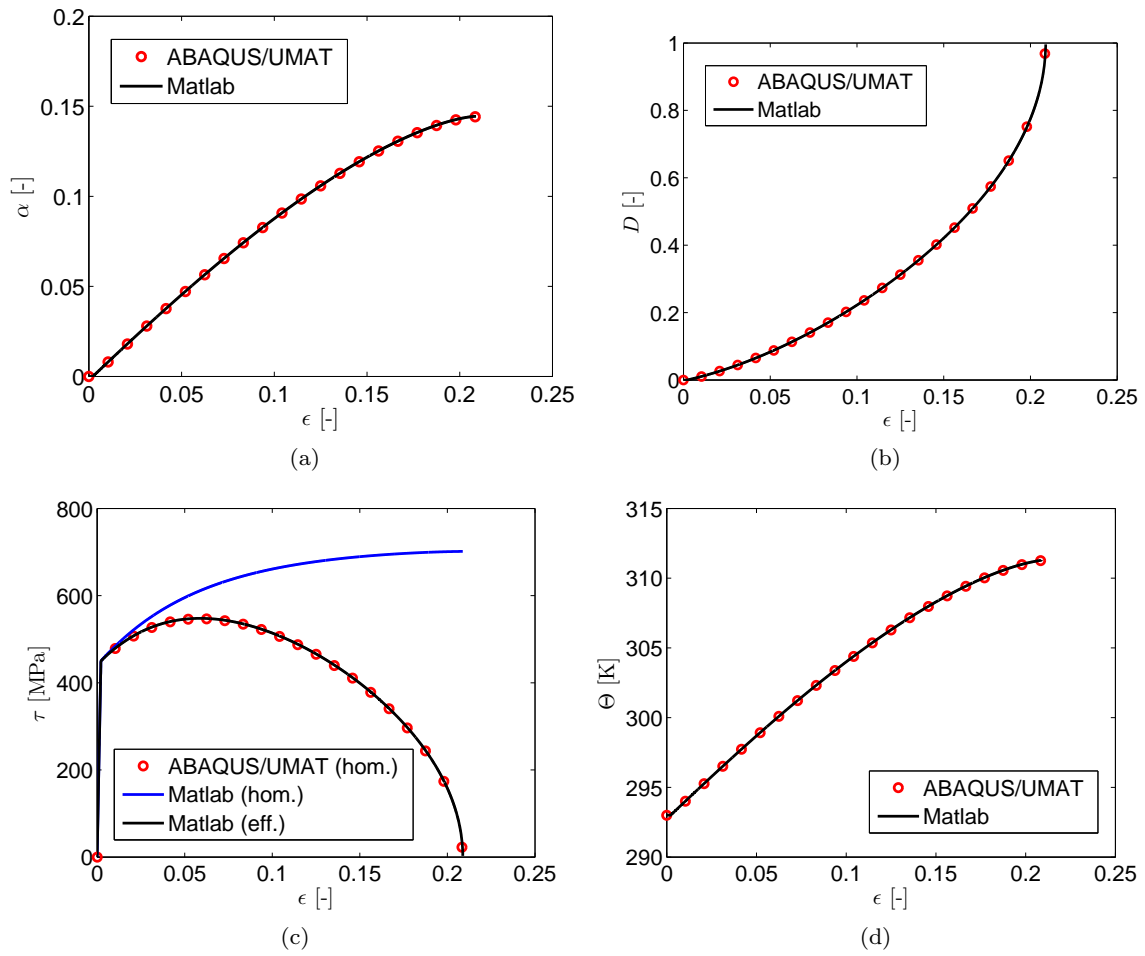
Figure 9.1.: Comparison of ABAQUS single 3D element with UMAT and MATLAB results for implementation verification: (a) α, (b) D, (c) effective and homogenized Kirchhoff stress in the direction of tension, (d) Θ.
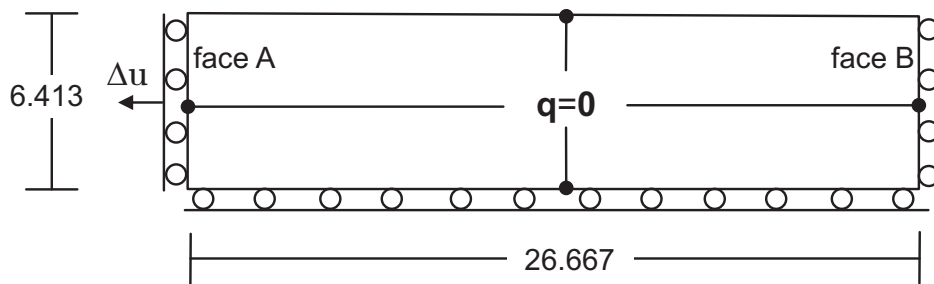
Figure 9.2.: Geometry and boundary conditions for tensile tests (all dimensions are in mm).

also investigated taking $\kappa^{\mathrm{vp}} = 500$ MPa and $\kappa^{\mathrm{vp}} = 1000$ MPa[14].

Considering damage evolution and mesh with $10{\times}20$ discretization, the load-displacement and the central temperature increment history plots are given in Figures 9.4.(a) and (b) respectively.

---

[14]In the most general case, instantaneous elasticity and inviscid plasticity bound the expansion of the damage affected yield surface with $0 \le \kappa^{\mathrm{vp}} < \infty$.

The initiation of the necking is signaled by the peak of the load deflection curves. The figures clearly reveal the effect of damage where the in absence of damage the neck is slightly delayed. Moreover, the abrupt loss in the load carrying capacity together with necking is precluded in the simulations where rate effects are considered. For the central temperature evolution, more rapid confinement of the plastic zone to the necked area in the middle of the bar in absence of rate affects results in a stronger raise in temperature at the specimen center.

Contour plots of temperature Θ, hardening strain-like variable α and damage D distribution at different displacements for damage-coupled 2D axisymmetric bar tension problem for 10×20 mesh and rate dependent solution are given in Figure 9.5. With neck development there occurs considerable temperature increase with inelastic dissipation. Also the central damage localization is more noticeable as compared to other fields. This is primarily due to the increased stress triaxiality ratio at the specimen center and it is in agreement with experimentally observed cup and cone fracture. Since the minimum of the hardening variable and damage ceases to evolve at latter stages it is understood that elastic unloading takes place in a considerable part of the specimen.

Figure 9.6 depicts the effect of viscosity on development of inelastic fields and temperature. In agreement with the given load-displacement plots, inclusion of rate affects delays neck formation and hence associated inelastic dissipation at the center whereas in the inviscid solution there occurs considerable damage development. Hence, a more concentrated plastic zone and a sharper curvature of the neck than the viscous results is observed. Together with the inclusion of viscosity, localized behavior of the rate independent analyses diffuse; that is, the deformation localized at the elements of the central band is distributed to a wider band. This also decreases the radius reduction at the center. In the inviscid analyses, intensities of both the maximum equivalent plastic strain and the temperature are higher than those of viscous analysis.

The mesh dependence of the doubly induced softening mechanism due to temperature and damage is tested together with considering the effect of viscosity for $\kappa^{\mathrm{vp}} = 500$ MPa. Figures 9.7.(a) and (b) show load-displacement curves for inviscid and viscous solutions, respectively. Although in both of the cases the mesh effect is considerably small, in the inviscid case, a more noticeable branching among solutions starting just after the peak is observed. For the rate dependent solution this branching seems to be further bypassed. This is parallel to the observations in the literature on viscous regularization, [326]. The difference in responses for 10×20 and 20×40 meshes could be attributed to the rather coarse nature of 10×20 mesh, hence classical mesh dependence of finite element solutions. Further differences with mesh refinement, however, is due to damage. In the rate independent solution, together with the refined mesh the analysis is terminated earlier at smaller deformations. Besides, the post peak response has a sharper decrease compared to the rate dependent solution where a rather diffuse localization is observed.

Figures 9.8.(a) and 9.8.(b) show central temperature development for inviscid and viscous solutions for different mesh refinement levels. In agreement with Figure 9.7 the central localization of temperature with further mesh refinement is for the regularized solution is not as strong as the regularized one.
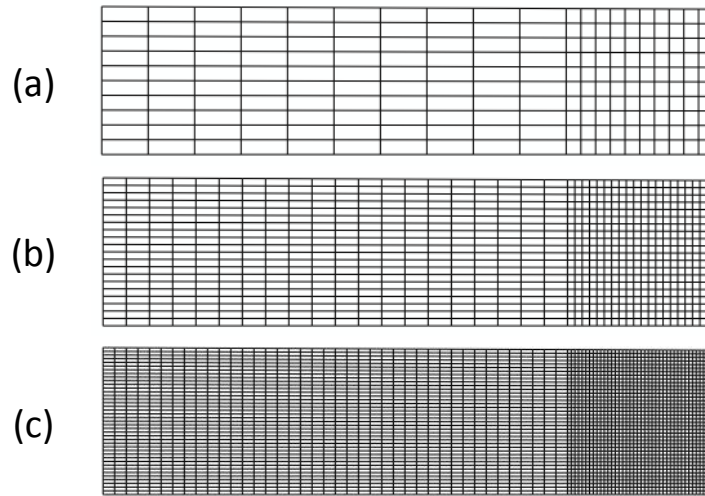
Figure 9.3.: Finite element meshes, (a) 10×20, (b) 20×40 and (c) 40×80.

(a)	(b)
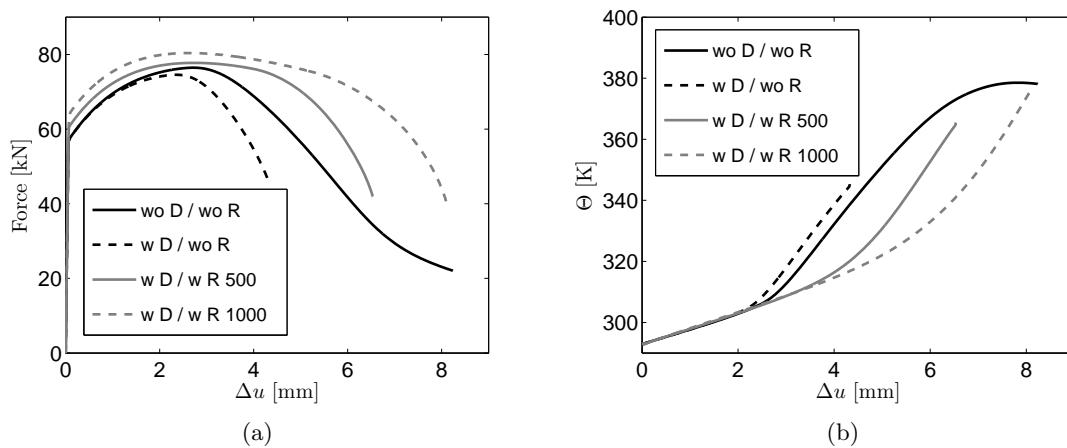
Figure 9.4.:   History plots for axisymmetric tension problem for 10×20 mesh, (a) Load-displacement curves, (b) Temperature evolution at the central node. The codes wo D and w D stand for without and with damage effect, respectively. The codes wo R, w R 500 and w R 1000 stand for without rate effect, with rate effect with $\kappa^{vp} = 500$ MPa and with rate effect with $\kappa^{vp} = 1000$ MPa, respectively.

9.5.3.   Localization of Rectangular Bar

In this 3D example, the localization in a rectangular bar with the geometry is investigated:

$$\text{width/thickness/length} = 16/4/52 \text{ mm}$$

This problem was studied in [275] in absence of damage. Contraction-free boundary conditions are applied during displacement controlled tensile loading of the bar. Since no geometrical imperfections are introduced, these boundary conditions result in a homogeneous state of stress throughout the loading. In order to trigger neck, thermal boundary conditions are arranged as to account for convective heat exchange on the entire free surface of the specimen (except for the symmetry surfaces) given by the expression $q_n = h\,[\Theta_\infty - \Theta]$. Here, $h = 17.5 \times 10^{-3}$ N/mmsK denotes the convection coefficient and $\Theta_\infty = 293$ K represents the temperature of the
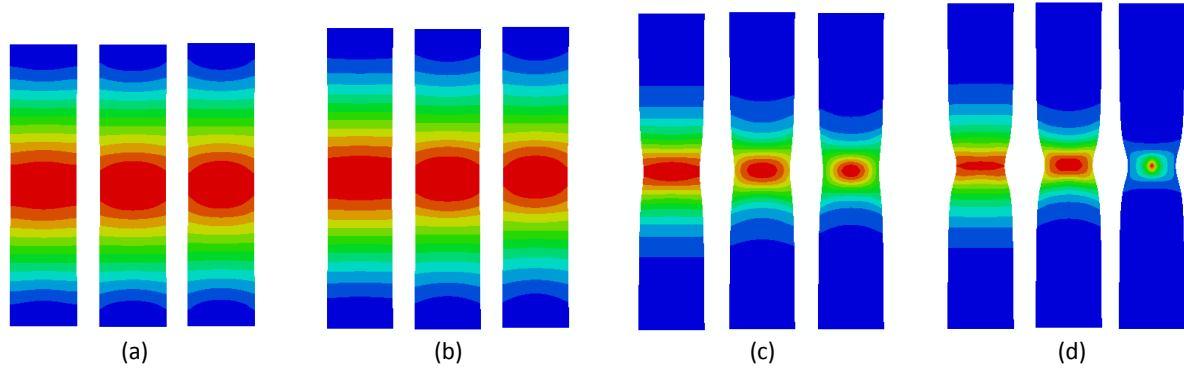
Figure 9.5.: Contour plots of temperature Θ, hardening strain-like variable α and damage D distribution at different displacements for damage-coupled 2D axisymmetric bar tension problem for 10×20 mesh and rate independent solution. (a) $\Delta u = 2 \times 0.25$ mm, min/max $\Theta = 293.6/294.1$, min/max $\alpha = 5.095 \times 10^{-3}/9.014 \times 10^{-3}$, min/max $D = 6.387 \times 10^{-4}/1.190 \times 10^{-3}$, (b) $\Delta u = 2 \times 2.00$ mm, min/max $\Theta = 300.3/303.2$, min/max $\alpha = 5.686 \times 10^{-2}/8.368 \times 10^{-2}$, min/max $D = 1.023 \times 10^{-2}/1.707 \times 10^{-2}$, (c) $\Delta u = 2 \times 3.50$ mm, min/max $\Theta = 301.1/328.8$, min/max $\alpha = 6.086 \times 10^{-2}/3.741 \times 10^{-1}$, min/max $D = 1.115 \times 10^{-2}/1.434 \times 10^{-1}$, (d) $\Delta u = 2 \times 4.325$ mm, min/max $\Theta = 301.3/347.2$, min/max $\alpha = 6.086 \times 10^{-2}/6.541 \times 10^{-1}$, min/max $D = 1.115 \times 10^{-2}/9.872 \times 10^{-1}$.
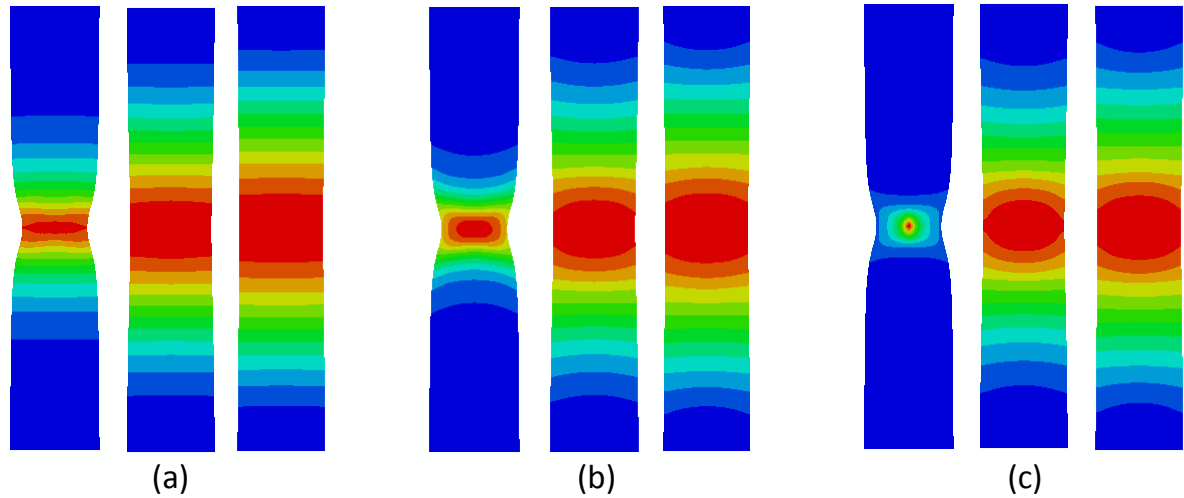
Figure 9.6.: Contour plots of temperature Θ, hardening strain-like variable α and damage D distributions at $\Delta u = 2 \times 0.25$ mm for damage-coupled 2D axisymmetric bar tension problem for 10×20 mesh and for $\kappa^{vp} = 0$ (left), $\kappa^{vp} = 500$ (center) and $\kappa^{vp} = 1000$ (right). (a) min/max (left) $\Theta = 301.3/347.2$, (center) $\Theta = 306.5/320.4$, (right) $309.7/317.0$, (b) min/max (left) $\alpha = 6.086 \times 10^{-2}/6.541 \times 10^{-2}$, (center) $\alpha = 9.697 \times 10^{-2}/2.157 \times 10^{-1}$, (right) $\alpha = 1.173 \times 10^{-2}/1.763 \times 10^{-1}$, (c) min/max (left) $D = 1.115 \times 10^{-2}/9.872 \times 10^{-1}$, (center) $D = 2.187 \times 10^{-2}/6.712 \times 10^{-2}$, (right) $D = 3.001 \times 10^{-2}/5.466 \times 10^{-2}$.

surrounding (infinite) medium. With self-heating by mechanical dissipation, an uneven temperature distribution, and, hence inhomogeneous stress distribution occurs over the specimen. Thus, necking develops.

Only one-eighth of the specimen is modeled using the symmetry in loading as well as geom-
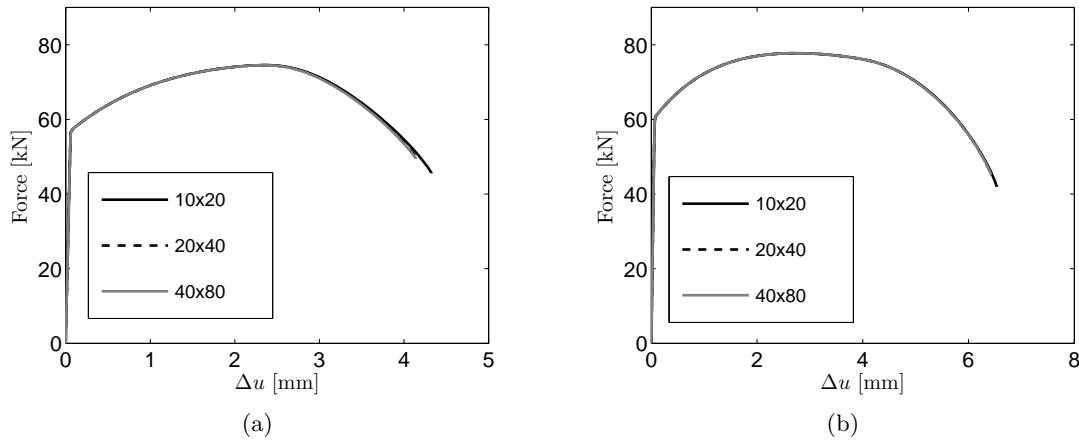
Figure 9.7.: Load-displacement curves for 10×20, 20×40 and 40×80 discreatizations. (a) Rate independent solution with $\kappa^{vp} = 0$. (b) Rate dependent solution with $\kappa^{vp} = 500$ MPa.
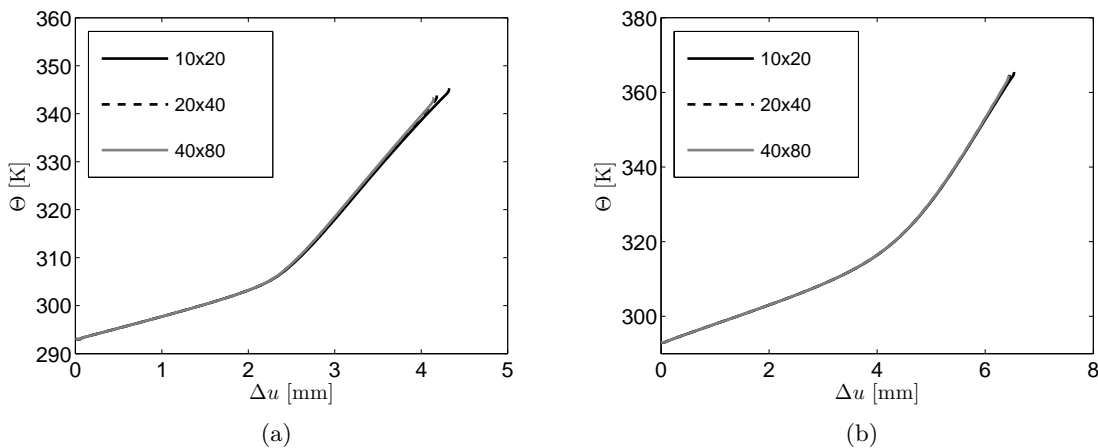
Figure 9.8.: Central temperature development with self-heating for 10×20, 20×40 and 40×80 discreatizations. (a) Rate independent solution with $\kappa^{vp} = 0$. (b) Rate dependent solution with $\kappa^{vp} = 500$ MPa.

etry. Discretization of the modeled part consists of 1280 8-node full integration temperature displacement elements of type C3D8T with trilinear displacement and temperature interpolations. Like before, the loading is applied under constant velocity with 1 mm/s. The analyses are conducted for damage coupled and uncoupled cases with viscosity parameter $\kappa^{\mathrm{vp}} = 100$ MPa. Except for this, the material parameters are the ones given in Table 9.1. For comparison reasons cases without heat convection, i.e., homogeneous solutions are also accounted for.

The load-displacement and the central temperature increment history plots are given in Figures 9.9.(a) and (b) respectively. It is seen that the models for which convective heat transfer from the surface is accounted for show a relatively rapid decrease in force response after the peak which signals the development of the neck. With damage coupling, a considerable softening is observable. Temperature development at central section of the specimen for the case with damage coupling and heat convection is given in Figure 9.9.(b). In agreement with the thermally triggered necking results given in [275], the maximal temperature difference in the

specimen rapidly increases with the development of the neck at which the deformation as well as self-heating with dissipative inelastic processes are localized. At the specimen ends, on the other hand, the temperature remains approximately constant also dictated by the surface heat convection.

Figure 9.10 depics the temperature development during loading whereas in Figures 9.11 and 9.12 corresponding damage and hardening strain-like variable evolutions are given. Unlike the homogeneous solution for which the specimen section remains rectangular along the specimen length, the deformed cross section in the necked zone exhibits double curvature: concave in direction of the width and convex in direction of the thickness in agreement with [275]. Thus, although in the homogeneous case the stress triaxiality ratio remains as $1/3$, as a result of the curvature development three-dimensional state of stress prevails at the central section. This in turn results in amplified damage accumulation and subsequent local failure, i.e., locally damage reaches 1. For the homogeneous solution, the damage magnitude at $\Delta u = 2 \times 5.96$ mm is only $D = 5.259 \times 10^{-2}$ which is far from critical. At the same deformation level the temperature and hardening development on the other hand are 317.9 K and $\alpha = 1.978 \times 10^{-1}$, respectively. Since heat convection through surface is not allowed, there occurs no temperature gradients and hence the homogeneous solution is equivalent to an adiabatic analysis.

Finally, Figures 9.13 show temperature and strain hardening variable contour plots, damage uncoupled case. In absence of damage, this localized deformation problem is transformed into a diffuse necking problem where the reduction of the central area is less than that of damage coupled analysis. Also the development of temperature as well as plastic flow is noticeably smaller than those occurring in a damage coupled analysis.
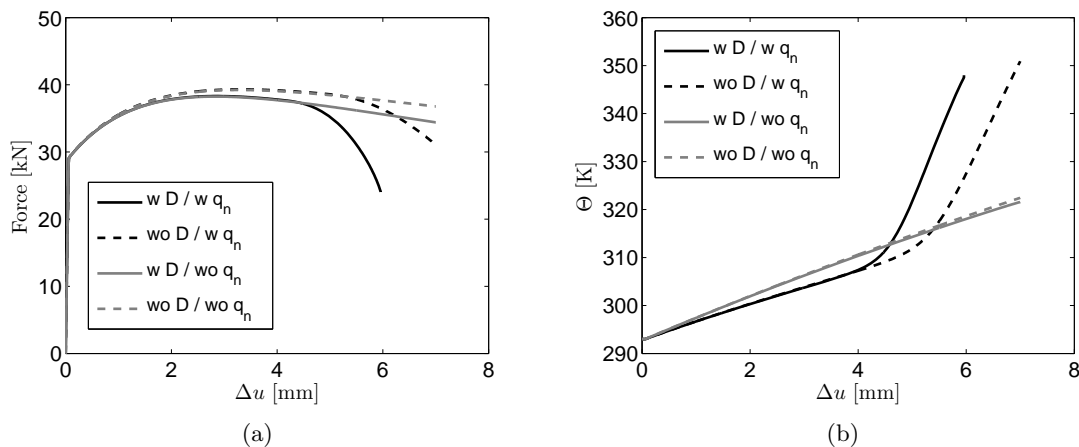
Figure 9.9.: (a) Load-displacement curves for rate dependent solutions with and without damage and heat convection at free surfaces. (b) Development of temperature at central node for for rate dependent solutions with and without damage and heat convection at free surfaces. In (a) and (b), the identifiers w D and wo D stand for with and without damage, respectively whereas the identifiers w q_n and wo q_n respectively denote with and without heat convection at free surface.
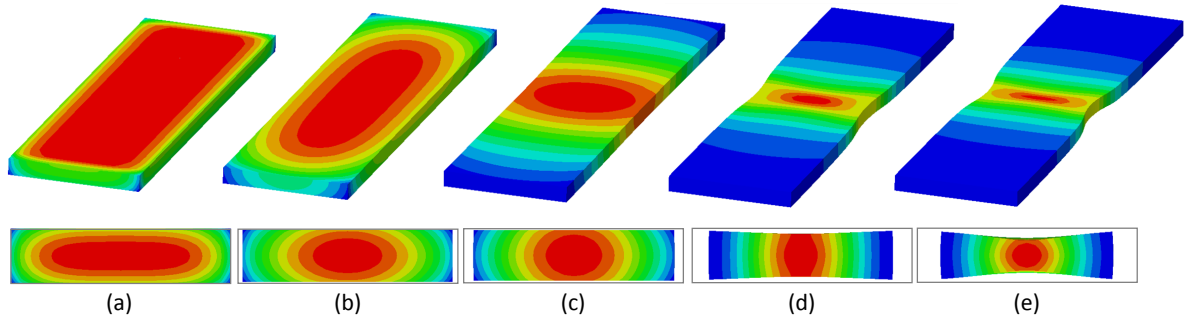
Figure 9.10.: Contour plots of temperature distribution at different displacements for damage-coupled 3D rectangular bar tension problem rate dependent solution. At top, distributions over the central plane along the plate plane are shown. At the bottom, central transverse section distributions are given. The outer frame denotes the undeformed shape to highlight the amount of deformation by necking. (a) $\Delta u = 2 \times 0.25$ mm, min/max $\Theta = 293.1/293.8$ K, (b) $\Delta u = 2 \times 2.75$ mm, min/max $\Theta = 301.4/302.9$ K, (c) $\Delta u = 2 \times 4.50$ mm, min/max $\Theta = 304.4/311.5$ K, (d) $\Delta u = 2 \times 5.45$ mm, min/max $\Theta = 303.6/334.8$ K, (e) $\Delta u = 2 \times 5.96$ mm, min/max $\Theta = 303.2/349.9$ K.
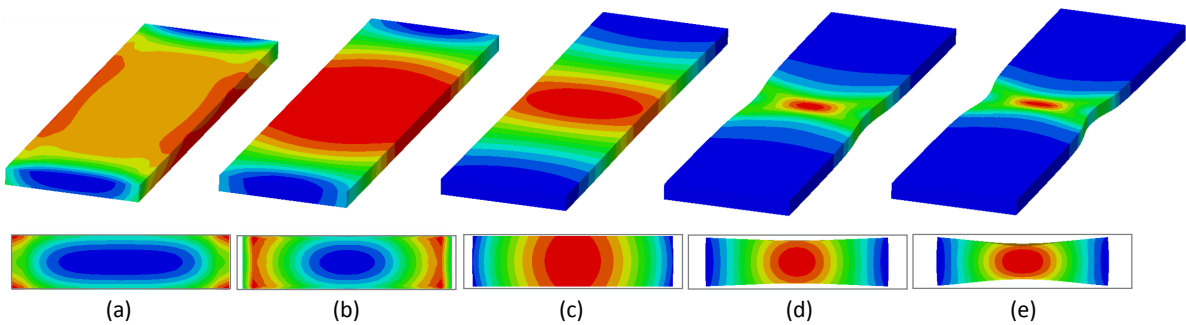
Figure 9.11.: Contour plots of hardening strain-like variable α distribution at different displacements for damage-coupled 3D rectangular bar tension problem rate dependent solution. At top, distributions over central plane along plate plane are shown. At the bottom, central transverse section distributions are given. The outer frame denotes the undeformed shape to highlight the amount of deformation by necking. (a) $\Delta u = 2 \times 0.25$ mm, min/max $\alpha = 7.199 \times 10^{-3}/7.210 \times 10^{-3}$, (b) $\Delta u = 2 \times 2.75$ mm, min/max $\alpha = 9.576 \times 10^{-2}/9.650 \times 10^{-2}$, (c) $\Delta u = 2 \times 4.50$ mm, min/max $\alpha = 1.330 \times 10^{-1}/1.789 \times 10^{-1}$, (d) $\Delta u = 2 \times 5.45$ mm, min/max $\alpha = 1.333 \times 10^{-1}/4.609 \times 10^{-1}$, (e) $\Delta u = 2 \times 5.96$ mm, min/max $\alpha = 1.333 \times 10^{-1}/7.378 \times 10^{-1}$.
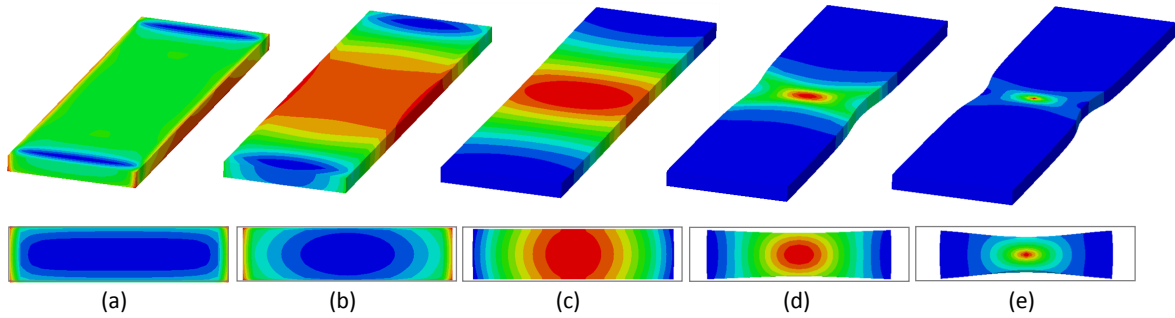
Figure 9.12.:   Contour plots of damage D distribution at different displacements for damage-coupled 3D rectangular bar tension problem rate dependent solution. At top, distributions over central plane along plate plane are shown. At the bottom, central transverse section distributions are given. The outer frame denotes the undeformed shape to highlight the amount of deformation by necking. (a) $\Delta u = 2 \times 0.25$ mm, min/max $D = 9.500 \times 10^{-4}/9.527 \times 10^{-4}$, (b) $\Delta u = 2 \times 2.75$ mm, min/max $D = 2.064 \times 10^{-2}/2.086 \times 10^{-2}$, (c) $\Delta u = 2 \times 4.50$ mm, min/max $D = 3.185 \times 10^{-2}/4.686 \times 10^{-2}$, (d) $\Delta u = 2 \times 5.45$ mm, min/max $D = 3.185 \times 10^{-2}/1.910 \times 10^{-1}$, (e) $\Delta u = 2 \times 5.96$ mm, min/max $D = 3.185 \times 10^{-2}/9.948 \times 10^{-1}$.
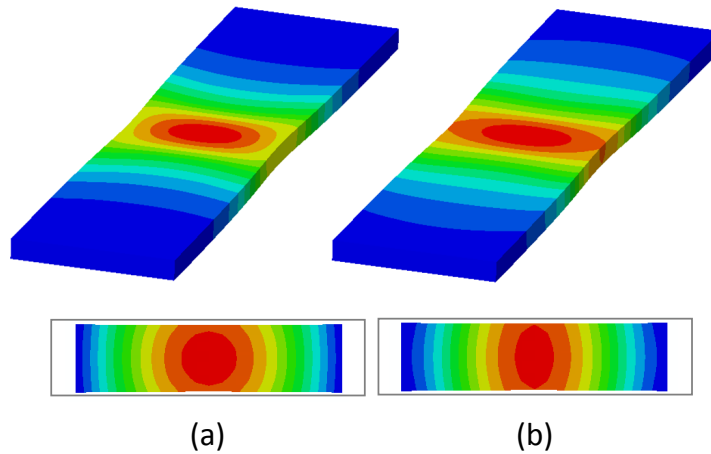
Figure 9.13.:   Contour plots of (a) hardening strain-like variable α and (b) temperature distribution at $\Delta u = 2 \times 5.96$ mm for 3D rectangular bar tension problem rate dependent solution without damage effects. As seen in absence of damage development, area reduction during neck development is considerably less. Hence, plastic flow and associated temperature development is smaller. At top, distributions over central plane along plate plane are shown. At the bottom, central transverse section distributions are given. The outer frame denotes the undeformed shape to highlight the amount of deformation by necking. (a) min/max $\alpha = 1.571 \times 10^{-1}/3.291 \times 10^{-1}$, (b) min/max $\Theta = 306.1/326.6$ K.

9.6. Closure

In this chapter, an extension of [275] and its follow up works [14], [15], to rate dependent damage-coupled thermomechanics is proposed. It is shown that, once the extensive property of the entropy is exploited, together with a temperature dependent damage dissipation potential, its decomposition into elastic, viscoplastic and damage parts is possible, with with corresponding structural changes. Besides it is shown that in addition to those mutual interactions of the mechanical and thermal fields presented in [275], there exist damage induced effects on thermal and other mechanical fields. The framework utilizes a principal axes formulation where the stresses are derived utilizing a hyperelastic potential quadratic elastic HENCKY strains. This supplies handiness in derivations and implementation of the framework. The resulting thermomechanical problem is solved for a staggered approach with the isothermal split. The derived forms are implemented as ABAQUS/UMAT and UMATH subroutines and utilized in a set of example problems involving geometrical imperfection triggered necking of an axisymmetric bar and thermally triggered necking of a 3D rectangular bar. The first problem reveals that, for a quasi-static analysis, doubly softening mechanism is prone to the problem of spurious mesh dependence due to the loss of ellipticity of the initial boundary value problem. Especially, in the absence of rate effects the mesh dependence is higher whereas inclusion of rate effects acts as a localization limiter. With the second problem, it is shown that triaxiality increase at the center by necking triggered by surface convection of heat accelerates damage rate considerably and consequently reduces global total strain to failure as compared to the homogeneous analysis without surface heat convection (hence without necking).

9.A. Auxiliary Derivations

Derivations for the Local Tangent. Using Equation (9.4.27) and assuming $Y^{\mathrm{d}} - Y_0^{\mathrm{d}} > 0$ the components for the local JACOBIAN for the simultaneous local integration scheme can be given as

$$\frac{\partial r_1}{\partial \Delta \gamma} = -\frac{2}{3} q^{\triangleleft}(\alpha, \Theta) + 2\mu \frac{1}{1-D} + m \, \kappa^{\mathrm{vp}} \left[\frac{t_\star}{\Delta t} \right]^m \Delta \gamma^{m-1}, \tag{9.A.1}$$

$$\frac{\partial r_1}{\partial D} = 2\mu \frac{\Delta \gamma}{[1-D]^2}, \tag{9.A.2}$$

$$\frac{\partial r_2}{\partial \Delta \gamma} = -\beta - \Delta \gamma \, s \, \beta \frac{1}{\langle Y^{\mathrm{d}} - Y_0^{\mathrm{d}} \rangle} \frac{\partial Y^{\mathrm{d}}}{\partial \Delta \gamma}, \tag{9.A.3}$$

$$\frac{\partial r_2}{\partial D} = 1 - \Delta \gamma \, \beta \left[\frac{r}{1-D} + \frac{s}{\langle Y^{\mathrm{d}} - Y_0^{\mathrm{d}} \rangle} \frac{\partial Y^{\mathrm{d}}}{\partial D} \right], \tag{9.A.4}$$

where $q^{\triangleleft} = \partial q(\alpha, \Theta) / \partial \alpha$ together with

$$\beta := \frac{1}{[1-D]^r} \left[\frac{\langle Y^{\mathrm{d}} - Y_0^{\mathrm{d}} \rangle}{a(\Theta)} \right]^s \quad \text{and} \quad \frac{\partial r_2}{\partial Y^{\mathrm{d}}} = -\Delta \gamma \, s \, \beta \frac{1}{\langle Y^{\mathrm{d}} - Y_0^{\mathrm{d}} \rangle}. \tag{9.A.5}$$

Derivations for the Mechanical Tangent Moduli. Using the viscoplastic/damage correction given in Equation (9.4.22), for a given principal stress component τ_A one has

$$\frac{\partial \tau_A}{\partial \epsilon_B^{\mathrm{e,\,tri}}} = [1-D] \frac{\partial \tilde{\tau}_A^{\mathrm{tri}}}{\partial \epsilon_B^{\mathrm{e,\,tri}}} - 2\mu \Delta \gamma \frac{\partial n_A}{\partial \epsilon_B^{\mathrm{e,\,tri}}}, \quad \frac{\partial \tau_A}{\partial \Delta \gamma} = -2\mu \, n_A \quad \text{and} \quad \frac{\partial \tau_A}{\partial D} = -\tilde{\tau}_A. \tag{9.A.6}$$

Using $\delta_{AB}^{\mathrm{dev}} = \delta_{AB} - 1/3$, with δ_{AB} representing the KRONECKER delta which is given as

$$\delta_{AB} := \begin{cases} 1 & \text{if } A = B \,, \\ 0 & \text{otherwise} \,. \end{cases} \tag{9.A.7}$$

Accordingly, using Equation (9.3.10) one can find

$$\frac{\partial \tilde{\tau}_A^{\mathrm{tri}}}{\partial \epsilon_B^{\mathrm{tri}}} = H + 2\mu \delta_{AB}^{\mathrm{dev}} \quad \text{and} \quad \frac{\partial n_A}{\partial \epsilon_B^{\mathrm{tri}}} = \frac{2\mu}{\|\tilde{\boldsymbol{s}}^{\mathrm{tri}}\|} \left[\delta_{AB}^{\mathrm{dev}} - n_A \, n_B \right] \,. \tag{9.A.8}$$

Derivations for the Thermal Tangent Modulus. In the view of Equation (9.4.24), for given inelastic dissipation Ω_{mech} using

$$\frac{\partial \Omega_{\mathrm{mech}}}{\partial Y^{\mathrm{d}}} = \frac{\Delta\gamma}{\Delta t} \beta \left[1 + s \frac{Y^{\mathrm{d}}}{\langle Y^{\mathrm{d}} - Y_0^{\mathrm{d}} \rangle} \right] \,, \tag{9.A.9}$$

and $q^{\triangleright} = \partial q(\alpha, \Theta)/\partial \Theta$ one has

$$\frac{\partial \Omega_{\mathrm{mech}}}{\partial \Theta} = \frac{\Delta\gamma}{\Delta t} \left[\sqrt{\frac{2}{3}} q^{\triangleright}(\alpha, \Theta) - s \, \beta \, g_{\omega^{\mathrm{d}}}'(\Theta) \, a_0 \frac{Y^{\mathrm{d}}}{a(\Theta)} \right] + \frac{\partial \Omega_{\mathrm{mech}}}{\partial Y^{\mathrm{d}}} \frac{\partial Y^{\mathrm{d}}}{\partial \Theta} \,, \tag{9.A.10}$$

$$\frac{\partial \Omega_{\mathrm{mech}}}{\partial \Delta\gamma} = \frac{\Omega_{\mathrm{mech}}}{\Delta\gamma} + \frac{\Delta\gamma}{\Delta t} \left[\frac{2}{3} q^{\triangleleft}(\alpha, \Theta) - \frac{2\mu}{1 - D} \right] + \frac{\partial \Omega_{\mathrm{mech}}}{\partial Y^{\mathrm{d}}} \frac{\partial Y^{\mathrm{d}}}{\partial \Delta\gamma} \,, \tag{9.A.11}$$

$$\frac{\partial \Omega_{\mathrm{mech}}}{\partial D} = -\frac{\Delta\gamma^2}{\Delta t} \frac{2\mu}{[1 - D]^2} + r \, \beta \frac{\Delta\gamma}{\Delta t} \frac{Y^{\mathrm{d}}}{1 - D} + \frac{\partial \Omega_{\mathrm{mech}}}{\partial Y^{\mathrm{d}}} \frac{\partial Y^{\mathrm{d}}}{\partial D} \,. \tag{9.A.12}$$

For the local tangent, additional derivations include the following

$$\frac{\partial r_1}{\partial \Theta} = \sqrt{\frac{2}{3}} g_{\omega^{\mathrm{vp}}}'(\Theta) \left[\tau_{y0,0} - q(\alpha, \Theta_0) \right] \,, \tag{9.A.13}$$

$$\frac{\partial r_2}{\partial \Theta} = \Delta\gamma \, s \, \beta \left[g_{\omega^{\mathrm{d}}}'(\Theta) \frac{a_0}{a(\Theta)} - \frac{1}{\langle Y^{\mathrm{d}} - Y_0^{\mathrm{d}} \rangle} \frac{\partial Y^{\mathrm{d}}}{\partial \Theta} \right] \,. \tag{9.A.14}$$

Using Equation (9.3.12) one reaches

$$\frac{\partial Y^{\mathrm{d}}}{\partial \Theta} = \frac{\partial \tilde{\Psi}^{\Theta\mathrm{e}}(J^{\mathrm{e}}, \Theta)}{\partial \Theta} = -3 \, H \, \alpha_\Theta \log(J^{\mathrm{e}}) \,. \tag{9.A.15}$$

Using $\partial(\bullet)/\partial\epsilon_B \equiv \partial(\bullet)/\partial\epsilon_B^{\mathrm{e, tri}}$ one reaches

$$\frac{\partial r_1}{\partial \epsilon_B} = -2\mu \, n_B \quad \text{and} \quad \frac{\partial r_2}{\partial \epsilon_B} = -\Delta\gamma \, s \, \beta \frac{1}{Y^{\mathrm{d}}} \frac{\partial Y^{\mathrm{d}}}{\partial \epsilon_B^{\mathrm{e, tri}}} \tag{9.A.16}$$

where Equation (9.A.16.1) is computed using $\|\tilde{s}\| := \left[\tilde{s}_1^2 + \tilde{s}_2^2 + \tilde{s}_3^2 \right]^{1/2}$ and

$$\frac{\partial \|\tilde{s}^{\mathrm{tri}}\|}{\partial \epsilon_B^{\mathrm{e, tri}}} = 2\mu \, n_B \,. \tag{9.A.17}$$

Derivations for the Plastic Dissipation. Using the proposed VON MISES yield potential and degree one homogeneity property of the yield potential, one may derive the following equivalence for the plastic part of the dissipation expression

$$
\begin{aligned}
\Omega_{\text{mech}}^{\text{vp}} &= \boldsymbol{\tau} : \left[-\frac{1}{2} \mathcal{L}_v \boldsymbol{b}^{\text{e}} \cdot [\boldsymbol{b}^{\text{e}}]^{-1} \right] + q\,\dot{\alpha} \\
&= [1-D]\,[\tilde{\boldsymbol{s}} + \tilde{p}\mathbf{1}] : \left[\frac{\dot{\gamma}}{1-D} \frac{\tilde{\boldsymbol{s}}}{\|\tilde{\boldsymbol{s}}\|} \right] + q(\alpha, \Theta) \left[\sqrt{\frac{2}{3}}\dot{\gamma} \right] \qquad (9.\text{A}.18) \\
&= \dot{\gamma} \left[\|\tilde{\boldsymbol{s}}\| + \sqrt{\frac{2}{3}} q(\alpha, \Theta) \right]
\end{aligned}
$$

with $\tilde{\boldsymbol{\tau}} = \boldsymbol{\tau}/[1-D]$, $\tilde{\boldsymbol{\tau}} = \tilde{p}\mathbf{1} + \tilde{\boldsymbol{s}}$ and $\tilde{p}\mathbf{1} : \tilde{\boldsymbol{s}} = 0$, and consequently $[\boldsymbol{\tau}/[1-D]] : \tilde{\boldsymbol{s}} = \tilde{\boldsymbol{s}} : \tilde{\boldsymbol{s}} = \|\tilde{\boldsymbol{s}}\|^2$.

Derivations for the Damage Conjugate Variable. Derivation of any of

$$
\frac{\partial Y^{\text{d}}}{\partial \epsilon_B^{\text{e, tri}}}, \quad \frac{\partial Y^{\text{d}}}{\partial \Delta\gamma} \quad \text{and} \quad \frac{\partial Y^{\text{d}}}{\partial D} \qquad (9.\text{A}.19)
$$

exploits the chain rule as follows

$$
\frac{\partial Y^{\text{d}}}{\partial [\bullet]} = \frac{\partial Y^{\text{d}}}{\partial J^{\text{e}}} \frac{\partial J^{\text{e}}}{\partial [\bullet]} + \sum_{A=1}^{3} \frac{\partial Y^{\text{d}}}{\partial \bar{\epsilon}_A^{\text{e}}} \frac{\partial \bar{\epsilon}_A^{\text{e}}}{\partial [\bullet]}, \qquad (9.\text{A}.20)
$$

where $[\bullet]$ represents one of $\epsilon_{n+1,B}^{\text{tri}}$, $\Delta\gamma$ or D. The following relations hold

$$
\frac{\partial Y^{\text{d}}}{\partial J^{\text{e}}} = H \frac{\log(J^{\text{e}})}{J^{\text{e}}} - 3\,H\,\alpha_\Theta\,[\Theta - \Theta_0]\,\frac{1}{J^{\text{e}}} \quad \text{and} \quad \frac{\partial Y^{\text{d}}}{\partial \bar{\epsilon}_A^{\text{e}}} = 2\mu\,\bar{\epsilon}_A^{\text{e}} \qquad (9.\text{A}.21)
$$

together with

$$
\frac{\partial J^{\text{e}}}{\partial \epsilon_B^{\text{e, tri}}} = J^{\text{e}}, \quad \frac{\partial J^{\text{e}}}{\partial \Delta\gamma} = 0 \quad \text{and} \quad \frac{\partial J^{\text{e}}}{\partial D} = 0\,. \qquad (9.\text{A}.22)
$$

Computing the deviator of both sides of Equation (9.4.20) and using the plastic incompressibility one has

$$
\bar{\epsilon}_A^{\text{e}} = \bar{\epsilon}_A^{\text{e, tri}} - \frac{\Delta\gamma}{1-D}\,n_A\,, \qquad (9.\text{A}.23)
$$

with which one may derive

$$
\frac{\partial \bar{\epsilon}_A^{\text{e}}}{\partial \epsilon_B^{\text{e, tri}}} = \frac{\partial \bar{\epsilon}_A^{\text{e, tri}}}{\partial \epsilon_B^{\text{e, tri}}} - \frac{\Delta\gamma}{1-D} \frac{\partial n_A}{\partial \epsilon_B^{\text{e, tri}}}\,, \qquad (9.\text{A}.24)
$$

with

$$
\frac{\partial \bar{\epsilon}_A^{\text{e, tri}}}{\partial \epsilon_B^{\text{e, tri}}} = \delta_{AB}^{\text{dev}}\,. \qquad (9.\text{A}.25)
$$

Finally, the following identities prove useful

$$
\frac{\partial \bar{\epsilon}_A^{\text{e}}}{\partial D} = -\frac{\Delta\gamma}{[1-D]^2}\,n_A \quad \text{and} \quad \frac{\partial \bar{\epsilon}_A^{\text{e}}}{\partial \Delta\gamma} = -\frac{1}{1-D}\,n_A\,. \qquad (9.\text{A}.26)
$$

10. A Thermomechanically Consistent Constitutive Theory for Modeling Micro-Void and/or Micro-Crack Driven Failure in Metals at Finite Strains

In this chapter, within a continuum approximation, a thermomechanical finite strain plasticity model which incorporates the blended effects of micro-heterogeneities in the form of micro-cracks and micro-voids is presented. The former accounts for cleavage-type of damage without any volume change whereas the latter is a consequence of plastic void growth. Limiting the context to isotropy, for cleavage damage a scalar damage variable $d \in [0,1]$ is incorporated. Its conjugate variable, the elastic energy release rate, and evolution law follow the formal steps of thermodynamics of internal variables requiring postulation of an appropriate damage dissipation potential. The growth of void volume fraction f is incorporated using a Gurson-type porous plastic potential postulated at the effective stress space following continuum damage mechanics principles. Since the growth of microvoids is driven by dislocation motion around voids the dissipative effects corresponding to the void growth are encapsulated in the plastic flow. Thus, the void volume fraction is used as a dependent variable using the conservation of mass. The predictive capability of the model is tested through uniaxial tensile tests at various temperatures $\Theta \in [-125°\text{C},125°\text{C}]$. It is shown, via fracture energy plots, that temperature driven ductile-brittle transition in fracture mode is well captured. With an observed ductile-brittle transition temperature around $-50°\text{C}$, at lower temperatures fracture is brittle dominated by d whereas at higher temperatures it is ductile dominated by f.

10.1. Introduction

Mechanistically, ductile fracture is explained by nucleation, growth and coalescence of microvoids. Brittle fracture, on the other hand, stems from the inter- or intra-granular cleavage with microcrack nucleation, growth and coalescence [11]. Both ductile and brittle fracture is observed in bcc metals. The transition from one mode to the other is mainly controlled by temperature[1]: At lower temperatures fracture is brittle whereas at higher temperatures it is ductile.

One of the most widely used modeling approach for plasticity with microvoid growth is that of Gurson, [110]. Derived using homogenization over void-rigid plastic matrix aggregates and limit analysis, the yield potential of Gurson's plasticity has hydrostatic stress dependence. A natural outcome of this formulation is irreversible volume change, i.e., plastic dilatation. This model is modified by Tvergaard and Needleman, by the introduction of void shape effects as well

---

[1]Stress triaxiality ratio and loading rate may also affect fracture mode.

as acceleration in the void growth during void coalescence, to be named as Gurson-Tvergaard-Needleman porous plasticity model [308] and by Chu and Needleman to account for void nucleation effects [75] along with other contributors, e.g., [304, 306, 305, 229, 224, 225].

There are various modeling approaches for cleavage in metallic materials. The deterministic model by Ritchie-Knott-Rice, [260], relies on a temperature and rate independent critical stress over the cleavage grain. Once the principal stresses averaged out over one or two grain-size region exceeds this threshold, the brittle fracture emanates. This threshold does not necessitate the presence of plastic flow. Incorporation of plastic flow is realized in Beremin's statistical model which, being based on the Weibull weakest link theory, reflects random nature of brittle fracture, see, e.g., [52, 223]. Another simple yet powerful approach to brittle fracture is the so-called energy limiters [318, 319, 320]. By enforcing saturation in the strain energy function, energy limiters automatically bound stresses in the constitutive equations. Although useful, none of these models postulate an internal damage variable to account for gradual material deterioration by microcrack nucleation. Thus, dissipation associated with brittle fracture is not incorporated. Continuum damage mechanics remedies this gap by introducing scalar or tensorial damage variables and their conjugate variables which allows not only modeling of stiffness and strength degradation but also determination of inelastic dissipation, [175, 178]. For the recent developments in brittle fracture modeling, the reader is refered to [217, 13, 216] and [88].

The present work introduces a thermodynamically consistent continuum approximation of micro-void and/or micro-crack driven failure at finite strains. To this end, in the spirit of Chaboche and coworkers [71] Gurson's porous plasticity model is blended with Lemaitre's continuum damage mechanics. The blended constitutive model has two damage variables: the void volume fraction f and the brittle damage variable d. Material fails by evolution of both damage sources. Since the growth of microvoids is driven by dislocation motion around voids, dissipative effects corresponding to the void growth are encapsulated in the plastic flow. Thus, the void volume fraction is a dependent variable using conservation of mass. For cleavage damage, a scalar variable is incorporated whose conjugate variable, the elastic energy release rate, and evolution law follow the formal steps of thermodynamics of internal variables requiring postulation of an appropriate damage dissipation potential. Hence, the brittle damage process is realistically reflected on a thermomechanically consistent ground. By these properties, the proposed model forms an appropriate basis for modeling fracture with ductile-brittle transitions driven by temperature or triaxiality.

Among various modeling attempts to the ductile-brittle transition problem in the literature, see, e.g., [337, 230, 271, 42, 134], the most common one is based on a collective use of Gurson-type porous plasticity along with either Ritchie-Knott-Rice or Beremin model, see, e.g., [230, 134, 281]. However, these approaches suffer from the mentioned inherent weaknesses pertaining to brittle fracture models. The noteworthy features of this work can be summarized as follows:

- Since the main motivation stems from modeling temperature driven ductile-brittle transition of fracture, unlike [71], thermal coupling is considered.

- Unlike [71], finite strains are accounted for making use of a hyperelastic-plastic-type formulation relying on multiplicative decomposition of deformation gradient into recoverable and irrecoverable parts following [114].

- Although in the current study the focus is set on thermoelastic, plastic and damage isotropy, incorporation of brittle anisotropic damage is possible within the presented for-

malism.

- Using the kinematic coupling between plasticity and continuum damage, brittle damage evolution necessitates plastic flow which is consistent for metallic materials.

- Unlike cited ductile-brittle transition modeling approaches, current modeling approach accounts for gradual strength and stiffness loss as well as energy dissipation associated with brittle damage.

- The model framework can also be exploited for fracture development under low triaxiality regimes for which Gurson model is known to be ineffective.

10.2. Fundamental Kinematics

Let $\mathcal{B} \in \mathbb{R}^3$ be the material (initial), $\overline{\mathcal{B}} \in \mathbb{R}^3$ the intermediate and $\mathcal{B}_t \in \mathbb{R}^3$ the spatial (current) configurations of a body. The motion of the body is described by a one-to-one mapping $\boldsymbol{\varphi}$: $\mathcal{B} \to \mathcal{B}_t \subset \mathbb{R}^3$. The deformation gradient $\boldsymbol{F} := \partial_{\boldsymbol{X}} \varphi$, is defined as the linear mapping of referential material tangents on their spatial counterparts, in which $\boldsymbol{X}$ defines the material coordinates in the reference configuration. The Jacobian of the deformation gradient is defined as $J = \det(\boldsymbol{F}) = \rho_0/\rho$, where ρ_0 and ρ are densities at initial and spatial configurations, respectively. Multiplicative decomposition of the deformation gradient in recoverable $\boldsymbol{F}^{\mathrm{r}}$ and irrecoverable $\boldsymbol{F}^{\mathrm{p}}$ parts is postulated such that

$$\boldsymbol{F} := \boldsymbol{F}^{\mathrm{r}} \cdot \boldsymbol{F}^p, \tag{10.2.1}$$

with $J^{\mathrm{r}} := \det(\boldsymbol{F}^{\mathrm{r}})$ and $J^{\mathrm{p}} := \det(\boldsymbol{F}^p)$. The recoverable part is associated with distortion of the crystal and the plastic part of the deformation gradient $\boldsymbol{F}^p$ encapsulates the dislocation movements through its isochoric part [Håkansson *et al.*, 2006]. $\boldsymbol{F}^{\mathrm{r}}$ is further partitioned into elastic and thermal parts using $\boldsymbol{F}^{\mathrm{r}} := \boldsymbol{F}^e \cdot \boldsymbol{F}^\theta$. With this decomposition an additional imagined configuration $\widehat{\mathcal{B}}$ is introduced, which corresponds to a stress-free thermoplastic deformation where thermal expansion (or contraction) is driven by temperature change $\Delta\Theta = \Theta - \Theta_0$, where Θ and Θ_0 represent the current and the initial temperature, respectively. The spatial velocity gradient is given by $\boldsymbol{l} := \dot{\boldsymbol{F}} \cdot \boldsymbol{F}^{-1}$ which is additively decomposed into the rate of deformation tensor $\boldsymbol{d} = \mathrm{sym}(\boldsymbol{l})$ and the rate of spin tensor $\boldsymbol{w} = \mathrm{skw}(\boldsymbol{l})$ via $\boldsymbol{l} = \boldsymbol{d} + \boldsymbol{w}$, respectively. The recoverable and irrecoverable right Cauchy-Green deformation tensors are defined as $\boldsymbol{C}^r = [\boldsymbol{F}^{\mathrm{r}}]^\top \cdot \boldsymbol{F}^{\mathrm{r}}$ and $\boldsymbol{C}^p = [\boldsymbol{F}^{\mathrm{p}}]^\top \cdot \boldsymbol{F}^{\mathrm{p}}$, respectively. Similar partition, which proves convenient in the following developments, applies for $\boldsymbol{l}$ as well via $\boldsymbol{l} = \boldsymbol{l}^{\mathrm{r}} + \boldsymbol{l}^{\mathrm{p}}$ where $\boldsymbol{l}^{\mathrm{r}} := \dot{\boldsymbol{F}}^{\mathrm{r}} \cdot [\boldsymbol{F}^{\mathrm{r}}]^{-1}$ and $\boldsymbol{l}^{\mathrm{p}} = \boldsymbol{F}^r \cdot \boldsymbol{L}^{\mathrm{p}} \cdot [\boldsymbol{F}^{\mathrm{r}}]^{-1}$ with $\boldsymbol{L}^{\mathrm{p}} := \dot{\boldsymbol{F}}^{\mathrm{p}} \cdot [\boldsymbol{F}^{\mathrm{p}}]^{-1}$. Letting recoverable logarithmic strain tensor defined by $\boldsymbol{e}^{\mathrm{r}}_{\log} := \ln(\sqrt{\boldsymbol{C}^{\mathrm{r}}})$, its partition into volumetric and isochoric parts reads $\boldsymbol{e}^{\mathrm{r}}_{\log,\mathrm{vol}} := 1/3 \ln J^{\mathrm{r}} \boldsymbol{1} = 1/3 \, \mathrm{tr}(\boldsymbol{e}^{\mathrm{r}}_{\log}) \boldsymbol{1}$ and $\boldsymbol{e}^{\mathrm{r}}_{\log,\mathrm{iso}} := \ln(\sqrt{J^{\mathrm{r}-2/3}\boldsymbol{C}^r}) = \mathrm{dev}\,\boldsymbol{e}^{\mathrm{r}}_{\log}$, respectively. Configurations and fundamental mappings are given in Figure 10.1.

The assumption of a representative volume element with uniformly distributed spherical voids with a total volume of $\mathrm{d}V^{\mathrm{v}}$ and plastically incompressible matrix with a total volume of $\mathrm{d}V^{\mathrm{m}}$ with $\mathrm{d}V^{\mathrm{v}} + \mathrm{d}V^{\mathrm{m}} = \mathrm{d}V$, lets one define the void volume fraction $f = \mathrm{d}V^{\mathrm{v}}/\mathrm{d}V$. Now, taking $J^{\mathrm{v}} = \mathrm{d}V/\mathrm{d}V^{\mathrm{m}}$ and letting the initial volume of the matrix be $\mathrm{d}V^{\mathrm{m}0}$ one defines $J^{\mathrm{v}0} = \mathrm{d}V^0/\mathrm{d}V^{\mathrm{m}0}$. Since the matrix material is allowed to experience only thermoelastic dilatations one sets $J^{\mathrm{r}} = \mathrm{d}V^{\mathrm{m}}/\mathrm{d}V^{\mathrm{m}0}$. Thus, with $J = J^{\mathrm{r}}J^{\mathrm{p}} = \mathrm{d}V/\mathrm{d}V^0$ one has $J^{\mathrm{p}} = J^{\mathrm{v}}/J^{\mathrm{v}0}$. Taking

logarithms and the material time derivatives of both sides one reaches $\overline{\ln(J^{\mathrm{p}})} = \overline{\ln(J^{\mathrm{v}})}$. Using $\overline{\ln(J^{\mathrm{p}})} = \mathrm{tr}(\boldsymbol{L}^{\mathrm{p}})$ one concludes that

$$\dot{f} = [1 - f]\,\mathrm{tr}(\boldsymbol{L}^{\mathrm{p}})\,. \tag{10.2.2}$$

Hence, being dependent on $\mathrm{tr}(\boldsymbol{L}^{\mathrm{p}})$, f is part of the problem kinematics; in other words, the void growth is linked to the dislocation motion around the void. In this sense, it is not an independent state variable. On the other hand, the rather brittle micro-crack and micro-cleavage mechanisms are not fully accounted for by dislocation glide. Hence, in the current thermodynamic formalism, their treatment requires the introduction of a new state variable whose evolution necessitates postulation of an independent dissipation potential. To this end, continuum damage $d \in [0, 1]$ phenomenologically reflects the softening response associated with accumulated micro-cracks. The interpretation of the envisioned framework is given on the right-hand side of Figure 10.1. Without loss of generality, independent of the scale hierarchy depicted the void free matrix is plastically incompressible - hence, above definitions are valid.
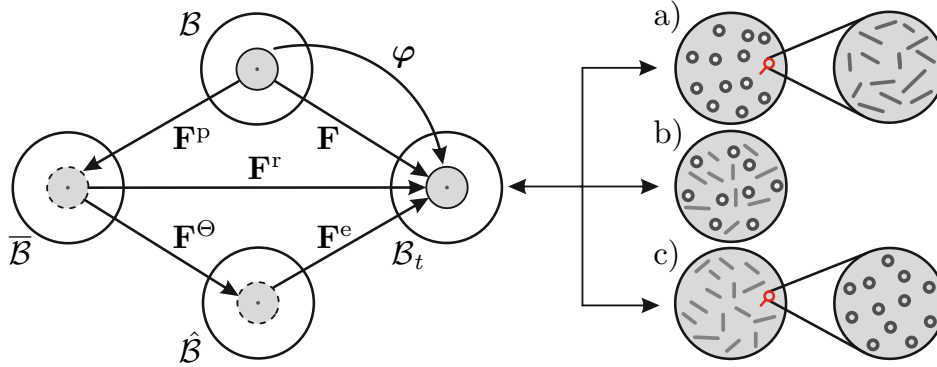
Figure 10.1.: On the left-hand side, the local multiplicative decomposition of the deformation gradient $\boldsymbol{F}$ into recoverable $\boldsymbol{F}^r := \boldsymbol{F}^e \cdot \boldsymbol{F}^\Theta$ and irrecoverable $\boldsymbol{F}^p$ parts and corresponding configurations are given. One the right-hand side, possible interpretations of the current framework are listed. (a) voids at upper scale and cracks at lower scale, (b) voids and cracks at identical scale, (c) cracks at upper scale and voids at lower scale.

10.3.   Thermodynamical Formulation

10.3.1.   General Theory

Let ψ denote the Helmholtz free energy per unit reference mass. Then, the first law of thermo-dynamics is expressed in reference configuration as

$$\rho_0 \Theta \dot{\eta} = \boldsymbol{\tau} : \boldsymbol{d} - \rho_0 \dot{\Theta} \eta - \rho_0 \dot{\psi} - J \mathrm{div}\,\boldsymbol{q} + \rho_0 r\,, \tag{10.3.1}$$

where $\boldsymbol{\tau}$ is the Kirchhoff stress tensor, Θ is the absolute temperature, η is the entropy per unit mass, $\boldsymbol{q}$ is the spatial heat flux and r is the body heat source per unit mass. With an abuse of notation, let $\psi = \psi(\boldsymbol{\mathcal{I}})$, with $\boldsymbol{\mathcal{I}}$ being the set of internal variables, the second law of thermodynamics supplies the following dissipation inequality represented in the reference configuration (see also [Bargmann and Ekh, 2013])

$$\mathcal{D}_{\mathrm{loc}} = \boldsymbol{\tau} : \boldsymbol{d} - \rho_0 \partial_{\boldsymbol{\mathcal{I}}} \psi \cdot \dot{\boldsymbol{\mathcal{I}}} - \frac{J}{\Theta} \boldsymbol{q} \cdot \mathbf{grad}\,\Theta \geq 0\,. \tag{10.3.2}$$

An additive decomposition into thermomechanical and conductive parts is further assumed $\mathcal{D}_{\text{loc}} = \mathcal{D}_{\text{loc}}^{\text{thermech}} + \mathcal{D}_{\text{loc}}^{\text{con}}$ with

$$
\begin{aligned}
\mathcal{D}_{\text{loc}}^{\text{thermech}} &:= \boldsymbol{\tau} : \boldsymbol{d} - \rho_0 \partial_{\boldsymbol{\mathcal{I}}} \psi \cdot \dot{\boldsymbol{\mathcal{I}}} \geq 0 \,, \\
\mathcal{D}_{\text{loc}}^{\text{cond}} &:= -\frac{J}{\Theta} \boldsymbol{q} \cdot \mathbf{grad} \, \Theta \geq 0 \,.
\end{aligned}
\tag{10.3.3}
$$

The latter inequality is satisfied by a generalized Fourier law adapted for the heat flux even in the presence of damage. The fulfillment of the former requires selection of the set $\boldsymbol{\mathcal{I}}$ and its appropriate evolution laws. With $\boldsymbol{\mathcal{I}} = \{\boldsymbol{C}^r, d, \alpha, \Theta\}$, where d is the scalar isotropic damage variable and α is the plastic hardening variable, Equation (10.3.3.1) reads

$$
\begin{aligned}
\mathcal{D}_{\text{loc}}^{\text{thermech}} = &\left[\boldsymbol{\tau} - 2\rho_0 [\boldsymbol{F}^{\text{r}}]^{\top} \cdot \partial_{\boldsymbol{C}^r} \psi \cdot \boldsymbol{F}^r \right] : \boldsymbol{d}^{\text{r}} \\
&+ \boldsymbol{\tau} : \boldsymbol{F}^r \cdot \boldsymbol{L}^{\text{p}} \cdot [\boldsymbol{F}^{\text{r}}]^{-1} - [\eta + \rho_0 \partial_{\Theta} \psi] \dot{\Theta} \\
&- \rho_0 \partial_d \psi \dot{d} - \rho_0 \partial_\alpha \psi \dot{\alpha} \geq 0 \,,
\end{aligned}
\tag{10.3.4}
$$

with $\dot{\boldsymbol{C}}^r = 2[\boldsymbol{F}^{\text{r}}]^{\top} \cdot \boldsymbol{d}^{\text{r}} \cdot \boldsymbol{F}^r$ and $\boldsymbol{\tau} : \boldsymbol{w} = 0$ since $\boldsymbol{w} = -\boldsymbol{w}^{\top}$. The following state laws are derived in order for inequality (10.3.4) to be valid for arbitrary $\boldsymbol{d}^{\text{r}}$ and $\dot{\Theta}$

$$
\begin{aligned}
\boldsymbol{\tau} &:= 2\rho_0 [\boldsymbol{F}^{\text{r}}]^{\top} \cdot \partial_{\boldsymbol{C}^r} \psi \cdot \boldsymbol{F}^r \,, \quad \beta := \rho_0 \partial_\alpha \psi \,, \\
Y &:= -\rho_0 \partial_d \psi \,, \quad \eta := -\rho_0 \partial_\Theta \psi \,,
\end{aligned}
\tag{10.3.5}
$$

where Y and β refer to the effective elastic energy release rate and the conjugate internal force variable of the plastic isotropic hardening. Substituting these back into the right-hand side of the inequality (10.3.4), one has the following reduced purely mechanical form

$$
\mathcal{D}_{\text{loc}}^{\text{red}} = \boldsymbol{\tau} : \boldsymbol{F}^r \cdot \boldsymbol{L}^{\text{p}} \cdot \boldsymbol{F}^{r-1} + Y\dot{d} - \beta\dot{\alpha} \geq 0 \,.
\tag{10.3.6}
$$

Let $\boldsymbol{\Sigma} := [\boldsymbol{F}^{\text{r}}]^{\top} \cdot \boldsymbol{\tau} \cdot [\boldsymbol{F}^r]^{-\top}$ denote the Mandel stress tensor. With reference to the intermediate configuration one has $\boldsymbol{\tau} : \boldsymbol{F}^r \cdot \boldsymbol{L}^{\text{p}} \cdot [\boldsymbol{F}^{\text{r}}]^{-1} = \boldsymbol{\Sigma} : \boldsymbol{L}^{\text{p}}$ and Equation (10.3.6) can be rearranged to give

$$
\mathcal{D}_{\text{loc}}^{\text{red}} = \boldsymbol{\Sigma} : \boldsymbol{L}^{\text{p}} - \beta\dot{\alpha} + Y\dot{d} \geq 0 \,.
\tag{10.3.7}
$$

This clearly depicts the work-conjugacy of the plastic part of the velocity gradient $\boldsymbol{L}^{\text{p}}$ defined at intermediate configuration and the Mandel stress tensor $\boldsymbol{\Sigma}$. With the assumption of elastic isotropy, one has $[\boldsymbol{F}^{\text{r}}]^{\top} \cdot \boldsymbol{\tau} \cdot [\boldsymbol{F}^r]^{-\top} = [\boldsymbol{R}^{\text{r}}]^{\top} \cdot \boldsymbol{\tau} \cdot \boldsymbol{R}^{\text{r}}$ where $\boldsymbol{R}^{\text{r}}$ is the elastic rotation found using the polar decomposition of the recoverable deformation gradient $\boldsymbol{F}^r = \boldsymbol{R}^{\text{r}} \cdot \boldsymbol{U}^{\text{r}}$ with $\boldsymbol{U}^{\text{r}} = \sqrt{\boldsymbol{C}^{\text{r}}}$ representing the recoverable stretch tensor. Hence, in the subsequent developments the use $\boldsymbol{\Sigma} = [\boldsymbol{R}^{\text{r}}]^{\top} \cdot \boldsymbol{\tau} \cdot \boldsymbol{R}^{\text{r}}$ is made. That is, $\boldsymbol{\Sigma}$ amounts to the rotated Kirchhoff stress tensor. Hence, both $\boldsymbol{\Sigma}$ and $\boldsymbol{\tau}$ share identical invariants which gains importance while postulating the plastic potential.

Finally, introducing the dissipation potential Υ as

$$
\Upsilon(\boldsymbol{\Sigma}, \beta, Y, d, f) := \phi^p(\boldsymbol{\Sigma}, \beta; d, f) + \phi^d(Y; d) \,,
\tag{10.3.8}
$$

and applying the generalized normality rule one derives the following evolution equations which satisfy the positiveness of the dissipation along with loading/unloading conditions $\lambda \geq 0$, $\phi^p \leq 0$, $\lambda \phi^p = 0$

$$
\boldsymbol{L}^{\text{p}} = \lambda \partial_{\boldsymbol{\Sigma}} \Upsilon = \lambda \partial_{\boldsymbol{\Sigma}} \phi^p \,, \quad \dot{\alpha} = -\lambda \partial_\beta \Upsilon = -\lambda \partial_\beta \phi^p \,, \quad \dot{d} = \lambda \partial_Y \Upsilon = \lambda \partial_Y \phi^d \,,
\tag{10.3.9}
$$

where λ is the plastic multiplier. This way, through a kinematic coupling, evolution of brittle damage is linked to plastic flow. This condition expresses the fact that brittle failure can only occur when plastic deformation occurs which is an appropriate assumption for cleavage in metallic materials, [Beremin, 1983]. On the contrary, Ritchie-Knott-Rice criterion for brittle fracture, for instance, does not require plastic flow [Ritchie *et al.*, 1973].

10.3.2.   Specification of the Constitutive Forms

The choice of the form of the Helmholtz free energy function ψ constitutes the basis in deriving the constitutive equations for the representative volume element. In the current treatment, an additively decomposed Helmholtz free energy into elastic, plastic and thermal parts is selected via $\psi = \psi^{\mathrm{e}} + \psi^{\mathrm{p}} + \psi^{\Theta}$. For the elastic part one can further apply a volumetric deviatoric split using $\psi^{\mathrm{e}} = \psi^{\mathrm{e}}_{\mathrm{vol}} + \psi^{\mathrm{e}}_{\mathrm{iso}}$ and, following a Lemaitre-type formalism, state coupling is applied only in between micro-crack damage and thermoelasticity using

$$
\begin{aligned}
\rho_0 \, \psi^{\mathrm{e}}_{\mathrm{vol}} &= [1-d]\kappa \left[\frac{1}{2}[\mathrm{tr}(\boldsymbol{e}^{\mathrm{r}}_{\mathrm{log}})]^2 - 3\alpha_\Theta[\Theta - \Theta_0]\mathrm{tr}(\boldsymbol{e}^{\mathrm{r}}_{\mathrm{log}}) \right] , \\
\rho_0 \, \psi^{\mathrm{e}}_{\mathrm{iso}} &= [1-d]\mu \, [\mathrm{dev}\,\boldsymbol{e}^{\mathrm{r}}_{\mathrm{log}} : \mathrm{dev}\,\boldsymbol{e}^{\mathrm{r}}_{\mathrm{log}}] ,
\end{aligned}
\tag{10.3.10}
$$

in the reference configuration. $\kappa = E/3[1-2\nu]$ and $\mu = E/2[1+\nu]$ are the elastic bulk modulus and shear modulus, respectively with E representing the modulus of elasticity and ν denoting the elastic Poisson's ratio. For the plastic part one uses

$$
\rho_0 \, \psi^{\mathrm{p}} = [1 - f_0][\tau_{\mathrm{m},\infty} - \tau_{\mathrm{m},0}] \left[\alpha + \frac{1}{\omega_{\mathrm{m}}} \left[\exp(-\omega_{\mathrm{m}}\alpha) - 1 \right] \right]
\tag{10.3.11}
$$

in the reference configuration. Hence, the isotropic plastic hardening of the representative volume element is taken to obey an exponential behavior, where $\tau_{\mathrm{m},0}$ and $\tau_{\mathrm{m},\infty}$ denote the initial and saturated Kirchhoff-type matrix yield stresses and ω_{m} is the matrix hardening saturation rate. The link between the material matrix and the representative volume element is reflected in the factor $[1 - f_0]$. The reason of using $[1 - f_0]$ rather than $[1 - f]$ is due to the Kirchhoff stress based hardening formulation which complies with the space of the postulated yield function, [Håkansson *et al.*, 2006].

Using the transformation $\boldsymbol{\tau} = [\boldsymbol{R}^{\mathrm{r}}]^{\top} \cdot \boldsymbol{\Sigma} \cdot \boldsymbol{R}^{\mathrm{r}}$, the plastic potential $\phi^p(\boldsymbol{\Sigma}, \beta; d, f)$ can be reparametrized to give $\phi^p(\overline{\boldsymbol{\tau}}, \beta, f)$ with the effective stress definition $\overline{\boldsymbol{\tau}} = \boldsymbol{\tau}/[1-d]$. Based on an analysis of a single spherical void in a spherical shell presented in [110] where the change of void shape is neglected, the effectively isotropic yield function ϕ^p, representing approximate form for the yield surface of a randomly voided solid containing a volume fraction f of voids is then defined as

$$
\phi^p(\overline{\boldsymbol{\tau}}, \beta, f) := \frac{1}{2\tau_{\mathrm{m}}} \left[\overline{\tau}^2_{\mathrm{eq}} + 2f\,\tau^2_{\mathrm{m}} \cosh\left(\frac{\mathrm{tr}\,\overline{\boldsymbol{\tau}}}{2\tau_{\mathrm{m}}} \right) - \tau^2_{\mathrm{m}}[1 + f^2] \right] \leq 0 ,
\tag{10.3.12}
$$

where $\overline{\tau}_{\mathrm{eq}}$ is introduced as the effective equivalent Kirchhoff stress through $\overline{\tau}_{\mathrm{eq}} = \sqrt{3/2\,[\mathrm{dev}\,\overline{\boldsymbol{\tau}} : \mathrm{dev}\,\overline{\boldsymbol{\tau}}]}$. Note that $\overline{\tau}_{\mathrm{eq}} = \overline{M}_{\mathrm{eq}} := \sqrt{3/2\,[\mathrm{dev}\,\overline{\boldsymbol{M}} : \mathrm{dev}\,\overline{\boldsymbol{M}}]}$ as well as $\mathrm{tr}\,\boldsymbol{\tau} = \mathrm{tr}\,\boldsymbol{M}$. The matrix flow stress is represented by $\tau_{\mathrm{m}} = \tau_{\mathrm{m},0} + \beta_{\mathrm{m}}$ with $\beta_{\mathrm{m}} = \beta/[1 - f_0]$ denoting the matrix hardening.

Remark 1. For fully developed plastic flow, i.e., $\phi^p(\overline{\boldsymbol{\tau}}, \beta) = 0$, under traceless stress state with $\mathrm{tr}\,\overline{\boldsymbol{\tau}}/2\tau_{\mathrm{m}} \to 0$ one has $\cosh\,(\mathrm{tr}\,\overline{\boldsymbol{\tau}}/2\tau_{\mathrm{m}}) \to 1$. Hence, $\overline{\tau}^2_{\mathrm{eq}} = [1 - f]^2\,\tau^2_{\mathrm{m}}$, which can be rearranged, using the effective stress definition, to give

$$
\tau_{\mathrm{eq}} = [1 - d][1 - f]\tau_{\mathrm{m}} .
$$

This depicts the effect of two distinct damage sources on the material response and the link between the fictitious effective material subscale free of defects and the mesoscopic behavior as depicted in the scenarios given in Figure 10.1.   ∎

Remark 2. In the spirit of [Håkansson *et al.*, 2006], the motivation for the evolution laws is considered in the absence of micro-voids, however, with micro-cracks. Accordingly, the flow potential reduces to $\phi^{\mathrm{p}}(\overline{\tau}, \beta) = \overline{\tau} - \tau_m \leq 0$. Following associative plasticity, the evolution laws for $\boldsymbol{L}^{\mathrm{p}}$ and α are governed by the normality rule

$$\boldsymbol{L}^{\mathrm{p}} = \lambda \frac{\partial \phi^p}{\partial \boldsymbol{M}} = \frac{\lambda}{1-d} \frac{3}{2} \frac{\mathrm{dev}\, \overline{\boldsymbol{M}}}{\tau_{\mathrm{m}}} \quad \text{and} \quad \dot{\alpha} = -\lambda \frac{\partial \phi^p}{\partial \beta} = \lambda \,.$$

Defining the equivalent plastic strain rate as $\dot{\epsilon}^{\mathrm{p}} = \sqrt{2/3\, \boldsymbol{L}^{\mathrm{p}} : \boldsymbol{L}^{\mathrm{p}}}$ and using $\dot{\alpha} = \lambda$ one reaches $\dot{\epsilon}^{\mathrm{p}} = \dot{\alpha}/[1-d]$. Hence, the rate of plastic work w^{p} in the reference configuration reads

$$w^{\mathrm{p}} = \mathrm{dev}\, \boldsymbol{M} : \boldsymbol{L}^{\mathrm{p}} = [1-d]\tau_{\mathrm{m}}\dot{\epsilon}^{\mathrm{p}} \,.$$

Thus, in comparison to [Håkansson *et al.*, 2006], the effect of the cleavage damage is also involved in the work equivalence relation.   ∎

In the light of the Remark 2, and following [Håkansson *et al.*, 2006], the validity of the following definitions is postulated for the porous plasticity model as well

$$\dot{\alpha} = \lambda \quad \text{and} \quad \dot{\epsilon}^{\mathrm{p}} = \frac{\dot{\alpha}}{1-d} \,. \tag{10.3.13}$$

Hence Equation (10.3.13.1) is replaced with Equation (10.3.9.2) for the definition of $\dot{\alpha}$ in the foregoing developments. Also, the following generalization of the plastic work equivalence is postulated

$$[1-f_0][1-d]\dot{\epsilon}^{\mathrm{p}}\tau_{\mathrm{m}} = \boldsymbol{\Sigma} : \boldsymbol{L}^{\mathrm{p}} \,, \tag{10.3.14}$$

which gains importance in definition of the total mechanical dissipation. Note that for a Cauchy-type matrix yield stress $\sigma_{\mathrm{m}} = 1/J^{\mathrm{r}}\tau_{\mathrm{m}}$ one has $[1-f_0][1-d]\dot{\epsilon}^{\mathrm{p}}\tau_{\mathrm{m}} = 1/J[1-f][1-d]\dot{\epsilon}^{\mathrm{p}}\sigma_{\mathrm{m}}$.

Due to the dependence of ϕ^p on the trace of the stress tensor, $\boldsymbol{l}^p$ is not traceless. Consequently, plastic dilatant effects are incorporated. Hence, the void volume fraction is associated with the plastic dilatant strains through the mass balance relation $\dot{f} = [1-f]\,\mathrm{tr}(\boldsymbol{L}^{\mathrm{p}})$, also given in Equation (10.2.2). Thus, unlike the isotropic continuum damage variable d, one does not need an additional dissipation potential in evaluation of the void volume fraction rate since it is plastic flow that accounts for the dissipation associated. The rate of d, on the other hand, is derived using a dissipation potential using Equation (10.3.9.3). ϕ^d is selected to take the form of Lemaitre-type damage dissipation potential [Lemaitre 1996]

$$\phi^d(Y) = \frac{S}{[1+m][1-d]^n} \left[\frac{\langle Y - Y_0 \rangle}{S} \right]^{m+1} , \tag{10.3.15}$$

where m, n, S and Y_0 are associated material parameters. Y_0 represents the threshold value of strain energy release rate governing the initiation of cleavage damage.

Now, using Equations (10.3.5) along with the defined potentials in Equations (10.3.10) and

(10.3.11), one arrives at explicit forms of the conjugate variables $\mathbf{\Sigma}$, β and Y as

$$
\begin{aligned}
\mathbf{\Sigma} &= [1 - d] \left[\kappa \mathrm{tr}(\boldsymbol{e}^{\mathrm{r}}_{\log}) \mathbf{1} + 2\mu \, \mathrm{dev}\, \boldsymbol{e}^{\mathrm{r}}_{\log} - 3\kappa \alpha_{\Theta} [\Theta - \Theta_0] \mathbf{1} \right] , \\
\beta &= [1 - f_0][\tau_{\mathrm{m},\infty} - \tau_{\mathrm{m},0}] \left[1 - \exp(-\omega_{\mathrm{m}} \alpha) \right] , \\
Y &= \kappa \left[\frac{1}{2} [\mathrm{tr}(\boldsymbol{e}^{\mathrm{r}}_{\log})]^2 - 3\alpha_{\Theta}[\Theta - \Theta_0]\mathrm{tr}(\boldsymbol{e}^{\mathrm{r}}_{\log}) \right] + \mu \left[\mathrm{dev}\, \boldsymbol{e}^{\mathrm{r}}_{\log} : \mathrm{dev}\, \boldsymbol{e}^{\mathrm{r}}_{\log} \right] ,
\end{aligned}
\tag{10.3.16}
$$

where the matrix hardening is represented with $\beta_{\mathrm{m}} = \beta/[1 - f_0] = [\tau_{\mathrm{m},\infty} - \tau_{\mathrm{m},0}] \left[1 - \exp(-\omega_{\mathrm{m}} \alpha) \right]$.

For the plastic flow and the evolution of d, one uses Equations (10.3.9.1) and (10.3.9.3) along with the dissipation potential components given in Equations (10.3.12) and (10.3.15), respectively. The hardening variable rate $\dot{\alpha}$ obeys Equation (10.3.13.1). Collectively, the evolution equations read

$$
\begin{aligned}
\boldsymbol{L}^{\mathrm{p}} &= \frac{\lambda}{1 - d} \left[\frac{3}{2} \frac{\mathrm{dev}\bar{\mathbf{\Sigma}}}{\tau_{\mathrm{m}}} - \frac{1}{2} f \sinh\left(\frac{q_2 \mathrm{tr}\bar{\mathbf{\Sigma}}}{2\tau_{\mathrm{m}}} \right) \mathbf{1} \right] , \\
\dot{\alpha} &= \lambda , \\
\dot{d} &= \frac{\lambda}{[1 - d]^n} \left[\frac{\langle Y - Y_0 \rangle}{S} \right]^m ,
\end{aligned}
\tag{10.3.17}
$$

where $\bar{\mathbf{\Sigma}} = \mathbf{\Sigma}/[1 - d]$. Now, substituting Equations (10.3.16) and (10.3.17) into the right-hand side of Equation (10.3.7) together with using Equation (10.3.14), the mechanical dissipation reads

$$
\mathcal{D}^{\mathrm{red}}_{\mathrm{loc}} = [1 - f_0][1 - d]\,\dot{\epsilon}^{\mathrm{p}} \tau_{\mathrm{m},0} + \dot{\epsilon}^{\mathrm{p}} \frac{1}{[1 - d]^{n-1}} Y \left[\frac{\langle Y - Y_0 \rangle}{S} \right]^m .
\tag{10.3.18}
$$

The second term reflects the dissipative effect of cleavage-type damage which is not accounted for in [Håkansson *et al.*, 2006]. Equation (10.3.18) is always nonzero, hence, the second law of thermodynamics is fulfilled. For convenience, a summary of the constitutive model is given in **BOX 1**.

BOX 1. A summary of the proposed model for general 3D stress-state.

i. Multiplicative kinematics

$$\boldsymbol{F} = \boldsymbol{F}^{\mathrm{r}} \cdot \boldsymbol{F}^{\mathrm{p}} \quad \text{and} \quad \boldsymbol{F}^{\mathrm{r}} = \boldsymbol{F}^{\mathrm{e}} \cdot \boldsymbol{F}^{\Theta} .$$

ii. Thermoelastic stress-strain relationship

$$\boldsymbol{\Sigma} = [1 - d] \left[\kappa \mathrm{tr}(\boldsymbol{e}_{\mathrm{log}}^{\mathrm{r}}) \boldsymbol{1} + 2\mu \, \mathrm{dev} \, \boldsymbol{e}_{\mathrm{log}}^{\mathrm{r}} - 3\kappa\alpha_{\Theta}[\Theta - \Theta_0] \boldsymbol{1} \right] .$$

iii. State laws for hardening and damage conjugate variables

$$\beta = [1 - f_0][\tau_{\mathrm{m},\infty} - \tau_{\mathrm{m},0}] \left[1 - \exp(-\omega_{\mathrm{m}}\alpha) \right] ,$$

$$Y = \kappa \left[\frac{1}{2}[\mathrm{tr}(\boldsymbol{e}_{\mathrm{log}}^{\mathrm{r}})]^2 - 3\alpha_{\Theta}[\Theta - \Theta_0]\mathrm{tr}(\boldsymbol{e}_{\mathrm{log}}^{\mathrm{r}}) \right] + \mu \left[\mathrm{dev} \, \boldsymbol{e}_{\mathrm{log}}^{\mathrm{r}} : \mathrm{dev} \, \boldsymbol{e}_{\mathrm{log}}^{\mathrm{r}} \right] .$$

iv. Matrix yield stress and hardening

$$\tau_{\mathrm{m}} = \tau_{\mathrm{m},0} + \beta_{\mathrm{m}} \quad \text{and} \quad \beta_{\mathrm{m}} = \frac{\beta}{1 - f_0} .$$

v. Thermoelastic domain in stress space (single surface)

$$\mathbb{E}_{\boldsymbol{\tau}} = \left\{ [\overline{\boldsymbol{\tau}}, \beta, f] \in \mathbb{S} \times \mathbb{R}^+ \times \mathbb{R}^+ : \phi^{\mathrm{p}}(\overline{\boldsymbol{\tau}}, \beta, f) \leq 0 \right\} ,$$

where $\mathbb{S}$ represents the vector space of *symmetric* second-order tensors and

$$\phi^p(\overline{\boldsymbol{\tau}}, \beta, f) = \frac{1}{2\tau_{\mathrm{m}}} \left[\overline{\tau}_{\mathrm{eq}}^2 + 2f \, \tau_{\mathrm{m}}^2 \cosh\left(\frac{\mathrm{tr} \, \overline{\boldsymbol{\tau}}}{2\tau_{\mathrm{m}}}\right) - \tau_{\mathrm{m}}^2[1 + f^2] \right] .$$

vi. Flow rule (associative model)

$$\boldsymbol{L}^{\mathrm{p}} = \frac{\lambda}{1 - d} \left[\frac{3}{2} \frac{\mathrm{dev}\overline{\boldsymbol{\Sigma}}}{\tau_{\mathrm{m}}} - \frac{1}{2} f \sinh\left(\frac{\mathrm{tr}\overline{\boldsymbol{\Sigma}}}{2\tau_{\mathrm{m}}}\right) \boldsymbol{1} \right] .$$

vii. Evolution equations for hardening, damage and porosity

$$\dot{\alpha} = \lambda \quad \text{and} \quad \dot{\epsilon}^{\mathrm{p}} = \frac{\lambda}{1 - d} ,$$

$$\dot{d} = \frac{\lambda}{[1 - d]^n} \left[\frac{\langle Y - Y_0 \rangle}{S} \right]^m ,$$

$$\dot{f} = [1 - f]\mathrm{tr}(\boldsymbol{L}^{\mathrm{p}}) .$$

viii. Kuhn-Tucker loading/unloading (complementarity) conditions

$$\lambda \geq 0, \ \phi^{\mathrm{p}}(\overline{\boldsymbol{\tau}}, \beta, f) \leq 0, \ \lambda\phi^{\mathrm{p}}(\overline{\boldsymbol{\tau}}, \beta, f) = 0 .$$

ix. Consistency condition

$$\lambda\dot{\phi}^{\mathrm{p}}(\overline{\boldsymbol{\tau}}, \beta, f) = 0 .$$

10.4.   Application - Uniaxial Tension

In this section, first a systematic reduction of the theory to monotonic uniaxial tension is presented. Solution of the resultant reduced equation set allows conduction of some parametric studies which show predictive capabilities of the model.

10.4.1.   Specification of Equations for Uniaxial Tensile State of Stress

Let $\boldsymbol{e}_1$, $\boldsymbol{e}_2$ and $\boldsymbol{e}_3$ denote orthogonal unit vectors associated with $x-$, $y-$ and $z-$directions. Tensile loading in $x-$direction is considered where the material motion is free in $y-$ and $z-$directions. This corresponds to a uniaxial state of stress and triaxial state of strain with

$$\boldsymbol{\tau} = \tau \boldsymbol{e}_1 \otimes \boldsymbol{e}_1 \quad \text{and} \quad \boldsymbol{F} = \lambda_1 \boldsymbol{e}_1 \otimes \boldsymbol{e}_1 + \lambda_2 [\boldsymbol{e}_2 \otimes \boldsymbol{e}_2 + \boldsymbol{e}_3 \otimes \boldsymbol{e}_3],\qquad(10.4.1)$$

where λ_1 and λ_2 represent principal stretches in $x-$ and $y-$ (equivalently $z-$) directions. With Equation (10.4.1.1) following equivalences hold: $\tau_{\text{eq}} = \tau = \operatorname{tr} \boldsymbol{\tau}$. Also, in absence of rotation, i.e., $\boldsymbol{R}^r = \mathbf{1}$, one has $\boldsymbol{\tau} \equiv \boldsymbol{M}$. Using Equation (10.4.1.2) the Jacobian of the deformation gradient becomes $J = \lambda_1 \lambda_2^2$. In analogy to Equation (10.4.1.2), the recoverable and irrecoverable parts of the deformation gradient can be given as

$$\begin{aligned}
\boldsymbol{F}^{\text{r}} &= \lambda_1^{\text{r}} \boldsymbol{e}_1 \otimes \boldsymbol{e}_1 + \lambda_2^{\text{r}} [\boldsymbol{e}_2 \otimes \boldsymbol{e}_2 + \boldsymbol{e}_3 \otimes \boldsymbol{e}_3], \\
\boldsymbol{F}^{\text{p}} &= \lambda_1^{\text{p}} \boldsymbol{e}_1 \otimes \boldsymbol{e}_1 + \lambda_2^{\text{p}} [\boldsymbol{e}_2 \otimes \boldsymbol{e}_2 + \boldsymbol{e}_3 \otimes \boldsymbol{e}_3].
\end{aligned}\qquad(10.4.2)$$

The recoverable part given in Equation (10.4.2.1) is further decomposed into the elastic and thermal parts viz. $\boldsymbol{F}^{\text{r}} = \boldsymbol{F}^{\text{e}} \cdot \boldsymbol{F}^{\Theta}$, where, with the assumption of thermally isotropic material $\boldsymbol{F}^{\theta}$ is defined as a spherical tensor with $\boldsymbol{F}^{\theta} := \lambda^{\Theta} \mathbf{1}$. Accordingly, in the given orthogonal triad one has

$$\begin{aligned}
\boldsymbol{F}^{\text{e}} &= \lambda_1^{\text{e}} \boldsymbol{e}_1 \otimes \boldsymbol{e}_1 + \lambda_2^{\text{e}} [\boldsymbol{e}_2 \otimes \boldsymbol{e}_2 + \boldsymbol{e}_3 \otimes \boldsymbol{e}_3], \\
\boldsymbol{F}^{\Theta} &= \lambda^{\Theta} [\boldsymbol{e}_1 \otimes \boldsymbol{e}_1 + \boldsymbol{e}_2 \otimes \boldsymbol{e}_2 + \boldsymbol{e}_3 \otimes \boldsymbol{e}_3].
\end{aligned}\qquad(10.4.3)$$

Hence, the right Cauchy Green deformation tensor $\boldsymbol{C} = \boldsymbol{F}^{\top} \cdot \boldsymbol{F}$ computes

$$\boldsymbol{C} = [\lambda_1^{\text{e}}]^2 [\lambda_1^{\text{p}}]^2 [\lambda^{\Theta}]^2 \boldsymbol{e}_1 \otimes \boldsymbol{e}_1 + [\lambda_2^{\text{e}}]^2 [\lambda_2^{\text{p}}]^2 [\lambda^{\Theta}]^2 [\boldsymbol{e}_2 \otimes \boldsymbol{e}_2 + \boldsymbol{e}_3 \otimes \boldsymbol{e}_3].\qquad(10.4.4)$$

Now, using the definition of the logarithmic strain $\boldsymbol{e}_{\log} = 1/2 \log \boldsymbol{C}$ one reaches

$$\boldsymbol{e}_{\log} = \boldsymbol{e}_{\log}^{\text{e}} + \boldsymbol{e}_{\log}^{\text{p}} + \boldsymbol{e}_{\log}^{\Theta},\qquad(10.4.5)$$

where

$$\begin{aligned}
\boldsymbol{e}_{\log}^{\text{e}} &= \log \lambda_1^{\text{e}} \boldsymbol{e}_1 \otimes \boldsymbol{e}_1 + \log \lambda_2^{\text{e}} [\boldsymbol{e}_2 \otimes \boldsymbol{e}_2 + \boldsymbol{e}_3 \otimes \boldsymbol{e}_3], \\
\boldsymbol{e}_{\log}^{\text{p}} &= \log \lambda_1^{\text{p}} \boldsymbol{e}_1 \otimes \boldsymbol{e}_1 + \log \lambda_2^{\text{p}} [\boldsymbol{e}_2 \otimes \boldsymbol{e}_2 + \boldsymbol{e}_3 \otimes \boldsymbol{e}_3], \\
\boldsymbol{e}_{\log}^{\Theta} &= \log \lambda^{\Theta} [\boldsymbol{e}_1 \otimes \boldsymbol{e}_1 + \boldsymbol{e}_2 \otimes \boldsymbol{e}_2 + \boldsymbol{e}_3 \otimes \boldsymbol{e}_3].
\end{aligned}\qquad(10.4.6)$$

Equation (10.4.5) encapsulates an additive decomposition in logarithmic strains carried out from a multiplicative decomposition of the deformation gradient. For convenience, the notations $e_{\log}^{\text{e}} = \log \lambda_1^{\text{e}}$, $e_{\log}^{\text{p}} = \log \lambda_1^{\text{p}}$ and $e_{\log}^{\Theta} = \log \lambda^{\Theta}$ are made use of. Letting $\lambda^{\Theta} := \exp \int_{\Theta_0}^{\Theta} \alpha_{\Theta}(\theta) d\theta$ and $\alpha_{\Theta}(\Theta)$ represent the linear[2] thermal expansion coefficient, omitting the dependence of α_{Θ} on the

---

[2]The volumetric thermal expansion coefficient, on the other hand, amounts for $3\alpha_{\Theta}(\Theta)$ for thermally isotropic materials.

temperature one finds $J^\Theta := \det(\boldsymbol{F}^\theta) = [\lambda^\Theta]^3 = \exp[3\alpha_\Theta[\Theta - \Theta_0]]$ where $\lambda^\Theta = \exp[\alpha_\Theta[\Theta - \Theta_0]]$. Thus $e_{\log}^\Theta = \alpha_\Theta[\Theta - \Theta_0]$. The elastic stress definition given in Equation (10.3.16) and the vanishing stress components in $y-$ and $z-$directions reveal $\log \lambda_2^e = -\nu \log \lambda_1^e$ and supplies

$$\tau = [1 - d]E\left[e_{\log}^r - \alpha_\Theta[\Theta - \Theta_0]\right] . \tag{10.4.7}$$

Also the total recoverable logarithmic strain tensor $\boldsymbol{e}_{\log}^r = \boldsymbol{e}_{\log}^e + \boldsymbol{e}_{\log}^\Theta$ reads

$$\boldsymbol{e}_{\log}^r = [e_{\log}^e + e_{\log}^\Theta]\boldsymbol{e}_1 \otimes \boldsymbol{e}_1 + [-\nu e_{\log}^e + e_{\log}^\Theta][\boldsymbol{e}_2 \otimes \boldsymbol{e}_2 + \boldsymbol{e}_3 \otimes \boldsymbol{e}_3] , \tag{10.4.8}$$

for which the volumetric and the deviatoric parts are computed as

$$\begin{aligned}
\operatorname{tr}\boldsymbol{e}_{\log}^r &= [1 - 2\nu]e_{\log}^e + 3e_{\log}^\Theta , \\
\operatorname{dev}\boldsymbol{e}_{\log}^r &= \frac{2}{3}[1 + \nu]e_{\log}^e\boldsymbol{e}_1 \otimes \boldsymbol{e}_1 - \frac{1}{3}[1 + \nu]e_{\log}^e[\boldsymbol{e}_2 \otimes \boldsymbol{e}_2 + \boldsymbol{e}_3 \otimes \boldsymbol{e}_3] .
\end{aligned} \tag{10.4.9}$$

Using Equation (10.4.9) along with Equation (10.3.16.3) gives the elastic energy release rate $e_{\log}^e$ as

$$Y = \frac{1}{2}\left[E[e_{\log}^e]^2 - 9\kappa[\alpha_\Theta]^2[\Theta - \Theta_0]^2\right] , \tag{10.4.10}$$

or in terms of $e_{\log}^r$ as

$$Y = \frac{1}{2}E[e_{\log}^r]^2 - Ee_{\log}^r\alpha_\Theta[\Theta - \Theta_0] - 3\kappa[1 + \nu][\alpha_\Theta]^2[\Theta - \Theta_0]^2 . \tag{10.4.11}$$

Finally, using $\boldsymbol{L}^p := \dot{\boldsymbol{F}}^p \cdot [\boldsymbol{F}^p]^{-1}$ one has

$$\boldsymbol{L}^p = \frac{\dot{\lambda}_1^p}{\lambda_1^p}\boldsymbol{e}_1 \otimes \boldsymbol{e}_1 + \frac{\dot{\lambda}_2^p}{\lambda_2^p}[\boldsymbol{e}_2 \otimes \boldsymbol{e}_2 + \boldsymbol{e}_3 \otimes \boldsymbol{e}_3] \equiv \dot{\boldsymbol{e}}^p . \tag{10.4.12}$$

For convenience, the complete reformulation of the model under uniaxial tension is given in **BOX 2**. The rate equations together with the given yield function form a differential-algebraic equation set which is solved semi-explicitly. To this end, the vector of unknowns is represented by $\boldsymbol{x} = \{\tau, \alpha, f\}$. Assuming $\boldsymbol{x} = \boldsymbol{x}(\Delta\lambda)$, where $\Delta\lambda$ denotes the incremental plastic multiplier, the yield function is reformulated as a nonlinear function of $\Delta\lambda$ with $\phi^p(\boldsymbol{x}(\Delta\lambda))$. Applying Taylor series expansion to ϕ^p with backward-Euler integration of the unknowns leads to an iterative solution with $\Delta\lambda^{\langle k+1 \rangle} = \Delta\lambda^{\langle k \rangle} - [\phi^p]^{\langle k \rangle}/[\partial\phi^p/\partial\boldsymbol{x} \cdot \partial\boldsymbol{x}/\partial\Delta\lambda]^{\langle k \rangle}$ where $\langle k \rangle$ represents the iteration index. The iterations are run under a desired tolerance where unknowns updates are realized at each iteration. The integration of d is realized subsequent to the convergence in a staggered manner using the converged incremental plastic multiplier.

BOX 2. A reduction of the proposed model to monotonic uniaxial tension.

---

   i. Additive kinematics

$$e_{\log} = e_{\log}^{\mathrm{r}} + e_{\log}^{\mathrm{p}} \quad \text{and} \quad e_{\log}^{\mathrm{r}} = e_{\log}^{\mathrm{e}} + e_{\log}^{\Theta},$$

  where $e_{\log}^{\Theta} = \alpha_{\Theta}[\Theta - \Theta_0]$.

  ii. Thermoelastic stress-strain relationship

$$\tau = [1 - d]E\left[e_{\log}^{\mathrm{r}} - \alpha_{\Theta}[\Theta - \Theta_0]\right].$$

 iii. State laws for hardening and damage conjugate variables

$$\beta = [1 - f_0][\tau_{\mathrm{m},\infty} - \tau_{\mathrm{m},0}]\left[1 - \exp(-\omega_{\mathrm{m}}\alpha)\right],$$

$$Y = \frac{1}{2}E[e_{\log}^{\mathrm{r}}]^2 - Ee_{\log}^{\mathrm{r}}\alpha_{\Theta}[\Theta - \Theta_0] - 3\kappa[1 + \nu][\alpha_{\Theta}]^2[\Theta - \Theta_0]^2.$$

 iv. Matrix yield stress and hardening

$$\tau_{\mathrm{m}} = \tau_{\mathrm{m},0} + \beta_{\mathrm{m}} \quad \text{and} \quad \beta_{\mathrm{m}} = \frac{\beta}{1 - f_0}.$$

  v. Thermoelastic domain in stress space (single surface)

$$\mathbb{E}_\tau = \left\{[\overline{\tau}, \beta, f] \in \mathbb{R}^+ \times \mathbb{R}^+ \times \mathbb{R}^+ : \phi^{\mathrm{p}}(\overline{\tau}, \beta, f) \le 0\right\},$$

  where

$$\phi^p(\overline{\tau}, \beta, f) = \frac{1}{2\tau_{\mathrm{m}}}\left[\overline{\tau}^2 + 2f\,\tau_{\mathrm{m}}^2\cosh\left(\frac{\overline{\tau}}{2\tau_{\mathrm{m}}}\right) - \tau_{\mathrm{m}}^2[1 + f^2]\right].$$

 vi. Flow rule (associative model)

$$\dot{e}_{\log}^{\mathrm{p}} = \frac{\lambda}{1 - d}\left[\frac{\overline{\tau}}{\tau_{\mathrm{m}}} - \frac{1}{2}f\sinh\left(\frac{\overline{\tau}}{2\tau_{\mathrm{m}}}\right)\right].$$

 vii. Evolution equations for hardening, damage and porosity

$$\dot{\alpha} = \lambda \quad \text{and} \quad \dot{\epsilon}^{\mathrm{p}} = \frac{\lambda}{1 - d},$$

$$\dot{d} = \frac{\lambda}{[1 - d]^n}\left[\frac{\langle Y - Y_0\rangle}{S}\right]^m,$$

$$\dot{f} = \frac{3}{2}\frac{\lambda[1 - f]}{1 - d}f\sinh\left(\frac{\overline{\tau}}{2\tau_{\mathrm{m}}}\right).$$

 viii. Kuhn-Tucker loading/unloading (complementarity) conditions

$$\lambda \ge 0, \ \phi^{\mathrm{p}}(\overline{\tau}, \beta, f) \le 0, \ \lambda\phi^{\mathrm{p}}(\overline{\tau}, \beta, f) = 0.$$

 ix. Consistency condition

$$\lambda\dot{\phi}^{\mathrm{p}}(\overline{\tau}, \beta, f) = 0.$$

10.4.2.   Results and Discussions

The derivations correspond to a single material point loaded under uniaxial stress state. Hence, there is no heat conduction. The heat generation by dissipative inelastic processes is also disregarded and simulations are conducted at ten different constant temperatures $\Theta_1 \ldots \Theta_{10}$ of equal temperature steps from $-125°$C to $125°$C where $\Theta_1 = -125°$C and $\Theta_{10} = 125°$C. All analyses start from a stress-free configuration. Since $T = T_0$ throughout the loading, no thermal strains occur. Moreover, during loading the stress triaxiality ratio η defined as $\eta := \mathrm{tr}\boldsymbol{\tau}/3\tau_{\mathrm{eq}}$ is constant and equal to $1/3$. Due to lack of sufficient stress triaxiality, void growth occurs slowly. In order to accelerate void growth and obtain realistic failure strains, a rather high initial void volume content with $f_0 = 0.055$ is selected. Moreover, following Tvergaard and Needleman [?], f in the yield function definition given in Equation (10.3.12) is replaced by f^* which encapsulates acceleration of the void growth during the void coalescence via

$$f^*(f) = f + \langle f - f_{\mathrm{c}} \rangle \frac{f_{\mathrm{u}}^* - f_{\mathrm{f}}}{f_{\mathrm{f}} - f_{\mathrm{c}}} \ . \tag{10.4.13}$$

Here, f_{c} and f_{f} describe the critical void volume fraction at incipient coalescence and the fraction at failure, respectively. Finally, $f_{\mathrm{u}}^* = 1/q_1$. For thermal properties and matrix hardening, steel-like but hypothetical parameters are selected. For convenience, Table 10.1 compiles the material parameters used at reference temperature $\Theta_{\mathrm{ref}} = 25°$C.

Table 10.1.: Selected steel-like material parameters.

Parameter	Symbol	Value	Unit
Thermal expansion coef.	α_Θ	10^{-5}	K^{-1}
Melting temperature	Θ_{melt}	1717	K
Reference temperature	Θ_{ref}	298	K
Young's modulus	E	210	GPa
Poisson's ratio	ν	0.3	$[-]$
	$\tau_{\mathrm{m},\infty}$	1000	MPa
Matrix hardening	$\tau_{\mathrm{m},0}$	500	MPa
	ω_{m}	15	$[-]$
	f_0	0.055	$[-]$
Gurson model	f_{c}	0.075	$[-]$
	f_{f}	0.10	$[-]$
	f_{u}^*	1	$[-]$
	Y_0	3	MPa
Lemaitre model	m	1	$[-]$
	n	2	$[-]$
	S	0.25	MPa

The temperature effect on the matrix yield stress is adapted using data available in the literature [Ritchie *et al.* 1973]. Accordingly, defining homologous temperature Ω with $\Omega := [\Theta - \Theta_{\mathrm{ref}}]/[\Theta_{\mathrm{melt}} - \Theta_{\mathrm{ref}}]$, one computes the matrix yield stress as $\beta_{\mathrm{m}}(\Omega) = t_y(\Omega)\beta_{\mathrm{m}}$ where $t_y(\Omega) = 1846\Omega^4 - 520.36\Omega^3 + 50.422\Omega^2 - 1.9124\Omega + 1$. Figure 10.2 depicts the variation of t_y as a function of Θ.
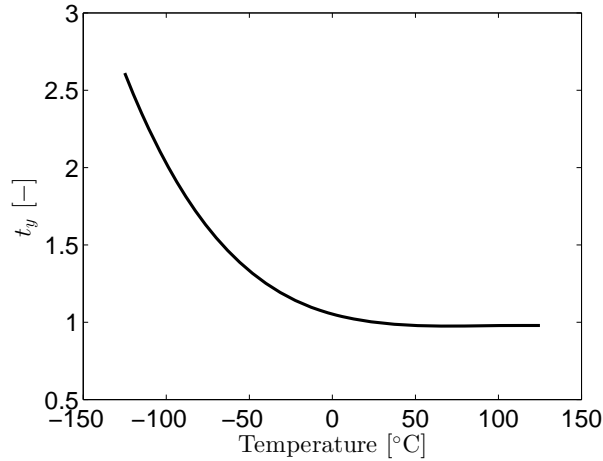
Figure 10.2.: Temperature effect on the yield stress as a scaling factor adapted from [Ritchie et al. 1973]. Room temperature is taken as $25°C$ at which the yield stress factor is unity. Beyond room temperature there occurs only a slight decrease within the range of selected temperature interval. The curve is represented by a continuous function of the homologous temperature Ω with $t_y(\Omega) = 1846\Omega^4 - 520.36\Omega^3 + 50.422\Omega^2 - 1.9124\Omega + 1$.

Two conditions are used in decision of the material failure: In the first one local instability condition is considered with $d\tau/d\epsilon < 0$, whereas in the second one a sufficient loss of the stress bearing capacity of the material point is taken into account with $\tau < \text{TOL}$ where $\text{TOL} = 0.01 \times \tau_{\text{m},0}$. The former could be seen as a consequence of Drucker's stability postulate or more elaborate discontinuous bifurcation analyses which locates the initiation of localization as a precursor to fracture through the vanishing determinant of the acoustic tensor. For both failure criteria the absorbed energy to failure, i.e., the area under the stress-strain curves, are computed and plotted for corresponding temperatures. The results are shown in Figures 10.3 and 10.4. In each figure the stress, damage and void volume fraction plots as a function of the axial logarithmic strain are given for $\Theta_1 \ldots \Theta_{10}$. Also the failure energy plots are given. The stress plots for both criteria show that at higher temperatures plastic strains are considerably larger than those at lower temperatures. It is seen that, in agreement with the presented results of [Doghri 1995], the accumulation of damage components d and f at the point of stability loss are lower than that of loss of complete load carrying capacity. Note that for due to lack of sufficient void volume fraction accumulation for $\Theta_1 \ldots \Theta_3$ with the criterion $\tau < \text{TOL} \times \tau_{\text{m},0}$, d reaches close to its theoretical limit $d = 1$. The occurrence of a kink and subsequent rather accelerated drop of the stress response for increased temperatures is due to the enforced void coalescence condition.

It is notable that, although a drastic difference is observed in continuum damage variable evolution for different temperatures the void volume fraction is less sensitive to the yield value changes. Two main differences are observed in d evolution curves for different temperatures: First the damage initiation strains and second the damage evolution rates. The former is due to the fact that the evolution of d requires the damage driving force Y reach the threshold Y_0. Higher yield stress at lower temperatures allows fulfillment of this requirement easily. At higher temperatures, i.e., $\Theta_5 \ldots \Theta_{10}$, Y never reaches Y_0, and thus d ceases to evolve. Then, the whole softening mechanism is controlled by the void growth, hence failure is ductile. With the same

token, higher Y observed at lower temperatures results in an increased rate of damage evolution. Then, the whole softening mechanism is controlled by the evolution of d, hence failure is brittle.

In both material failure assumptions, the failure energy density plots show a sharp increase in the energy demand with temperature around $-50°$C. Hence, the desired ductile-brittle transition in the failure mode was possible where $-50°$C point amounts for the ductile-brittle transition temperature. The energy demand until complete stress loss is slightly over double the energy demand until neck, but the main characteristics of the curve is not changed. There results show that the proposed framework proves useful in modeling temperature driven ductile-brittle transition of the fracture mode in metallic materials.
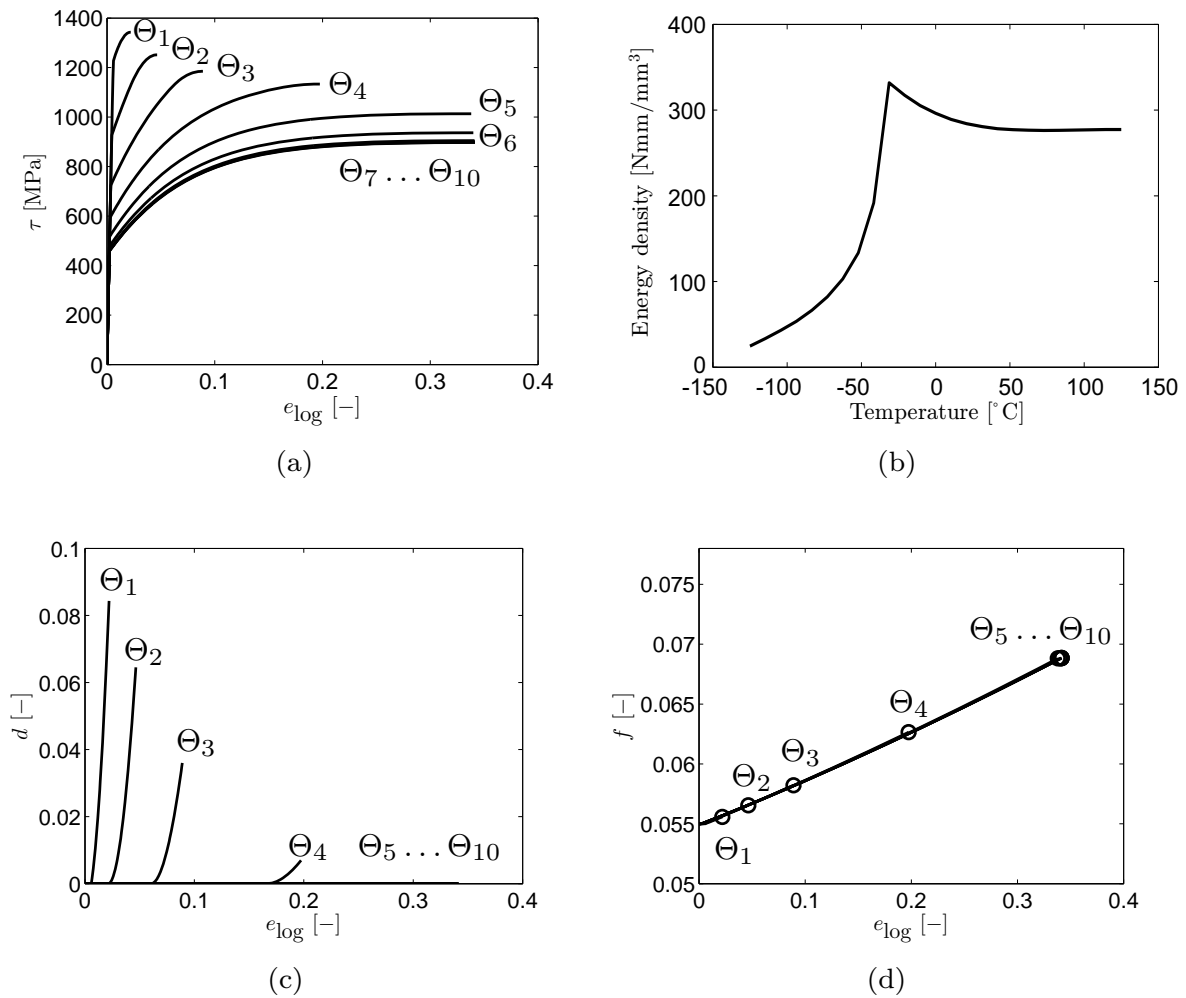
Figure 10.3.: Results for criterion $d\tau/de_{log} < 0$ at 10 different temperatures $\Theta_1 \ldots \Theta_{10}$ of equal temperature steps from $-125°C$ to $125°C$ where $\Theta_1 = -125°C$ and $\Theta_{10} = 125°C$: (a) stress-strain curves, (b) energy per unit (reference) volume computed using $\int \tau de_{log}$, as seen a sharp ductile-brittle transition is observed in energy density demand until neck where the ductile-brittle transition temperature is around $-50°C$, (c) damage d accumulation until neck, (d) void volume fraction f accumulation until neck. The markers show f values reached at each temperature.

(a)   (b)

(c)   (d)
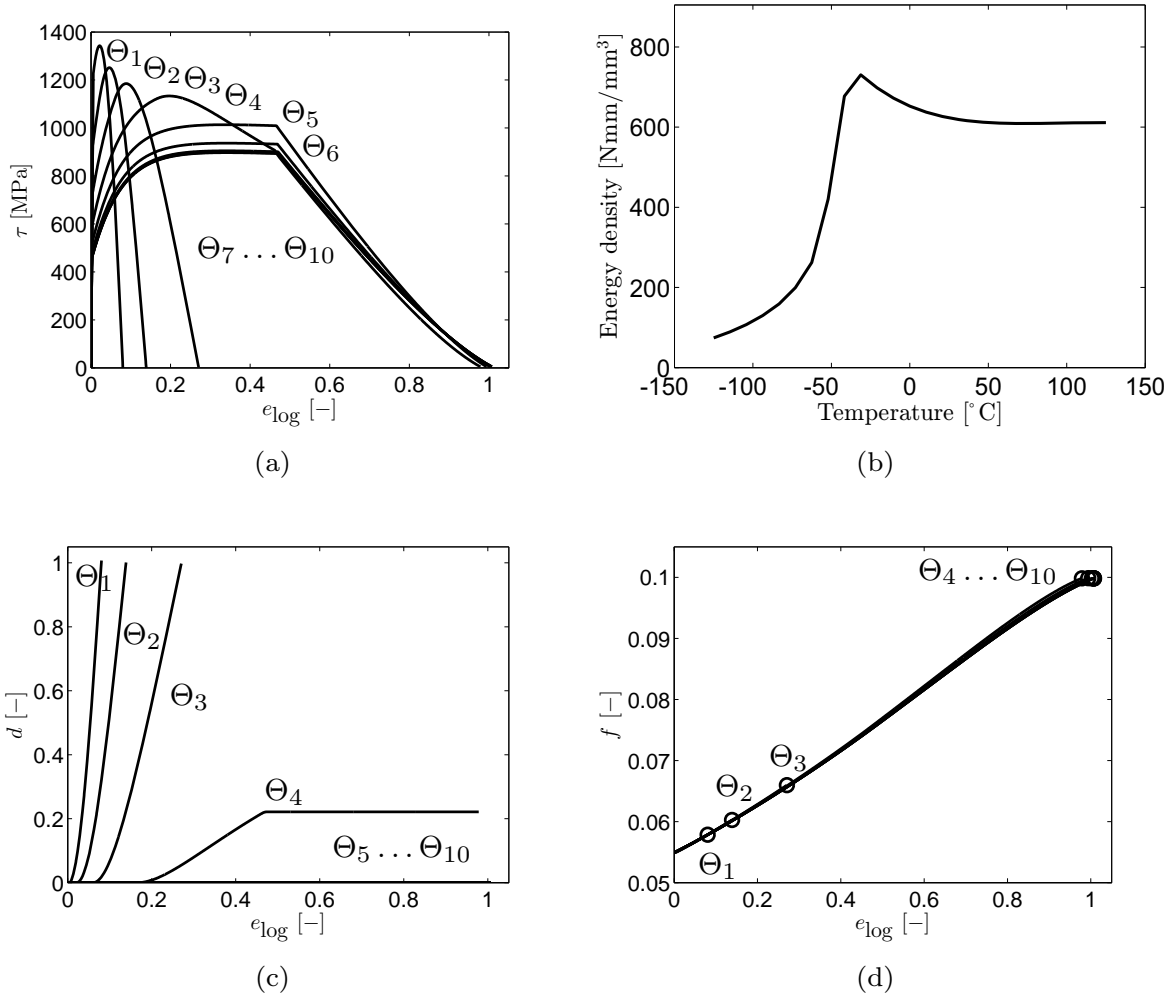
Figure 10.4.: Results for criterion $\tau < TOL$ where $TOL = 0.01 \times \tau_{m,0}$ at 10 different temperatures $\Theta_1 \ldots \Theta_{10}$ of equal temperature steps from $-125°C$ to $125°C$ where $\Theta_1 = -125°C$ and $\Theta_{10} = 125°C$: (a) stress-strain curves, (b) energy per unit (reference) volume computed using $\int \tau de_{log}$, as seen a sharp ductile-brittle transition is observed in energy density demand until complete loss of load carrying capacity where the ductile-brittle transition temperature is around $-50°C$, (c) damage d accumulation until neck, (d) void volume fraction f accumulation until neck. The markers show f values reached at each temperature.

10.5.   Conclusion

A theoretical framework for coupled porous thermoplasticity and continuum damage mechanics has been formulated preserving isotropy, within a thermodynamic consistency at finite strains. Multiplicative split of the deformation gradient in elastic, plastic and thermal parts has been utilized as a basis for finite strain kinematics. The framework aims at modeling blended mechanisms of simultaneous micro-void and micro-crack driven material degradation. Hence, the building blocks are selected as the Gurson-type porous plasticity and Lemaitre-type continuum damage mechanics. Considering the possible application of the proposed model as the ductile-to-brittle transition of the fracture mode, the main advantage that the proposed model shows over the widely-used framework (e.g., porous plasticity for ductile failure and Ritchie-Knott-

Rice or Beremin local approaches to cleavage) is that the energy dissipation associated with the cleavage-type of fracture is accounted for within the formalism of continuum damage mechanics. The isotropic damage variable d introduced via Lemaitre formalism is able to take care of the strength and stiffness degradation related to the micro-cracks without volumetric changes, whereas void volumetric changes are encapsulated in the evolution of the void volume fraction f. The evolution of d is formulated by a damage dissipation potential which devises the energy release rate Y_0 as a threshold for cleavage damage to initiate at the process zone. The evolution of f follows the mass conservation relation which does not necessitate an additional dissipation potential. Extension of the model to anisotropic cleavage damage is possible through a fully intermediate configuration formulation of the yield function. The predictive capability of the model is demonstrated through application problems assuming uniaxial state of stress. It is shown by absorbed energy plots for different temperatures that for the presented parameter set remedying limitations of the limited stress triaxiality conditions, the model predicts the temperature driven ductile-brittle transition of fracture mode sufficiently well.

Part IV.

Experimental Approaches for Mechanical Characterization of Plasticity and Damage

11. Characterization of Anisotropy of Sheet Metals Employing Inhomogeneous Strain Fields for Yld2000-2D Yield Function

In this chapter, a method to include the distribution of strains in the identification of the planar anisotropy of sheet metals is proposed. The method includes the optical measurement of strains on a flat specimen with a varying cross-section and an inverse parameter identification scheme which minimizes the differences between the numerical simulation results and the experimental measurements by using Levenberg-Marquardt algorithm. The main advantage is the reduction of the needed number of material tests especially for complex material models, under the assumption of negligible kinematic hardening. The utilized specimen geometry covers a deformation state between uniaxial tension and plane strain tension cases. In order to supply additional information to the inverse scheme, the equi-biaxial stress state obtained from layer compression test is also included in the definition of the objective function. The anisotropy of the sheet is modeled with the Yld2000-2D model which is implemented as a VUMAT subroutine for ABAQUS/EXPLICIT. Numerical tests point out that the orientation of the specimen defines the quality of the found yield loci. The proposed method is applied to characterize the commercial aluminum alloy AA6016-T4 and the obtained material parameters are used to analyze a deep drawn car hood geometry. The results show that the use of the strain distribution is a crucial point in identification of the planar anisotropy. The yield loci obtained with the proposed method are in accordance with the conventionally obtained yield stresses and $r-$values.

11.1. Introduction

Sheet metals exhibit a certain texture which leads to differences in the plastic behavior along different loading directions and stress states. For that reason assumption of isotropy is no longer applicable in the numerical analyses. Instead the assumption of orthotropic material behavior is the common practice which postulates symmetry along the rolling, transverse and normal directions of the sheet metal. The Hill'48 model [122], is a widely used quadratic yield criterion, which is utilized especially to model anisotropic steel sheets. When reduced to planes stress condition the number of needed material parameters reduces to 3, which can be obtained by uniaxial tension tests at 0°, 45° and 90° to the rolling direction. Hill presented an enhanced version of this model in order take the equi-biaxial stress state into consideration, which is an improvement aiming accurate modeling of aluminum alloys with an additional material parameter [123]. Barlat and coworkers proposed different sets of yield functions. Yld91 takes the uniaxial yield stress values at 0°, 45° and 90°, together with the equi-biaxial yield stress as material parameters [37]. This model is followed by Yld94, Yld9Yld96 and Yld2000-2D, [33, 38, 34]. Among them Yld2000-2D is widely used and is also implemented in a number of commercial codes. This is a non-quadratic plane stress yield function having 8 material parameters which can be

identified by the yield stresses and strain ratios in three uniaxial cases, $0°$, $45°$ and $90°$ and one equi-biaxial tension case. Banabic and coworkers [27], proposed another model, BBC2000 with 7 material parameters. An improvement of this model, BBC2005, is proposed by Banabic and coworkers in [25, 26] using the same material tests with Yld2000-2D. The yield function proposed by Vegter and van den Boogaard [317] utilizes quadratic Bezier functions that are fitted to the experimentally obtained strain ratios and stresses at different orientations. This model requires 17 free material parameters when the experiments are performed at $0°$, $45°$ and $90°$. The consequence of these complex material models is the need for various test set-ups, such as uniaxial tensile test, shear test, biaxial tension test, plane strain tensile test, layer compressions test, etc. [163].

The increasing flexibility and accuracy of the yield conditions leads to an increase in the number and complexity of the necessary material tests, which are tried to be kept at feasible levels especially from the industrial point of view. Most of these tests do not have a worldwide standard, meaning that each laboratory uses its own specimen geometry and testing conditions and this makes it difficult to transfer and compare the results of different test institutes. A final disadvantage of the mentioned variety of tests is the need for an assumption of homogeneous stress and strain states in the plastic zone of the specimens, in order to be able to calculate the material parameters analytically. This assumption fails for many specimen geometries especially with increasing deformation.

On the other side, the inverse methods enable the usage of unusual test set-ups or even the forming process itself due to their flexibility in the definition of the objective functions [311]. These methods use conventionally experimental measures like tool forces and tool displacements for optimization [97, 98]. However these integral measures are not helpful in identifying the planar anisotropy of the sheet metals. To gain more information on the specimen, optical measurement devices capable of capturing strain distributions on the specimen are also employed together with inverse parameter identification [146, 194, 212, 252]. There are different approaches to assess this additional information in the characterization framework. One common approach is the virtual fields method (VFM) which relies on the virtual work principle. The application of this method to characterization problems with cyclic loads at small strains [244] and extensions to large plastic deformations with anisotropy [261] reveals that the method is an effective tool for material characterization. Another common approach is the finite element model updating method (FEMU). This perspective of parameter identification is based on kinematic full- field measurements, iterative utilization of the finite element method for the solution of the direct problem and an optimization algorithm for the minimization of the differences between the actual and computed measures. A complete overview and comparison of the mentioned approaches is given by Avril et al. [18].

The present chapter focuses on the identification of the planar anisotropy of sheet metals utilizing the FEMU approach. A flexible yield condition, Yld2000-2D is selected and material parameters are identified by using the strain field measurements on specimens with a varying cross-section. The relation between the supplied information to the inverse scheme and the obtained solutions is studied and the outcomes of this study are tested numerically and experimentally.

11.2. Material Model and Implementation

Assuming $\boldsymbol{a}$, $\boldsymbol{b}$, and $\boldsymbol{c}$ as three second order tensors, together with the Einstein's summation convention on repeated indices, $\boldsymbol{c} = \boldsymbol{a} \cdot \boldsymbol{b}$ represents the single contraction product with $c_{ik} = a_{ij}b_{jk}$. $d = \boldsymbol{a} : \boldsymbol{b}$ represents the double contraction product with $d = a_{ij}b_{ij}$ where d is a scalar. $(\dot{\bullet})$ denotes the material time derivative.

Let $\boldsymbol{d} = \mathrm{sym}\,(\boldsymbol{l})$ represent the spatial rate of deformation tensor, where $\boldsymbol{l} = \dot{\boldsymbol{F}} \cdot \boldsymbol{F}^{-1} = \partial_{\boldsymbol{x}}\boldsymbol{v}$ denotes the spatial velocity gradient, with $\boldsymbol{v} = \partial_t \boldsymbol{x}$. The kinematics of the current framework relies on the additive decomposition of the symmetric part of the rotated rate of deformation tensor, which preserves validity in the context of metal plasticity due to infinitesimal elastic strains compared to the larger plastic strains,

$$\widehat{\boldsymbol{d}} = \widehat{\boldsymbol{d}}^e + \widehat{\boldsymbol{d}}^p \,, \tag{11.2.1}$$

with $\widehat{\boldsymbol{d}}^e$ and $\widehat{\boldsymbol{d}}^p$ respectively denoting the elastic and plastic rotated rate of deformation tensors with $\widehat{\boldsymbol{d}} = \boldsymbol{R}^\top \cdot \boldsymbol{d} \cdot \boldsymbol{R}$. Here, $\boldsymbol{R}$ denotes the rotation tensor which can be derived from the deformation gradient using the polar decomposition theorem, $\boldsymbol{F} = \boldsymbol{R} \cdot \boldsymbol{U} = \boldsymbol{V} \cdot \boldsymbol{R}$ where $\boldsymbol{U}$ and $\boldsymbol{V}$ respectively denote the right and left stretch tensors. The Cauchy stress tensor, $\boldsymbol{\sigma}$, in this corotational form gives $\widehat{\boldsymbol{\sigma}} = \boldsymbol{R}^\top \cdot \boldsymbol{\sigma} \cdot \boldsymbol{R}$ where a hypoelastic relation $\dot{\widehat{\boldsymbol{\sigma}}} = \boldsymbol{\mathcal{C}}^e : \widehat{\boldsymbol{d}}^e$ is assumed with $\boldsymbol{\mathcal{C}}^e$ denoting the elastic constitutive tensor. Due to anisotropy, the yield function $\widehat{\Phi}^p(\widehat{\boldsymbol{\sigma}}, q)$ is postulated in the rotationally neutralized frame. Let $\overline{\sigma}$ denote the equivalent stress and σ_0 denote the initial yield stress in rolling direction. First, the following generic form of the yield function is defined where nonlinear isotropic hardening is taken into account

$$\widehat{\Phi}^p(\widehat{\boldsymbol{\sigma}}, q) = \overline{\sigma} - [\sigma_0 + q] \,, \tag{11.2.2}$$

where $q(\overline{\alpha})$ represents the expansion of the yield locus due to isotropic hardening where a is the isotropic hardening strain like variable. A saturation type dependence is selected, which reads

$$q(\overline{\alpha}) = K\overline{\alpha} + [\sigma_\infty - \sigma_0][1 - \exp(-\delta\overline{\alpha})] \,, \tag{11.2.3}$$

where K, σ_∞ and δ denote material parameters.

For the anisotropic yield function Yld2000-2D, the equivalent stress $\overline{\sigma}$ is defined as a degree one homogeneous function of $\widehat{\boldsymbol{\sigma}}$ as follows

$$\overline{\sigma} = \left[\frac{1}{2}\right]^{1/a} [|X_1' - X_2'| + |2X_2'' - X_1''| + |2X_1'' - X_2''|]^{1/a} \,, \tag{11.2.4}$$

where X_i' and X_i'', i=1,2,3, respectively denote the principal values of tensors $\boldsymbol{X}' = \boldsymbol{L}' \cdot \widehat{\boldsymbol{\sigma}}$ and $\boldsymbol{X}'' = \boldsymbol{L}'' \cdot \widehat{\boldsymbol{\sigma}}$ where $\boldsymbol{L}'$ and $\boldsymbol{L}''$ are defined in terms of material parameters α_i, $i = 1, 2, \ldots, 8$ as proposed by Barlat et al. [34]. Exponent a reflects the polycrystal structure.

Denoting the plastic multiplier with $\dot{\gamma}$, Normality postulate and plastic work identity gives the following evolutionary equations for $\widehat{\boldsymbol{d}}^p$ and $\dot{\overline{\alpha}}$

$$\widehat{\boldsymbol{d}}^p = \dot{\gamma}\, \partial_{\widehat{\boldsymbol{\sigma}}}\widehat{\Phi}^p(\widehat{\boldsymbol{\sigma}}, q) \,, \quad \dot{\overline{\alpha}} = \dot{\gamma} \,, \tag{11.2.5}$$

In solution of local integration algorithms in a strain driven nature of FEM, it is typical to assume that for a typical time step $\Delta t = t_{n+1} - t_n$ the solution at time t_n is known as $\{\widehat{\boldsymbol{\sigma}}_n, \widehat{\varepsilon}_n^p, \overline{\alpha}_n\}$ and

the solution at time t_{n+1} is sought for $\{\widehat{\boldsymbol{\sigma}}_{n+1}, \widehat{\varepsilon}^p_{n+1}, \overline{\alpha}_{n+1}\}$. Following integrations are defined in the rotationally neutralized coordinates

$$\Delta\widehat{\varepsilon}_{n+1} = \int_{t_n}^{t_{n+1}} \widehat{\boldsymbol{d}}\, dt\,, \quad \Delta\widehat{\varepsilon}^e_{n+1} = \int_{t_n}^{t_{n+1}} \widehat{\boldsymbol{d}}^e\, dt\,, \quad \Delta\widehat{\varepsilon}^p_{n+1} = \int_{t_n}^{t_{n+1}} \widehat{\boldsymbol{d}}^p\, dt\,, \tag{11.2.6}$$

where

$$\widehat{\varepsilon}_{n+1} = \widehat{\varepsilon}_n + \Delta\widehat{\varepsilon}_{n+1}\,, \quad \widehat{\varepsilon}^e_{n+1} = \widehat{\varepsilon}^e_n + \Delta\widehat{\varepsilon}^e_{n+1}\,, \quad \widehat{\varepsilon}^p_{n+1} = \widehat{\varepsilon}^p_n + \Delta\widehat{\varepsilon}^p_{n+1}\,. \tag{11.2.7}$$

An elastic predictor-plastic corrector type operator split is pursued, where the elastic prediction is carried out assuming the trial values, where the trial stress and yield surface expansion respectively read:

$$\begin{aligned}
\widehat{\boldsymbol{\sigma}}^{trial}_{n+1} &= \widehat{\boldsymbol{\sigma}}_n + \boldsymbol{\mathcal{C}}^e : \Delta\widehat{\varepsilon}_{n+1}\,, \\
q^{trial}_{n+1} &= K\overline{\alpha}^{trial}_{n+1} + [\sigma_\infty - \sigma_0][1 - \exp(-\delta\overline{\alpha}^{trial}_{n+1})]\,.
\end{aligned} \tag{11.2.8}$$

In above $\overline{\alpha}^{trial}_{n+1} = \overline{\alpha}_n$. Within the time step, the elastic or plastic character of the status is checked by inserting the trial stresses into the yield function, $\widehat{\Phi}^{p,trial}_{n+1} = \widehat{\Phi}^p(\widehat{\boldsymbol{\sigma}}^{trial}_{n+1}, q^{trial}_{n+1})$. Once $\widehat{\Phi}^{p,trial}_{n+1} < 0$ is satisfied, an elastic state at time t_{n+1} is defined and the trial values does not require any correction. Otherwise, plastic flow is due.

During flow, together with an implicit backward Euler integration and using $\Delta\gamma_{n+1} = \Delta t \times \dot\gamma_{n+1}$, return mapping in the residual form becomes

$$\begin{aligned}
\boldsymbol{R}^p_{n+1} &= -\widehat{\varepsilon}^p_{n+1} + \widehat{\varepsilon}^p_n + \Delta\gamma_{n+1}\partial_{\widehat{\boldsymbol{\sigma}}}\widehat{\Phi}^p_{n+1}\,, \\
R^\Phi_{n+1} &= \widehat{\Phi}^p_{n+1}\,.
\end{aligned} \tag{11.2.9}$$

Using $\Delta\widehat{\varepsilon}^{p,(k)}_{n+1} = \boldsymbol{\mathcal{C}}^{e,-1} : \Delta\widehat{\boldsymbol{\sigma}}^{(k)}_{n+1}$ where (k) is the iteration index, linearization of the equation set 11.2.9 gives

$$\begin{aligned}
\boldsymbol{0} &= \boldsymbol{R}^{p,(k)}_{n+1} + \boldsymbol{\mathcal{C}}^{e,-1} : \Delta\widehat{\boldsymbol{\sigma}}^{(k)}_{n+1} + \Delta\gamma^{(k)}_{n+1}\partial_{\widehat{\boldsymbol{\sigma}}}\widehat{\boldsymbol{r}}^{(k)}_{n+1} : \Delta\widehat{\boldsymbol{\sigma}}^{(k)}_{n+1} + \Delta\Delta\gamma^{(k)}_{n+1}\widehat{\boldsymbol{r}}^{(k)}\,, \\
0 &= R^{\Phi,(k)}_{n+1} + \widehat{\boldsymbol{r}}^{(k)}_{n+1} : \Delta\widehat{\boldsymbol{\sigma}}^{(k)}_{n+1} + [\partial_{\Delta\gamma_{n+1}}\widehat{\Phi}^{p,(k)}_{n+1}]\Delta\Delta\gamma^{(k)}_{n+1}\,.
\end{aligned} \tag{11.2.10}$$

where $\widehat{\boldsymbol{r}}^{(k)}_{n+1} = \partial_{\widehat{\boldsymbol{\sigma}}}\widehat{\Phi}^{p,(k)}_{n+1}$ and using chain rule of differentiation $\partial_{\Delta\gamma_{n+1}}\widehat{\Phi}^{p,(k)}_{n+1} = -q^{\star,(k)}_{n+1}$ with $q^\star = \partial_{\overline{\alpha}}q$ denoting the hardening modulus. $\Delta\widehat{\boldsymbol{\sigma}}^{(k)}_{n+1}$ and $\Delta\Delta\gamma^{(k)}_{n+1}$ denote iterative increments of $\widehat{\boldsymbol{\sigma}}_{n+1}$ and $\Delta\gamma_{n+1}$, respectively. Using Equation (11.2.10), one can iteratively update the incremental plastic multiplier $\Delta\gamma^{(k+1)}_{n+1}$ with

$$\Delta\gamma^{(k+1)}_{n+1} = \Delta\gamma^{(k)}_{n+1} + \Delta\Delta\gamma^{(k)}_{n+1}\,, \tag{11.2.11}$$

where computation of $\Delta\Delta\gamma^{(k)}_{n+1}$ requires a simple substitution of $\Delta\widehat{\boldsymbol{\sigma}}^{(k)}_{n+1}$ from Equation (11.2.10).1

$$\Delta\widehat{\boldsymbol{\sigma}}^{(k)}_{n+1} = -\boldsymbol{\mathcal{A}}^{(k)}_{n+1} : [\boldsymbol{R}^{p,(k)}_{n+1} + \Delta\Delta\gamma^{(k)}_{n+1}\widehat{\boldsymbol{r}}^{(k)}_{n+1}]\,, \tag{11.2.12}$$

to Equation (11.2.10).2

$$\Delta\Delta\gamma^{(k)}_{n+1} = \frac{R^{\Phi,(k)}_{n+1} - \widehat{\boldsymbol{r}}^{(k)}_{n+1} : \boldsymbol{\mathcal{A}}^{(k)}_{n+1} : \widehat{\boldsymbol{R}}^{p,(k)}_{n+1}}{\widehat{\boldsymbol{r}}^{(k)}_{n+1} : \boldsymbol{\mathcal{A}}^{(k)}_{n+1} : \widehat{\boldsymbol{r}}^{(k)}_{n+1} + q^{\star,(k)}_{n+1}}\,, \tag{11.2.13}$$

where

$$\mathcal{A}_{n+1}^{(k)} = [\mathcal{C}^{e,-1} + \Delta\gamma_{n+1}^{(k)}\partial_{\widehat{\boldsymbol{\sigma}}}\widehat{\boldsymbol{r}}_{n+1}^{(k)}]^{-1}\,. \tag{11.2.14}$$

For the analytical forms for first and second derivatives of the yield function for plane stress state the reader is referred to Yoon et al. [346]. Finally, one can compute the updated plastic strains or equivalently updated stresses using Equation (11.2.12)

$$\widehat{\boldsymbol{\sigma}}_{n+1}^{(k+1)} = \widehat{\boldsymbol{\sigma}}_{n+1}^{(k)} + \Delta\widehat{\boldsymbol{\sigma}}_{n+1}^{(k)}\,. \tag{11.2.15}$$

The iterations will run until the norm of the residuals settle within a desired tolerance. This ends the backward Euler return mapping scheme for the plastic correction which falls into a general closest point projection type algorithm, see e.g. [273]. Once the converged stresses are carried out at the rotationally neutralized configuration, a final transformation to the current configuration is required using $\boldsymbol{\sigma}_{n+1} = \boldsymbol{R}_{n+1} \cdot \widehat{\boldsymbol{\sigma}}_{n+1} \cdot \boldsymbol{R}_{n+1}^{\top}$. This framework is implemented as a VUMAT subroutine for ABAQUS/EXPLICIT.

11.3. Material and the Conventional Characterization

Throughout this chapter the aluminum alloy AA6016-T4 with 1.0 mm thickness is used. This is a heat treatable Al-Mg-Si alloy, which is especially used for autobody panels because of its good formability, surface appearance and age hardening character.

The flow curve of the material is obtained by uniaxial tension tests in rolling direction. Denoting initial and stagnation yield stresses as σ_0 and σ_∞, respectively, letting K and δ denote two material constants, during plastic flow the flow stress can be represented as

$$\overline{\sigma} = K\overline{\alpha} + \sigma_\infty - [\sigma_\infty - \sigma_0]\exp(-\delta\overline{\alpha})\,, \tag{11.3.1}$$

The conventional characterization of the sheet material for the Yld2000-2D model requires 3 tensile tests in rolling direction (0), 45 to the rolling direction (45) and transverse direction (90), and a test for the equi-biaxial stress state [34]. By each test the yield stresses and the corresponding r-values are obtained. In this study the equi-biaxial stresses are obtained with a layer compression test. Since the used test set-up does not allow the measurement of the strains in high strain values, the rb value is taken to be equal to 1.0. The yield stresses, rvalues, the corresponding Yld2000-2D parameters and the flow curve constants of AA6016-T4 can be seen in Table 11.1. As recommended in [34] for FCC materials the exponent, a, of the Yld2000-2D model is taken to be equal to 8.0.

Table 11.1.: Conventionally obtained material parameters of AA6016-T4 (all stresses in MPa).

σ_0	σ_{45}	σ_{90}	σ_b	r_0	r_{45}	r_{90}	r_b	σ_∞	
112.5	107.4	110.0	115.1	0.85	0.48	0.77	1.00	223.3	
α_1	α_2	α_3	α_4	α_5	α_6	α_7	α_8	K	δ
0.979	0.998	0.885	1.008	1.001	0.965	0.953	1.242	308.9	20.1

11.4. Selection of the Specimen Geometry

The main concern in this study is to capture the deformation field on the sheet specimen and exploit this information for the characterization of the anisotropy of the material. Therefore the specimen geometry and the type of the loading are of great importance in terms of the supplied input for the characterization scheme. This work focuses on two main aspects of the specimen geometry:

- The geometry should enable the generation of an inhomogeneous deformation field which serves as a cloud of information on yield loci for the parameter identification.

- The density of information captured on the specimen with the optical measurement system should be identical for different deformation states, rather than favoring a specific type of deformation.

For the purpose of obtaining inhomogeneity there exist two main perspectives in the literature: cutting out holes in the specimen and using notched specimens. In the case of holes, the obtained deformation localizes rapidly in the vicinity of the hole and therefore it is hard to control the deformation in that region. The abrupt localization can be captured by optical measurement systems. However this information would be a small portion of the obtained deformation on the whole specimen and this violates the second aspect mentioned at the beginning. Therefore specimen with notches is selected in this study and different specimens with a varying cross-section are analyzed numerically (Figure 11.1). In this analysis, the largest and the smallest widths, W1 and W2, are kept constant at 20 and 30 mm, respectively. Three different radius values are used to analyze the usability of the strain distributions. These values represent two extreme cases with sharp and mild notches and a case in between.
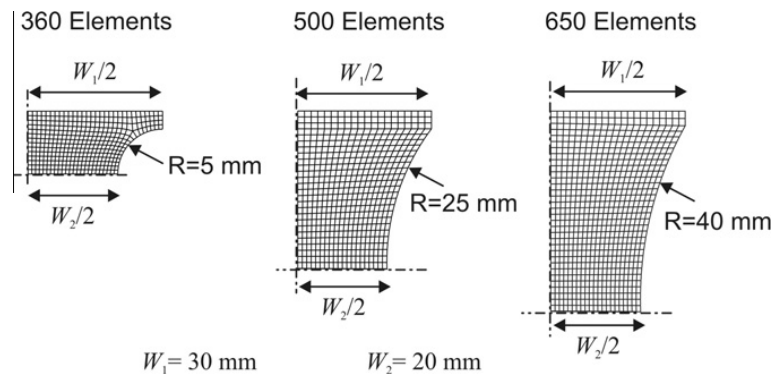
Figure 11.1.: Analyzed specimen geometries and the finite element meshes with varying notch radii.

Since the main concern here is the analysis of the deformation distribution, the numerical analyses were performed using von Mises yield criterion with isotropic hardening in ABAQUS/EXPLICIT. Due to symmetry, only 1/4 of the specimen is modeled with fully integrated shell elements having 7 integration points in the thickness direction. In each model the average element size is selected to be nearly equal to 0.5 mm after a convergence analysis, leading to approximately 20 elements on the horizontal symmetry axis. The corresponding number of elements varies from 360 to 650 depending on the geometry.

The tool displacement for each specimen is selected in such a way that an equivalent plastic strain of 0.20 is obtained at the center of the specimen, i.e. intersection of the horizontal and vertical symmetry axes. Therefore different tool displacements are used for each specimen. The value 0.20 for equivalent plastic strain represents a safe value not to exceed the limits of the uniaxial tensile test. By this way the need for extrapolation functions for the flow curve extensions is avoided and only the actually measured tensile flow curves are utilized.

Figure 11.2.a presents the equivalent plastic strain distribution on the horizontal symmetry axis. The specimen with 5 mm radius exceeds the set value 0.2 with a value of 0.5 around the notches. Therefore with this geometry it is hard to set a tool displacement, with respect to a selected maximum strain not to exceed the flow curve limits. If the tool displacements are to be set with respect to the maximum strains around the notches, the values for displacements are too small and it will be hard to analyze the deformation in different increments. Therefore the specimen with 5 mm radius is eliminated. The other two geometries have the same amount of strain hardening on the horizontal symmetry axis although the deformation state is not completely uniaxial tension. The deformation states on the specimens can be analyzed in the principal strain space which is widely used for the forming limit analyses. Figure 11.2.b shows the position of the finite elements in the principal strain space at the same tool displacements used in Figure 11.2.a for the cases with 25 and 40 mm radii. For the purpose of clearness the 5 mm radius is not shown in the figure. However, it should be noted that the different deformation states observed on the strain diagram from this specimen represents a very small portion of the specimen around the notch and therefore just like the specimens with hole it contradicts to the aspects of this study mentioned before. The specimen with 40 mm radius shows hardly a deformation gradient. Nearly almost all of the elements are in the vicinity of the uniaxial tension line presented in the figure. On the other hand, the deformation state of the specimen with 25 mm radius lies between the uniaxial tension and plane strain tension states and the distribution does not favor a certain deformation state. Because of these two reasons the specimen with 25 mm radius is selected for the rest of the study.
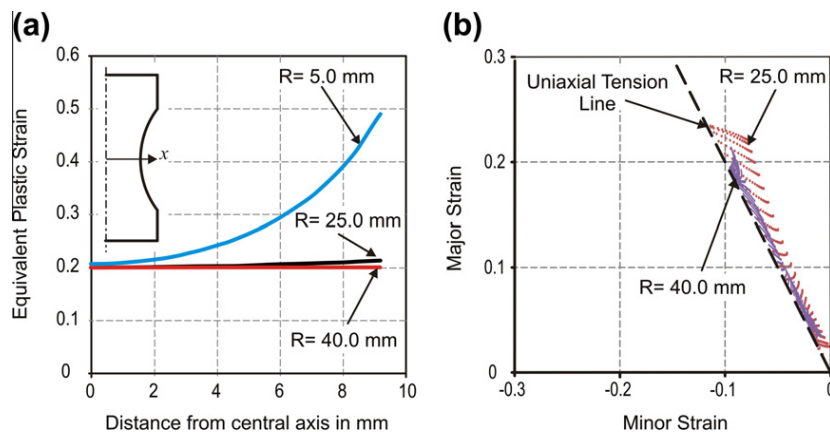
Figure 11.2.: (a) Equivalent plastic strain distribution on the horizontal centerline, (b) Principal strain distribution on the specimens with notches having 25 and 40 mm radius.

Figure 11.3 presents the major and minor strains on the specimen predicted by the finite element simulations for the material AA6016-T4 in rolling direction at the maximum tool displacement of 4 mm with the material parameters listed in Table 11.1. Again this tool displacement is set by keeping the strain hardening in the limits of the flow curves obtained by the tensile tests.
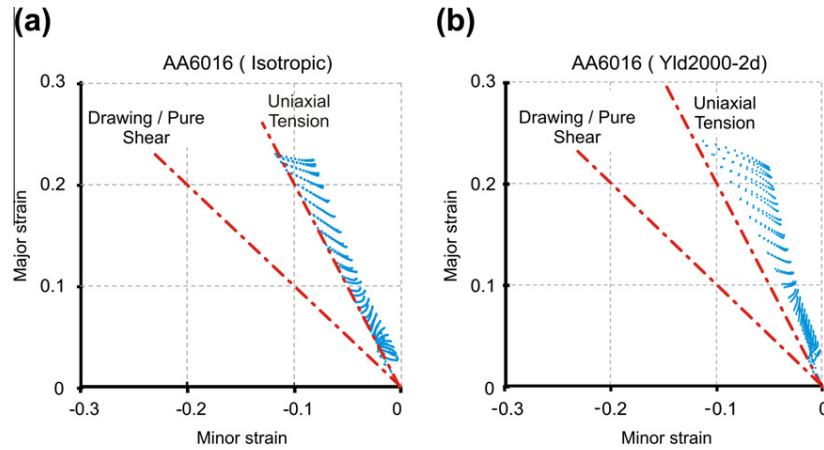
Figure 11.3.: Major and minor strain distribution obtained from the finite element simulations of AA6016-T4 for (a) isotropic and (b) anisotropic cases.

When the problem is simulated with von Mises yield condition for an isotropic case (Figure 11.3.a), the deformation is between uniaxial tension and plane strain tension states. The material points on the vertical symmetry line of the specimen lie directly on the uniaxial tension line on the strain diagram. The deformation state changes significantly when the material is simulated with Yld2000-2D material model (Figure 11.3.b). The points are shifted in the direction of plane strain tension state. This can be visualized by considering the Lankford's coefficients ($r-$values) of the material which are all lower than 1.0. In uniaxial tension case the plastic strain in the thickness direction is larger than the strains in transverse direction. This plastic behavior in uniaxial tension case shows itself also in this specimen geometry. As compared to the hypothetical isotropic case, anisotropic material does not flow much in the width direction. This shifts the strain states on the specimen closer to the plane strain tension state.

The analysis performed in this section points out three key aspects about the used geometry.

- The specimen allows different strain states between uniaxial tension and plane strain tension without losing the control on the reached highest strain hardening

- The specimen can reflect the anisotropy of the tested material with the strain distribution on the surface.

- At any instance of the test there exist material points with different strain hardening level, meaning that they lie on different yield loci.

All of these aspects can be captured with an optical strain measurement system. This information will be used to characterize the anisotropy of the sheet materials. However in terms of the parameter identification, it is not possible to obtain an analytical closed form formulation utilizing the experimentally measured local strains and tool forces. Therefore an inverse methodology is applied to solve this problem and this will be discussed in the next section.

11.5.   Inverse Parameter Identification Scheme

The parameter identification scheme in this chapter is considered as an optimization problem, in which all of the parameters are found simultaneously by minimizing an objective function

consisting of differences between the numerically computed and experimentally measured values of selected material responses. In this respect, for each increment of the optimization, finite element simulations should be performed with a new set of predicted material parameters and the results should be compared with the experimental measurements in an automated manner. In this framework the selection of the objective function, optimization algorithm and automated comparison of the results are the crucial elements and will be discussed here.

The main difficulty in comparing the results is that the discretization of the optical measurement results is different than the finite element simulations. In other words, the location, dimension and number of the facets used for the optical measurement do not match with the finite elements of the numerical simulations. In order to be able to compare the simulation results with the experiments, simulation results should be obtained at the exact location of the experimental measurement points. For that reason a parameter mapping algorithm is constructed, in which the enclosing finite element of each experimental measurement point is found according to the procedure described by Jayadevan and Narasimhan [139] and the local coordinates of the measurement points are found in these elements. By the help of the shape functions, the nodal values are interpolated to the coordinates of the measurement point. This algorithm is used at each predefined increment of tool displacement. In the analyses presented in the foregoing sections 4 mm of tool displacement is divided into 8 equal intervals. Hence, for each 0.5 mm of tool displacement the tool forces and principal strains are recorded in the experiments. At the same increments the same responses are also extracted from the simulation results and for each increment parameter mapping is applied. At the end of this step, the tool forces and principal strains of the same material points are obtained at the same tool displacement increments from the simulations and the experiment.

For the conventional characterization of the sheets with respect to Yld2000-2D material model uniaxial tension tests in $0°$, $45°$, $90°$ and a test for the equi-biaxial tension state are needed. In the previous section it was shown that the deformation obtained from the specimen lies between the uniaxial tension and plane strain tension cases. Hence, the region in the vicinity of the equi-biaxial tension state is not covered by the specimen. For that reason, to enrich the objective function, the experimentally measured equi-biaxial stress value is used. In each iteration, the equi-biaxial stress, σ_b is calculated analytically with the alpha values predicted by the optimization algorithm. The difference of this value from the experimentally measured σ_b is also added to the definition of the objective function. At the end, the objective function, Φ, consisting of 3 sub-functions having principal strains, forces and σ_b differences is defined as follows:

$$\Phi = \Phi_{\text{train}} + \Phi_{\text{force}} + \Phi_{\sigma_b}, \qquad (11.5.1)$$

where

$$\Phi_{\text{train}} = \sum_{i=1}^{n_{\text{inc}}} \sum_{j=1}^{n_{\text{elem}}} \left[[\varepsilon_{1,ij}^{\text{sim}} - \varepsilon_{1,ij}^{\text{exp}}]^2 + [\varepsilon_{2,ij}^{\text{sim}} - \varepsilon_{2,ij}^{\text{exp}}]^2 \right],$$

$$\Phi_{\text{force}} = \sum_{i=1}^{n_{\text{inc}}} [F_i^{\text{sim}} - F_i^{\text{exp}}]^2 \times C_1, \qquad (11.5.2)$$

$$\Phi_{\sigma_b} = [\sigma_b^{\text{analytical}} - \sigma_b^{\text{exp}}]^2 \times C_2.$$

where n_{inc} and n_{elem} are the number of tool displacement increments and number of elements in the optical measurements respectively. C_1 and C_2 are defined as follows:

$$C_1 = \frac{\Phi_{\text{strain}}^{\text{initial guess}}}{\Phi_{\text{force}}^{\text{initial guess}}} \quad \text{and} \quad C_2 = \frac{\Phi_{\text{strain}}^{\text{initial guess}}}{\Phi_{\sigma_b}^{\text{initial guess}}}. \qquad (11.5.3)$$

In this analysis the relative weighting between strains, forces or stresses is avoided, meaning that all these variables are equally relevant for the material characterization. For that reason the scaling factors C1 and C2 in Equation (11.5.3) are used. This scaling is performed in two steps. First a test run is performed just with the initial guesses and the contributions of the strains, forces and σ_b are calculated once. In this test run there exist orders of magnitude of difference between these values. Hence, in the second step the values of the functions of stress and forces are scaled down to the strain contributions by multiplying with a scalar. By this way, in the first increment performed with the initial guesses, the contribution of strains, forces and rb to the objective function are all equal and the same scalar values are used throughout the iterations.

Having formed the objective function, the identification procedure is now a non-linear least-square problem and the function is minimized using the Levenberg-Marquardt algorithm [180, 204]. With the introduction of a scalar controlling the magnitude and direction of the iterations, the algorithm calculates a search direction that is between the Gauss-Newton direction and steepest descent direction and therefore eliminates the disadvantages of the Gauss-Newton method especially in the proximity of the optimum solution. The needed Jacobian matrix is calculated by the finite difference method by a perturbation of each α_k with an absolute value of 0.01. Since the Levenberg-Marquardt algorithm is a gradient based algorithm, the required number of simulations to reach the convergence is not larger than 60 in most of the cases in this study, which is a considerable value as compared to the generic algorithms where one order of magnitude larger number of simulations is required. In order to automate the whole inverse scheme, a MATLAB code is written which starts finite element simulations in ABAQUS, reads the outputs of the simulations by calling a PYTHON script, compares the results with the experimental measurements, builds and minimizes the objective function. The main framework of this scheme can be seen in Figure 11.4.
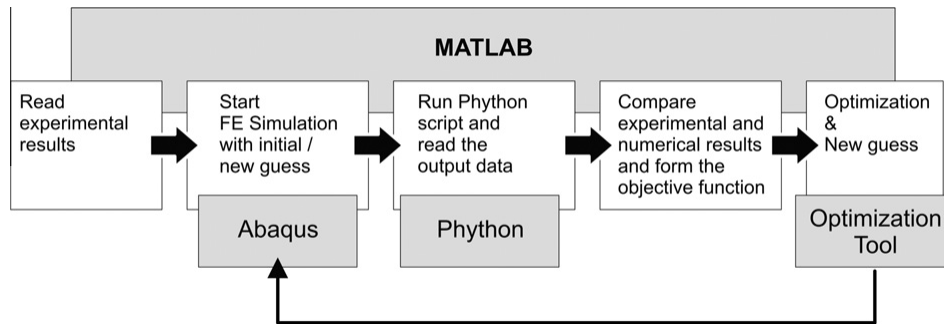
Figure 11.4.: Framework of the inverse scheme used for parameter identification.

As mentioned before the scope of this study is to identify the planar anisotropy of the sheet metals, rather than the hardening behavior. Therefore it is assumed that the flow curve is known and only the coefficients α_k are varied throughout the iterations. However, it should be noted that when all of the 8 parameters are varied simultaneously without any constraining equation, the obtained yield loci do not necessarily reflect the yield stress of the material designated by the flow curve in rolling direction. In the graphical representation, the predicted yield loci, at the horizontal axis in stress space, do not assume the value of the yield stress obtained in the rolling direction. In order to avoid this artificial scaling of the flow curve in rolling direction, following relation between the material parameters is obtained:

$$|L'_{11} - L'_{21}|^8 + |2L''_{21} + L''_{11}|^8 + |2L''_{11} + L''_{21}|^8 = 2 \,, \tag{11.5.4}$$

or in terms of the α_k,

$$\left|\frac{2\alpha_1 + \alpha_2}{3}\right|^8 + \left|\frac{2\alpha_3 - 2\alpha_4}{3}\right|^8 + \left|\frac{4\alpha_5 - \alpha_6}{3}\right|^8 = 2 , \qquad (11.5.5)$$

where the definition of the linear transformation functions L' and L'' are presented by Barlat et al. [34]. By the help of this relation one parameter becomes dependent to others and therefore only 7 of the ak are varied in the parameter identification scheme. As the initial guess, all of the parameters are set to 1.0, having an isotropic material at the beginning.

11.6.   Results and Discussion

11.6.1.   Numerical Application

In order to study the applicability of the inverse parameter identification scheme, a numerical framework is constructed. In this framework, firstly finite element simulations of the proposed specimen modeled at 0, 45 and 90 to the rolling direction are performed using the experimentally obtained Yld2000-2D parameters. The tool forces, tool displacements and principal strains on the specimen are recorded at different increments as if they were actual experimental results. The identification scheme is then applied to obtain the fictitious experiment results. Since the main concern is the planar anisotropy of the sheet, the experimental flow curve of the material is used in all simulations and it is not a part of the parameter identification. Therefore only the 7 coefficients of the Yld2000-2D model are varied throughout the identification procedure.

With this numerical framework the results of the inverse scheme are checked quantitatively by direct comparison with the input values used for the numerical experiments. As obtained from the early investigations mentioned in Section 5, a maximum tool displacement of 4.0 mm is used in order to remain in the limits of the experimental flow curve. The numerical analysis is conducted with 6 different cases and the results are tabulated in Table 11.2 in terms of the percentage errors of the predicted material parameters and the results of these cases will be discussed next.

Table 11.2.: Percentage errors of the obtained material parameters for six cases.

case	α_1	α_2	α_3	α_4	α_5	α_6	α_7	α_8
1. 0°	17.47	−24.85	−6.69	−5.51	−0.20	9.08	0.57	−5.60
2. 90°	15.42	−9.82	1.69	0.00	−5.09	9.82	−1.92	−1.67
3. 0° and 90°	−0.06	0.06	0.12	−0.01	0.00	−0.03	0.19	0.09
4. 45°	−0.50	0.94	0.92	0.02	−0.18	−0.64	−0.04	0.01
5. 45° w/o strain cont.	12.27	−12.71	−6.56	−0.44	0.32	6.80	0.24	−0.06
6. 45° w/o σ_b cont.	17.47	−19.84	−11.86	0.20	1.40	23.40	1.37	−0.95

11.6.1.1.   Case 1: Specimen in 0° to Rolling Direction

This case results in maximum errors of 25% in the predicted alphas. This is because of the deformation state of the specimen in 0, which is between the uniaxial tension and plane strain tension. In the stress space this is the region around the $x-$axis of the yield locus in the first quadrant that is also coincident with the rolling direction. Hence, the provided information

does not include any information around the vertical axis in the first quadrant. This lack of information causes the optimization algorithm to find a solution that matches around the rolling direction and biaxial point but not necessarily in the transverse direction. This fact shows itself clearly when the identification results are compared with the fictitious experiment results, as in Figure 11.5.a. There is almost a one to one match between the predicted and input yield loci between horizontal axis and biaxial point, σ_b, whereas around the 90°-tension region there are discrepancies, as a result of the errors in alphas.
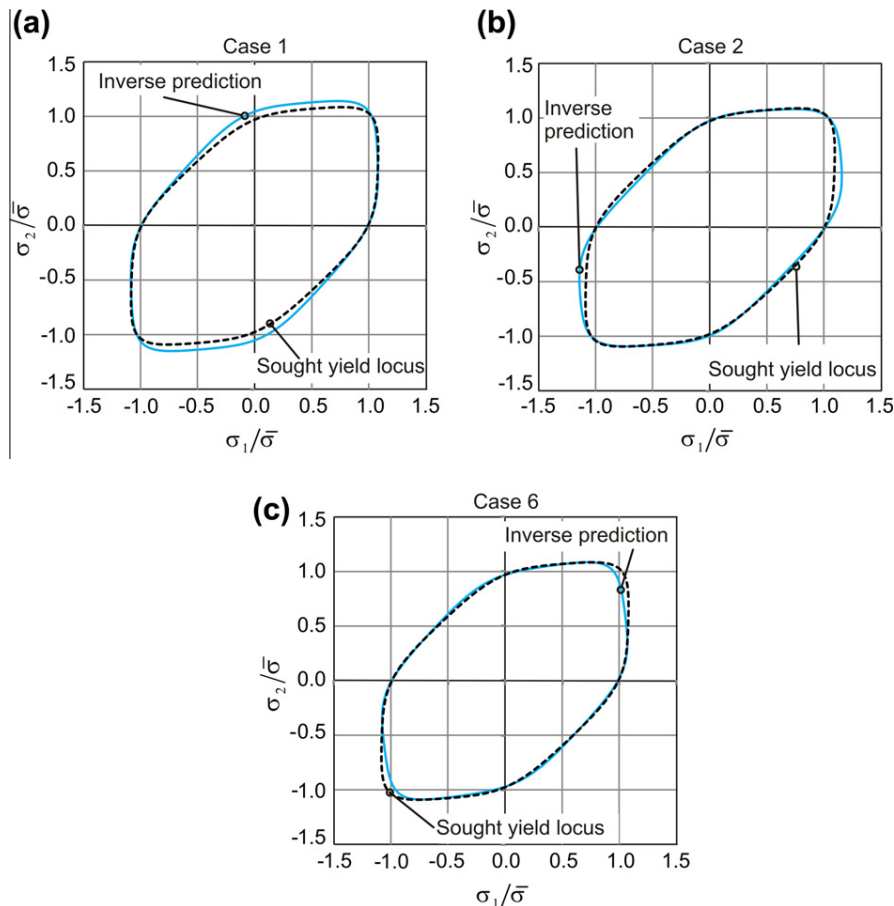
Figure 11.5.: Comparison of the predicted yield loci with the sought yield loci for the cases (a) specimen in 0° and (b) specimen in 90°, (c) specimen in 45° - without the contribution of the equi-biaxial stresses in the objective function.

11.6.1.2. Case 2: Specimen in 90° to Rolling Direction

The results with this specimen show a very similar tendency as the case 1. Again, because of the supplied information in 90°-tension region, a total match cannot be obtained for the whole first quadrant (Figure 11.5.b). The good prediction of the yield stress in rolling direction is because of the dependency of the parameters which is governed by the Equation (11.5.5). It should be noted that although the absolute value of this point is analytically correct, the slope at that point and the predictions in the neighboring plane strain tension regions are quite unsatisfactory.

11.6.1.3. Case 3: Specimens in 0° and 90° to Rolling Direction Simultaneously

This case is designed to overcome the disadvantages of the first two cases by combining them. Using the two specimens simultaneously means that at each iteration two simulations are performed, one being in 0° and one in 90°. After the simulations the elements of the objective function for each case are formed and they are scaled in such a way the contribution of the strains from the two orientations equals the contribution of the forces of the two cases and the contribution of the equi-biaxial point to form the final objective function. From the Table 11.2 it can be seen that maximum errors in this case are two orders of magnitude smaller than the first two cases and the sought alpha's are found with a maximum error of 0.2%. Hence, the enrichment of the information supplied to the inverse scheme with two orientations enabled the successful prediction of the material parameters.

11.6.1.4. Case 4: Specimen in 45° to Rolling Direction

This case is analyzed to obtain a deformation state between the first two cases. It is seen that the maximum error is less than 1% of the sought parameters. This is again the result of the supplied information to the inverse scheme. It should be noted that in the conventional characterization the coefficients α_7 and α_8 are computed from the uniaxial tension tests and therefore the predictions of this case provides the best results for these two parameters among all cases.

11.6.1.5. Case 5: Specimen in 45° to Rolling Direction without Contribution of Strains

This case is performed in order to study the impact of the principal strain field in the definition of the objective function. Therefore, in this case the principal strains are not included in the objective function. In other words, the whole inverse scheme is based on the force-displacement curve and the biaxial point. The specimen in 45° is used as it proved itself as a suitable orientation in the latter case. The maximum error in this case rises up to 13%. The direct comparison of the case 4 and 5 shows that the strain field on the specimen provides information about the planar anisotropy which helps to identify the material coefficients together with the tool forces.

11.6.1.6. Case 5: Specimen in 45° to Rolling Direction without Contribution of Equibiaxial Stress Value, σ_b

This case is designed in order to study the effect of the equibiaxial stress state in the definition of the objective function. Hence, in this case the σ_b value is not included in the objective function. The maximum error in material parameters in this case increases to 23% as compared to case 4. It can be seen in Figure 11.5.c that the equibiaxial point is not predicted correctly, as expected, with an error of 5%. It must be noted that the lack of information in the vicinity of the equibiaxial point also affects the prediction in the neighboring stress states.

The numerical analysis performed in this section does not involve any experimental noise, any violation of the assumptions like kinematic hardening or any other aspect that may arise in the experiments, building an ideal environment for characterization. For that reason the objective function takes the exact value zero, when the characterization is successful. Hence, the errors obtained in cases 1, 2, 5 and 6 would be more dominant in actual experiments. However, one to

one correlation between the predicted material parameters and the provided information about the plastic behavior remains the same. The analysis has shown clearly that it should not be expected from the inverse scheme to find a solution that covers the regions where no input is supplied. The last two cases present also the importance of the strain distribution and biaxial stress state for the characterization of the anisotropy coefficients.

11.6.2.   Experimental Application

The outcomes of the previous section will be applied experimentally in this section. For that reason specimens with the decided geometry are prepared as seen in the Figure 11.6.a. In order to measure the strains on the specimen, digital image correlation method is used. Therefore a stochastic pattern is sprayed on each specimen in order to be able to track the material points with the gray level analysis in the photos taken by digital cameras during the experiment with 1 Hz frequency. The whole optical measurement region is divided into facets having 1 mm edge length. The tests are performed on a universal tensile testing machine with a tool speed of 1.0 mm/min leading to quasi-static forming rates.
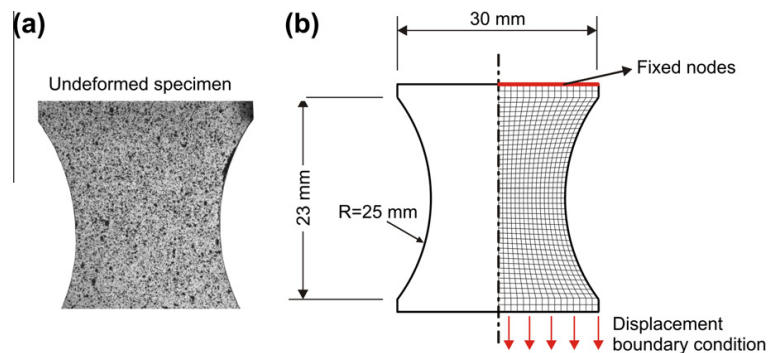
Figure 11.6.: (a) Specimen with the stochastic pattern, (b) geometry of the selected specimen and the finite element discretization.

The specimen geometry is modeled with 720 fully integrated shell elements in ABAQUS/EXPLICIT. Due to the symmetry, only one half of the geometry is modeled (Figure 11.6.b). As in the previous analyses, the tool displacement is set as 4.0 mm to remain in the limits of the experimental flow curve. Since the flow curve is known, only the material parameters of the Yld2000-2D model are varied. The relation in Equation (11.5.5) is also used here and only 7 of the free parameters are varied. The exponent a of the yield function is taken to be equal to 8.0. As in the previous section, all the parameters are set to 1.0 for the initial guess and the two successful cases in Section 6.1, case 3 and case 4, are applied in the experimental characterization

The obtained yield loci with the two cases can be seen in Figure 11.7, together with the numerical values of the material parameters presented in Table 11.3. For comparison, yield locus which is obtained conventionally from the tension tests and layer compression tests are also plotted. The difference between the absolute stress values is in both cases less than 5%. There are some dissimilarities in the slopes that can be observed around the plane strain tension regions. However, both cases can predict the initial anisotropy of the material. It should be noted that the utilized inverse scheme does not take the r-values or the yield stress of the material at different orientations as input. Nevertheless the yield stress in 90° or the slopes of the yield locus at the axes, which eventually reflect the $r-$values, are predicted correctly.

Table 11.3.: Material parameters obtained with the conventional and inverse methods.

method	α_1	α_2	α_3	α_4	α_5	α_6	α_7	α_8
conventional	0.979	0.998	0.885	1.008	1.001	0.965	0.953	1.242
45°	0.973	1.008	0.980	1.010	0.986	0.904	0.960	1.142
0° and 90°	0.977	0.977	0.987	1.020	0.989	0.900	0.981	1.114
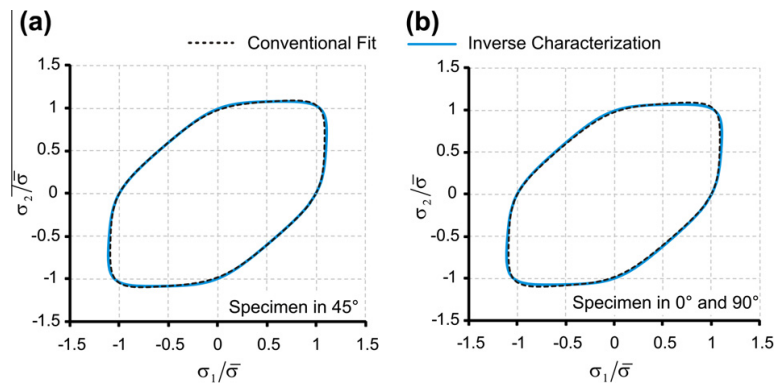
Figure 11.7.: Comparison of conventionally and inversely obtained yield loci (a) with the specimen in 0° (case 4) and (b) with the specimens in 0° and 90° (case 3).

The comparison of the force-displacement curves of the experiments and finite element simulations is presented in Figure 11.8. In both cases the numerical force predictions are higher than the experimental forces. Among all, the maximum difference occurs in the case of the 45° specimen, with a maximum difference of 10%. The deviations are even lower with the other case utilizing specimens in 0° and 90°. The force-displacement curves are directly related to the hardening behavior of the material. Hence, the difference in the force values can be due to the assumption of isotropic hardening in this study. The kinematic or distortional hardening behavior is not included in the characterization scheme. In reality the changes in the straining path during the experiments, which is the case for this specimen, can lead to different stress states and therefore to different force values.
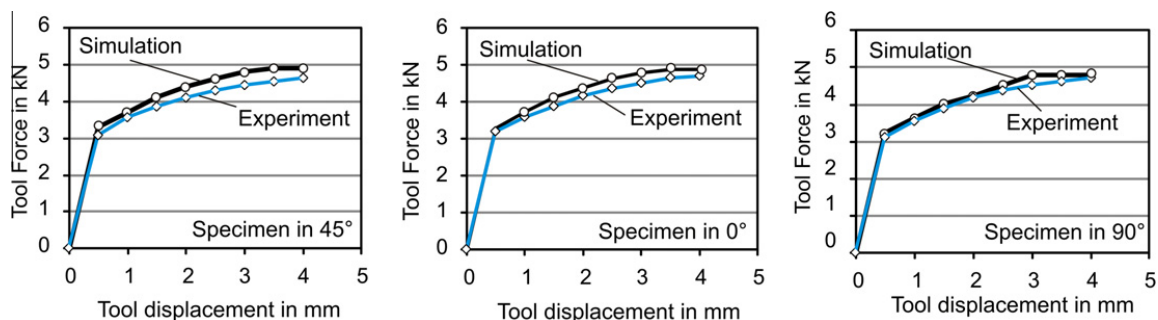
Figure 11.8.: Experimental and numerical tool force-displacement diagrams for three orientations.

The major strain distributions from the finite element simulations and experiments at a tool displacement of 4 mm can be seen in Figure 11.9 for each specimen orientation. The distribution of the strains in both cases is in accordance with the experiments. The values show some discrepancies especially on the outer edge at the horizontal symmetry axis. The numerical

results in those regions are larger than the measurements in all orientations. However it should be noted that the optical measurements do not supply information in the vicinity of the free edges because of lack of material points and therefore it is not possible to compare the results on the outer edge.
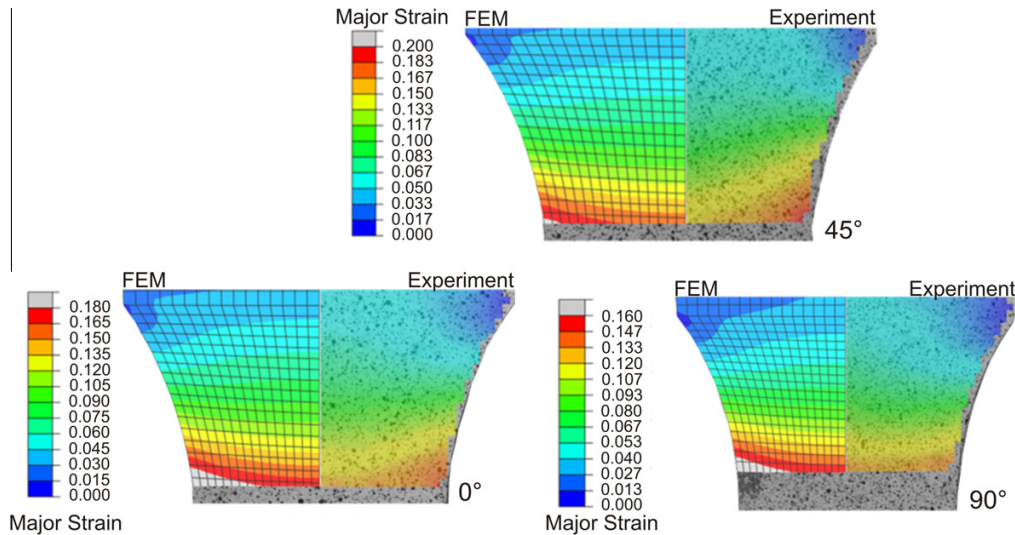
Figure 11.9.: Comparison of the experimentally and numerically obtained major strain distributions at a tool displacement of 4.0 mm for the three orientations.

The figures in this section are actually visual interpretations of the objective function that is used in the characterization, which is composed of the strain distributions, tool forces and equibiaxial stress. Since no relative weighting between these elements are applied, the inverse scheme tries to find a global minimum by considering each element equally. Hence the reached solution satisfies each condition equally as presented in the figures.

11.6.3. Experimental Verification

A representative car hood geometry, which is scaled to a smaller size, is used for verifying the obtained Yld2000-2D parameters (Figure 11.10.a). This geometry, which represents an industrial product, has side walls that flow through the drawbeads and builds a complicated pattern of deformation. All the blanks were cut from the identical charge used for the characterization section having the rolling direction along the short side of the hood geometry. In the experiments a blankholder force of 450 kN is used and the punch displacement is set to 130 mm. The strains on the outer surface of the final product are measured optically with the optical forming analysis tool, ARGUS System of the company GOM. A grid of circular dots is applied to the blank with an initial spacing of 2 mm by printing (Figure 11.10.b). These dots undergo the same deformation of the sheet and therefore the spacing of the dots is changed after the forming process which can be captured by taking the pictures of the hood by a CCD camera from different angles. The 3D positions of the centers of these dots are obtained using photogrammetric algorithms which leads to the strain tensor on the sheet surface [267].

The problem is simulated with LS-Dyna using 16000 shell elements with adaptive remeshing. Besides the Yld2000-2D model the Hill'48 model is also included in the analyses since the model is still in use as a basic model for anisotropic sheets. The yield loci of the material are shown in Figure 11.10.c with respect to the two yield conditions. At the equi-biaxial stress state, the
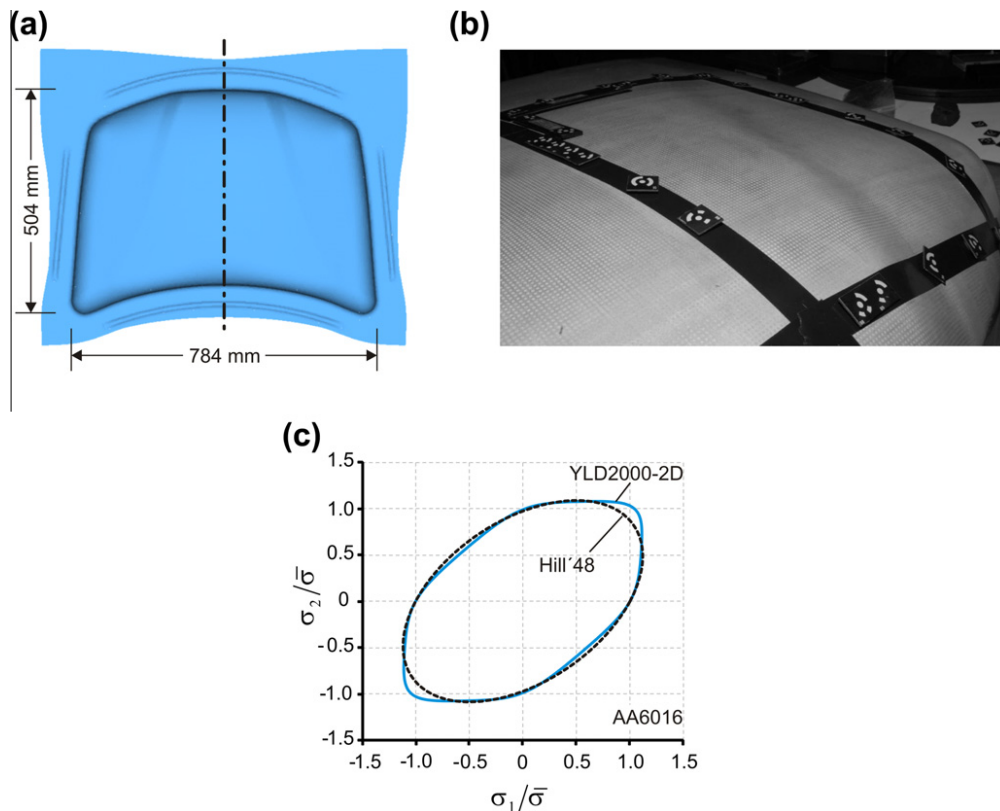
Figure 11.10.: (a) Scaled car hood geometry, (b) applied grid on the sheet surface, (c) yield locus of AA6016-T4 according to Hill'48 and Yld2000-2D material models.

two yield loci diverge from each other, since Hill'48 does not consider this stress state in the identification of the parameters.

The results of the optical measurement are compared with the numerical results (see Figure 11.11) by taking two different sections as the references. The first section cuts the workpiece diagonally and the second section goes through the rear side wall at the half height. For comparison, the thickness distributions are presented here which are calculated from the major and minor strains assuming volume constancy

Because of the large dimensions of the workpiece, strain measurements on the whole workpiece are performed by dividing the geometry in sub-sections. The gaps that are found in the figure are caused by the measurement gaps between these sections. Both models predict similar thicknesses where moderate deformations occur. It can be seen that, the plastic behavior of AA6016-T4 is oversimplified by the Hill'48 model as expected. The thicknesses in the corner regions of the geometry predicted by this model are 12% lower than the actual measurements. On the other hand, the predictions of the Yld2000-2D model tend to be closer to the measured thicknesses. The two yield loci differ from each other especially around the equi-biaxial tension state. This stress state is observed around the corner of the hood geometry where the sheet is stretched in two principal directions. The Hill'48 model predicts more thinning around these regions since the needed stresses for the plastic flow are lower compared to the Yld2000-2D model.
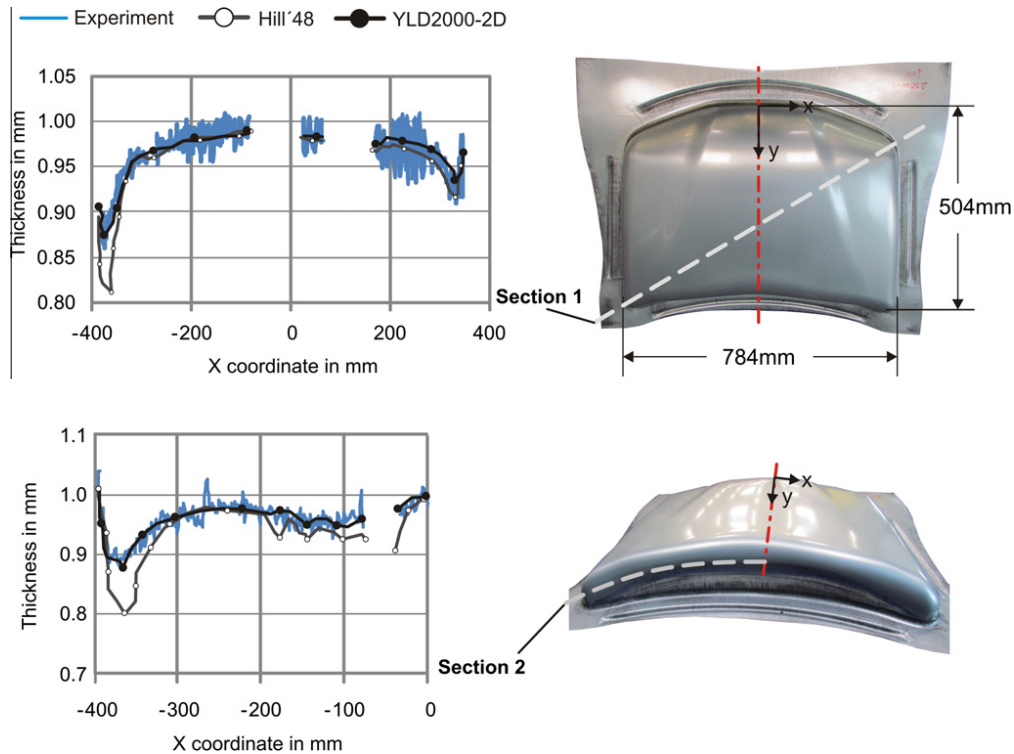
Figure 11.11.: The comparison of the thicknesses from the simulation results and the experimental measurements along two different sections.

11.6.4.   Conclusion

The appropriateness of the utilization of strain distributions for identifying the planar anisotropy is analyzed in this chapter. The utilization of an optically measured strain field together with the conventionally used integral measures such as force and displacement, improves the quality of the supplied information for an inverse parameter identification of planar anisotropy. Although it takes longer computation times, it is shown that, the usage of simultaneous experiments is possible and meaningful, if there are significant changes of material properties along different orientations. Since the flexibility of the used yield condition is an important issue, Yld2000-2D model is also implemented and used in this study. More complex yield functions that have more material parameters should be tested within this framework. The kinematic hardening is assumed to be neglected through this study. Consequently the current method cannot give accurate results, if the considered material shows a pronounced anisotropic hardening behavior. In such a case, the obtained solution would represent an average between the initial yield locus and subsequent yield loci. Therefore the proposed method has to be further developed in order to include isotropic-kinematic hardening models.

12. A Cyclic Twin Bridge Shear Test for Identification of Kinematic Hardening Parameters

In this chapter, a twin bridge cyclic shear test with in-plane torsion is proposed for identification of kinematic hardening parameters for metallic sheets. Besides its practicality, noteworthy advantages of the test are a) reduced loads on the experimental device as compared to a one-sided shear test, b) identical orientation of the principal stresses with respect to the rolling direction in both of the shear bridges, e.g. which cannot be realized by the Miyauchi shear test and c) no premature termination by instability mechanisms such as buckling or necking. Two main disadvantages appear to be a) preclusion of the use of analytically solved initial value problem in parameter identification due to diffusivity of the plastic region around the shear bridges, b) smeared out anisotropic material response proportional with the width of the shear bridge. As a remedy for the former, an inverse parameter identification methodology is used to determine the hardening parameters using an objective function devising the measured moment and rotation angle. For the latter, an optimum shear bridge width is selected which also minimizes the edge effect where shear equilibrium is not possible. A combined nonlinear isotropic and kinematic hardening model respectively based on Voce and Armstrong-Frederick is selected as the material model, which is implemented as a Vumat subroutine for Abaqus/Explicit. Strain controlled tests are conducted over three different classes of steel sheet materials, namely a mild steel DC06, a dual phase steel DP600 and a Transformation Induced Plasticity steel TRIP700. These tests with one single cycle including a forward shearing and a reverse shearing phase aimed merely the Bauschinger effect. Variations with different stress and strain based loading cycles for phenomena like shakedown, ratcheting, mean stress relaxation, cyclic hardening and softening are not explored and left beyond the scope of the current study. The results, besides showing the applicability of the test to the kinematic hardening parameter identification purposes also show that the Armstrong Frederick model falls short to capture the cyclic response of the selected materials, especially advanced high strength steels DP600 and TRIP700.

12.1. Introduction

Industrial steels show various measures of the Bauschinger effect, i.e. early re-yielding at load reversal, depending on the microstructural mechanisms playing role. At early stages of deformation, monotonic loads cumulate dislocations in front of barriers to form dislocation pile-ups. With load reversal, these are dissolved to a certain degree, with the dislocation motion diverging from the barrier. For steels with multiple phases a load reversal will cause a likely consequence, this time motivated by relative strength and flow stress of constituent phases, [127, p. 312], [243]. This kind of path dependence of hardening has a dominating effect on localization into shear bands, amount of spring-back, punch force demand, wall thickness of the sheet in sheet

metal forming, see e.g. [237] and [299] among many others, where strain path nonlinearities are common, e.g. successive bending unbending when the sheet passes the die radius. Phenomenologically this is modeled with kinematic hardening models where a translation of the yield locus in the direction of plastic loading in the principal stress space is assumed. Models developed within this context can be classified in two groups: single surface models, for example the Prager-Ziegler linear hardening rule [356], [94] or [70] and multi- or bounding surface models such as [222], [99] or [347].

Any material model, which is after prediction of a physical phenomenon comes with a cost of material constants which need to be defined, a process also known as mechanical material identification. Cyclic tests with reversed strain and/or stress paths are preferred in the evaluation of the extent of the Bauschinger effect of the material, as well as the predictive capability of the proposed material model and also in determining regarding material constants. In this chapter, a twin bridge cyclic shear test for metallic sheets with in-plane torsion is proposed for this purpose. Some positive features of the test are:

- Very practical during testing ad specimen change,

- Insensitive to geometrical instability mechanisms such as buckling or necking,

- Reduced anisotropy smearing with bridging rather then utilization of a continuous specimen,

- Supplied wide shear region with reduced edge effects,

- Reduced loads on the experimental device as compared to a one-sided shear test,

- Orientation equivalence of the principal stress triads in both of the shear bridges, which is not the case in classical Miyauchi shear test with a continuous specimen,

- Extendible for low triaxiality fracture characterization.

Nevertheless, adaption of an analytical closed form solution in parameter identification is ceased due to the nonuniform plastic strain distribution which diffuses out of the bridge. As a remedy an inverse parameter identification methodology, where the direct step is handled with finite element analysis, is developed with an objective function based on least squares of the measured and simulated torque differences for controlled tool rotation.

Proposed test and inverse methodology is conducted on three materials, namely a mild steel DC06, a dual phase steel DP600 and a Transformation Induced Plasticity Steel TRIP700. The motivation is twofold: Gathering input for parameter identification phase as well as evaluation of the extent of the Bauschinger effect that the materials show, depending on their distinct micro-structures. The mild steel DC06 is widely used for automotive components such as hood, roof or crashboxes. This deep drawing steel has a plain ferrite matrix granting a high formability. DC06 consists of only one phase and therefore shows the Bauschinger-Effect due to the dissolving of dislocation pile-ups. The DP600 and the TRIP700, both high strength steels, combine good formability and ductility with a high tensile strength. Recently, numerous research work are done analyzing these two material grades, i.e. examining the dynamic crash behavior, see e.g. [82], [238], or the springback behavior, see e.g. [237], [121]. Both steels show multiple microstructural phases, where the ferrite phase is responsible for the ductility and the martensite phase provides the high strength [190]. TRIP steels show in addition a retained autenite phase,

transforming to martensite during deformation and producing additional hardening [327], [206]. For these multiphase steels, the Bauschinger-effect may also be a result of different strengths of the phases, see e.g. [243], in addition to the relaxation of the dislocation pile-ups at other barriers. Since theoretical evaluation of these models is beyond the scope of this study, within this text Armstrong-Frederick nonlinear kinematic hardening model will be used in simulating path dependence of material hardening and early re-yielding admitting its shortcomings in predicting certain phenomena like work hardening stagnation and decreased elasticity modulus with straining.

12.2. A Critical Overview of Sheet Metal Tests for Mechanical Parameter Identification with a Specific Reference to Their Availability to Cyclic Testing

Testing techniques to identify hardening behavior of metals and other materials exist in manifold variants. A classification of these numerous methods can be done according to the loading stress state and the specimen geometry such as sheet, bulk, profiles etc. Since this chapter is focusing on sheet metals, material tests for this geometry class will be discussed in detail. In Table 12.1, several categories of sheet metal tests are listed, according to the stress state.

The most commonly used method is the uniaxial tensile test, standardized for both sheet and bulk specimen at monotonic loading. A major advantage is the known homogeneous one-dimensional stress state in the specimen, allowing accurate evaluation of material behavior by analytical equations. Cyclic testing in terms of alternately applying tension and compression is an obvious way to identify kinematic hardening behavior in form of the Bauschinger-Effect, [4]. The disadvantages of the tensile test are visible in three effects: necking, changing strain rates and buckling. Necking limits the achievable strain by tensile loading, the change in the strain rate can be compensated with some effort if required. A more important issue is the buckling tendency when compression loads are applied on a thin sheet specimen, making additional support necessary. Support against buckling can be realized in different ways as demonstrated by [294], [165], [65] and [348]. Tension-compression tests can also be conducted without supporting fixtures, when the specimen length is kept small, as shown by [329]. However, the achievable compression strain is quite low, which makes this method suitable for fatigue analysis, but partly tedious for straining behavior. In order to obtain higher strains without supporting fixtures, similar to the uniaxial test, plane-strain tensile tests can also be loaded for compression, as described by [10] and [92]. To create plane strain tensile deformation in a specimen, the width has to be designed larger so a horizontal contraction is prohibited. The experimental effort is higher than the uniaxial test, while a perfect homogeneous plane strain distribution can hardly be realized. Since the usage of plane strain tensile tests is to identify a specific point or boundary for the yield locus, this test is usually not chosen for characterizing kinematic hardening.

To identify the first quadrant of the yield locus, especially the equibiaxial-stress state, the biaxial tensile test, [118], and the hydraulic bulge test, [242], can be used. Similar to the uniaxial tensile test, the biaxial tensile and the hydraulic bulge test show changing strain rates. Both tests are not suitable for a load reversal, because of the buckling tendency in a cruciform specimen and the lacking possibility to apply any pressure from the upper side of a bulge specimen. However, the biaxial tensile test can still realize nonlinear strain paths, if the two tensile arms are controlled separately, [164].

Table 12.1.: *Overview of sheet tests - Stress state, homogeneity and suitability for cyclic testing.*

ID	Test method	Principal stress state	Stress/strain field uniformity	Reversed loading
1.	(Uniaxial) Tension-Compression test	$\begin{bmatrix} \sigma & 0 & 0 \\ 0 & 0 & 0 \\ 0 & 0 & 0 \end{bmatrix}$	Homogeneous	Limited (buckling)
2.	Biaxial tensile test	$\begin{bmatrix} a\sigma & 0 & 0 \\ 0 & b\sigma & 0 \\ 0 & 0 & 0 \end{bmatrix}$	Partly homogeneous	No
3.	Hydraulic bulge test	$\begin{bmatrix} \sigma & 0 & 0 \\ 0 & \sigma & 0 \\ 0 & 0 & 0 \end{bmatrix}$	Strain evaluated at top of specimen	No
4.	Bending test	$\begin{bmatrix} \sigma & 0 & 0 \\ 0 & \sigma/2 & 0 \\ 0 & 0 & 0 \end{bmatrix}$	Stress and strain changes through the sheet thickness	Yes
5.	Shear test	$\begin{bmatrix} \sigma & 0 & 0 \\ 0 & -\sigma & 0 \\ 0 & 0 & 0 \end{bmatrix}$	Partly homogeneous	Yes

Another alternative is loading by cyclic bending. [349] introduced a device for uniform bending, involving a rotating step motor clamping on one side of a sheet strip while the other end of the specimen is fixed on a slide rail with no degree of freedom in rotation. [99] used a three-point bending test to identify hardening parameters. To minimize friction effects, [55] suggested a contactless pure bending device for cyclic testing. A main issue of sheet bending test is the calculation of stresses, because of the different loading on the material, with higher stresses near the sheet surface and almost no load at the neutral fiber. Although bending of a narrow strip will cause a one-dimensional stress state, tension and compression occur depending on the position relative to the neutral fiber. Therefore, a stress strain curve cannot be directly extracted from any measured data, which makes inverse methods necessary. This is also the reason why bending tests are normally not used for monotonic loadings, due to the high effort for calculation of stresses.

Compared to the previously described testing techniques for cyclic loadings, shear tests have certain advantages. In-plane shearing is symmetrical for both shear directions which is a pleasant characteristic for reversed loadings. Usually, the shear deformation is realized by a translational movement of opposing edges, distorting a rectangular area to a parallelogram. It can be shown, that a shear test working as described above does have a constant strain rate, because the sheared area is not changing. This is a general advantage of all shear tests which is very important when shear tests are carried out at higher temperatures. Despite the above mentioned convenient characteristics, shear tests have to be carefully designed. The homogeneity of the shear zone is depending on its dimensions, as discussed by [58]. Due to the inhomogeneous distribution of stress and strain in the sheared area, the shear bridge width should be significantly larger than the height. In Literature, various specimen geometries and test devices were described [299], [256], [220]. Two opposing shear forces with shifted lines of action cause high reaction moments which are the reasons for high loadings in the clamps and guides. All shear tests have to cope with relative movement underneath the clamps and high experimental effort to compensate undesired reaction moments. For sheet metal characterization, the one-sided

shear test and the Miyauchi-test with two shear bridges are popular amongst other shear tests. While the Miyauchi specimen, [220], can avoid a global reaction moment by using two symmetrically arranged shear zones, identical behavior of both shear zones cannot be guaranteed because the principal stress directions are rotated by 90°. This is particularly relevant when the yield locus is shifted from the origin, which can be the result of previous plastic deformations.

Another shear test approach can be seen in the ASTM Standard B831-05. This suggested specimen uses the kinematics of a tensile test and realizes the shear deformation by diagonal slits in the sample geometry. [211] used a modified geometry based on this specimen for cyclic shear testing of sheet metals. The experimental effort can be reduced because the clamping devices are located at the upper and lower ends far away from the shear gauges and therefore only loaded by normal forces almost without rotation moments. Still, the specimen may show rotation of the shear gauge at larger deformation and buckling at compression loads, which make additional supporting devices necessary. Buckling for compression loads can be prevented by supporting devices without applying friction on the shear zone itself.

The plane torsion test, firstly introduced by [199] and further developed by [250] and [43], is an alternative way to load a sheet specimen by in plane shearing. Plane torsion is applied on a round sheet specimen by rotating the inner part against the outer rim. The free area in between is deformed partly, whereas the highest stress and strains occur near the inner clamps. To conduct cyclic plane torsion tests, [199] used distorted radial lines to track the deformation history. [341] proposed a more efficient way to analyze cyclic plane torsion tests using digital image correlation, which is able to obtain multiple cyclic shear curves from one single specimen tested. The plane torsion test creates a high information density on every specimen due to the gradient of stress and strain over the radius. A disadvantage is the distribution of load over the whole circumference, averaging any effect of the anisotropy.

12.3.   Twin Bridge Shear Specimen

Based on the plane torsion test described in the previous section, [61] introduced a modified geometry with two shear bridges as shown in Figure 12.1(a). Two round slits are cut out of the material, thus the shear deformation is localized in the two bridges, when the outer grip is twisted in-plane against the inner grip, as can be seen in Figure 12.2(a). Compared to the full specimen for the in-plane torsion test, an averaging of the anisotropic behavior over the whole circumference is avoided. By arranging two identical shear zones on opposing positions, the specimen can be twisted stably while the shear direction is the same relative to the rolling direction. Figure 12.2(b) shows the characteristic geometrical features of a shear zone.

The width of the shear zone is defined by the angle and the radius r_m of the slits. In the following, the dimensions of the twin bridge specimen is chosen as:

$$r_m = 21.5 \text{ mm}, \quad \Delta r = 1 \text{ mm}, \quad \Delta \vartheta = 20°, \quad t = 1 \text{ mm}. \tag{12.3.1}$$

The radius of the inner clamps is 15 mm, the radius of the outer clamps is 30 mm. A specimen is shown in Figure 12.1(b). Depending on the arrangement of the slit geometry and slit position, linearization of the kinematic relations can be applied to receive equations for the shear stress and shear strain:

$$\gamma = \tan(\alpha) = \frac{\theta r_m}{\Delta r}, \quad \tau = \frac{M}{2t\Delta\vartheta r_m^2}. \tag{12.3.2}$$

(a) Geometry.   (b) Specimen.
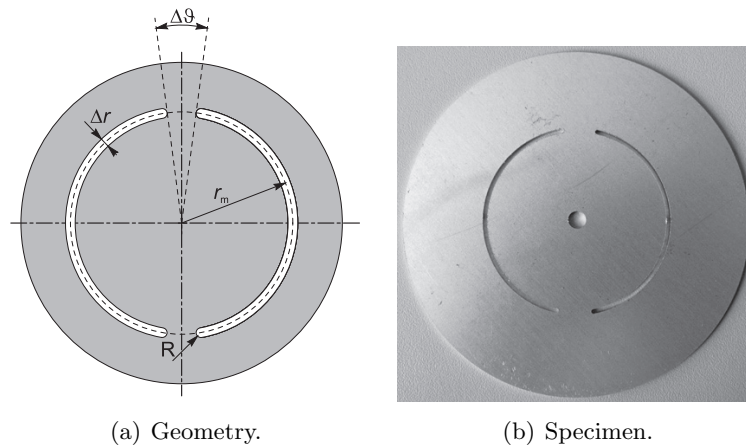
Figure 12.1.: Twin bridge shear specimen based on the in-plane torsion test.

(a) Schematic design of the test.   (b) Shear zone.
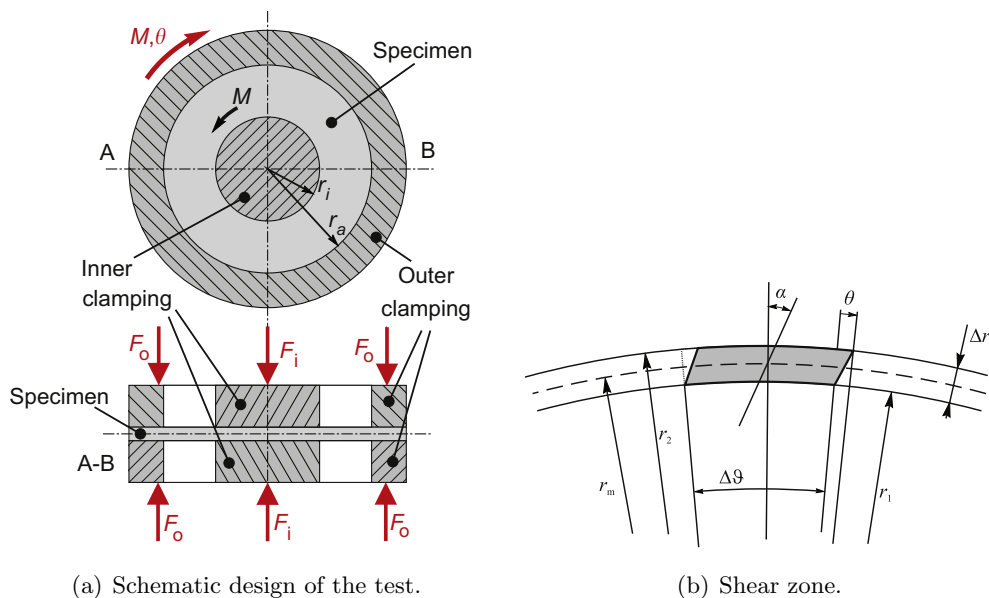
Figure 12.2.: Clamping of the specimen and shear zone geometry.

In Table 12.2, an overview of the previously described shear tests are given. Compared to these available tests, the twin bridge shear test avoids the drawbacks for each test. It does not show unwanted reaction moments because the torque moment is already the applied loading, it shows identical behavior for both shear zones, it has no limitations in compression load like the specimen according to the ASTM standard, and it does not average the influence of the anisotropy like the conventional in-plane torsion test.

In a numerical analysis of the specimen the deformation field is shown in Figures 12.3(a) and 12.4(a) for rotation angles of 0.5° and 2.7°. The regions with an equivalent plastic strain of 0.005 or more is colored. Two issues can be analyzed when considering these figures. Firstly, due to the inhomogeneous distribution of strains, not all parts of the shear zone is loaded by ideal shearing. In Figures 12.3(b) and 12.4(b), the strain of each element is drawn in the principal strain plane. The green area represents the pure shear deformation. As can be seen there, the major part between the slits can be seen as pure shear, while the deviations at the edges remain

Table 12.2.: Overview of shear tests.

ID	Shear test variant	Experimental characteristics	Load characteristics in shear zone
1.	Single-side	High load on clamps, unwanted rotation moment	Simple shear
2.	Miyauchi	Two symmetrical shear zones provide more stability	Shear zones under different load directions
3.	ASTM B831-05	Conducted like a tensile test, buckling tendency and limitations in compression	Rotation of the shear zone at larger strains
4.	In-plane torsion	In-plane rotation of sheet, high strains achievable	Measured torque is averaged over whole circumference for anisotropy
5.	Twin bridge shear test	Like the in-plane torsion test, reduced loads, no unwanted reaction moments	No averaging over anisotropy, both bridges loaded in the same direction

small. The second issue is the diffuse outspread of plastic deformation to the surrounding regions of the shear gauge.

<center>(a)   (b)</center>
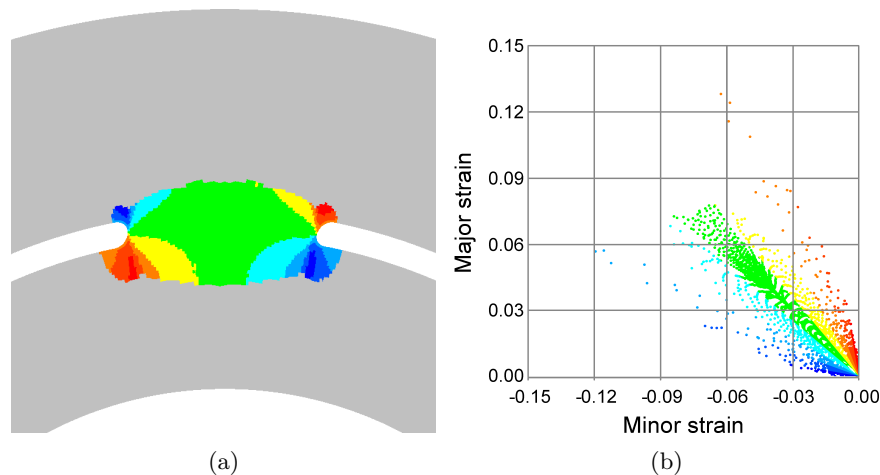
Figure 12.3.: Development of shear strain at rotation angle θ = 0.5°: (a) Contours for strain ratio, (b) Strain components in major principal directions.

As a result, Equation (12.3.2) cannot be applied to obtain correct strain values. The calculated strains will be larger compared to the real plastic shear strain in the shear zone, as shown in Figure 12.5(a). For DC06 and DP600, the measured shear strain using digital image correlation is compared to the theoretical values according to Equation (12.3.2). With increasing rotation angle θ, significantly lower curves are measured for both materials. In Figure 12.5(b), the quotient of measured shear strain and calculated shear strain is plotted over θ. Here, the differences between DC06 and DP600 become visible. While DC06 shows an almost constant quotient of 0.4, the quotient for DP600 is smoothly increasing until this value due to its different hardening behavior. It is obvious that a direct calculation of strains cannot be done from the
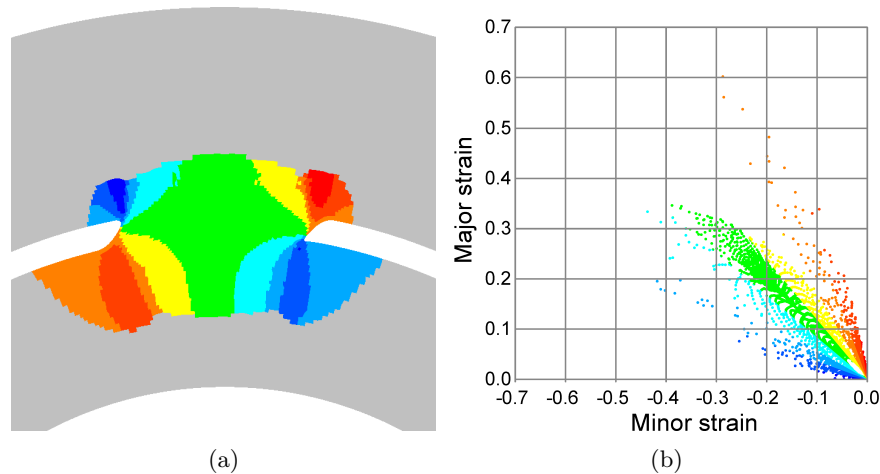
Figure 12.4.: Development of shear strain at rotation angle θ = 2.7°: (a) Contours for strain ratio, (b) Strain components in major principal directions.

measured rotation angle. However, Equation (12.3.2) is not affected by the elastic deformation and thus is applicable for the shear stress τ.
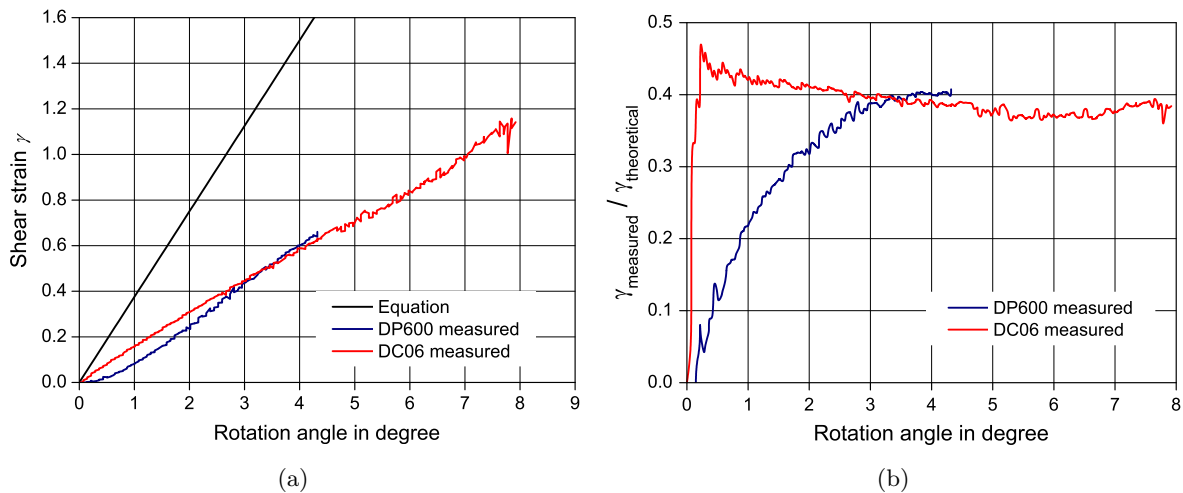
Figure 12.5.: (a) Comparison of measured to theoretically calculated shear strain, (b) Development of the quotient of measured shear strain to calculated shear strain.

There are several possibilities to avoid or minimize errors in the strain data when conducting the twin bridge test. One approach can be measuring the shear strain by digital image correlation. This would provide direct information from the shear zone without involving the rotation angle but requires higher experimental effort in specimen preparation and calibration of the measurement devices. Another way is to position the clamping in direct proximity of the shear bridges, leaving no free space around it. This would reduce the diffuse plastic region beneath the shear bridge, but is not able to complectly prevent erroneous strain calculation using the rotation angle due to slipping underneath the clamps. Such a clamping leaving only a small gap would complicate optical strain measurements during testing. Instead of clamping the free area to avoid diffuse deformation outspread next to the shear bridge, a weakening of the shear bridge by reducing the sheet thickness locally will also lead to a more concentrated deformation field

in the desired region. However, cutting out material in order to reduce the sheet thickness is an expensive procedure, increasing the preparation time and cost for each specimen considerably. A completely different solution would be an inverse approach to determine material parameters directly without any measured strain information, only using the measured data of torque, angle and a finite element model. Especially for a model which involves combined isotropic and kinematic hardening behavior, this strategy would be most effective, since no additional measurement and experimental devices need to be set up or modified.

The experimental device is identical to the setup of the standard in-plane torsion test described by [341], as shown in Figure 12.6. A ZWICK universal testing machine realizes the inner clamping force, while the outer clamps are tightened by screws. The moment is provided by a servo motor and a worm gear. The rotation is applied on the outer parts of the device, while the inner clamps are fixed and loaded by the universal testing machine. During testing, the rotation angle and the torque moment are measured at a sampling rate of 5 Hz.
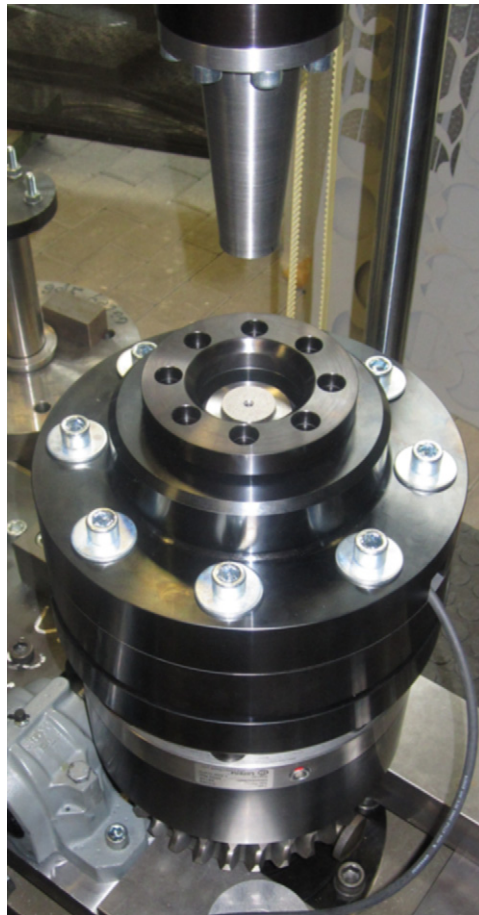
Figure 12.6.: Experimental device for the twin bridge shear test.

The Experiments were conducted for one single straining cycle, at first twisting until a certain rotation angle and then twisting back until the rotation angle is 0° again. The strain rate resulting from the rotation speed is about $\dot{\gamma} \simeq 0.01$ per second.

12.4. Inverse Parameter Identification Scheme

As in many sheet metal characterization tests like Miyauchi test or plane strain tension test, the proposed twin bridge shear test has a plastic deformation zone which loses its homogeneity with the increasing deformation. This makes it difficult to apply analytical methods to calculate the strain and stresses in the plastic zone from the measured moments and rotation angles. In addition, the twin bridge shear test show a diffuse plastic region around the shear bridge which does not allow the application of a analytical equation to calculate the strain using the rotation angle, as described above. Therefore an inverse parameter identification scheme is utilized to obtain the material parameters. Inverse methods enable the usage of unusual test set-ups or even the forming process itself [311], since the assumption of homogeneous deformation fields is not needed anymore. The application of this method in the field of metal forming makes use of the experimental measures like tool forces and tool displacements, [97] and [98]. The implemented scheme in this chapter identifies the material parameters in an iterative way, in which for each iteration a finite element simulation is run and the numerical results are compared to the experimental ones.

As the reference, the moment-angle curves of the experiments are used. In order to form the objective function which is minimized by the optimization algorithm the experimental and numerical curves having different discretizations are linearly interpolated at the same rotation angle values. For each forward and backward curve 100 integration intervals are used, adding up to 200 data points for one cycle. No relative weighting between the forward and backward curves is applied. The objective function is then formed by calculating the differences in moments at the same shear angles and adding the squares of differences. By this way the objective function is formed as follows:

$$\Phi = \Phi_{\text{forward}} + \Phi_{\text{backward}}, \tag{12.4.1}$$

where the additive components Φ_{forward} and Φ_{backward} are

$$\Phi_{\text{forward}} = \sum_{i=1}^{n_f} \left[\frac{M_{\text{exp},i} - M_{\text{sim},i}}{M_{\text{elastic}}} \right]^2 \quad \text{and} \quad \Phi_{\text{backward}} = \sum_{i=1}^{n_b} \left[\frac{M_{\text{exp},i} - M_{\text{sim},i}}{M_{\text{elastic}}} \right]^2. \tag{12.4.2}$$

In order to minimize the objective function the Trust Region Reflective Method is utilized which suits itself to nonlinear least square optimization problems, [80] and [81]. The optimization process involves the approximate solution of a large linear system based on the method of preconditioned conjugate gradients (PCG).

The finite element model that is to be run in each iteration is constructed in ABAQUS/EXPLICIT, see Figure 12.7, with 4676 shell elements with reduced integration.

In order to automate the whole optimization process a MATLAB code is written which starts the ABAQUS simulations, reads the outputs by calling a PYTHON script, compares the results with the experimental measurements, builds and minimizes the objective function, Figure 12.8.

The used material model is an Armstrong-Frederick Kinematic Hardening model whose details are given in the appendices. Material Parameters are (Voce+AF):

$$q(\alpha) = K\alpha + [\sigma^\infty - \sigma^0][1 - \exp(-\delta\alpha)]. \tag{12.4.3}$$

The initial yield stress values, σ^0, of the analyzed materials are obtained from the uniaxial tension tests in the rolling direction and they are set as constants. Only the remaining 4 material parameters are varied along the iterations. As the initial guess, the same values are given for
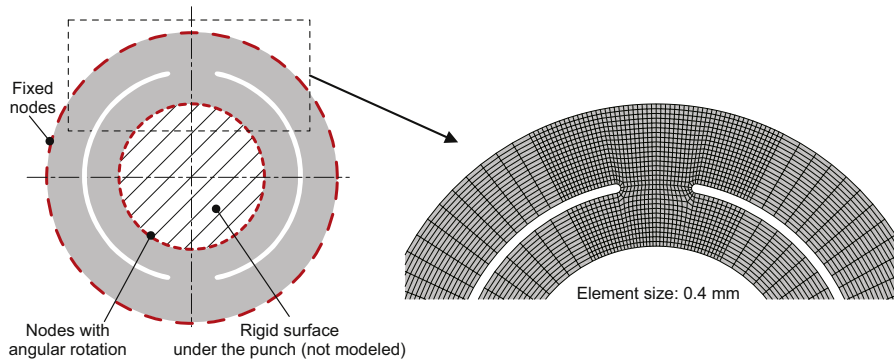
Figure 12.7.: Finite element model of the proposed specimen.
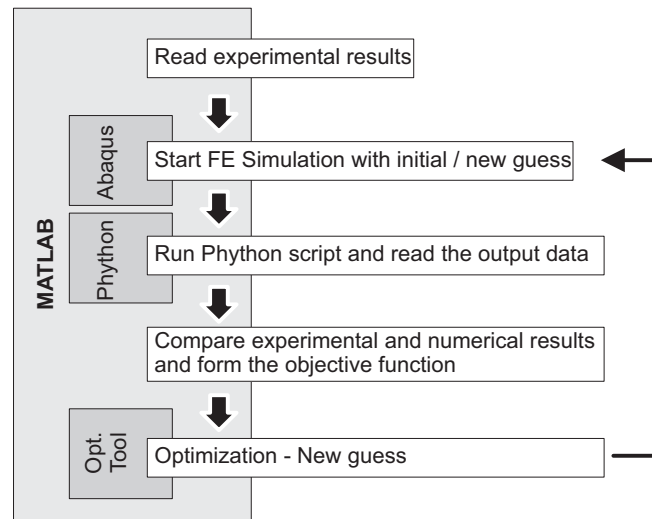
Figure 12.8.: Framework of the optimization algorithm.

each material. These values are selected in such a way that they only represent the expected order of magnitudes of the parameters. Therefore for the stress-like measures $\sigma^\infty = 100$, $C = 100$ and $Q = 100$ and for the exponent $\delta = 10$ are selected as the initial guesses.

Throughout the analysis the progress of the values of the objective function and material parameters are tracked in order to check whether the parameters converge to a stable value. The normalized values of the material parameters and the objective function for the case of DP600 can be seen in Figure 12.9. The objective function is reduced drastically after 30 iterations being equal to 0.4% of the initial value. However, the iterations go on and after 80 iterations the minimum is reached with 0.2% of the initial value. After this point the algorithm perturbates the parameters (peaks in the figure) and go back again to the values obtained at 80th iteration and the change in the material parameters is less than 0.1%. The values at that point are used as the result of the parameter identification procedure.The development of the material parameters of TRIP700 shows a similar behavior. In the case of DC06 the objective function is reduced more rapidly compared to the DP600. Just after 25 iterations the objective function value is reduced to 0.1% of its initial value. After this point the change in the guessed material parameters merely consists of the perturbations of the optimization algorithm.

(a)

(b)

(c)
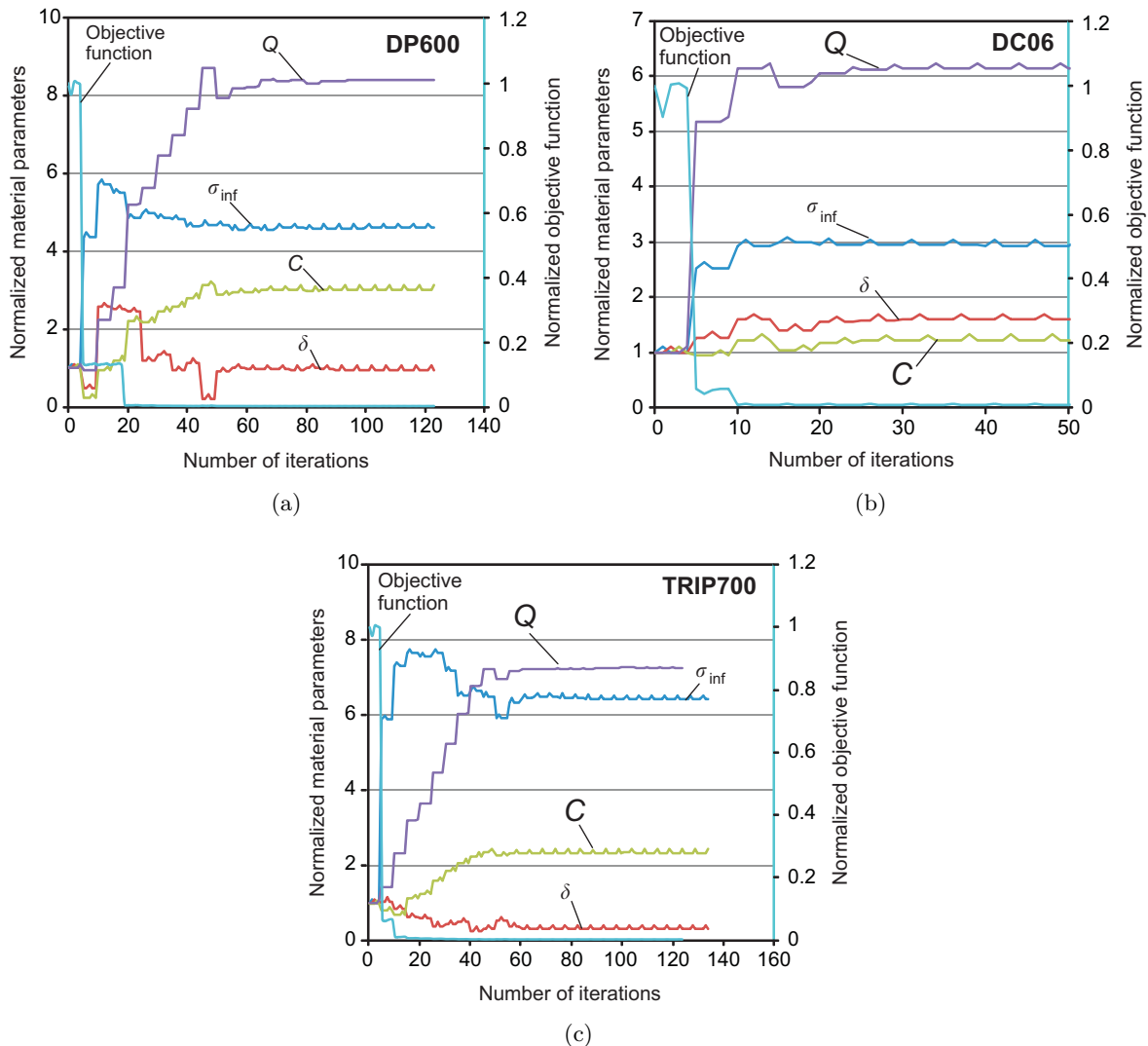
Figure 12.9.: Course of the material parameters and objective functions along the iterations for DP600, DC06 and TRIP700.

12.5.   Results and Discussion

The measured results of the cyclic experiments and the corresponding results from the parameter identification can be seen in the Figures 12.10(a), 12.10(b) and 12.10(c). Each diagram contains three curves showing the moment over the rotation angle. Although the experimental curves are resulting from the measured moment and rotation angle, they show the same characteristics as a material stress strain curve. After an linear increase representing the elastic zone, the plastic hardening is also reproduced. The elastic unloading and load reversal show smooth transition and a lower moment measured after the re-yielding.

The experimental results can be compared to the identified material parameters according to the combined hardening model and the model showing only pure isotropic hardening. To obtain the curve for isotropic hardening, the kinematic parts of the material model was set inactive, while the experimental data is considered for the initial monotonic loading until the point of load reversal. This would represent the default material model of the common finite element codes,

(a) DC06.

(b) DP600.

(c) TRIP700.
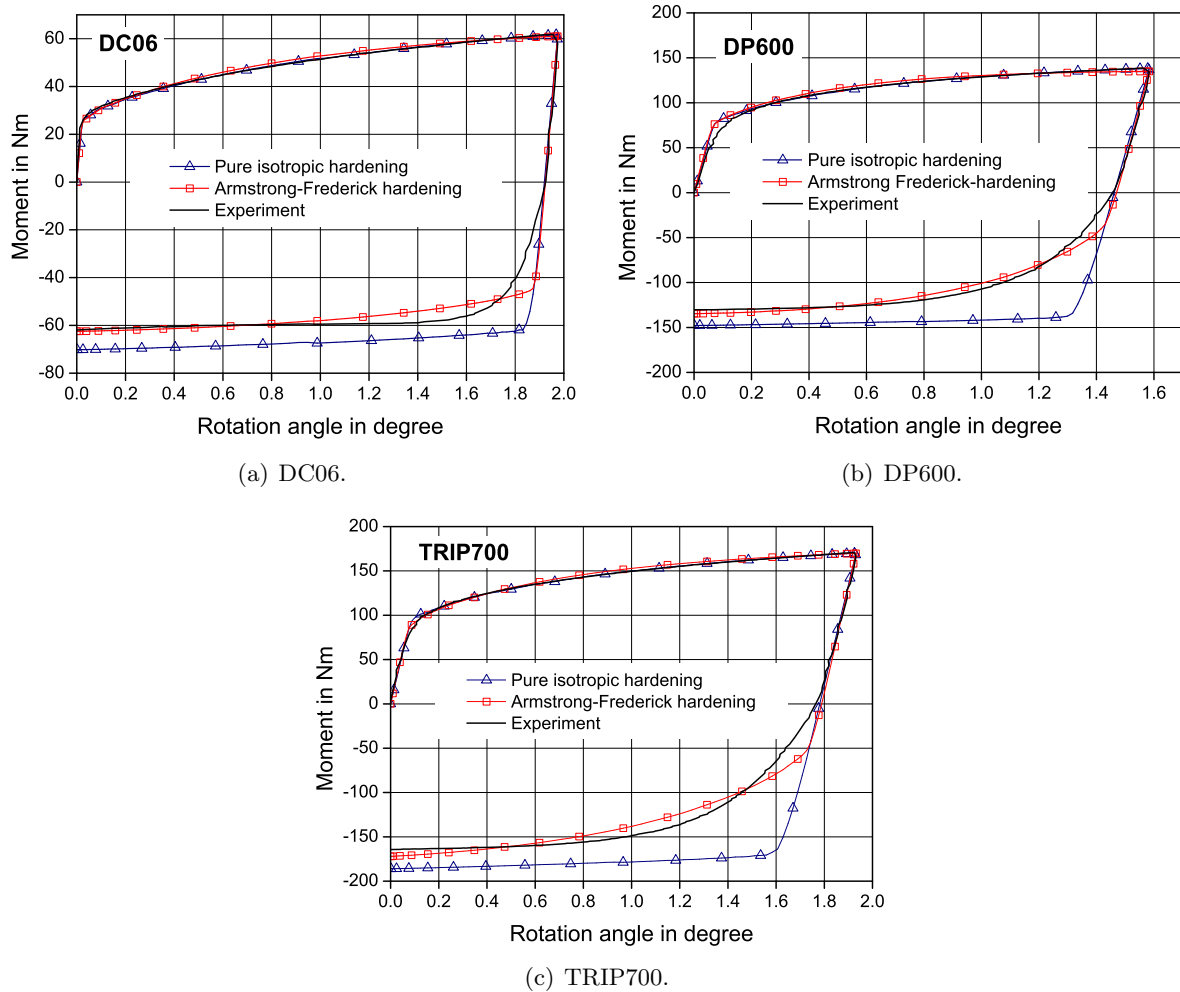
Figure 12.10.: Resultant curves for cyclic shearing.

when no kinematic hardening is considered. In the case of the deep drawing steel DC06 the monotonic hardening can be reproduced correctly by both models. During load reversal, both models miss the smooth transition which begins at about -10 Nm. The resolved curves stick to a linear elastic unloading path. However, the combined modeling is able to fit the material behavior again after a certain amount of reversed shearing. It is noticeable that the isotropic and combined kinematic hardening curves are almost parallel after re-yielding.

The DP600 alloy was not predicted well at the initial hardening phase. It seems that the first transition between elastic and plastic deformation is smooth already, which may be the result of the dual phase structure with different yield strengths. The response at the load reversal point shows again a much better result by the combined hardening model, while the isotropic hardening model clearly overestimates the stress for re-yielding. TRIP700 was better reproduced at the initial hardening zone compared to DP600, although it has a multiphase microstructure, too. The combined model again is significantly better at the transition zone at load reversal, however not perfectly fitting again as for the other materials. It is obvious that all three steels exhibit a certain portion of kinematic hardening, showing a smooth transition at re-yielding and a lower stress level during the reversal of the shear deformation. As a summary, the obtained parameter values are listed in Table 12.3.

Since moment and angle curves are integral values they do not directly provide any information about the strain distribution inside the shear zone. However, it can be shown that the strain distribution is correctly predicted in the numerical simulation during the parameter identification process. In Fig. 12, the major strains are compared for DC06 between an optical measurement and the numerical calculation during the last iteration of the parameter identification procedure. Figure 12.11(c) shows the position and direction of the longitudinal and transverse cut. In Figures 12.11(a) and 12.11(b) the major strain is drawn over the cut length for the rotation angles $\theta = 1°$ and $\theta = 2°$. Considering the strain state in Figs. 3 and 4, shear condition can be assumed on the section cuts, leading to the same but negative values for the minor strains. For both cuts, a good agreement between simulation and experimental results can beseen. The longitudinal cut shows lower strains in the center and increasing strain to the outer regions and a decrease again next to the edges, where the optical strain measurement cannot provide reliable data anymore. The transverse cut shows the highest strain in the center and decreasing values on both sides. Therefore, the proposed method is capable of correctly predicting the inhomogeneity within the shear zone, allowing reliable parameter identification only using moment and angle data.

(a)

(b)

(c)
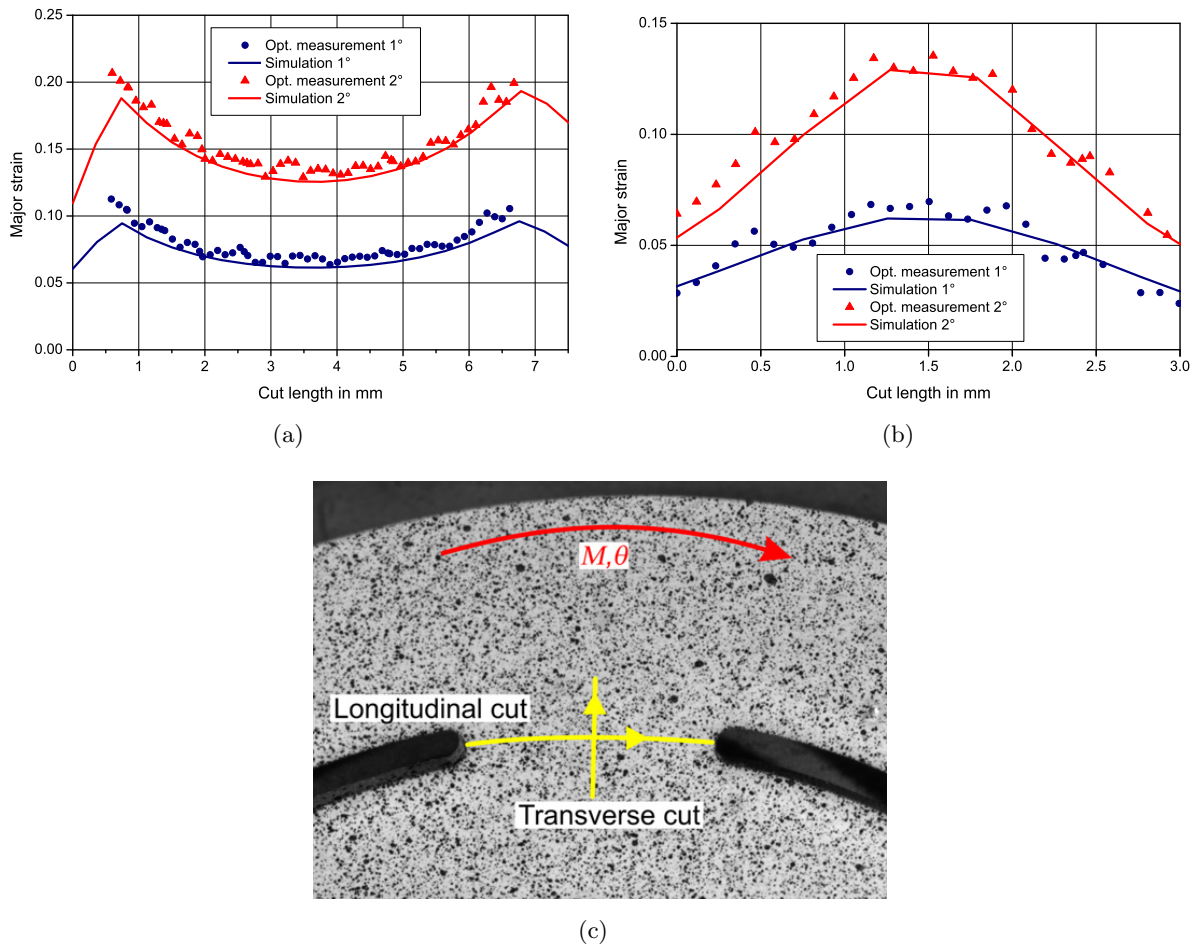
Figure 12.11.: Comparison of major strains in the shear zone between optical strain measurement and numerical analysis for DC06. (a) longitudinal section cut; (b) transverse section cut; (c) position of sections.

In the Figures 12.12(a), 12.12(b) and 12.12(c), the stress strain curve at monotonic uniaxial

tensile loading according the identified parameters is drawn and compared to experimental data obtained by uniaxial tensile tests. It can be seen that good accordance between the curves can be found for DC06 and DP600. TRIP700 shows less hardening in the experiment, while the initial hardening zone was predicted correctly. The differences found in the comparison to monotonic flow curves may be the result of anisotropic yielding of the material and the different hardening behavior of the sheets at shear and uniaxial tensile loading.

(a) DC06.

(b) DP600.

(c) TRIP700.
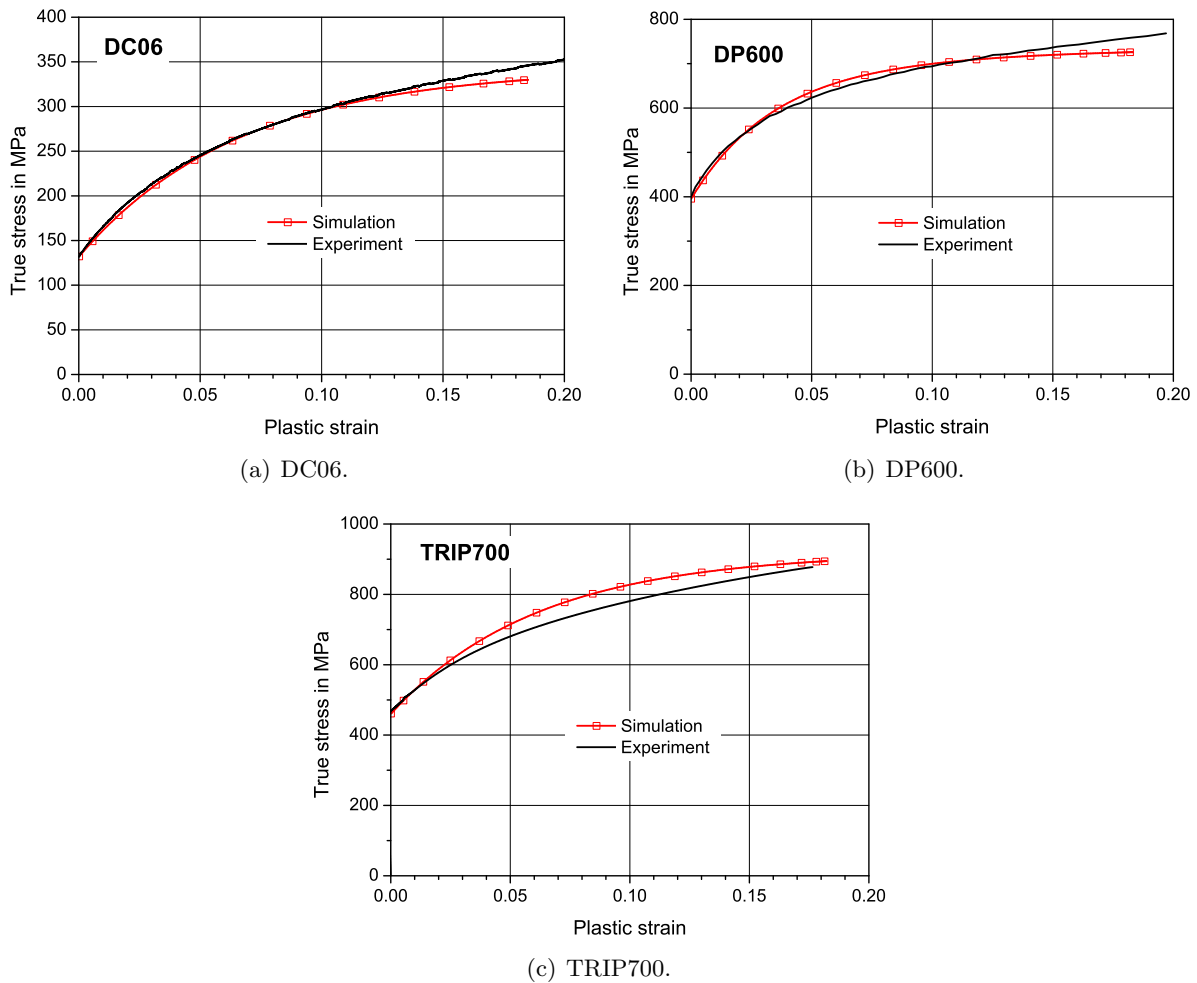
Figure 12.12.: Comparison of calculated monotonic flow curves to experimental flow curves.

The results of these three tested steel sheet materials show the principal suitability of the plane torsion test to identify material parameters for the kinematic hardening models. However, a perfect match in the re-yielding phase failed for all materials. The reason can be found in the limitations of the chosen material model, i.e. by the Armstrong-Frederick hardening rule.

Table 12.3.: Identified material parameters for the combined isotropic-kinematic hardening model.

ID	Material	σ_0 (fixed) (MPa)	σ_∞ (MPa)	δ	C	Q
1.	DC06	132	293.31	16.04	12.23	613.51
2.	DP600	395	460.35	9.60	30.26	8408.43
3.	TRIP700	460	283.51	7.37	77.86	5285.62

12.6. Conclusion and Future Perspectives

A twin bridge cyclic shear test for metallic sheets with in-plane torsion is proposed for path dependent hardening investigation. With a critical comparison with other known sheet metal tests including ones with shear state of stress the advantages and the disadvantages of the current proposal are explained. Depicted parameter identification methodology follows an inverse approach where simulations devise finite element method due to intrinsic limitations pertaining to diffuse structure of plastic flow. Bauschinger effect in three classes of steels with distinct micro-structures, namely DC06, DP600 and TRIP700, are evaluated by the proposed test and the parameters for the selected combined (Voce type nonlinear) isotropic (Armstrong Frederick nonlinear) are quantified. Although the smooth re-yielding cannot be fully reproduced, this being a limitation of the selected material model, proposed test proves to be an efficient one for identification of Bauschinger effect and relevant phenomena. Accordingly it is plausible to expect better fits in combination with a more appropriate material model selection of which was left beyond the aim of this study. As a future study, the drawback of diffuse plastic flow pattern can be remedied by mechanically weakening the specimen bridge (relative to the rest of the specimen) to localize plastic flow. Numerical investigations show that such geometries let one use accurately the analytically derived closed form solutions, which eliminates the need for relatively computationally costly finite element analysis. This can be supplied by reducing the sheet thickness locally with subtractive processes like milling, or stiffening the unclamped area with e.g. complete tool coverage. At first sight, uncertainties regarding the material mechanical properties with subtraction processes and slipping in tool-specimen interface seems to be the problems deserving further attention. The test also constitutes a promising potential for low triaxiality fracture parameter identification, which is the subject of a growing interest in the literature, see e.g. [224, 338] and [29].

12.A. Armstrong-Frederick Kinematic Hardening Model

In the following equations pertaining the implemented combined isotropic-kinematic hardening model is given. Let $\boldsymbol{F} := \partial_{\boldsymbol{X}} \boldsymbol{x}$ define the deformation gradient of the nonlinear map $\boldsymbol{\varphi} : \mathfrak{B}_0 \times \mathbb{R} \to \mathbb{R}^3$. Particle positions at the reference, $\mathfrak{B}_0$, and current configurations, $\mathfrak{B}$, are respectively denoted by $\boldsymbol{X}$ and $\boldsymbol{x} = \boldsymbol{\varphi}(\boldsymbol{X}, t)$. $\boldsymbol{d} = \mathrm{sym}(\boldsymbol{l})$ represents the spatial rate of deformation tensor, where $\boldsymbol{l} = \dot{\boldsymbol{F}} \cdot \boldsymbol{F}^{-1} = \partial_{\boldsymbol{X}} \boldsymbol{v}$ denotes the spatial velocity gradient, with $\boldsymbol{v} = \partial_t \boldsymbol{x}$. The small strain kinematics of the current framework relies on the ansatz of additive decomposition of the total strain, $\boldsymbol{\varepsilon}$, into elastic, $\boldsymbol{\varepsilon}^e$, and plastic portions[1], $\boldsymbol{\varepsilon}^p$.

$$\boldsymbol{\varepsilon} = \boldsymbol{\varepsilon}^e + \boldsymbol{\varepsilon}^p. \tag{12.A.2}$$

Let $\boldsymbol{\chi} = \{\boldsymbol{\varepsilon}^e, \boldsymbol{A}, \alpha\}^\top$ and $\boldsymbol{\varsigma} = \{\boldsymbol{\sigma}, \boldsymbol{X}, q\}^\top$ denote the vectors of all strain-like variables and their associated dual variables of a purely mechanical problem, respectively. $\boldsymbol{A}(\boldsymbol{\sigma})$ and $\alpha(q)$ respectively denote the kinematic hardening and isotropic hardening strain(stress)-like variables. Proposing appropriate free energy functions and following standard steps of the second principle of thermodynamics which dictates a non-negative mechanical dissipation supplies us the

---

[1]For finite strains, a corotational framework is assumed where rate additive forms of the spatial rate of deformation tensor is assumed, with

$$\boldsymbol{d} = \boldsymbol{d}^e + \boldsymbol{d}^p. \tag{12.A.1}$$

following state equations:

$$\boldsymbol{\sigma} = \lambda \operatorname{tr}(\boldsymbol{\varepsilon}^e)\mathbf{1} + 2\mu\,\boldsymbol{\varepsilon}^e\,, \quad \boldsymbol{X} = \frac{2}{3}Q_X\boldsymbol{A}\,, \quad q = [\sigma_\infty - \sigma_0][1 - \exp(-\delta\alpha)]\,. \tag{12.A.3}$$

Here, all yet undefined symbols refer to material constants. Postulating the yield potential Φ^p

$$\Phi^p := \sigma_{eq} - [\sigma_0 + q(\alpha)]\,, \tag{12.A.4}$$

where $\sigma_{eq} = \sqrt{[\boldsymbol{\sigma} - \boldsymbol{X}] : \boldsymbol{H} : [\boldsymbol{\sigma} - \boldsymbol{X}]}$ and σ_0 is the initial yield stress. $\boldsymbol{H}$ is the constant structural tensor, responsible for the inherent plastic symmetry. For initial plastic isotropy one has $\boldsymbol{H} = 3/2\,\boldsymbol{\mathcal{I}}^{\mathrm{dev}}$ where $\boldsymbol{\mathcal{I}}^{\mathrm{dev}}$ is the deviatoric part of the fourth-order symmetric identity tensor, $\boldsymbol{\mathcal{I}}^{\mathrm{sym}} = 1/2\,[\mathbf{1}\overline{\otimes}\mathbf{1} + \mathbf{1}\underline{\otimes}\mathbf{1}]$, with $\boldsymbol{\mathcal{I}}^{\mathrm{dev}} = \boldsymbol{\mathcal{I}}^{\mathrm{sym}} - 1/3\,[\mathbf{1}\otimes\mathbf{1}]$. Applying the normality rule for $\dot{\boldsymbol{\varepsilon}}^p$ and $\dot{\alpha}$, gives the following evolution equations $\dot{\boldsymbol{\chi}}$

$$\dot{\boldsymbol{\varepsilon}}^p = \dot{\gamma}\frac{\boldsymbol{H} : [\boldsymbol{\sigma} - \boldsymbol{X}]}{\sigma_{eq}}\,, \quad \dot{\boldsymbol{A}} = \dot{\gamma}\left[\frac{\boldsymbol{H} : [\boldsymbol{\sigma} - \boldsymbol{X}]}{\sigma_{eq}} - C_X\boldsymbol{A}\right]\,, \quad \dot{\alpha} = \dot{\gamma}\,. \tag{12.A.5}$$

Here $\dot{\gamma}$ is the so-called plastic multiplier. The presented framework results in a differential-algebraic (DA) set of equations. The evolutionary equations give account for differential forms whereas the algebraic equation comes from the yield function. In solution of such a system in a strain driven nature of FEM, it is typical to assume that for a typical time step $\Delta t = t_{n+1} - t_n$ the solution at t_n is known as $\{\boldsymbol{\sigma}_n, \boldsymbol{X}_n, \boldsymbol{\varepsilon}_n^p, \boldsymbol{A}_n, \alpha_n\}$ and the solution at t_{n+1} is sought for $\{\boldsymbol{\sigma}_{n+1}, \boldsymbol{X}_{n+1}, \boldsymbol{\varepsilon}_{n+1}^p, \boldsymbol{A}_{n+1}, \alpha_{n+1}\}$. Utilizing an elastic predictor plastic/damage corrector type operator split, it is possible to reiterate the total problem. The elastic prediction is made by,

$$\boldsymbol{\varepsilon}_{n+1}^{p,\mathrm{trial}} = \boldsymbol{\varepsilon}_n^p\,, \quad \boldsymbol{A}_{n+1}^{\mathrm{trial}} = \boldsymbol{A}_n\,, \quad \alpha_{n+1}^{\mathrm{trial}} = \alpha_n\,, \tag{12.A.6}$$

where the trial state is defined as

$$\boldsymbol{\sigma}_{n+1}^{\mathrm{trial}} = \boldsymbol{\mathcal{C}}^e : [\boldsymbol{\varepsilon}_{n+1} - \boldsymbol{\varepsilon}_{n+1}^{p,\mathrm{trial}}]\,, \quad \boldsymbol{X}_{n+1}^{\mathrm{trial}} = \frac{2}{3}Q_X\boldsymbol{A}_{n+1}^{\mathrm{trial}}\,, \quad q_{n+1}^{\mathrm{trial}} = q(\alpha_{n+1}^{\mathrm{trial}})\,. \tag{12.A.7}$$

Within the time step, the elastic or plastic character of the status is checked by inserting the trial stresses into the yield function,

$$\Phi_{n+1}^{p,\mathrm{trial}} = \Phi^p\left(\boldsymbol{\sigma}_{n+1}^{\mathrm{trial}}, \boldsymbol{X}_{n+1}^{\mathrm{trial}}, q_{n+1}^{\mathrm{trial}}\right) = \begin{cases} \leq 0 \implies \mathrm{elastic}\,, \\ > 0 \implies \mathrm{plastic}\,. \end{cases} \tag{12.A.8}$$

Once $\Phi_{n+1}^{p,\mathrm{trial}} \leq 0$ is satisfied, an elastic state at t_{n+1} is defined and the trial values does not require any correction. Otherwise, a plastic state is due, and following corrections named as return mapping trial state should be realized to fulfill the yield condition at effective stress space. Using the following abbreviations for brevity

$$\partial_{\boldsymbol{\sigma}}\Phi^p|_{n+1}^{(k)} \to \boldsymbol{r}_{n+1}^{(k)}\,, \quad \partial_{\boldsymbol{X}}\Phi^p|_{n+1}^{(k)} \to -\boldsymbol{r}_{n+1}^{(k)}\,, \quad \partial_q\Phi^p|_{n+1}^{(k)} \to \varsigma_{n+1}^{(k)}\,, \tag{12.A.9}$$

the incremental plasticity parameter, $\delta\gamma_{n+1}^{(k)}$, can be found using

$$\delta\gamma_{n+1}^{(k)} = \frac{\Phi_{n+1}^{p,(k)}}{\boldsymbol{r}_{n+1}^{(k)} : \boldsymbol{\mathcal{C}}^e : \boldsymbol{r}_{n+1}^{(k)} + \frac{2}{3}Q_X\,[\boldsymbol{r}_{n+1}^{(k)} : \boldsymbol{s}_{n+1}^{(k)}] - \varsigma_{n+1}^{(k)}}\,, \tag{12.A.10}$$

which is used through iterations with $\Delta\gamma_{n+1}^{(k+1)} = \Delta\gamma_{n+1}^{(k)} + \delta\gamma_{n+1}^{(k)}$ with $\Delta\gamma_{n+1}^{(0)} = 0$. Iterations with computation of the variable updates are continued until $\Phi^p(\boldsymbol{\sigma}_{n+1}, \boldsymbol{X}_{n+1}, q_{n+1}) \leq TOL$.

The algorithm utilized in the following falls in the class of cutting plane algorithms [273], taking advantage of the great generality and implementation convenience proposed. It is crucial to note that, as also remarked in [273], the algorithm merely requires essential response function derivations. However, unlike closest point projection algorithms significant errors may be introduced for large time steps. Thus the method should better be used only with explicit transient simulations, where the Courant condition severely limits the allowable time steps.

12.B. Analytical Solution for Uniform Simple Shear

Under strain controlled shearing, one has the following total strain and strain rate tensors,

$$\varepsilon = \frac{1}{2} \begin{pmatrix} 0 & \gamma & 0 \\ \gamma & 0 & 0 \\ 0 & 0 & 0 \end{pmatrix} \quad \text{and} \quad \dot{\varepsilon} = \frac{1}{2} \begin{pmatrix} 0 & \dot{\gamma} & 0 \\ \dot{\gamma} & 0 & 0 \\ 0 & 0 & 0 \end{pmatrix} . \tag{12.B.1}$$

With omission of the elastic strains one has under simple shear conditions $\varepsilon^p \simeq \varepsilon$. Similar tensorial forms are valid for other strain and stress measures as far as the nonzero terms are considered due to the proportional nature of the loading. Accordingly the von Mises equivalent plastic strain rate $\dot{\alpha}$ reads

$$\dot{\alpha} = \frac{1}{\sqrt{3}} \dot{\gamma} , \tag{12.B.2}$$

and equivalent von Mises equivalent stress become

$$\sigma_{eq} = \sqrt{3} \left| \sigma_{12} - X_{12} \right| . \tag{12.B.3}$$

The evolution equation set then reads

$$\left. \begin{aligned} \dot{\varepsilon}_{12}^p &= \frac{\sqrt{3}}{2} \dot{\gamma} \ \text{sign}(\sigma_{12} - X_{12}) , \\ \dot{A}_{12} &= \frac{\sqrt{3}}{2} \dot{\gamma} \ \text{sign}(\sigma_{12} - X_{12}) - \frac{3}{2} \frac{C_X}{Q_X} X_{12} , \\ \dot{\alpha} &= \dot{\gamma} , \end{aligned} \right\} \tag{12.B.4}$$

which is subjected to

$$\sqrt{3} \left| \sigma_{12} - X_{12} \right| - \left[\sigma_y + q(\alpha) \right] = 0 . \tag{12.B.5}$$

For monotonic loading conditions, i.e. $\text{sign}(\sigma_{12} - X_{12}) = 1$, and using the conjugate stress definition for kinematic hardening and equivalent strain definition, one has

$$\dot{X}_{12} = \dot{\gamma} \left[\frac{1}{3} Q - \frac{1}{\sqrt{3}} C_X X_{12} \right] . \tag{12.B.6}$$

Here, immediate integration is possible to give

$$X_{12} = \frac{1}{\sqrt{3}} \frac{Q}{C_X} \left[1 - \exp\left(-C_X \frac{1}{\sqrt{3}} \gamma \right) \right] , \tag{12.B.7}$$

which gives kinematic hardening stress like variable. For isotropic hardening stress one has

$$q(\alpha) = \left[\sigma_\infty - \sigma_0 \right] \left[1 - \exp\left(-\delta \frac{1}{\sqrt{3}} \gamma \right) \right] . \tag{12.B.8}$$

Eventually one can find σ_{12}, using these definitions by

$$\sigma_{12} = X_{12} + \frac{1}{\sqrt{3}} \left[\sigma_y + q(\alpha) \right] ,$$

(12.B.9)

from which one can compute the moment, for the monotonic loading

$$M = 2t\Delta\vartheta r_m^2 \left[\begin{array}{c} \frac{1}{\sqrt{3}}\frac{Q}{C_X} \left[1 - \exp\left(-C_X \frac{1}{\sqrt{3}}\gamma \right) \right] \\ + \frac{1}{\sqrt{3}} \left[\sigma_y + [\sigma_\infty - \sigma_0] \left[1 - \exp\left(-\delta \frac{1}{\sqrt{3}}\gamma \right) \right] \right] \end{array} \right] ,$$

(12.B.10)

which completes this part.

13. A Grooved In-Plane Torsion Test for the Investigation of Shear Fracture in Sheet Materials

In this chapter, the grooved in-plane torsion test is proposed as a shear fracture test for sheet materials. Unlike conventional simple shear tests, which are prone to incipient cracking at the free edges, this test uses radially continuous specimens, as firstly introduced by [200]. In order to control the fracture position, a radial groove is cut out which allows to keep the fracture away from the clamping area. Thus, this test is able to create material fracture under ideal shear conditions i.e., the condition of vanishing triaxiality at the observable region of the test. Accordingly, the recent shear extended damage and fracture models for the selected material classes can be validated and/or qualified. With the help of finite element analysis (FEA), the corresponding fracture strains for the steel DP1000 were investigated using the proposed shear test and, additionally, three tensile tests conducted on notched specimens which cause fracture at moderate to high triaxialities. These are used to fit the fracture loci of some shear enhanced fracture criteria which were recently been proposed in the literature. The FEA shows that the proposed test provides fracture development under constantly zero triaxiality and zero Lode parameter conditions. Moreover, among the selected criteria, the model proposed by [192] delivers the best results for selected experimental set. The developed test is ideally suitable for fracture parameter identification of sheet materials which do not show pronounced in-plane anisotropy, e.g. dual phase steels. Furthermore, this test is not limited to metallic materials.

13.1. Introduction

The formability of metallic sheet materials is relatively limited for the loading paths under generalized shear stress states [154]. Conventional forming limit diagrams, which are mainly based on the measurement of surface strains till onset of necking, fall short to predict shear governing failure at vanishing and low stress triaxialities [183]. In [325] it was found that the microscopic mechanism of fracture depends on the martensitic volume and distribution in DP steels. In the sheet metal forming practice, the lower limit[1] of the admissible stress triaxiality η is assumed to be $-1/3$ i.e., buckling under uniaxial compression. Shear fracture is represented by triaxiality $\eta = 0$ and lies within the considered interval of triaxiality for sheet metal forming. Hence, the determination of the shear fracture limits is required. For this purpose, recent material characterization studies for fracture are reconsidered taking into account the shear mode of fracture.

---

[1]Selecting the von Mises equivalent stress, it is conventional to assume the admissible triaxiality interval for sheet metal forming as $-\frac{1}{3} \leq \eta \leq +\frac{2}{3}$ with the assumption of *plane stress* due to thin sheets, where $\eta = \frac{2}{3}$ represents the biaxial tensile stress state. The choice of the upper limit of triaxiality is realistic only when the post-necking response is excluded. Otherwise the state of plane stress is broken and triaxial stress states develop. A typical consequence is the premature fracture prediction of the FEA, which uses thin shell elements.

The existing mechanical tests for shear fracture have some disadvantages, which are namely

- fracture occurence at the free edges due to inhomogeneous stress distribution, thus failing to achieve crack initiation under desired shear conditions

- varying triaxiality and Lode parameter during plastic deformation until crack

In the current study, a novel torsional test, the so called grooved in-plane torsion test is presented, which was developed for the investigation of ductile failure of planar sheets. Unlike in original in-plane torsion test, grooved specimens free of slits are used. The aim is to achieve shear fracture in sheet materials supplying ideal shearing conditions of the material points at the fracture zone throughout the deformation history with vanishing instantaneous (and thus average) triaxiality, $\eta = 0$, and Lode parameter[2], $\theta = 0$. This test is free of the mentioned edge effects. Due to the relatively simple specimen morphology, the test allows a direct determination of the equivalent strain at fracture from digital image correlation (DIC) results. Hence, an inverse analysis does not have to be involved for the parameter identification.

13.2.   Current State Of Shear Fracture Testing For Sheet Materials

Various shear tests for the characterization of plastic material behavior of sheet metals are known in literature, however, not all are suitable for the identification of shear fracture. In Table 13.1, an overview of available shear test approaches is given with corresponding references and comments on the test characteristics and purposes. Two main aims exist when performing a shear test: the characterization of plastic hardening (e.g. determination of the flow curve, identification and partition of isotropic and kinematic hardening) and the characterization of formability and fracture behavior.

13.2.1.   Shear and Torsion Tests for Characterization of Plastic Hardening

Figure 13.1 shows five specimen approaches for the determination of the flow curve in shear tests. One can distinguish between translational and rotational fixture movements. Typical shear test kinematics is achieved by a parallel displacement of two opposing edges in opposite directions. In numerous publications, like [128], this principle is followed by testing a single sided shear specimen (see Figure 13.1.(b). Basically with the same kinematics but with two symmetrical shear zones, a specimen design by [220] was suggested in order to avoid the unwanted reaction moment on the fixtures (Figure 13.1.(a). The ASTM B831 Standard suggests a much simpler clamping configuration by using the kinematics of tensile tests. The complexity is moved to the specimen design, involving diagonal cuts in the specimen (see Figure 13.1.(c). The advantage is the compatibility of this specimen with testing devices designed for tensile tests. However, the shear zone may rotate during deformation. [211] presented a modified version of this specimen with additional supporting fixtures in order to stiffen the regions without plastic deformation as well as allow cyclic loadings.

Torsion tests for sheet materials are still rarely applied. The initial work for the in-plane torsion test was done by [199], who proposed this test in order to investigate cyclic hardening of copper. A round sheet specimen is clamped concentrically in the center and at the outer rim and

---

[2]A detailed summary of these expressions are given on Section 13.3.1.

Table 13.1.: Shear tests for sheet materials.

Publications	Loading	Characteristics	Purpose
[220]	Translational	Planar shear test with two symmetrical zones	Plastic hardening
[128], [256], [58]	Translational	Planar shear test with one single shear zone	
ASTM B831, [211]	Translational	Planar shear test with slits suitable for tensile test kinematics	
[297]	Torsional	In-plane torsion to reach high strains	
[61], [342]	Torsional	Modified in-plane torsion test with slits	Formability, fracture
[29], [221]	Translational	Grooved shear specimen geometry (Butterfly)	
[270]	Translational	Shear specimen with slits for tensile loading	
[137], ASTM D5379	Translational	Shearing of notched bars	
[200]	Torsional	In-plane torsion test	

torsioned in the sheet plane. Shear deformation is created in the free ring-shaped area between the clamps. Further developments by [297] allow the usage of the in-plane torsion test for the flow curve determination. The in-plane torsion test is free of edge effects due to the absence of any edges. Thus, a high deformation can be achieved. Recent developments suggest applying optical strain measurements in this test [341]. [61] proposed a modification of the torsion specimen, the so called *twin bridge shear test*, with round slits in order to obtain a shear test with specific orientation to the rolling direction. [344] showed that this specimen modification produces results which are comparable to the Miyauchi specimen and the shear test according to ASTM B831.
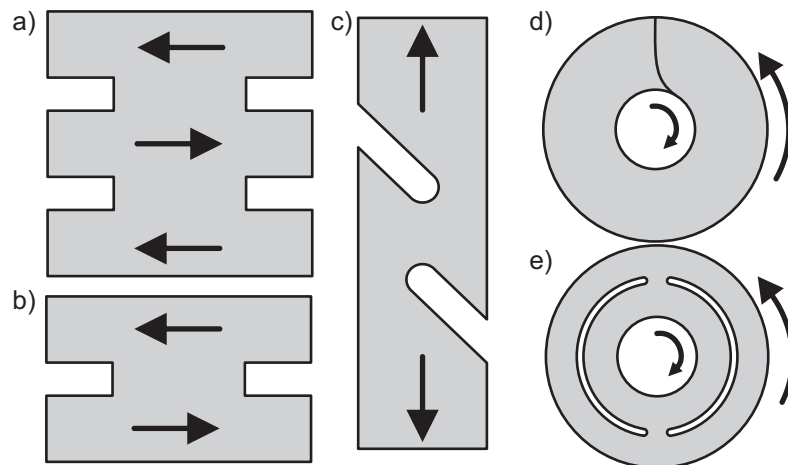
Figure 13.1.: Shear tests for characterization of hardening behavior of sheet materials.

13.2.2. Shear Tests for Fracture and Formability Testing of Sheets

As the above described approaches are originally designed for the determination of plastic hardening, they are not generally suitable for the characterization of formability limits by fracture. The shear tests and the twin bridge specimen are affected by edge effects which are explained in Section 13.1. Moreover, inhomogeneous stress and strain distributions within these tests lead to stress states which deviate significantly from the simple shear state, especially at both ends of the shear zone. For flow curve determination, the influence of this effect can be reduced by increasing the ratio of length to width. [58] suggested a proportion of 10:1. The position of the incipient fracture is very important for the fracture analysis. For the mentioned shear tests, which involve discontinuities at the sheared stress carrying zone, the crack tends to emanate at the edges where the tensile stress state is dominant. Hence, the material failure under shear conditions cannot be guaranteed. Obviously, the stress states at the crack tip process zone for a propagating crack has additional complexities. This drawback of edge effects does not exist for the in-plane torsion test without slits. The application of this test for formability testing is shown by [200], where failure occurs at the inner clamping. However, the shear stress state overlaps with the clamping pressure at this position.

Hence, the main challenge for the experimental characterization of sheet metal failure under simple shear loading is avoiding the crack initiation at free edges, while maintaining a desired and constant stress triaxility and lode parameter for simple shear. Figure 13.2 shows schematically four specimen designs which were originally developed with this intention. An early approach with notched bars was suggested by [137] (Figure 13.2a). A modified version of this specimen is standardized as ASTM D5379, which aims at fracture testing of composite materials. The crack initiation is enforced at the sharp notches, however, with huge impact of edge effects. [270] presented a specimen with cutouts for formability testing (Figure 13.2.(b). It contains two regions dedicated to shear deformation. The applied tensile load also causes deformation on three tensile regions, in the center and at the outer edges. Thus, the stress values in the deformed areas cannot be directly calculated from the applied force. Similar to the conventional shear tests, the crack is also initiated at the edges, where the stress state cannot be considered as simple shear. In order to obtain crack initiation inside the material and not at the free edges, [29] suggested a specimen with locally reduced sheet thickness (Figure 13.2.(c). [221] used a similar specimen with a groove to reduce the sheet thickness. The result of a detailed analysis showed that the crack beginning can be located within the material. However, it cannot be guaranteed that the starting point is at the exact center of the shear zone. In addition, it was found that the triaxiality is changing during deformation. That means the stress state at the beginning of plastic deformation has changed when fracture occurs.

In contrast, a low triaxiality test method for tubes does exist, as suggested by [106]. In their work, the specimen designs according to [188] and [39] are used. These tubular specimen have notches at the inner and/or outer side, which creates a predetermined shear fracture point when torsion is applied. Comparable approaches for sheet materials are not known yet.

13.2.3. Requirements for an Ideal Shear Test for Fracture

From the brief review in this section, one can see that the characterization of shear fracture of sheet material is experimentally challenging. As far as the shear fracture investigation is concerned, an ideal mechanical test should have the following features:
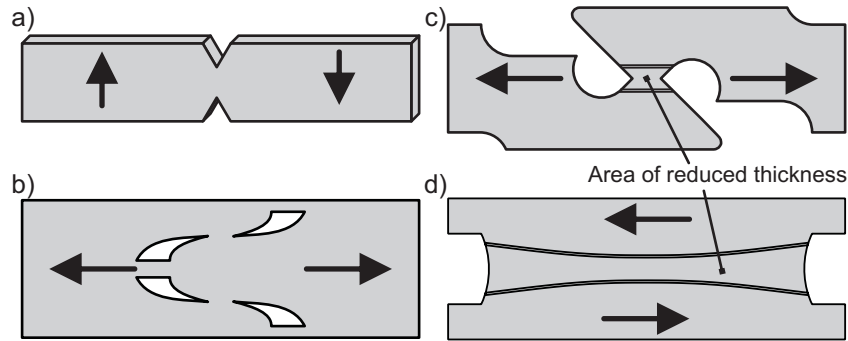
Figure 13.2.: Shear tests for the investigation of fracture and formability of sheet materials by (a) [137], (b) [270], (c) [29], and (d) [221].

- Ensuring an in-plane traceless shear stress state with vanishing instantaneous stress triaxiality ratio $\eta = 0$ and Lode parameter $\bar{\theta} = 0$ at the point of incipient cracking throughout the whole deformation history

- Possibility to control the location of the crack for digital imaging

- Determination of the stress and equivalent strain at fracture without need for reverting to an inverse procedure

Considering all the above described specimen approaches, none of the yet proposed shear tests can fulfill all these requirements. If such an ideal shear test were available, it would be possible to investigate all the proposed fracture criteria and determine parameters under exactly defined conditions. Thus, in this chapter, a novel shear specimen for sheet materials is introduced which allows the investigation of shear fracture at exact shear stress conditions.

13.3. Theory - Enhanced Shear Fracture Approaches Accounting for Shear Fracture

Ductility of metallic materials is defined as the ability of the material to deform preserving its continuity at the macro scale. After [59] had revealed that increasing the hydrostatic pressure extends the ductility of metals, the interest shifted to the influence of the stress state on the formability. However, the mathematical models aiming at fracture prediction in metallic materials had long concentrated merely on the effect of triaxiality, which is the ratio of the hydrostatic pressure and equivalent stress. The studies of [208] and [259] presented models quantifying the growth of idealized void structures in a rigid matrix in hydrostatic stress fields. Driven by numerical and experimental studies on the relations between void mechanisms and ductile fracture, several fracture models have been proposed in the last five decades. Well known examples are the model by [78] with an energy based approach and the model of [143], which can be applied for different temperatures and strain rates. The models developed on this track gave accurate predictions only for moderate to high triaxiality ratios. Low triaxiality ductile fracture engaged considerable interest in the theoretical and the experimental solid mechanics communities since the pioneering study of [29], which shows the non-monotonic dependence of the equivalent fracture strain on triaxiality. On the one side, micro-void dynamics and interaction based descriptions of the observed phenomena are involved in theoretical developments. On the other side, new constitutive models [192] or the modification of the existing ones for moderate

to high triaxiality ratios are proposed [224, 339]. In these proposals, the Lode parameter or an equivalent measure is frequently devised as an additional degree of freedom in addition to the triaxiality and equivalent plastic strain rate.

Before proceeding further, the characterization of the stress state of a material point is presented in detail . In the following section, the notations for triaxiality and lode parameter which are used in this chapter are also introduced, since various notations with slight differences can be found in literature, especially for the Lode parameter.

13.3.1. Characterization of the Stress State

Note that the total (true) Cauchy stress tensor $\boldsymbol{\sigma}$ has the following invariants, I_i, $i = 1, 2, 3$

$$ I_1 = \mathrm{tr}\left(\boldsymbol{\sigma}\right), \quad I_2 = \frac{1}{2}\left[\mathrm{tr}\left(\boldsymbol{\sigma}\right)^2 - \mathrm{tr}\left(\boldsymbol{\sigma}^2\right)\right], \quad I_3 = \det\left(\boldsymbol{\sigma}\right). \tag{13.3.1} $$

where tr($\bullet$) denotes the trace of ($\bullet$). Letting σ_i with $i = 1, 2, 3$ denote the principal stress components, the invariants read

$$ I_1 = \sigma_1 + \sigma_2 + \sigma_3, \quad I_2 = \sigma_1\sigma_2 + \sigma_1\sigma_3 + \sigma_2\sigma_3, \quad I_3 = \sigma_1\sigma_2\sigma_3. \tag{13.3.2} $$

The hydrostatic stress p, then, can be defined in terms of I_1

$$ p = \frac{1}{3}I_1 = \frac{\sigma_1 + \sigma_2 + \sigma_3}{3}. \tag{13.3.3} $$

With this definition, the deviatoric principal stress components S_1, S_2, and S_3 are defined as $S_1 = \sigma_1 - p$, $S_2 = \sigma_2 - p$, and $S_3 = \sigma_3 - p$. The deviatoric invariants of the stress tensor J_i, $i = 1, 2, 3$ can be defined as

$$ J_1 = 0, \quad J_2 = S_1^2 + S_2^2 + S_3^2, \quad J_3 = S_1 S_2 S_3. \tag{13.3.4} $$

Using the definition of J_2 and the relation between the total and deviatoric components of the principal stress components, the equivalent von Mises stress $\sigma_{vM} = \sqrt{[3/2]\,J_2}$ can be defined in terms of the principal stress components as follows

$$ \sigma_{vM} = \frac{1}{\sqrt{2}}\sqrt{[\sigma_1 - \sigma_2]^2 + [\sigma_2 - \sigma_3]^2 + [\sigma_3 - \sigma_1]^2}. \tag{13.3.5} $$

The triaxiality η, using $\eta = p/\sigma_{vM}$ reads

$$ \eta = \frac{\sqrt{2}}{3}\frac{\sigma_1 + \sigma_2 + \sigma_3}{\sqrt{[\sigma_1 - \sigma_2]^2 + [\sigma_2 - \sigma_3]^2 + [\sigma_3 - \sigma_1]^2}}. \tag{13.3.6} $$

For the definition of the shear dependence of damage, the location of the stress point on the yield locus is best achieved through the use of spherical coordinates and the Lode parameter. Hence, it is possible to distinguish between axisymmetric stress states and generalized plane strain stress states. In the literature, different measures are used for this purpose. In the following, the notation used in this chapter is introduced and the fracture criteria in terms of a consistent set of parameters, that is $(\eta, \bar{\theta})$, where the definition of $\bar{\theta}$ is clarified in the following lines, applying necessary transformations are attempted to be presented.

First, the Lode angle θ is defined in the interval $0 \leq \theta \leq \frac{\pi}{3}$, beginning at the tensile stress
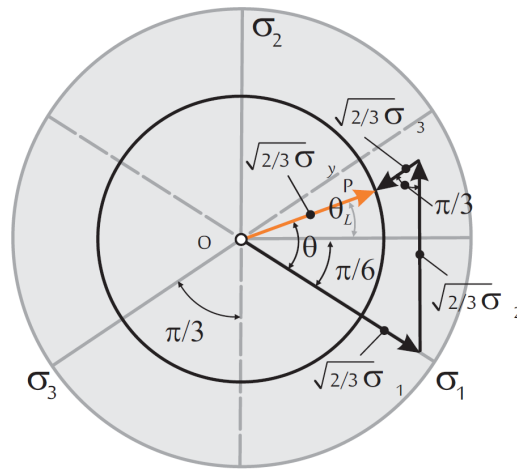
Figure 13.3.: Definition of the Lode angle on $\Pi-plane$. $\theta = 0$ for axisymmetric tension, $\theta = \pi/6$ for plane stress shear and $\theta = \pi/3$ for axisymmetric compression.

axis as given in Figure 13.3. For $\theta = 0$ and $\theta = \frac{\pi}{3}$, there are uniaxial (axisymmetric) tensile and compressive stress states, respectively, whereas for $\theta = \frac{\pi}{6}$ one has shear stress state. A variable frequently used in the literature is the Lode parameter $\bar{\theta}$ which is linked to the Lode angle by

$$\bar{\theta} = 1 - \frac{6\theta}{\pi} \, . \tag{13.3.7}$$

Note that the range is $-1 \leq \bar{\theta} \leq 1$, where for for $\bar{\theta} = 1$ and $\bar{\theta} = -1$ there are uniaxial (axisymmetric) tensile and compressive stress states, respectively, whereas for $\bar{\theta} = 0$ there is shear stress state. The interpretation of this variable is simple compared to θ due to its simple limits and the sign of $\bar{\theta}$ which directly gives a sense of the tensile and compressive character of the stress state. $\bar{\theta}$ can be linked to the so-called normalized third deviatoric invariant of the stress tensor ξ by the following expressions allows the computation of the Lode parameter $\bar{\theta}$ for a given stress state

$$\bar{\theta} = 1 - \frac{2}{\pi} \arccos(\xi) \quad \text{with} \quad \xi = \frac{27}{2} \frac{J_3}{\sigma_{vM}^3} \, . \tag{13.3.8}$$

Another interpretation of the Lode parameter as used in the model of [192] is given, for the range $-1 \leq L \leq 1$, as

$$L = \frac{2\sigma_2 - \sigma_1 - \sigma_3}{\sigma_1 - \sigma_3} \, . \tag{13.3.9}$$

Assuming an ordered set of principal stresses $\sigma_1 > \sigma_2 > \sigma_3$, the definition of a shear state of stress can also be done through the normalized maximum shear stress $2[\tau_{\max}/\sigma_{vM}]$, where $\tau_{\max} = [1/2][\sigma_1 - \sigma_3]$. Note that for pure hydrostatic stress states, $2[\tau_{\max}/\sigma_{vM}]$ vanishes whereas, for uniaxial tension and compression, $2[\tau_{\max}/\sigma_{vM}]$ has the value of 1 and -1, respectively. In case of a simple shear stress state, $2[\tau_{\max}/\sigma_{vM}] = 2/\sqrt{3}$ can be found. $2[\tau_{\max}/\sigma_{vM}]$ could be linked to L using $2[\tau_{\max}/\sigma_{vM}] = 2/\sqrt{L^2 + 3}$. Finally, the following relation bridges the gap between $\bar{\theta}$ and L and allows to represent all the fracture criteria studied in the current chapter in terms of the pair $(\eta, \bar{\theta})$ consistently

$$\sin\left(\frac{\pi\bar{\theta}}{6}\right) = -\frac{L}{\sqrt{L^2 + 3}} \, . \tag{13.3.10}$$

13.3.2.   Fracture Criteria

In the current study, only the models referred to as the fracture criteria where the generic representation of the ductile fracture criterion can be given as $D = \int f\left(\boldsymbol{T}\right) d\varphi$ with D and φ denoting the damage indicator and the equivalent plastic strain, respectively, are dealt with where $f\left(\boldsymbol{T}\right)$ is a generic function of stress. Approaches with coupled fracture and plastic behavior are not considered here. Using above definitions, the generic form of the fracture criteria can be reiterated in the following form as $D = \int f\left(\eta, \overline{\theta}\right) d\varphi$. For strictly proportional loading paths, the pair $(\eta, \overline{\theta})$ is constant and so is the integrand. Thus, the equivalent plastic strain at fracture φ_f is defined as

$$\varphi_f = \frac{D_f}{f\left(\eta, \overline{\theta}\right)} \ , \tag{13.3.11}$$

where D_f is the damage indicator at fracture. Giving such closed form expressions for the fracture strain in terms of η and $\overline{\theta}$ is only possible for strictly proportional loading cases. Taking the flow curve definition for the material to be in the power form $\sigma_{vM} = A\varphi^n$, a set of fracture criteria, given in terms of critical equivalent strain to fracture are summarized in the following.

Rice and Tracey Model (RT).   Being among the earliest fracture criteria, the model according to [259] considers the growth of a spherical void in a cubic cell under a remote loading field. This criterion calculates the equivalent (plastic) fracture strain φ_f as a function of η only, while the Lode parameter $\overline{\theta}$ is not considered:

$$\varphi_f\left(\eta\right) = c_1 + c_2 \exp(-c_3\eta) . \tag{13.3.12}$$

The Cockcroft Latham Model (CL).   The model of [78] constitutes an energy-based ductile fracture criterion considering a critical threshold for the plastic work done by the maximum tensile principal stress. The corresponding equivalent fracture strain φ_f, which is a function of both η and $\overline{\theta}$, reads

$$\varphi_f\left(\eta, \overline{\theta}\right) = \frac{C}{\eta + \dfrac{2}{3}\cos\left(\dfrac{\pi}{6}[1 - \overline{\theta}]\right)} \ . \tag{13.3.13}$$

The Pressure Modified Maximum Shear Model (PMMS).   Being among the models proposed by the MIT Crashworthiness Lab., this damage model is an extension of the maximum shear stress model by accounting for the effect of the stress triaxiality ratio. The equivalent fracture strain φ_f is calculated by

$$\varphi_f\left(\eta, \overline{\theta}\right) = \left[\frac{A}{c_2}\left[c_1\eta + \frac{\sqrt{3}}{3}\cos\left(\frac{\overline{\theta}\pi}{6}\right)\right]\right]^{-\frac{1}{n}} . \tag{13.3.14}$$

Note that above closed form is made possible assuming a power type hardening, $\sigma_{vM} = A\varphi^n$.

Modified Mohr Coulomb (MMC).   The closed form solution for the equivalent fracture strain for the empirical Modified Mohr Coulomb fracture criterion [183] assumes a power-type hard-

ening $\sigma_{vM} = A\varphi^n$ and results in the following function of both η and $\overline{\theta}$

$$
\varphi_f\left(\eta, \overline{\theta}\right) = \left[\frac{A}{c_2}\left[c_3 + \frac{\sqrt{3}}{2-\sqrt{3}}[1-c_3]\left[\sec\left(\frac{\overline{\theta}\pi}{6}\right) - 1\right]\right] \times \right.
$$
$$
\left. \times \left[\sqrt{\frac{1+c_1^2}{3}}\cos\left(\frac{\overline{\theta}\pi}{6}\right) + c_1\left[\eta + \frac{1}{3}\sin\left(\frac{\overline{\theta}\pi}{6}\right)\right]\right]\right]^{-\frac{1}{n}}.
$$
(13.3.15)

As seen, apart from the hardening variables, this model requires three parameters.

Model of Lou and Huh (LH).   This phenomenological model, developed by [192], considers the damage evolution motivated by the micro-mechanical phenomena of void nucleation, growth, and coalescence. The growth of voids is accounted for materializing the stress triaxiality whereas the effects of void coalescence are incorporated by normalized maximum shear stress. The equivalent plastic strain takes account of the continuous nucleation of voids as a measure of the material flow. It also scales both the void growth and coalescence. In its original setting, the model reads

$$
\varphi_f = C\left[\frac{2\tau_{\max}}{\sigma_{vM}}\right]^{-a}\left[\frac{\langle 1+3\eta\rangle}{2}\right]^{-b},
$$
(13.3.16)

where C, a, and b are material parameters. The corresponding equivalent fracture strain φ_f as a function of both η and $\overline{\theta}$ reads

$$
\varphi_f\left(\eta, \overline{\theta}\right) = C\left[\sqrt{\left[\frac{1}{3}\sin^{-2}\left(\pi\frac{\overline{\theta}}{6}\right) - \frac{1}{3}\right]^{-1} + 3}\right]^{-a}\left[\frac{\langle 1+3\eta\rangle}{2}\right]^{-b}.
$$
(13.3.17)

It should be noted that the closed form expression for the Lou and Huh fracture criterion does not explicitly depend on the functional form of the flow curve. This property makes the model more flexible since sticking to the power form can be highly limiting. Hence the model can be used for materials showing hardening regimes other than power type hardening.

The above mentioned models are implemented as Vusdfld subroutines for Abaqus/Explicit and used initially in the mechanical resolution of the developed grooved in plane torsion test for shear fracture. Then, complementing the shear test results with the results of a set of notched tensile tests, the identification of the parameters for the listed fracture criteria is attempted. Based on the comparison of the qualities of the fits, the most appropriate fracture criteria for the selected class of materials are identified and the corresponding fracture curves are given. Hence, two aims that are defined in the introduction of the chapter i.e., firstly development of an ideal shear test, then, validation of the shear extended materials models, are carried out.

13.4.   Design of Test Specimen

13.4.1.   Expected Advantages of the New Specimen

Considering the proposed requirements for an ideal shear fracture test at the end of Section 13.2, a new specimen based on the in-plane torsion test is designed. By cutting out a smooth, circular groove in the whole circumference, the highest loading is located in the bottom of the groove while no edges and edge effects disturb the ideal shear conditions. With this specimen design, the following advantages are expected:

- The specimen is loaded in planar simple shear without edge effects. Triaxiality η and Lode parameter $\bar{\theta}$ are expected to remain zero during the whole deformation history.

- The incipient crack is trapped at the grooved region, away from the boundaries in contact with the tools.

- The shear stress can be calculated using the torque loading and the local thickness in the groove during deformation and at the point of fracture.

- The equivalent strain can also be determined using optical strain measurements based on digital image correlation.

In the following, the experimental approach is described in detail and the question if the suggested specimen can match these expectations is analyzed.

13.4.2. Test Set-up

For the in-plane torsion testing, the experimental device at the Institute of Forming Technology and Lightweight Construction is used which was presented in [341] (see Figure 13.4). The test setup is integrated in a universal testing machine which is used to produce the inner clamping force. In the experiments of the current study, a clamping force of 50 kN was applied on the inner fixture with an circular area of 30 mmin diameter. In order to prevent slipping, the clamping surface is structured by a corrugation with a rectangular grid of small pyramids, as shown in Figure 13.5. The grid distance is 1.0 mm. In the very center of the inner clamps, a centering pin is inserted to ensure concentric position of the torsion specimen, which also possesses a center hole. The outer clamps are applied manually by a clamping ring, which also possesses a surface corrugation. Transferred through a worm gear, the rotation and the torque are applied on the outer clamps, while the inner fixture remains stationary during the deformation. The maximum load of this testing machine is ca. 1500 Nm. A rotary encoder and a torque sensor are integrated in the setup in order to measure the rotation angle and the moment. The rotation speed was set to $0.05°/$s.

Optical strain measurements can be conducted since the deformed area is visible during testing. In this work, a GOM ARAMIS 5 MDIC System is used for 3D optical strain measurement. A section of ca. 90° of the specimen is visible in the measurement area, where the spatial resolution of about 0.1 mm is achieved.

13.4.3. Specimen Design

Bauer showed that the area next to the inner clamps are affected by the clamping force [?]. However, the influence vanishes for the rest of the specimen after a radial distance as large as the sheet thickness. Therefore, a new specimen design based on the in-plane torsion test is developed in this work using circular grooves. The aim is to generate an ideal shear loading until fracture without any unwanted edge effects and deviating stress components, as for example by the clamping pressure. Figure 13.6 shows the suggested geometry. A round groove is cut from one side of the in-plane torsion specimen by milling. The groove is defined by the diameter of the circular milling path d_b, the groove depth t_n, and the groove radius r_n. Since the shear stress can be calculated by $\tau = M/[2\,\pi\,r^2]$ for each radial position r on the specimen with the local thickness t, if the torque M is known, the value of the diameter d_b has tobe chosen as small as possible without an overlap of groove and inner clamping area. This is necessary
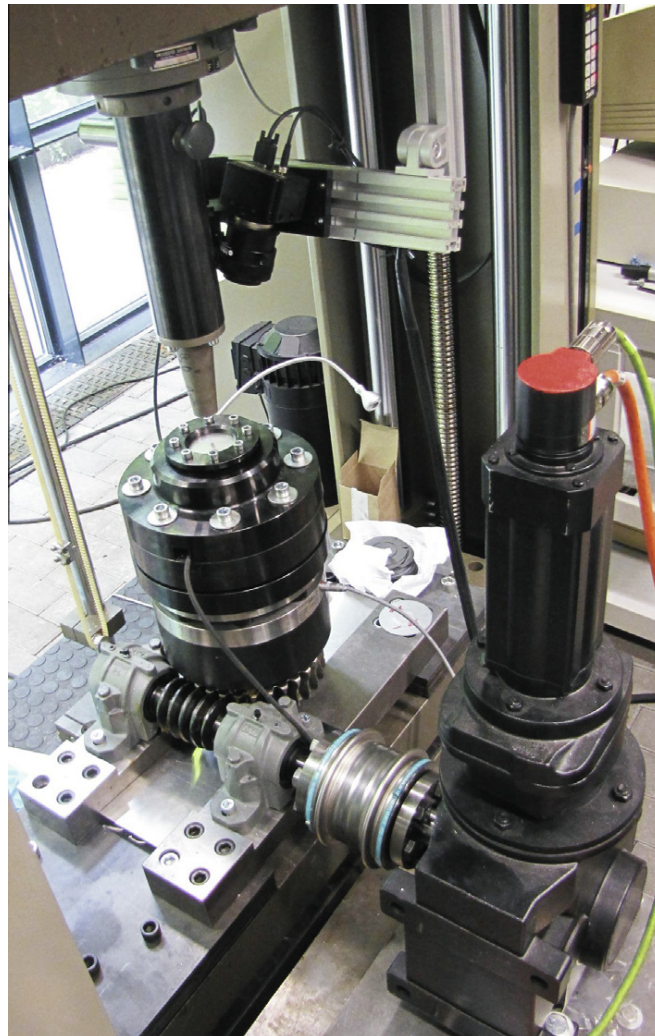
Figure 13.4.: In-plane torsion test set-up integrated in a universal tensile testing machine (Yin et al., 2011).
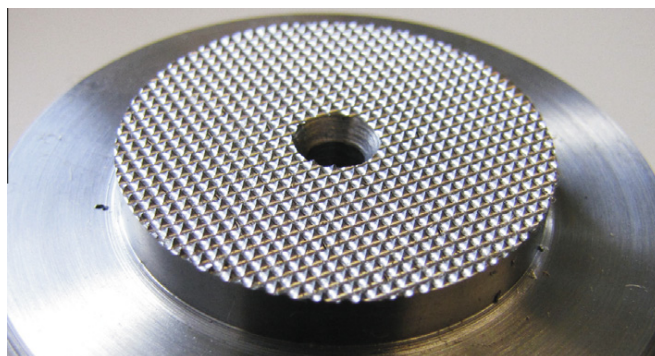
Figure 13.5.: Surface corrugation by a rectangular grid of small pyramids on the clamping devices (Yin, 2014).

to achieve the highest stresses in the groove bottom instead at the area next to the inner clamps.

The groove radius in this study is chosen to be $r_n = 4$ mm according the availability of the milling tools. Thus, the radius is smooth in order to prevent edge effects. Since the material properties may vary over the thickness, the specimen is not cut from both sides. Instead, an optimal cut depth of 50% of the thickness is preferred. This would still provide a representative material response for all sheet thickness layers. However, the initial production attempts show that the cut depth has to be controlled after milling due to the accuracy of the cutting process.
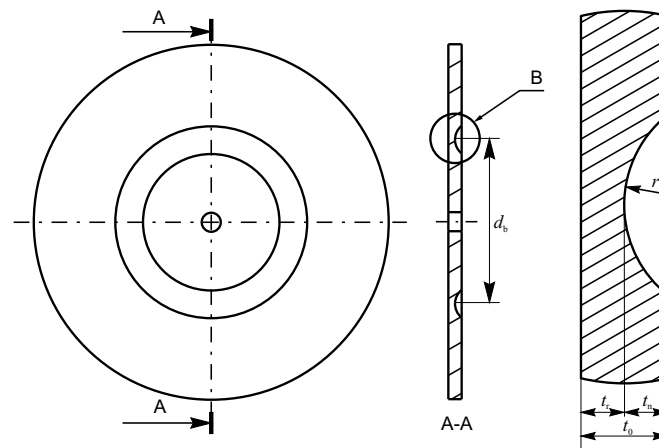
Figure 13.6.: Design of grooved in-plane torsion specimen.

For the following work, a DP1000 steel with a thickness of 1.55 mm is tested. The inner and outer clamping radius of the test set-up is 15.0 mm and 30.0 mm. The blank cutting process is conducted using a laser cutting device. To create the groove, a spherical ball cutter with a diameter of 8 mm is used for a milling path diameter of $d_b = 36$ mm. The specimen is positioned using a centering hole during the milling process. The final specimen is shown in Figure 13.7. The initial thickness is 1.55 mm and the cut depth is 0.85 mm. Thus, the minimum thickness is 0.7 mm.
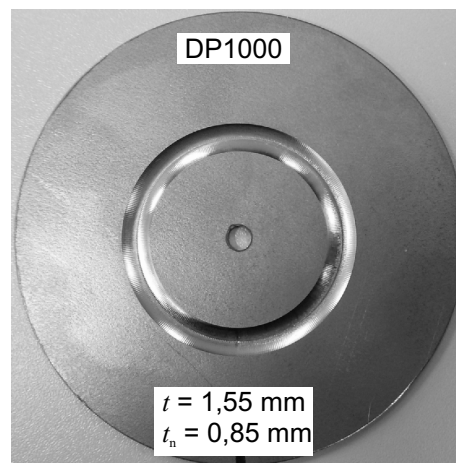
Figure 13.7.: In-plane torsion specimen made of DP1000 with circular groove.

13.4.4.   Experimental Results and Repeatability

Three specimens made of DP1000 are tested within this study. It is important to ensure a good repeatability of the results, especially for the load peak representing the point for fracture in the grooved specimen. Two ways of evaluating the specimen are compared to each other in Figure 13.8. On the left side, the three curves of the specimens show similar initial and hardening phases. However, the point of fracture seems to occur between a rotation angle of $10°$ and $12°$. As a remedy, the rotation angle of the specimen can be taken directly from an optical strain measurement system. On the right side of Figure 13.8, the inner and outer edge of the groove are tracked optically and the relative angle is recorded. Since the area of interest is exactly in the groove, this way to obtain the angle avoids any error sources, like slipping of the clamps and elastic tool deformations, without losing useful information. Furthermore, tracking the groove edges is both convenient for the optical measurement as well as the finite element simulation later on for the optimization process, as the edges are well defined and visible. Hence, the resulting torque-edge-angle curves show quite a good accordance with each other, indicating the point of fracture at an angle of $\simeq 6.8°$. As a consequence, the second approach to determine the torque-angle curve is used for the following analysis.
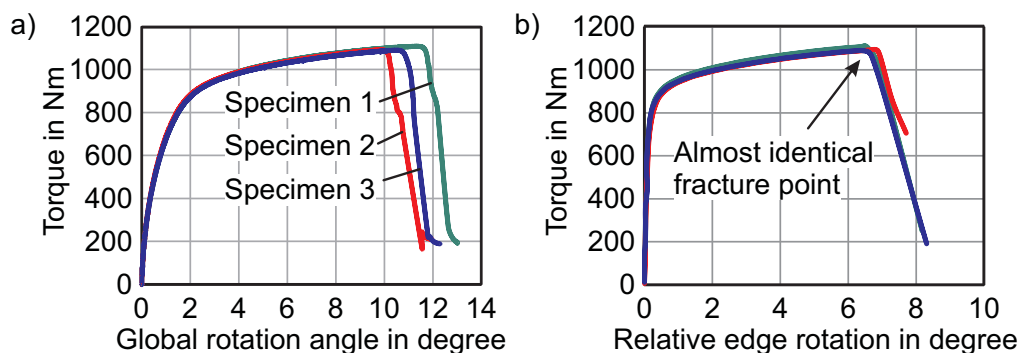
Figure 13.8.: Comparison of torque-angle curves using (a) the global angle from the incremental rotary encoder and (b) the local relative distortion of the groove edges.

Taking a look on the resulting strain distribution, Figure 13.9 shows two images of the DIC result with the strain countour as an overlay on the taken image. The distribution of the equivalent plastic strain according to von Mises is given, proving that the strain is concentrated in a small circular band in the groove. For the state of $6.6°$, the pattern for the optical strain measurement becomes severely distorted, causing gaps in the measurement. As the color indicates, the achieved strain reaches almost values of 1.0, which is by far exceeding the measurable strain in a uniaxial tensile test.

In Figure 13.10, the resulted fracture is shown in a closer view. After reaching the fracture point, the crack appears and progresses quickly over the full circumference. The specimen is is separated to an outer ring and an inner part.

Since crack occurence and crack shape are meeting the expectations, the exact crack position would be interesting for further analysis. By comparison of optically measured strains to the groove depth in Figure 13.11, one can see that the crack does not occur at the very center of the groove bottom. The figure shows the strains along a radial cut for the two states at edge rotation of $4.3°$ and $6.6°$. The groove depth is also measured optically by the same DIC system. Since the optical strain measurement system is calibrated to measure strains exactly, but not for the purpose of distance measuring, the precision of the results can be seen critically. However,
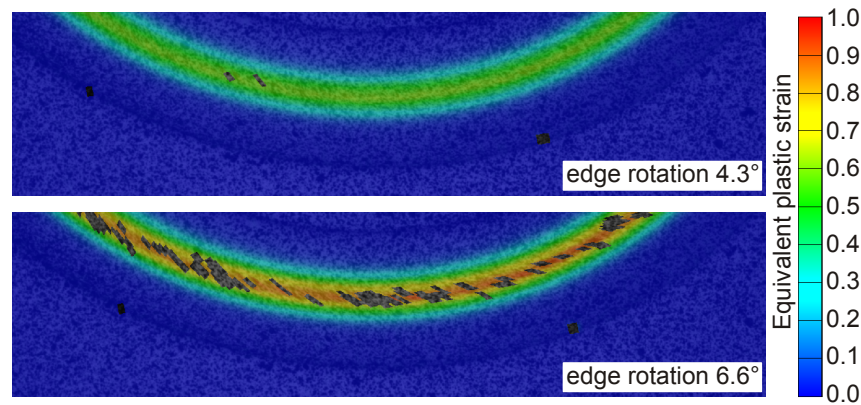
Figure 13.9.: Strain distribution measured by DIC at the stage of 4.3° and 6.6° groove edge rotation, showing the circular localization band at the bottom of the groove.
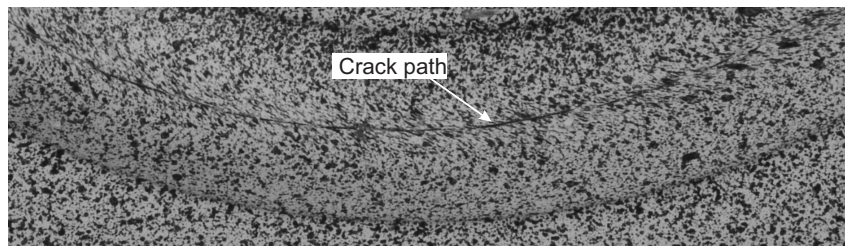
Figure 13.10.: Crack at the bottom of the groove.

it is visible that the maximal deformation is shifted to the rotation center instead of being at the groove bottom. The shifted position of the maximal stress and strain occurrence should be taken considering the measured strain and the local sheet thickness which is slightly higher than at the bottom of the groove.

13.4.5. FEA in Evaluation of the Test Results

For modeling shear test, a full 3D modelis constructed where the minimum mesh size of the utilized reduced integration elements is around 0.085 mm. Eight reduced integration hexahedral elements through thickness is used, where the minimum thickness at the bottom of the groove is 0.7 mm. The hardening of DP1000 is characterized by the flow rule according to the power law with $A = 1370$ MPa and $n = 0.0752$. The equivalent plastic strain distribution over the section at the incipient cracking time from the experiments, which is defined as the time of rapid drop in experimental moment angle curves, as a result of the conducted simulations are given in Figure 13.12.

The material flow is trapped at the grooved section as intended, where the radial location of the maximum value is close to the bottom of the groove. The element corresponding to the maximum equivalent plastic strain over the section is selected as the critical element as shown in Figure 13.12. Once the stress triaxiality ratio and the Lode parameter histories are analyzed for the critical point to fracture, as given in Figure 13.13, one sees that both values are at the vicinity of zero throughout the test. This clearly shows that the test supplies desired ideal conditions for shear fracture parameter identification since the instantaneous values match for the stress dependent functions triaxiality and Lode parameter. This is to say that the average values also read zero as aimed at.
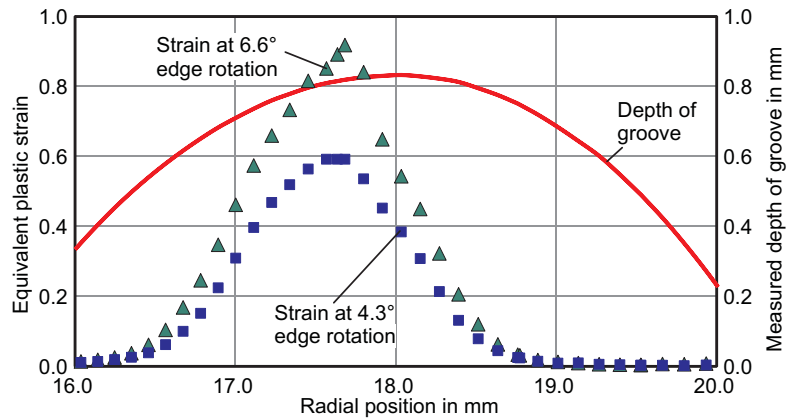
Figure 13.11.: Measured strain distribution using DIC at two different stages, showing the shifted radial position of the strain localization in good agreement with the theoretically calculated position of the stress peak.
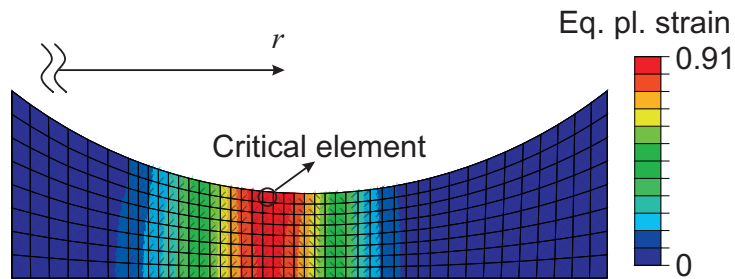
Figure 13.12.: Equivalent plastic strain contours over the specimen section at the failure rotation. r represents the radius measured from the center of the specimen. The critical element represents the element with maximum equivalent plastic strain.
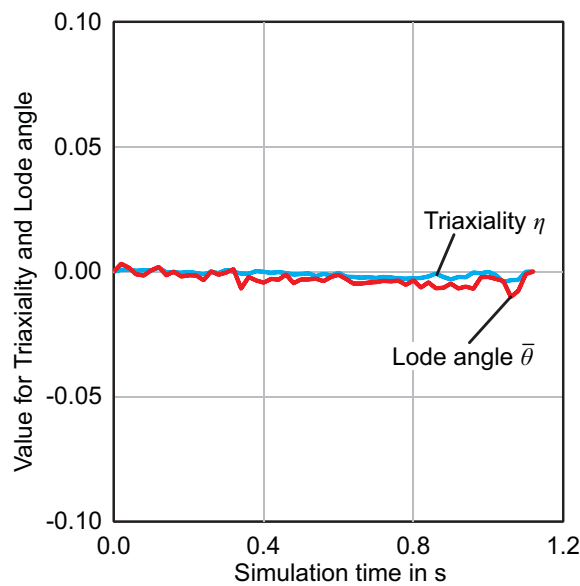
Figure 13.13.: Stress triaxiality ratio and Lode angle parameter histories throughout the shearing test for the critical elements identified in Figure 13.12.

13.4.6. Disadvantages and Limits of the New Specimen

Despite the good performance of this specimen for the tested DP1000 material, the disadvantages and limits of the proposed in-plane torsion specimen should be mentioned in order to ensure a serious scientific discussion and provide the basis for further improvements. At the current state, following issues are noted:

- **Anisotropy**: As a general drawback for in-plane torsion tests, anisotropic yielding of sheet materials cannot be investigated due to the specimen design. The orientation-dependent material behavior cannot be distinguished since the measured torque is an average value for the full circumference of the specimen. High strength dual phase steels exhibit almost isotropic yielding in the sheet plane, therefore, the error due to anisotropy in the presented results is negligible.

- **Bulging of very ductile, thin sheets**: In some piloting tests on different sheet materials, shear fracture could not be achieved for very ductile deep drawing steel grades like DC04 or DC06. These materials tend to buckle in the groove at larger strains instead of showing cracks. Further studies may investigate the influence of the groove radial position in order to evoke fracture before buckling. In addition, the sheet thickness and the groove depth can play important roles.

- **Specimen manufacturing**: While the laser cutting process for the round sheet specimen is simple, the machining of the groove requires more effort. Control of depth and concentric position of the groove is essential for this test. Due to the small residual material thickness, a small deviation from the nominal thickness can cause large errors in the stress calculation afterwards. Repeatability of the machining process and the surface roughness after cutting are also key aspects. In order to ensure the correct stress calculation, the depth and the thickness at the groove bottom are measured for each tested specimen by tactile coordinate measuring before testing.

- **Strain measurement**: As for all strain measurements using DIC, the strain gradient of the measurement influences the results. Especially for fracture strains, high strains are concentrated in a small area where the crack occurs. The reliability of the measurements depends strongly on the selected resolution, the evaluation algorithm, and the size of the involved neighboring area. This is a general issue for all fracture tests with optically measured fracture strain. However, at the current state-of-the-art, no better solutions for the strain measurement are available.

- **Maximum transferable torque of test device**: The used device in this work has a limit of about 1,300 Nm for the maximum torque. This causes a natural limit for the processable specimen thickness and groove radius. However, the real limit is smaller since the inner clamps can slip depending on the hardness of the specimen. Although slipping of the clamps does not cause an error of the stress or strain measurement, the achievement of fracture may be hindered due to the limited transferable torque at the inner fixtures.

13.5. Parameter Identification

As given before, identified from the moment-angle curves of the conducted in-plane torsion test, the flow curve of the material can be represented in sufficient accuracy with a power type hardening with $\sigma_y = A\varphi^n$ according to Hollomon where $A = 1370$ MPa and $n = 0.0752$. This leaves

the parameters of the fracture criteria to be identified only. The uncoupled structure of the fracture criteria allows the identification process at post processing because the damage has no effect on the flow curve in these models.

Although the developed shear test facilitates optimal conditions for shear fracture development, mathematically it constitutes an output for a single pair in the $(\eta, \bar{\theta})$ space. Each fracture locus, on the other hand, represents a continuous surface in the same space. Hence the identification of the parameters of the selected fracture criteria requires additional tests preferably spanning a broad range of stress triaxiality ratio and Lode parameter values. Since the current study aims at the promotion and mechanical justification of the proposed shear fracture test and not at a detailed analysis of an overall parameter identification strategies, the experimental results are extended by only three additional notched tensile tests with different notch radii. The experimental data of the notched tensile test were taken from [350]. With these additional tests, the database consists of a total of four points which can be used to identify parameters for at most four parameter models (in order to preclude an under-determined system). Material parameters controlling the identified flow curve are already known and do not need to be identified anymore for the considered models. Following the hybrid experimental numerical parameter identification strategy proposed in [191], the equivalent fracture strains φ_f and the corresponding averages for the stress triaxiality ratio η_{ave}, and the Lode angle parameter $\bar{\theta}_{ave}$ for the selected material are defined as listed in Table 13.2.

Table 13.2.: Triaxiality (average), Lode angle, and fracture strain measured for the notched tensile test and the grooved in-plane torsion test.

Test	η_{ave}	$\bar{\theta}_{ave}$	φ_f
NT, $R = 5$ mm	0.660	0.108	0.665
NT, $R = 10$ mm	0.627	0.249	0.710
NT, $R = 20$ mm	0.596	0.376	0.784
ST	0	0	0.910

To fit the fracture surfaces of the damage models to the data listed in Table 13.2 the toolbox of sftool in MATLAB is used. A summary of the results is given in Table 13.3[3] From this table it can be seen that models of LH and MMC show well fitting properties. In comparison, the LH model requires fewer parameters than the MMC model which involves also the hardening curve. The PMMS model also performs well. The RT model does not fit well the listed fracture points mainly due to the sensitivity of the material fracture to the Lode angle parameter. Finally, the single parameter CL model gave a negative R^2 value, which is a statement of an unacceptable fit.

In Figure 13.14, the equivalent fracture strain is given in the triaxiality space within the range of $-\frac{1}{3} \leq \eta \leq \frac{2}{3}$. All five fracture criteria with the above identified parameters are plotted within this diagram. The determined shear fracture point with the new proposed grooved specimen can be directly found in this diagram. However, the notched tensile fracture points with triaxialities in the range of $0.59 < \eta < 0.66$ are not visible in the plane stress triaxiality plane due to slightly varying Lode angle values. Nevertheless, the five curves show that the models are more or less capable of representing the experimental data given. The shear fracture point can be captured by all models except the CL model. Discrepancies and large differences can be found in the

---

[3]Note that the coefficient of determination, R^2, a number between 0 and 1, is used to describe how well a regression line fits a set of data. It being near 1 is an indication of the high quality of the fit of the regression line, while R^2 closer to 0 indicates that the regression line does not fit the data well.

Table 13.3.: Determined parameters for the fracture criteria.

Model	Parameters	R^2
LH	$a = 8.0$; $b = 0.30$; $C = 2.34$	1.0
MMC	$c_1 = 0.021$; $c_2 = 747.8$ MPa; $c_3 = 0.95$	1.0
PMMS	$c_1 = 0.026$; $c_2 = 785.1$ MPa	0.89
RT	$c_1 = 0$; $c_2 = 0.91$; $c_3 = 0.38$	0.89
CL	$C = 0.68$	< 0

area of uniaxial tension around $\eta = \pi/3$ and compressive stress states with $\eta < 0$ due to lack of experimental data at these loading conditions. The PMMS model tends to unrealistic high fracture strains for uniaxial tension with the data provided. The RT model exhibits an almost linear behavior in this view despite the flexibility of three parameters. The LH model by [192] and the MMC model by [183] give similar results.
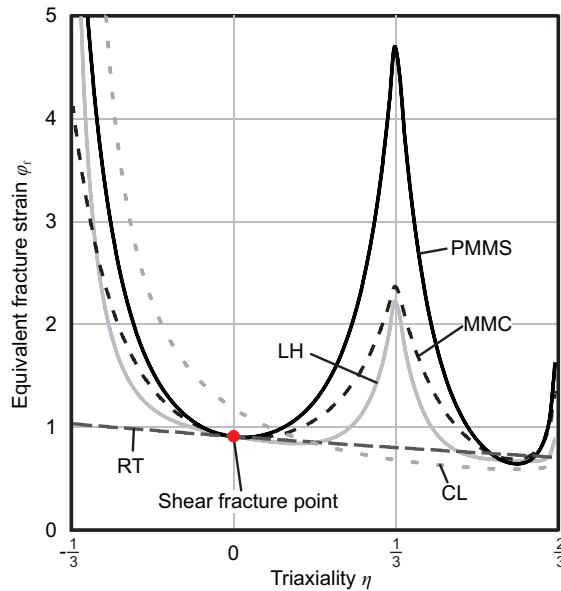
Figure 13.14.: Plot of the fracture locus for DP1000 for the five fracture criteria represented at the triaxiality (η) space for plane stress conditions for the identified parameters.

The rest of the analysis will focus on the outputs of the LH model. For a validation of the identified damage parameters, the simulations are performed this time with the developed VUS-DFLD subroutine for the LH model using the identified damage parameters. Once the damage accumulation reaches the critical value at a Gauss point, the corresponding reduced integration element is eliminated from the computational stack i.e., the so-called element deletion procedure is devised to create crack propagation. A comparison of the load-displacement curves for the notched tests are given in Figure 13.15. As seen in this figure, although a variation between the instant and average triaxialities is unavoidable for the conducted tests and the surface fitting for the fracture loci are done using average values, the load-displacement curves show acceptable results, at least for the total elongation at fracture. The load gap between the experimental and computed curves are mainly related to the form of the yield curve which is identified from the shear test mainly.

The comparison of the experimental and numerical force-displacement curves for the shear test
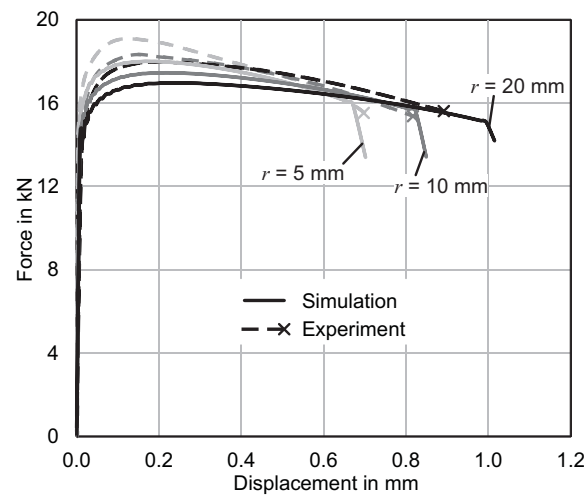
Figure 13.15.: The load-displacement diagram comparison of the experimental outputs and the simulations for the notched tensile tests by [350] where the LH model is used for determination of the incipient cracking.

is given in Figure 13.16. Since the flow curve identification relies on this test, there is an overall agreement between the experimentally and numerically handled plots. As far as the time of fracture is concerned, there is a slight premature prediction of the Lou and Huh model, which is acceptable. The reason for the fact that the simulations show a rapid drop after a kink rather than a smooth transition as seen in the experimental outputs during fracture propagation is that, in the simulation, the fracture happens suddenly through the whole radius where the elements are deleted. In the experiments this is not the case due to local heterogeneities. Moreover, the newly evolved surfaces during fracture might come into contact due to a possible loss of cyclic symmetry conditions.
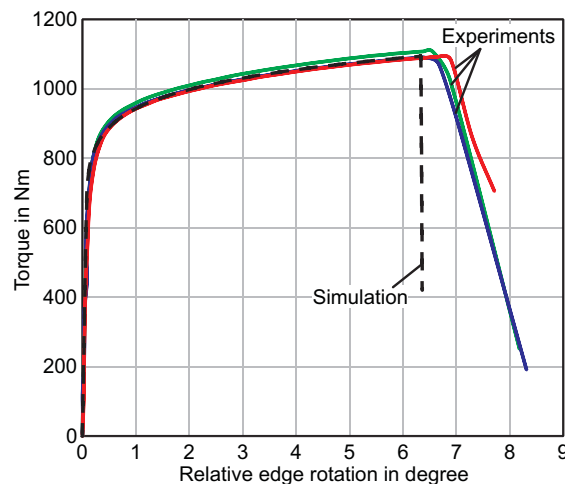
Figure 13.16.: The load-displacement diagram comparison of the experimental outputs and the simulations for the shear test where the Lou Huh model is used for determination of the incipient cracking.

The distribution of the damage indicator for the LH model is given in Figure 13.17. This distribution agrees well with the equivalent plastic strain distributions given in Figure 13.12. The outcome of this good agreement of the distributions is twofold: Firstly, this justifies once

more that the aimed ideal shear conditions are present. Secondly, it is understood that the experimental readings of the maximum shear strain by means of a DIC system at the deformed specimen surface are sufficient to determine the shear fracture strain. This brings a considerable feasibility for the determination of the test results and even makes finite element analysis and an inverse method unnecessary provided the test results could be processed using certain DIC systems with sufficient resolution. A final note on Figure 13.17 is that the fracture emanates from the critical element and along the corresponding column of elements. This ends of with a continuous slit in the form of a ring.
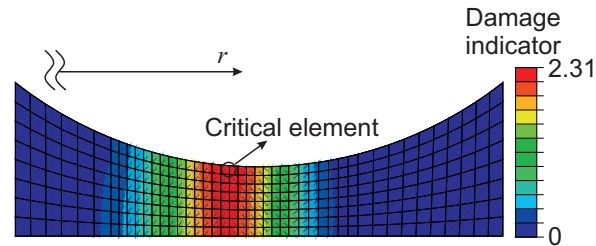
Figure 13.17.: Damage indicator contours over the specimen section at the incipient failure. r represents the radius measured from the center of the specimen. The critical element represents the element with maximum damage indicator.

13.6.   Conclusion and Outlook

Marciniak's original intention in using in plane torsion test was to investigate sheet metal formability [200]. In the current chapter, a return back to these the very roots of the in-plane torsion test is aimed at. The grooved in-plane torsion test is proposed as a shear fracture test for metallic sheets. The test uses round planar sheet specimens and in addition, a continuous radial groove is cut out from one side. With this new specimen, incipient cracking due to edge effects can be avoided. Furthermore, the location of the shear fracture can be controlled and positioned away from the boundaries in contact with the tools. This lets one have a clear view of the fracture process zone using digital image correlation systems for identifying the equivalent strain at fracture. FEA shows that the test is capable of creating material fracture under ideal shear conditions i.e., the condition of constantly triaxiality $\eta = 0$ and Lode parameter $\bar{\theta} = 0$ throughout the deformation. Accordingly, it is suitable to validate and/or quantify the recent shear extended damage and fracture models for the selected material classes. If the knowledge of material fracture at exact shear loading is required, this test is superior to all other known tests for sheet materials. As a model study, an attempt for parameter identification for a set of selected fracture criteria by complementing the currently developed shear test with notched tensile tests with various notch radii conducted on DP1000 specimens is presented. Among the selected criteria, the models proposed by [192] and [183] deliver the best results for selected experimental set.

For the outlook, many aspects are to be mentioned which require additional research work. This new test specimen needs further development although the model study provides good results. The process limits have to be found for ductile and thin sheet materials in order to achieve fracture before bulging. As an alternative to the machining process, the groove can also be produced by electrical discharging in form of die sinking. The influence of different cutting processes on the groove surface may also be interesting. Due to averaging effects, the developed

test is ideally suitable for sheet materials which do not show pronounced in-plane anisotropy, e.g. dual phase steel sheets. Its application is not limited to metallic materials either. In the future work, one main advantage of this test can be the ability to combine the characterization of kinematic hardening and shear fracture since load reversals can be achieved conveniently with the in-plane torsion test. Moreover, the grooved in-plane torsion specimen can also be used to characterize (monotonic) shear flow curves for high strength steels up to very high strains. As seen in the current study, equivalent strains of up to 0.9 were measured for DP1000. No other known test for sheet materials can reach strains like that for this material class.

14. Conclusions

The observed behavior of metallic materials in response to thermal and mechanical stimuli depends on the underlying microstructural changes and can vary greatly depending upon the magnitude and multiaxiality of loading and the magnitude of homologous temperature. The current thesis focuses on the phenomenological modeling approaches related to different microstructural mechanisms responsible for plastic hardening, ductile and brittle damage as well as complementary experimental mechanical characterization methodologies.

The presentation of the topics are divided in four main parts. In Part I, cross hardening as a path dependent hardening model for metallic sheets is studied. The model considers a fourth-order anisotropy tensor whose evolution encapsulates the dynamic and the latent hardening effects of dislocation structures parallel and orthogonal to the loading direction. Extensions of the original Levkovitch–Svendsen model, as presented in [181], to rate dependence in a Johnson–Cook formalism is considered in Chapter 2 together with an application of spring back prediction in industrial forming process of IF steel DC06 sheets in which the cross hardening effects with strain path change is evident. The role of reduction in yield locus curvature by cross hardening on the formability of metallic sheets is studied in Chapter 3 considering the first quadrant of the in-plane principal strain space. In absence of dynamic hardening component, strictly proportional strain paths give identical results for models with and without cross hardening. Hence, in order to invoke strain path variations, a stochastic finite element based Marciniak-Kuczyński and Nakazima tests are considered. A delayed localization with cross hardening is observed for all considered strain paths except for the plane strain path. This stability increase is linked to the decreased local curvature of the yield locus at the loading point which impedes the rotation of the normal for associated plastic flow. In the original Levkovitch–Svendsen model parallel and orthogonal projections used in controlling dynamic and latent hardening are based on the unit plastic flow direction $\boldsymbol{n}_p = \dot{\boldsymbol{E}}_p/|\dot{\boldsymbol{E}}_p|$. In Chapter 4, the use of the radial direction $\boldsymbol{n}_s = [\boldsymbol{S} - \boldsymbol{X}]/|\boldsymbol{S} - \boldsymbol{X}|$ is proposed instead. It is shown both analytically and numerically that, this remedies the undesired plastic strengthening in direction of the active proportional loading path even in the absence of dynamic hardening contribution, as observed in initially anisotropic materials.

This is followed localization, local and nonlocal fracture modeling approaches including low triaxiality shear fracture at room temperature, as given in Part II. Chapter 5 gives a detailed experimental numerical investigation of ductile fracture development in DP1000 steel sheets during free bending process. Observed fractures emanate at free surfaces at the apex of the bend. Fractographic studies attest a blended Mode I Mode II fracture driven by cavitation and subsequent strain localization. The numerical studies materializing a local version of Gurson's porous plasticity model with a shear modification made it possible to reproduce experimentally observed softening induced localization bands under plane strain constraint and consequent fracture patterns. In the local models, the size of the localization band is controlled by the selected mesh size. In this sense, the mesh size acts as a length scale associated with ductile damage. A

more powerful mesh objective approach for natural control of the localization size and reflection of size effects is through nonlocal formulations which incorporate a material length parameter. For ductile fracture this relates to the inter-particle spacing. In Chapter 6, a non-local extension of shear modified Gurson's porous plasticity model is established and used in investigation of the deformation and fracture behavior of P91 steel during small punch testing of disks with different thicknesses. The experimental studies demonstrate that for thinner disks diffuse necking with membrane stretching followed by a localized deformation precedes fracture whereas shear localization prevails for thicker ones. Comparison of the numerically and experimentally determined results show a considerable agreement in the force-displacement curves as well as the fracture patterns. Comparing the shear damage controlling parameter k_w identified for each DP1000 and P91 steel, it is observed that shear damage contribution in fracturing of DP1000 steels is more dominant with higher k_w value at corresponding scale of each test. For P91, values of k_w as high as that of DP1000 result in premature fracture, a result which gets more pronounced with increasing disk thickness. Due to smaller strain and stress gradients emerging in the small punch test for specimens without notch, similar estimations for different mesh sizes were observed for local and nonlocal formulations, until the severe localization phase.

In Chapter 7, two empirical extensions of the classical Lemaitre's damage model are investigated. Weighting damage evolution for the compressive principal stress components, the first extension considers a quasi-unilateral damage evolution. The second extension adds a shear stress dependent term in the evolution equation of damage. Material characterization studies conducted on the available database for proportional strain paths reported in the literature show that the two introduced modifications makes the model sufficiently flexible especially as compared to the common fracture criteria used in analysis of many manufacturing simulations. The implications of the modifications in the metal forming practice are also discussed.

Part III extends the discussion on damage, localization and fracture to account for the role of temperature. In Chapter 8 a unified thermo-plastic constitutive model combining the non-local RKR brittle damage model with the nonlocal Gurson's porous plasticity is established to predict temperature driven ductile-brittle transition in small punch test of P91 steel disks. Associated length scales are computed depending on the underlying material microstructure as well as conducted simulations. Both small- and large-scale yielding conditions are considered through notched and unnotched specimens, respectively. Comparison of experimental and numerical load-displacement curves as well as optical and SEM images of the fractured disks demonstrating the crack patterns and fracture surface morphologies validates the applied modeling strategy whose key ingredient is the temperature dependence of the yield stress.

Chapters 9 and 10, which are rather theoretical in nature, focus on development of thermo-mechanical frameworks which make use of the internal variable theory of thermodynamics for damage-coupled finite plasticity with nonlinear isotropic hardening. Underlying kinematics uses multiplicative decomposition of the deformation gradient into elastic and inelastic parts. In Chapter 9 an extension of [275] to rate dependent damage-coupled thermomechanics is studied. This allows modeling damage induced effects on thermal and other mechanical fields, such as deteriorated head conduction as well as reduction of mechanical stiffness and strength. It is demonstrated that decomposition of entropy into elastic, viscoplastic and damage parts is possible through a temperature dependent damage dissipation potential. Developed model is used in simulation of a set of example problems involving geometrical imperfection triggered necking of an axisymmetric bar and thermally triggered necking of a 3D rectangular bar. It is shown that surface convection of heat triggers necking which in turn causes increase of triaxiality at the

specimen center. This substantially accelerates the emergent damage rate and reduces global fracture strain of the specimen as compared to the homogeneous solution. The results also reveal the role of rate effect as a localization limiter for the current doubly softening model, with both damage and temperature.

In Chapter 10, the problem of ductile-brittle transition is revisited, establishing a thermodynamically consistent constitutive approach which considers both brittle and ductile damage development making use of two scalar state variables, d and f. d constitutes brittle damage variable whose kinetic relation relies on the postulated damage dissipation potential. The evolution of the void volume fraction f, on the other hand, relies on conservation of mass. Any dissipation associated with f, is thus that of plastic flows. Absorbed energy plots computed for various temperatures for uniaxial states of stress show that the model is capable of reflecting ductile-brittle transition. In agreement with Chapter 1, temperature dependence of the material yield stress is an indispensable ingredient of the model. Proposed model is advantageous as compared to the approach presented in Chapter 1 of this part which uses Gurson-type porous plasticity for ductile failure and Ritchie-Knott-Rice model for brittle fracture, since the energy dissipation associated with the cleavage-type of fracture is accounted for. Also, extension of the model to anisotropic brittle damage is possible within the same continuum thermodynamics formalism.

Part IV focuses on mechanical material characterization tests for sheet metals. In Chapter 11 use of optical strain field measurements in inverse parameter identification for plastic anisotropy is proposed in addition to the conventional force and displacement data. To span a wide strain path spectrum yet to provide a room for sufficient material deformation, smoothly notched tensile test specimens are used. Applications with 8 parameter Yld2000-2D model show that the proposed methodology proves useful in identification of model parameters while keeping the number of required characterization tests at a reasonable limit. This gains more importance considering time pressure in industrial applications and also more complex yield loci with more material parameters.

In Chapters 12 and 13 in-plane torsion test is explored with two specimen variants. With slitted disk specimens, cyclic twin bridge shear test is studied in Chapter 12 in characterization of kinematic hardening parameters. An inverse approach through finite element simulations is required due to lack of a closed form solution. Applications to three distinct steel classes, namely DC06, DP600 and TRIP700, demonstrates the usefulness of the test in characterization of Bauschinger effect and relevant phenomena. The last chapter of the thesis, Chapter 13, focuses on low triaxiality fracture parameter identification, which is the subject of a growing interest in the literature, see, e.g., [224, 338, 29] among others. To this end monotonic in-plane torsion tests exploiting radially grooved round planar sheet specimens is considered. Avoiding slits with continuous radial groove not only helps avoiding edge fracture but also provides control on the fracture location. This allows in situ identification of fracture strain through digital image correlation systems. The numerical studies with finite element analysis show that, as intended, fracture initiates within the groove under ideal shear conditions with vanishing triaxiality $\eta = 0$ and Lode parameter $\bar{\theta} = 0$. Thus, the test is suitable to characterize shear fracture for metallic sheets.

Bibliography

[1] European Structural Integrity Society (ESIS) Technical Committee 8, Numerical Round Robin on Micro-Mechanical Models. Technical report, 1997.

[2] ASM Handbook, Vol. 8: Mechanical Testing and Evaluation, ASM International. Technical report, 2000.

[3] ABAQUS Documentation, Dassault Systèmes, Providence, RI, USA. Technical report, 2012.

[4] A. Abel and R. K. Ham. The cyclic strain behaviour of crystals of aluminum-4 wt.% copper-i. the bauschinger effect. *Acta Metallurgica*, 14(11):1489–1494, 1966.

[5] M. Abendroth and M. Kuna. Determination of deformation and failure properties of ductile materials by means of the small punch test and neural networks. *Computational Material Science*, 28:633–644, 2003.

[6] M. Abenroth and M. Kuna. Identification of ductile damage and fracture parameters from the small punch test using neural networks. *Engineering Fracture Mechanics*, (73):710–725, 2006.

[7] J. Aboudi, S. Arnold, and B. Bednarcyk. *Micromechanics of Composite Materials A Generalized Multiscale Analysis Approach*. Elsevier Science and Technology, 2012.

[8] R. Akeret. Failure mechanisms in the bending of aluminum sheets and limits of bendability. *Aluminium*, 54:117–123, 1978.

[9] L. Anand, M. E. Gurtin, S. P. Lele, and C. Gething. A one-dimensional theory of strain-gradient plasticity: Formulation, analysis, numerical results. *Journal of the Mechanics and Physics of Solids*, 53:1789–1826, 2005.

[10] L. Anand and S. R. Kalidindi. The process of shear band formation in plane strain compression of fcc metals: Effects of crystallographic texture. *Mechanics of Materials*, 17(2-3):223–243, 1994.

[11] T. L. Anderson. *Fracture Mechanics: Fundamentals and Applications*. CRC Press, 2004.

[12] H. Andersson. Analysis of a model for void growth and coalescence ahead of a moving crack tip. *Journal of the Mechanics and Physics of Solids*, 25(3):217–233, 1977.

[13] A. Andrieu, A. Pineau, J. Besson, D. Ryckelynck, and O. Bouaziz. Bimodal Beremin-type model for brittle fracture of inhomogeneous ferritic steels: Theory and applications. *Engineering Fracture Mechanics*, 95:84–101, 2012.

[14] F. Armero and J. C. Simo. A new unconditionally stable fractional step method for non-linear coupled thermomechanical problems. *International Journal for Numerical Methods in Engineering*, 35(4):737–766, 1992.

[15] F. Armero and J. C. Simo. A priori stability estimates and unconditionally stable product formula algorithms for nonlinear coupled thermoplasticity. *International Journal of Plasticity*, 9(6):749–782, 1993.

[16] J. Asaro. Material modelling and failure modes in metal plasticity. *International Journal of Mechanical Sciences*, 4:343–373, 1985.

[17] G. Atkins. Fracture mechanics and metal forming: damage mechanics and the local approach of yesterday and today. In H. P. Rossmanith, editor, *Fracture Research in Retrospect: An anniversary volume in honour of G.R. Irwin's 90th birthday*. CRC Press, Rotterdam: Balkema, 1997.

[18] S. Avril, M. Bonnet, A.-S. Bretelle, M. Grédiac, F. Hild, P. Ienny, F. Latourte, D. Lemosse, S. Pagano, E. Pagnacco, and F. Pierron. Overview of identification methods of mechanical parameters based on full-field measurements. *Experimental Mechanics*, 48(4):381–402, 2008.

[19] H. Badreddine, K. Saanouni, and A. Dogui. On non-associative anisotropic finite plasticity fully coupled with isotropic ductile damage for metal forming. *International Journal of Plasticity*, 26(11):1541–1575, 2010.

[20] Y. Bai and T. Wierzbicki. A new model of metal plasticity and fracture with pressure and Lode dependence. *International Journal of Plasticity*, 24:1071–1096, 2008.

[21] Y. Bai and T. Wierzbicki. Application of extended Mohr-Coulomb criterion to ductile fracture. *International Journal of Fracture*, 161:1–20, 2010.

[22] J. Baik, J. Kameda, and O. Buck. Development of small punch tests for ductile-brittle transition temperature measurement of embrittled Ni-Cr steels. *ASTM*, STP 888-EB:92–111, 1986.

[23] A. Baltov and A. Sawczuk. A rule of anisotropic hardening. *ACTA Mechanica*, 1(2):81–92, 2012.

[24] D. Banabic. *Sheet Metal Forming Processes: Constitutive Modelling and Numerical Simulation*. Springer-Verlag, Berlin, Heidelberg, 2010.

[25] D. Banabic, H. Aretz, D. S. Comsa, and L. Paraianu. An improved analytical description of orthotropy in metallic sheets. *International Journal of Plasticity*, 21(3):493–512, 2005.

[26] D. Banabic, D. S. Comsa, M. Sester, M. Selig, W. Kubli, K. Mattiasson, and M. Sifvant. Influence of constitutive equations on the accuracy of prediction in sheet metal forming simulation. In *Proceedings of the 7th International Conference and Workshop on Numerical Simulation of 3D Sheet Metal Forming Processes*, pages 7–42, 2008.

[27] D. Banabic, T. Kuwabara, T. Balan, D. S. Comsa, and D. Julean. Non-quadratic yield criterion for orthotropic sheet metals under plane-stress conditions. *International Journal of Mechanical Sciences*, 45(5):797–811, 2003.

[28] Y. Bao, X. Teng, and T. Wierzbicki. On the application of stress triaxiality formula for plane strain fracture testing. *Journal of Engineering Materials and Technology*, 131:021002–1–10, 2009.

[29] Y. Bao and T. Wierzbicki. On fracture locus in the equivalent strain and stress triaxiality space. *International Journal of Mechanical Sciences*, 46(1):81–98, 2004.

[30] Y. Bao and T. Wierzbicki. On the cut-off value of negative triaxiality. *International Journal of Fracture*, 72(7):1049–1069, 2005.

[31] L. Bardella. A deformation theory of strain gradient crystal plasticity that accounts for geometrically necessary dislocations. *Journal of the Mechanics and Physics of Solids*, 54:128–160, 2006.

[32] S. Bargmann, B. Svendsen, and M. Ekh. An extended crystal plasticity model for latent hardening in polycrystals. *Computational Mechanics*, 48:631–648, 2011.

[33] F. Barlat, R. C. Becker, Y. Hayashida, Y. Maeda, M. Yanagawa, K. Chung, J. C. Brem, D. J. Lege, K. Matsui, S. J. Murtha, and S. Hattori. Yielding description for solution strengthened aluminum alloys. *International Journal of Plasticity*, 13(4):385–401, 1997.

[34] F. Barlat, J. C. Brem, J. W. Yoon, K. Chung, R. E. Dick, D. J. Lege, F. Pourboghrat, S. H. Choi, and E. Chu. Plane stress yield function for aluminum alloy sheets-Part I: Theory . *International Journal of Plasticity*, 19(9):1297–1319, 2003.

[35] F. Barlat, J. J. Gracio, M. G. Lee, E. F. Rauch, and G. Vincze. An alternative to kinematic hardening in classical plasticity. *International Journal of Plasticity*, 27(9):1309–1327, 2011.

[36] F. Barlat, J. Ha, J. J. Gracio, M. G. Lee, E. F. Rauch, and G. Vincze. Extension of homogeneous anisotropic hardening model to cross-loading with latent effects. *International Journal of Plasticity*, 46:130–142, 2013.

[37] F. Barlat, D. J. Lege, and J. C. Brem. A six component yield function for anisotropic materials. *International Journal of Plasticity*, 7:693–712, 1991.

[38] F. Barlat, Y. Maeda, K. Chung, M. Yanagawa, J. C. Brem, Y. Hayashida, D. J. Lege, K. Matsui, S. J. Murtha, S. Hattori, R. C. Becker, and S. Makosey. Yield function development for aluminum alloy sheets. *Journal of the Mechanics and Physics of Solids*, 1997.

[39] I. Barsoum and J. Faleskog. Rupture mechanisms in combined tension and shear experiments. *International Journal of Solids and Structures*, 44(6):1768–1786, 2007.

[40] C. Barthel, B. Klusemann, R. Denzer, and B. Svendsen. Modeling of a thermomechanical process chain for sheet steels. *International Journal of Mechanical Sciences*, 74:46–54, 2013.

[41] C. Barthel, V. Levkovitch, and B. Svendsen. Modeling of sheet metal forming processes taking into account distortional hardening. *International Journal of Material Forming*, 1:105–108, 2008.

[42] R. C. Batra and M. Lear. Simulation of brittle and ductile fracture in an impact loaded prenotched plate. *International Journal of Fracture*, 126(2):179–203, 2004.

[43] M. Bauer. *Ermittlung der Fliesskurven von Feinblechen im ebenen Torsionsversuch*. PhD thesis, 1989.

[44] J. Bauschinger. Über die Veränderung der Elastizitätsgrenze und des Elastizitätsmoduls verschiedener Metalle. *Civilingenieur*, (27):289–348, 1881.

[45] Z. Bazant, T. B. Belytschko, and T. P. Chang. Continuum theory for strain softening. *Journal of the Engineering Mechanics Division ASCE*, 110(12):1666–1692, 1984.

[46] C. D. Beachem and G. R. Yoder. Elastic-plastic fracture by homogeneous microvoid coalescence tearing along alternating shear planes. *Metallurgical Transactions*, 4(4):1145–1153, 1973.

[47] R. Becker. An analysis of shear localization during bending of a polycrystalline sheet. *ASME. Journal of Applied Mechanics*, 59:491–496, 1992.

[48] R. Becker and A. Needleman. Effect of yield surface curvature on necking and failure in porous plastic solids. *ASME. Journal of Applied Mechanics*, 53(3):491–499, 1986.

[49] A. Behrouzi, C. Soyarslan, B. Klusemann, and S. Bargmann. Inherent and induced anisotropic finite visco-plasticity with applications to the forming of DC06 sheets. *International Journal of Mechanical Sciences*, 89:101–111, 2014.

[50] T. Belytschko, Y. Y. Lu, and L. Gu. Element-free Galerkin methods. *International Journal for Numerical Methods in Engineering*, 37:229–256, 2004.

[51] M. Ben Bettaieb, X. Lemoine, O. Bouaziz, A. M. Habraken, and L. Duchêne. A finite element analysis of the bending and the bendability of metallic sheets. *International Journal of Material Forming*, 4(3):283–297, 2011.

[52] F. Beremin. A local criterion for cleavage fracture of a nuclear pressure vessel steel. *Metallurgical Transactions*, 14A:2277–2287, 1983.

[53] J. Besson. Damage of ductile materials deforming under multiple plastic or viscoplastic mechanisms. *International Journal of Plasticity*, 25(11):2204–2221, 2009.

[54] M. B. Bettaieb, X. Lemoine, L. Duchêne, and A. M. Habraken. Simulation of the bending process of hardening metallic sheets using damage model. Part I: Theoretical development and numerical implementation. *Materials Science and Engineering: A*, 528(1):434–441, 2010. Special Topic Section: Local and Near Surface Structure from Diffraction.

[55] S. H. A. Boers, M. G. D. Geers, and V. G. Kouznetsova. Contactless and frictionless pure bending. *Experimental Mechanics*, 50(6):683–693, 2010.

[56] N. Bonora, D. Gentile, A. Pirondi, and G. Newaz. Ductile damage evolution under triaxial state of stress: theory and experiments. *International Journal of Plasticity*, 21(5):981–1007, 2005.

[57] N. Bonora, A. Ruggiero, L. Esposito, and D. Gentile. CDM modeling of ductile failure in ferritic steels: Assessment of the geometry transferability of model parameters . *International Journal of Plasticity*, 22(11):2015–2047, 2006. Damage and Fracture: Modeling and Experiments.

[58] S. Bouvier, H. Haddadi, P. Levee, and C. Teodosiu. Simple shear tests: Experimental techniques and characterization of the plastic anisotropy of rolled sheets at large strains. *Journal of Materials Processing Technology*, 172:96–103, 2006.

[59] P. W. Bridgman. Studies in large plastic flow and fracture with special emphasis on the effects of hydrostatic pressure. *McGraw-Hill, New York*, 1952.

[60] D. Broek. *Elementary Engineering Fracture Mechanics*. Springer, 1982.

[61] A. Brosius, Q. Yin, A. Güner, and A. E. Tekkaya. A new shear test for sheet metal characterization. *Steel Research International*, 82(4):323–328, 2011.

[62] L. M. Brown and J. D. Embury. The initiation and growth of voids at second phase particles. *In Proceedings of the Third International Conference on the Strength of Metals and Alloys, Institute of Metals, London*, 25 (3):164, 1973.

[63] M. Brunig. An anisotropic ductile damage model based on irreversible thermodynamics. *International Journal of Plasticity*, 19:1679–1713, 2003.

[64] M. Brunig and S. Ricci. Non-local continuum theory of anisotropically damaged metals. *International Journal of Plasticity*, 21:1346–1382, 2005.

[65] J. Cao, W. Lee, H. S. Cheng, M. Seniw, H. P. Wang, and K. Chung. Experimental and numerical investigation of combined isotropic-kinematic hardening behavior of sheet metals. *International Journal of Plasticity*, 25(5):942–972, 2009.

[66] T. S. Cao. Numerical simulation of 3D ductile cracks formation using recent improved Lode-dependent plasticity and damage models combined with remeshing. *International Journal of Solids and Structures*, 51:2370–2381, 2014.

[67] T. S. Cao, A. Gaillac, P. Montmitonnet, and P. O. Bouchard. Identification methodology and comparison of phenomenological ductile damage models via hybrid numerical-experimental analysis of fracture experiments conducted on a zirconium alloy. *International Journal of Solids and Structures*, 50:3984–3999, 2013.

[68] B. G. Çakan, C. Soyarslan, S. Bargmann, and P. Hähner. Ductile fracture under large-scale yielding conditions: Experimental and computational study of the small punch test. *Materials*, 10(10) - 1185, 2017.

[69] CEN Workshop Agreement. Small punch test method for metallic materials. Technical Report CWA 15627, 2006.

[70] J. L. Chaboche. Time-independent constitutive theories for cyclic plasticity. *International Journal of Plasticity*, 2(2):149–188, 1986.

[71] J. L. Chaboche, M. Boudifa, and K. Saanouni. A CDM approach of ductile damage with plastic compressibility. *International Journal of Fracture*, 137(1):51–75, 2006.

[72] A. Chatterjee, D. Chakrabarti, A. Moitra, and A. K. Bhaduri. Effect of normalization temperatures on ductile-brittle transition temperature of a modified 9Cr-1Mo steel. *Material Science & Engineering A*, 618:219–231, 2014.

[73] B. K. Choundhary, D. P. Rao Palaparti, and I. Samuel. Analysis of tensile stress-strain and work-hardening behavior in 9Cr-1Mo ferritic steel. *Metallurgical and Materials Transactions A*, 44A:212–223, 2013.

[74] J. Christoffersen and J. W. Hutchinson. A class of phenomenological corner theories of plasticity. *Journal of the Mechanics and Physics of Solids*, 27(5):465–487, 1979.

[75] C. C. Chu and A. Needleman. Void nucleation effects in biaxially stretched sheets. *ASME. Journal of Engineering Materials and Technology*, 102(3):249–256, 1980.

[76] T. Clausmeyer, G. Gerstein, S. Bargmann, B. Svendsen, A. H. van den Boogaard, and B. Zillmann. Experimental characterization of microstructure development during loading path changes in bcc sheet steels. *Journal of Materials Science*, 48(2):674–689, 2013.

[77] T. Clausmeyer, A. H. van den Boogaard, M. Noman, M. Gershteyn, M. Schaper, B. Svendsen, and S. Bargmann. Phenomenological modeling of anisotropy induced by evolution of the dislocation structure on the macroscopic and microscopic scale. *International Journal of Material Forming*, 4(10):141–154, 2011.

[78] M. G. Cockcroft and D. J. Latham. Ductility and the workability of metals. *Journal of the Institute Metals*, 96:33–39, 1968.

[79] B. D. Coleman and M. E. Gurtin. Thermodynamics with internal state variables. *The Journal of Chemical Physics*, 47(2):597–613, 1967.

[80] T. F. Coleman and Y. Y. Li. On the convergence of interior-reflective newton methods for nonlinear minimization subject to bounds. *Mathematical Programming*, 67(1-3):189–224, 1994.

[81] T. F. Coleman and Y. Y. Li. An interior trust region approach for nonlinear minimization subject to bounds. *Siam Journal on Optimization*, 6(2):418–445, 1996.

[82] S. Curtze, V. T. Kuokkala, M. Hokka, and P. Peura. Deformation behavior of TRIP and DP steels in tension at different temperatures over a wide range of strain rates. *Materials Science And Engineering: A*, 507(1-2):124–131, 2009.

[83] C. T. D. Reckwerth. The principle of generalized energy equivalence in the continuum damage mechanics. In K. Hutter and H. Baaser, editors, *Deformation and Failure in Metallic Materials, Springer-Verlag, Berlin Heidelberg*, pages 381–406, 2003.

[84] L. A. B. da Cunda, E. Bittencourt, and G. Creus. Analysis of ductile damage coupled with thermoplasticity by the FEM. In S. Idelsohn, E. Oñate, and E. Dvorkin, editors, *Computational Mechanics New Trends and Applications, CIMNE, Barcelona, Spain*, pages 1–13, 1998.

[85] M. Dao and M. Li. A micromechanics study on strain-localization-induced fracture initiation in bending using crystal plasticity models. *Philosophical Magazine A*, 81(8):1997–2020, 2001.

[86] E. A. de Souza Neto and D. Perić. A computational framework for a class of fully coupled models for elastoplastic damage at finite strains with reference to the linearization aspects. *Computer Methods in Applied Mechanics and Engineering*, 130(1):179–193, 1996.

[87] E. A. de Souza Neto, D. Perić, and D. R. J. Owen. *Computational Methods for Plasticity: Theory and Applications.* John Wiley and Sons Ltd, Chichester, UK, 2008.

[88] F. P. Duda, A. Ciarbonetti, P. J. Sánchez, and A. E. Huespe. A phase-field/gradient damage model for brittle fracture in elastic–plastic solids. *International Journal of Plasticity*, 65:269–296, 2015.

[89] L. P. Evers, W. A. M. Brekelmans, and M. G. D. Geers. Scale dependent crystal plasticity framework with dislocation density and grain boundary effects. *International Journal of Solids and Structures*, 41:5209–5230, 2004.

[90] H. P. Feigenbaum and Y. F. Dafalias. Directional distortional hardening in metal plasticity within thermodynamics. *International Journal of Solids and Structures*, 44:7526–7542, 2007.

[91] H. P. Feigenbaum and Y. F. Dafalias. Simple model for directional distortional hardening in metal plasticity within thermodynamics. *ASCE Journal of Engineering Mechanics*, 134(9):730–738, 2008.

[92] P. Flores, F. Bonnet, and A. M. Habraken. Plane strain test for metal sheet characterization. *Key Engineering Materials*, 344:135–142, 2007.

[93] A. G. Franklin. Comparison between a quantitative microscope and chemical methods for assessment of non-metallic inclusions. *Journal of the Iron and Steel Institute*, 207:181–186, 1969.

[94] C. O. Frederick and P. J. Armstrong. A mathematical representation of the multiaxial bauschinger effect. *Materials at High Temperatures*, 24(1):1–26, 2007.

[95] A. Ganczarski. *Thermo-Damage Coupling Modelling and Applications for Creep Conditions*, pages 317–349. Springer, Berlin, Heidelberg, 2003.

[96] B. Gardey, S. Bouvier, V. Richard, and B. Bacroix. Texture and dislocation structures observation in a dual-phase steel under strain-path changes at large deformation. *Materials Science and Engineering: A*, 400–401(0):136–141, 2005.

[97] J. C. Gelin and O. Ghouati. An inverse method for determining viscoplastic properties of aluminum-alloys. *Journal of Materials Processing Technology*, 45(1-4):435–440, 1994.

[98] J. C. Gelin and O. Ghouati. The inverse approach for the determination of constitutive equations in metal forming. *CIRP Annals-Manufacturing Technology*, 44(1):189–192, 1995.

[99] L. M. Geng and R. H. Wagoner. Role of plastic anisotropy and its evolution on springback. *International Journal of Mechanical Sciences*, 44(1):123–148, 2002.

[100] M. M. Gharbi, C. Labergere, H. Badreddine, C. Soyarslan, A. Weinrich, M. Hermes, S. Chatti, H. Sulaiman, K. Saanouni, and A. E. Tekkaya. Advanced experimental–numerical investigations of cold bending of high strength steels. In *Steel Research International, Special Edition: 10th International Conference on Technology of Plasticity, ICTP2011*, pages 877–883, 2011.

[101] A. Ghazanfari and A. Assempour. Calibration of forming limit diagrams using a modified Marciniak–Kuczyński model and an empirical law. *Materials and Design*, 34:185–191, 2012.

[102] A. Ghiotti, F. S., S. Bruschi, and B. P. F. Modelling of the Mannesmann effect. *CIRP Annals-Manufacturing Technology*, 58:255–258, 2009.

[103] A. Ghosh. The influence of strain hardening and strain-rate sensitivity on sheet metal forming. *Journal of Engineering Materials and Technology*, 99(3):264–274, 1977.

[104] A. K. Ghosh and W. A. Backofen. Strain hardening and instability in biaxially streched sheets. *Metallurgical Transactions*, 4(4):1113–1123, 1973.

[105] G. Goodwin. Application of strain analysis to sheet metal forming problems in the press shop. Technical Report 680093, SAE Technical Paper, 1968.

[106] S. M. Graham, T. Zhang, X. Gao, and M. Hayden. Development of a combined tension-torsion experiment for calibration of ductile fracture models under conditions of low triaxiality. *International Journal of Mechanical Sciences*, 54(1):172–181, 2012.

[107] B. Gülçimen, A. Durmuş, S. Ülkü, R. C. Hurst, K. Turba, and P. Hähner. Mechanical characterisation of a P91 weldment by means of small punch fracture testing. *International Journal of Pressure Vessels and Piping*, 105-106:28–35, 2013.

[108] B. Gülçimen and P. Hähner. Determination of creep properties of a P91 weldment by small punch testing and a new evaluation approach. *Materials Science and Engineering: A*, 588:125–131, 2013.

[109] A. Güner, C. Soyarslan, A. Brosius, and A. E. Tekkaya. Characterization of anisotropy of sheet metals employing inhomogeneous strain fields for Yld2000-2D yield function. *International Journal of Solids and Structures*, 49(25):3517–3527, 2012.

[110] A. L. Gurson. Continuum theory of ductile rupture by void nucleation and growth-Part I. Yield criteria and rules for porous ductile media. *Journal of Engineering Materials and Technology*, 99:2–15, 1977.

[111] L. Gurson. *Plastic flow and fracture behavior of ductile materials incorporating void nucleation, growth, and interaction.* PhD thesis, Brown University, 1975.

[112] J. S. Ha and E. Fleury. Small punch tests to estimate the mechanical properties of steels for steam power plant: II. Fracture Toughness. *International Journal of Pressure Vessels and Piping*, 75:707–713, 1998.

[113] H. Haddadi, S. Bouvier, M. Banu, C. Maier, and C. Teodosiu. Towards an accurate description of the anisotropic behaviour of sheet metals under large plastic deformations: Modelling, numerical analysis and identification. *International Journal of Plasticity*, 22(12):2226–2271, 2006.

[114] P. Håkansson, M. Wallin, and M. Ristinmaa. Thermomechanical response of non-local porous material. *International Journal of Plasticity*, 22(11):2066–2090, 2006. Damage and Fracture: Modeling and Experiments.

[115] R. Hambli, A. Mkaddem, and A. Potiron. Damage prediction in L-bending processes using FEM. *The International Journal of Advanced Manufacturing Technology*, 22(1):12–19, 2003.

[116] R. Hambli, A. Mkadem, and A. Potiron. Finite element damage modeling in bending processes. *Journal of Materials Processing Technology*, 147(3):302–310, 2004.

[117] O. Hamdane, J. Bouquerel, I. Proriol-Serre, and J. B. Vogt. Effect of heat treatment on liquid sodium embrittlement of T91 martensitic steel. *Journal of Materials Processing Technology*, 211:2085–2090, 2011.

[118] A. Hannon and P. Tiernan. A review of planar biaxial tensile test systems for sheet metal. *Journal of Materials Processing Technology*, 198(1-3):1–13, 2008.

[119] N. R. Hansen and H. L. Schreyer. A thermodynamically consistent framework for theories of elastoplasticity coupled with damage. *International Journal of Solids and Structures*, 31(3):359–389, 1994.

[120] H. Z. Hencky. Zur Theorie Plastischer Deformationen und der hierdurch im Material hervorgerufenen Nachspannungen. *Journal of Applied Mathematics and Mechanics / Zeitschrift für Angewandte Mathematik und Mechanik*, 4:232–334, 1924.

[121] T. B. Hilditch, J. G. Speer, and D. K. Matlock. Influence of low-strain deformation characteristics of high strength sheet steel on curl and springback in bend-under-tension tests. *Journal of Materials Processing Technology*, 182(1-3):84–94, 2007.

[122] R. Hill. A theory of the yielding and plastic flow of anisotropic metals. *Proceedings of the Royal Society of London A: Mathematical, Physical and Engineering Sciences*, 193(1033):281–297, 1948.

[123] R. Hill. Constitutive modelling of orthotropic plasticity in sheet metals. *Journal of the Mechanics and Physics of Solids*, 38(3):405–417, 1990.

[124] S. Hiwatashi, A. van Bael, P. van Houtte, and C. Teodosiu. Modelling of plastic anisotropy based on texture and dislocation structure. *Compuational Material Science*, 9:274–284, 1997.

[125] B. Holmedal, P. van Houtte, and Y. An. A crystal plasticity model for strain-path changes in metals", international journal of plasticity. *International Journal of Plasticity*, 24(8):702–707, 2008.

[126] W. F. Hosford. A generalized isotropic yield criterion. *ASME. Journal of Applied Mechanics*, E. 39:607–, 1972.

[127] W. F. Hosford. *Mechanical behavior of materials*. Cambridge Univ. Press, Cambridge, 2005.

[128] Z. Hu, E. F. Rauch, and C. Teodosiu. Work-hardening behavior of mild steel under stress reversal at large strains. *International Journal of Plasticity*, 8(7):839–856, 1992.

[129] D. Hull. *Fractography: Observing, Measuring and Interpreting Fracture Surface Topography*. Cambridge University Press, 1999.

[130] E. Husser, S. Bargmann, and E. Lilleodden. Computational modeling of intrinsically induced strain gradients during compression of c-axis oriented magnesium single crystal. *Acta Materialia*, 71:206–219, 2014.

[131] E. Husser, T. Clausmeyer, G. Gershteyn, and S. Bargmann. Determination of average dislocation densities in metals by analysis of digitally processed tem images. *Material Science and Engineering Technology*, 44(6):541–546, 2013.

[132] J. Hutchinson and K. Neale. Influence of strain-rate sensitivity on necking under uniaxial tension. *Acta Metallurgica*, 25(8):839–846, 1977.

[133] J. W. Hutchinson and K. W. Neale. *Sheet Necking-III. Strain-Rate Effects*, pages 269–285. Springer US, Boston, MA, 1978.

[134] G. Hütter, T. Linse, S. Roth, U. Mühlich, and M. Kuna. A modeling approach for the complete ductile-brittle transition region: cohesive zone in combination with a non-local gurson-model. *International Journal of Fracture*, 185(1):129–153, 2014.

[135] A. Ibrahimbegovic and F. Gharzeddine. Finite deformation plasticity in principal axes: from a manifold to the euclidean setting. *Computer Methods in Applied Mechanics and Engineering*, 1999.

[136] K. Inal, K. Neale, and A. Aboutajeddine. Forming limit comparisons for FCC and BCC sheets. *International Journal of Plasticity*, 21(6):1255–1266, 2005.

[137] N. Iosipescu. New accurate procedure for single shear testing of metals. *Journal of Materials*, 3:537–566, 1967.

[138] J. Jackiewicz. Calibration and evaluation of a combined fracture model of microvoid growth that may compete with shear in polycrystalline microstructure by means of evolutionary algorithms. *Computational Materials Science*, 45:133–149, 1969.

[139] K. R. Jayadevan and R. Narasimhan. Finite element simulation of wedge indentation. *Computers & Structures*, 57(5):915–927, 1995.

[140] X. Jia and Y. Dai. Small punch tests on martensitic/ferritic steels F82H, T91 and Optimax-A irradiated in SINQ Target-3. *Journal of Nuclear Materials*, 323:360–367, 2003.

[141] N. Y. Jin and A. T. Winter. Dislocation structures in cyclically deformed [001] copper crystals. *Acta Metallurgica*, 32(8):1173–1176, 1984.

[142] G. J. Johnson and W. H. Cook. A constitutive model and data for metals subjected to large strains, high strain rates and high temperatures. *Proc. 7th International Symposium on Ballistics, The Hague*, pages 541—-547, 1983.

[143] G. R. Johnson and W. H. Cook. Fracture characteristics of three metals subjected to various strains, strain rates, temperatures and pressures. *Engineering Fracture Mechanics*, 21:31–48, 1985.

[144] J. W. Ju. Isotropic and anisotropic damage variables in continuum damage mechanics. *Journal of Engineering Mechanics*, 116:283—287, 1990.

[145] L. M. Kachanov. Time of the rupture process under creep conditions. *Izv Akad Nauk SSR*, 273:26–31, 1958.

[146] J. Kajberg and G. Lindkvist. Characterisation of materials subjected to large strains by inverse modelling based on in-plane displacement fields. *International Journal of Solids and Structures*, 41(13):3439–3459, 2004.

[147] S. R. Kalidini, C. A. Bronkhorst, and L. Anand. Crystallographic texture evolution during bulk deformation processing of fcc metals. *Journal of the Mechanics and Physics of Solids*, 40:537–569, 1992.

[148] A. P. Karafillis and M. C. Boyce. A general anisotropic yield criterion using bounds and a transformation weighting tensor. *Journal of the Mechanics and Physics of Solids*, 41:1859–1886, 1993.

[149] S. Keeler and W. Backofen. Plastic instability and fracture in sheets stretched over rigid punches. *Transactions of the American Society for Metals*, 56:25–48, 1963.

[150] A. S. Khan and M. Baig. Anisotropic responses, constitutive modeling and the effects of strain-rate and temperature on the formability of an aluminum alloy. *International Journal of Plasticity*, 27(4):522–538, 2011.

[151] D. Kim, H. Kim, J. H. Kim, M.-G. Lee, K. J. Kim, F. Barlat, Y. Lee, and K. Chung. Modeling of forming limit for multilayer sheets based on strain-rate potentials. *International Journal of Plasticity*, 75:63–99, 2015. Special Issue: Metal Forming – Challenges in Constitutive and Fracture Modeling.

[152] J. H. Kim, M.-G. Lee, D. Kim, and F. Barlat. Numerical procedures for predicting localization in sheet metals using crystal plasticity. *Computational Materials Science*, 72:107–115, 2013.

[153] J. H. Kim, J. H. Sung, D. K. Matlock, D. Kim, and R. H. Wagoner. Influence of low-strain deformation characteristics of high strength sheet steel on curl and springback in bend-under-tension tests. *International Journal of Material Forming*, 3:187—-190, 2010.

[154] J. H. Kim, J. H. Sung, K. Piao, and R. Wagoner. The shear fracture of dual-phase steel. *international Journal of Plasticity*, 27:1658–1676, 2011.

[155] R. Kishore and T. K. Sinha. Modification of microstructure and the alligatoring damage in a modified 9Cr-1Mo steel. *Journal of Nuclear Materials*, 273:334–337, 1999.

[156] R. L. Klueh and A. T. Nelson. Ferritic/martensitic steels for next-generation reactors. *Journal of Nuclear Materials*, 371:37–52, 2007.

[157] S. Kobayashi, S. Oh, and T. Altan. *Metal Forming and Finite Element Method*. Oxford University Press, 1989.

[158] D. P. Kroese and Z. I. Botev. Spatial process generation. *arXiv:1308.0399*, 2013.

[159] M. Kuroda and V. Tvergaard. Shear band development predicted by a non-normality theory of plasticity and comparison to crystal plasticity predictions. *International Journal of Solids and Structures*, 2001.

[160] M. Kuroda and V. Tvergaard. Shear band development in anisotropic bent specimens. *European Journal of Mechanics-A/Solids*, 23(5):811–821, 2004.

[161] M. Kuroda and V. Tvergaard. Effects of texture on shear band formation in plane strain tension/compression and bending. *International Journal of Plasticity*, 23(2):244–272, 2007.

[162] T. Kurtyka and M. Zyczkowski. Evolution equation for distortional plastic hardening. *International Journal of Plasticity*, 12(2):81–98, 1996.

[163] T. Kuwabara. Advances in experiments on metal sheets and tubes in support of constitutive modeling and forming simulations. *International Journal of Plasticity*, 23(3):385–419, 2007. NUMISHEET2005 Conference.

[164] T. Kuwabara, M. Kuroda, V. Tvergaard, and K. Nomura. Use of abrupt strain path change for determining subsequent yield surface: Experimental study with metal sheets. *Acta Materialia*, 48(9):2071–2079, 2000.

[165] T. Kuwabara, Y. Morita, Y. Miyashita, and S. Takahashi. Elastic-plastic behavior of sheet metal subjected to in-plane reverse loading. *Proceedings of the 5th International Symposium on Plasticity and Its Current Applications*, pages 841–844, 1995.

[166] P. Ladeveze and J. Lemaitre. Damage effective stress in quasi-unilateral conditions. *IUTAM Congress Proceedings, Lyngby (Danemark)*, 25, 1984.

[167] H. Lämmer and C. Tsakmakis. Discussion of coupled elastoplasticity and damage constitutive equations for small and finite deformations. *International Journal of Plasticity*, 16(5):495–523, 2000.

[168] P. Larour. Strain rate sensitivity of automotive sheet steels: influence of plastic strain, strain rate, temperature, microstructure, bake hardening and pre-strain. *ISBN 978-3-8322-9149-5, RWTH Aachen University*, 2010.

[169] J. B. Leblond, G. Perrin, and J. Devaux. Bifurcation effects in ductile metals with damage delocalization. *Journal of Applied Mechanics*, 61:236–242, 1994.

[170] E. H. Lee. Elastoplastic deformation at finite strains. *ASME Journal of Applied Mechanics*, 36:1–6, 1969.

[171] J. Lee, I. Kim, and A. Kimura. Application of small punch test to evaluate sigma-phase embrittlement of pressure vessel cladding material. *Journal of Nuclear Science and Technology*, 40:664–671, 2003.

[172] J. S. Lee, J. I. Jang, B. W. Lee, Y. Choi, S. G. Lee, and D. Kwon. An instrumented indentation technique for estimating fracture toughness of ductile materials: A critical indentation energy model based on continuum damage mechanics. *Acta Materialia*, 54:1101–1109, 2006.

[173] M.-G. Lee, D. Kim, C. Kim, M. Wenner, R. Wagoner, and K. Chung. A practical two-surface plasticity model and its application to spring-back prediction. *International Journal of Plasticity*, 23(7):1189–1212, 2007.

[174] J. Lemaitre. Evaluation of dissipation and damage in metals. In *Proceedings of I.C.M., vol. 1, Kyoto, Japan*, 1971.

[175] J. Lemaitre. *A Course on Damage Mechanics*. Springer Verlag, Berlin, 1996.

[176] J. Lemaitre, A. Benallal, and D. Marquis. Lifetime prediction of structures in anisothermal viscoplasticity coupled with damage. *Nuclear Engineering and Design*, 133:345–360, 1992.

[177] J. Lemaitre and R. Desmorat. *Engineering Damage Mechanics*. Springer-Verlag, Berlin, Heidelberg, 2005.

[178] J. Lemaitre, R. Desmorat, and M. Sauzay. Anisotropic damage law of evolution. *European Journal of Mechanics-A/Solids*, 19(2):187–208, 2000.

[179] J. Lemonds and A. Needleman. Finite element analysis of shear localization in rate and temperature dependent solids. *Mechanics of Materials*, 5:339–361, 1986.

[180] K. Levenberg. A method for the solution of certain non-linear problems in least squares. *The Quarterly of Applied Mathematics*, 2(164-168):17–39, 1944.

[181] V. Levkovitch and B. Svendsen. Accurate hardening modeling as basis for the realistic simulation of sheet forming processes with complex strain-path change. In J. M. A. Cesar de Sa, editor, *9th International Conference on Numerical Methods in Industrial Forming Processes (NUMIFORM 2007), Porto, Portugal*, Vol. 2. AIP Conference Proceedings, pages 1331–1336, 2007.

[182] S. Li, E. Hoferlin, A. van Bael, P. van Houtte, and C. Teodosiu. Finite element modeling of plastic anisotropy induced by texture and strain-path change. *International Journal of Plasticity*, 19(5):647–674, 2003.

[183] Y. Li, M. Luo, J. Gerlach, and T. Wierzbicki. Prediction of shear-induced fracture in sheet metal forming. *Journal of Materials Processing Technology*, 210(14):1858–1869, 2010.

[184] Y. Z. Li, R. Hurst, K. Matocha, and P. Cizek. Local approach to determine fracture toughness from small punch test. *Proceedings of 1st International Conference on small punch test and other miniature testing techniques, Ostrava, Czech Republic*, 2010.

[185] W. Lievers, A. Pilkey, and D. Lloyd. The influence of iron content on the bendability of AA6111 sheet. *Materials Science and Engineering: A*, 361(1):312 – 320, 2003.

[186] W. B. Lievers, A. K. Pilkey, and M. J. Worswick. The co-operative role of voids and shear bands in strain localization during bending. *Mechanics of Materials*, 35(7):661–674, 2003.

[187] R. C. Lin, W. Brocks, and J. Betten. On internal dissipation inequalities and finite strain inelastic constitutive laws: Theoretical and numerical comparisons. *International Journal of Plasticity*, 22(10):1825–1857, 2006.

[188] U. S. Lindholm, A. Nagy, G. R. Johnson, and J. M. Hoegfeldt. Large strain, high strain rate testing of copper. *Journal of Engineering Materials and Technology*, 102(4):376, 1980.

[189] T. Linse and G. H˙ Simulation of crack propagation using a gradient-enriched ductile damage model based on dilatational strain. *Engineering Fracture Mechanics*, 95:13–28, 2012.

[190] D. T. Llewellyn and D. J. Hillis. Dual phase steels. *Ironmaking & Steelmaking*, 23(6):471–478, 1996.

[191] Y. Lou and H. Huh. Prediction of ductile fracture for advanced high strength steel with a new criterion: Experiments and simulation. *Journal of Materials Processing Technology*, 213(8):1284–1302, 2013.

[192] Y. Lou, H. Huh, S. Lim, and K. Pack. New ductile fracture criterion for prediction of fracture forming limit diagrams of sheet metals. *International Journal of Solids and Structures*, 49:3605–3615, 2012.

[193] X. Z. Lu and L. C. Chan. Numerical simulation for thermal and RT forming light sheet materials using a new combined model of M-K theory and shear localization criterion. *The International Journal of Advanced Manufacturing Technology*, 83(1):357–363, 2016.

[194] R. Mahnken and E. Stein. Parameter identification for finite deformation elasto-plasticity in principal directions. *Computer Methods in Applied Mechanics and Engineering*, 1997.

[195] L. Malcher and E. N. Mamiya. An improved damage evolution law based on continuum damage mechanics and its dependence on both stress triaxiality and the third invariant. *International Journal of Plasticity*, 59:232–261, 2014.

[196] M. P. Manahan, A. S. Argon, and O. K. Harling. The development of a miniaturized disk bend test for determination of post irradiation mechanical properties. *Journal of Nuclear Materials*, 104:1545–1550, 1981.

[197] X. Mao and H. Takahashi. Development of a further-miniaturized specimen of 3 mm diameter for TEM disk (ϕ 3 mm) small punch tests. *Journal of Nuclear Materials*, 150(1):42–52, 1987.

[198] N. L. Maoût, S. Thuillier, and P. Y. Manach. Aluminum alloy damage evolution for different strain paths-application to hemming process. *Engineering Fracture Mechanics*, 76(9):1202–1214, 2009.

[199] Z. Marciniak. Influence of the sign change of the load on the strain hardening curve of a copper test subject to torsion. *Archiwum Mechaniki Stosowanj*, (13):743–751, 1961.

[200] Z. Marciniak and J. Kołodziejski. Assessment of sheet metal failure sensitivity by method of torsioning the rings. *J. Proc. 7th Biennual Congress of the IDDRG*, pages 61–64, 1972.

[201] Z. Marciniak and K. Kuczyński. Limit strains in the processes of stretch-forming sheet metal. *International Journal of Mechanical Sciences*, 9(9):609–620, 1967.

[202] Z. Marciniak, K. Kuczyński, and T. Pokora. Influence of the plastic properties of a material on the forming limit diagram for sheet metal in tension. *International Journal of Mechanical Sciences*, 15(10):789–800, 1973.

[203] E. B. Marin and P. R. Dawson. On modelling the elasto-viscoplastic response of metals using polycrystal plasticity. *Computer Methods in Applied Mechanics and Engineering*, 165(1-4):23–41, 1998.

[204] D. W. Marquardt. An algorithm for least-squares estimation of nonlinear parameters. *Journal of the Society for Industrial and Applied Mathematics*, 11(2):431–441, 1963.

[205] J. E. Marsden and T. J. R. Hughes. *Mathematical Foundations of Elasticity*. Dover, New York, 1994.

[206] O. Matsumura, Y. Sakuma, and H. Takechi. Enhancement of elongation by retained austenite in intercritical annealed 0.4C-1.5Si-0.8Mn steel. *Transactions of the Iron and Steel Institute of Japan*, 27(7):570–579, 1987.

[207] G. A. Maugin. *The Thermomechanics of Plasticity and Fracture*. Cambridge University Press, Cambridge, 1992.

[208] F. A. McClintock. A criterion of dcutile fracture by the growth of holes. *Journal of Applied Mechanics*, 35:363–371, 1968.

[209] M. E. Mear and J. W. Hutchinson. Influence of yield surface curvature on flow localization in dilatant plasticity. *Mechanics of Materials*, 4(3):395–407, 1985.

[210] A. Menzel, M. Ekh, K. Runesson, and P. Steinmann. A framework for multiplicative elastoplasticity with kinematic hardening coupled to anisotropic damage. *International Journal of Plasticity*, 21(3):397–434, 2005.

[211] M. Merklein and B. M. Forward and reverse simple shear test experiments for material modeling in forming simulations. *Steel Research International, Special Edition: 10th International Conference on Technology of Plasticity, ICTP 2011*, (1):702–707, 2011.

[212] M. H. H. Meuwissen, C. W. J. Oomens, F. P. T. Baaijens, R. Petterson, and J. D. Janssen. Determination of the elasto-plastic properties of aluminium using a mixed numerical-experimental method. *Journal of Materials Processing Technology*, 1998.

[213] M. A. Meyers and K. K. Chawla. *Mechanical Behavior of Materials*. Cambridge University Press, 2009.

[214] C. Miehe. Aspects of the formulation and finite element implementation of large strain isotropic elasticity. *International Journal for Numerical Methods in Engineering*, 37(12):1981–2004, 1994.

[215] C. Miehe. A theory of large-strain isotropic thermoplasticity based on metric transformation tensors. *Archive of Applied Mechanics*, 66(1):45–64, 1995.

[216] C. Miehe, M. Hofacker, L. M. Schänzel, and F. Aldakheel. Phase field modeling of fracture in multi-physics problems. Part II. Coupled brittle-to-ductile failure criteria and crack propagation in thermo-elastic–plastic solids. *Computer Methods in Applied Mechanics and Engineering*, 294:486–522, 2015.

[217] C. Miehe, F. Welschinger, and M. Hofacker. Thermodynamically consistent phase-field models of fracture: Variational principles and multi-field fe implementations. *International Journal for Numerical Methods in Engineering*, 83(10):1273–1311, 2010.

[218] J. Min, L. G. Hector, J. Lin, and J. T. Carter. Analytical method for forming limit diagram prediction with application to a magnesium ZEK100-O alloy. *Journal of Materials Engineering and Performance*, 22(11):3324–3336, 2013.

[219] J. Min, J. Lin, J. Li, and W. Bao. Investigation on hot forming limits of high strength steel 22MnB5. *Computational Materials Science*, 49(2):326–332, 2010.

[220] K. Miyauchi. A proposal of a planar simple shear test in sheet metals. *Scientific Papers of RIKEN*, (78):27–42, 1984.

[221] D. Mohr and S. Henn. Calibration of Stress-triaxiality Dependent Crack Formation Criteria: A New Hybrid Experimental-Numerical Method. *Experimental Mechanics*, 47(6):805–820, 2007.

[222] Z. Mróz. On description of anisotropic work hardening. *Journal of the Mechanics and Physics of Solids*, 15(3):163–&, 1967.

[223] F. Mudry. A local approach to cleavage fracture. *Nuclear Engineering and Design*, 105:65–76, 1987.

[224] K. Nahshon and J. W. Hutchinson. Modification of the Gurson Model for shear failure. *European Journal of Mechanics-A/Solids*, 27(1):1–17, 2008.

[225] K. Nahshon and Z. Xue. A modified Gurson model and its applications to punch-out experiments. *Engineering Fracture Mechanics*, 76:997–1009, 2009.

[226] K. Nakazima, T. Kikuma, and K. Asuka. Study on the formability of steel sheet. Technical Report 264, Yawata Technical Report, 1968.

[227] K. Narasimhan and R. H. Wagoner. Finite element modeling simulation of in-plane forming limit diagrams of sheets containing finite defects. *Metallurgical Transactions A*, 22(11):2655–2665.

[228] A. Needleman and J. R. Rice. Limits to ductility set by plastic flow localization. In Koistinen, P. D. and Wang, N. -M., editor, *Mechanics of Sheet Metal Forming*, Plenum Press, New York, pages 237–268, 1978.

[229] A. Needleman and V. Tvergaard. Dynamic crack growth in a nonlocal progressively cavitating solid. *European Journal of Mechanics-A/Solids*, 17(3):421–438, 1998.

[230] A. Needleman and V. Tvergaard. Numerical modeling of the ductile-brittle transition. *International Journal of Fracture*, 101:73–97, 2000.

[231] E. V. Nesterova, B. Bacroix, and C. Teodosiu. Experimental observation of microstructure evolution under strain-path changes in low-carbon IF steel. *Materials Science and Engineering: A*, 309–310(0):495–499, 2001. Dislocations 2000: An International Conference on the Fundamentals of Plastic Deformation.

[232] K. L. Nielsen and V. Tvergaard. Effect of a shear modified Gurson model on damage development in a FSW tensile specimen. *International Journal of Solids and Structures*, 46:587–601, 2009.

[233] K. L. Nielsen and V. Tvergaard. Ductile shear failure or plug failure of spot welds modelled by modified gurson model. *Engineering Fracture Mechanics*, 77:1031–1047, 2010.

[234] S. D. Norris. A comparison of the disk bend test and the Charpy impact test for fracture property evaluation of power station steels. *International Journal of Pressure Vessels and Piping*, 74:135–144, 1997.

[235] R. W. Ogden. *Non-Linear Elastic Deformations*. Ellis Horwood Limited, 1984.

[236] N. Ohno and D. Okumura. Higher-order stress and grain size effects due to self-energy of geometrically necessary dislocations. *Journal of the Mechanics and Physics of Solids*, 55:1879–1898, 2007.

[237] M. C. Oliveira, J. L. Alves, B. M. Chaparro, and L. F. Menezes. Study on the influence of work-hardening modeling in springback prediction. *International Journal of Plasticity*, 23(3):516–543, 2007.

[238] S. Oliver, T. B. Jones, and G. Fourlaris. Dual phase versus trip strip steels: Microstructural changes as a consequence of quasi-static and dynamic tensile testing. *Materials Characterization*, 58(4):390–400, 2007.

[239] M. Ortiz and J. C. Simo. An analysis of a new class of integration algorithms for elastoplastic constitutive relations. *International Journal for Numerical Methods in Engineering*, 23:353–366, 1986.

[240] J. Oudin, B. Bennani, and P. Picard. Models for microvoid nucleation, growth and coalescence in elastoplasticity, finite element reference modelling. In Ghosh, S.K. and Predeleanu, M., editor, *Material Processing Defects*, Elsevier Science B.V, pages 107—122, 1995.

[241] M. Oyane, T. Sato, K. Okimoto, and S. Shima. Criteria for ductile fracture and their applications. *Journal of Mechanical Working Technology*, 4:65–81, 1980.

[242] W. Panknin. *Der hydraulische Tiefungsversuch und die Ermittlung von Fließkurven*. PhD thesis, 1959.

[243] E. S. Perdahcıoğlu and H. J. M. Geijselaers. Constitutive modeling of two phase materials using the mean field method for homogenization. *International Journal of Material Forming*, 4(2):93–102, 2011.

[244] F. Pierron, S. Avril, and V. T. Tran. Extension of the virtual fields method to elasto-plastic material identification with cyclic loads and kinematic hardening. *International Journal of Solids and Structures*, 2010.

[245] M. P. Pietryga, I. N. Vladimirov, and S. Reese. A finite deformation model for evolving flow anisotropy with distortional hardening including experimental validation. *Mechanics of Materials*, 44(0):163–173, 2012.

[246] G. Pijaudier-Cabot and Z. Bazant. Nonlocal damage theory. *Journal of Engineering Mechanics ASCE*, 113(10):1512–1533, 1987.

[247] F. M. A. Pires, E. A. de Souza Neto, and D. R. J. Owen. On the finite element prediction of damage growth and fracture initiation in finitely deforming ductile materials. *Computer Methods in Applied Mechanics and Engineering*, 193:5223–5256, 2004.

[248] A. Pirondi, N. Bonora, D. Steglich, W. Brocks, and D. Hellmann. Simulation of failure under cyclic plastic loading by damage models. *International Journal of Plasticity*, 22(11):2146–2170, 2006.

[249] J. Plesek, H. P. Feigenbaum, and Y. F. Dafalias. Convexity of yield surface with directional distortional hardening rules. *ASCE Journal of Engineering Mechanics*, 136(4):477–484, 2010.

[250] K. Pöhlandt and A. E. Tekkaya. Torsion testing-plastic-deformation to high strains and strain rates. *Materials Science and Technology*, 1(11):972–977, 1985.

[251] P. Poruks, I. Yakubtsov, and J. D. Boyd. Martensite-ferrite interface strength in a low-carbon bainitic steel. *Scripta Materialia*, 54(1):41–45, 2006.

[252] T. Pottier, F. Toussaint, and P. Vacher. Contribution of heterogeneous strain field measurements and boundary conditions modelling in inverse identification of material parameters. *European Journal of Mechanics-A/Solids*, 30(3):373–382, 2011.

[253] H. L. D. Pugh. Metalworking using fluid pressure. *Annual Reviews of Material Research*, 75:253–290, 1972.

[254] M. Rabahallah, T. Balan, S. Bouvier, B. Bacroix, F. Barlat, K. Chung, and C. Teodosiu. Parameter identification of advanced plastic strain rate potentials and impact on plastic anisotropy prediction. *International Journal of Plasticity*, 25(3):491–512, 2009.

[255] Y. Rabotnov. Creep rupture. In M. Hetenyi and W. Vincenti, editors, *Applied Mechanics Proceedings of the 12th International Congress of Applied Mechanics*, pages 320–342. Springer-Verlag, Berlin, 1968.

[256] E. F. Rauch. Plastic anisotropy of sheet metals determined by simple shear tests. *Materials Science And Engineering: A*, 241(1-2):179–183, 1998.

[257] E. F. Rauch and J. H. Schmitt. Dislocation substructures in mild steel deformed in simple shear. *Materials Science and Engineering: A*, A113:441–448, 1989.

[258] E. F. Rauch and S. Thuillier. Rheological behaviour of mild steel under monotonic loading conditions and cross-loading. *Materials Science and Engineering: A*, A164:255–259, 1993.

[259] J. R. Rice and D. M. Tracey. On the ductile enlargement of voids in triaxial stress field. *Journal of the Mechanics and Physics of solids*, 17:201–217, 1969.

[260] R. O. Ritchie, J. F. Knott, and J. R. Rice. On the tensile relationship between critical tensile stress and fracture toughness in mild steel. *Journal of the Mechanics and Physics of Solids*, 21:395–410, 1973.

[261] M. Rossi and F. Pierron. Identification of plastic constitutive parameters at large deformations from three dimensional displacement fields. *Computational Mechanics*, 49(1):53–71, 2012.

[262] F. Roters, P. Eisenlohr, L. Hantcherli, D. D. Tjahjanto, T. R. Bieler, and D. Raabe. Overview of constitutive laws, kinematics, homogenization and multiscale methods in crystal plasticity finite-element modeling: Theory, experiments, applications. *Acta Materialia*, 58(4):1152–1211, 2010.

[263] K. Saanouni and J. L. Chaboche. Computational damage mechanics: application to metal forming simulation (Chapter 3.06). In S. Idelsohn and E. Oñate and E. Dvorkin, editor, *Comprehensive Structural Integrity. Elsevier Ltd., Amsterdam*, pages 319—374, 2003.

[264] R. Safdarian. Forming limit diagram prediction of tailor welded blank by modified M–K model. *Mechanics Research Communications*, 67:47–57, 2015.

[265] Saje, M. and Pan, J. and Needleman, A. Void nucleation effects on shear localization in porous plastic solids. Technical Report Report NSF-ENG76-16421/7 Brown University, 1980.

[266] J. Sarkar, T. R. G. Kutty, K. T. Conlon, D. S. Wilkinson, J. D. Embury, and D. J. Lloyd. Tensile and bending properties of AA5754 aluminum alloys. *Materials Science and Engineering: A*, 316:52–59, 2001.

[267] M. Schneider, H. Friebe, and K. Galanulis. Validation and optimization of numerical simulations by optical measurements of tools and parts. In *Proceedings of the IDDRG 2008 International Conference*, pages 373–384, 2008.

[268] B. Shashank Dutt, M. Nani Babu, S. Venugopal, G. Sasikala, and A. K. Bhaduri. Effect of test temperature on fracture toughness of modified 9Cr-1Mo steel. *Materials Science and Technology*, 27 (10):1527–1533, 2011.

[269] B. Shi and J. Mosler. On the macroscopic description of yield surface evolution by means of distortional hardening models: application to magnesium. *International Journal of Plasticity*, 44:1–22, 2013.

[270] D. R. Shouler and J. M. Allwood. Design and use of a novel sample design for formability testing in pure shear. *Journal of Materials Processing Technology*, 210(10):1304–1313, 2010.

[271] A. Shterenlikht. *3D CAFE modelling of transitional ductile-brittle fracture in steels*. PhD thesis, University of Sheffield, 2003.

[272] J. C. Simo. Algorithms for static and dynamic multiplicative plasticity that preserve the classical return mapping schemes of the infinitesimal theory. *Computer Methods in Applied Mechanics and Engineering*, 99(1):61–112, 1992.

[273] J. C. Simo and T. J. R. Hughes. *Computational Inelasticity*. Springer, 1998.

[274] J. C. Simo and J. W. Ju. On continuum damage-elastoplasticity at finite strains. *Computational Mechanics*, 5(5):375–400, 1989.

[275] J. C. Simo and C. Miehe. Associative coupled thermoplasticity at finite strains: Formulation, numerical analysis and implementation. *Computer Methods in Applied Mechanics and Engineering*, 98(1):41–104, 1992.

[276] J. C. Simo and R. L. Taylor. Consistent tangent operators for rate-independent elastoplasticity. *Computer Methods in Applied Mechanics and Engineering*, 48(1):101–118, 1985.

[277] A. Simone. *Continuous-Discontinuous Modelling of Failure*. PhD thesis, Technische Universiteit Delft, 2003.

[278] C. Soyarslan. *Modeling Damage for Elastoplasticity*. PhD thesis, Middle East Technical University, 2008.

[279] C. Soyarslan and S. Bargmann. Thermomechanical formulation of ductile damage coupled to nonlinear isotropic hardening and multiplicative viscoplasticity. *Journal of the Mechanics and Physics of Solids*, 91:334–358, 2016.

[280] C. Soyarslan, M. M. Gharbi, and A. E. Tekkaya. A combined experimental-numerical investigation of ductile fracture in bending of a class of ferritic-martensitic steel. *International Journal of Solids and Structures*, 49:1608–1626, 2012.

[281] C. Soyarslan, B. Gülçimen, S. Bargmann, and P. Hähner. Modeling of fracture in small punch tests for small- and large-scale yielding conditions at various temperatures. *International Journal of Mechanical Sciences*, 106:266–285, 2016.

[282] C. Soyarslan, B. Klusemann, and S. Bargmann. A directional modification of the Levkovitch-Svendsen cross-hardening model based on the stress deviator. *Mechanics of Materials*, 86:21–30, 2015.

[283] C. Soyarslan, B. Klusemann, and S. Bargmann. The effect of yield surface curvature change by cross hardening on forming limit diagrams of sheets. *International Journal of Mechanical Sciences*, 117:53–66, 2016.

[284] C. Soyarslan, H. Richter, and S. Bargmann. Lode parameter dependence and quasi-unilateral effects in continuum damage mechanics: Models and applications in metal forming. *Key Engineering Materials*, 651-653(10):187–192, 2015.

[285] C. Soyarslan, H. Richter, and S. Bargmann. Variants of Lemaitre's damage model and their use in formability prediction of metallic materials . *Mechanics of Materials*, 92:58–79, 2016.

[286] C. Soyarslan and A. E. Tekkaya. Prevention of internal cracks in forward extrusion by means of counter pressure: a numerical treatise. *Steel Research International*, 80:671–679, 2009.

[287] C. Soyarslan and A. E. Tekkaya. Finite deformation plasticity coupled with isotropic damage: Formulation in principal axes and applications. *Finite Elements in Analysis and Design*, 46:668–683, 2010.

[288] C. Soyarslan, A. E. Tekkaya, and U. Akyuz. Application of continuum damage mechanics in discontinuous crack formation: Forward extrusion chevron predictions. *Journal of Applied Mathematics and Mechanics / Zeitschrift für Angewandte Mathematik und Mechanik*, 88/6:436–453, 2008.

[289] C. Soyarslan, I. C. Türtük, B. Deliktas, and S. Bargmann. A thermomechanically consistent constitutive theory for modeling micro-void and/or micro-crack driven failure in metals at finite strains. *International Journal of Applied Mechanics*, 0(0):1650009, 0.

[290] D. Steglich, J. Bohlen, X. Tian, S. Riekehr, N. Kashaev, S. Bargmann, D. Letzig, K. U. Kainer, and N. Huber. Crashworthiness of Magnesium Sheet Structures. In Stone, I. and McKay, B. and Fan, Z. Y., editor, *Light Metals Technology 2013*, volume 765 of

Materials Science Forum, pages 590–594, 2013. 6th International Light Metals Technology Conference (LMT 2013), Brunel University, BCAST, Old Windsor, England, July 24-26, 2013.

[291] P. Steinmann, C. Miehe, and E. Stein. Comparison of different finite deformation inelastic damage models within multiplicative elastoplasticity for ductile materials. *Computational Mechanics*, 13(6):458–474, 1994.

[292] S. Stören and J. Rice. Localized necking in thin sheets. *Journal of the Mechanics and Physics of Solids*, 23(6):421–441, 1975.

[293] T. Tabata, H. Fujita, M.-A. Hiraoka, and K. Onishi. Dislocation behaviour and the formation of persistent slip bands in fatigued copper single crystals observed by high-voltage electron microscopy. *Philosophical Magazine A*, 47(6):841–857, 1983.

[294] Z. Tan, C. Magnusson, and B. Persson. The Bauschinger effect in compression-tension of sheet metals. *Materials Science and Engineering: A*, 183(1-2):31–38, 1994.

[295] C. Tasan. *Micro-mechanical Characterization of Ductile Damage in Sheet Metal*. PhD thesis, Eindhoven University of Technology (TU/e), 2010.

[296] G. I. Taylor and H. Quinney. The latent energy remaining in a metal after cold working. *Proceedings of the Royal Society of London*, 143(849):307–326, 1934.

[297] A. E. Tekkaya, K. Pöhlandt, and K. Lange. Determining stress-strain curves of sheet metal in the plane torsion test. *CIRP Annals-Manufacturing Technology*, 31(1):171–174, 1982.

[298] C. Teodosiu and Z. Hu. Evolution of the intragranular microstructure at moderate and large strains: modelling and computational significance. In S. Shen and P. Dawson, editors, *Simulation of Materials Processing: Theory, Methods and Applications, Balkema, Rotterdam*, pages 173–182, 1995.

[299] S. Thuillier and P. Y. Manach. Comparison of the work-hardening of metallic sheets using tensile and shear strain paths. *International Journal of Plasticity*, 25(5):733–751, 2009.

[300] Thyssen Krupp Materials International. Material data sheet-alloy steel tubes for high-temperature service. Technical Report Material data sheet P91/T91 10/2011, 2011.

[301] N. Triantafyllidis, A. Needleman, and V. Tvergaard. On the development of shear bands in pure bending. *International Journal of Solids and Structures*, 18(2):121–138, 1982.

[302] K. Turba, B. Gülçimen, Y. Z. Li, D. Blagoeva, P. Hähner, and R. C. Hurst. Introduction of a new notched specimen geometry to determine fracture properties by small punch testing. *Engineering Fracture Mechanics*, 78(16):2826–2833, 2011.

[303] V. Tvergaard. Effect of kinematic hardening on localized necking in biaxially stretched sheets. *International Journal of Mechanical Sciences*, 20(9):651–658, 1978.

[304] V. Tvergaard. Influence of voids on shear band instabilities under plane strain conditions. *International Journal of Fracture*, 17:389–407, 1981.

[305] V. Tvergaard. Influence of void nucleation on ductile shear fracture at a free surface. *Journal of the Mechanics and Physics of Solids*, 30:399–425, 1982.

[306] V. Tvergaard. On localization in ductile materials containing spherical voids. *International Journal of Fracture*, 18:237–252, 1982.

[307] V. Tvergaard. Ductile shear fracture at the surface of a bent specimen. *Mechanics of Materials*, 6(1):53–69, 1987.

[308] V. Tvergaard and A. Needleman. Analysis of the cup-cone fracture in a round tensile bar. *Acta Metallurgica*, 32:157–169, 1984.

[309] V. Tvergaard and A. Needleman. Effects of nonlocal damage in porous plastic solids. *International Journal of Solids and Structures*, 32:1063–1077, 1995.

[310] A. Uenishi and C. Teodosiu. Constitutive modelling of the high strain rate behaviour of interstitial-free steel. *International Journal of Plasticity*, 20(4–5):915–936, 2004.

[311] J. Unger, M. Stiemer, A. Brosius, B. Svendsen, H. Blum, and M. Kleiner. Inverse error propagation and model identification for coupled dynamic problems with application to electromagnetic metal forming. *International Journal of Solids and Structures*, 45(2):442–459, 2008.

[312] H. S. Valberg. *Applied Metal Forming: Including FEM Analysis*. Cambridge University Press, Cambridge, 2010.

[313] A. H. van den Boogaard and M. van Riel. Non-proportional deformation paths for sheet metal: experiments and models. In Hora, P., editor, *3rd Forming Technology Forum Zurich 2009 - Constitutive Modeling of Kinematic and Anisotropic Hardening Effects for Ductile Materials*, Institute of Virtual Manufacturing, ETH Zurich, pages 57–62, 2009.

[314] M. van Riel. *Strain path dependency in sheet metal – experiments and models*. PhD thesis, Twente University, 2009.

[315] M. van Riel and A. H. van den Boogaard. Stress-strain responsesfor continuous orthogonal strain path changes with increasing sharpness. *Scripta Materialia*, 57(5):381–384, 2007.

[316] M. Čanadija and J. Brnić. Associative coupled thermoplasticity at finite strain with temperature-dependent material parameters. *International Journal of Plasticity*, 20(10):1851–1874, 2004.

[317] H. Vegter and A. H. van den Boogaard. A plane stress yield function for anisotropic sheet material by interpolation of biaxial stress states. *International Journal of Plasticity*, 22(3):557–580, 2006.

[318] K. Y. Volokh. Nonlinear elasticity for modeling fracture of isotropic brittle solids. *ASME. Journal of Applied Mechanics*, 71(1):141–143, 2004.

[319] K. Y. Volokh. Hyperelasticity with softening for modeling materials failure. *Journal of the Mechanics and Physics of Solids*, 55(10):2237–2264, 2007.

[320] K. Y. Volokh. Non-linear thermoelasticity with energy limiters. *International Journal of Non-Linear Mechanics*, 76:169–175, 2015.

[321] W. von Lode. Versuche über den Einfluß der mittleren Hauptspannug auf die Fließgrenze. *Zeitschrift für angewandte Mathematik und Mechanik*, 5(2):142–144, 1925.

[322] R. H. Wagoner and J. L. Chenot. *Metal Forming Analysis*. Cambridge University Press, Cambridge, 2001.

[323] R. H. Wagoner, H. Lim, and M.-G. Lee. Advanced issues in springback. *International Journal of Plasticity*, 45:3–20, 2013.

[324] J. Wang, V. Levkovitch, F. Reusch, B. Svendsen, J. Huetink, and M. van Riel. On the modeling of hardening in metals during non-proportional loading. *International Journal of Plasticity*, 24(6):1039–1070, 2008.

[325] W. Wang and X. Wei. The effect of martensite volume and distribution on shear fracture propogation of 600-1000 mpa dual phase sheet steels in the process of deep drawing. *international Journal of Mechanical Sciences*, 67:100–107, 2013.

[326] W. M. Wang, L. J. Sluys, and R. de Borst. Viscoplasticity for instabilities due to strain softening and strain-rate softening. *International Journal for Numerical Methods in Engineering*, 40(20):3839–3864, 1997.

[327] G. Wassermann. *Untersuchungen an einer Eisen-Nickel-Legierung über die Verformbarkeit während der γ-α-Umwandlung: (Mitteilg aus d. Zentrallaboratorium d. Wernerwerks d. Firma Siemens & Halske, A.-G.)*. Verl. Stahleisen, 1937.

[328] G. Weber and L. Anand. Finite deformation constitutive equations and a time integration procedure for isotropic, hyperelastic-viscoplastic solids. *Computer Methods in Applied Mechanics and Engineering*, 79(2):173–202, 1990.

[329] M. Widmark, A. Melander, and F. Meurling. Low cycle constant amplitude fully reversed strain controlled testing of low carbon and stainless sheet steels for simulation of straightening operations. *International Journal of Fatigue*, 22(4):307–317, 2000.

[330] H. H. Wisselink and J. Huetink. Application of nonlocal damage models to sheet forming applications. In Koistinen, P. D. and Wang, N. -M., editor, *COMPLAS 2007, IX International Conference on Computational Plasticity, Barcelona*, 2007.

[331] H. H. Wisselink and J. Huetink. Prediction of the bendability of sheet metals using nonlocal damage models. *Materials Innovation Institute*, 1:217–224, 2008.

[332] J. Witulski, M. Trompeter, and A. E. Tekkaya. Coated polymers for rapid tooling of deep drawing tools. *Proc. 2nd International Conference Process Machine Interactions, 10.-11.06.2010, Vancouver, BC (Canada)*, 57(5):381–384, 2010.

[333] P. Wriggers, C. Miehe, M. Kleiber, and J. C. Simo. On the coupled thermomechanical treatment of necking problems via finite element methods. *International Journal for Numerical Methods in Engineering*, 33(4):869–883, 1992.

[334] L. Xia and C. Fong Shih. A computational approach to ductile crack growth under large scale yielding conditions. *Journal of the Mechanics and Physics of Solids*, 43(3):389–413, 1995.

[335] L. Xia and C. Fong Shih. Ductile crack growth-I. A numerical study using computational cells with microstructurally-based length scales. *Journal of the Mechanics and Physics of Solids*, 43:233–259, 1995.

[336] L. Xia and C. Fong Shih. Ductile crack growth-III. Transition to cleavage fracture incorporating statistics. *Journal of the Mechanics and Physics of Solids*, 44(4):603–639, 1996.

[337] L. Xia and C. Fong Shih. A fracture model applied to the ductile/brittle regime. *Journal de Physique IV*, 6:363–372, 1996.

[338] L. Xue. Constitutive modeling of void shearing effect in ductile fracture of porous materials. *Engineering Fracture Mechanics*, 75(11):3343–3366, 2008. Local Approach to Fracture (1986-2006): Selected papers from the 9th European Mechanics of Materials Conference.

[339] L. Xue and T. Wierzbicki. Ductile fracture initiation and propagation modeling using damage plasticity theory. *Engineering Fracture Mechanics*, 75:3276–3293, 2008.

[340] H. Yamamoto. Conditions for shear localization in the ductile fracture of void-containing materials. *International Journal of Fracture*, 14(4):347–365, 1978.

[341] Q. Yin, A. Brosius, and A. E. Tekkaya. Modified plane torsion tests for sheet metal characterization. *Steel Research International, Special Edition: 10th International Conference on Technology of Plasticity, ICTP 2011*, (1):696–701, 2011.

[342] Q. Yin, C. Soyarslan, A. Güner, A. Brosius, and A. E. Tekkaya. A cyclic twin bridge shear test for the identification of kinematic hardening parameters. *International Journal of Mechanical Sciences*, 59(1):31–43, 2012.

[343] Q. Yin, C. Soyarslan, K. Isik, and A. E. Tekkaya. A grooved in-plane torsion test for the investigation of shear fracture in sheet materials. *International Journal of Solids and Structures*, 66:121–132, 2015.

[344] Q. Yin, B. Zillmann, S. Suttner, G. Gerstein, M. Biasutti, A. E. Tekkaya, M. F. X. Wagner, M. Merklein, M. Schaper, T. Halle, and A. Brosius. An experimental and numerical investigation of different shear test configurations for sheet metal characterization. *International Journal of Solids and Structures*, 51:1066–1074, 2014.

[345] L. Yingzhi. New approach to determine fracture toughness from small punch test, Concept Report, August 2010. Technical report, 2010.

[346] J.-W. Yoon, F. Barlat, R. E. Dick, K. Chung, and T. J. Kang. Plane stress yield function for aluminum alloy sheets-Part II: FE formulation and its implementation . *International Journal of Plasticity*, 20(3):495–522, 2004. Owen Richmond Memorial Special Issue.

[347] F. Yoshida and T. Uemori. A model of large-strain cyclic plasticity and its application to springback simulation. *International Journal of Mechanical Sciences*, 45(10):1687–1702, 2003.

[348] F. Yoshida, T. Uemori, and K. Fujiwara. Elastic-plastic behavior of steel sheets under in-plane cyclic tension-compression at large strain. *International Journal of Plasticity*, 18(5-6):633–659, 2002.

[349] F. Yoshida, M. Urabe, and V. V. Toropov. Identification of material parameters in constitutive model for sheet metals from cyclic bending tests. *International Journal of Mechanical Sciences*, 40(2-3):237–249, 1998.

[350] Z. M. Yue, C. Soyarslan, H. Badreddine, K. Saanouni, and A. E. Tekkaya. Inverse identification of CDM model parameters for DP1000 steel sheets using a hybrid experimental-numerical methodology spanning various stress triaxiality ratios. *Key Engineering Materials*, 554-557:2103–2110, 2013.

[351] R. Zaera and J. Fernandez Saez. An implicit consistent algorithm for the integration of thermoviscoplastic constitutive equations in adiabatic conditions and finite deformations. *International Journal of Solids and Structures*, 43 (6):1594–1612, 2006.

[352] H. M. Zbib and E. C. Aifantis. A gradient-dependent flow theory of plasticity: application to metal and solid instabilities. *Applied Mechanics Reviews*, 42:S295–S304, 1989.

[353] C. Zhang, L. Leotoing, D. Guines, and E. Ragneau. Theoretical and numerical study of strain rate sensitivity on formability of sheet metal. In *NUMISHEET 2008*, pages 1–5, 2008.

[354] C. Zhang, L. Leotoing, D. Guines, and E. Ragneau. Theoretical and numerical study of strain rate influence on AA5083 formability. *Journal of Materials Processing Technology*, 209(8):3849–3858, 2009.

[355] A. D. Zidan and J. Brookfield. A technique for the determination of post-yield material properties from the small punch test. *The Journal of Strain Analysis for Engineering Design*, 38(4):367–376, 2003.

[356] H. Ziegler. A modification of Prager's hardening rule. *Quarterly of Applied Mathematics*, (17):55–65, 1959.